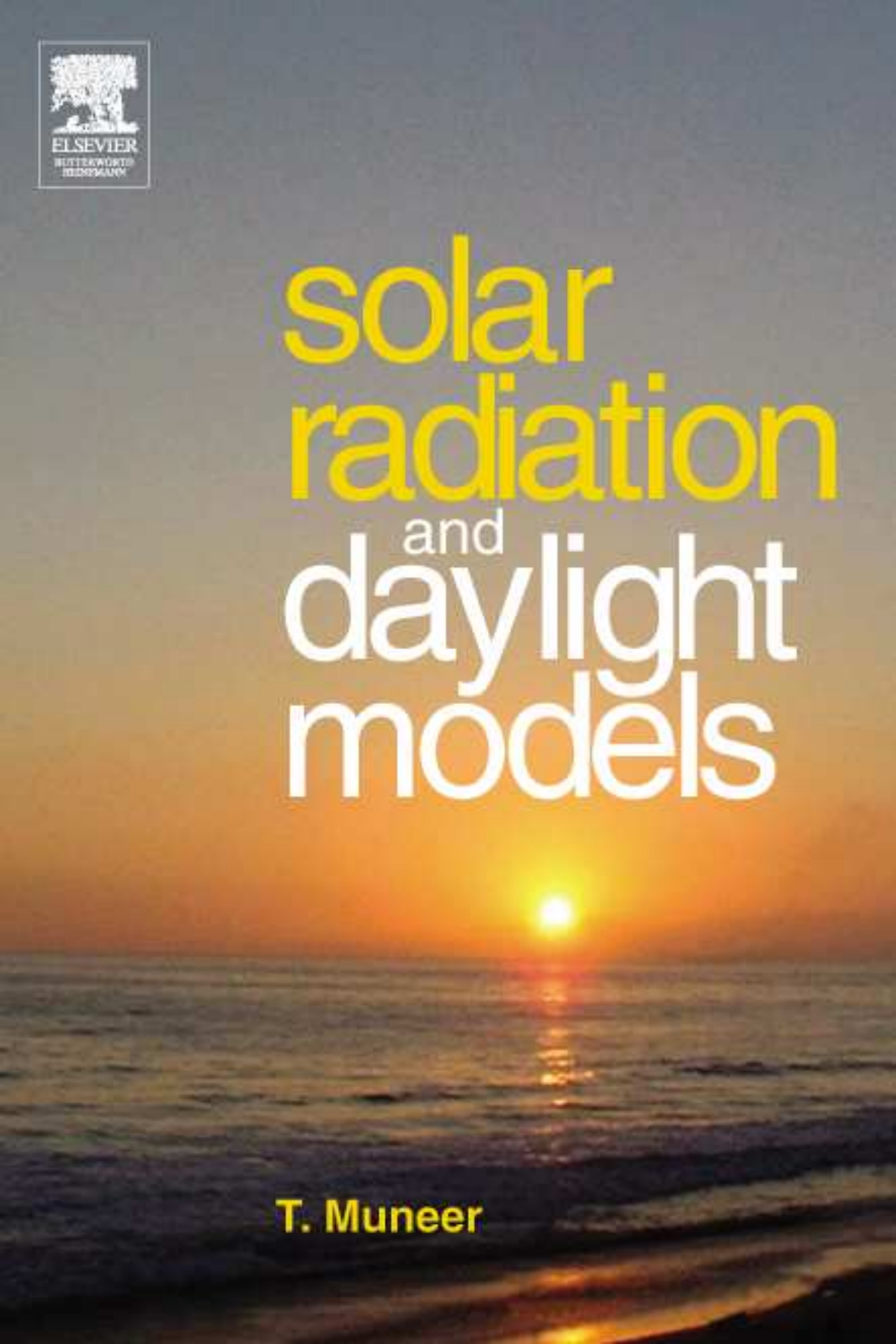
ELSEVIER
solar
radiation
and
daylight
models
T. Muneer

Solar Radiation and Daylight Models

Solar Radiation and Daylight Models

(with software available from companion web site)

T. Muneer
Napier University, Edinburgh

with a chapter on Solar Spectral Radiation
by C. Gueymard, Solar Consulting Services, Denver, Colorado

and

H. Kambezidis, National Observatory of Athens, Athens

ELSEVIER
BUTTERWORTH
HEINEMANN

AMSTERDAM • BOSTON • HEIDELBERG • LONDON • NEW YORK • OXFORD
PARIS • SAN DIEGO • SAN FRANCISCO • SINGAPORE • SYDNEY • TOKYO

Elsevier Butterworth-Heinemann
Linacre House, Jordan Hill, Oxford OX2 8DP
200 Wheeler Road, Burlington, MA 01803

First published 1997
Second edition 2004

British Library Cataloguing in Publication Data
A catalogue record for this book is available from the British Library

Library of Congress Cataloguing in Publication Data
A catalogue record for this book is available from the Library of Congress

ISBN 0 7506 5974 2

Typeset by Charon Tec Pvt. Ltd, Chennai, India
Printed and bound in Great Britain

For my parents

Low in the earth
I lived in the realms of ore and stone;
and then I smiled in many-tinted flowers;
Then roving with the wild and wandering hours,
Over earth and air and ocean's zone,
In a new birth,
I dived and flew,
And crept and ran,
And all the secret of my essence drew
Within a form that brought them all to view –
And then my goal,
Beyond the clouds, beyond the sky,
In angel form; and then away
Beyond the bounds of night and day*.

From *Masnavi-ye-Manavi (Spiritual Couplets)*
by Jalaluddin Rumi (1207–73), Persian mystical poet.

*Metaphorically, the sun is a 'whirling dervish'. The sect of the whirling dervishes was founded by Rumi's followers.

CONTENTS

FOREWORD

During the last decade there has been much research into solar radiation and daylighting in relation to environmental design. New data have been collected – particularly though the CIE/WMO Daylight Measurement Programme and its related projects – and new empirical models have been developed. Dr Muneer has been active in both aspects of the work.

Many numerical techniques now exist for calculating the distribution of radiation on and within buildings. This gives the designer a considerable predictive power, but it is at the cost of maintaining knowledge of a large and changing literature. Published algorithms vary in scope, accuracy and length; in some cases several alternative procedures are available for estimating the same physical quantity.

The value of this book is that an expert in the subject has made a personal selection of applicable formulae, and presented them in a comprehensive and consistent format, both on paper and in the form of computer programs. Books such as this are indispensable references for the research worker and for the practising engineer.

Peter Tregenza
University of Sheffield

PREFACE TO THE FIRST EDITION

The aim of this work is to provide both a reference book and text on solar radiation and daylight models. The book grew out of author's past 30 years of first hand experience of dealing with the relevant data from four continents: India, where the author grew up; USA, where he got his advanced schooling; Africa and UK where he taught and researched. Some of that work has been published in a series of technical articles. A concurrent and interesting activity in which the author is involved is the production of the new Chartered Institution of Building Services Engineers' *Guide for Weather and Solar Data*. This work provided an opportunity to liaise with colleagues from both sides of the Atlantic. The author was also fortunate to be awarded the Royal Academy of Engineering's fellowship to visit Japan on an extended study leave. Through this opportunity the author was able to examine the abundance of solar irradiance and illuminance data now being collected in the Far East. The models presented herein are applicable for a very wide range of locations worldwide, in particular though for the European, American, Indian and other locations in the Pacific Rim.

The text also emphasises the importance of good structure in the presentation of the computational algorithms. The chapters and sections have been divided in a manner which represents not only a chronological development of the knowledge base, but also the algorithmic flow from coarse to a more refined basis of calculation.

FORTRAN is one of the most widely used programming languages in engineering applications. A special feature of this text is that it includes 43 programs, provided in the *.For and *.Exe formats. The former format enables the user to make any changes such as providing data via prepared electronic files or to embed these routines in their own simulation or other programs. For example, the earlier work performed by the author involved liaison with the developers of ESP and SERI-RES building energy simulation packages to incorporate some of the enclosed solar radiation routines. The *.Exe files are for users who may not have access to FORTRAN compilers. These files may be run directly from the DOS or Windows XP.

The enclosed suite of FORTRAN programs, available from companion web site, were designed and written by the author, based on several years of his research and consultancy experience. The programs cover almost all aspects of solar radiation and daylight related computations. All programs included herein are introduced via examples and the readers are encouraged to try them out as they progress through the book. Exercises as well as project work are additionally provided to enable further practice on the routines. Towards this end electronic files (data bases) with solar and other data are also available from companion web site.

The following program copying policy is to be maintained. Copies are limited to a one person/one machine basis. Backup copies may be kept by each individual reader as required. However, further distribution of the programs constitutes a violation of the copy

agreement and hence is illegal. Although prepared with great care and subject to rigorous quality control checks, neither the author nor the publisher warrant the performance or the results that may be obtained by using the enclosed suite of computer programs. Accordingly, the accompanying programs are licensed on an 'as-is' basis. Their performance or fitness for any particular purpose is assumed by the purchaser or user of this book.

The author welcomes suggestions for additions or improvements.

PREFACE TO THE SECOND EDITION

Rapid sale of the first edition in a relatively short time plus the need to update information for an area of significant activity has dictated the need for the second edition of this book. Of late, the rapid deployment of solar photovoltaic technology across the globe has also demanded a need for the estimation of the local availability of the solar energy resource. In this respect the user will find that a considerable amount of new information, along with computational tools has been added in this edition.

New material and, in most cases, resulting computer programs on the following topics has been provided:

(a) Sun-path diagrams for abbreviated analysis.
(b) New data files on measured data sets of irradiance and illuminance.
(c) Distance between any two locations (solar radiation measurement site and location of its utilisation).
(d) Characterisation of sky clarity indices and solar climate for any given location.
(e) Corrections for sky-diffuse irradiance measurements using a shade-ring device.
(f) Quality control of measured solar radiation and daylight data including outlier analysis.
(g) Cloud radiation model.
(h) Page radiation model (developed by Emeritus Professor John Page).
(i) An extensive section on various forms of turbidity and their inter-relationships.
(j) Newer generation of turbidity-based radiation models.
(k) The European clear-sky solar radiation model (developed by Emeritus Professor John Page).
(l) Procedures for obtaining sunshine data from cloud cover information and vice versa.
(m) Frequency of occurrence of diffuse and global illuminance.
(n) Zenith luminance models.
(o) New all-sky CIE standard for sky luminance distribution.
(p) Spectral radiation.
(q) Detailed measured data sets of solar radiation and other meteorological parameters.
(r) Web sites that provide solar radiation and daylight data and other related information.

In response to a demand from readers and reviewers of this book a section on estimation of clear-sky solar irradiance for any part of the globe has been added.

Within the past 5 years there has been an acceleration of activity in the exploitation of solar energy and this has primarily resulted from protection of environment pressures. The Kyoto protocol for reduction of carbon dioxide has been an important instrument in this respect. Subsidies offered for the use of solar water heating and building integrated photovoltaic installations (BIPV technology) within the European Union countries have resulted in a rapid take-off of these and related technologies.

Another contributing factor that will eventually lead to the use of solar power within the transport sector is the spiralling monetary and environment costs associated with the current use of fossil fuels. With the rapid decline in the oil reserves within the Gulf of Mexico basin, Iraq has become the linchpin in the US strategy to secure cheap oil. Between Saudi Arabia and Iraq, with their respective proven oil reserves of 262 and 112 billion barrels, a staggering 40% of world's oil reserves is shared. With the US invasion of Iraq it appears that a new phase of 'Energy wars' has started that may indeed spill over to other Opec countries. The repercussions of such actions and the fact that cheaper oil resulting from the 'capture' of oil reserves will lead to a faster consumption may indeed herald the true age of solar energy. In this respect world political leaders would be well advised to promote renewable energy technologies. That is the only and truly sustainable action for the abatement of the effects of an increase in atmospheric greenhouse gas loading.

ACKNOWLEDGEMENTS

The author is indebted to the following individuals for their support: Z. Akber, W. A1-Naser, R. Angus, M. Asif, S. Baxter, K. Butcher, R. Claywell, F. Fairooz, S. Farhatullah, J. Fulwood, M. Gul, M. Gulam, B. Han, P. Haves, M. Holmes, A. Hussain, C. Kaldis, D. Kinghorn, Y. Koga, J. Kubie, A. Kudish, J. Lebrun, G. Levermore, P. Littlefair, G. Lopez, K. MacGregor, J. Mardaljevic, H. Nakamura, S. Natrajan, W. Platzer, G. Saluja, S. Samad, P. Tregenza, A. Wagner, G. Weir, A. Wright, B. Yallop, A. Young and X. Zhang.

The present text is the culmination of research undertaken by the author over the past two decades. Many organisations have either sponsored or actively supported author's scholarly programme of work, noteworthy among them are: Scottish Education Department; Robert Gordon University; General Electric plc; University College, Oxford; The Leverhulme Trust; Université de Liège, Belgium; The Royal Academy of Engineering, London; The Chartered Institution of Building Services Engineers, London; and The British Council through its offices in Germany and Greece. Their contributions are gratefully acknowledged.

The help extended by the publishers Neil Warnock-Smith, Alex Hollingworth and Sarah Hunt is particularly appreciated. The author is grateful to George Pringle and Steve Paterson for their assistance in producing the diagrams for this book. Mr and Mrs Samad of Manhattan Beach, California spent many evenings with the author with the view to capture 'that ideal snapshot' of sunset. That picture was used for the cover of this book. The author is grateful for the Samads for their hospitality. Above all the author would like to extend special thanks to his family for being extremely supportive throughout.

ELECTRONIC FILES AVAILABLE FROM THIS BOOK'S WEB SITE

A number of FORTRAN programs (.For), directly executable (.Exe) and other files that provide measured irradiance and illuminance data sets are available in this book's web site. The url is: www.bh.com/companions/0750659742/

The programs enable the user to undertake all manner of solar radiation and daylight related computations. Most of the programs accept the required input information from keyboard. However, a few programs require data files, samples of which are once again available from the above web site (see table below). The programs do not perform quality control checks on the user's input. As such it is important that all the requisite data are provided with care. Note that FORTRAN differentiates between real and integer numbers. Also important is the formatting of each file as in some cases the program accepts fixed-format data. This is particularly the case for all DAT, PRN and TXT files. Hence during the preparation of data files these sensitivities have to be borne in mind. The reader is advised that they ought to carefully examine the accompanying sample data files before they venture to incorporate their own data files.

Although prepared with great care and subject to rigorous quality control checks, neither the author nor the publisher warrants the performance or the results that may be obtained by using the enclosed suite of computer spreadsheets or programs. Accordingly, the accompanying programs are licensed on an 'as-is' basis. The purchaser or user of this book assumes their performance or fitness for any particular purpose.

Program name (.For extension)	Required input file	Output file produced
Prog3-2a	In3-2a.Csv	Out3-2a.Dat
Prog3-2b	In3-2.Prn	Out3-2b.Dat
Prog3-2c	In3-2.Prn	Out3-2c.Dat
Prog3-2d	In3-2d.Csv	Out3-2d.Dat
Prog3-2e	In3-2.Prn	Out3-2e.Dat
Prog3-2f	In3-2.Prn	Out3-2f.Dat
Prog3-5	In3-5.Csv	
Prog3-9	File1-1.Csv	Out3-9.Dat
Prog4-4	In4-4.Csv	Out4-4.Dat
Prog4-5	In4-4.Csv	Out4-5.Dat
Prog4-7a	In4-7a.Csv	Out4-7a.Dat
Prog4-7b	In4-7b.Txt	Out4-7b.Dat, Outlier.Dat
Prog4-7c	In4-7c.Dat	In4-7d.Dat
Prog4-7d	In4-7d.Dat	Out4-7d.Dat
Prog4-7e	In4-7e.Csv	Out4-7e.Dat
Prog4-8	Lebaron.Prn	

LIST OF FILES AVAILABLE FROM THIS BOOK'S WEB SITE

Computer programs

Prog1-1.For	Day number of the year for a given date
Prog1-2.For	Julian day number and day of the week for a given date
Prog1-3.For	Low precision algorithm for EOT and DEC
Prog1-4.For	Medium precision algorithm for EOT
Prog1-5.For	Medium precision algorithm for DEC
Prog1-6.For	High precision algorithm for EOT, DEC and solar geometry
Prog1-7.For	Sunrise, sunset and twilight times
Prog1-8.For	Distance between two locations
Prog2-1.For	Monthly-averaged horizontal global, diffuse and beam irradiation
Prog2-2.For	Daily horizontal global, diffuse and beam irradiation
Prog2-3.For	Monthly-averaged slope irradiation
Prog2-4.For	Daily slope irradiation
Prog3-1.For	Monthly-averaged hourly horizontal global, diffuse and beam irradiation
Prog3-2a.For	Hourly horizontal global and diffuse irradiation using MRM
Prog3-2b.For	Hourly horizontal global and diffuse irradiation using CRM
Prog3-2c.For	Hourly horizontal global and diffuse irradiation using PRM
Prog3-2d.For	Hourly horizontal global and diffuse irradiation using Yang's model
Prog3-2e.For	Hourly sunshine data generation from cloud information
Prog3-2f.For	Hourly cloud data generation from sunshine information
Prog3-3.For	Hourly diffuse fraction of horizontal global irradiation
Prog3-4a.For	Horizontal global and diffuse daylight illuminance, Perez et al. (1990) models
Prog3-4b.For	Horizontal and slope global, diffuse daylight illuminance and zenith luminance, Muneer–Kinghorn models
Prog3-5.For	Daylight factors for CIE overcast sky
Prog3-6.For	Frequency distribution of clearness index, US locations
Prog3-7.For	Frequency distribution of clearness index, tropical locations
Prog3-8.For	Frequency distribution of clearness index, UK and north European locations
Prog3-9.For	Frequency distribution of daylight illuminance, Tregenza (1986) model
Prog4-1.For	Solar climate indices
Prog4-2.For	Slope global, diffuse and beam irradiance, output for seven models

Prog4-3.For	Slope global, diffuse and beam illuminance, Perez et al. model
Prog4-4.For	Sky luminance distributions, relative coordinates
Prog4-5.For	Sky luminance distributions, absolute coordinates
Prog4-6a.For	Incidence angle of luminance from a given sky patch
Prog4-6b.For	Illuminance transmission functions for multiple glazed windows
Prog4-7a.For	Quality control of solar radiation data, turbidity analysis
Prog4-7b.For	Quality control of solar radiation data, outlier analysis
Prog4-7c.For	Time-series check for hourly solar radiation data
Prog4-7d.For	Completing time-series for hourly solar radiation data
Prog4-7e.For	Time-series check for 5 min data
Prog4-8.For	Shade ring correction factors to be applied to measured sky-diffuse irradiance
Prog7-1.For	Psychrometric properties, given dry- and wet-bulb temperatures
Prog7-2.For	Psychrometric properties, given dry-bulb temperature and relative humidity
Prog7-3.For	Conversion from daily to hourly temperatures

Input files

File1-1.Csv	DEC and EOT (must reside with Prog3-9.For)
In3-2.Csv	Sample input file for Prog3-2.For (must reside with Prog3-2.For)
In3-2d.Csv	Clear-sky hourly (LAT) measured data for Madras (Chennai), India
In3-2.Prn	Synoptic and solar radiation data for Bracknell, England (17 August 1990)
In3-5.Csv	Data file required for executing Prog3-5.For (must reside with Prog3-5.For)
In4-4.Csv	Data file required for executing Prog4-4.For and Prog4-5.For
In4-7a.Csv	Five-minute averaged solar radiation data for Bahrain, Arabian Gulf. Prog4-7a.For refers
In4-7b.Txt	k-kt data required for Prog4-7b.For
In4-7c.Dat	Checks for continuity of hourly data time-series. Prog4-7c.For refers
In4-7d.Dat	Output from Prog4-7c.For and input file required for Prog4-7d.For
In4-7e.Csv	Checks for continuity of 5 min time-series. Prog4-7e.For refers

Data files

File1-1.Xls	EOT and solar declination data for a complete leap year cycle
File2-1a.Csv	Mean-monthly meteorological data for the UK, January–June
File2-1b.Csv	Mean-monthly meteorological data for the UK, July–December
File3-1.Csv	Five-minute averaged measured solar data for Edinburgh, April 1993
File4-1.xls	Horizontal and slope solar radiation data for Bracknell, England
File4-2.xls	Hourly-averaged horizontal diffuse, global and beam-normal solar radiation data for Bracknell, England
File7-1.Csv	Dry-bulb temperature and humidity ratio data for psychrometric chart

LIST OF FIGURES

LIST OF TABLES

INTRODUCTION

Solar radiation and daylight are essential to life on earth. Solar radiation affects the earth's weather processes which determine the natural environment. Its presence at the earth's surface is necessary for the provision of food for mankind. Thus it is important to be able to understand the physics of solar radiation and daylight, and in particular to determine the amount of energy intercepted by the earth's surface. The understanding of the climatological study of radiation is comparatively new. Until 1960 there were only three stations in north-west Europe with irradiation records exceeding a 25 year period. In the UK it was only in the 1950s that Kipp solarimeters were installed by the Meteorological Office. Similarly, daylight was not recorded on a continuous basis and up to 1970 only seven sites across the UK measured horizontal illuminance. Furthermore, until 1992 there were no records of vertical illuminance for any location in the UK north of Watford (51.7°N) leaving the majority of the country without these measurements. At present vertical illuminance measurements exist for a short period and for only four sites across the country – Watford, Manchester, Sheffield and Edinburgh. These stations were operated in response to the call made by Commission Internationale de l'Éclairage (CIE) under which 1991 was declared the International Daylight Measurement Year. Table A1 (Appendix A) contains a list of daylight measurement stations worldwide.

Daylight is necessary for the production of all our agricultural produce and sustains the food chain through the process of photosynthesis. Photosynthesis is a biological phenomenon which describes the ability of plant life to convert light into chemical energy for growth. Daylight is one of the most important parts of the solar spectrum; it is the band of the sun's energy that we associate with day and night and has been the centre of much attention in recent years for a variety of reasons.

The initial research carried out by Ångström and others was concerned with the relationship between irradiation and the sunshine duration. Since then research in this field has come a long way. The aim of this book is to further the understanding of the physics of short-wave irradiation, with particular emphasis on the development of mathematical models for computational purposes. The terms solar radiation, irradiation, radiance, irradiance, luminance and illuminance are frequently encountered in the literature and a note on their use is perhaps appropriate at this stage. Solar radiation (W/m^2) or luminance (candela/m^2 (cd/m^2)) refers to the energy emanating from the sun. Luminance is the energy contained within the visible part of the solar radiation spectrum (0.39–0.78 μm). The term irradiation (W h/m^2 or J/m^2) and illumination (lumen-hour (lm-h)/m^2) refer to the cumulative energy incident on a surface in a given period of time. Irradiance (W/m^2) and illuminance (lm/m^2) refer to the instantaneous incident energy. As it would be expected, daylight and solar radiation possess similar physical characteristics and the modelling experience of one quantity helps the understanding of the other.

The interception of solar radiation by arbitrary surfaces is a function of their geometry and a determinant of their microclimatic interaction, i.e. the energy exchange between the surface and the surroundings. Estimation of horizontal irradiation is one task, assessment

of insolation (solar irradiation) on slopes is another. Insolation availability of arbitrary sloped surfaces is a prerequisite in many sciences. For example, agricultural meteorology, photobiology, animal husbandry, daylighting, comfort air-conditioning, building sciences and solar energy utilisation, all require insolation availability on slopes. In agricultural meteorology, the importance of net radiation in determining crop evaporation is well documented. It has been suggested that in the climate of the British Isles the annual enthalpy of evaporation from short grass is equal to the annual net radiation. A similar case occurs on a daily basis. Net radiation is also required in estimating the heating coefficient of a field, which is a key index for the soil germination temperature. The first step in determining net radiation is the incident short-wave radiation on the surface of the field, which may be situated on a slope.

Photosynthesis is an important phenomenon in photobiology. This term is commonly reserved for the process by which green plants are able to convert light into chemical energy. However, the absorption of energy is selective as far as the wavelength of the incident radiation is concerned. Therefore a spectral irradiation model is required in the applications of photobiology.

The effects of solar radiation are also of interest in the breeding of cattle, sheep and other livestock. It is usually the major factor limiting the distribution of stock in the tropics. The heat load on an animal is the result of solar irradiation and in some cases its magnitude could be several times the animal's normal heat production. Nature helps, however, in keeping down the heat load by having a low absorptivity of the animal's coat and by providing an insulating barrier in the form of thick fleece. Nevertheless, the limited ability of the animal to vaporise moisture, and thus regulate the dissipation of solar heat load, makes the effect of solar radiation on its surface an important factor. The problems of solar heat loads are not limited to the tropics. Even in Scotland, the insolation levels may induce a considerable load in the summer season.

The rising cost of electricity has provided the motive for making best use of daylight. Utilisation of daylight and solar radiation has led to new architectural developments. Typical design elements include atria, sloping facades and large windows. But although there are new opportunities for making use of daylight, there is a need for comprehensive information on appropriate calculations. By incorporation of realistic prediction methods, daylight and passive solar design can provide a reduction in energy costs. The need for prediction methods for daylight is even more genuine owing to the fact that worldwide there is very limited measured illuminance data.

There is an increasing concern over our planet's 'global warming'. Since 1765 levels of greenhouse gases have increased substantially. The accelerated warming of the planet is leading to considerable increase in monetary loss through flood damage. That information is presented in Figure I.

The worldwide use of energy is rising by 2.5% a year, most of which is attributable to the accelerated consumption in the developed countries. Table I presents the projections of future electricity demand. It has been estimated that, from a sustainability viewpoint the developed countries will have to cut their use of energy by a factor of 10 within a generation. Proponents of solar energy have gone to the extent that they are calling for a complete substitution of conventional sources of energy with renewables. Their thesis is that the use of fossil fuels for energy production, even in minor quantities would merely postpone the collapse of the global environment.

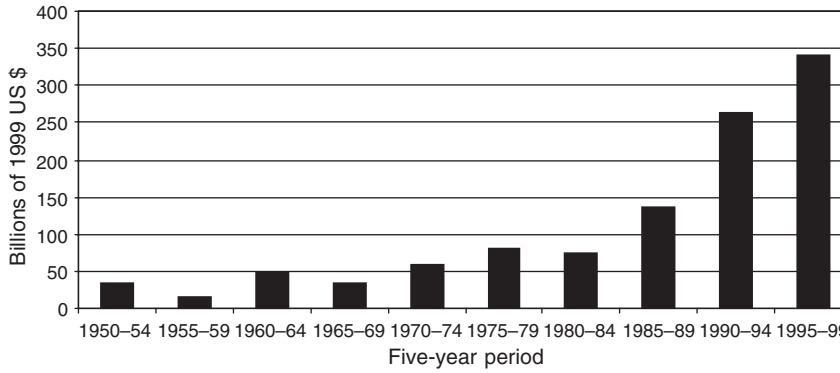

Figure I *Global direct economic losses from natural catastrophes*

Table I Projections of future electricity demand (TWh)

Region	1998	2010	2020
OECD-Europe	2875	3836	4492
OECD-North America	4362	5508	6363
OECD-Pacific	1236	1613	1865
Latin America	871	1409	2073
East Asia	708	1294	2030
South Asia	568	1070	1657
China	1234	2497	3857
Middle East	357	513	839
Former Soviet Union	1777	2491	3298
Africa	408	622	851
World total	14 396	20 853	27 325

Electricity production accounts for 39% of the UK's total CO_2 production. Electrical lighting in the UK accounts for an estimated 5% of the total primary energy consumed per annum. Exploitation of daylight can thus produce significant savings. Research has shown that savings of 20–40% are attainable for office buildings which utilise daylight effectively. The energy potential of daylight in the UK alone and using conventional windows has been estimated at around one million tonnes of coal equivalent per annum by the year 2020. However, a high density of urban structures can often lead to the loss of daylight amenity. Improper design of large glazed facades may also lead to the problem of glare. Innovative solutions have however emerged in recent years to overcome above-mentioned difficulties. One such solution incorporates capture of daylight via a mirrored light-pipe and then directing it to those areas of building which are starved of this amenity. The mirrored light transmission system gathers daylight via a polycarbonate dome at roof level and then transmits it downwards to interior spaces within buildings. The internal surface of the sun-pipe is coated with a highly reflective mirror finish material (typically with a reflectance in excess of 0.95) which helps in achieving a reasonable illuminance indoors when daylight is introduced via a light diffuser. The light reflecting tube is adaptable to incorporate any bends around building structural components. In a

further development, the 3M company has introduced a light-pipe with a total internal reflection material that enable transmission of daylight to distances of up to 40 m without any serious illuminance degradation.

Advances by a team of physicists at the University of Technology, Sydney are paving the way for a significant exploitation of daylight. The team are using materials coated on windows to introduce natural sunlight without its heat (infrared) content. Using the fruits of nanotechnology research the team have experimented with certain powders with a particle size of between 5 and 20 nm that are embedded within a thin plastic layer to allow visible light to pass through but curtail near-infrared part of solar radiation. The technique is based on the ability of these ultra-fine particles to cut out infrared photons, an electromagnetic effect called surface plasmon resonance. The technology thus offers an increased use of daylighting within buildings without increased energy consumption due to air conditioning.

The benefits and savings associated with daylight design are severalfold. Reduction of electrical lighting load due to the increased contribution of daylight results in lower sensible heat gains. This has the knock-on effect of lowering the cooling requirements of the buildings' air conditioning. As cooling plants are high consumers of electricity the costs associated with their operation can be as much as four times greater than that of heating. Furthermore the overall efficiency of a cooling plant is only 5% due to the energy conversions associated with refrigeration and losses accumulating from electricity generation, transmission and final consumption. Thus, any reduction in electrical lighting load produces a much larger saving in the primary energy consumption.

Buildings in the UK have traditionally been designed using daylight data recorded from the National Physical Laboratory in Teddington between 1933 and 1939. More recently new building constructions have employed illuminance data from Kew. The age of the data may not create any serious concern, although the clean air acts passed in major towns and cities across the country could possibly influence present daylight levels. There is, however, concern centring around the lack of illuminance data from the major part of the country. In a relevant study it was shown that values of average horizontal illuminance in the northern part of the UK varied significantly from those reported for Kew, e.g. the differences were found to be as much as 32%. These differences have far reaching consequences for a building's performance.

As a consequence of the absence of adequate measured illuminance data, building designers have to rely on predictive tools and models. These models should be capable of accurately predicting illuminance values from meteorological parameters such as solar radiation. There are algorithms which allow the prediction of illuminance when solar irradiation is provided as an input parameter. Thus validated insolation models will not only provide information on the interception of irradiation, but also on daylight.

It has also been reported in the literature that during the past quarter century many building air-conditioning systems were overdesigned. The resulting plant capacity at least in the UK building stock exceeds the true requirements by as much as 30%. This was due to the procedures used for load estimations. Two factors that may have contributed to the above overestimations are the assumption of isotropic diffuse irradiance for computing vertical surface energy gains and the use of hypothetical clear-sky irradiation data. During the past decade several new and better solar radiation algorithms have evolved. These models indicate that the isotropic assumption overestimates the energy

transmission through fenestration by as much as 40% for vertical surfaces in shade and over 20% for sun-facing surfaces under overcast conditions.

Modelling the availability of energy for the above-mentioned applications requires knowledge of slope irradiation and illuminance either on a monthly-averaged, daily (only applicable for irradiation) or hourly basis depending on how refined the analysis has to be. While modelling and simulation of energy systems would require determination of hourly horizontal and slope quantities, daily and monthly-averaged irradiation values would suffice for an abbreviated analysis. In the UK, e.g. currently horizontal hourly diffuse and global irradiations are recorded by the Meteorological Office for eight locations. Records for hourly global irradiation alone are available for a further 74 stations. For some of these locations these records exceed a period of 60 years. Slope irradiation measurements are however, available for only two sites, Easthampstead (51.4°N) and Lerwick (60.2°N) which lie at the southern and northern extremes of the UK. Across western Europe as well as in the USA, long-term records of slope irradiation are available for no more than a dozen locations. A similar situation exists in other parts of the world, e.g. in India only one and in China three stations presently log slope irradiance and illuminance.

Within the past 5 years there has been an acceleration of activity in the exploitation of solar energy and this has primarily resulted from protection of environment pressures. The Kyoto protocol for reduction of carbon dioxide (CO_2) has been an important instrument in this respect. Subsidies offered for the use of solar water heating and building integrated photovoltaic installations (BIPV technology) within the European Union (EU) countries have resulted in a rapid take-off of these and related technologies. In this respect the Berlin based consultancy Eclareon's report (Sunrise 2002) provides an account of renewable market penetration within the EU. Their report's findings are summarised in the Tables II and III.

To become competitive, renewable energy producers ought to find means to fill the monetary gap between their higher generation costs and the whole price of electricity available within the grid. In this respect the value of emissions reduction credit will help swing the balance incrementally in favour of renewables. In the EU penalties on fossil fuel emissions will add \$40/ton of CO_2. This is likely to increase to \$100/ton within the Kyoto compliance period of 2008–2012. Tables IV and V provide details of the prices of greenhouse emission credits that are either currently in practice or are being proposed and a comparison of electricity generating costs.

With the allocation of above emission credits, the per-kWh generation cost of renewables would drop by 1 US cent while the cost for coal- and gas-based generation would rise by 2 cents and 1 cent, respectively, thus reducing the gap between conventional and renewable electricity by up to 3 cents/kWh. However, with the PV generating costs being an order of magnitude higher than those of conventional sources significant investments would be needed to support the former technology to bring the economy of scales factor into play. The trends though are encouraging, i.e. during the past decade, the per peak Watt PV cost has dropped from \$6 to \$2.5 and year upon year PV module production has enjoyed a double-digit percentage increase. For instance, during the year 2002 the world total PV production capacity reached 540 MW, a 35% increase over 2001.

Another contributing factor that will eventually lead to the use of solar power within the transport sector is the spiralling monetary and environment costs associated with the current use of fossil fuels. However, a considerable amount of R&D money is being spent

Table II Installed thermal solar collector area for European countries

Country	1	2	3	4	5
Germany	420	615	900	3.71	45.1
Greece	195	181	160	2.98	283.4
Austria	141	168	169	2.34	288.9
France	16	23	38	0.55	9.3
Spain	33	40	50	0.45	11.4
Denmark	22	27	40	0.32	60.6
Italy	16	18	17	0.31	5.5
Switzerland	30	26	27	0.26	36.1
Portugal	5	6	8	0.25	25
Netherlands	30	32	35	0.21	13.5
Sweden	9	18	13	0.21	23.9
UK	9	10	11	0.21	3.5
Finland	9	10	10	0.03	5.9
Belgium	2	2	3	0.02	2.4
Ireland	1	0.3	0.3	0.003	0.9
Total	914	1171	1488	11.9	

Column labelled 1: Thousand m^2 installed in year 1999.
Column labelled 2: Thousand m^2 installed in year 2000.
Column labelled 3: Thousand m^2 installed in year 2001.
Column labelled 4: Million m^2 installed, cumulative.
Column labelled 5: Cumulative installed, m^2/thousand population.

Table III PV module price data ($/W)

Year	Average price
1990	4.5
1993	4.0
1996	4.0
1997	4.2
1998	4.0
2000	3.0
2005	2.0
2010	1.5

Table IV Emission credits for conserving greenhouse gases (USD/tonne)

Country/region	CO_2	SO_2	NO_x
USA	2.7	220	825
Ontario	2.2	220	825
UK	10–18		2200
The Netherlands	3–5		
EU	4.8		
Australia	8.9		

Table V Generating costs for electricity

	Generating costs (US cents/kWh)	
Technology	Mean	Range
Gas combined cycle	3.5	3.0–4.0
Coal	4.8	4.0–5.5
Nuclear	6	3.3–8.0
Wind	5.5	3.0–8.0
Biomass	6.5	4.0–9.0
Small hydro	7.5	5.0–10.0
Solar thermal	15	12.0–18.0
Solar PV	55	30.0–80.0

Table VI World fossil fuel reserves to production ratio, years (British Petroleum 1999 statistics)

North America	11
South and Central America	65
Europe	18
Africa	100
Asia-Pacific	42
World	62

by all leading automobile manufacturers on the development of hydrogen powered vehicles that either use fuel cell or internal combustion engines. In March 2003, the Japanese Honda company introduced the first fuel-cell car. The model FCX that weighs 1680 kg uses polymer proton exchange membrane technology and develops 81 kW brake-power by the reaction of hydrogen (stored at 350 bar pressure) and atmospheric oxygen.

With the rapid decline in the oil reserves within the Gulf of Mexico basin, Iraq has become the linchpin in the US strategy to secure cheap oil. Within the oil production sector the 'reserve/production ratio' is a key index that determines the period of exhaustion of fossil fuel and in this respect Table VI has been included herein. Between Saudi Arabia and Iraq, with their respective proven oil reserves of 262 and 112 billion barrels, a staggering 40% of world's oil reserves is shared. With the US invasion of Iraq it appears a new phase of 'energy wars' has started that may indeed spill over to other Opec countries. The repercussions of such actions and the fact that cheaper oil resulting from the 'capture' of oil reserves will lead to a faster consumption may indeed herald the true age of solar energy. In this respect world political leaders would be well advised to promote renewable energy technologies. That is the only and truly sustainable action for the abatement of the effects of an increase in atmospheric greenhouse gas loading. In this respect an extract of a study published in the year 2002 is presented below.

The above research team have argued that the transition of a hydrocarbon to hydrogen fuel economy is a natural transition phase in human development (see Figure II). Furthermore, they have shown that a single solar PV station of 250×250 km area, or 12 decentralised stations each of 72×72 km area would be sufficient to meet the year 2020

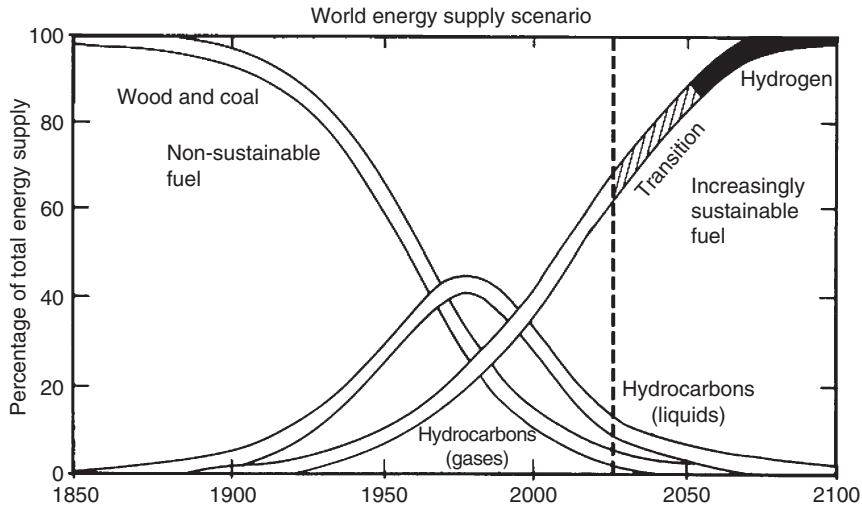

Figure II *World energy supply scenario*

world electricity demand. Hydrogen produced by electrolysis of water may be distributed via pipelines with staged compression. It has been worked out that for sustainable energy supply to Western Europe, a single decentralised station using a three stage compression plant will be able to supply hydrogen gas from the eastern most part of Saudi Empty Quarter to Adana, southern Turkey, a distance of 2500 km. An identical booster station would then be able to transport the gas to southern Germany, which is a further 2300 km away. Estimates show that a $9 \times 9\,\text{km}^2$ PV array area would be sufficient to provide a flow rate of 11.5 k/s of hydrogen through a 2-m diameter pipeline which translates to an annual capacity of 9 TWh. The respective sizes of a single solar PV station of $250\,\text{km}^2$, or a decentralised station of 72×72 km, conceptually built within the Saudi Empty Quarter are shown in Figure III. Table VII identifies those desert locations that are in proximity to large economies, which may possibly 'host' the solar hyper PV stations of the type identified above.

The aim of this work is to address the relevant topics mentioned in the preceding discussion, and provide those mathematical models and computer programs which enable computation of global, diffuse and beam irradiance and illuminance on arbitrary surfaces. It was shown above that estimation of solar radiation and daylight is required in a number of scientific and engineering applications. However, there are only a handful of specialist books, which address this subject with the required rigour. The past decade has seen a burst of activity in the relevant measurement and modelling spheres. As a consequence, previously available texts, which deal with the subject of solar radiation and daylight models, now appear dated. This book attempts to fill this gap. The present book is also different in its character, i.e. it presents a comprehensive suite of electronic programs, which cover most aspects of solar radiation and daylight calculations. These programs are available from companion web site. The programs are licensed on an 'as-is' basis.

With the dawn of the information technology revolution a significant proportion of what used to be printed material is now available in the electronic format. In such publications

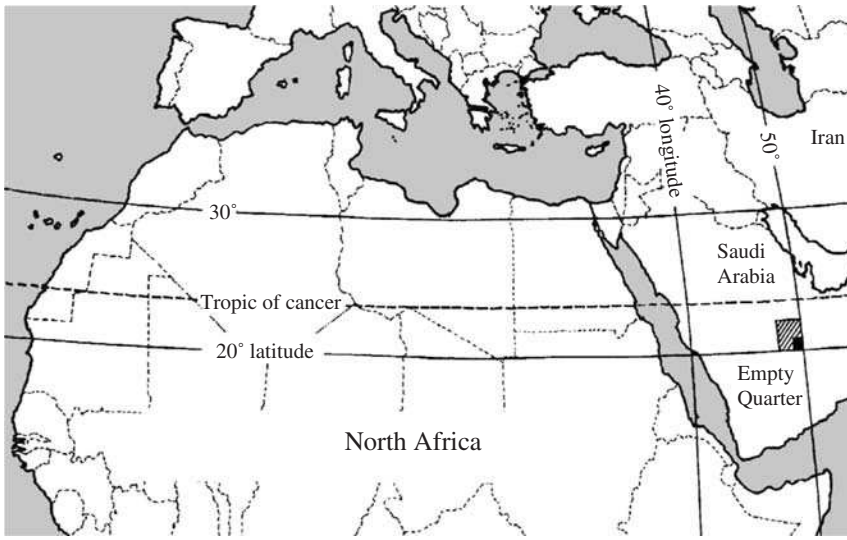

Figure III *Size of solar PV-hydrogen station in an arid region. Single hatched area represents an area of 250 km², solid-fill is 72 km²*

Table VII Arid/semi-arid locations around the globe with potential for installation of hyper PV stations

Energy markets	Arid/semi-arid location or desert
USA, Canada	Nevada, Baja
South America	Atacama (Chile)
OECD-Europe	Southern Spain
Middle East, OECD-Europe	Saudi Empty Quarter
China, CIS states	Gobi
India	Rajasthan
North Africa	Sahara
South Africa	Namibia, Kalahari
Australia	Great Victoria, Gibson, Tanami

the accompanying software enables the reader to resequence, reorganise and indeed create new material. The distinction between writer and reader is fast becoming blurred. As a matter of fact the experienced reader is able to push the boundaries of the electronic publication beyond the author's sphere of presentation. The medium and format of the present publication may be described as 'part soft, part hard', i.e. the text is available as a hard copy while the accompanying algorithms and basic weather data are presented in an electronic format. Electronic spreadsheets have come to be known as productivity software. However, in the present moment in time the more sophisticated building energy simulation programs continue to use FORTRAN as the developmental medium. Therefore all algorithms included in this book have been written in the current version of the latter language.

The advantage of having computer programs in an electronic format is that they may be copied and pasted in other larger simulation programs. This may be done effectively by

making the present FORTRAN codes as sub-routines or embedding them as part of the main body of user's own programs. Of course, the programs may also be used as independent modules to evaluate any desired solar property or quantity on a one-off or iterative basis. The programs are being made available both in the *.For and *.Exe formats. The *.Exe files will enable those users who do not have access to a FORTRAN compiler to execute any of the accompanying routines in the DOS or Windows XP environment.

1 FUNDAMENTALS

Introduction

The past decade has seen a boom in the construction of energy efficient buildings which use solar architectural features to maximise the exploitation of daylight, solar heat and solar-driven ventilation. Daylight and building services engineers have therefore become accustomed to the use of specialist software for the physical simulation of buildings. Many of these software programs operate in the FORTRAN environment and, with new releases of FORTRAN available for the development work, this area of activity will see even more growth. Despite the fact that presently languages, which are more structured than FORTRAN, e.g. C, are available, the former continues to be used widely in the engineering sector. Popular building physics simulation programs such as ESP and SERI-RES use the FORTRAN environment. 'The "Grand Challenges of Science and Engineering" for the foreseeable future will involve the use of FORTRAN-like programs on supercomputers' was an observation made in a recent report prepared for the President of the US, as quoted by Edgar (1992). After its creation in the 1950s, FORTRAN developed many different dialects. However, the current standard is FORTRAN 95 (Nyhoff and Leestma, 1995).

The Commission International de l'Éclairage (CIE) declared the year 1991 as the International Daylight Measurement Year. Consequently, new activity was seen across the globe on this front. This activity is called the International Daylight Measurement Programme (IDMP). In the UK as a result of the CIE call, horizontal and vertical illuminance and irradiation measurements have been carried out for four sites, i.e. Watford, Manchester, Sheffield and Edinburgh. These records are available on a minute-by-minute basis (Tregenza, 1994). Any sun position software which utilises data at this frequency warrants high accuracy. Thus older algorithms based on calculating the solar declination angle (DEC) and the equation of time (EOT) on once a day basis will gradually become obsolete. It is worth noting that astronomical almanacs report values of the above variables for 0 h Universal Time (UT).

In this chapter algorithm and software routines are presented which enable calculation of the sun's position and the related geometry. The present set of algorithms include low to high accuracy models. The high precision algorithm for solar position calculation was developed by Yallop (1992), a leading astronomer. These algorithms are dynamic and take account of the change of the above-mentioned parameters, year upon year. The validity period for the present high accuracy algorithm (Prog1-6.For and Prog1-6.Exe available from this book's web site) is from 1980 to 2050.

Disparate practice has been adopted by meteorological stations across the globe in measuring hourly solar radiation. While in the UK the irradiation data is available against apparent solar time (AST), many other countries use the local civil time (LCT) as the reference for all records. Under the CIE IDMP the illuminance was recorded worldwide against the LCT. It is therefore necessary that appropriate algorithms are available for the conversion from one system to another. Basic concepts and definitions are introduced herein, which are a prerequisite for obtaining sun's position.

1.1 Solar day

Our sun is only one of a very large number of stars that constitute our galaxy, the milky way. To be more precise there are around 100 billion stars within our galaxy and there are around 500 billion galaxies within the universe! Our sun, along with its entire solar system, is 26 thousand light years from the centre of the galaxy. The period of its revolution around the galaxy centre is 230 million years. Figure 1.1.1 shows a rough schematic of the position of our solar system within the galaxy.

A solar day is defined to be the interval of time from the moment the sun crosses the local meridian to the next time it crosses the same meridian. Owing to the fact that the earth rotates in a diurnal cycle as well as moves forward in its orbit, the time required for one full rotation of the earth is less than a solar day by about 4 min. Table 1.1.1 presents information on terrestrial and other related time cycles.

The earth's rotation about its own axis and its revolution around the sun is very involved. Over and above its rotation about its polar axis in one sidereal day and its orbital motion around the sun in a year, the tilt of earth's axis varies from 22 to 25 over a period of around 41 000 years. The greater the tilt, the more summer sunlight falls on the poles, partly contributing to glacial retreat. Furthermore, the earth wobbles like a spinning top in a cycle that lasts for 23 000 years, changing the fraction of sunlight that falls on each hemisphere. Lastly, the earth's path around the sun alternates between a circular to elliptical orbit with a

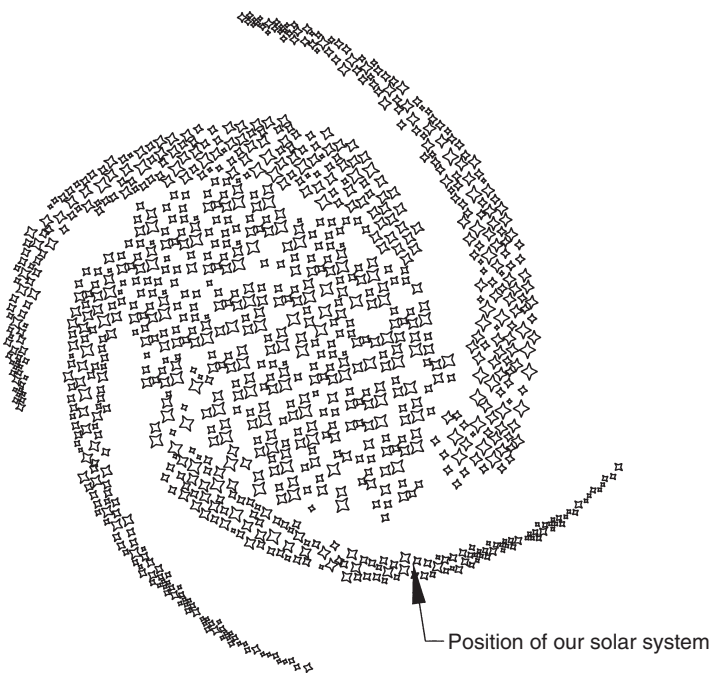

Figure 1.1.1 *Our solar system's motion around the milky way galactic centre. Our solar system is 26 thousand light years from the centre of the milky way galaxy. The period of its revolution around the galaxy centre is 230 million years*

period of 100 000 years. A circular orbit results in less sunlight over the course of the year. The above-mentioned terrestrial movements have been graphically shown in Figure 1.1.2. Further information in this respect may be obtained from the Lamont Doherty Earth Observatory of Brown University, USA.

A further point of interest is that owing to earth's tidal drag, the day length has been slowly increasing at the rate of 21.6 μs per year.

1.1.1 Day number

In many solar energy applications one needs to calculate the day number (DN) corresponding to a given date. DN is defined as the number of days elapsed in a given year up to a particular date. Examples of this application are the estimation of the EOT and DEC using low precision algorithms, and the extraterrestrial irradiance and illuminance at any given time. In the present section DN is obtained via Prog1-1.Exe. The FORTRAN routine for DN and the aforementioned .Exe file are available from the book's web site. Users may wish to incorporate the calculation of DN in their own FORTRAN routines and this would be facilitated by electronically copying Prog1-1.For in their programs.

Example 1.1.1

Calculate the DN corresponding to 1 March 1996 and 1 March 1997.

The output from Prog1-1.For is as follows:

DN = 61 (for 1 March 1996)
DN = 60 (for 1 March 1997)

Notice that the program takes account of the leap years.

1.1.2 Julian day number and day of the week

In many astronomical calculations it is often necessary to count the number of days elapsed since a predetermined reference date (fundamental epoch). By convention this date has been fixed as the Greenwich mean noon of 1 January 4713 BC. The number of days elapsed

Table 1.1.1 Time cycles and other related information

Length of tropical year as recorded in 2000 CE: 365.484 375 days
Time that the year has slowed since 1 CE: 10 s
Average decrease in terrestrial year due to decreasing angular velocity of earth: 0.5 s/century
Length of lunar year: 354.367 069 4 days
Date of enactment of Julian calendar: 46 BC
Date of enactment of Gregorian calendar: 1582 CE
Length of Gregorian year: 365.241 898 148 148 days
Length of time the Gregorian calendar had become misligned over the 414 years since enactment of Gregorian calendar: 2 h, 59 min and 12 s
Year in which the Gregorian calendar will be 1 day ahead of the true solar year: 4909 CE
Terrestrial year measured in oscillations of atomic cesium: 290 091 200 500 000 000

from this epoch to any given date is called the Julian day number (JDN). The calculation for JDN involves six steps and these are given in Duffett-Smith (1988).

The estimation of the day of the week is easy once JDN is known. This involves a three-step algorithm which is also available in Duffett-Smith (1988). Modern control algorithms for energy efficient buildings, such as optimum start algorithm, may find the use for the 'day of the week' routine to differentiate between weekdays and weekends.

Prog1-2.For and Prog1-2.Exe enable estimation of JDN and day of the week.

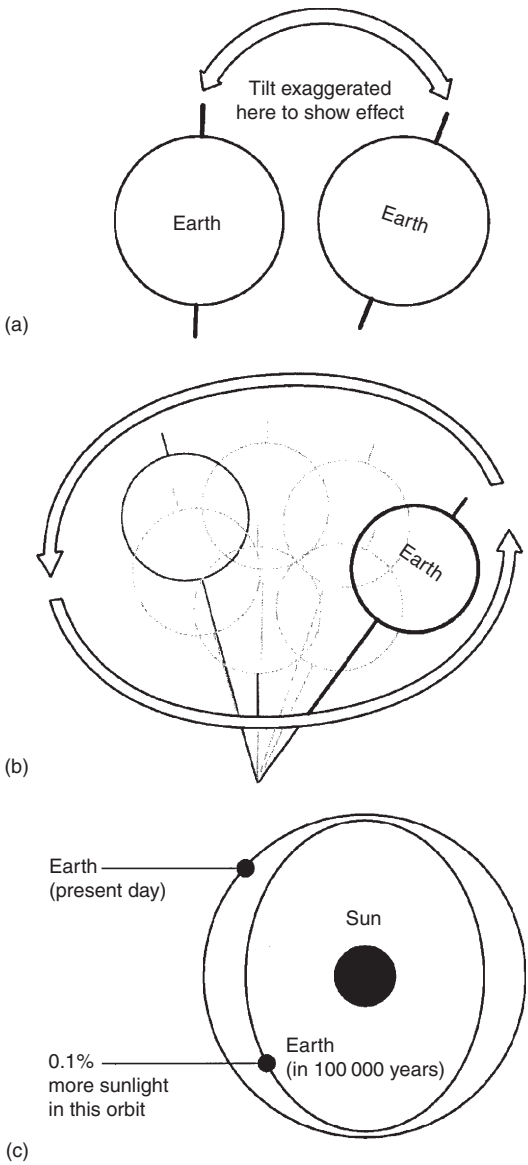

Figure 1.1.2 *Earth's rotational movements: changes in tilt, wobble and orbital changes: (a) Tilt: The tilt of earth's axis varies from 22° to 25° over 41 000 years. The greater the tilt, the more summer sunlight falls on the poles, contributing to glacial retreat. (b) Wobble: Earth wobbles like a toy in a cycle that lasts 23 000 years, changing the fraction of sunlight that strikes each hemisphere. (c) Orbit: The shape of earth's path around the sun ranges from circular to more elliptical over 100 000 years. A circular orbit means less sunlight over the course of the year*

Example 1.1.2

Find JDN and the day of the week corresponding to 25 December 1996.

Prog1-2.Exe provides the following output:

JDN = 2 450 442.5
day of the week = Wednesday

It is worth noting that JDN begins at 12 h UT and is therefore 0.5 day ahead of the civil time.

1.2 Equation of time

The solar day defined above varies in length throughout the year due to:

(a) the tilt of the earth's axis with respect to the plane of the ecliptic containing the respective centres of sun and the earth,
(b) the angle swept out by the earth–sun vector during any given period of time, which depends upon the earth's position in its orbit (see Figure 1.2.1).

Note that Table 1.2.1 presents information on the minimum and maximum earth–sun orbital distance along with data for other planets within our solar system.

Thus, the standard time (as recorded by clocks running at a constant speed) differs from the solar time. The difference between the standard time and solar time is defined as

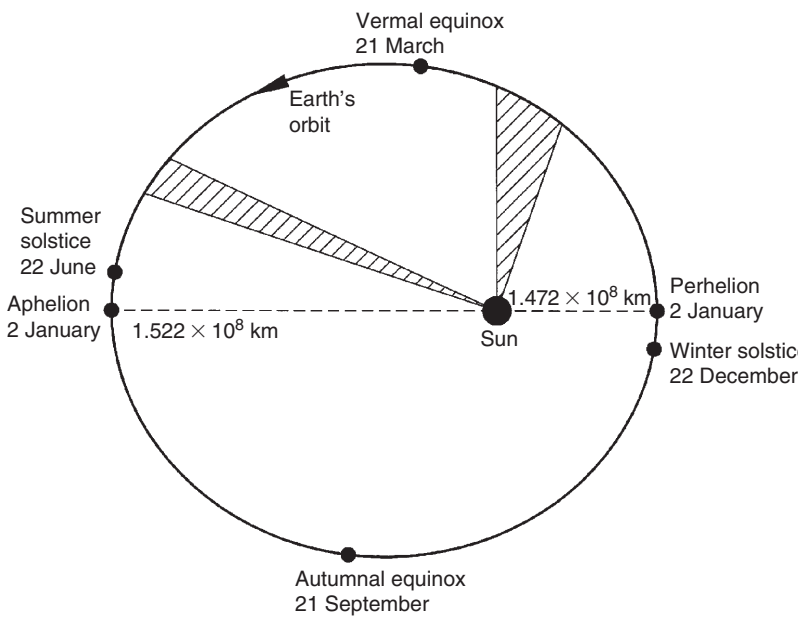

Figure 1.2.1 *Earth's orbit around the sun*

Table 1.2.1 Data related to solar planetary system

	Mercury	Venus	Earth	Mars	Jupiter	Saturn	Uranus	Neptune	Pluto
Distance (million km) from sun									
maximum	69.7	109	152	249	816	1507	3004	4537	7375
mean	57.9	108.2	149.6	227.9	778	1427	2870	4497	5900
minimum	45.9	107.4	147	206.7	741	1347	2735	4456	4425
Orbital period*	87.97d	224.7d	365.3d	687.0d	11.86y	29.46y	84.01y	164.8y	247.7y
Rotation period**	58.646	243.16	0.997	1.026	0.414	0.426	0.718	0.672	0.256
Orbital eccentricity	0.206	0.007	0.017	0.093	0.048	0.056	0.047	0.009	0.248
Axial inclination, degrees	2	178	23.4	24	3	26.4	98	28.8	122.5
Mass relative to earth	0.055	0.815	1	0.11	317.9	95.2	14.6	17.2	0.002
Volume relative to earth	0.056	0.86	1	0.15	1319	744	67	57	0.01

*d = terrestrial days and y = terrestrial years.
**Terrestrial days.

Table 1.2.2 Coefficients for Eq. (1.2.2)

k	$A_k \times 10^3$ (h)	$B_k \times 10^3$ (h)
0	0.2087	0.000 00
1	9.2869	−122.290 00
2	−52.2580	−156.980 00
3	−1.3077	−5.160 20
4	−2.1867	−2.982 30
5	−1.5100	−0.234 63

the EOT. EOT may be obtained as expressed by Woolf (1968):

$$\text{EOT} = 0.1236 \sin x - 0.0043 \cos x + 0.1538 \sin 2x + 0.0608 \cos 2x \tag{1.2.1}$$

where $x = 360\,(\text{DN} - 1)/365.242$, DN = 1 for 1 January in any given year. EOT may also be obtained more precisely as presented by Lamm (1981) as:

$$\text{EOT} = \sum_{k=0}^{5} A_k \cos(2\pi kN/365.25) + B_k \sin(2\pi kN/365.25) \tag{1.2.2}$$

where N is the day in the 4-year cycle starting after the leap year. Prog1-2.For discussed earlier is especially useful for such calculations and is incorporated in the present algorithm. Values of the A_k and B_k coefficients are given in Table 1.2.2. In any non-leap year,

Table 1.2.3 EOT: accuracy evaluation for the 21st day of each month

	Low: Eq. (1.2.1)		Medium: Eq. (1.2.2)		High: Yallop (1992)		AP (1993)*	
	(min)	(s)	(min)	(s)	(min)	(s)	(min)	(s)
January	−10	56	−11	8	−11	13	−11	14
February	−13	57	−13	43	−13	41	−13	41
March	−7	40	−7	30	−7	19	−7	19
April	2	40	1	14	1	12	1	13
May	4	21	3	28	3	28	3	29
June	−1	30	−1	28	−1	38	−1	38
July	−6	20	−6	18	−6	21	−6	21
August	−3	17	−3	19	−3	13	−3	14
September	8	46	6	43	6	46	6	46
October	16	23	15	8	15	17	15	16
November	14	24	14	23	14	13	14	12
December	2	13	2	13	2	06	2	05

* *Astronomical Phenomena* (1993).

EOT assumes the value of near zero for 0 h UT for 15 April, 13 June, 1 September and 25 December. A high precision routine for EOT is implicit in Yallop's algorithm which is presented in Section 1.4.

FORTRAN routines for EOT based on Eqs (1.2.1), (1.2.2) and Yallop's algorithm are respectively presented in Prog1-3.For, Prog1-4.For and Prog1-6.For. These FORTRAN files and the corresponding machine executable files are also available from the book's web site. Table 1.2.3 presents the accuracy evaluation of the above EOT models, compared against the reference *Astronomical Phenomena* (1993).

It may be of interest to note that up to early 17th century the EOT, then known as Equation Naturales, could be computed with an accuracy of half a minute. In 1675 Flamsteed Street, the first Astronomer Royal in England produced a technique to reduce the error in obtaining EOT to within 6 s. Today there are models available which enable EOT to be computed to an accuracy of 3 s over a range of 60 centuries, e.g. Hughes et al. (1989)!

Table 1.2.4 presents precise values of EOT and DEC for the year 2002. This table has especially been prepared for this book by the Royal Greenwich Observatory, Cambridge. The choice of this particular epoch was made due to it being the mid-year in the first leap year cycle of this millennium. The accuracy of this table is better than 1 s for EOT and 1 min of arc for the DEC. This table may be used as a reference for the next two decades. Typically, the variation of EOT, year on year, is around a 10th of a minute.

Example 1.2.1

Calculate the EOT for 2 February 1993 at 0 h Greenwich Mean Time (GMT).

Using the above-mentioned FORTRAN routines, Table 1.2.5 may be generated which enables the necessary accuracy evaluation.

Table 1.2.4 EOT and DEC for the year 2002* (all values are for 0 h UT)

		EOT		DEC				EOT		DEC				EOT		DEC				EOT		DEC	
		(min)	(s)	(deg)	(min)			(min)	(s)	(deg)	(min)			(min)	(s)	(deg)	(min)			(min)	(s)	(deg)	(min)
Jan.	0	−2	49	−23	6	Feb.	15	−14	9	−12	49	Apr.	2	−3	45	4	46	May	18	3	38	19	28
	1	3	17	23	2		16	14	6	12	28		3	3	27	5	9		19	3	36	19	41
	2	3	46	22	57		17	14	3	12	7		4	3	9	5	32		20	3	33	19	54
	3	4	14	22	52		18	13	58	11	46		5	2	52	5	55		21	3	29	20	6
	4	4	41	22	46		19	13	53	11	25		6	−2	34	6	18		22	3	25	20	18
	5	−5	8	−22	39		20	−13	48	−11	4		7	2	17	6	41		23	3	21	20	30
	6	5	35	22	32		21	13	41	10	42		8	2	1	7	3		24	3	16	20	42
	7	6	1	22	25		22	13	34	10	20		9	1	44	7	26		25	3	11	20	53
	8	6	27	22	18		23	13	26	9	58		10	1	28	7	48		26	3	5	21	3
	9	6	52	22	9		24	13	18	9	36		11	−1	12	8	10		27	2	58	21	14
	10	−7	17	−22	1		25	−13	9	−9	14		12	0	56	8	32		28	2	51	21	24
	11	7	42	21	52		26	12	59	8	52		13	0	40	8	54		29	2	44	21	33
	12	8	5	21	42		27	12	49	8	29		14	0	25	9	16		30	2	36	21	43
	13	8	28	21	33		28	12	39	8	7		15	0	10	9	37		31	2	28	21	51
	14	8	51	21	22	Mar.	1	12	27	7	44		16	0	4	9	59	Jun.	1	2	19	22	0
	15	−9	13	−21	12		2	−12	16	−7	21		17	0	18	10	20		2	2	10	22	8
	16	9	34	21	1		3	12	3	6	58		18	0	32	10	41		3	2	0	22	16
	17	9	55	20	49		4	11	51	6	35		19	0	45	11	2		4	1	51	22	23
	18	10	14	20	37		5	11	37	6	12		20	0	58	11	23		5	1	40	22	30
	19	10	33	20	25		6	11	24	5	49		21	1	11	11	43		6	1	30	22	37
	20	−10	52	−20	12		7	−11	10	−5	26		22	1	23	12	4		7	1	19	22	43
	21	11	9	19	59		8	10	56	5	3		23	1	35	12	24		8	1	7	22	49
	22	11	26	19	46		9	10	41	4	39		24	1	46	12	44		9	0	56	22	54
	23	11	42	19	32		10	10	26	4	16		25	1	57	13	4		10	0	44	22	59
	24	11	57	19	18		11	10	10	3	52		26	2	7	13	23		11	0	32	23	3
	25	−12	2	−19	3		12	−9	55	−3	29		27	2	17	13	42		12	0	19	23	8
	26	12	25	18	49		13	9	39	3	5		28	2	27	14	2		13	0	7	23	11
	27	12	38	18	33		14	9	22	2	41		29	2	36	14	20		14	0	6	23	15
	28	12	50	18	18		15	9	6	2	18		30	2	44	14	39		15	0	18	23	17
	29	13	1	18	2		16	8	49	1	54	May	1	2	52	14	57		16	0	31	23	20
	30	−13	12	−17	46		17	−8	32	−1	30		2	2	59	15	15		17	0	44	23	22
	31	13	21	17	29		18	8	15	1	6		3	3	6	15	33		18	0	57	23	24
Feb.	1	13	30	17	13		19	7	57	0	43		4	3	12	15	51		19	1	10	23	25
	2	13	38	16	56		20	7	40	0	19		5	3	18	16	8		20	1	23	23	26
	3	13	45	16	38		21	7	22	0	5		6	3	23	16	25		21	−1	36	23	26
	4	−13	51	−16	20		22	−7	4	0	28		7	3	27	16	42		22	1	49	23	26
	5	13	57	16	2		23	6	46	0	52		8	3	31	16	59		23	2	2	23	26
	6	14	1	15	44		24	6	28	1	16		9	3	34	17	15		24	2	15	23	25
	7	14	5	15	26		25	6	10	1	39		10	3	37	17	31		25	2	28	23	24
	8	14	9	15	7		26	5	52	2	3		11	3	39	17	47		26	−2	41	23	22
	9	−14	11	−14	48		27	−5	33	2	26		12	3	41	18	2		27	2	53	23	20
	10	14	13	14	29		28	5	15	2	50		13	3	42	18	17		28	3	6	23	18
	11	14	14	14	9		29	4	57	3	13		14	3	42	18	32		29	3	18	23	15
	12	14	14	13	49		30	4	39	3	37		15	3	42	18	46		30	3	30	23	12
	13	14	13	13	29		31	4	21	4	0		16	3	41	19	0	July	1	−3	42	23	8
	14	−14	12	−13	9	Apr.	1	−4	3	4	23		17	3	40	19	14		2	−3	53	23	4

(*continued*)

Table 1.2.4 *Continued*

	EOT		DEC			EOT		DEC			EOT		DEC			EOT		DEC	
	(min)	(s)	(deg)	(min)		(min)	(s)	(deg)	(min)		(min)	(s)	(deg)	(min)		(min)	(s)	(deg)	(min)
July 3	4	5	22	59	Aug. 18	3	59	13	13	3	10	46	3	48	18	14	57	19	8
4	4	16	22	55	19	3	46	12	54	4	11	5	4	12	19	14	45	19	22
5	4	26	22	49	20	3	32	12	34	5	11	23	4	35	20	14	31	19	36
6	−4	37	22	44	21	−3	17	12	15	6	11	41	−4	58	21	14	17	−19	49
7	4	47	22	38	22	3	2	11	55	7	11	59	5	21	22	14	2	20	3
8	4	57	22	31	23	2	47	11	34	8	12	16	5	44	23	13	46	20	15
9	5	6	22	24	24	2	31	11	14	9	12	33	6	7	24	13	30	20	28
10	5	15	22	17	25	2	15	10	54	10	12	49	6	30	25	13	12	20	40
11	−5	24	22	9	26	−1	59	10	33	11	13	5	−6	52	26	12	54	−20	52
12	5	32	22	1	27	1	42	10	12	12	13	20	7	15	27	12	35	21	3
13	5	39	21	53	28	1	24	9	51	13	13	35	7	37	28	12	16	21	14
14	5	47	21	44	29	1	7	9	30	14	13	50	8	0	29	11	55	21	24
15	5	53	21	35	30	0	48	9	8	15	14	4	8	22	30	11	34	21	35
16	−5	59	21	26	31	0	30	8	47	16	14	17	−8	44	Dec. 1	11	12	−21	44
17	6	5	21	16	Sep. 1	0	11	8	25	17	14	30	9	6	2	10	50	21	54
18	6	10	21	6	2	0	8	8	4	18	14	42	9	28	3	10	27	22	2
19	6	15	20	55	3	0	27	7	42	19	14	54	9	50	4	10	3	22	11
20	6	19	20	44	4	0	46	7	20	20	15	5	10	12	5	9	39	22	19
21	−6	22	20	33	5	1	6	6	57	21	15	15	−10	33	6	9	14	−22	27
22	6	25	20	21	6	1	26	6	35	22	15	25	10	55	7	8	48	22	34
23	6	27	20	9	7	1	46	6	13	23	15	34	11	16	8	8	23	22	40
24	6	29	19	57	8	2	7	5	50	24	15	43	11	37	9	7	56	22	47
25	6	30	19	44	9	2	27	5	28	25	15	50	11	58	10	7	29	22	52
26	−6	30	19	31	10	2	48	5	5	26	15	57	−12	18	11	7	2	−22	58
27	6	30	19	18	11	3	9	4	42	27	16	4	12	39	12	6	34	23	3
28	6	29	19	4	12	3	30	4	20	28	16	9	12	59	13	6	7	23	7
29	6	28	18	50	13	3	51	3	57	29	16	14	13	19	14	5	38	23	11
30	6	26	18	36	14	4	12	3	34	30	16	18	13	39	15	5	10	23	15
31	−6	24	18	22	15	4	33	3	11	31	16	21	−13	59	16	4	41	−23	18
Aug. 1	6	21	18	7	16	4	55	2	48	Nov. 1	16	23	14	18	17	4	12	23	20
2	6	17	17	52	17	5	16	2	24	2	16	25	14	37	18	3	43	23	23
3	6	13	17	36	18	5	38	2	1	3	16	26	14	56	19	3	13	23	24
4	6	8	17	21	19	5	59	1	38	4	16	26	15	15	20	2	44	23	25
5	−6	2	17	5	20	6	21	1	15	5	16	25	−15	33	21	2	14	−23	26
6	5	56	16	48	21	6	42	0	51	6	16	23	15	52	22	1	44	23	26
7	5	50	16	32	22	7	3	0	28	7	16	20	16	10	23	1	14	23	26
8	5	43	16	15	23	7	25	0	5	8	16	17	16	27	24	0	45	23	25
9	5	35	15	58	24	7	46	0	19	9	16	13	16	45	25	0	15	23	24
10	−5	27	15	41	25	8	7	0	42	10	16	8	−17	2	26	0	15	−23	23
11	5	18	15	23	26	8	27	1	5	11	16	2	17	19	27	0	45	23	21
12	5	8	15	5	27	8	48	1	29	12	15	55	17	35	28	1	14	23	18
13	4	58	14	47	28	9	8	1	52	13	15	47	17	51	29	1	44	23	15
14	4	47	14	29	29	9	29	2	15	14	15	39	18	7	30	2	13	23	12
15	−4	36	14	10	30	9	48	−2	39	15	15	30	−18	23	31	−2	42	−23	8
16	−4	24	13	52	Oct. 1	10	8	−3	2	16	15	20	−18	38	32	−3	10	−23	3
17	4	12	13	33	2	10	27	3	25	17	15	9	18	53					

*Prepared by Royal Greenwich Observatory, Cambridge, UK.

NB: Negative values are sparingly used in this table. Note that EOT has a negative value during the periods December 26–April 15 and June14–September 1. Likewise, DEC assumes a (−)ve value during the period September 24–March 20.

Table 1.2.5 Accuracy evaluation of EOT models (2 February 1993)

Source	Accuracy	Program name	Program output (h)	EOT (min)
Woolf (1968)	Low	Prog1-3.For	−0.2257	−13.5
Lamm (1981)	Medium	Prog1-4.For	−0.2265	−13.6
Yallop (1992)	High	Prog1-6.For	−0.228 2949	−13.7
HMNA (1993)	Reference	–		−13.7*

* Corresponds to 0 h UT.

1.3 Apparent solar time

Solar time is the time to be used in all solar geometry calculations. It is necessary to apply the corrections due to the difference between the longitude of the given locality (LONG) and the longitude of the standard time meridian (LSM). This correction is needed in addition to the above-mentioned EOT. Thus:

$$\text{AST} = \text{standard time (LCT)} + \text{EOT} \pm [(\text{LSM} - \text{LONG})/15] \tag{1.3.1}$$

All terms in the above equation are to be expressed in hours. The algebraic sign preceding the longitudinal correction terms contained in the square brackets should be inserted as positive for longitudes which lie east of LSM and vice versa. The LSM and LONG themselves have no sign associated with them.

Example 1.3.1

What is the AST for Madison, Wisconsin corresponding to 10:30 a.m. LCT on 2 February 1993? The following data is given: latitude = 43°N, longitude (LONG) = 89.4°W and LSM = 90°W.

Using Prog1-6.For, AST = 10.310 35 h (10:19 a.m.).

The above value is in agreement with the solution given in Example 1.5.1 of Duffie and Beckman (1980).

1.4 Solar declination

The angle between the earth–sun vector and the equatorial plane is called the DEC. As an adopted convention DEC is considered to be positive when the earth–sun vector lies northwards of the equatorial plane. Declination may also be defined as the angular position of the sun at noon (AST) with respect to the equatorial plane.

DEC may be obtained as expressed by Boes and reported in Kreider and Kreith (1981):

$$\text{DEC} = \sin^{-1}\{0.397\,95 \cos[0.985\,63(\text{DN} - 173)]\} \tag{1.4.1}$$

Note that in the above equation, the cosine term is to be expressed in degrees. The arc sine term will obviously be returned in radian.

Alternately, it may be computed, with a medium to high accuracy, using the algorithm presented by Duffett-Smith (1988). This algorithm involves the following steps:

Step 1 The start of epoch for this algorithm is fixed as 0.0 January 1990. For any given date (either before or after the above epoch) calculate the number of days, D, passed since the start of the epoch.

Step 2 Calculate $N = 360D/365.242\,191$; add or subtract multiples of 360 until N lies in the range of 0–360°.

Step 3 Find $M = N + \varepsilon_g - \omega_g$. If the result is negative, add 360°. Here ε_g and ω_g are respectively the ecliptic longitude of the sun at epoch (=279.403 303°) and the ecliptic longitude of perigee (=282.768 422°).

Step 4 Find $E_c = (360/\pi)\, e \sin M$, e is the eccentricity of orbit (=0.016 713).

Step 5 Find $\lambda = N + E_c + \varepsilon_g$; if the result is more than 360°, subtract 360.

Step 6 DEC $= \sin^{-1}(\sin\varepsilon \sin\lambda)$, where $\varepsilon = 23.441\,884°$ is the obliquity of the ecliptic, the angle between the planes of the equator and the ecliptic.

Yallop's algorithm (1992) given below enables a high precision computation of EOT and DEC. The present routine is valid for the period 1980–2050 and has an accuracy of 3 s for the EOT and 1 min of arc for DEC. For a given year (y), month (m), day (D), hour (h), minute (min) and second (s):

$$t = \{(\mathrm{UT}/24) + D + [30.6\,m + 0.5] + [365.25(y - 1976)] - 8707.5\}/365.25 \tag{1.4.2}$$

where UT $= h + (min/60) + (s/3600)$. In Eq. (1.4.2), if $m > 2$ then $y = y$ and $m = m - 3$, otherwise $y = y - 1$ and $m = m + 9$. In the above expression for t, $[x]$ denotes the integer part of x. The following terms are then determined:

$G = 357.528 + 35\,999.05t$
$C = 1.915 \sin G + 0.020 \sin 2G$
$L = 280.460 + 36\,000.770t + C$
$\alpha = L - 2.466 \sin 2L + 0.053 \sin 4L$
Greenwich Hour Angle, GHA $= 15\mathrm{UT} - 180 - C + L - \alpha$
If necessary add or subtract multiples of 360° to G, L and GHA to set them in the range 0–360°
obliquity of the ecliptic, $\varepsilon = 23.4393 - 0.013t$

DEC, $\delta = \tan^{-1}(\tan\varepsilon \sin\alpha)$
EOT $= (L - C - \alpha)/15$

FORTRAN 77 routines for DEC based on Eq. (1.4.1), Duffett-Smith (1988) and Yallop (1992) algorithms are respectively presented in Prog1-3.For, Prog1-5.For and Prog1-6.For. These FORTRAN files and the corresponding machine executable files are also available from the book's web site. The electronic data files, File1-1.Csv and File1-1.Xls, contain daily values of EOT and DEC computed for noon GMT. Where high computing speed is required this file may be used with the users' own routines.

Table 1.4.1 Accuracy evaluation of DEC models (2 February 1993)

Source	Accuracy	Program name	Program output (deg)
Kreider and Kreith (1981)	Low	Prog1-3.For	−17.1983
Duffett-Smith (1988)	Medium	Prog1-5.For	−16.8748
Yallop (1992)	High	Prog1-6.For	−16.8698
AP (1993)*	Reference	–	−16.8667**

* *Astronomical Phenomena*.
** Corresponds to 0 h UT.

Table 1.4.2 DEC: evaluation for the 21st day of each month*

	Low: Eq. (1.4.1)		Medium: Duffett-Smith (1988)		High: Yallop (1992)		AP (1993)**	
Accuracy	(deg)	(min)	(deg)	(min)	(deg)	(min)	(deg)	(min)
January	−21	53	−19	57	−19	57	−19	57
February	−12	47	−10	38	−10	38	−10	38
March	−1	20	0	9	0	9	0	9
April	11	5	11	48	11	47	11	47
May	19	50	20	9	20	8	20	8
June	23	27	23	26	23	26	23	26
July	20	27	20	31	20	31	20	31
August	11	47	12	11	12	11	12	11
September	0	7	0	47	0	47	0	47
October	−12	47	−10	38	−10	37	−10	37
November	−21	53	−19	52	−19	52	−19	52
December	−24	33	−23	26	−23	26	−23	26

** *Astronomical Phenomena*.
* Corresponds to 0 h GMT.

Example 1.4.1

Calculate DEC for Madison, Wisconsin corresponding to 10:30 a.m. LCT on 2 February 1993. Compare the results obtained using the algorithms due to Boes (Kreider and Kreith, 1981), Duffett-Smith (1988) and Yallop (1992).

Table 1.4.1 shows the above results for accuracy evaluations. Table 1.4.2 compares the DEC estimates obtained via the above three models, and compares them against the *Astronomical Phenomena* (1993).

As stated above, Table 1.2.4 provides high accuracy values of DEC. Year on year the variation of DEC is around a 10th of a degree of arc.

1.5 Solar geometry, SOLALT and SOLAZM

The sun's position in the sky can be described in terms of two angles: SOLALT, the elevation angle above the horizon and SOLAZM, the azimuth from north of the sun's beam

projection on the horizontal plane (clockwise = positive). These co-ordinates which describe the sun's position are dependent on GHA, the latitude (LAT) and longitude (LONG) of the location, and DEC. The solar geometry may now be obtained from the following equations:

$$\sin \text{SOLALT} = \sin \text{LAT} \sin \text{DEC} - \cos \text{LAT} \cos \text{DEC} \cos \text{GHA} \tag{1.5.1}$$

$$\cos \text{SOLAZM} = \frac{\cos \text{DEC} (\cos \text{LAT} \tan \text{DEC} + \sin \text{LAT} \cos \text{GHA})}{\cos \text{SOLALT}} \tag{1.5.2}$$

Manipulation of the above equation to convert SOLAZM values resulting from the arc cosine function of −90 to +90 to the desired 0–360° range is presented in Prog1-6.For.

The angle of incidence, INC, that the sun's beam strikes a sloped surface of any given tilt can then be calculated from the solar altitude, azimuth and the orientation of the surface as expressed by its wall azimuth angle (WAZ). The sign convention adopted for WAZ is the same as that used for SOLAZM, i.e. clockwise from North is considered positive:

$$\begin{aligned}\text{INC} = \cos^{-1}[&\cos \text{SOLALT} \cos(\text{SOLAZM} - \text{WAZ}) \sin \text{TLT} \\ &+ \cos \text{TLT} \sin \text{SOLALT}]\end{aligned} \tag{1.5.3a}$$

An alternate formulation for INC is also available in literature that avoids calculation of SOLAZM:

$$\begin{aligned}\text{INC} = &\sin \text{DEC} \sin \text{LAT} \cos \text{TLT} - \sin \text{DEC} \cos \text{LAT} \sin \text{TLT} \cos \text{WAZ2} \\ &+ \cos \text{DEC} \cos \text{LAT} \cos \text{TLT} \cos \omega \\ &+ \cos \text{DEC} \sin \text{LAT} \sin \text{TLT} \cos \text{WAZ2} \cos \omega \\ &+ \cos \text{DEC} \sin \text{TLT} \sin \text{WAZ2} \sin \omega\end{aligned} \tag{1.5.3b}$$

WAZ2 is the WAZ measured from due south, positive for orientations west of south and vice versa. The symbol ω in Eq. (1.5.3b) represents the solar hour angle, 15° for each hour displaced from the true solar noon.

Prog1-6.For contains outputs from both of the above formulations for INC. Figure 1.5.1 shows the angles relevant to the determination of sun's position and the geometry for a tilted surface. Table 1.5.1 compares the computations of the present routine against Kreider and Kreith (1981). The maximum difference between presently computed values of solar altitude and azimuth and those given by Kreider and Kreith (1981) may be up to 0.5°. The presently generated values of the solar co-ordinates are, of course, much more precise and the approximate nature of the older algorithms has thus been demonstrated. This is owing to the fact that the older algorithms use values of EOT and DEC for 0 h UT, whereas the present routine evaluates these for the precise moment for which the solar geometry is required.

Example 1.5.1

Calculate the solar altitude and sun's azimuth for Edinburgh, UK (lat. = 55.95°N and long. = 3.20°W) at 12 noon LCT on 21 March 1997. Also, find the angle of incidence of the sun's beam on a surface with a given tilt of 45° and orientation 15°W of south.

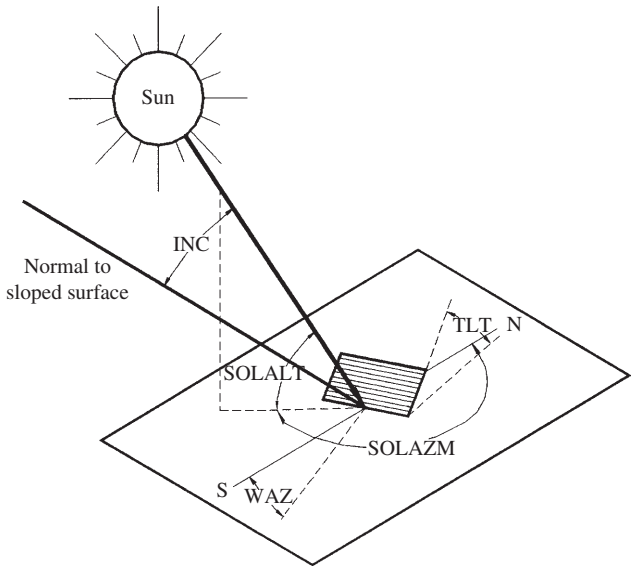

Figure 1.5.1 *Solar geometry of a sloped surface*

Table 1.5.1 Solar geometry: evaluation for the 21st day of each month*

	Solar altitude		Solar azimuth**	
	Prog1-6 (deg)	Kreider and Kreith (1981) (deg)	Prog1-6 (deg)	Kreider and Kreith (1981) (deg)
January	28.5	28.0	163.8	164.0
February	37.6	37.0	161.1	161.0
March	48.0	48.0	157.0	157.0
April	59.1	59.0	151.2	151.0
May	66.5	66.0	142.8	143.0
June	68.9	69.0	137.2	138.0
July	66.6	66.0	142.2	143.0
August	59.0	59.0	150.5	151.0
September	48.3	48.0	157.0	157.0
October	37.3	37.0	161.2	161.0
November	28.4	28.0	164.0	164.0
December	25.1	25.0	165.3	165.0

* Corresponds to 11 h AST for 40° N.
** Clockwise from true north.

Note that the required input value of the WAZ is 195° (=180 + 15).

For the above data Prog1-6.Exe produces the following output:

EOT = −0.1196 h
AST = 11.667 h
solar hour angle = −4.99°
DEC = 0.3626°

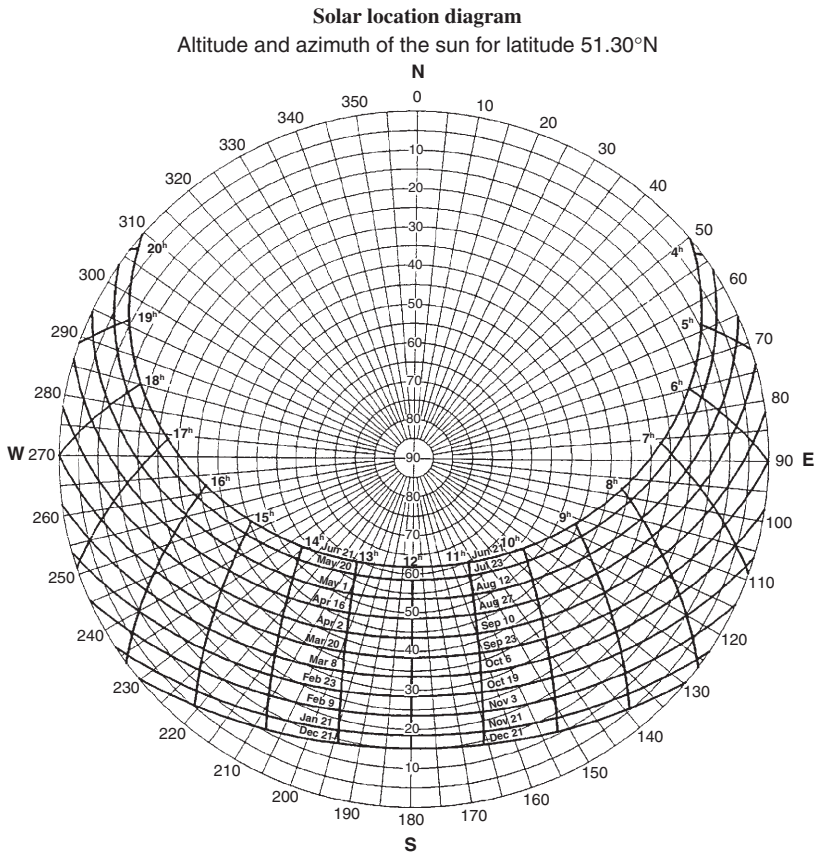

Figure 1.5.2 *Sun-path diagram for London, 50.5°N*

SOLALT = 34.27°
SOLAZM = 173.95°
INC (formulation 1: Eq. (1.5.3a)) = 19.35°
INC (formulation 2: Eq. (1.5.3b)) = 19.35°

The point of interest here is that SOLAZM is almost 6° away from the usually assumed value of 180° for solar noon LCT. For example, the solar geometry tables presented in *CIBSE Guide A2* (1982) do not draw a line of demarcation between the two time frames, LCT and AST. It has been demonstrated herein that this may lead to errors of the above-mentioned magnitude.

1.5.1 Sun-path (solar location) diagrams

In the above example the use of Prog1-6.Exe was demonstrated to precisely obtain solar geometry. Often architects prefer to use paper-based tools such as nomograms that provide a quick and ready reference for solar geometry for obtaining shadow profiles of surrounding landscape. Towards that end two nomograms, Figures 1.5.2 and 1.5.3, are provided for

two UK locations – London and Edinburgh. The use of this nomogram is now demonstrated via Example 1.5.2.

Note that nomograms for any given location may be produced by using Prog1-6.For after suitable modifications have been made to execute it in a dual-nested loop, one loop for given dates and the other for time of the day.

Example 1.5.2

Using Figure 1.5.3 which presents the sun-path diagram for Edinburgh (55.95°N), obtain the solar altitude and solar azimuth for 1 May at 1300 h solar time.

A graphical solution to the above problem may easily be obtained via intersection of the curvilinear lines for 1 May and 1300 h (13 h). The solar altitude and azimuth are respectively read off as 47.5° and 202°. Note that Prog1-6.Exe gives the corresponding outputs as 47.5125° and 201.7183°.

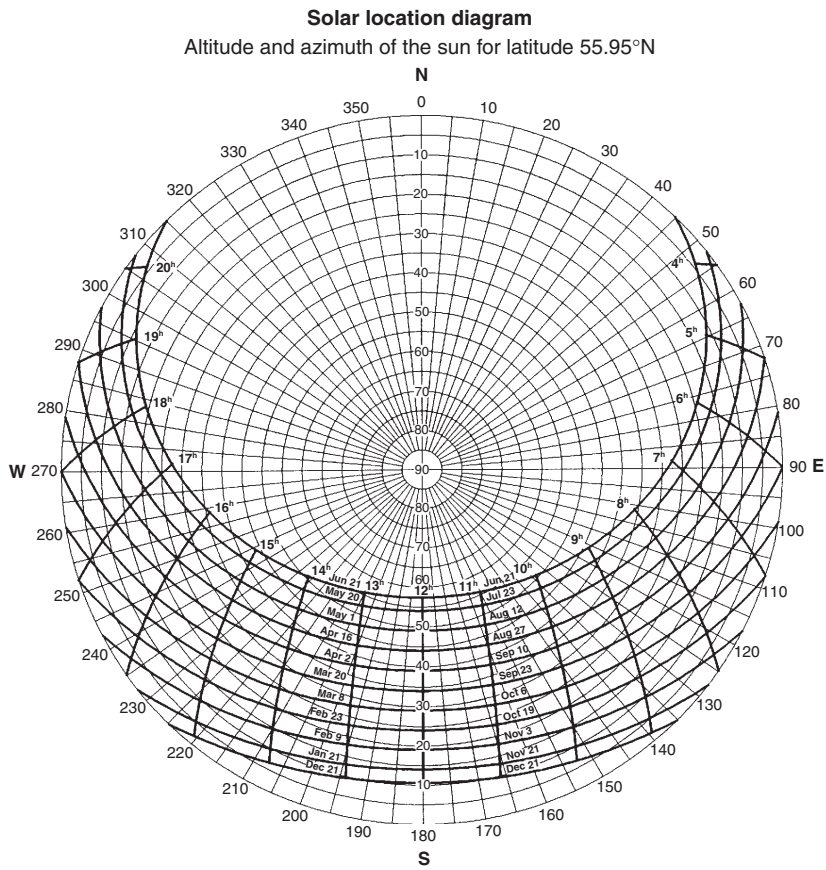

Figure 1.5.3 *Sun-path diagram for Edinburgh 55.95°N*

1.6 Astronomical sunrise and sunset

Figure 1.6.1 shows the sun-path geometry for a location with an approximate latitude of 50°N. Likewise, Figure 1.6.2 shows the sun's trajectory for a northerly location. Note the shift of solar azimuth angle for sunrise and sunset when the season changes from mid-winter to mid-summer.

Astronomers define sunrise and sunset as the moment at which the centre of the solar disk is along the horizon of the earth. It was shown above that sun's position in the sky could be determined in terms of the elevation angle (SOLALT) and the azimuth of the sun's beam from north (SOLAZM). Using Eq. (1.5.1), the sunrise/sunset instance may be

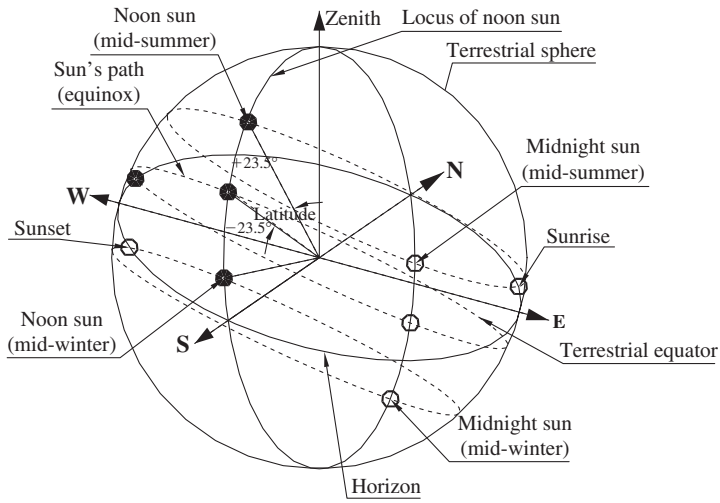

Figure 1.6.1 *Sun-path geometry for an approximate latitude of 50°N*

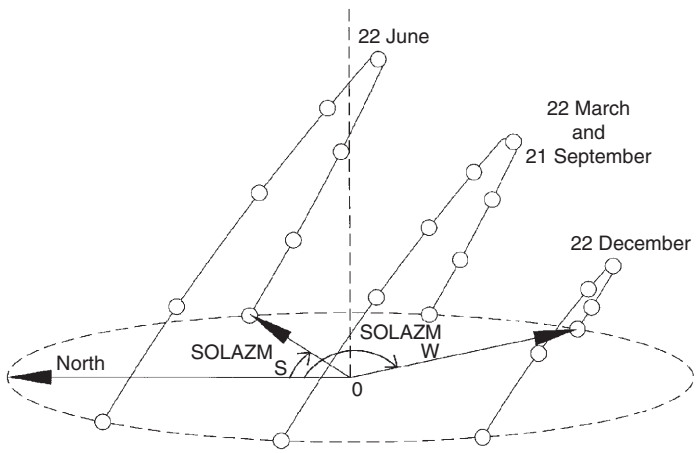

Figure 1.6.2 *Trace of sun's path for a northerly location*

computed by setting the SOLALT = 0. The sunrise/sunset instance may then be estimated by using Eq. (1.3.1) to obtain the standard time (LCT).

1.7 Actual sunrise and sunset

The actual sunrise and sunset do not occur at the time when the sun's elevation is zero. This is due to the refraction of light by terrestrial atmosphere. A ray of light travelling in vacuum from the sun which is actually below the earth's horizon is bent towards the earth by the heavier medium, air (the average refractive index of atmospheric air is 1.0003). Hence actual sunrise appears slightly before astronomical sunrise and actual sunset occurs after astronomical sunset. Further, for locations which are higher than the sea level, the sun will appear in the morning slightly earlier. Corrections have therefore to be made for the above refraction and altitude effects. These are expressed via the following equation for SOLALT which refers to the instance of actual sunrise or sunset:

$$\text{SOLALT} = -0.8333 - 0.0347H^{0.5} \tag{1.7.1}$$

H in the above equation is to be given in metres above sea level (m ASL). Equation (1.5.1) is then solved in conjunction with Eq. (1.3.1) to obtain the corresponding LCT.

1.8 Twilight

Twilight is defined as the pre-sunrise or post-sunset period of partial daylight and is caused by the reflection and scattering of sunlight towards the horizon of any terrestrial observer. Twilight has an important biological and socio-religious significance. At any one instant, the twilight zone covers 20–25% surface area of our globe and humans, on an average, live under the twilight band for a quarter of the time. In the tropics, due to the sun's steep descent towards the horizon, twilight occupies only 10–15% of the diurnal cycle. However, in the higher latitudes such as those of northern Europe, twilight occupies up to two-fifths of the annual cycle.

Soon after sunset the illuminance progressively diminishes in an exponential manner until the sun sinks to an elevation angle of $-18°$. This is the instance of the last stage of receipt of light emanating from the sun (astronomical twilight). The negative elevation angle, which corresponds to the period of twilight, is also expressed as the angle of depression. Thus, when SOLALT $= -18°$, the depression angle $= 18°$.

Various stages of twilight have been standardised, e.g. civil and nautical twilight, respectively, when the solar depression angles are 6° and 12° (see Figure 1.8.1). Civil twilight is the stage when enough illuminance exists to enable outdoor civil activity to continue unhindered without resorting to the use of electric street lighting. The nautical twilight is the stage which establishes the limit of the visibility of ships approaching a harbour.

The following illuminance figures (values in lux) for the above three stages of twilight have been attributed to the famous physicist Kimball. For a horizontal surface under a cloudless sky:

sun at zenith:	103 000
sun at horizon:	355

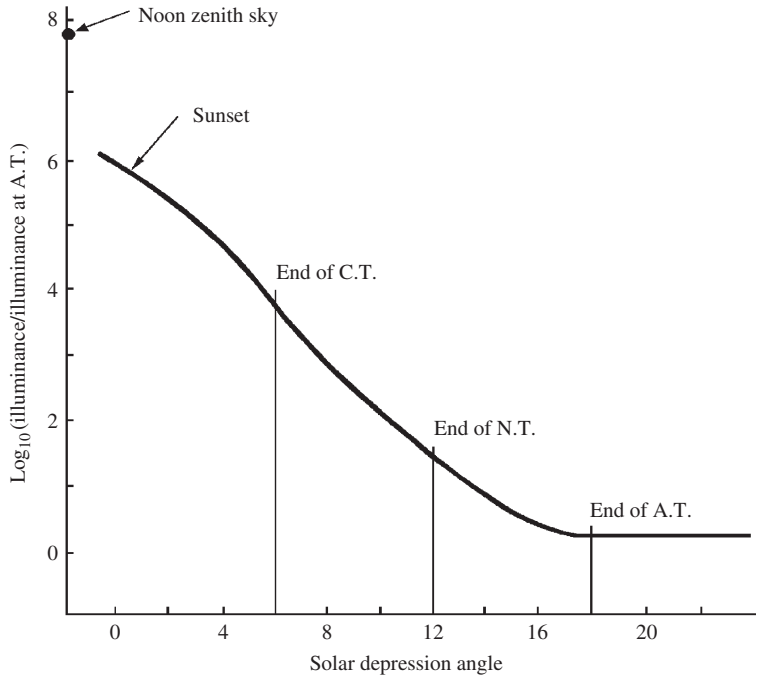

Figure 1.8.1 *Variation of daylight and twilight*

end of civil twilight:	4.3
end of astronomical twilight:	0.001
full moon at zenith:	0.215

It is with some fascination we note that the change in illuminance from noon to astronomical twilight is around 100 million! Even between the sunset to the end of twilight instance the change is about 400 000. Yet the human eye being a logarithmic sensor is able to cope with such wide ranging illuminance levels. Laboratory measurements of daylight and twilight are undertaken with sensors which operate in much narrower ranges.

An exhaustive review of the research undertaken on twilight phenomenon and its measurement has been presented by Rozenberg (1966). Presently, Prog1-7.Exe enables computation of the actual sunrise/sunset times and the above three stages of twilight. This is demonstrated via the following example.

Example 1.8.1

Calculate for the city of Edinburgh (lat. = 55.95°N, long. = 3.2°W and altitude = 35 m ASL) the sunrise/sunset times and the times for the end of civil, nautical and astronomical twilight for 1 March 1996.

Prog1-7.Exe produces the following output (in hours):

sunrise at	0702
sunset at	1748

astronomical twilight appears at	0500
nautical twilight appears at	0543
civil twilight appears at	0626

It is worth noting that at mid-summer, between Arctic Circle and 48.5°N, there is a belt with no true night, i.e. the astronomical twilight extends from sunset to sunrise. This is due to the fact that the solar depression angle for 21 June for 48.5°N (and even more so for the northerly latitudes) is less than 18°, the last stage of astronomical twilight. Thus, the temporal period of no true night progressively widens as one crosses to more northerly latitudes. Prog1-7.Exe has the capability to handle such cases with robustness. The reader is invited to use this particular software for any of the northern locations for dates around mid-summer, e.g. estimation of the data obtained in Example 1.8.1 for London for, say, 15 June.

1.9 Distance between two locations

In Chapter 2 of this book it will be shown that daily values of solar irradiation are more accurately estimated from local sunshine observations than by assignment from nearby pyranometric stations if the latter are more than 20 km away. For monthly-averaged daily totals this critical distance may be taken to be about 30 km. Thus, an algorithm is required which provides the distance between any two locations, pyranometric and candidate sites, to evaluate the applicability of the above constraints. The distance sought in this case is based on the principle of great circle navigation. The algorithm given below provides the distance and heading (for shortest flight path) from the source to destination.

If we denote the geographical latitudes of the source and destination, respectively, as LatS and LatD and the longitudes as LongS and LongD, then the distance between the locations is obtainable from the following suite of equations:

$$\text{Dterm} = [\sin(\text{LatS})\sin(\text{LatD}) + \cos(\text{LatS})\cos(\text{LatD})\cos(\text{LongD} - \text{LongS})] \quad (1.9.1)$$

$$\text{distance (nautical miles)} = 60(180/\pi)\cos^{-1}(\text{Dterm}) \quad (1.9.2)$$

$$\text{distance (km)} = \text{distance (miles)} \times 1.852 \quad (1.9.3)$$

$$\text{Hterm1} = (180/\pi)\cos^{-1}[\{\sin(\text{LatD}) - \sin(\text{LatS})\}/\{\cos(\text{LatS})(1 - \text{Dterm}^2)^{0.5}\}] \quad (1.9.4)$$

$$\text{Hterm2} = \sin(\text{LongS} - \text{LongD}) \quad (1.9.5)$$

$$\text{heading} = \text{Hterm1},\ \text{Hterm2} > 0 \quad (1.9.6a)$$

$$= 360 - \text{Hterm1},\ \text{Hterm2} < 0 \quad (1.9.6b)$$

Equation (1.9.2) provides the distance between the source and destination in nautical miles. The nautical mile is an international unit used in sea and air navigation, being 1852 m. Incidentally the older, British nautical mile = 6080 ft and hence this equals 1853 m. The nautical mile is defined as the distance subtended at the earth's equatorial plane by 1 min

Table 1.9.1 Distance between two locations: validation of Prog1-8.For (distances reported are between Dubai and a given destination)

	Latitude (north)		Longitude (east)		Prog1-8.Exe			
	(deg)	(min)	(deg)	(min)	(Naut. miles)	(km)	Emirates* (km)	% (error)
Amman	31	57	35	56	1093	2024	2020	0.2
Beirut	33	49	35	30	1150	2130	2140	−0.5
Bangkok	13	45	100	31	2636	4882	4876	0.1
Hong Kong	22	15	114	10	3212	5949	5943	0.1
Birmingham**	52	28	1	55	3025	5602	5600	0.0
Dusseldorf	51	17	6	47	2696	4993	5003	−0.2
Khartoum	15	38	32	33	1401	2595	2600	−0.2
Kuala Lampur	3	10	101	42	2985	5528	5544	−0.3
Dubai	25	18	55	18				

*Distance reported in Emirates Air flight magazine.
**Longitude west.

of longitude. A speed of one nautical mile per hour is defined as one knot, an international unit for designating sea, air and wind speeds.

A program for the above computational scheme is given in Prog1-8.For. The following example demonstrates its use.

Example 1.9.1

An hour-by-hour energy simulation is to be carried out for a prospective office building, to be situated in the city of Edinburgh (lat. = 55.95°N and long. = 3.2°W). While other climatological data is available from Turnhouse (local airport), solar radiation records are available only for Mylnefield, Dundee (56.45°N and 3.067°W). Calculate the shortest distance between the two sites in order to investigate the feasibility of using Mylnefield solar data for Edinburgh.

The output from Prog1-8.Exe is as follows:

distance = 56.2 km
heading = 8.4° (azimuth direction, clockwise from North)

Since the above distance is more than 30 km, neither the daily nor monthly-averaged solar radiation data from Mylnefield may reliably be used for Edinburgh.

Table 1.9.1 has been prepared as a measure of further validation of Prog1-8.For.

1.10 Solar radiation and daylight measurement

Routine measurement of diffuse solar energy from sky and the global (total) radiation incident on a horizontal surface is usually undertaken by an agency such as the national meteorological office. For this purpose the measurement network uses pyranometers, solarimeters or actinograph. Direct or beam irradiation is measured by a pyrheliometer

with a fast-response multijunction thermopile placed inside a narrow cavity tube. The aperture is designed such that it admits a cone of full angle around 6°. Most of the above irradiance sensors used across Europe are manufactured by Kipp and Zonen, while Eppley and Eko instruments are more widely used in the US and Japan, respectively.

The CM 22 is now regarded as the standard reference pyranometer due to its accuracy, stability and quality of construction. The sensing element consists of a thermal detector which responds to the total power absorbed without being selective to the spectral distribution of radiation. The heat energy generated by the absorption of radiation on the black disk flows through a thermal resistance to the heat sink. The resultant temperature difference across the thermal resistance of the disk is converted into a voltage which can be read by computer. The double glass construction minimises temperature fluctuations from the natural elements and reduces thermal radiation losses to the atmosphere. The glass domes can collect debris over time and weekly cleaning is recommended. Moisture is prevented due to the presence of silica gel crystals in the body of the CM 11. The pyranometers have a spectral response of between 335 and 2200 nm of the solar spectrum which includes the visible wavelength band.

For most stations diffuse irradiance is measured by placing a shadow band over a pyranometer, adjustment of which is required periodically. Coulson (1975) provides an excellent account of these adjustments and the associated measurement errors for the above sensors, a brief summary of which is provided herein. The object of this section is to familiarise the reader with the order of errors encountered in the measurement of solar radiation and daylight. This is very much needed to establish the upper limit of refinement in the modelling work, e.g. no model can surpass the accuracy of the measured quantity. The present state of solar radiation and daylight models is such that they are approaching the accuracy limits set out by the measuring equipment (Perez et al., 1990; Gueymard, 2003).

Radiation in the visible region of the spectrum is often evaluated with respect to its visual sensation effect on the human eye. The CIE meeting in 1924 resulted in the adoption of a standard of the above wavelength-dependent sensitivity. The CIE standardised sensitivity of daylight adapted human eye is presented in Table 1.10.1.

Table 1.10.1 CIE standard spectral relative sensitivity of the daylight adapted human eye

Wavelength (μm)	Relative sensitivity	Wavelength (μm)	Relative sensitivity	Wavelength (μm)	Relative sensitivity
0.38	0.0000	0.51	0.5030	0.64	0.1750
0.39	0.0001	0.52	0.7100	0.65	0.1070
0.40	0.0004	0.53	0.8620	0.66	0.0610
0.41	0.0012	0.54	0.9540	0.67	0.0320
0.42	0.0040	0.55	0.9950	0.68	0.0170
0.43	0.0116	0.56	0.9950	0.69	0.0082
0.44	0.0230	0.57	0.9520	0.70	0.0041
0.45	0.0380	0.58	0.8700	0.71	0.0021
0.46	0.0600	0.59	0.7570	0.72	0.0010
0.47	0.0910	0.60	0.6310	0.73	0.0005
0.48	0.1390	0.61	0.5030	0.74	0.0003
0.49	0.2080	0.62	0.3810	0.75	0.0001
0.50	0.3230	0.63	0.2650	0.76	0.0001

Illuminance measuring sensors are known as either photometers or daylight sensors. These sensors are similar in construction to the above-mentioned pyranometers. Daylight illuminance is not one of the quantities routinely measured by the meteorological networks. There is therefore a dearth of measured illuminance data. However, in 1991 in response to the call made by CIE's IDMP, new activity was seen across the globe. For example during 1991–95 a total of 14 daylight and solar radiation measurement stations were operational in Japan. In France, UK and the USA the respective number of stations were 5, 4 and 3. Most of the European sensors in current use were manufactured by the German vendors PRC Krochmann while the Japanese equipment has been built by Tokyo-based EKO company.

Owing to the fact that there is a relative abundance of solar radiation data it is common practice to correlate the illuminance values against irradiation figures. Such models are known as luminous efficacy models and will be described in Chapter 3.

In many countries, diurnal duration of bright sunshine is measured at a wide number of places. The hours of bright sunshine is the time during which the sun's disk is visible. For over a century these data have been measured using the well-known Campbell–Stokes sunshine recorder which uses a solid glass spherical lens to burn a trace of the sun on a treated paper, the trace being produced whenever the beam irradiation is above a critical level. Although the above critical threshold varies loosely with the prevailing ambient conditions, the sunshine recorder is an economic and robust device and hence used widely.

The limitations of the Campbell–Stokes sunshine recorder are well known and have been discussed in *Observers' Handbook* (1969), Painter (1981) and Rawlins (1984). Some of the associated limitations with this device are that the recorder does not register a burn on the card below a certain level of incident radiation (about 150–300 W/m^2). On a clear day with a cloudless sky the burn does not start until 15–30 min after sunrise and usually ceases about the same period before sunset. This period varies with the season. On the other hand under periods of intermittent bright sunshine the burn spreads. The diameter of sun's image formed by the spherical lens is only about 0.7 mm. However, a few seconds' exposure to bright sunshine may produce a burnt width of about 2 mm. As such, intermittent sunshine may be indistinguishable from a longer period of continuous sunshine.

In the past a more sophisticated photoelectric sunshine recorder called the Foster sunshine switch (Foster and Foskett, 1953) has been used by the US Weather Service. This device incorporates two photovoltaic cells, one shaded and the other exposed to solar beam. Incident beam irradiation above a given threshold produces a differential output from the above two cells, the diurnal duration of which determines the hours of bright sunshine.

1.10.1 Equipment error and uncertainty

With any measurement there exist errors, some of which are systematic and others inherent of the equipment employed. Angus (1995) has provided an account of the measurement errors associated with solar irradiance and illuminance measurements. These are summarised herein. The most common sources of error arise from the sensors and their construction. These are broken down into the most general types of error as follows:

(a) cosine response
(b) azimuth response
(c) temperature response

(d) spectral selectivity
(e) stability
(f) non-linearity
(g) thermal instability
(h) zero offset due to nocturnal radiative cooling.

To be classed as a secondary standard instrument (such as the CM 11) pyranometers have to meet the specifications set out by World Meteorological Organisation (WMO).

Of all the aforementioned errors, the cosine effect is the most apparent and widely recognised. This is the sensor's response to the angle at which radiation strikes the sensing area. The more acute the angle of the sun, i.e. at sunrise and sunset, the greater this error (at altitude angles of sun below 6°). Cosine error is typically dealt with through the exclusion of the recorded data at sunrise and sunset times.

The azimuth error is a result of imperfections of the glass domes, and in the case of solarimeters the angular reflection properties of the black paint. This is an inherent manufacturing error which yields a similar percentage error as the cosine effect.

Like the azimuth error, the temperature response of the sensor is an individual fault for each cell. The photometers are thermostatically controlled, and hence the percentage error due to fluctuations in the sensor's temperature are reduced. However, the CM 11 pyranometers have a much less elaborate temperature control system. The pyranometers rely on the two glass domes to prevent large temperature swings. Ventilation of the instrument is an additional recommended option.

The spectral selectivity of the CM 11 is dependent on the spectral absorptance of the black paint and the spectral transmission of the glass. The overall effect contributes only a small percentage error to the measurements. Each sensor possesses a high level of stability with the deterioration of the cells resulting in approximately $\pm 1\%$ change in the full scale measurement per year. Finally, the non-linearity of the sensors is a concern especially with photometers. It is a function of illuminance or irradiance levels. It however tends to contribute only a small percentage error towards the measured values. Table 1.10.2 provides details of the above-mentioned uncertainties. In addition to the above sources of equipment-related errors care must be taken to avoid operational errors such as incorrect sensor levelling and orientation of the vertical sensors, as well as improper screening of the vertical sensors from ground-reflected radiation.

1.10.2 Operational errors

(a) Complete or partial shade-ring misalignment
(b) Dust, snow, dew, water droplets, bird droppings, etc.
(c) Incorrect sensor levelling
(d) Shading caused by building structures
(e) Electric fields in the vicinity of cables
(f) Mechanical loading on cables
(g) Orientation and/or improper screening of the vertical sensors from ground-reflected radiation
(h) Station shut down
(i) Improper application of diffuse shade-ring correction factor
(j) Inaccurate programming of calibration constants.

Table 1.10.2 WMO classification of pyranometers

Characteristic	Secondary standard	First class	Second class
Resolution (smallest detectable change in W/m^2)	±1	±5	±10
Stability (percentage of full scale, change/year)	±1	±2	±5
Cosine response (percentage deviation from ideal at 10° solar elevation on a clear day)	<±3	<±7	<±15
Azimuth response (percentage deviation from ideal at 10° solar elevation on a clear day)	<±3	<±5	<±10
Temperature response (percentage maximum error due to change of ambient temperature within the operating range)	±1	±2	±5
Non-linearity (percentage of full scale)	±0.5	±2	±5
Spectral sensitivity (percentage deviation from mean absorptance 0.3–3 μm)	±2	±5	±10
Response time (99% response)	<25 s	<1 min	<4 min

The sources of operation-related errors itemised above are self-explanatory. It is good practice to protect cables from strong electric fields such as elevator shafts. Another source of error that may arise is from cables under mechanical load (piezoelectric effects). The piezoelectric effect is the production of electrical polarisation in a material by the application of mechanical stress. Failure to protect cables from the above sources may produce 'spikes' in the data and these are shown as unusually high values of irradiance. Figure 1.10.1 demonstrates the sources of error categorised under items (a) and (b) discussed above. Such errors are best highlighted via cross plotting the diffuse ratio (the ratio of horizontal sky diffuse and the total or global irradiance) against clearness index (the ratio of horizontal global to extraterrestrial irradiance). Any serious departure of data from the normally expected envelope is thus identified. Further light is shed on this quality control procedure in Chapter 3.

Figure 1.10.2 highlights error categorised under item (f).

1.10.3 Diffuse-irradiance data measurement errors

Historically, meteorological offices worldwide have used shade-ring correction procedure that is based on the assumption of an isotropic sky. However, during the past 15 years a number of alternate, more precise methods that are based on a realistic, anisotropic sky have been established (15–16). The older, isotropic-sky corrected diffuse-irradiation records are slightly higher for overcast conditions and lower by up to 10% for clear-sky conditions. It is imperative that due care is taken in using a precise and validated shade-ring correction procedure since any errors in horizontal diffuse-irradiance records will be multiplied by a large factor when horizontal beam irradiance and subsequently the total slope energy computations are undertaken.

1.10.4 Types of sensors and their accuracies

A survey of radiation instruments undertaken by Lof et al. (1965) showed that of the 219 sensors in use across Europe, 65 were of the CM11 type pyranometers while 107 sensors were the simpler and less expensive Robitzch actinographs with a bimettalic temperature

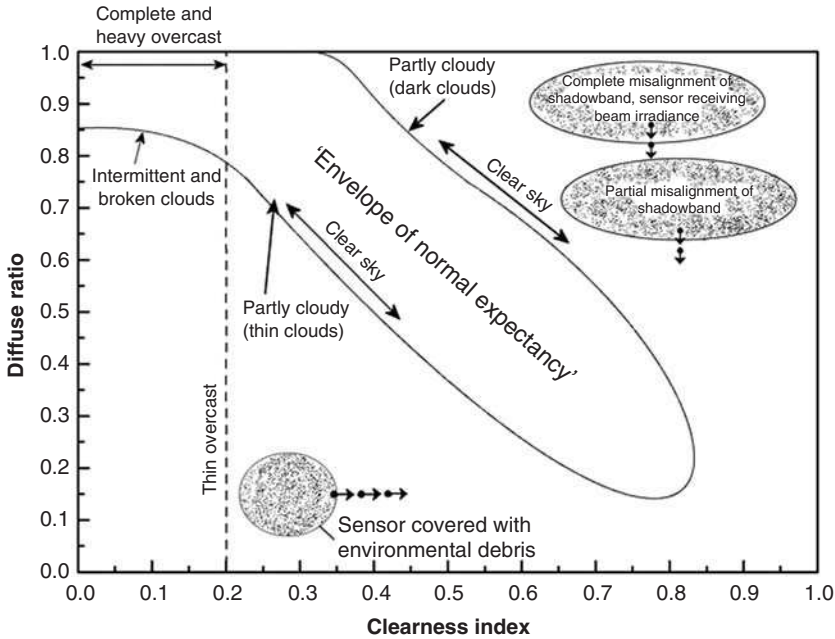

Figure 1.10.1 *Demonstration of the sources of measurement errors*

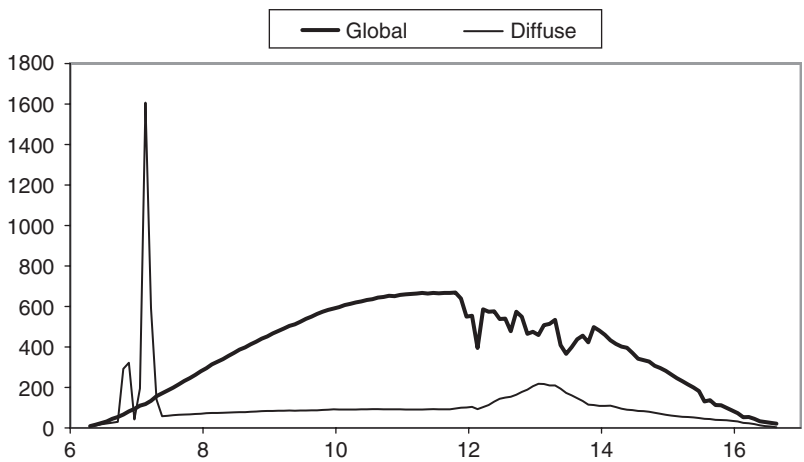

Figure 1.10.2 *Demonstration of problems associated with mechanical loading of cables connecting datalogger to irradiance sensor. Note:5 min averaged data for Bahrain for 12 December 2001 (x-axis: the time of the day, y-axis: irradiance, W/m^2)*

element. The latter instrument is also quite popular in the developing Asian (89 such sensors were reported to be in use), African (16 sensors) and South American (47 sensors) countries where maintenance is often the key factor. The author has in the past visited a solar radiation measurement station in the middle of the Sahara desert and seen the Robitzch actinograph faithfully recording a regular trace of irradiation. The weekly changeover of the recording chart makes this instrument an ideal choice for remote locations. Although not in use with the North American meteorological network, it is known to be of use over there in biological and agriculture-related work (Coulson, 1975).

Drummond (1965) estimates that accuracies of 2–3% are attainable for daily summations of radiation for pyranometers of first class classification. Individual hourly summations even with carefully calibrated equipment may be in excess of 5%. Coulson (1975) infers that the errors associated with routine observations may be well in excess of 10%. Isolated cases of poorly maintained equipment but those which are in the regular network may exhibit monthly-averaged errors of 10% or more. The Robitzch actinograph, even with all the modifications to improve its accuracy is suitable only for daily summations. At this interval it provides an accuracy of around 10%. However, not all designs of the latter sensor can claim even this level of accuracy. These figures must be borne in mind when evaluating the accuracy of the relevant computational models.

1.10.5 Innovative developments

Delta-T device of Cambridge, England have produced a new instrument that measures the horizontal global and diffuse irradiance as well as sunshine duration from a single, stationary sensor. Unlike the Campbell–Stokes sunshine recorder the Delta-T device neither requires any cards or shade ring for the measurement of sky-diffuse irradiance. The BF3 model, shown in Figure 1.10.3, enables simultaneous recording of the above-mentioned three sets of data. The electronic outputs are compatible with electronic data loggers and work at any latitude.

Figure 1.10.3 *The BF3 sensor (photo courtesy of Delta-T, Cambridge, England)*

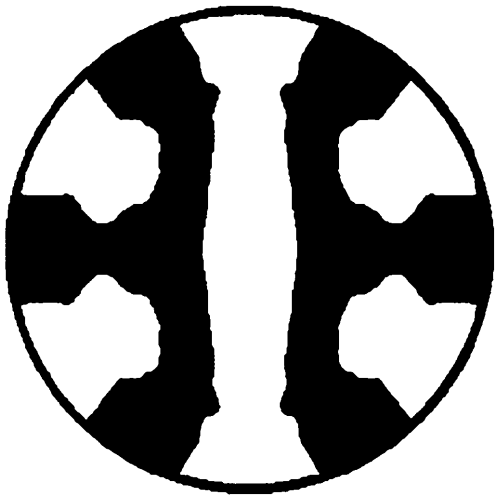

Figure 1.10.4 *Hemispherical shading pattern for Delta-T BF3 irradiance sensor*

The device uses a system of photodiodes and a shading pattern such that wherever the sun is in the sky at least one photodiode is always exposed to the full solar beam and at least another one diode is always completely shaded. All photodiodes receive an equal sampling of diffuse light from the rest of the sky hemisphere. A special layout of seven photodiodes on a hexagonal grid, covered by a hemispherical shading pattern, ensures the satisfaction of the above constraints. A sketch of the shading pattern of BF3 is shown in Figure 1.10.4, plotted in a 180° fisheye lens view.

The sensor has a digital output of sunshine presence. This is defined by the WMO as the duration with irradiance greater than 120 W/m^2 in the direct beam measured perpendicular to the beam. The microprocessor algorithm uses the measured global and diffuse irradiance to provide an estimate of sunshine duration.

An account of BF3's performance, evaluated against Kipp and Zonen irradiance sensors and Campbell–Stokes sunshine recorders, has been presented by Wood et al. (2003).

1.11 Statistical evaluation of models

Checking on the adequacy of the mathematical model describing any physical process such as a given solar radiation model is important not only in the final stages of the work programme, but more particularly in the initial phase. An examination of residuals is recommended. The procedure is to produce a graph of the residuals d (the difference between observed Y_o and calculated Y_c values of the dependent variable) plotted against the independent variable X or the observed value Y_o.

If the residuals fall in a horizontal band as shown in Figure 1.11.1(a), the model may be judged as adequate. If the band widens as X or Y_o increases, displayed in Figure 1.11.1(b), this indicates a lack of constant variance of the residuals. The corrective measure in this case is a transformation of the Y variable. A plot of the residuals such as Figure 1.11.1(c) indicates the absence of an independent variable in the model under examination. If, however, a plot such as Figure 1.11.1(d) is obtained, a linear or quadratic term would have to be added.

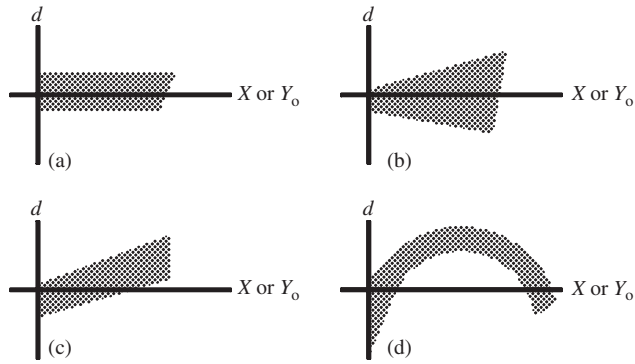

Figure 1.11.1 *Plot of residuals for evaluating the adequacy of the model: (a) adequacy, (b)* Y_o *needs transformation, (c) missing linear independent variable and (d) missing linear or quadratic independent variable*

In the forthcoming chapters a number of models will be presented wherein one dependent variable is regressed against one or several independent variables. Often correlation between two quantities is also to be examined. In solar energy literature it has become common practice to refer regression models as 'correlation equations'. Strictly speaking this is wrong usage of statistician's language. Correlation is the degree of relationship between variables and one seeks to determine how well a linear or other model describes the relationship. On the other hand, regression is a technique of fitting linear or non-linear models between a dependent and a set of independent variables. Thus fitting an equation of the form:

$$Y = a_0 + a_1 X \tag{1.11.1}$$

for n pairs of (X,Y) is an example of linear regression. On the other hand fitting:

$$Y = a_0 \exp(a_1 X) + b_0 \sin(b_1 X) \tag{1.11.2}$$

is an example of a non-linear model. A number of low-priced software packages are available which adequately cover the requirements of fitting linear and non-linear models. The popular spreadsheet packages such as Lotus 1-2-3 (a product of Lotus Corporation) and Excel (a product of Microsoft Corporation) as well as more specialist statistical packages such as SOLO and BMDP (products of BMDP Statistical Software Inc., California) are a few examples. For handling very large data arrays one has to resort to FORTRAN and C environments. The text *Numerical Recipes* by Press et al. (1992), with its companion electronic suite of programs, offers solutions at this end. All of the above packages use robust and efficient routines which obviate any particular need for developing optimisation programs from scratch. In the following paragraphs, a brief discussion on the statistical examination of models is provided.

1.11.1 Coefficient of determination r^2

The ratio of explained variation, $\sum(Y_c - Y_m)^2$, to the total variation, $\sum(Y_o - Y_m)^2$, is called the coefficient of determination. Y_m is the mean of the observed Y values. The ratio lies

between zero and one. A high value of r^2 is desirable as this shows a lower unexplained variation.

1.11.2 *Coefficient of correlation* r

The square root of the coefficient of determination is defined as the coefficient of correlation *r*. It is a measure of the relationship between variables based on a scale ranging between $+1$ and -1. Whether *r* is positive or negative depends on the inter-relationship between *x* and *y*, i.e. whether they are directly proportional (*y* increases and *x* increases) or vice versa.

Once *r* has been estimated for any fitted model its numerical value may be interpreted as follows. Let us assume that for a given regression model $r = 0.9$. This means $r^2 = 0.81$. It may be concluded that 81% of the variation in *Y* has been explained (removed) by the model under discussion, leaving 19% to be explained by other factors.

1.11.3 *Student's* t*-distribution*

Often the modeller is faced with the question as to what quantitative measure is to be used to evaluate the value of r^2 obtained for any given model (Owen and Jones, 1990). Clearly, r^2 would depend on the size of the data population. For example, a lower value of r^2 obtained for a model fitted against a large database may or may not be better than another model which used a smaller population. In such situations, the Student's *t*-test may be used for comparing the above two models. The following example demonstrates the use of this test of significance for r^2.

Example 1.11.1

For a given location a regression model between average clearness index ($\overline{K}_T$) and monthly-averaged sunshine fraction (n/N) gives $r^2 = 0.64$ for 12 pairs of data points. Using Student's *t*-test investigate the significance of *r*.

The test statistic $t = (n-2)^{0.5}\{r/\sqrt{(1-r^2)}\}$, where *n* is the number of data points and $(n-2)$ is the degrees of freedom (d.f.).

Thus:

$$\text{Test statistic } t = (12-2)^{0.5}\{0.8/\sqrt{(1-0.64)}\} = 4.216$$

In this example there are 10°d.f. Thus from Table 1.11.1 the value of $r = 0.8$ is significant at 99.8% but not at 99.9% (note that for d.f. $= 10$ and $t = 4.216$ lies between 4.144 and 4.587 corresponding to columns for 0.998 and 0.999 respectively).

In layman terms this means that using the above regression model, K_T may be estimated with a 99.8% confidence.

1.11.4 *Mean bias error, mean of absolute deviations and root mean square error*

To enable further insight in the performance evaluation of a model, mean bias errors (MBEs), mean of absolute deviations (MADs) and root mean square errors (RMSEs)

Table 1.11.1 Percentile values for Student's *t*-distribution

d.f	$P = 0.95$	0.98	0.99	0.998	0.999
1	12.706	31.821	63.657	318.310	636.620
2	4.303	6.965	9.925	22.327	31.598
3	3.182	4.541	5.841	10.214	12.924
4	2.776	3.747	4.604	7.173	8.610
5	2.571	3.365	4.032	5.893	6.869
6	2.447	3.143	3.707	5.208	5.959
7	2.365	2.998	3.499	4.785	5.408
8	2.306	2.896	3.355	4.501	5.041
9	2.262	2.821	3.250	4.297	4.781
10	2.228	2.764	3.169	4.144	4.587
15	2.131	2.602	2.947	3.733	4.073
20	2.086	2.528	2.845	3.552	3.850
25	2.060	2.485	2.787	3.450	3.725
30	2.042	2.457	2.750	3.385	3.646
40	2.021	2.423	2.704	3.307	3.551
60	2.000	2.390	2.660	3.232	3.460
120	1.980	2.358	2.617	3.160	3.373
200	1.972	2.345	2.601	3.131	3.340
500	1.965	2.334	2.586	3.107	3.310
1000	1.962	2.330	2.581	3.098	3.300
∞	1.960	2.326	2.576	3.090	3.291

may be obtained. These are defined as:

$$\text{MBE} = \sum (Y_c - Y_o)/n \tag{1.11.3a}$$

$$\text{MAD} = \sum \text{abs}(Y_c - Y_o)/n \tag{1.11.3b}$$

$$\text{RMSE} = \left[\sum (Y_c - Y_o)^2/n\right]^{1/2} \tag{1.11.4}$$

The above formulae provide MBE, MAD and RMSE which have the same physical units as the dependent variable, *Y*. In some instances non-dimensional MBE (NDMBE), MAD (NDMAD) and RMSE (NDRMSE) are required. These are obtained as:

$$\text{NDMBE} = \sum \left[(Y_c - Y_o)/Y_o\right]/n \tag{1.11.5a}$$

$$\text{NDMAD} = \sum \text{abs}[(Y_c - Y_o)/Y_o]/n \tag{1.11.5b}$$

$$\text{NDRMSE} = \left\{\sum [(Y_c - Y_o)/Y_o]^2/n\right\}^{1/2} \tag{1.11.6}$$

The MBE provides a measure of the overall trend of a given model, i.e. predominantly overestimating (positive values) or underestimating (negative values). The MAD is similar to RMSE and provides a measure of absolute deviations.

1.11.5 Outlier analysis

Often in solar radiation studies one encounters data that lie unusually far removed from the bulk of the data population. Such data are called 'outliers'. One definition of an outlier is that it lies three or four standard deviations or more from the mean of the data population. The outlier indicates peculiarity and suggests that the datum is not typical of the rest of the data. As a rule, an outlier should be subjected to particularly careful examination to see whether any logical explanation may be provided for its peculiar behaviour. Automatic rejection of outliers is not always very wise. Sometimes an outlier may provide information that arises from unusual conditions. Outliers may however be rejected if the associated errors may be traced to erroneous observations due to any one or a combination of factors described in Sections 1.10.1–1.10.3.

Statistically, a 'near outlier' is an observation that lies outside 1.5 times the inter-quartile range. The inter-quartile is the interval from the 1st quartile to the 3rd quartile. The *near outlier* limits are mathematically defined by:

$$\text{Lower outlier limit: 1st quartile} - 1.5(\text{3rd quartile} - \text{1st quartile}) \tag{1.11.7}$$

$$\text{Upper outlier limit: 3rd quartile} + 1.5(\text{3rd quartile} - \text{1st quartile}) \tag{1.11.8}$$

Likewise, *far outliers* are defined as the data whose limits are defined below:

$$\text{Lower limit: 1st quartile} - 3(\text{3rd quartile} - \text{1st quartile}) \tag{1.11.9}$$

$$\text{Upper limit: 3rd quartile} + 3(\text{3rd quartile} - \text{1st quartile}) \tag{1.11.10}$$

A high number of outliers in a given data set signifies that the observations have a high degree of variability or a large set of suspect data indicating poor station operation.

For a more rigorous discussion on outlier analysis reference is made to Draper and Smith (1998) and Montgomery and Peck (1992).

1.12 Exercises

1.12.1 Calculate the EOT and DEC for 12 h on 15 October 2002 using the FORTRAN executable routines Prog1-3.Exe through to Prog1-6.Exe. Compare your computations with the figures given in Table 1.2.3.

1.12.2 Calculate the solar altitude and solar azimuth for 12 h LCT on 15 October 2002 for Belfast (54.583°N and 5.917°W) using Prog1-6.Exe. What would be the error in the estimation of the above angles if the difference between the AST and LCT was disregarded. Also obtain the incidence angle of the sun's beam on a south facing vertical surface.

1.12.3 Estimate the twilight illuminance under a clear sky for London (51.5°N and 0.167°W) at 10 p.m. on 21 June. You may use Prog1-6.Exe to obtain the solar altitude (or solar depression angle) and then use Figure 1.8.1 to interpolate the required illuminance.

1.12.4 Long-term records of solar radiation are available for Sutton Bonnington in England (52.833°N and 1.25°W). Calculate the distance between this location and Leicester (52.633°N and 1.083°W) and hence check the validity of the above-mentioned records for the latter site. (Hint: recall that in Section 1.9 the limiting distance for the applicability of use of such data was shown to be 30 km).

References

Angus, R.C. (1995) *Illuminance Models for the United Kingdom*. PhD thesis, Napier University, Edinburgh.

Astronomical Phenomena (1993). HM Nautical Almanac Office, HMSO, London.

CIBSE Guide A2 (1982) Chartered Institution of Building Services Engineers, London.

Coulson, K.L. (1975) *Solar and Terrestrial Radiation*. Academic Press, New York.

Draper, N. and Smith, H. (1998) *Applied Regression Analysis*. Wiley, New York.

Drummond, A.J. (1965) Techniques for the measurement of solar and terrestrial radiation fluxes in plant biological research: a review with special reference to arid zones. *Proc. Montpiller Symp.*, UNESCO.

Duffett-Smith, P. (1988) *Practical Astronomy with Your Calculator*, 3rd edn. Cambridge University Press, Cambridge, UK.

Duffie, J.A. and Beckman, W.A. (1980) *Solar Engineering Thermal Processes*. John Wiley and Sons, New York.

Edgar, S.L. (1992) *FORTRAN for the 90s*. W.H. Freeman and Co, New York.

Foster, N.B. and Foskett, L.W. (1953) A photoelectric sunshine recorder. *Bull. Am. Met. Soc*. 34, 212.

Gueymard, C. (2003) Direct solar transmittance and irradiance predictions with broadband models. Part I: detailed theoretical performance assessment. *Solar Energy*, 74, 355.

Hughes, D.W., Yallop, B.D. and Hohenkerk, C.Y. (1989) The equation of time. *Mon. Not. R. Astr. Soc.* 238, 1529.

Kreider, J.F. and Kreith, F. (1981) *Solar Energy Handbook*. McGraw-Hill, New York.

Lamm, L.O. (1981) A new analytic expression for the equation of time. *Solar Energy*, 26, 465.

Lof, G.O.G., Duffie, J.A. and Smith, C.O. (1965) World distribution of solar radiation. *Solar Energy*, 10, 27.

Montgomery, D. and Peck, E. (1992) *Introduction to Linear Regression Analysis*. Wiley, New York.

Nyhoff, L. and Leestma, S. (1995) *FORTRAN 77 and Numerical Methods for Engineers and Scientists*. Prentice Hall, Englewoods Cliff, New Jersey.

Observers' Handbook (1969) HMSO, London.

Owen, F. and Jones, R. (1990) *Statistics*. Pitman Publishing, London.

Painter, H.E. (1981) The performance of a Campbell–Stokes sunshine recorder compared with a simultaneous record of the normal incidence irradiance. *Met. Mag.* 110, 102–87.

Perez, R., Ineichen, P. and Seals, R. (1990) Modelling daylight availability and irradiance components from direct and global irradiance. *Solar Energy*, 44, 271.

Press, W.H., Teukolsky, S.A., Vetterling, W.T. and Flannery, B.P. (1992) *Numerical Recipes in FORTRAN: The Art of Scientific Computing*. Cambridge University Press, Cambridge, UK.

Rawlins, F. (1984) The accuracy of estimates of daily global irradiation from sunshine records for the United Kingdom. *Met. Mag.* 113, 187.

Rozenberg, G.V. (1966) *Twilight – A Study in Atmospheric Optics*. Plenum Press, New York.

Tregenza, P.R. (1994) *UK International Daylight Measurement Programme*. Architecture Department, University of Sheffield, UK.

Wood, J., Muneer, T. and Kubie, J. (2003) Evaluation of a novel sensor for measuring global and diffuse irradiance, and sunshine duration. *ASME, J. Solar Energy Eng.* 125(February), 43.

Woolf, H.M. (1968) *Report NASA TM-X-1646*. NASA, Moffet Field, CA, USA.

Yallop, B.D. (1992) *Technical Note*. Royal Greenwich Observatory, Cambridge.

2 DAILY IRRADIATION

Introduction

Solar energy or daylight utilisation for any site is dependent upon the quantity of the available flux. Obviously, the flux impinging upon any arbitrary surface undergoes monthly as well as diurnal variations. The measurement of the energy received from the sun, on horizontal as well as sloped surfaces, is an expensive affair. As such, few locations in the world have reliable, long-term measured irradiation data sets. Daylight records are even scarcer.

Most radiation data are given as the energy received on a horizontal surface. Since only very few applications use this configuration, there is a genuine need for insolation estimations to be carried out for sloped surfaces of any given aspect. The accuracy of these models varies from 40–50% for abbreviated techniques to the limits set out by the accuracy of the measuring equipment for modern sophisticated models (Colliver, 1991).

The frequency at which solar radiation data are required depends on the application. While in agricultural meteorology monthly-averaged or even annual-energy budget would suffice, detailed simulation studies warrant computation of inclined surface irradiation at an hourly or sub-hourly level. With the increasing interest being shown in photovoltaics (PV), researchers are demanding data to be provided at a minute's frequency. For an abbreviated analysis of solar energy systems, daily values have been used. Yet for other applications monthly-averaged hourly irradiation data are employed.

Measurements made by meteorological departments in most countries are in a manner such that the different climatic and geographical regions are covered. Usually, the number of stations which measure daily global horizontal radiation exceeds those which report both global and diffuse values. Again, fewer stations measure radiation values on an hourly rather than a day-integrated basis. A typical measurement strategy may be categorised in the following manner:

(a) global horizontal irradiation recorded on a day-integrated basis,
(b) diffuse and global horizontal irradiation recorded on a day-integrated basis,
(c) global horizontal irradiation recorded on an hourly-integrated basis,
(d) diffuse and global horizontal irradiation recorded on an hourly basis,
(e) irradiation recorded on surfaces of several orientations and tilts in addition to normal incidence beam radiation using a pyrheliometer.

The Meteorological Office network for the UK contains 56 stations in the first category (Meteorological Office, 1980a). The number of stations in the second, third, fourth and fifth categories are 23, 26, 19 and 2 respectively (Muneer and Saluja, 1985).

For any locality, where solar energy-related simulation study is to be undertaken, the amount of incident solar radiation on a given plane can be predicted with an accuracy dictated by the available data. The prediction will be more refined if it is based on detailed data, e.g. models utilising global and diffuse values will be more accurate compared to those based on global values alone.

In this chapter those models are presented which enable calculation of diffuse and global horizontal irradiation on a daily, monthly and annual basis.

2.1 Monthly-averaged daily horizontal global irradiation

Initial modelling work carried out in many countries was involved in relating daily horizontal global irradiation to duration of bright sunshine. The first phase of that work involved the development of regression equations from monthly-averaged data. However, work has progressed since then and equations which use data recorded at daily intervals have also been developed. Full exploitation may therefore be made by linking the relationships under discussion with the daily relationship between horizontal diffuse and global irradiation. In the subsequent sections analysis will be presented which enables estimation of diurnal horizontal as well as sloped global and diffuse irradiation. Figure 2.1.1 shows the scheme for estimation of monthly-averaged daily slope irradiation.

The original Ångström (1924) regression equation related monthly-averaged daily irradiation to clear day irradiation. However, this method poses the difficulty of defining a clear day. To overcome this difficulty several workers, including Page (1961), Lof et al. (1966), Schulze (1976), Hawas and Muneer (1983), Nagrial and Muneer (1984), Garg and Garg (1985), Turton (1987) and Jain and Jain (1988) have developed relationships of the form given by the following equation:

$$\overline{G} = \overline{E}\,[a + b(n/N)] \tag{2.1.1}$$

where $\overline{G}$ and $\overline{E}$ are the monthly-averaged daily terrestrial and extraterrestrial irradiation on a horizontal surface, n is the average daily hours of bright sunshine and N is the day

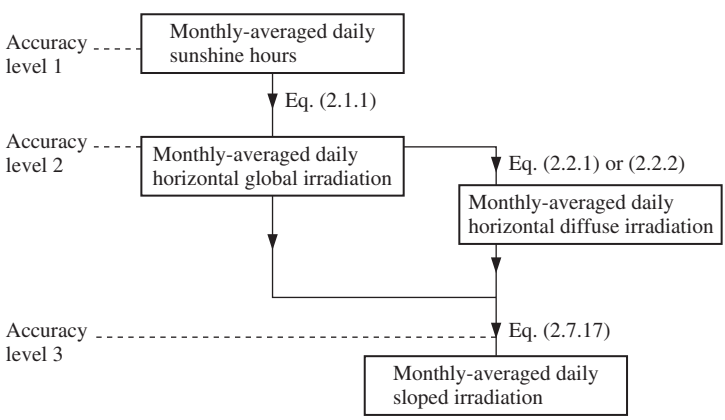

Figure 2.1.1 *Calculation scheme for monthly-averaged daily sloped irradiation*

length, obtained by:

$$\omega_s = \cos^{-1}(-\tan \text{LAT} \tan \text{DEC}) \tag{2.1.2}$$

$$N = (2\omega_s/15) \tag{2.1.3}$$

where ω_s is expressed in degrees. DEC is the solar declination angle obtained via Prog1-3.For, Prog1-5.For or Prog1-6.For (refer to Chapter 1). The ratio n/N is known as fractional possible sunshine. The extraterrestrial irradiation, E (some authors refer to it as the radiation received under the absence of any atmosphere) may be calculated by:

$$E(\text{kW h/m}^2) = (0.024/\pi)I_{SC}[1 + 0.033\cos(360\,\text{DN}/365)] \times [\cos \text{LAT} \cos \text{DEC} \sin \omega_s + (2\pi\omega_s/360)\sin \text{LAT} \sin \text{DEC}] \tag{2.1.4}$$

In the above equation I_{SC} is the solar constant ($=1367\,\text{W/m}^2$). Note that a more accurate value of I_{SC} and the relevant discussion is provided in Chapter 5. Klein (1977) has recommended average days for each month which receive extraterrestrial energy equal to the average energy receipt of the entire month. This is indeed a useful routine since it results in a large time saving. Table 2.1.1 gives the recommended days for each month (seel column heads) and also provides the values of E for a range of latitudes. These values have been obtained via Prog2-1.Exe. The computational routine is given in Prog2-1.For.

Figure 2.1.2 shows the scatter plot for Eq. (2.1.1) for four Indian locations as presented by Hawas and Muneer (1983). A strong correlation between the two quantities under discussion is evident. Similar plots, each showing a strong correlation, have been presented by the above researchers.

In the UK, Meteorological Office records daily fractional sunshine for 231 locations. Likewise, there are a large number of stations recording this variable around the globe. Thus the usefulness of this model lies in its capability to predict daily insolation for all of these sites. Colliver (1991) has presented a most comprehensive monthly-averaged irradiation data set for 1200 locations worldwide using the approach under discussion. Page and Lebens (1986) has also tabulated such data for 13 sites in the UK.

Table 2.1.2 provides values of the '*a*' and '*b*' coefficients for selected sites around the globe, and Prog2-1.For lists the routine for computing $\bar{G}$. The above coefficients have been presented by Lof et al. (1966) for many sites around the world. Note that '*a*' and '*b*' have to be determined empirically and is indeed a shortcoming of the so-called Ångström relationship.

Table 2.1.1 Monthly-averaged horizontal daily extraterrestrial irradiation (kW h/m^2)

Lat. (deg)	Jan. 17	Feb. 16	Mar. 16	Apr. 15	May 15	Jun. 11	Jul. 17	Aug. 16	Sep. 15	Oct. 15	Nov. 14	Dec. 10
60	0.942	2.333	4.630	7.548	10.070	11.279	10.687	8.544	5.664	2.995	1.251	0.639
50	2.501	4.012	6.182	8.647	10.579	11.434	11.004	9.404	7.060	4.647	2.851	2.120
40	4.185	5.638	7.547	9.518	10.915	11.483	11.183	10.051	8.243	6.194	4.522	3.791
30	5.850	7.132	8.685	10.119	11.001	11.309	11.125	10.432	9.176	7.574	6.141	5.480
20	7.407	8.436	9.559	10.426	10.806	10.873	10.799	10.524	9.831	8.737	7.631	7.090
10	8.795	9.504	10.144	10.426	10.324	10.171	10.197	10.317	10.188	9.647	8.933	8.550
0	9.961	10.301	10.421	10.119	9.564	9.213	9.330	9.815	10.236	10.272	10.001	9.808

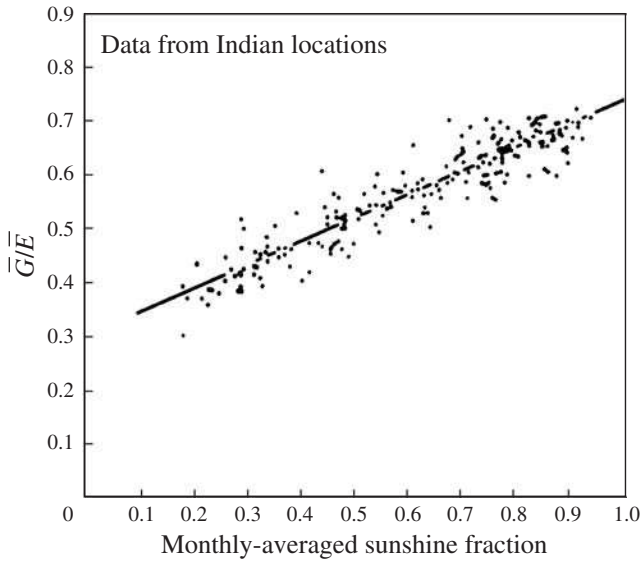

Figure 2.1.2 *Relationship between average clearness index and sunshine fraction*

The following example demonstrates the use of Prog2-1.Exe.

Example 2.1.1

Using monthly-averaged sunshine data for June presented in Table B1, calculate the available horizontal global, diffuse and beam irradiation for London, England. Note that an electronic version of Table B1 is available from the book's web site (File2-1.Csv).

The output generated by Prog2-1.Exe is as follows:

day length = 16.324 h
daily extraterrestrial irradiation = 11.413 kW h/m^2
monthly-averaged global, diffuse and beam irradiation = 4.73, 2.51 and 2.21 kW h/m^2.

The above value for global irradiation is comparable to that given by Cowley (1978) (5 kW h/m^2).

Suehrcke (2000) has presented an elegant and simple relationship that enables estimation of $\overline{G}$ from the monthly-averaged daily bright sunshine fraction and clear-sky clearness index, $\overline{G}_{\text{clear}}/\overline{E}$. Thus:

$$\overline{G}/\overline{E} = (n/N)(\overline{G}_{\text{clear}}/\overline{E}) \tag{2.1.5}$$

Suehrcke has argued that $\overline{G}_{\text{clear}}/\overline{E}$ varies narrowly between 0.65 and 0.75. Given this small range of variation, in the absence of specific site information, an average value of 0.7 may be assumed for $\overline{G}_{\text{clear}}/\overline{E}$, thus giving Eq. (2.1.5) the potential for worldwide application.

Driesse and Thevenard (2002) have evaluated the above claim. They have used measurements from 700 sites, compiled by the World Radiation Data Centre with over 70 000

Table 2.1.2 Coefficients for use in Eq. (2.1.1)

Location	*a*	*b*	Source
Stanleyville, Zaire	0.280	0.400	Page (1961)
Nairobi, Kenya	0.240	0.560	
Leopoldville, Zaire	0.210	0.520	
Pretoria, South Africa	0.270	0.460	
Durban, South Africa	0.330	0.350	
Capetown, South Africa	0.200	0.590	
Sao Paolo, Brazil	0.240	0.580	
Kew, England	0.150	0.680	
Rothamsted, England	0.160	0.600	
Bracknell, England	0.150	0.700	
Cambridge, England	0.170	0.680	
Garston, England	0.140	0.680	
London, England	0.130	0.650	
Malange, Angola	0.340	0.340	Lof et al. (1966)
Hamburg, Germany	0.220	0.570	
Tamanrasset, Algeria	0.300	0.430	
Buenos Aires, Argentine	0.260	0.500	
Nice, France	0.170	0.630	
Darien, Manchuria	0.360	0.230	
Charleston, SC, USA	0.480	0.090	
Atlanta, Ga, USA	0.380	0.260	
Miami, Fl, USA	0.420	0.220	
Madison, Wi, USA	0.300	0.340	
El Paso, Tx, USA	0.540	0.200	
Albuquerque, NM, USA	0.410	0.370	
New Delhi, India	0.341	0.446	Garg and Garg (1985)
Jodhpur, India	0.309	0.484	
Ahmedabad, India	0.302	0.464	
Calcutta, India	0.327	0.400	
Nagpur, India	0.293	0.460	
Bombay, India	0.292	0.464	
Poona, India	0.330	0.453	
Goa, India	0.279	0.514	
Madras, India	0.340	0.399	
Trivandrum, India	0.393	0.357	
Average for 18 Indian locations	0.299	0.448	Hawas and Muneer (1993)
Southern China	0.16	0.53	Lam and Li (1996)
Karachi, Pakistan	0.335	0.391	Nagrial and Muneer (1984)
Lahore, Pakistan	0.326	0.314	
Multan, Pakistan	0.423	0.239	
Quetta, Pakistan	0.436	0.337	
Locations between 20°S and 22°N	0.300	0.400	Turton (1987)
Average for eight Zambian locations	0.240	0.513	Jain and Jain (1988)
Gebze, Turkey	0.226	0.418	Tiris et al. (1996)

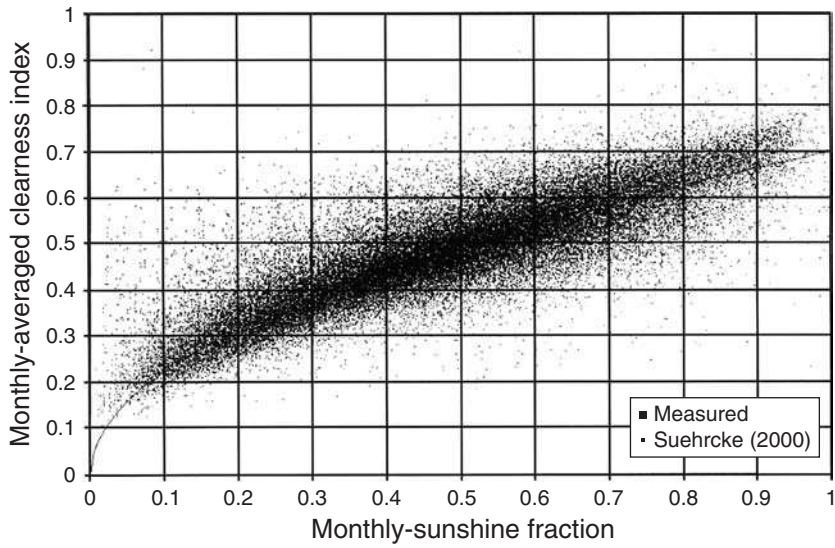

Figure 2.1.3 *Driesse and Thevenard's (2002) evaluation of Suehrcke's 'universal' relationship (Eq. (2.1.3))*

sunshine and radiation data. The relevant plot is shown in Figure 2.1.3. It may be noted that there is a considerable dispersion in the values of solar radiation. This variation (root mean square errors, RMSEs) was found to be around 12%. The latter team has fitted the above data to find regressed values of globally applicable Ångström *a* and *b* coefficients. These values are 0.2336 and 0.4987 respectively. Using the latter 'universal' coefficients the performance of Suehrcke and Angstrom procedures for estimating $\overline{G}$ was found to be on a par.

2.2 Monthly-averaged daily horizontal diffuse irradiation

Global irradiation on a slope is the sum of its direct (beam), diffuse and ground-reflected components. Starting from a horizontal global and diffuse irradiation database, beam irradiation can be evaluated from the difference of the former quantities. This, in turn, can be employed for determining the beam irradiation on a slope. The slope diffuse component is not so straightforward to evaluate. It may be computed from the angular, radiance distribution of the sky. The distribution of the sky-diffuse radiance, which is anisotropic in nature, depends on the condition of the sky and determination of it is a fairly involved task. Likewise, the ground-reflected component may be computed given the horizontal diffuse and global irradiation. However, it is also of an anisotropic nature and precise evaluation of it poses difficulties.

It is clear from the preceding discussion that, if the above-mentioned approach is adopted, the first step in the estimation of slope irradiation would be to acquire knowledge of horizontal global as well as diffuse irradiation. Therefore in the first instance, for those locations at which only horizontal global irradiation is recorded, a method is needed

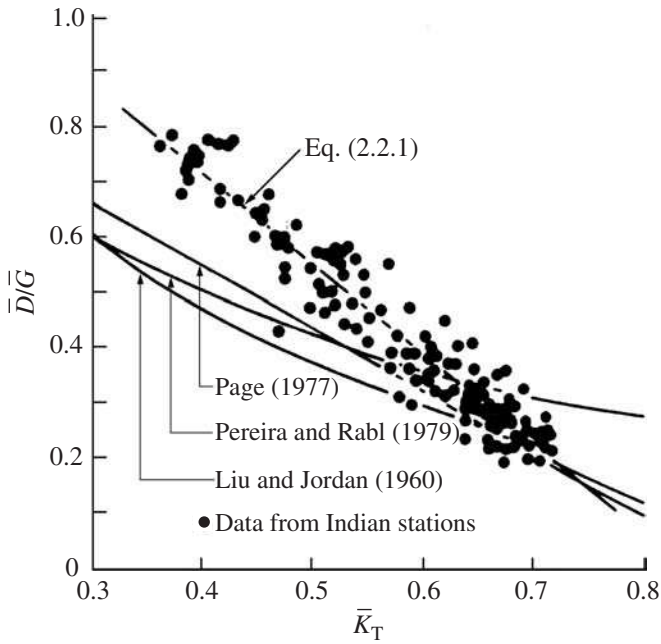

Figure 2.2.1 *Variation of monthly-averaged diffuse ratio against clearness index*

to estimate the diffuse component. One way is to study the regression between the two quantities at locations where appropriate data are available and hence establish models which may be used to predict the diffuse component. The models obtained from data recorded on a monthly-averaged basis differ from those obtained from data collected on an individual day-to-day basis.

A regression between monthly-averaged values of diffuse and global irradiation was first developed by Liu and Jordan (1960) in the form of $\bar{D}/\bar{G}$ as a function of $\bar{K}_T = \bar{G}/\bar{E}$, where $\bar{D}$ is the monthly-average daily diffuse radiation incident on a horizontal surface. Many investigators across the world have confirmed the validity of this approach. However, they found that measured data differs from that predicted by Liu–Jordan's model. As such, questions have been raised about the generality of Liu–Jordan's regression. Figure 2.2.1 shows the regressions proposed by Liu and Jordan (1960) and Pereira and Rabl (1979) for USA, Page (1977) for the UK and Hawas and Muneer (1984) for India. Page's relationship was derived from shade-ring corrected measurements at 10 stations. However, no such corrections were applied to the measurements at Blue Hill, Massachusetts which Liu and Jordan used in their work. Pereira and Rabl used beam radiation data measured by pyrheliometer at five stations in the US and hence avoided use of a shade-ring correction factor.

Hawas and Muneer's work was based on long-term measurements undertaken at 13 stations in India for the period 1957–75 (Meteorological Office, 1980b). A shade-ring correction factor was applied to the diffuse data. Monthly values of the diffuse ratio are shown in Figure 2.2.1 as a function of monthly clearness indices for all months and stations considered. Each point in the figure represents monthly-average daily values over

the whole period of observation for any given station. The model proposed by Hawas and Muneer for the Indian sub-continent is:

$$\overline{D}/\overline{G} = 1.35 - 1.61\overline{K}_{\mathrm{T}} \tag{2.2.1}$$

Figure 2.2.1 shows that the Indian regression curve differs markedly from the other two regressions, i.e. the diffuse ratio is much higher. Mani and Chacko (1973), in their analysis of solar radiation characteristics for India also found the diffuse irradiation to be much higher than that for Europe and West Africa. They reported that the highest values of diffuse irradiation occur during the monsoon months when the sky is covered by cloud layers of varying types and densities. The results obtained by Choudhury (1963) for New Delhi also indicate high values of diffuse irradiation.

Pereira and Rabl (1979) have reported a weak effect of changing season upon the regression under discussion. However, no appreciable seasonal variations have been reported by Page (1961) and Hawas and Muneer (1984). This result is in accordance with the study of Stanhill (1966) for Gilat.

To conclude, for the desert and tropical locations which experience high turbidities, Eq. (2.2.1) is recommended. However, for temperate climates and for locations out with the tropics, Eq. (2.2.2) given by Page (1977) may be used. This equation is based on eight UK and nine worldwide locations:

$$\overline{D}/\overline{G} = 1.00 - 1.13\overline{K}_{\mathrm{T}} \tag{2.2.2}$$

Example 2.2.1

Using monthly-averaged measured irradiation data for April presented in Table 2.2.1, calculate the available horizontal diffuse irradiation for Eskdalemuir, Scotland. Compare the result against the corresponding measured value which is also provided in Table 2.2.1.

Prog2-1.Exe estimates $\overline{D} = 1.77\,\mathrm{kW\,h/m^2}$. This may be compared against the measured value of $1.94\,\mathrm{kW\,h/m^2}$.

2.3 Annual-averaged diffuse irradiation

Using the analysis presented in Section 2.2 it is logical to investigate an annual regression between the diffuse ratio and the corresponding clearness index. Figure 2.3.1, based on data from widely different locations, indicates a strong correlation between $D_{\mathrm{an}}/G_{\mathrm{an}}$ and $K_{\mathrm{T,an}}$. The following equation gives the regression model:

$$D_{\mathrm{an}}/G_{\mathrm{an}} = 1 - 1.04K_{\mathrm{T,an}} \tag{2.3.1}$$

Hawas and Muneer (1984) have shown that the ratio of annual global to extraterrestrial irradiation, $K_{\mathrm{T,an}}$, varies for the tropics between 0.53 and 0.61. The ratio of annual values of diffuse to extraterrestrial irradiation, $K_{\mathrm{D,an}}$, varies in a very narrow range, i.e. between 0.22 and 0.25, with an average of 0.233. This value is close to that reported by Stanhill (1966) for Gilat (0.237). The above ratio is also comparable to the values for UK locations

Table 2.2.1 Monthly-averaged horizontal daily global and diffuse irradiation (kW h/m^2)

Month	1	2	3	4	5	6	7	8	9	10	11	12
Jersey 49.183°N and 2.183°W												
Global	0.80	1.59	2.86	4.27	5.30	5.96	5.56	4.53	3.36	2.12	0.98	0.64
Diffuse	0.57	0.95	1.46	2.15	2.59	2.68	2.68	2.32	1.68	1.10	0.64	0.44
Easthampstead 51.383°N and 0.783°W												
Global	0.62	1.24	2.32	3.32	4.41	5.22	4.70	3.90	2.92	1.70	0.91	0.53
Diffuse	0.45	0.83	1.36	2.01	2.64	2.76	2.75	2.26	1.69	1.02	0.58	0.38
London 51.517°N and 0.017°W												
Global	0.56	1.14	2.06	3.12	4.10	5.03	4.46	3.58	2.69	1.59	0.81	0.48
Diffuse	0.40	0.73	1.22	1.89	2.40	2.55	2.55	2.07	1.50	0.92	0.53	0.33
Aberporth 52.133°N and 4.567°W												
Global	0.63	1.36	2.58	3.99	4.88	5.54	5.10	4.08	3.07	1.71	0.83	0.53
Diffuse	0.48	0.86	1.43	2.16	2.56	2.76	2.81	2.34	1.69	1.03	0.59	0.39
Cambridge 52.217°N and 0.1°E												
Global	0.61	1.28	2.35	3.28	4.56	5.14	4.65	3.59	2.86	1.66	0.93	0.49
Diffuse	0.45	0.83	1.38	2.00	2.66	2.92	2.76	2.19	1.63	1.00	0.58	0.36
Aldergrove 54.650°N and 6.217°W												
Global	0.48	1.15	2.18	3.63	4.34	5.24	4.37	3.59	2.65	1.38	0.73	0.39
Diffuse	0.33	0.73	1.31	2.08	2.61	2.86	2.76	2.34	1.59	0.89	0.46	0.28
Eskdalemuir 55.317°N and 3.200°W												
Global	0.38	1.12	2.01	3.25	3.90	4.67	4.06	3.42	2.31	1.29	0.65	0.34
Diffuse	0.28	0.68	1.25	1.94	2.40	2.72	2.51	2.16	1.45	0.81	0.41	0.23
Lerwick 60.133°N and 1.183°W												
Global	0.21	0.79	1.76	3.28	3.94	4.81	4.16	3.35	2.06	1.03	0.37	0.14
Diffuse	0.18	0.51	1.11	1.98	2.46	2.72	2.75	2.11	1.35	0.69	0.28	0.12

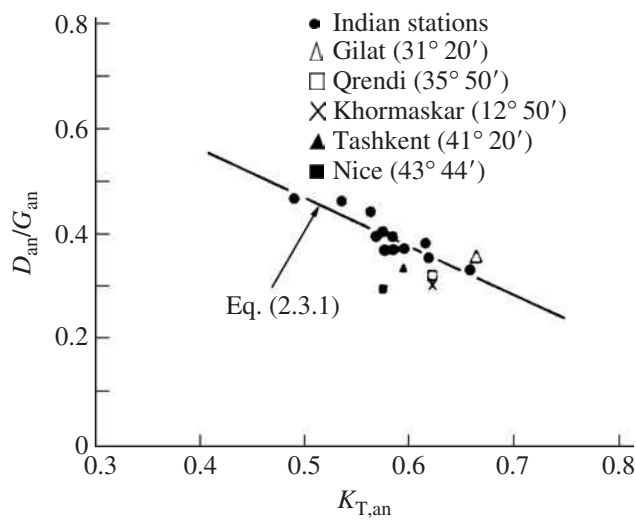

Figure 2.3.1 *Variation of annual-averaged diffuse ratio against clearness index*

obtained by the present author as may be seen in Table 2.3.1. This is a very interesting phenomenon since the annual-average extraterrestrial irradiation may easily be computed (either from Prog2-1.For or Table 2.1.1), and using a universal value of 0.233 for $K_{D,an}$ the annual receipt of diffuse radiation obtained for any locality.

Mani and Chacko (1973) have also provided an annual-average value of 0.35 for the ratio of annual values of diffuse to global irradiation D_{an}/G_{an}. This is comparable to the values of 0.36 for Gilat (Stanhill, 1966) and 0.3 for Southern Africa (Drummond, 1956).

Example 2.3.1

Using monthly-averaged data presented in Table 2.2.1, calculate the annual receipt of diffuse irradiation for Easthampstead, England (51.4°N). Use the abbreviated method for computing the annual irradiation quantities shown in Section 2.3.

The abbreviated estimates do not warrant the use of a computer and may easily be carried out on an electronic calculator. Using Table 2.1.1 the annual-averaged daily extraterrestrial irradiation is obtained via interpolation as 6.542 kW h/m^2. Annual-average global irradiation is obtained from Table 2.2.1 as 2.65 kW h/m^2. Using Eq. (2.3.1), D_{an} is now obtained as 1.53 kW h/m^2. The measured value of D_{an} from Table 2.2.1 is 1.56 kW h/m^2.

Note that in this $K_{D,an} = 0.238$ which is within 2% of the above quoted universal value of 0.233 (see Table 2.3.1).

Table 2.3.1 Annual irradiation data for worldwide locations

Station	Country	$K_{T,an}$	D_{an}/G_{an}	$K_{D,an}$
Ahmedabad	India	0.58	0.38	0.22
Bhaunagar	India	0.61	0.36	0.22
Bombay	India	0.56	0.40	0.22
Calcutta	India	0.53	0.47	0.25
Goa	India	0.59	0.38	0.23
Jodhpur	India	0.65	0.34	0.22
Madras	India	0.57	0.41	0.24
Nagpur	India	0.58	0.38	0.22
New Delhi	India	0.61	0.39	0.24
Poona	India	0.58	0.40	0.23
Shillong	India	0.49	0.47	0.23
Trivandrum	India	0.56	0.45	0.25
Visakhapatnam	India	0.58	0.38	0.22
Gilat	Israel	0.66	0.36	0.24
Jersey	UK	0.47	0.51	0.24
Easthampstead	UK	0.40	0.59	0.24
London	UK	0.38	0.58	0.22
Aberporth	UK	0.44	0.56	0.25
Cambridge	UK	0.41	0.60	0.24
Aldergrove	UK	0.41	0.61	0.25
Eskdalemuir	UK	0.37	0.61	0.23
Lerwick	UK	0.39	0.63	0.24
Average				0.233

2.4 Daily horizontal global irradiation

Figure 2.4.1 shows the scheme for obtaining daily sloped irradiation. As will be demonstrated herein, this scheme uses statistically different models when compared with the models presented in Sections 2.1 and 2.2. A set of linear regression equations between daily global irradiation and the duration of bright sunshine was obtained by Cowley (1978) for 10 stations in Great Britain. These equations enable the estimation of daily incident radiation, rather than monthly-averaged quantity discussed in Section 2.1. Cowley (1978) used the above equations to produce a set of irradiation maps for Great Britain using sunshine data from 132 stations. Cowley's equation is given as:

$$G = E[d\{(a/100) + (b/100)\,(n/N)\} + (1 - d)a'] \tag{2.4.1}$$

where $d = 0$ if $n = 0$, otherwise $d = 1$ if $n > 0$, and a' = average ratio of G/E for overcast days. Table B1 provides values of 'a' and 'b'.

Cowley's choice of Eq. (2.4.1), rather than Eq. (2.1.1), has been justified on the grounds that it results in lower RMSEs.

Rawlins (1984) has further investigated the accuracy of Cowley's model by its examination against data from 21 independent stations. The reported RMSEs lie in the range of 15–20%. If, however, the monthly-averaged daily estimates are to be compared, an accuracy of 3–9% is claimed. An interesting conclusion drawn by Rawlins is that individual daily irradiation is more accurately estimated from local sunshine observations than by assignment from nearby radiometric stations, if these are more than 20 km away. For monthly averages the critical distance increases to about 30 km. It was also shown that the use of sunshine values from a location 50 km away may typically increase the RMSEs of daily estimates from 14% to 22%.

It was shown in Section 2.1 that the regression coefficients for monthly-averaged irradiation are available for worldwide locations (see Table 2.1.2). Cowley's work, however, has not been extended for other geographic regions. At least for the UK, it nevertheless presents an opportunity to compute daily horizontal as well as slope irradiation by linking the above model with those to be presented in Sections 2.5 and 2.7.

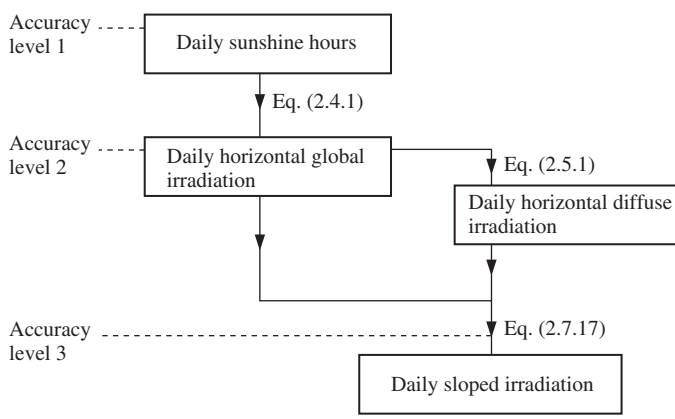

Figure 2.4.1 *Calculation scheme for daily sloped irradiation*

Table B1 presents the above a, a' and b coefficients (for use in Eq. (2.4.1)) for 15 locations in the UK.

Example 2.4.1

On 25 August 1983, 10.1 h of sunshine was recorded at Easthampstead, England (51.4°N). Calculate the available horizontal global and diffuse irradiation using Cowley's model (Eq. (2.4.1)).

We note from Table B1 that for a neighbouring site, London, $a = 0.24$, $b = 0.6$ and $a' = 0.15$. Using these coefficients Prog2-2.Exe enables us to obtain horizontal global, diffuse and beam irradiation values of 5.87, 1.87 and 4 kW h/m^2 (daily diffuse irradiation is computed within Prog2-1.Exe using Eq. (2.5.1)). The measured values for daily global and diffuse irradiation were, respectively, 5.37 and 2.06 kW h/m^2.

2.5 Daily horizontal diffuse irradiation

A regression equation which relates the diffuse fraction of daily global irradiation (diffuse ratio) to the ratio of daily global to extraterrestrial irradiation (clearness index) was also originally developed in the pioneering work of Liu and Jordan (1960). Their correlation is based on data for one location, namely Blue Hill, Massachusetts. No correction was made for the shade ring, and one value of daily extraterrestrial irradiation was used for the middle of the month, for computation of the daily clearness index K_T. Pereira and Rabl (1979) re-investigated the correlation of Liu and Jordan using 1–4 years of pyrheliometric data for five stations in the USA (Albuquerque, New Mexico; Fort Hood, Texas; Livermore, California; Raleigh, North Carolina and Maynard, Massachusetts).

The extraterrestrial irradiation was calculated for each individual day. The latter procedure has been followed by all other investigators who developed similar correlations for different regions. A seasonal trend was reported by Pereira and Rabl. However, the regression equation was fitted for the entire data as one group.

A parallel study, for the last of the four stations mentioned above, was conducted by Erbs et al. (1982) to develop two seasonal correlations, one for winter ($\omega_s < 1.4208$ rad) and the other for the rest of the year ($\omega_s > 1.4208$ rad). Averaged values of the diffuse ratio D/G over finite intervals of K_T were used in the above investigations. Rao et al. (1984) used a year's data for Corvallis, Oregon, to develop an annual as well as seasonal regression. Individual values of D/G against K_T were used, thus obtaining a more representative value for r^2 (the coefficient of determination).

Several investigators developed similar correlations for other geographical regions. The works of Choudhary (1963) and Muneer and Hawas (1984) for India, Ruth and Chant (1976) and Tuller (1976) for Canada, Stanhill (1966) for Israel, Bartoli et al. (1982) for Italy and Saluja and Muneer (1986) for the UK are now examined. These studies have confirmed the validity of Liu and Jordan's approach to correlate D/G and K_T.

Choudhary (1963) used only 3 months of data for New Delhi, and found a higher D/G ratio compared to the Liu–Jordan model. He attributed this to a higher dust content over New Delhi and his small sample of data. Muneer and Hawas (1984) used 3 years of data for 13 stations in India, spanning from 8.5°N to 28.5°N latitude, to develop correlations for

individual stations and for the entire region of India. Individual values of D/G were plotted against K_T and used for regression purposes. The averaged values give a 'false' sense of high r^2 value for the regressed equation and do not portray a true picture of the scatter of individual points. Muneer and Hawas (1984) found that a good correlation exists between D/G and K_T for the individual location ($r^2 = 0.893-0.95$) and for the entire Indian region ($r^2 = 0.89$). Figure 2.5.1 shows the regression curves for four Indian locations.

Ruth and Chant (1976) used 7 years of data for four Canadian stations (Toronto, Montreal, Goose Bay and Resolute Bay). They found that their diffuse ratios were higher than those reported by Liu and Jordan. In a later study Pereira and Rabl (1979) reported the proximity of their results for the US stations to those of Ruth and Chant. A latitude dependence was reported by Ruth and Chant and use of the correlation for individual locations was suggested.

Tuller (1976) made a parallel study for the same four Canadian stations using 1 year of daily data. He found a latitude effect to be present with the grouped correlation closer to the one due to Choudhary (1963). Tuller also investigated the effect of surface reflectivity on the diffuse irradiation. He concluded that this effect was responsible for only 27% of the variance in diffuse transmission coefficient D/E. Stanhill (1966) studied the relationship using 3 years of data for Gilat, a semi-arid location in Israel. He also found a departure of the diffuse ratio from that suggested by Liu and Jordan. He attributed his and Choudhary's (1963) results to the higher dust content of stations situated in semi-arid locations.

Bartoli et al. (1982) have studied correlation for Macerata and Genova in Italy using data for 6 and 8 years, respectively. They have reported regressions for these two stations on an individual basis rather than grouping the data together.

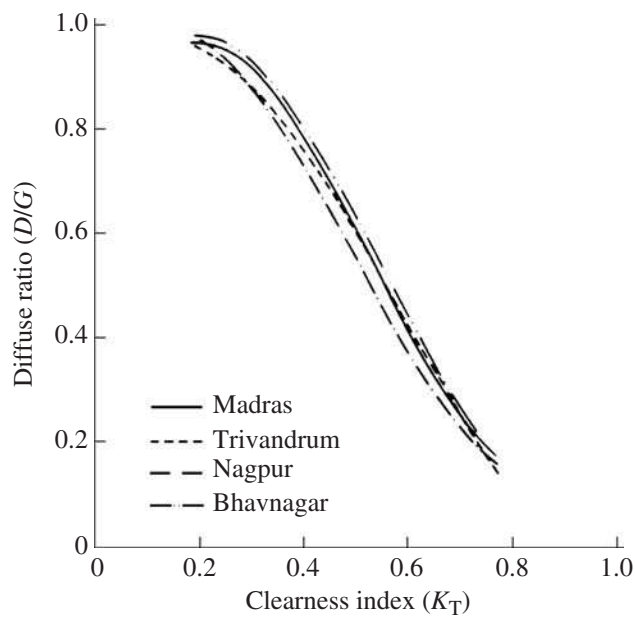

Figure 2.5.1 *Regression curves for daily diffuse ratio – Indian locations*

Saluja and Muneer (1986) used 3 years daily diffuse and global irradiation data from five locations in the UK (Easthampstead, Aberporth, Aldergrove, Eskdalemuir and Lerwick) to develop individual as well as a single regression model. The regressed curves for UK are shown in Figure 2.5.2.

Liu and Jordan used uncorrected diffuse radiation data while other investigators used the corrected data to compensate the obstruction caused by the shade ring or shadow band. A shift of the diffuse ratio curve above that due to Liu and Jordan, first reported by Choudhary (1963) and then by Tuller (1976), can be attributed to this reason, rather than the effect of dust. This observation is made after taking into account the increased diffuse ratios associated with higher turbidities in dust-laden atmospheres. The consequent increment is not so dramatic as to offset the effect of uncorrected diffuse radiation data.

The above paragraphs provide a brief review of the regressions which have been developed between D/G and K_T for various regions in different continents. All of the above-mentioned investigators used daily-integrated values of diffuse and global solar radiation, rather than hourly or minute-by-minute recordings.

Other investigators have attempted a different approach. Mani and Rangarajan (1983) followed the approach of Hay (1979). Their procedure is as follows: instead of regressing D/G against K_T, regression is performed for D'/G' against G'/E, where D' and G' are diffuse and global radiation quantities (calculated from sunshine and radiation data) which strike the ground before undergoing multiple reflections with the atmosphere. This is done by using standardised values of atmospheric, cloud base and ground albedo. Hawas and Muneer (1984) in a study for 18 Indian stations found negligible difference between the methods due to Liu and Jordan (1960) and Hay (1979). This may be attributed to the non-existent snow cover at most locations in the tropics.

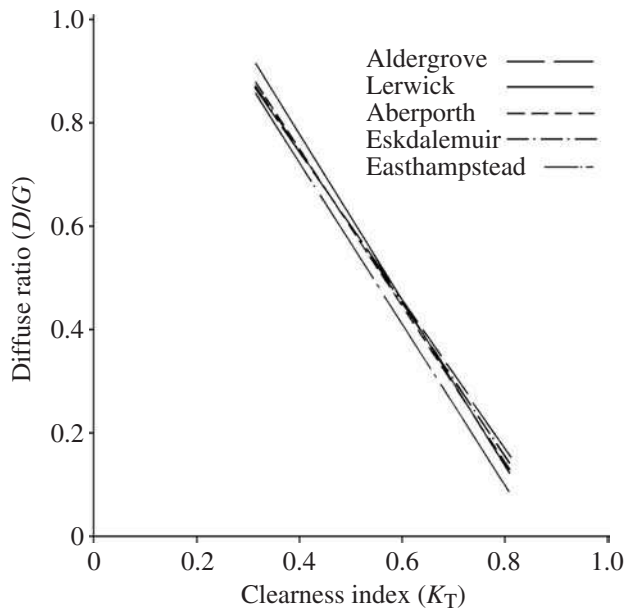

Figure 2.5.2 *Regression curves for daily diffuse ratio – UK locations*

Smietana et al. (1984), using detailed (1 min) measurements for Davis, California, have shown that days with disparate weather conditions produced different regressions between D/G and K_T. They have shown that the large scatter around the polynomial regression curve could be reduced by grouping days with equal amounts of per cent sunshine. They concluded in their study that D/G is not a unique function of K_T. However, the use of D/G and K_T ratios on a minute-by-minute basis does not validate their claim in the strict sense as applied to daily values. One may refer to the study of Erbs et al. (1982) in which different regressions were developed for D/G against K_T based on hourly- and daily-integrated data. A further discussion on the inequality of regressions based on different time scales will be provided in Section 2.6.

Le Baron and Dirmhirn (1983) have used 2 years data for two locations in the USA, to investigate the limitations of the Liu–Jordan models for locations with varied snow cover and elevation. The two locations on which their study is based are Hidden Peak Site (high elevation with undisturbed snow cover over a large area and time) and Salt Lake City (a lower elevation site with relatively short-lived snow cover). They report a drastic shift of the Liu–Jordan regression curve under an influence of heavy snow cover. Hay (1979) has attributed this phenomenon to the increased diffuse radiation due to multiple reflections between the snow-covered ground and clouds.

Thus, recapitulating the results of the studies mentioned above, we arrive at the following conclusions:

(a) The validity of Liu and Jordan's approach in considering the correlation between the daily diffuse ratio and the daily clearness index has been confirmed by a large number of investigators in various countries.
(b) The original regression curve proposed by Liu and Jordan was based on uncorrected diffuse irradiation data, and as such, it predicts lower values of the diffuse fraction.
(c) It can be demonstrated via Figure 2.5.1 that without any serious loss of accuracy a global curve may be used for any candidate location.

Figure 2.5.3 shows the regressed curves, discussed above, for Canada, India, the US and the UK. The recommended global model for the diffuse ratio is:

$$D/G = 0.962 + 0.779K_T - 4.375K_T^2 + 2.716K_T^3, \quad K_T > 0.2 \tag{2.5.1a}$$

$$D/G = 0.98 \quad \text{for} \quad K_T < 0.2 \tag{2.5.1b}$$

Example 2.5.1

On 25 August 1983, 5.37 kW h/m^2 of horizontal global irradiation was recorded at Easthampstead, England (51.4°N). Calculate the diffuse irradiation for this day.

Prog2-2.Exe computes the horizontal diffuse irradiation as 2.17 kW h/m^2. The corresponding measured value was 2.06 kW h/m^2. We note by comparing the solutions of Examples 2.4.1 and 2.5.1 that the estimate of diffuse irradiation is significantly improved if we initiate the computation with measured value of global irradiation rather than sunshine data. This is due to two reasons: (a) the latter procedure involves a two-step

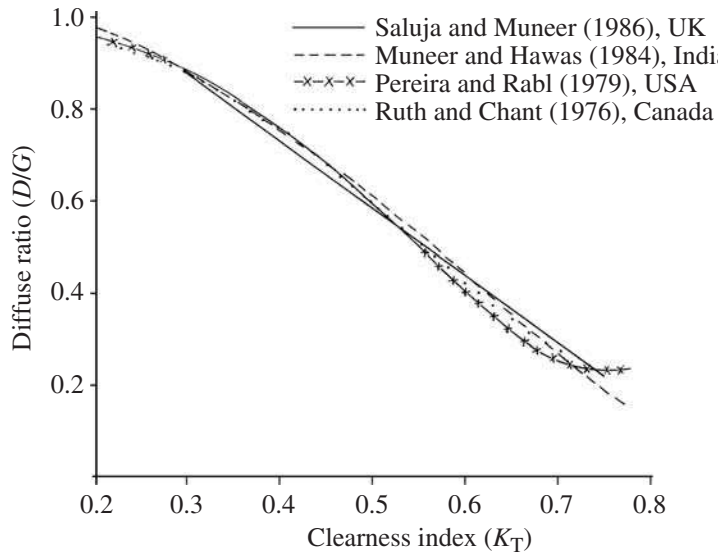

Figure 2.5.3 *Regression curves for daily diffuse ratio – worldwide locations*

procedure with the consequent compounding of errors and (b) the sunshine records are of a much poorer quality than pyranometric data. Nevertheless, in the absence of any measured irradiation the sunshine data at least enables rough estimates to be made.

2.6 The inequality of the daily- and monthly-averaged regressions

As shown above, a number of studies have been carried out in which the daily diffuse component has been regressed against daily global irradiation. These may be broadly classified as:

(a) regressions based on daily values,
(b) regressions based on monthly-averaged values.

A review of the former type of regressions was made in the above sections. In their pioneering work, Liu and Jordan (1960) obtained both of the above-mentioned regressions for the US. Erbs et al. (1982) have re-established these regressions for the US using pyrheliometric data. Also, Muneer and Hawas (1984) have established these regressions for India.

Monthly-averaged regressions obtained by Liu and Jordan and Erbs et al. were in fact derived from the daily-based regressions in conjunction with the frequency of the daily clearness index. On the other hand Muneer and Hawas have used measured data to obtain both of the above-mentioned regressions. The outcome of these studies was that the two relationships differ in their functional form.

Furthermore, for the UK Page (1977) has developed a monthly-averaged regression while Saluja and Muneer (1986) have developed a daily-based regression. In Section 2.5 this

regression was shown to be markedly different from the corresponding daily regression. As pointed out in the preceding section, some authors on occasions have failed to appreciate the fundamental difference between the two relationships under discussion. Muneer and Saluja (1985) have pointed out the erroneous approach of some of the above-mentioned studies.

The aim of this section is to provide a theoretical proof, extracted from the works of Muneer (1987) and Saluja et al. (1988), that the relationship between daily quantities differs from that based on monthly-averaged values.

Assume that the relationship between daily diffuse/global irradiation and clearness index is represented by:

$$\frac{D}{G} = a_0 + a_1 K_T \tag{2.6.1}$$

where a_0 and a_1 are constants, and also that the relationship between monthly-averaged daily diffuse/global irradiation and clearness index is represented by the regression equation:

$$\frac{\overline{D}}{\overline{G}} = b_0 + b_1 \overline{K}_T \tag{2.6.2}$$

where b_0 and b_1 are constants.

The relationships for daily and monthly-averaged values would be the same if, and only if, $a_0 = b_0$ and $a_1 = b_1$. The present objective is to prove that the relationships are *not* the same by showing that the assumption $a_0 = b_0$ and $a_1 = b_1$ leads to a contradiction.

If E denotes the daily extraterrestrial irradiation, then:

$$\frac{\overline{D}}{\overline{G}} = \frac{\overline{D}/E}{\overline{G}/E} = \frac{\int_0^1 \frac{D}{G} K_T \, df}{\int_0^1 K_T \, df}$$

also:

$$\overline{K}_T = \int_0^1 K_T \, df \tag{2.6.3}$$

In the above integrations, df represents the time increment. For a fuller explanation of the clearness index distribution the reader is referred to Liu and Jordan (1960). Equation (2.6.2) can be written as:

$$\frac{\int_0^1 \frac{D}{G} K_T \, df}{\overline{K}_T} = b_0 + b_1 \overline{K}_T$$

or:

$$\int_0^1 \frac{D}{G} K_T \, df = b_0 \overline{K}_T + b_1 \overline{K}_T^2 \tag{2.6.4}$$

However, using Eq. (2.6.1) it may be shown that:

$$\int_0^1 \frac{D}{G} K_T \, df = \int_0^1 (a_0 + a_1 K_T) K_T \, df$$

and so Eq. (2.6.4) becomes:

$$\int_0^1 (a_0 K_T + a_1 K_T^2) df = b_0 \overline{K}_T + b_1 \overline{K}_T^2 \tag{2.6.5}$$

Now if $a_0 = b_0$ and $a_1 = b_1$, Eq. (2.6.5) becomes:

$$\int_0^1 (a_0 K_T + a_1 K_T^2) df = a_0 \overline{K}_T + a_1 \overline{K}_T^2$$

which reduces to:

$$a_1 \int_0^1 K_T^2 \, df = a_1 \overline{K}_T^2$$

or, since $a_1 \neq 0$:

$$\int_0^1 K_T^2 \, df - \overline{K}_T^2 = 0 \tag{2.6.6}$$

Now the LHS of Eq. (2.6.6) may be proved equal to $\int_0^1 (K_T - \overline{K}_T)^2 df$ as follows:

$$\begin{aligned} \int_0^1 (K_T - \overline{K}_T)^2 \, df &= \int_0^1 (K_T^2 - 2\overline{K}_T K_T + \overline{K}_T^2) \, df \\ &= \int_0^1 K_T^2 \, df - 2\overline{K}_T \int_0^1 K_T \, df + \overline{K}_T^2 \int_0^1 df \\ &= \int_0^1 K_T^2 \, df - 2\overline{K}_T^2 + \overline{K}_T^2 \end{aligned}$$

Thus:

$$\int_0^1 (K_T - \overline{K}_T)^2 \, df = \int_0^1 K_T^2 \, df - \overline{K}_T^2 \tag{2.6.7}$$

$(K_T - \overline{K}_T)^2 > 0$, since $K_T \neq \overline{K}_T$ (see Eq. (2.6.3)). Hence $\int_0^1 (K_T - \overline{K}_T)^2 df > 0$ and thus $\int_0^1 K_T^2 df - \overline{K}_T^2 > 0$ (see Eq. (2.6.7)). But this contradicts Eq. (2.6.6). Therefore, the assumption $a_0 = b_0$ and $a_1 = b_1$ must be false. It follows that the relationships for daily values and monthly-averaged values, represented by Eqs (2.6.1) and (2.6.2), respectively, are different.

The above proof applies for linear relationships between D/G and K_T and between $\overline{D}/\overline{G}$ and $\overline{K}_T$. Proofs based on polynomial relationships may be obtained by following the above approach. It is worth mentioning that the monthly-averaged relationship between and $\overline{D}/\overline{G}$ and $\overline{K}_T$ developed by Page (1977) and the relationship between D/G and K_T established by Saluja and Muneer (1986) in Section 2.5 for the UK are both linear.

2.7 Daily slope irradiation

Daily horizontal global and diffuse irradiation data can be used to estimate slope irradiation provided R, the ratio of global irradiation on a slope to that on a horizontal surface, is known. Mathematically, R is expressed as:

$$R = G_{TLT}/G \tag{2.7.1}$$

R can be further decomposed in terms of the contribution of the beam and diffuse components of global irradiation:

$$R_B = B_{TLT}/B \tag{2.7.2}$$

$$R_D = D_{TLT}/D \tag{2.7.3}$$

Thus:

$$R = R_B(B/G) + R_D(D/G) \tag{2.7.4}$$

As a first approximation, the above equation assumes an ideally non-reflecting foreground. The angular correction for the beam component may be solved analytically using the principles of solar geometry. Duffie and Beckman (1991) present equations, based on the work of Liu and Jordan (1962) and Klein (1977), for surfaces sloped towards the equator and also for a sloped surface of any orientation. The former set of equations are simpler but the latter are quite involved, certainly for manual calculations. Muneer and Saluja (1988) have shown that the second set of equations, mentioned above, are not applicable for vertical surfaces with north, east and west aspects, e.g. for these aspects indeterminate quantities are generated. Equations (2.7.5)–(2.7.8), based on the work of Liu and Jordan (1962), Klein (1977) and Muneer and Saluja (1988), enable computation of monthly or daily sloped irradiation on vertical surfaces with eastern, western and northern aspects, and any sloping surface facing south.

For sloped surfaces Liu and Jordan (1962) have shown that:

$$R_B = \int_{\omega_s'}^{\omega_s} I_0\tau \cos \mathrm{INC}\, d\omega / 2 \int_0^{\omega_s} I_0\tau \sin \mathrm{SOLALT}\, d\omega \tag{2.7.5}$$

I_o is the normal incidence extraterrestrial irradiance, and as it is a constant it cancels out from the numerator and denominator. The atmospheric transmissivity of the beam of irradiance τ is a function of the time of the day and in general R_B can be evaluated only when this functional relationship is known. However, Liu and Jordan (1962) have shown that at the equinox $\omega_s = \omega_s' = \pi/2$, R_B is independent of τ. Thus for the equinox (21 March and 21 September) τ will cancel out from Eq. (2.7.5). For sloped surfaces in the northern hemisphere facing the equator the expression for R_B may be shown to take the form:

$$R_B = \frac{\cos \mathrm{DEC} \cos(\mathrm{LAT} - \mathrm{TLT}) \sin \omega_s' - \omega_s' \sin \mathrm{DEC} \sin(\mathrm{LAT} - \mathrm{TLT})}{\cos \mathrm{LAT} \cos \mathrm{DEC} \sin \omega_s + \omega_s \sin \mathrm{LAT} \sin \mathrm{DEC}} \tag{2.7.6a}$$

and, for surfaces in the southern hemisphere facing the equator:

$$R_B = \frac{\cos \mathrm{DEC} \cos(\mathrm{LAT} + \mathrm{TLT}) \sin \omega_s' - \omega_s' \sin \mathrm{DEC} \sin(\mathrm{LAT} + \mathrm{TLT})}{\cos \mathrm{LAT} \cos \mathrm{DEC} \sin \omega_s + \omega_s \sin \mathrm{LAT} \sin \mathrm{DEC}} \tag{2.7.6b}$$

Liu and Jordan's work is based on an isotropic sky. However, as will be demonstrated in Chapter 4, the isotropic model generates large errors for slope irradiation, in particular north-facing surfaces. It was shown in Sections 2.4 and 2.5 that the sky-diffuse component is often the major component of the total incident solar energy. As such, Muneer and Saluja (1988) have presented an anisotropic model for obtaining monthly as well as daily

slope irradiation. Following the analysis of Muneer and Saluja (1988) the expression for R_B for a vertical surface facing north may be obtained as:

$$R_B = \frac{\begin{array}{c}\sin \text{DEC} \cos \text{LAT}\{\omega_s - \cos^{-1}(\tan \text{DEC}/\tan \text{LAT})\} \\ -\cos \text{DEC} \sin \text{LAT}\{\sin \omega_s - \sqrt{(1 - \tan^2 \text{DEC}/\tan^2 \text{LAT})}\}\end{array}}{\cos \text{LAT} \cos \text{DEC} \sin \omega_s + \omega_s \sin \text{LAT} \sin \text{DEC}} \quad (2.7.7a)$$

For months with little or no receipt of beam radiation a much more simpler model has also been proposed:

$$R_B = 0.4 \quad (2.7.7b)$$

Similarly, the expression for R_B for a vertical surface facing east or west is given by:

$$R_B = \frac{\cos \text{DEC}(1 - \cos \omega_s)}{2(\cos \text{LAT} \cos \text{DEC} \sin \omega_s + \omega_s \sin \text{LAT} \sin \text{DEC}} \quad (2.7.8)$$

Muneer and Saluja's (1988) model is based on an anisotropic treatment of the sky-diffuse radiation. In the application of this model, fuller details of which are provided in Chapter 4, the fraction of the time any given surface faces the sun (F_{sun}), or remains in shade (F_{shade}), is to be determined. For a vertical surface facing north:

$$F_{sun} = \omega_s - \text{arc cos}(\tan \text{DEC}/\tan \text{LAT}) \quad (2.7.9)$$

For any sloped surface facing south:

$$F_{sun} = \omega_s'/\omega_s \quad (2.7.10)$$

where ω_s' is obtained from:

$$\omega_s' = \min[\omega_s, \text{ arc cos}(-\tan(\text{LAT} - \text{TLT})\tan \text{DEC})] \quad (2.7.11)$$

The sun's motion is symmetric about east- and west-facing surfaces. Hence for either of the two cases:

$$F_{sun} = 0.5 \quad (2.7.12)$$

Having obtained F_{sun}, F_{shade} is then obtained as:

$$F_{shade} = 1 - F_{sun} \quad (2.7.13)$$

The daily anisotropic model may then be described as follows. For overcast days (i.e. when $G = D$):

$$G_{TLT} = D(F_{shade}\, T_{shade} + F_{sun}\, T_{overcast}) \quad (2.7.14)$$

The 'tilt factors' T_{shade} and $T_{overcast}$ are the ratios of the diffuse irradiation on a slope to that on a horizontal surface. The values of these factors depend upon the tilt of the surface and the radiance distribution of the sky for the respective case. For vertical surfaces $T_{shade} = 0.36$ and $T_{overcast} = 0.4$ (Muneer and Saluja, 1988).

For non-overcast days (i.e. when $G > D$):

$$G_{\mathrm{TLT}} = (G - D)R_{\mathrm{B}} + D\{(R_{\mathrm{B}}F + T_{\text{non-overcast}})(1 - F)\, F_{\text{sun}} + T_{\text{shade}}\, F_{\text{shade}}\} \qquad (2.7.15)$$

where $T_{\text{non-overcast}}$ is the tilt factor for the sunlit surface under non-overcast conditions (for a vertical surface $T_{\text{non-overcast}} = 0.63$). F is the modulating function which 'mixes' the diffuse circumsolar and background sky irradiation and is given by:

$$F = \frac{G - D}{E} \qquad (2.7.16)$$

If the ground-reflected irradiation is assumed to be isotropic the total sloped irradiation is obtained from:

$$G_{\mathrm{TLT}} = BR_{\mathrm{B}} + DR_{\mathrm{D}} + G_{\rho}[(1 - \cos\mathrm{TLT})/2] \qquad (2.7.17)$$

In the above equation ρ is the ground albedo (see Chapter 6).

Table 2.7.1 and Figures 2.7.1–2.7.4 enable comparison of the respective performance of the above two procedures to obtain monthly-averaged and individual daily slope irradiation for Easthampstead and Lerwick. On an individual day-to-day basis the anisotropic method outperforms the isotropic model. However, as would be expected, the monthly

Table 2.7.1 Monthly-averaged daily irradiation for Easthampstead (51.383°N) (kW h/m^2)

Month	G	D	$G_{\mathrm{TLT,N}}$	$G_{\mathrm{TLT,E}}$	$G_{\mathrm{TLT,S}}$	$G_{\mathrm{TLT,W}}$
Measured values						
January	0.62	0.45	0.19	0.36	0.82	0.34
February	1.24	0.83	0.33	0.75	1.49	0.69
March	2.32	1.36	0.52	1.29	2.02	1.18
April	3.32	2.01	0.83	1.80	2.15	1.71
May	4.41	2.64	1.18	2.25	2.11	2.12
June	5.22	2.76	1.41	2.69	2.20	2.53
Computed values, Muneer's model						
January	0.62	0.45	0.18	0.42	1.10	0.42
February	1.24	0.83	0.33	0.82	1.73	0.82
March	2.32	1.36	0.54	1.49	2.42	1.49
April	3.32	2.01	0.80	1.95	2.20	1.95
May	4.41	2.64	1.06	2.46	2.14	2.46
June	5.22	2.76	1.10	2.88	2.13	2.88
MBE, %			−7	15	16	24
Computed values, isotropic model						
January	0.62	0.45	0.22	0.42	0.93	0.42
February	1.24	0.83	0.41	0.81	1.45	0.81
March	2.32	1.36	0.68	1.48	2.07	1.48
April	3.32	2.01	–	1.95	2.01	1.95
May	4.41	2.64	–	2.47	2.11	2.47
June	5.22	2.76	–	2.90	2.20	2.90
MBE, %			9	15	0	25

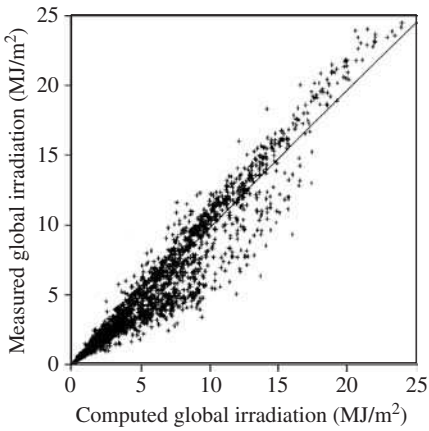

Figure 2.7.1 *Measured versus computed daily sloped irradiation for Easthampstead, UK (isotropic model)*

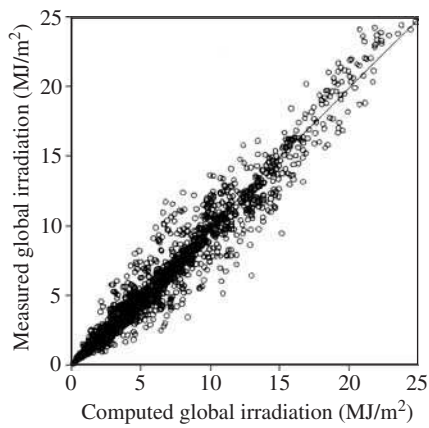

Figure 2.7.2 *Measured versus computed daily sloped irradiation for Easthampstead, UK (anisotropic model)*

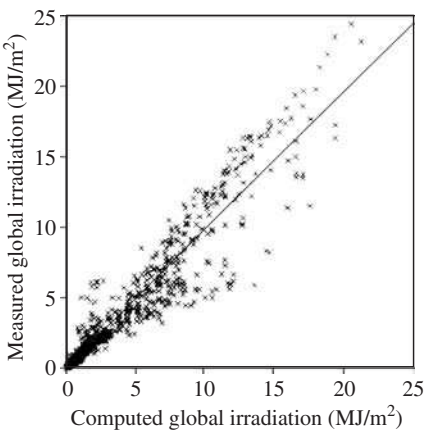

Figure 2.7.3 *Measured versus computed daily sloped irradiation for Lerwick, UK (isotropic model)*

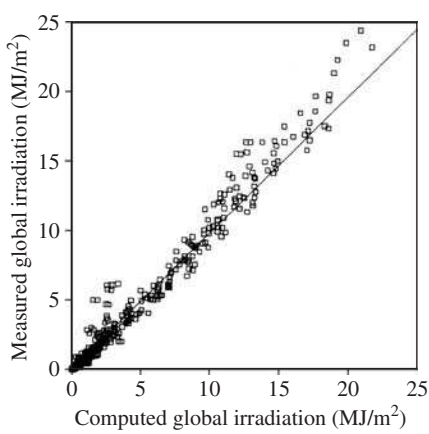

Figure 2.7.4 *Measured versus computed daily sloped irradiation for Lerwick, UK (anisotropic model)*

averaging procedure masks the intricate details. Both of the above procedures are, however, quite restrictive and cumbersome. A much more precise method for obtaining averaged-daily sloped irradiation will be introduced in Chapter 4. The procedure requires as a first step the decomposition of averaged-daily values into hourly values, to be introduced in Chapter 3.

2.8 Exercises

2.8.1 Monthly-averaged weather data for 15 principle locations is given in Table B1. Calculate monthly-averaged horizontal daily global and diffuse irradiation for London.

Compare your results with the long-term figures reported by the Meteorological Office (1980a) given in Table 2.2.1. You may use Prog2-1.Exe for the above task.

2.8.2 Using the computed monthly-averaged horizontal daily global and diffuse irradiation (Exercise 2.8.1) prepare a table for irradiation on vertical surfaces with principal cardinal aspects. You may use Prog2-3.Exe.

2.8.3 On 28 April 1993 the following irradiation were logged in Edinburgh (55.95°N and 3.2°W) (values in kW h/m^2):

global, horizontal = 5.883
diffuse, horizontal = 2.010
north, vertical = 0.878
east, vertical = 2.08
south, vertical = 4.53
west, vertical = 4.05.

Use Prog2-4.Exe to estimate vertical slope irradiation for the cardinal aspects. Perform computations using the isotropic and Muneer and Saluja model. Compare your figures against measured data given above and comment on the error statistics.

2.8.4 File 2-1.Xls contains clear-sky hourly radiation and daily sunshine data for two Indian locations. Use Eq. (2.1.1) and Table 2.1.2 to compute daily total irradiation from sunshine information. Compare your results with the measured data provided.

References

Ångström, A.K. (1924) On the computation of global radiation from records of sunshine. *Arkiv. Geof*. 2(22), 471.

Bartoli, B., Cuomo, V. and Amato, U. (1982) Diffuse and beam components of daily global radiation in Genova and Macerata. *Solar Energy* 28, 307.

Choudhury, N.K.O. (1963) Solar energy at New Delhi. *Solar Energy* 7, 44.

Colliver, D.G. (1991) Solar Energy in Agriculture. *Energy in World Agriculture*, ed. B.F. Parker. Elsevier, Amsterdam.

Cowley, J.P. (1978) The distribution over Great Britain of global solar radiation on a horizontal surface. *Met. Mag*. 107, 357.

Driesse, A. and Thevenard, D. (2002) A test of Suehrcke's sunshine–radiation relationship using a global data set. *Solar Energy* 72, 167.

Drummond, A.J. (1956) On the measurement of sky radiation. *Arch. Materiol. Vienna* B7, 414.

Duffie, J.A. and Beckman W.A. (1991) *Solar Engineering of Thermal Processes*. Wiley, New York.

Erbs, D.G., Klein, S.A. and Duffie, J.A. (1982) Estimation of the diffuse fraction of hourly, daily and monthly-averaged global radiation. *Solar Energy* 28, 293.

Garg, H.P. and Garg, S.N. (1985) Correlation of monthly-average daily global, diffuse and beam radiation with bright sunshine hours. *En. Conv. Mgmt*. 25, 409.

Hawas, M. and Muneer, T. (1983) Correlation between global radiation and sunshine data for India. *Solar Energy* 30, 289.

Hawas, M. and Muneer, T. (1984) Study of diffuse and global radiation characteristics in India. *En. Conv. Mgmt*. 24, 143.

Hay, J.E. (1979) Calculation of monthly mean solar radiation for horizontal and inclined surfaces. *Solar Energy* 23, 301.

Jain, S. and Jain, P.C. (1988) A comparison of the Ångström-type correlations and the estimation of monthly average daily global irradiation. *Solar Energy* 40, 93.

Klein, S.A. (1977) Calculation of monthly-average insolation on tilted surfaces. *Solar Energy* 19, 325.

Lam, J. and Li, D. (1996) Regression analysis of solar radiation and sunshine duration. *Architect. Sci. Rev.* 39, 15.

Le Baron, B. and Dirmhirn, I. (1983) Strengths and limitations of the Liu and Jordan model to determine diffuse from global irradiance. *Solar Energy* 31, 167.

Liu, B.Y.H. and Jordan, R.C. (1960) The inter-relationship and characteristic distribution of direct, diffuse and total solar radiation. *Solar Energy* 4, 1.

Liu, B.Y.H. and Jordan, R.C. (1962) Daily insolation on surfaces tilted towards the equator. *ASHRAE J*. 3, 53.

Lof, G.O.G., Duffie, J.A. and Smith, C.O. (1966) World distribution of solar radiation. *Engineering Experiment Station Report 21*, University of Wisconsin, Madison, USA.

Mani, A. and Chacko, O. (1973) Solar radiation climate of India. *Solar Energy* 14, 139.

Mani, A. and Rangarajan, S. (1983) Techniques for the precise estimation of hourly values of global, diffuse and direct solar radiation. *Solar Energy* 31, 577.

Meteorological Office (1980a) *Solar Radiation data for the United Kingdom 1951–75*. MO 912. Meteorological Office, Bracknell.

Meteorological Office (1980b) *Radiation: Short Period Averages 1957–75*. Meteorological Office, Pune, India.

Muneer, T. and Hawas, M. (1984) Correlation between daily diffuse and global radiation for India. *En. Conv. Mgmt.* 24, 151.

Muneer, T. and Saluja, G. (1985) A brief review of models for computing solar radiation on inclined surfaces. *En. Conv. Mgmt*. 25, 443.

Muneer, T. (1987) *Solar Radiation Modelling for the United Kingdom*. PhD Thesis. CNAA, London.

Muneer, T. and Saluja, G.S. (1988) Estimation of daily inclined surface solar irradiation – an anisotropic model. *Proc. Inst. Mech. Engrs*. 202, 333.

Nagrial, M. and Muneer, T. (1984) Relationship between global radiation and sunshine hours for Pakistan. *Proc. Int. Conf. on Science – Past, Present and Future*. Islamabad, Pakistan.

Page, J.K. (1961) *Proc U.N. Conf. on New Sources of Energy*, paper no. 35/5/98.

Page, J.K. (1977) *The Estimation of Monthly Mean Value of Daily Short Wave Irradiation on Vertical and Inclined Surfaces from Sunshine Records for Latitudes 60°N to 40°S*. BS32, Department of Building Science, University of Sheffield, UK.

Page, J.K. and Lebens, R. (1986) *Climate in the United Kingdom*. HMSO, London.

Pereira, M.C. and Rabl, A. (1979) The average distribution of solar radiation – correlations between diffuse and hemispherical and between daily and hourly insolation values. *Solar Energy* 22, 155.

Rao, C.R.N., Bradley, W.A. and Lee, T.Y. (1984) The diffuse component of the daily global solar irradiation at Corvallis, Oregon. *Solar Energy* 32, 637.

Rawlins, F. (1984) The accuracy of estimates of daily global irradiation from sunshine records for the United Kingdom. *Met. Mag.* 113, 187.

Ruth, D.W. and Chant, R.E. (1976) The relationship of diffuse radiation to total radiation in Canada. *Solar Energy* 18, 153.

Saluja, G.S. and Muneer, T. (1986) Correlation between daily diffuse and global irradiation for the UK. *BSER & T* 6, 103.

Saluja, G.S., Muneer, T. and Smith, M.E. (1988) Methods for estimating solar radiation on a horizontal surface. *Ambient Energy* 9, 59.

Schulze, R.E. (1976) Physically based method of estimating solar radiation from suncards. *Agricul. Met.* 16, 85.

Smietana, P.J., Flocchini, R.G., Kennedy, R.L. and Hatfield, H.L. (1984) A new look at the correlation of K_d and K_t ratio models using one-minute measurements. *Solar Energy* 32, 99.

Stanhill, G. (1966) Diffuse sky and cloud radiation in Israel. *Solar Energy* 10, 96.

Suehrcke, H. (2000) On the relationship between duration of sunshine and solar radiation on the earth's surface: Ångström's equation revisited. *Solar Energy* 68, 417.

Tiris, M., Tiris, C. and Ture, I.E. (1996) Correlations of monthly-average daily global, diffuse and beam radiation with hours of bright sunshine in Gebze, Turkey. *En. Conv. Mgmt*. 37, 1417.

Tuller, S.E. (1976) The relationship between diffuse, total and extraterrestrial solar radiation. *Solar Energy* 18, 259.

Turton, S.M. (1987) Relationship between total radiation and sunshine duration in the humid tropics. *Solar Energy* 38, 353.

3 HOURLY HORIZONTAL IRRADIATION AND ILLUMINANCE

Introduction

It was pointed out in the previous chapter that irradiation data are usually available as the amount of short-wave energy received on a horizontal surface. The frequency at which solar radiation data are required depends on the application. With the advent of cheap and yet powerful desk-top computers it is now possible to perform energy-system simulations using hourly or sub-hourly data. Such simulations, however, require reliable estimates of slope surface irradiation and illuminance which may be computed from the corresponding horizontal global and diffuse energy data. The UK radiation measurement network is one of the best in Europe, yet long-term hourly data for the latter two quantities are available for only a dozen sites. Therefore, methods are required for estimations to be carried out from long-term records of daily irradiation or other meteorological parameters such as humidity, pressure and sunshine. In this chapter models are presented which enable computation of hourly or instantaneous irradiance and illuminance.

3.1 Monthly-averaged hourly horizontal global irradiation

It has been pointed out earlier that hourly irradiation data leads to more accurate modelling of solar energy processes. Since daily irradiation is measured at more sites than its hourly counterpart, it is logical to consider the correlation between the two. Several meteorological stations publish their data in terms of monthly-averaged values of daily global irradiation. Where such measurements are not available, it may be possible to obtain them from the long-term sunshine data via models presented in Chapter 2.

In this section, the correlation between hourly and daily global radiation is examined. The models presented in this and the following section should be used for long-term averaged hourly computations. Figure 3.1.1 shows the calculation scheme for averaged hourly irradiation.

The original work in this field is attributed to Whillier (1956). Liu and Jordan (1960) extended Whillier's work and developed a set of regression curves, shown in Figure 3.1.2, which illustrates the effect of the displacement of the hour from solar noon, and the day length, on the ratio of hourly to daily global irradiation (r_G).

Collares-Pereira and Rabl (1979) reconfirmed the correctness of the plots of Liu and Jordan and, by using a least-squares fit, obtained:

$$r_G = \frac{\pi}{24}(a' + b' \cos \omega)\frac{\cos \omega - \cos \omega_s}{\sin \omega_s - \omega_s \cos \omega_s} \tag{3.1.1}$$

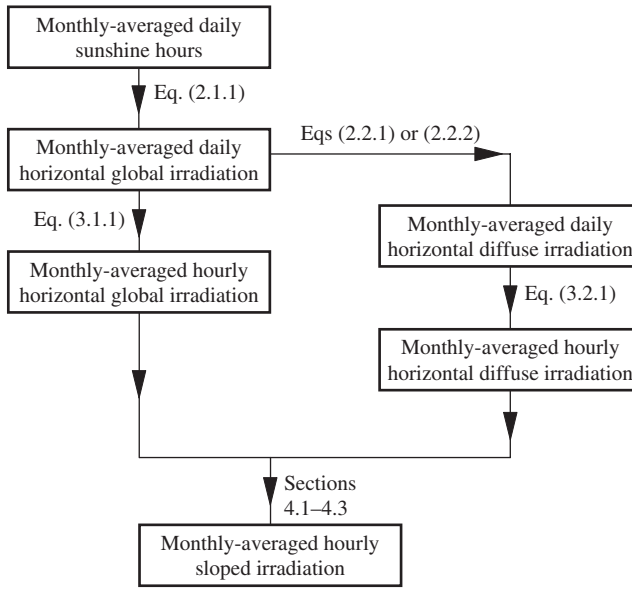

Figure 3.1.1 *Calculation scheme for monthly-averaged hourly sloped irradiation*

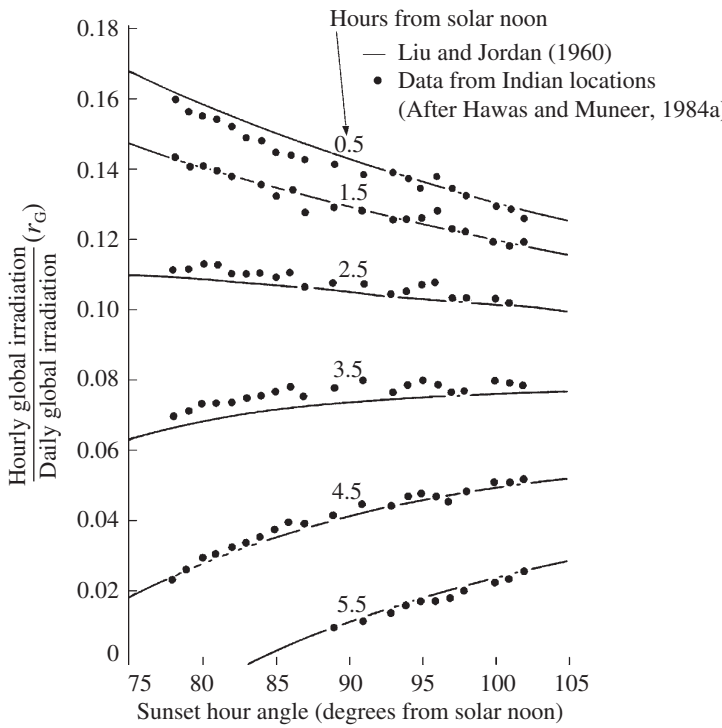

Figure 3.1.2 *Ratio of hourly to daily global irradiation*

where:

$$a' = 0.409 + 0.5016 \sin(\omega_s - 1.047) \quad (3.1.2)$$

$$b' = 0.6609 - 0.4767 \sin(\omega_s - 1.047) \quad (3.1.3)$$

Iqbal (1979) tested the applicability of Liu–Jordan model for three Canadian locations (Toronto, Winnipeg and Vancouver). He found a good agreement, barring the 4.5 h curve. Hawas and Muneer (1984a) used 20 years of averaged data for 13 locations in India to test Liu and Jordan's approach. Figure 3.1.2 shows their data plotted along with Liu and Jordan's regression curves. The scatter of the points is noticeable, and in two cases (2.5 and 3.5 h), a definite shift from Liu and Jordan's regression curves is apparent.

In all the studies reported here, recordings on either side of solar noon have been lumped together. Iqbal (1979) has drawn attention to the problem of asymmetry around solar noon. For Vancouver, he has reported morning values consistently lower than the corresponding afternoon values, while for Montreal no definite pattern was found.

Saluja and Robertson (1983) have also observed that the computed values of yearly long-term averages of irradiation on east- and west-facing surfaces for Aberdeen, Easthampstead and Kew differed from those for other locations in the UK, e.g. higher morning irradiation.

Example 3.1.1

Refer to the extreme right hand column of Table 3.1.1 which provides the monthly-averaged daily global irradiation for Eskdalemuir, Scotland (Meteorological Office, 1980). Evaluate the use of Eq. (3.1.1) to obtain hourly estimates. Note that the time reference in this and the subsequent section is solar time.

Prog3-1.For enables the above estimations to be carried out. An error analysis is also provided. It is evident that barring the sunrise/sunset period the Liu–Jordan model provides reasonable estimates of averaged hourly irradiation for the UK.

Gueymard (2000) has presented a more generalised method of obtaining hourly-averaged global irradiation. Using a large data set of 135 stations encompassing very diverse geographic locations (82.5°N to 67.6°S) and climates, he has presented two new models for such predictions provided their daily counterparts are known beforehand. Alongside those new models a review and validation of a number of recent developments has also been undertaken by Gueymard (2000). The most accurate of these was reported to be 'daily integration model'. This model is described below by means of definition of a number of variables and their inter-relationships:

Step 1 $k = 24/\pi$

Step 2 $\sin h_0 = qA(\omega_s)/\omega_s$, $q = \cos \mathrm{LAT} \cos \mathrm{DEC}$ and $A(\omega_s) = \sin \omega_s - \omega_s \cos \omega_s$

Step 3 Day length (in hours), $S_0 = k\omega_s$

Step 4 $r_0 = (\cos \omega - \cos \omega_s)/[kA(\omega_s)]$

Step 5 $a_1 = 0.413\,41K_t + 0.611\,97K_t^2 - 0.018\,86K_tS_0 + 0.007\,59S_0$, and

$a_2 = \max(0.054, 0.281\,16 + 2.2475K_t - 1.761\,18K_t^2 - 1.845\,35 \sin h_0 + 1.6811 \sin^3 h_0)$

Step 6 $B(\omega_0) = \omega_0(0.5 + \cos^2 \omega_0) - 0.75 \sin 2\omega_0$

Step 7 $r_G = r_0[1 + q(a_2/a_1)kA(\omega_0)r_0]/[1 + q(a_2/a_1)B(\omega_0)/A(\omega_0)]$

An evaluation of Gueymard's model is provided in Example 3.2.2.

Table 3.1.1 Monthly-averaged hourly horizontal irradiation for Eskdalemuir (55.3°N and 3.2°W)

		Time (h)												
Month		6.5	7.5	8.5	9.5	10.5	11.5	12.5	13.5	14.5	15.5	16.5	17.5	Total $\bar{G}$
Measured Values (W h/m^2)														
January	I_G	0	0	8	36	64	83	81	67	36	8	0	0	381
	I_D	0	0	8	28	47	56	56	47	28	8	0	0	281
February	I_G	3	14	61	125	172	197	194	164	117	58	14	0	1119
	I_D	3	11	42	75	103	117	114	100	72	42	11	0	683
March	I_G	19	81	153	219	267	286	289	258	208	147	75	19	2014
	I_D	17	53	97	133	164	172	169	156	128	94	53	17	1250
April	I_G	92	178	269	333	369	400	403	361	308	244	164	86	3247
	I_D	61	108	156	189	217	233	233	211	181	147	103	61	1936
May	I_G	147	231	297	358	411	422	428	397	358	303	225	144	3900
	I_D	94	142	178	214	242	261	258	244	217	183	139	94	2397
June	I_G	186	281	361	406	458	486	500	464	414	347	269	186	4669
	I_D	114	156	203	236	267	281	281	267	233	197	156	114	2717
Computed Values (W h/m^2)														
January	I_G	0	0	0	35	68	87	87	68	35	0	0	0	380
	I_D	0	0	0	29	50	60	60	50	29	0	0	0	278
February	I_G	0	12	66	121	167	192	192	167	121	66	12	0	1116
	I_D	0	10	47	77	99	110	110	99	77	47	10	0	686
March	I_G	11	73	144	211	265	294	294	265	211	144	73	11	1996
	I_D	10	57	99	133	157	170	170	157	133	99	57	10	1252
April	I_G	88	165	246	319	376	406	406	376	319	246	165	88	3200
	I_D	66	112	153	187	211	223	223	211	187	153	112	66	1904
May	I_G	142	218	295	363	415	442	442	415	363	295	218	142	3750
	I_D	101	144	184	215	238	250	250	238	215	184	144	101	2264
June	I_G	191	270	348	416	467	494	494	467	416	348	270	191	4372
	I_D	123	164	201	231	252	263	263	252	231	201	164	123	2468
Error (%)														
January	I_G	0	0	0	−3	6	4	8	2	−3	0	0	0	0
	I_D	0	0	0	4	6	8	8	6	4	0	0	0	−1
February	I_G	0	−14	8	−3	−3	−3	−1	2	4	13	−14	0	0
	I_D	0	−10	13	3	−4	−6	−3	−1	7	13	−10	0	0
March	I_G	−43	−9	−6	−4	−1	3	2	3	1	−2	−3	−43	−1
	I_D	−40	8	2	0	−4	−1	0	1	4	5	8	−40	0
April	I_G	−4	−7	−9	−4	2	1	1	4	3	1	1	2	−1
	I_D	8	3	−2	−1	−3	−4	−4	0	4	4	9	8	−2
May	I_G	−4	−5	−1	1	1	5	3	4	1	−3	−3	−2	−4
	I_D	7	2	3	1	−2	−4	−3	−3	−1	0	4	7	−6
June	I_G	3	−4	−4	3	2	2	−1	1	1	0	0	3	−6
	I_D	8	5	−1	−2	−6	−6	−6	−6	−1	2	5	8	−9

3.2 Monthly-averaged hourly horizontal diffuse irradiation

Long-term averages of hourly diffuse irradiation can be computed from monthly-average values of daily diffuse irradiation if the ratio of hourly to daily diffuse irradiation, r_D is

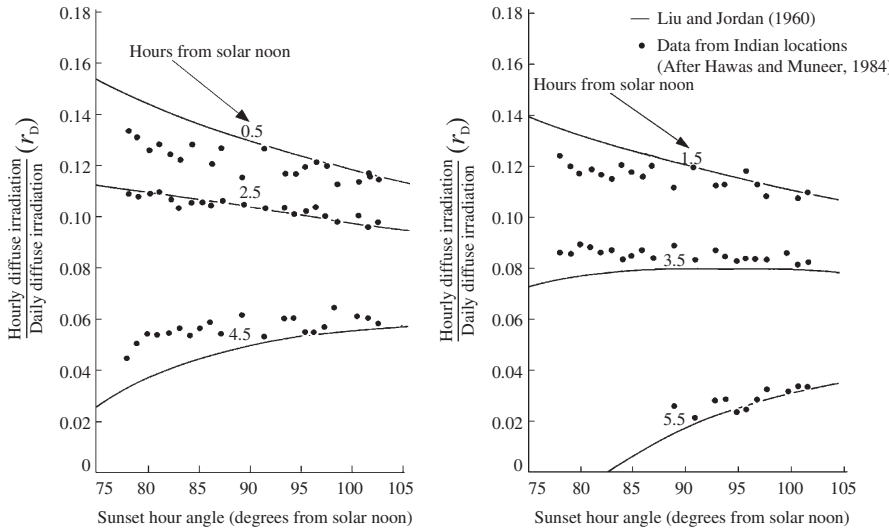

Figure 3.2.1 *Ratio of hourly to daily diffuse irradiation*

known. Liu and Jordan (1960) have presented a theoretical model:

$$r_D = \frac{\pi}{24} \frac{\cos \omega - \cos \omega_s}{\sin \omega_s - \omega_s \cos \omega_s} \tag{3.2.1}$$

The model shows good agreement with measured data for North America as confirmed by Iqbal (1979).

Collares-Pereira and Rabl (1979) have suggested the possibility of refinement of the above r_D model by incorporating the dependence of the transmission coefficient, τ_D on $\bar{K}_T$ and including the angle of incidence in the relationship. In their study of data from 13 Indian locations, Hawas and Muneer (1984a) found considerable data scatter around the r_D model. Indeed, different trends, reflecting a location dependence were reported by Hawas and Muneer (1984a). Their averaged data points are superimposed on Liu and Jordan's regression curves, shown in Figure 3.2.1. The Indian data points show a compressed range of r_D and a noticeable scatter for the 2.5 h curve. Individual monthly values of r_D for the instance of 0.5 solar hour for all Indian locations are shown in Figure 3.2.2. The order of scatter indicates that the r_D model is unsuitable for computing hour-by-hour irradiation.

The effect of $\bar{K}_T$ on r_D was investigated by Hawas and Muneer (1984a). A sample plot is shown in Figure 3.2.3. A consistently decreasing trend of r_D with increasing $\bar{K}_T$ is apparent. The constant value as predicted by the Liu–Jordan model is also shown.

Mani and Rangarajan (1983) have also presented a set of curves for Indian locations, noticeably different from those obtained by Liu and Jordan.

Hay (1976; 1979) attempted to correlate the hourly global and diffuse radiation (I'_G and I'_D respectively) incident before multiple reflections between the ground and sky to the measured hourly global horizontal radiation $\bar{I}_G$ and the fractional possible sunshine $\bar{n}/\bar{N}$.

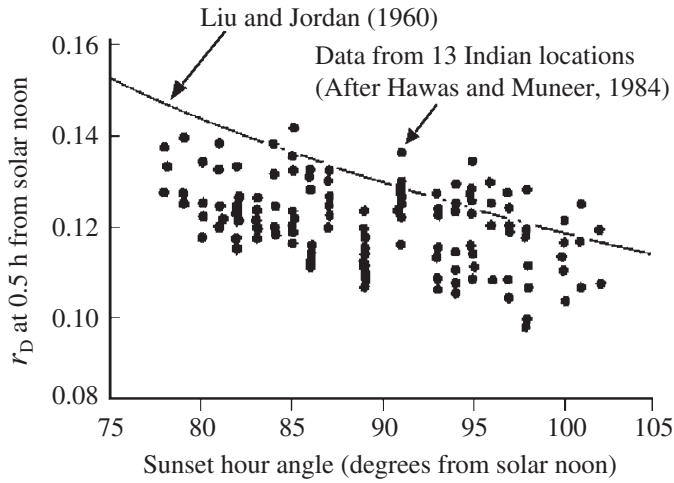

Figure 3.2.2 *Individual (not averaged) values of* r_D *at 0.5 h from solar noon*

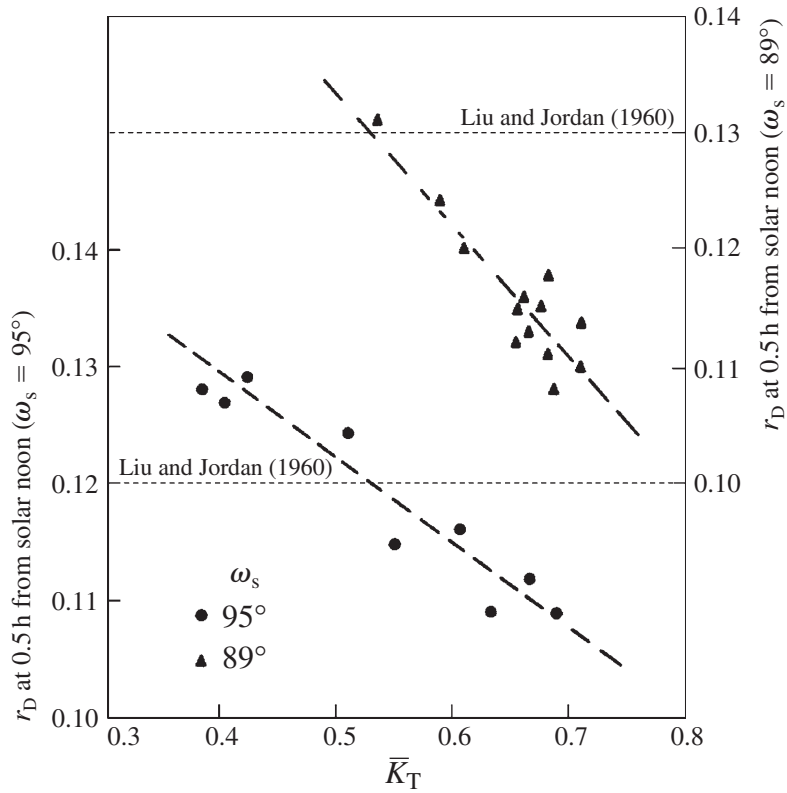

Figure 3.2.3 r_D *at 0.5 h from solar noon for two fixed values of* ω_s

Hay's model is as follows:

$$\bar{I}_G - \bar{I}'_G = \bar{I}_G \rho[\rho_a(\bar{n}/\bar{N}) + \rho_c(1 - \bar{n}/\bar{N})] \tag{3.2.2}$$

$$\bar{I}_D - \bar{I}'_D = \bar{I}_G \rho[\rho_a(\bar{n}/\bar{N}) + \rho_c(1 - \bar{n}/\bar{N}] \tag{3.2.3}$$

$$\frac{\bar{I}'_D}{\bar{I}'_G} = 0.9702 + 1.6688\frac{\bar{I}'_G}{\bar{I}_E} - 21.303\left(\frac{\bar{I}'_G}{I_E}\right)^2 + 51.288\left(\frac{\bar{I}'_G}{I_E}\right)^3 - 50.081\left(\frac{\bar{I}'_G}{I_E}\right)^4 + 17.551\left(\frac{\bar{I}'_G}{I_E}\right)^5 \tag{3.2.4}$$

Here ρ, ρ_a and ρ_c are respectively the albedo of the ground, clear sky and clouds. In order to compute $\bar{I}_D$, one has to calculate $\bar{I}'_G$ by Eq. (3.2.2) using $\bar{I}_G$, proceed to compute $\bar{I}'_D$ by Eq. (3.2.4) and then compute $\bar{I}_D$ by Eq. (3.2.3). Iqbal (1983) has compared the accuracy of Liu and Jordan's method with that of Hay's for Canadian locations. The Liu–Jordan model was found to provide better accuracy, in addition to being simpler and straightforward.

Table 3.1.1 enables evaluation of the r_D model of Eq. (3.2.1) for Eskdalemuir data. The estimations were carried out using Prog3-1.For. In this case it may be noted that the accuracy is better than that of the r_G model of Eq. (3.1.1).

Example 3.2.1

Refer to Table 3.1.1, wherein the measured monthly-averaged daily global irradiation, $\bar{G}$ is given as 1.119 kW h/m^2. Using Prog2-1.For, with its built-in Eq. (2.2.2), compute the monthly-averaged daily diffuse irradiation $\bar{D}$. Comment on the use of your computed value of $\bar{D}$ to obtain the hourly estimates.

Prog2-1.For provides $\bar{D} = 0.666$ kW h/m^2. This figure is within 2% of the corresponding measured value. The hourly diffuse irradiation estimates may also be obtained with good accuracy as demonstrated in Table 3.1.1.

Example 3.2.2

Refer to Table 3.2.1, wherein the measured monthly-averaged daily global and diffuse irradiation (kW h/m^2) for Chennai, India are given as 5.824 and 2.857, respectively. Using

Table 3.2.1 Monthly-averaged hourly horizontal irradiation (W/m^2) for Chennai (11.0°N and 78.25°E)

Hour ending at	I_G, Measured	I_G, Eq. (3.1.1)	I_G, Gueymard	I_D, Measured	I_D, Eq. (3.2.1)
7	95	108	109	72	71
8	258	265	268	159	154
9	437	434	437	235	228
10	602	591	595	291	289
11	726	714	718	328	332
12	794	780	784	341	354
Daily totals (kW h/m^2)	5.824			2.857	

Prog3-1.For obtain hourly estimates of the two irradiation components using Eq. (3.1.1) and Gueymard methods for global and Eq. (3.2.1) for diffuse irradiation.

The computed values are displayed in Table 3.2.1 alongside the respective measured data. We note that:

(a) in general terms the concordance between measured and computed data sets is good;
(b) although it is claimed that the Gueymard method generally improves the global irradiation estimates, the improvement is not obvious in this case;
(c) at least in this particular instance Eq. (3.2.1) provides a fairly accurate means of obtaining hourly-averaged diffuse irradiation.

3.3 Hourly horizontal global irradiation

It was shown above that Liu–Jordan models may only be used to obtain hourly irradiation data from long-term records of monthly-averaged daily values. Building simulation programs however need detailed hour-by-hour data. In the absence of measured irradiation data, a reliable computational method is the meteorological radiation model (MRM). This model estimates the beam transmission through the terrestrial atmosphere based on its attenuation due to mixed gases (such as oxygen, nitrogen and carbon dioxide), water vapour, ozone and aerosols. Figure 3.3.1 shows the schematic for obtaining hourly irradiation from other measured meteorological parameters. The physical basis of MRM and its performance evaluation is provided in the following sections.

3.3.1 The extraterrestrial solar spectrum

Solar spectral wavelengths are measured in micrometres ($1\,\mu m = 10^{-6}m$), nanometres ($1\,nm = 10^{-9}m$) or Ångströms ($1\,Å = 10^{-8}m$) units. Most broadband solar radiation

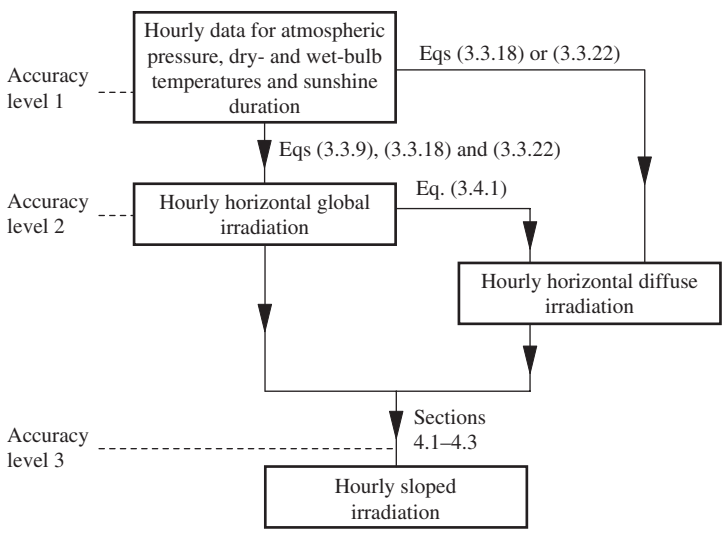

Figure 3.3.1 *Calculation scheme for hourly sloped irradiation*

sensors work in the 300 nm–3μm band since this region covers 98% of the energy radiated by the sun. The distribution of the solar spectral irradiance is not uniform in the range of 250 nm–25μm, i.e. that part of electromagnetic spectrum which starts with ultraviolet (UV) radiation and ends in the near infrared (NIR) region. New developments on the spectral distribution are reported by Gueymard (1995; 2003). In this respect further information is provided in Chapter 5. The summation of all energy received at individual wavelengths in the extraterrestrial solar spectrum equals the solar constant I_{Sc} ($=1367\,W/m^2$). This value of I_{Sc} has been used throughout this book. This is the irradiance received on a surface normal to the sun's rays at the top of the earth's atmosphere and at a sun–earth distance equal to 1 astronomical unit (AU) ($1\,AU = 1.496 \times 10^{11}\,m$) occurring at the vernal and autumnal equinoxes. The energy of the solar spectrum is approximately distributed as follows: UV (8%), visible band (46%) and NIR (46%).

3.3.2 Solar radiation transmission through the earth's atmosphere

To understand the atmospheric transmission of solar radiation it is important to know the composition of the earth's atmosphere. Excluding the water vapour content, the other natural constituents are given in Table 3.3.1 which is based on the *US Standard Atmosphere* (1976). The atmosphere extends to an altitude of 100 km or a pressure of 0.0005 mbar. The naturally occurring gases which play a significant role in the absorption of solar radiation are O_2, N_2 and CO_2 (mixed gases), O_3, H_2O and aerosols. More details are provided in Chapter 5.

3.3.2.1 Mixed gases

The depletion of molecular oxygen by solar UV radiation starts at an altitude of 90 km. Therefore, the concentration of O_2 decreases and that of atomic oxygen increases.

Table 3.3.1 Normal composition of clean atmosphere

Gas	Content (ppmv)
Nitrogen	78 084 000.000
Oxygen	20 948 000.000
Argon	934 000.000
Carbon dioxide	333 000.000
Neon	1 818.000
Ozone	1 200.000
Helium	524.000
Methane	150.000
Krypton	114.000
Hydrogen	50.000
Nitrous oxide	27.000
Carbon monoxide	19.000
Xenon	8.900
Ammonia	0.400
Water vapour	0.400
Sulfur dioxide	0.100
Nitrogen dioxide	0.100
Nitric oxide	0.050
Hydrogen sulfide	0.005

Because molecular nitrogen is difficult to dissociate, its concentration in the atomic form remains very small even at high altitudes.

3.3.2.2 Ozone

This dry air constituent is created in the upper atmosphere mainly by UV solar radiation. At ground level, it is formed through decomposition of nitrous oxide (NO) that enters the atmosphere as a pollutant. The total amount of ozone (l_o) in the atmosphere as a vertical column is given in units of atmosphere centimetres (atm-cm). This is the height of gaseous O_3 in a vertical column of unit area brought to normal temperature and surface pressure (NTP). Values of l_o are measured worldwide and are readily available, e.g. *Red Book* (1992) or given by an approximate formula due to Van Heuklon (1979):

$$l_o = J + \{A + C \sin[D(\mathrm{DN} + F)] + G \sin[H(\mathrm{LONG} + I)]\}[\sin^2(B\ \mathrm{LAT})] \qquad (3.3.1)$$

where l_o is in milli-atm-cm units, $J = 235$ (the equatorial annual average value of l_o) and A, C, D, F, G, H, I and B are constants given in Table 3.3.2.

3.3.2.3 Water vapour

The amount of water vapour in the entire depth of the atmosphere is referred to as precipitable water l_w. This is the total amount of water vapour (cm) in zenith's direction. l_w can be measured by radiometers or estimated from either radiosonde data or via any one of the available empirical models. One such model is given by Eq. (3.3.2) (Perez et al., 1990) which is based on Reitan's (1963) formulation and validated for 15 US locations by Wright et al. (1989):

$$l_w = \exp(0.07\mathrm{DPT} - 0.075) \qquad (3.3.2)$$

The dew-point temperature (DPT) may be obtained from dry-bulb temperature and either wet-bulb temperature or relative humidity (RH). The computational scheme and routines are provided in Chapter 7.

Table 3.3.2 Coefficients for use in Eq. (3.3.1)

Coefficient	Northern hemisphere	Southern hemisphere
A	150	100
C	40	30
D	0.9865	0.9865
F	−30	152.625
G	20	20
H	3°	2°
I, longitude > 0	20°	−75°
I, longitude < 0	0°	−75°
J	235	235
B	1.28	1.5
Latitude	N = +ve, S = −ve	
Longitude	E = +ve, W = −ve	

3.3.2.4 Aerosols

An aerosol is a small solid or liquid particle that remains suspended in the air following the motion of the air stream. Coagulated water vapour molecules following the motion of the air are an example. All suspended particles showing variation in volume, distribution, size, form and material composition are aerosols. They are responsible for the 'haze' and are either of terrestrial origin (e.g. industrial smoke, volcanic eruptions, sandstorms and forest fires) or of marine origin (e.g. salt crystals and ocean spray). Suspended water and ice particles in fog and clouds are not classified as aerosols. Similarly, rain, snow and hail are not aerosol particles. Aerosol particles range in radius from 0.001 to 100 μm.

3.3.2.5 Relative and absolute optical air mass

The attenuation of solar energy by molecules and aerosols in the atmosphere is a function of the type and number of molecules and aerosols in the path of the solar rays. The density of the molecules (or aerosols) multiplied by the path length traversed by a solar ray represents the mass of a substance in a column of unit cross-section. This is called optical air mass or simply air mass. The ratio of the air mass in a slant path in the atmosphere to the air mass in the zenith direction is called relative air mass m. From the definition it is implied that m takes different values for various solar elevation angles. For a homogeneous atmosphere m may be obtained via Kasten's (1993) formula which provides an accuracy of 99.6% for zenith angles up to 89°:

$$m = [\sin \mathrm{SOLALT} + 0.505\,72(\mathrm{SOLALT} + 6.079\,95)^{-1.6364}]^{-1} \tag{3.3.3a}$$

A modified relationship for air mass has also been provided by Gueymard (1993a) in the form of Eq. (3.3.3b):

$$m = [\sin \mathrm{SOLALT} + 0.001\,767\,59(\mathrm{SOLALT}(94.375\,15 - \mathrm{SOLALT})^{-1.215\,63})]^{-1} \tag{3.3.3b}$$

The above equations are applicable to a standard pressure p_0 of 1013.25 mbar at sea level. For other pressures the air mass may be corrected as:

$$m' = m(p/1013.25) \tag{3.3.4}$$

where p is the atmospheric pressure (in mbar) at height h (metres above sea level). If p is not known an approximate formula due to Lunde (1980) may be used:

$$p/p_0 = \exp(-0.000\,118\,4h) \tag{3.3.5}$$

3.3.3 Attenuation of beam solar radiation

Radiative transfer through terrestrial atmosphere has been discussed at length by Chandrasekhar (1950), Goody (1964), Kondratyev (1969), Barbaro et al. (1979) and several others. When solar radiation enters the earth's atmosphere a part of the incident energy is lost by the mechanisms of scattering and absorption. The scattered radiation is called diffuse radiation, while that part which arrives at the surface of the earth directly from the sun is called direct or beam radiation. According to the Bouguer–Lambert law, also known as Beer's law (circa 1760), the attenuation of light through a medium is proportional to the

distance traversed in the medium and the local flux of radiation. This law is written as:

$$I_B = I_E \exp(-km) \tag{3.3.6}$$

where I_E is the hourly averaged or instantaneous extraterrestrial irradiance on a horizontal surface, and k is known as the total attenuation coefficient, extinction coefficient or optical thickness. I_E may be computed from:

$$I_E = 1367[1 + 0.033\cos(0.017\,202\,4\mathrm{DN})]\sin \mathrm{SOLALT} \tag{3.3.7}$$

Defining the transmission coefficient as $\tau = \exp(-km)$, Eq. (3.3.6) may be written as:

$$I_B = I_E\tau \tag{3.3.8}$$

3.3.3.1 Rayleigh and Mie scattering

When an electromagnetic wave strikes a particle, part of the incident energy is scattered in all directions. If the particle size is smaller than the wavelength, the phenomenon is called Rayleigh scattering. However, if the particle is of the order of the wavelength the process is known as Mie scattering. In the atmosphere, air molecules cause Rayleigh scattering and aerosols Mie scattering. Therefore if τ_r and τ_α are the respective transmittances for the Rayleigh and Mie scattering and τ_g, τ_o, and τ_w the mixed gases, ozone and water vapour transmittances, Eq. (3.3.8) becomes:

$$I_B = I_E\tau_r\tau_\alpha\tau_g\tau_o\tau_w \tag{3.3.9}$$

3.3.3.2 Ångström's turbidity coefficients for aerosol scattering

Ångström (1929; 1930) suggested a single formula for $k_{\alpha\lambda}$, generally known as Ångström's turbidity formula:

$$k_{\alpha\lambda} = \beta\lambda^{-\alpha} \tag{3.3.10}$$

where β is the Ångström's turbidity coefficient, α the wavelength exponent and λ the wavelength (μm). β is a measure of the amount of the aerosols in the atmosphere in the zenith direction. Typically, it varies in the range 0–0.5. α is an index of the size distribution of the aerosol particles. Large values of this coefficient indicate a higher ratio of small to large particles. α typically ranges from 0.5 to 2.5, but a value of 1.3 is commonly employed as originally suggested by Ångström for natural atmospheres. Negative values of this coefficient have however been reported for polluted atmospheres.

The transmittance coefficient due to aerosol scattering may be written as:

$$\tau_\alpha = \int_{\lambda=0.3\,\mu\mathrm{m}}^{3\,\mu\mathrm{m}} \tau_{\alpha\lambda}\,\mathrm{d}\lambda = \int_{\lambda=0.3\,\mu\mathrm{m}}^{3\,\mu\mathrm{m}} \exp(-\beta\lambda^{-\alpha}m_\alpha)\mathrm{d}\lambda \tag{3.3.11}$$

Therefore if estimations of the pair α, β exist for any location, a value of τ_α can be deduced. An alternate way of estimating τ_α is the relationship of Bird and Hulstrom (1981) given as:

$$k_\alpha = 0.2758k_{\alpha,\lambda=0.5\,\mu\mathrm{m}} + 0.35k_{\alpha,\lambda=0.5\,\mu\mathrm{m}} \tag{3.3.12}$$

where $k_{\alpha,\lambda=0.35\,\mu\mathrm{m}}$ and $k_{\alpha,\lambda=0.5\,\mu\mathrm{m}}$ are the attenuation coefficients due to aerosol scattering at the wavelengths 350 nm (no molecular absorption) and 500 nm (ozone weak absorption).

For UK these values have been given by Muneer et al. (1996) as 0.72 and 0.56. It is worth mentioning that geographical variations have a significant influence on k_α, e.g. its respective value for UK and the US are 0.394 and 0.387. Note that Shettle and Fenn (1975) have also provided the relevant information.

3.3.3.3 Atmospheric transmittances

The following section provides equations for estimating the transmittances required to obtain the terrestrial beam irradiance. A total of 14 coefficients [COF(i), i = 1,14] are required in Eqs (3.3.13)–(3.3.17). These coefficients are given in Table 3.3.3 for the respective climates of northern Europe and southern Europe/USA.

According to Iqbal (1983):

$$\tau_\alpha = \exp[-k_\alpha^{\mathrm{COF(1)}}\,(1 + k_\alpha - k_\alpha^{\mathrm{COF(2)}})m'^{\mathrm{COF(3)}}] \tag{3.3.13}$$

Also according to Lacis and Hansen (1974):

$$\tau_\mathrm{o} = 1 - [0.1611x_\mathrm{o}(1 + 139.48x_\mathrm{o})^{-0.3035} - 0.002\,715x_\mathrm{o}(1 + 0.044x_\mathrm{o} + 0.0003x_\mathrm{o}^2)^{-1}],$$
$$x_\mathrm{o} = l_\mathrm{o}m \tag{3.3.14}$$

According to Davies et al. (1975):

$$\tau_\mathrm{r} = \mathrm{COF(4)} - \mathrm{COF(5)}m' + \mathrm{COF(6)}m'^2 - \mathrm{COF(7)}m'^3 + \mathrm{COF(8)}m'^4 \tag{3.3.15}$$

According to Lacis and Hansen (1974):

$$\tau_\mathrm{w} = 1 - \mathrm{COF(9)}x_\mathrm{w}[(1 + \mathrm{COF(10)}x_\mathrm{w})^{\mathrm{COF(11)}} + \mathrm{COF(12)}x_\mathrm{w}]^{-1},$$
$$x_\mathrm{w} = l_\mathrm{w}m \tag{3.3.16}$$

Table 3.3.3 Coefficients for Eqs (3.3.13)–(3.3.17)

	UK/northern Europe			USA/southern Europe
i	Clear SF = 1	Overcast SF = 0	Non-overcast SF > 0	Clear SF = 1
1	1.492 90	0.843 73	2.114 30	0.873
2	0.398 80	0.719 97	0.353 40	0.7088
3	0.743 83	1.040 70	1.059 30	0.9108
4	0.892 02	0.049 52	0.832 50	0.972
5	0.074 01	0.068 16	−0.021 60	0.082 62
6	0.009 96	0.010 87	0.017 40	0.009 33
7	0.000 94	0.000 97	0.000 70	0.000 95
8	0.000 18	−0.000 10	0.000 20	0.000 437
9	2.430 00	3.438 15	3.446 20	2.4959
10	80.187 00	71.764 20	77.024 80	79.034
11	0.578 67	0.131 81	0.414 00	0.6828
12	6.362 00	5.030 57	3.358 40	6.385
13	0.012 35	0.013 18	0.012 30	0.0127
14	0.257 81	0.268 15	0.253 80	0.26

According to Bird and Hulstrom (1981):

$$\tau_g = \exp[-\mathrm{COF}(13)m'^{\mathrm{COF}(14)}] \tag{3.3.17}$$

Numerical values of the above 14 coefficients for clear, overcast and non-overcast sky conditions are given in Table 3.3.3.

3.3.4 The meteorological radiation model

MRM estimates the horizontal beam and diffuse components from just ground-based meteorological data – air temperature, atmospheric pressure, RH (or wet-bulb temperature) and sunshine duration. Such data is readily available worldwide. MRM is therefore an extremely useful tool. Moreover, the model can estimate the horizontal solar components (diffuse, beam and global irradiance) on an hourly, monthly-averaged hourly, daily or monthly-averaged daily basis. Historically, the theoretical approaches used within MRM may be traced to the works of Chandrasekhar and Elbert (1954), Sekera (1956), Coulson (1959), Dave (1964) and Kambezidis et al. (1996). The complete set of sub-models were, however, presented by Kambezidis and Papanikolou (1989) followed by an improved version by Muneer and Gul (1998).

3.3.4.1 MRM at an hourly level

This model enables hour-by-hour computation of beam, diffuse and global irradiance. Its accuracy is most precise for clear-sky conditions and worst during overcast periods. Some of the air mass and transmission models presented in the above sections have one limitation, i.e. they return unreasonably high values at low solar altitudes. The readers' attention is therefore drawn towards the solution incorporated in this text which is to exclude from computations those instances when the solar altitude is less than 7°. This control was found to be quite effective in dealing with broadband as well as spectral irradiance calculations presented in Chapter 5.

MRM for clear skies

MRM is a broadband empirical algorithm. The clear-sky diffuse irradiance model is based on the works of Dave (1979), Bird and Hulstrom (1979) and Pisimanis et al. (1987):

$$I_D = I_E\tau_{\alpha\alpha}\tau_g\tau_o\tau_w\left[\frac{0.5(1-\tau_r)}{1-m+m^{1.02}} + \frac{0.84(1-\tau_{\alpha s})}{1-m+m^{1.02}}\right] \tag{3.3.18}$$

$$\tau_{\alpha\alpha} = 1 - 0.1(1-\tau_\alpha)(1-m+m^{1.06}) \tag{3.3.19}$$

$$\tau_{\alpha s} = 10^{-0.045^{m'^{0.7}}} \tag{3.3.20}$$

The global irradiance on horizontal surface I_G is given by:

$$I_G = (I_B + I_D)\left(\frac{1}{1-r_s r'_\alpha}\right) \tag{3.3.21}$$

where r_s is the ground albedo (a standard value of 0.2 is often quoted), and $r'_\alpha = 0.0685 + 0.17(1-\tau'_\alpha)$ is the albedo of the cloudless sky. τ'_α is the Rayleigh scattering transmittance computed at $m = 1.66$.

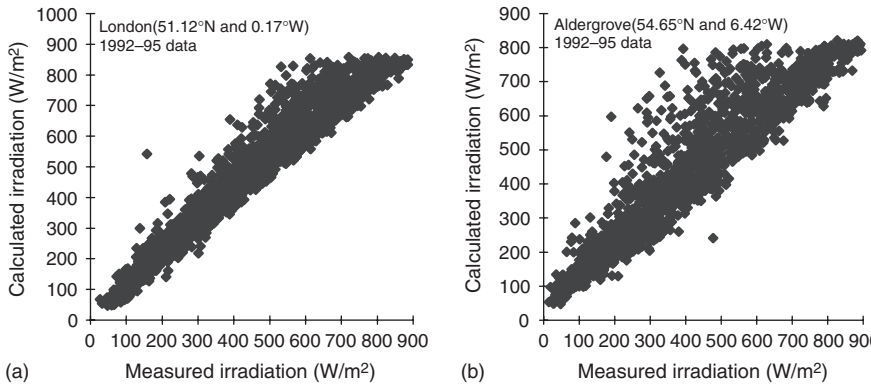

Figure 3.3.2 *Evaluation of MRM for clear skies: (a) London and (b) Aldergrove*

Table 3.3.4 Accuracy evaluation of hourly MRM, 1985–94 data

	Overcast (0–200 W/m^2)				Part-overcast (200–600 W/m^2)				Clear (600–1000 W/m^2)			
Location	MBE (W/m^2)	RMSE (W/m^2)	MBE (%)	RMSE (%)	MBE (W/m^2)	RMSE (W/m^2)	MBE (%)	RMSE (%)	MBE (W/m^2)	RMSE (W/m^2)	MBE (%)	RMSE (%)
Camborne	33	63	33	63	25	112	6	28	−37	111	−5	14
London	37	61	37	61	52	87	13	22	36	61	4	8
Bracknell	30	57	30	57	30	77	8	19	1	69	0	9
Aberporth	21	46	21	46	4	60	1	15	−51	75	−6	9
Hemsby	32	90	32	90	28	174	7	44	−77	171	−10	21
Finningley	26	54	26	54	26	65	6	16	10	47	1	6
Aldergrove	26	52	26	52	11	65	3	16	−28	69	−4	9
Mylnefield	36	72	36	72	19	115	5	29	−68	122	−8	15
Aberdeen	23	56	23	56	19	69	5	17	−13	69	−2	9
Stornoway	12	38	12	38	6	60	2	15	−33	61	−4	8

The performance of the above model is shown in Figure 3.3.2 and Table 3.3.4. It is apparent that under clear skies the model provides satisfactory results. This is to be expected, though, as transmission under such conditions is quite well defined. Contrary to this the overcast skies are the most difficult to model. This is discussed below.

MRM for overcast skies

In this case Eq. (3.3.18) may be used to obtain I_D which also equals the global irradiation I_G. It is well known that overcast skies are most difficult to model owing to their indistinguishable trace on the relevant meteorological variables, i.e. a dense, dark overcast as well as a thin cloud, both register nil sunshine duration. However, the irradiation would be widely different for the above two extremes. Figure 3.3.3 shows the behaviour of MRM for two UK locations. As would be expected there is considerable scatter in this case. An attempt may be made to improve this model via identification of the above two extreme weather conditions. For example, the rain amount may be used as an index to determine the presence of dark overcast. However, such attempts have only rarely been reported in the literature. One reason for this may be due to the fact that the absolute error in energy

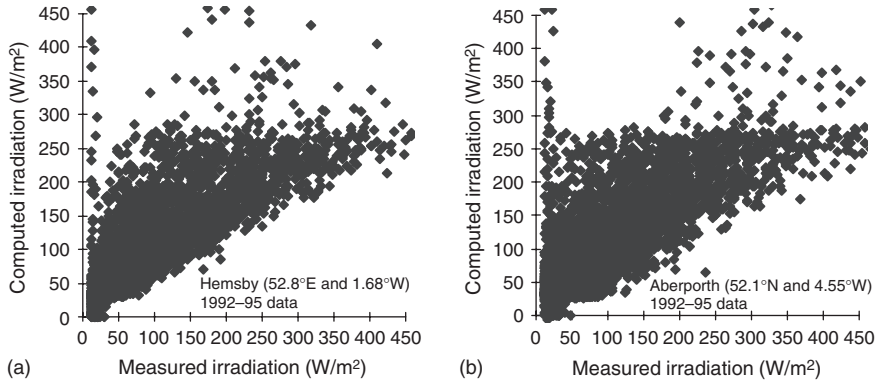

Figure 3.3.3 *Evaluation of MRM for overcast skies: (a) Hemsby and (b) Aberporth*

estimation is low under overcast conditions. It must be borne in mind that the absolute, rather than the relative error, is the crucial criterion, e.g. the error in calculating daylight illuminance or the energy collection from a solar collector will depend on the absolute deviation of the estimated irradiance. Fortuitously, MRM offers an almost constant deviation, small relative error for high clear-sky irradiance levels and vice versa.

MRM for non-overcast skies

In the above two sections the procedure to obtain irradiation under the two extreme sky conditions was presented. Real skies are, however, rarely clear or completely overcast and hence irradiance models for intermediate skies are very desirable. Some modellers, e.g. Pisimanis et al. (1987), have attempted to obtain intermediate-sky irradiation by interpolating the clear and overcast irradiation with the sunshine fraction (SF) as the weighing factor. Muneer et al. (1996) have, however, shown that such an approach leads to excessive scatter of the computed quantities. They have proposed an alternate, more reliable approach which is summarised below.

Muneer et al. (1996) have produced a correlation between hourly diffuse to beam ratio (DBR $= I_D/I_B$) and beam clearness index ($K_B = I_B/I_E$). Plots for two locations in the UK are shown in Figure 3.3.4. The generalised correlation is given as:

$$\mathrm{DBR} = a\,K_B^{-b} \tag{3.3.22}$$

where $a = 0.285$ and $b = 1.006$ for UK.

Figure 3.3.5 shows the results for non-overcast conditions. Table 3.3.4 presents statistical error analysis of the hourly MRM model undertaken by Muneer et al. (1996) against 100 station-year data within the UK. Broad conclusions which may be drawn from these tables are that:

(a) The mean bias errors (MBEs) suggest that under overcast conditions the model is capable of computing hourly irradiation with an accuracy of 30% (30 W/m^2).
(b) Under part-overcast conditions the errors are in the range of 8% (28 W/m^2).
(c) As it would be expected the model performs the best under clear-sky regimes, the accuracy in this case being better than 6% (40 W/m^2). The scatter is also kept

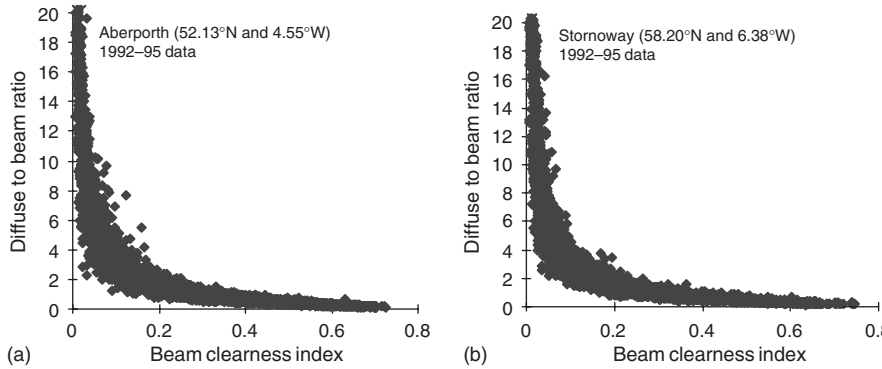

Figure 3.3.4 *Correlation between hourly diffuse and beam irradiation: (a) Aberporth and (b) Stornoway*

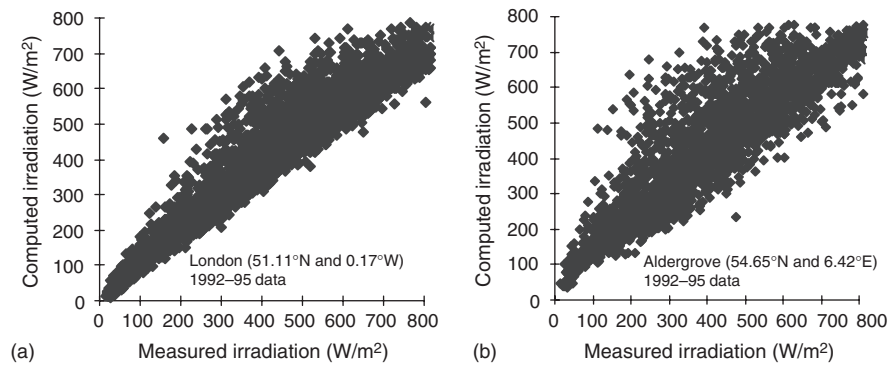

Figure 3.3.5 *Evaluation of MRM for non-overcast skies: (a) London and (b) Aldergrove*

fairly low for the entire non-overcast set of conditions. This result is in agreement with the works of Gueymard (1993a,b) and Grindley et al. (1995). The latter mentioned team have shown that such models can indeed estimate clear-sky irradiance to an accuracy of 4%. Their conclusions were based on 1 min instantaneous measurements undertaken at Cambridge, UK.

Example 3.3.1

Table 3.3.5 provides measured hourly weather data for London, UK. Using the MRM model, obtain hourly horizontal global and diffuse irradiation.

In cases such as these, Prog3-2a.For may be used to generate the output shown in Table 3.3.5. Note that the format for the given data file is year, month, day, hour, dry- and wet-bulb temperatures, atmospheric pressure (h Pa) and sunshine fraction.

It is evident that for the non-overcast conditions, global irradiation estimates are better than the corresponding diffuse values. This is due to the fact that under such conditions

Table 3.3.5 Data for Examples 3.3.1 and 3.4.1: London (51.5°N and 0.2°W), 14 April 1995 (Prog3-2.For and Prog3-3.For refer)

					Measured		MRM Computed			
Hour	Dry-bulb temperature (°C)	Wet-bulb temperature (°C)	Atmospheric pressure (mbar)	SF	I_G (W/m^2)	I_D (W/m^2)	I_G (W/m^2)	I_D (W/m^2)	Eq. (3.4.1) I_D (W/m^2)	Eq.(3.4.2) I_D (W/m^2)
6	9.2	7.5	1038	0	66	44	100	100	54	40
7	8.8	7.1	1039	0.4	206	96	203	140	116	78
8	10.0	7.8	1039	1	345	139	435	193	157	123
9	10.7	7.8	1039	0.9	490	159	528	237	170	136
10	12.9	9.3	1039	1	619	170	642	267	167	137
11	14.8	10.1	1038	1	675	195	689	284	185	178
12	15.4	10.7	1037	1	705	204	684	284	183	178
13	16.1	10.7	1037	1	672	203	644	268	187	184
14	16.7	10.8	1036	1	600	198	559	237	183	166
15	17.3	11.2	1035	1	469	199	437	194	189	169
16	17.3	11.4	1034	1	283	184	296	140	190	172
17	17.1	11.5	1033	0	140	122	54	54	121	110
18	16.5	11.3	1033	0	54	51	9	9	49	44
Daily totals				9.3	5324	1964	5280	2406	1951	1715

beam irradiation, the dominant component, is obtained first. There is, however, a multiplicative error in the estimation of diffuse irradiation.

MRM for low solar altitudes

It was mentioned in Section 3.3.2 that Kasten's (1993) formula for air mass provides sufficiently good accuracy for solar altitudes in excess of 1°. Other expressions for air mass and transmissions, e.g. Eq. (3.3.15) have been given by Davies et al. (1975). Experience suggests that for solar altitudes less than 7° it is unwise to use the above transmission expressions. The following procedure may be followed in such infrequent circumstances.

Adapting Eq. (2.1.1) for an hourly time interval, the horizontal global irradiation may be obtained from the corresponding extraterrestrial quantity and the hourly sunshine fraction. The diffuse irradiation may then be computed using an hourly diffuse ratio model due to Orgill and Hollands (1977). This procedure is presented in Section 3.4.

3.3.4.2 MRM for daily- and monthly-averaged irradiation

MRM is basically an hourly or sub-hourly solar radiation model. Its use may also be extended to estimate hourly or sub-hourly illuminance by either fitting the model against concurrent weather and illuminance data, or via the use of luminous efficacy models, to be introduced in Section 3.5. If the model is fitted for illuminance calculations (in this case it would be appropriate to call the model as meteorological illuminance model, MIM) the 14 coefficients provided in Table 3.3.3 would be tuned more closely to the short-wave transmission in the daylight band. Since the visible band represents nearly half of the total energy it would be reasonable to assume that the transmission coefficients would not be too indifferent to the ones obtained for the broadband model.

The hourly MRM may be used to produce day-integrated irradiation with a high degree of accuracy. Figure 3.3.6 shows a plot which enables such a visual performance

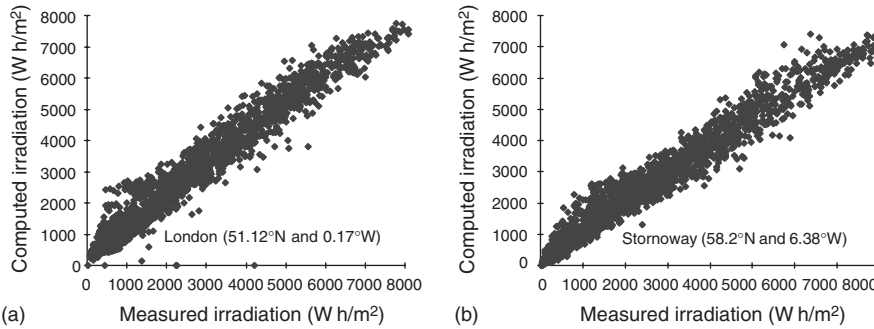

Figure 3.3.6 *Performance of the MRM model for daily irradiation: (a) London and (b) Stornoway*

evaluation. Tables 3.3.6 and 3.3.7 show the error statistics for monthly-averaged hourly and daily irradiation, obtained via summing the long-term computed and measured values.

MRM is a convenient and powerful tool which enables hourly irradiation and illuminance computations to be carried out for a very large number of locations worldwide, e.g. in the UK alone there are around 300 locations for which the required meteorological data are available. In contrast long-term irradiation data values are available for less than 5% of the above locations.

3.3.5 Cloud-cover radiation model

Although sunshine measuring stations are more numerous than those measuring insolation, they are still less in comparison to those that undertake cloud measurements. The cloud-cover data are more numerous and, in some instances, geographically better distributed than sunshine data.

Attempts to parameterise the dependence of radiation fluxes on cloud amount and type have been made by many authors in the past, e.g. Haurwitz (1945; 1948), Lumb (1964) and Parker (1971). As quoted by Iqbal (1983), it has long been known that a relationship exists between insolation and the amount of sky covered by clouds (Kimball, 1919).

Kimura and Stephenson (1969) used cloud opacity as the measure of cloud cover. Data from Ottawa were analysed to obtain seasonal numerical values for coefficients involved in their regression. Their results have been applied universally in the ASHRAE (2002) model using total cloud amount instead of opacity. Later on, Won (1977) found that Kimura and Stephenson's coefficients varied regionally and seasonally. Brinsfield et al. (1984) predicted solar radiation on a horizontal surface for any latitude as a function of total opaque cloud cover. Kasten and Czeplak (1980) have furthered the work done by Haurwitz by considering 10 years (1964–73) of continuous hourly data from Hamburg for their research.

Formulations based on the type and state of the clouds are quite complex. Clouds vary from thin, transparent cirrus, exerting little influence on global radiation to thick and dark thunderstorm clouds, which may reduce the global radiation to 1% of its normal value. The brightness of the same cumulus cloud may greatly vary, depending on its position with regard to sun. Also, there are a few stations at which each cloud layer is separately observed, and at which both the type and extent of every layer is noted.

Table 3.3.6 Evaluation of the MRM for monthly-averaged hourly irradiation (W h/m^2) Bracknell (51.383°N and 0.783°W)

Month	7*	7†	8*	8†	9*	9†	10*	10†	11*	11†	12*	12†	13*	13†	14*	14†	15*	15†	16*	16†	17*	17†
Global irradiation																						
1	0	0	7	0	37	49	78	103	113	141	131	153	125	144	95	111	56	56	17	0	1	0
2	77	0	104	30	89	113	147	170	183	207	200	223	189	218	165	185	119	127	64	56	15	0
3	46	43	118	138	199	225	263	295	302	349	331	370	318	348	277	298	222	232	146	140	67	50
4	136	157	362	265	446	358	377	442	420	493	442	494	424	480	379	436	315	348	236	251	145	139
5	475	227	582	330	421	431	484	508	513	540	523	552	505	526	463	475	396	404	308	318	213	218
6	233	247	334	355	419	433	476	487	501	523	517	550	511	512	471	474	415	417	329	328	238	228
7	216	227	317	328	402	411	472	487	518	536	533	547	507	517	469	479	423	418	338	334	247	237
8	172	183	282	289	382	387	450	461	484	504	504	511	491	496	443	440	380	359	287	266	184	171
9	89	100	176	194	264	284	319	348	355	392	374	416	356	381	312	331	243	248	161	162	80	64
10	34	21	99	113	172	191	235	249	271	279	271	285	237	266	191	212	137	146	70	59	18	0
11	3	0	30	20	74	91	120	139	149	166	156	170	136	147	98	108	50	52	13	0	1	0
12	0	0	8	0	38	46	78	96	106	124	116	132	105	119	74	80	33	17	6	0	0	0
Diffuse irradiation																						
1	0	0	6	0	28	37	55	78	75	100	86	108	82	102	65	82	41	48	14	0	0	0
2	76	0	98	22	63	83	97	122	119	147	132	158	130	153	114	132	83	97	47	50	14	0
3	34	31	79	98	125	147	164	185	183	212	198	221	189	214	168	192	138	154	96	105	49	47
4	85	104	268	160	316	207	219	246	243	270	255	277	247	270	221	247	186	208	144	158	95	99
5	379	145	425	197	207	244	240	280	262	299	337	303	334	296	247	273	214	237	173	191	126	139
6	141	159	192	210	236	255	263	285	281	307	290	315	285	304	270	284	238	251	189	207	141	154
7	125	147	172	199	213	241	248	279	271	299	278	311	268	301	252	280	229	248	183	206	138	153
8	230	117	280	171	326	219	231	256	253	279	258	286	249	280	234	257	210	220	167	174	112	119
9	56	72	102	129	148	175	182	211	202	233	210	242	200	231	178	201	145	164	103	114	56	56
10	23	15	61	78	99	124	132	157	151	176	152	179	135	167	113	140	85	100	47	46	14	0
11	3	0	22	15	51	68	79	101	97	117	101	120	92	107	69	81	38	43	11	0	0	0
12	0	0	7	0	28	34	53	70	70	90	75	95	68	85	51	61	25	16	5	0	0	0

* Measured irradiance for the hour shown (W/m^2), † Computed irradiance for the hour shown (W/m^2).

Table 3.3.7 Performance of the MRM for monthly-averaged daily irradiation (W h/m^2)

	Stornoway					Bracknell				
Month	G-m	G-c	D-m	D-c	SF	G-m	G-c	D-m	D-c	SF
1	333	339	338	267	1.0	664	755	452	560	1.8
2	909	934	632	666	2.2	1303	1407	848	977	2.6
3	1906	1976	1189	1320	3.3	2266	2464	1514	1609	3.5
4	3164	3204	2238	2047	4.4	3405	3793	2081	2307	5.0
5	4953	4818	2585	2752	7.1	4638	4823	2917	2829	6.6
6	4577	4505	2786	2946	5.3	4851	4946	3504	3030	6.4
7	3994	3861	2689	2731	4.1	4735	4795	2943	2923	6.8
8	3071	3121	2194	2234	3.6	4170	4172	2612	2497	6.5
9	2365	2331	1514	1570	3.8	2834	2923	1626	1838	4.7
10	1173	1189	783	860	2.5	1706	1802	1244	1183	3.6
11	474	483	344	370	1.4	877	930	700	661	2.3
12	224	195	182	155	0.8	524	577	507	444	1.4

G-m: G-measured, G-c: G-computed, D-m: D-measured and D-c: D-computed.

Gul and Muneer (1998) and Muneer and Gul (2000) have extended the work of Kasten and Czeplak (1980) towards the development of cloud-cover radiation model (CRM) and an account of those works is presented here.

The CRM needs only cloud-cover data as the key input to generate hour-by-hour global, beam and diffuse horizontal irradiation.

3.3.5.1 Kasten–Czeplak model

Using Hamburg data, Kasten and Czeplak (1980) have developed a cloud model that first obtains solar radiation under cloudless sky, I_{Gc}. They have shown that I_{Gc} depends on solar elevation angle and may be obtained by:

$$I_{Gc} = (A \sin \text{SOLALT} - B) \tag{3.3.23a}$$

Furthermore, they have shown that the ratio of global irradiation I_G for a given cloud amount N octa, to I_{Gc} is independent of SOLALT:

$$I_G / I_{Gc} = 1 - C(N/8)^D \tag{3.3.23b}$$

The values of A, B, C and D coefficients for Hamburg are provided in Table 3.3.8. The diffuse component is then calculated from:

$$I_D / I_G = 0.3 + 0.7(N/8)^2 \tag{3.3.24}$$

The beam component will then be obtained as the difference of global and diffuse irradiation.

3.3.5.2 Gul–Muneer model

The coefficients A through to D involved in the above model were re-fitted by Gul and Muneer (1998) using data from UK locations and these coefficients are also provided in Table 3.3.8. The validity of the model under discussion was checked using 9 years hourly

Table 3.3.8 Coefficients for CRM to be used in Eqs (3.3.23a) and (3.3.23b)

Locations	*A*	*B*	*C*	*D*
Massachusetts, USA	1098	63	0.75	3.4
Hamburg, Germany	910	30	0.75	3.4
Aldergrove, UK	956	34	0.70	3.1
Stornoway, UK	979	45	0.73	3.4
Finningley, UK	902	36	0.71	3.7
Aberporth, UK	1024	54	0.71	4.2
London, UK	948	49	0.71	3.4

Table 3.3.9 Statistical evaluation of CRM

Location	K_t	MAD (W/m^2)	RMSE (W/m^2)
Aldergrove, UK	<0.2	53	60
	>0.2 to <0.6	67	85
	>0.6	62	87
Stornoway, UK	<0.2	49	59
	>0.2 to <0.6	60	78
	>0.6	50	72
Finningley, UK	<0.2	31	42
	>0.2 to <0.6	48	66
	>0.6	50	72
Aberporth, UK	<0.2	47	56
	>0.2 to <0.6	60	76
	>0.6	72	98
London, UK	<0.2	32	41
	>0.2 to <0.6	52	73
	>0.6	61	87
Davos, Switzerland	<0.2	52	75
	>0.2 to <0.6	87	118
	>0.6	121	160
Zurich, Switzerland	<0.2	59	79
	>0.2 to <0.6	71	94
	>0.6	89	118

database (1985–93) for five UK sites and 3 years database (1993–95) for two Swiss sites. Table 3.3.9 presents those results. In Table 3.3.9 the data have been grouped in three bands of clearness index. Under overcast conditions ($K_t < 0.2$) the MBEs and MADs are quite high. The poor performance of CRM under overcast conditions is attributed to the fact that data on cloud type is neither included nor readily available. For part-overcast ($K_t = 0.2$–0.6) conditions the errors are quite low with MBE in the range of 5–8%, MADs being 17–22% and root mean square errors (RMSEs) being 23–40%. For clear skies ($K_t > 0.6$) the MBE vary in the range of 9–13%.

Prog3-2b.For enables estimation of global and diffuse irradiation from cloud-cover data. Note that the required input data file, In3-2.Prn, has the following data fields for any

given day's data: hour, global and diffuse irradiation (W/m^2), SF, cloud cover in oktas, dry- and wet-bulb temperatures, atmospheric pressure (h Pa) and solar altitude (degrees).

Lam and Li (1998) have explored the incorporation of multiple linear regressions between global irradiation and cloud cover involving solar altitude. They have reported an improvement of 5% accuracy increase with such regressions. The latterly mentioned model is given as follows:

$$I_G = 217 - 485(N/8) + 696 \sin \text{SOLALT} \tag{3.3.25a}$$

$$I_D = 30.5 - 62.9(N/8) + 294.7 \sin \text{SOLALT} \tag{3.3.25b}$$

So long as the sky is not completely obscured by clouds the record of duration of bright sunshine where available is as a rule a better indicator of insolation than is the cloudiness index. Since cloud observations are abundantly available for many stations that have no sunshine records it is useful to have a relation between cloud data and insolation. The continuous sunshine trace through the hour, obviously provides much more detailed information than a spot reading of the cloud cover. Haurwitz (1948) has shown that a much stronger correlation exists between insolation and sunshine than between insolation and cloudiness. According to Bennett (1969), sunshine explains 70–85% of the insolation variance. Cloud cover, on the other hand, seldom explains more than 70% and frequently less than 50% of insolation variance.

3.3.6 Page radiation model

The page radiation model (PRM) evolved from the development of the European Solar Radiation Atlas (ESRA, 2000).

3.3.6.1 Clear-sky radiation model

The clear-sky radiation model was originally developed by Page and Lebens (1986) as a key component needed in the development of the ESRA. This cloudless sky model predicts the irradiation on horizontal surfaces as a function of solar altitude and air mass 2 Linke turbidity factor, after incorporating the standard corrections to mean solar distance, and the air-mass adjustment for station height. The cloudless sky direct beam and diffuse irradiation on the horizontal surface are separately estimated and global irradiation is then obtained by summation.

3.3.6.2 Estimation of direct-beam irradiation

The solar beam normal irradiation depends on the solar altitude and Linke turbidity factor. As pointed out earlier in this chapter, outside the atmosphere at mean solar distance the beam irradiation is $1367\,W/m^2$. The orbit of the sun is slightly eccentric and so the earth–sun distance varies slightly across the year. This influences the extraterrestrial irradiation. Within ESRA the correction factor to allow for the varying solar distance, K_d, is calculated from the following expression:

$$K_d = 1.0 + 0.033\,44 \cos(J' - 2.80) \tag{3.3.26}$$

where J' = day angle, which is the day number in the year divided by 365.25.

The beam irradiation normal to the surface is calculated as:

$$I_{Bn} = I_E K_d \exp(-m \times 0.8662 T_{LK} \delta_r(m)) \quad (3.3.27a)$$

where m is the optical air mass corrected for station pressure as calculated by Kasten's formulation (1993). This has been discussed in detail earlier on in this chapter (see Eq. (3.3.3)). T_{LK} is the air mass 2 Linke turbidity factor and $\delta_r(m)$ is the Rayleigh optical depth at air mass m. These parameters will be described in detail in the following sections.

The beam irradiation on a horizontal surface from the cloudless sky is calculated as:

$$I_{Bc} = I_{Bn} \sin \text{SOLALT} \quad (3.3.27b)$$

In addition to the air mass 2 Linke turbidity factor the model also uses some other direct inputs. These include the following:

(a) *Atmospheric pressure*: The hourly surface pressure is used in the assessment of the relative air mass (Eq. (3.3.4)).
(b) *Vapour pressure*: The vapour pressure is determined from the observed dry- and wet-bulb temperatures at each hour and is used in the estimation of the maximum possible beam irradiation.
(c) *Present weather code*: If any of the hourly observations report haze or mist (weather code = 5) at any time between 0800 and 1600 h that hour is classified as hazy, and the air mass 2 Linke turbidity factor is raised by two units.

3.3.6.3 The air mass 2 Linke turbidity factor, T_{LK}

Linke's turbidity factor (T_{LK}) is defined as the number of clean, dry atmospheres that would produce the same total depletion (or give rise to the same intensity) of direct solar radiation as that produced by the actual atmosphere (Linke, 1922; Robinson, 1966). It summarises the turbidity of the atmosphere, and hence the attenuation of the direct-beam solar radiation and the importance of the diffuse fraction. The larger the Linke turbidity factor, the larger the attenuation of the radiation by the clear-sky atmosphere.

T_{LK} does not exclusively explain the turbidity caused by aerosol because the quantity is also affected by the absorption of solar radiation in the visible and NIR regions by water vapour. It depends on the optical thickness of the clean and dry atmosphere which is very sensitive to the relative optical air mass m. Therefore, the Linke turbidity factor depends on m, and consequently, on solar elevation at the instant of its evaluation. It is possible to convert any T_{LK} value into a standard one with respect to a fixed m value chosen as a reference. Such a standard value of T_{LK} will be independent of m, i.e. of the solar elevation at the instant of evaluation, and hence, strictly representative of the atmospheric turbidity. A value of $m = 2$ as reference value has been adopted based on the work by Kasten (1993); it corresponds to a solar elevation of 29.9°.

The air mass 2 Linke turbidity factors under discussion are the historically based values, but the solar elevation dependence is assessed here using the new formulation of the Rayleigh optical depth. The new formula with the conversion factor 0.8662 in Eq. (3.3.27) produces accurate predictions at low solar elevations. The values for T_{LK} for UK locations are shown in Table 3.3.10.

Table 3.3.10 Monthly values of estimated clear day air mass 2 Linke turbidity factors for UK

Site	Latitude (deg/min)	Longitude (deg/min)	Ht. (m)	Jan.	Feb.	Mar.	Apr.	May	Jun.	Jul.	Aug.	Sep.	Oct.	Nov.	Dec.
Lerwick	60 08N	01 11W	82	2.7	3.0	2.1	2.8	2.7	2.0	2.1	2.8	2.5	2.4	2.8	*
Stornoway	58 13N	06 19W	9	4.1	3.8	2.9	3.3	3.2	2.8	3.4	4.7	3.7	3.6	3.8	3.8
Aughton	53 33N	02 55W	54	4.3	4.0	3.1	3.6	3.9	3.6	3.7	4.7	4.1	4.0	4.4	4.0
Aberporth	52 08N	04 34W	133	4.4	3.5	2.9	3.3	3.3	3.0	3.2	4.2	3.7	3.9	4.4	3.9
Efford	50 44N	02 12W	16	3.9	3.7	3.2	3.7	3.8	3.9	4.1	4.7	3.9	3.8	4.0	3.5
Camborne	50 13N	05 19W	87	3.9	3.5	3.2	3.5	3.6	3.6	3.7	4.3	3.6	3.6	3.8	3.5
Jersey airport	49 13N	02 12W	84	3.4	3.4	3.0	3.5	3.6	3.3	3.7	4.3	3.7	3.5	3.6	3.1
Aberdeen	57 12N	02 13W	65	4.5	4.2	3.0	3.7	2.7	2.8	3.3	3.9	3.8	3.6	4.7	4.5
Mylnefield	56 27N	03 04W	30	3.9	3.4	2.2	2.9	2.7	2.7	3.0	4.1	2.7	3.1	4.1	3.3
Shanwell	56 26N	02 52W	4	4.3	3.8	3.0	3.3	3.3	3.1	3.2	4.4	3.3	3.7	4.1	4.0
Edinburgh	55 57N	03 20W	61	4.6	3.6	3.5	3.5	3.5	3.4	3.6	4.1	3.4	3.3	3.1	4.9
Hemsby	52 41N	01 41E	13	4.4	4.1	3.4	3.5	3.8	3.9	4.0	4.6	4.0	4.0	4.2	4.0
E. Malling	51 17N	00 27E	37	4.3	4.1	3.3	3.6	3.9	3.6	3.8	4.8	4.3	4.1	4.1	4.0
Aviemore	57 12N	03 50W	220	3.8	2.8	2.5	3.0	3.1	2.3	2.6	3.2	3.1	3.0	3.4	3.2
Eskdalemui	55 19N	03 12W	242	3.9	3.3	2.5	3.3	3.5	3.3	3.4	4.0	3.2	3.3	3.7	3.5
Hazlerigg	54 01N	02 45W	95	4.0	3.5	2.5	3.1	3.4	3.1	3.1	3.7	3.3	3.3	3.9	3.3
Finningley	53 29N	01 00W	17	4.6	3.9	3.2	3.9	4.0	3.7	4.0	5.2	4.1	3.7	4.1	4.1
Broom's B[3]	52 16N	00 34E	75	4.1	4.0	3.4	3.7	4.0	3.7	4.0	4.9	4.1	4.0	4.2	4.1
Silsoe	52 01N	00 25W	59	3.3	3.3	2.8	3.0	3.4	3.2	3.6	4.5	3.7	3.4	3.4	2.7
Rothamsted	51 48N	00 21W	128	NA	4.0	2.4	3.6	3.6	3.8	3.9	4.5	4.2	3.5	4.1	3.4
Hoddesdon	51 47N	00 00E	47	4.0	3.4	3.0	3.4	3.5	3.8	3.9	5.0	4.0	3.8	3.7	3.4
Wallingford	51 36N	01 10W	49	4.6	3.5	NA	3.6	4.7	4.1	4.2	5.2	4.5	3.5	4.1	4.1
London WC	51 31N	00 07W	77	4.4	4.1	3.4	4.0	4.2	4.1	4.5	5.3	4.5	4.1	4.6	3.9
Bracknell	51 23N	00 47W	73	4.3	4.0	3.4	3.9	4.0	3.8	4.0	4.9	4.1	3.8	4.1	3.6
Crawley	51 05N	00 13W	144	3.8	3.4	3.2	3.9	4.0	3.9	4.0	4.9	4.0	3.8	3.6	3.3

Source: J Page.
* Sun too low for methodology to be applicable.

Ineichen and Perez (2002) have proposed a new formulation for Linke turbidity (T_{LIP}) which they claim is independent of the air mass. The formulation may be expressed as:

$$b = 0.664 + 0.163/\exp(-\text{station height, metres}/8000) \tag{3.3.28a}$$

$$T_{\mathrm{LIP}} = 1 + [11.1 \ln(bI_{\mathrm{o}}/I_{\mathrm{B,ncl}})]/m \tag{3.3.28b}$$

where I_{o} and $I_{\mathrm{B,ncl}}$ are respectively, the sun–earth distance corrected extraterrestrial and normal beam clear-sky irradiance.

Using one clear day's irradiance data (29 March 2000) recorded at Bahrain the Linke– and Ineichen–Perez turbidities were inter-compared. The basic irradiance data are presented in File In4-7a.Csv and the relevant program is Prog4-7a.For. Figure 3.3.7 presents those results. The variation in the above two turbidity indices seems to be of a similar order, as may also be seen by the following statistics for T_{LK} and T_{LIP} respectively: averages 4.06 and 3.83, standard deviations 0.20 and 0.18, coefficients of variation 5.0 and 5.0.

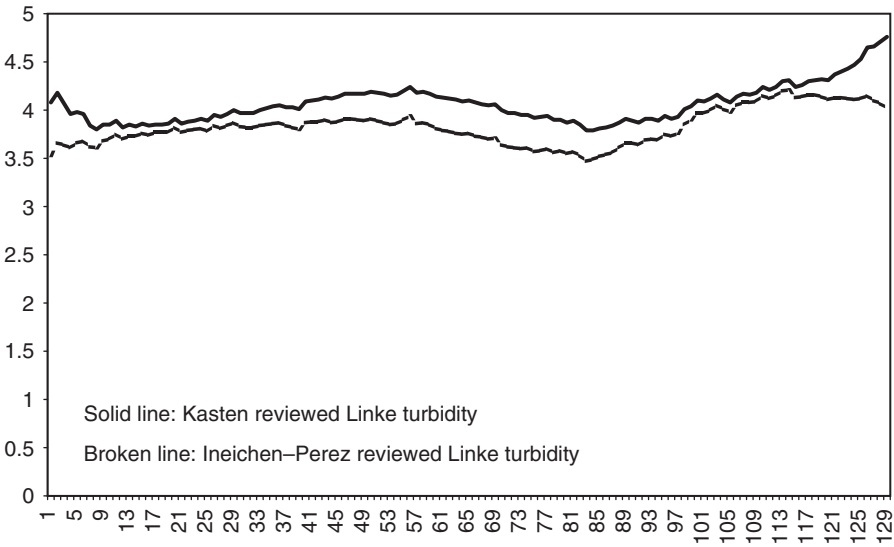

Figure 3.3.7 *Comparison of Linke and Ineichen–Perez reviewed Linke turbidity for Bahrain data: 29 March 2000*

3.3.6.4 Rayleigh optical depth

Following a recent reassessment by Kasten (1993), Page recommended the algorithm modified by Kasten to determine the Rayleigh optical depth as a function of air mass:

$$\delta_r(m) = [6.6296 + 1.7513m - 0.1202m^2 + 0.0065m^3 - 0.00013m^4]^{-1} \qquad (3.3.29)$$

3.3.6.5 Estimation of clear-sky diffuse irradiation

In this model the diffuse irradiation of the cloudless sky depends on the solar altitude and air mass 2 Linke turbidity factor. As the sky becomes more turbid the diffuse irradiation increases while the beam irradiation decreases.

The diffuse modelling is carried out in two stages. First of all the value of diffuse transmittance Trd(n) is established for day n. This is the theoretical diffuse irradiation on a horizontal surface with the sun vertically overhead for the air mass 2 Linke turbidity factor T_{LK} selected.

The following second order polynomial expression is used:

$$\text{Trd}(n) = -21.657 + 41.752T_{LK} + 0.519\,05(T_{LK})^2 \qquad (3.3.30)$$

Then the solar elevation function, F(SOLALT), is evaluated using:

$$F(\text{SOLALT}) = C(0) + C(1)\sin \text{SOLALT} + C(2)\sin^2 \text{SOLALT} \qquad (3.3.31)$$

The values of the coefficients used to determine $C(0)$, $C(1)$ and $C(2)$ are only dependent on the air mass 2 Linke turbidity factor T_{LK}. They are found from the following expressions:

$$C(0) = 0.264\,63 - 0.061\,581 T_{LK} + 0.003\,140\,8(T_{LK})^2 \tag{3.3.32a}$$

$$\text{If } \mathrm{Trd}(n) \times C(0) < 3\ \mathrm{W/m^2} \quad \text{then } C(0) = 3/\mathrm{Trd}(n) \tag{3.3.32b}$$

$$C(1) = 2.0402 + 0.018\,945 T_{LK} - 0.011\,161(T_{LK})^2 \tag{3.3.32c}$$

$$C(2) = -1.3025 + 0.039\,231 T_{LK} + 0.008\,507\,9(T_{LK})^2 \tag{3.3.32d}$$

The cloudless sky diffuse irradiation is then given by:

$$I_{Dc} = K_d \times \mathrm{Trd}(n) \times F(\mathrm{SOLALT}) \tag{3.3.33}$$

Total global irradiation under clear-sky conditions is then calculated as:

$$I_{Gc} = I_{Dc} + I_{Bc}$$

3.3.6.6 Actual beam irradiation

The actual beam irradiation under a part-cloudy sky is estimated from the cloudless sky beam irradiation, and the observed sunshine in the hour. A correction is then applied to allow for the characteristic defects of the sunshine recorder which typically contains over-estimates of actual sunlight with broken cloud. The beam radiation is thus not linearly related to the sunshine in the hour.

Case 1

The following expression is used when the solar elevation is above 8° and the hourly sunshine is less than 0.9 h:

$$I_B = I_{Bc} \times \mathrm{SF} \times \text{sunshine amount correction factor} \tag{3.3.34}$$

The sunshine amount correction factor is given by:

$$\text{If } \mathrm{SF} < 0.9, \quad \text{sunshine amount correction factor} = 0.0021 + 0.3808\mathrm{SF} + 0.4961\mathrm{SF}^2$$

Case 2

The following expression is used under very sunny conditions with the solar elevation above 8° and the hourly sunshine $\mathrm{SF} > 0.8$ and $N > 2$ oktas. The modelled clear-sky diffuse irradiation is increased to allow for the combined effects of high sun and high cloud using the following seasonal expressions based on cloud amount.

For period April through to September (for Northern hemisphere):

$$\text{Corrected diffuse} = I_{Dc}/(1.089 - 0.0506N) \tag{3.3.35a}$$

Table 3.3.11 Perrin de Brichambaut formulation

		T_{LK}: vapour pressure at surface (mb)			
Colour of sky	Visibility at surface (km)	3–5	5–8	9–16	18–30
Deep blue	>100	2.0	2.3	2.6	2.9
Pure blue	60–100	2.6	2.9	3.2	3.5
Pale blue	30–50	3.4	3.7	4.0	4.3
Around conurbations	Added by Page	3.8	4.1	4.4	4.7
Milky blue to whitish	12–25	4.9	5.2	5.6	5.8
	Precip. wv (cm)	0.5	1.0	2.0	4.3

For period October through to March (for Northern hemisphere):

$$\text{Corrected diffuse} = I_{Dc}/(0.945 - 0.0262N) \tag{3.3.35b}$$

The estimated beam irradiation is then found by difference between the quality controlled global radiation and the cloud adjusted diffuse radiation.

Case 3
When the solar elevation is below 8°, the following simple beam model is used:

$$I_B = I_{Bc}(1 - N/8) \tag{3.3.36}$$

3.3.6.7 Extreme clarity clear-sky model

In order to establish credible upper limits over the wide range of air mass 2 Linke turbidity factors that may occur in practice, a second beam irradiation calculation is performed. This calculation uses the observed vapour pressure at the site. The model of Perrin de Brichambaut is used which takes account of vapour pressure, but requires good knowledge of the climate to assess the colour of the sky. The assumption is made that the sky conditions are exceptionally clear, and the colour of the sky is set as deep blue. Thus the Linke turbidity factor is estimated from the actual vapour pressure with the sky colour set to its lowest possible value of 1, thus giving the lowest reasonable Linke turbidity factor to be expected for the given observed vapour pressure and surface pressure. This calculation provides the greatest acceptable observable beam strength. The values of T_{LK} for different vapour pressures and states of sky are shown in Table 3.3.11. The model also provides control values of the maximum acceptable values of hourly global irradiation using the cloudless sky model described above.

3.3.6.8 Overcast sky radiation model

The key initial input into the daily overcast sky model is the daily transmittance for the overcast conditions. This is the ratio of the overcast daily irradiation on horizontal plane to the extraterrestrial daily irradiation (see Chapter 2).

3.3.6.9 Conversion from daily to hourly diffuse irradiation

The daily global radiation information has next to be linked into the overcast sky diffuse irradiation model which deals with the effects of solar elevation on overcast day irradiation.

Table 3.3.12 Perraudeau sky types coefficients

	$A(0)$	$A(1)$	$A(2)$
Overcast sky	-6.7133×10^{-3}	$+0.78600$	$+0.22401$
Intermediate overcast sky	-9.2023×10^{-3}	$+0.61541$	$+0.39851$
Intermediate median sky	-3.6029×10^{-3}	$+0.90169$	$+0.10364$
Intermediate blue sky	$+7.5027 \times 10^{-3}$	$+1.15360$	-0.16453
Blue sky	$+3.8175 \times 10^{-2}$	$+1.54580$	-0.59980

This associated hourly overcast radiation model is based on the estimation of the overcast sky transmittance with the sun directly overhead combined with the application of an overcast sky solar elevation function to estimate the overcast day global irradiation value at any solar elevation. If the hourly transmittance were constant, the correction would be equal to the sine of the solar altitude. As this is not so, a second order sine polynomial is used to calculate the overcast day solar elevation function. The formula used to calculate the overcast day irradiation at any hour is:

$$I_{\mathrm{Do}} = K_{\mathrm{d}}\,\mathrm{Trd}(n)[A(0) + A(1)\sin \mathrm{SOLALT} + A(2)\sin^2 \mathrm{SOLALT}] \tag{3.3.37}$$

where $\mathrm{Trd}(n)$ is the overcast day transmittance and $A(0)$, $A(1)$ and $A(2)$ are constants dependent on sky type. The term in square brackets is the solar elevation function. The solar elevation function was estimated for the five sky types using the observations of Perraudeau at Nantes from 1991 to 1994. The values obtained for each of Perraudeau's sky types are set out in Table 3.3.12.

3.3.6.10 Estimating the overcast day transmittance

The overcast day transmittance is found from the daily overcast day transmittance by firstly integrating the solar elevation function, over the day, and then dividing the daily transmittance by the integral of the hourly transmittance. The integrations are achieved using the hour angles from solar noon in radians, at the beginning and end of each integration period. The sunset hour angle defines the limits for integration at the end of the day, and the sunrise hour angle defines the limits for integration at the beginning of the day. It is assumed that the rate of change of declination is slow enough to treat the noon declination as representative for the day.

The hourly irradiation is thus given by:

$$I_{\mathrm{Do}} = (12/\pi)\,K_{\mathrm{d}}\mathrm{Trd}(n) \int_{\omega\mathrm{sunrise}}^{\omega\mathrm{sunset}} \{A(0) + A(1)\sin \mathrm{SOLALT} + A(2)\sin^2 \mathrm{SOLALT}\}\mathrm{d}\omega \tag{3.3.38}$$

Expressing $\sin \mathrm{SOLALT}$ in terms of LAT, DEC and ω:

$$\sin \mathrm{SOLALT} = \cos \mathrm{LAT} \cos \mathrm{DEC} \cos \omega + \sin \mathrm{LAT} \sin \mathrm{DEC} \tag{3.3.39}$$

and setting:

$$B(0) = A(0) + A(1)\sin \mathrm{LAT} \sin \mathrm{DEC} + A(2)\sin^2 \mathrm{LAT} \sin^2 \mathrm{DEC} + A(2)\,(\cos^2 \mathrm{LAT} \cos^2 \mathrm{DEC})/2$$

$B(1) = A(1)$ cos LAT cos DEC + 2 $A(2)$ sin LAT sin DEC cos LAT cos DEC

$B(2) = A(2)$ (cos^2 LAT cos^2 DEC)/4

We obtain:

$$I_{\mathrm{Do}} = (12/\pi)K_{\mathrm{d}}\mathrm{Trd}(n)[B(0)\omega + B(1)\sin\omega + B(2)\sin(2\omega)]\Big]_{\omega\mathrm{sunrise}}^{\omega\mathrm{sunset}} \tag{3.3.40}$$

3.3.6.11 Global radiation model

The estimated global irradiation is then estimated as:

$$I_{\mathrm{G}} = \{I_{\mathrm{Gc}} - I_{\mathrm{Do}}\}\mathrm{SF} + I_{\mathrm{Do}} \tag{3.3.41}$$

The complete FORTRAN program for PRM is included in Prog3-2c.For. Note that the required input data file, In3-2.Prn, has the following data fields for any given day's data: hour, global, diffuse irradiation (W/m^2), sunshine fraction, cloud cover in oktas, dry- and wet-bulb temperatures, atmospheric pressure (h Pa) and solar altitude (degrees).

Table 3.3.13 provides an evaluation of the above three hourly models for computing horizontal global irradiance. Data from five UK locations was used in this instance. In this scheme the values of MBE and RMSE for any given model are added for each location and

Table 3.3.13 Evaluation of hourly models, horizontal global irradiance

	MBE (W/m^2)			RMSE (W/m^2)			Score (W/m^2)		
Location	CRM	MRM	PRM	CRM	MRM	PRM	CRM	MRM	PRM
(a) Overcast skies ($K_t < 0.2$)									
London/London	33	53	6	54	65	34	87	118	40
Bracknell/Heathrow	38	53	−1	63	67	43	101	120	44
Finningley/Finningley	33	51	2	57	63	47	90	114	49
Aughton/Ringway	55	55	5	83	74	131	138	129	136
Stornoway/Stornoway	37	51	−2	57	64	66	94	115	68
Total							510	596	337
(b) Intermediate skies ($0.2 < K_t < 0.6$)									
London/London	2	18	21	69	66	64	71	84	85
Bracknell/Heathrow	−6	5	20	81	80	99	87	85	119
Finningley/Finningley	−1	0	22	71	68	113	72	68	135
Aughton/Ringway	−2	−3	17	87	92	130	89	95	147
Stornoway/Stornoway	1	4	13	72	82	98	73	86	111
Total							392	418	597
(c) Clear skies ($K_t > 0.6$)									
London/London	−56	−11	88	95	38	122	151	49	210
Bracknell/Heathrow	−86	−40	93	129	71	153	215	111	246
Finningley/Finningley	−55	−22	96	91	49	178	146	71	274
Aughton/Ringway	−101	−75	95	142	122	213	243	197	308
Stornoway/Stornoway	−95	−77	81	122	108	149	217	185	230
Total							972	613	1268

then a total 'score' is obtained. The model that produces the lowest score is then chosen as the best model for a given sky condition (see the boxed score for each sky condition). The conclusion from this analysis is that the PRM, the CRM and the MRM respectively produce the lowest score (and hence most accurate) for overcast, intermediate and clear sky.

3.3.7 Other turbidity-based radiation models

In the previous section the PRM that was primarily based on Linke turbidity was presented. In this section a discussion on other turbidity indices, namely Ångström, Scheupp and Unsworth–Monteith turbidity, are presented.

3.3.7.1 Atmospheric turbidity indices

The most accurate measure of turbidity is the spectral aerosol optical depth (Paltridge and Platt, 1976). Values of turbidity are determined, indirectly, by measuring the depletion of the solar beam at particular wavelengths. Atmospheric turbidity is characterised by four turbidity indices. The Ångström (β) and Schuepp (B) turbidity coefficients are spectral in nature, in that they reference the spectral aerosol optical depth to a common wavelength, i.e. 1.0 μm for β and 0.5 μm for B (Ångström, 1929; Schuepp, 1949). The Unsworth–Monteith (τ_a) and Linke (T_{LK}) turbidity coefficients, in contrast, are broadband in nature; they are estimated by reversing or inverting models that estimate broadband beam irradiance when the latter is measured. The Unsworth–Monteith turbidity coefficient is, by definition, equal to the broadband aerosol optical depth (Unsworth and Monteith, 1972) which is the sum of the aerosol absorption and scattering coefficients integrated over the entire depth of the atmosphere.

Turbidity measurements are inherently difficult and expensive. Based on the work of Gueymard (1993; 1994), Power (2001) has proposed a technique that circumvents the above procedure to obtain turbidity from computations that use potential clear-sky beam irradiance data. In Power's research, parameterisation of clear-sky beam irradiance as a function of atmospheric attenuation processes allows estimation of monthly-averaged turbidity from broadband beam irradiation, sunshine and other readily available climate data. The approach circumvents the need for clear-sky conditions.

Unsworth and Monteith (1972) indicate that for clear-sky conditions it is relatively straightforward to calculate the theoretical direct solar irradiance normal to the solar beam I^*_{Bn} received by a surface below a clean atmosphere containing known amounts of absorbing and scattering gases.

I^*_{Bn} is dependent upon the following parameters:

(a) the solar constant I_{Sc},
(b) the sun–earth distance,
(c) the total water vapour and ozone content of the atmosphere (assuming that the concentrations of other absorbing gases are constant),
(d) the path length of the solar beam through the atmosphere.

I^*_{Bn} depends mainly on the water vapour content of the atmosphere and the path length.

Water vapour content is conveniently expressed as precipitable water; this being the depth of liquid water which would result if all the water vapour in a vertical column from

Table 3.3.14 Values of I_{Bn} (W/m^2), the irradiance of the solar beam at normal incidence at mean solar distance below an aerosol-free atmosphere, as functions of air mass and precipitable water content of the atmosphere

Precipitable water (mm)	Air mass, m	1	1.5	2	3	4	5	6
	SOLALT	90°	42°	30°	20°	14.5°	11.5°	9.6°
5		1100	1055	1010	940	885	835	800
10		1090	1035	990	915	860	810	775
15		1080	1020	975	900	845	800	760
20		1065	1010	960	890	835	790	750
30		1050	990	945	870	820	770	730
40		1035	980	930	860	805	755	720

the earth's surface to the limits of the atmosphere were to condense. Unsworth and Monteith (1972) indicate that values of precipitable water over Britain lie in the range 5–33 mm, with low values occurring in winter. Historic data on the seasonal variations in precipitable water over the earth's surface are given in Bannon and Steele (1960). More recent data are available through several URLs, e.g. www.badc.rl.ac.uk and www.aeronet.gsfc.nasa.gov websites.

The path length of the solar beam through the atmosphere may be expressed in terms of the air mass, e.g. Eq. (3.3.3).

Unsworth and Monteith (1972) tabulate I_{Bn} for a range or precipitable water and air mass and this table is reproduced as Table 3.3.14. The values in this table are, however, based on the older solar constant of 1353 W/m^2, assuming a fixed atmospheric ozone content of 3 mm and assuming mean sun–earth distance. They also indicate that the measured direct irradiance I_{Bn} is in fact usually less than the theoretically derived value I^*_{Bn}. The additional attenuation is usually ascribed to aerosol in the atmosphere and is described mathematically by a turbidity coefficient. Unsworth and Monteith (1972) suggest the use of the coefficient τ_a defined by:

$$\tau_a = -\frac{1}{m}\ln\left(\frac{I_{Bn}}{I^*_{Bn}}\right) \tag{3.3.42}$$

Rodgers et al. (1981) have presented a comparison between the Unsworth–Monteith and Schuepp turbidity coefficients and this information is shown in Table 3.3.15.

In the remainder of this section relationships between the above mentioned turbidity indices are presented. This will enable the user to use any given solar radiation model with a required turbidity index that is not known, but may be derived from other given turbidity. For a more elaborate physical treatment, rather than the generally empirical relationships discussed below, see Gueymard (1998).

The relationship between B and τ_a

The relationship between B and τ_a can be determined from Figure 3.3.8, reproduced from Rodgers et al. (1981).

Table 3.3.15 Typical values of the Schuepp turbidity coefficient for different types of weather with derived values of Monteith and Unsworth's τ_a values

Schuepp, B	Monteith and Unsworth derived τ_a	Domain of validity
0.050	0.09	Clear weather in winter
0.100	0.19	Fine weather in the summer in the country
0.150	0.28	Fine weather in the summer in towns
0.200	0.37	Hazy weather
0.250	0.45	Heavy warm hazy weather in summer

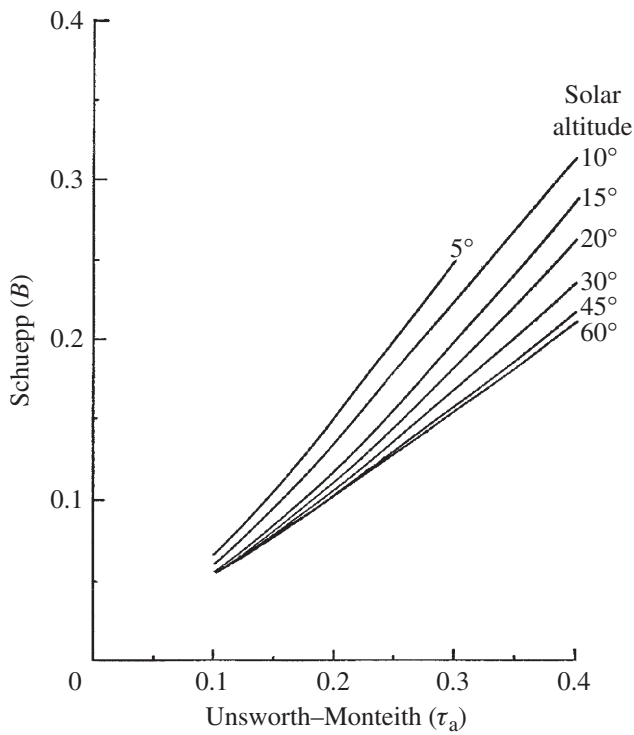

Figure 3.3.8 *Inter-relationship between Schuepp and Unsworth–Monteith turbidity factors*

The relationship between B and β

Ångström (1929; 1930) put forward the following relationship between aerosol optical thickness $\delta_\alpha(\lambda)$ turbidity coefficient, β and the wavelength exponent α as follows:

$$\delta_\alpha(\lambda) = \beta\, \lambda^{-\alpha}$$

It is possible to show that B and β are inter-related as follows:

$$B = 2^\alpha\, \beta \log_{10} e$$

Kambezidis et al. (1998a,b; 2001) have provided mean seasonal and diurnal values of B and β for Athens, Greece. The range of these turbidities are as follows:

B_{summer}: Range = 0.10–0.35 (mean = 0.20)

B_{winter}: Range = 0.03–0.11 (mean = 0.08)

β_{summer}: Range = 0.10–0.68 (mean = 0.35)

β_{winter}: Range = 0.01–0.07 (mean = 0.05)

α_{summer}: Range = 0.25–1.20 (mean = 0.75)

α_{winter}: Range = 1.80–2.50 (mean = 2.25)

The annual mean for α was found to be 1.3.

The relationship between T_{LK} and τ_a

The relationship between T_{LK} and τ_a can be derived from the following expression given by Robinson (1966):

$$T_{LK} = P(m)\,(\log I_{Sc} - \log I_{Bn})$$

where $P(m)$ is a function of air mass only. Robinson has tabulated $P(m)$ for a range of air masses from 0.5 to 10. From Unsworth–Monteith I_{Bn} is given by:

$$I_{Bn} = I^{*}_{Bn} \exp(-\tau_a\, m)$$

and hence by eliminating I_{Bn} between the above two equations T_{LK} is given by:

$$T_{LK} = P(m)(\log I_{Sc} - \log I^{*}_{Bn} + (\log e)\tau_a m) \tag{3.3.43a}$$

The relationship found was that, for a fixed altitude and turbidity, T_{LK} increased by 0.1 for every 5 mm of precipitable water content increment above 15 mm. Similarly, T_{LK} decreased by 0.1 for every 5 mm of precipitable water decrement below 15 mm. Figure 3.3.9 shows the relationship between T_{LK} and τ_a.

Based on several years of measurements for Athens, Greece Kambezidis et al. (1993) have regressed the turbidities under discussion as follows:

$$T_{LK} = 14.37\tau_a + 1.62 (R^2 = 0.88) \tag{3.3.43b}$$

They have also provided the frequency of occurrence of T_{LK} and τ_a. The statistics for T_{LK} is provided below:

T_{LK}	1–1.3	1.3–2.6	2.6–3.9	3.9–5.2	5.2–6.5
Frequency of occurrence (%)	0.8	0.8	30.0	37.6	30.8

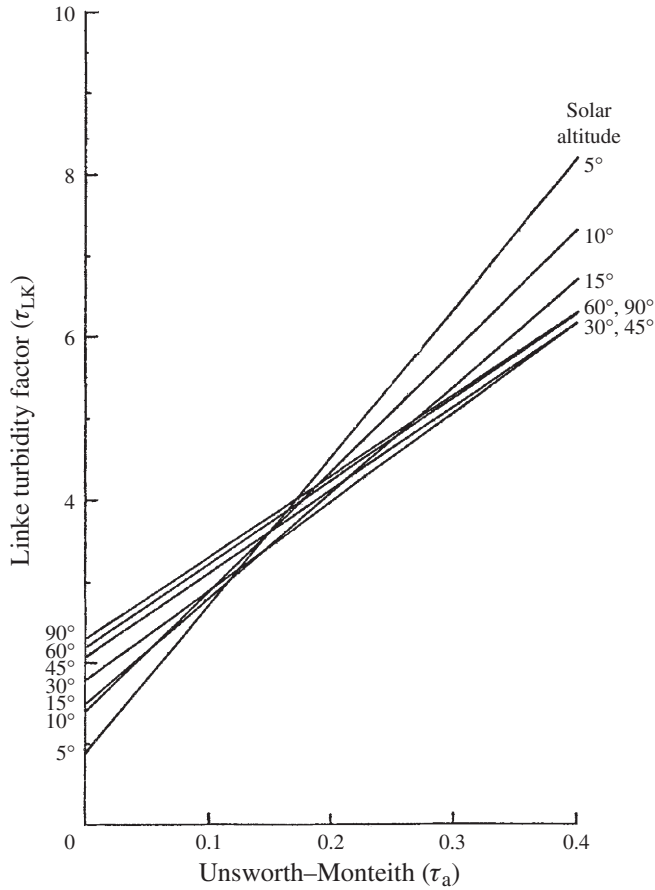

Figure 3.3.9 *Inter-relationship between Linke and Unsworth–Monteith turbidity factors*

Relationship between B and T_{LK}

Valko's work (1966) has been summarised by Rodgers et al. (1981). Based on the former work an empirical formula between B and T_{LK} as a function of optical air mass m and precipitable water content w is available. Thus:

$$T_{LK} = \left(B + 0.54\right)\left(1.75 \log\left(\frac{w}{m} + 0.1\right) + 12.75\right) - 5.4 \tag{3.3.44}$$

where w is in mm and $0 \leqslant B \leqslant 0.4$.

Relationship between β and T_{LK}

Grenier et al. (1994) have presented a simple empirical relationship between β and T_{LK}:

$$\beta = -0.113 + 0.065 T_{LK} \tag{3.3.45a}$$

Furthermore, they have provided similar relationships for dry- ($0.5 < w < 1.6$ cm), medium humidity- ($1.2 < w < 3.2$ cm) and wet (or tropical) climates with $w > 2.8$ cm, respectively as follows:

$$\beta = -0.120 + 0.071 T_{LK} \tag{3.3.45b}$$

$$\beta = -0.128 + 0.070 T_{LK} \tag{3.3.45c}$$

$$\beta = -0.138 + 0.069 T_{LK} \tag{3.3.45d}$$

Likewise, relationships between β and T_{LK} for temperate climates of Avignon, France and Potsdam, Germany are, repsectively:

$$\beta = -0.103 + 0.052 T_{LK} \tag{3.3.45e}$$

$$\beta = -0.100 + 0.050 T_{LK} \tag{3.3.45f}$$

Abdelrahman et al. (1988) have undertaken turbidity measurements for Dhahran, Saudi Arabia, which has a semi-arid climate. Their inter-relationships between the above turbidities are:

$$\beta = -0.1326 + 0.0433 T_{LK} \tag{3.3.45g}$$

Based on 9 years of hourly measurements (1991–99), Li and Lam (2002) have provided Ångström and Linke turbidity values for southern China. The range for the above turbidities was noted to be in the respective ranges of 0.1–0.18 and 3.7–5.3, with the lower values occurring in December and the highest turbidities reported for the month of May.

Under the aegis of ESRA (2000), values of T_{LK} for large number of locations have been made available. Using Eqs (3.3.43)–(3.3.45) along with Figures 3.3.8 and 3.3.9 any given T_{LK} value may be converted to the other three turbidity indices – Ångström, Schuepp and Unsworth–Monteith. Furthermore, monthly Linke turbidity factor may be estimated from the sum of the Ångström regression coefficients ($a + b$). These monthly coefficients are given in Table 2.1.2 for several sites around the globe.

The simple formulae used are:

$$T_{LK} = f_m - f_m(a + b) \quad \text{for monthly mean values} \tag{3.3.46a}$$

and:

$$T_{LK} = f_c - f_c(a + b) \quad \text{for clear day value} \tag{3.3.46b}$$

A research programme carried out around 1980 for a limited range of European sites yielded the values of f_m and f_c given in Table 3.3.16.

Table 3.3.17 provides rough guideline values for selecting the Linke turbidity factor.

The use of the above turbidity factors lies in their utilisation in the estimation of beam normal irradiance. In this respect Gueymard (2003) has undertaken an extensive survey of a whole family of the relevant models, a synopsis of which is presented below.

Table 3.3.16 Values of f_m and f_c month by month for use in Eqs (3.3.46a) and (3.3.46b)

	Jan.	Feb.	Mar.	Apr.	May	Jun.	Jul.	Aug.	Sep.	Oct.	Nov.	Dec.
f_m	10.7	13.2	15.4	17.1	18.5	16.9	18.2	17.0	14.9	12.8	11.3	9.5
f_c	13.5	13.9	13.4	15.4	15.4	15.4	14.9	16.3	14.6	13.2	12.8	11.6

Table 3.3.17 Approximate values of T_{LK}

	T_{LK}
Very clear cold air in winter	$T_{LK} = 2$
Clear warm air	$T_{LK} = 3$
Moist warm air	T_{LK} 4–6
Polluted air	$T_{LK} > 6$

Gueymard's (2003) work is related to the performance of broadband direct irradiance predictions under clear skies. For this task he has selected 19 models from an extensive literature survey. In addition, two new models were specifically developed for his study to provide state-of-the-art broadband transmittances models associated with the atmospheric extinction processes. The SMARTS spectral radiative code was selected to provide reference transmittance and irradiance values, corresponding to concurrent solar position and atmospheric conditions data.

The possible atmospheric inputs for the models evaluated by Gueymard, besides solar altitude, are:

(a) site pressure, p (h Pa),
(b) precipitable water in the vertical column, l_w (cm),
(c) reduced vertical ozone column amount, l_o (in atm-cm),
(d) reduced vertical nitrogen dioxide column amount in the stratosphere (atm-cm),
(e) reduced vertical nitrogen dioxide column amount in the troposphere (atm-cm),
(f) Ångström's spectral turbidity coefficient, β,
(g) Ångström's wavelength exponent, α,
(h) Unsworth–Monteith's broadband turbidity coefficient, τ_a.

In conclusion of his study, Gueymard has short-listed four high-performance models one of which is the Yang turbidity-based model. The latter model has the capability of predicting beam as well as diffuse irradiance once the Ångström turbidity β is specified.

Yang's model

This recent clear-sky solar radiation model (Yang et al. 2001) is based on a product of atmospheric transmittances as explained above in Section 3.3.4. Due to some inconsistencies in the air-mass pressure correction in the published equations, those actually used here take subsequent, unpublished corrections into account. Those corrections were obtained by Gueymard. The main steps in computation of beam (τ_B) and diffuse irradiance transmittances are given below. Note that m' and I_E are obtained from application of Eqs (3.3.4) and (3.3.7) respectively:

$$\tau_r = \exp[-0.008\,735m'(0.5474 + 0.014\,24m' - 0.000\,383\,4m'^2 + 0.000\,004\,59m'^3) - 4.08]$$

$$\tau_o = \exp[-0.0365(mu_o)^{-0.2864}]$$

$$\tau_g = \exp(-0.0117m'^{0.3139})$$

$$\tau_w = \min[1.0,\ 0.909 - 0.036\ln(mw)]$$

$$\tau_a = \exp\{-m\beta[0.6777 + 0.1464m\beta - 0.006\,26(m\beta)^2]^{-1.3}\}$$

$$\tau_B = \tau_r\tau_o\tau_g\tau_w\tau_a - 0.013, \quad \text{and} \quad \tau_D = \tau_o\tau_g\tau_w(1 - \tau_a\tau_r) + 0.013$$

The horizontal beam and diffuse irradiance are then obtained by multiplication of their respective transmittances with I_E.

Note that Gueymard's evaluation of Yang's model for beam irradiance showed satisfactory performance. However, caution must be exercised for diffuse irradiance estimation.

Prog3-2d.For provides the code for Yang's model and has been furnished by Gueymard for this publication. Note that the required input data file, In3-2d.Csv, has the following data fields for any given day's data: year, month, day, hour, minute and dry- and wet-bulb temperatures.

Note however, that as opposed to the original routine, which required β, the present author has altered present code to allow an input of Linke turbidity factor. The code then computes β using Grenier's regression (Eq. (3.3.45a)). This action was undertaken in view of the fact that data on Linke turbidity factor are available for a very wide number of locations and its possible estimation through the use of Eq. (3.3.46). Should any other turbidity factor be available for any given candidate site, the above inter-relationships may be used to obtain β.

Yang has also provided approximate formulations for β and u_o for any location on earth (in terms of the site latitude) so that the model truly becomes universal. However, for preservation of accuracy local and temporal data for w, β and u_o should be sought for dependable estimates of irradiance.

For completion of this section the above-mentioned formulations for β and u_o, as reported by Yang et al. (2001), are provided herein:

$$\beta = \overline{\beta} + \Delta\beta,$$
$$\overline{\beta} = (0.025 + 0.1\cos\text{LAT})\exp(-0.7z/1000) \quad \text{and } \Delta\beta = \pm(0.02 \sim 0.06)$$

z is the station height in masl.

$$u_o = 0.44 - 0.16\{[(\text{LAT} - 80)/60]^2 + [(d - 120)/(263 - \text{LAT})]^2\}^{0.5}$$

$$d = \text{DN} \quad \text{for DN} < 300$$

else:

$$d = \text{DN} - 366$$

The application of Prog3-2d.For will now be demonstrated through the following example.

Example 3.3.2

Five minute averaged data for a clear day (29 March 2000) for Bahrain, Arabian Gulf (26°13′N and 50°39′E) is available within the Bahrain zipped file from the companion web site. File In3-2d.Csv may thus be created from that data after carefully studying the required format from listing of Prog3-2d.For.

Use Yang's model provided in Prog3-2d.For to obtain horizontal beam, diffuse and global irradiance.

Note in accordance with Bahraini turbidity data provided in Figure 4.7.4, a T_{LK} value of 4.0 was used for clear-sky conditions. Furthermore, in view of absence of given data for p-atm and u_o, respective default values of 1013.25 h Pa and 0.3 atm-cm suggested by Gueymard (2003) were used. A plot generated from the output file Out3-2d.Dat, shown in Figure 3.3.10, displays good concordance between computed and measured global irradiance (top plot). The output obtained from MRM (Prog3-2a.For) is also included in the latter figure (bottom plot). Both plots include the best-fit lines, their respective regression equations and R^2 values to enable evaluation of the performance of the respective models.

Example 3.3.3

Clear-sky hourly (LAT) measured data for Chennai, India are provided in File In3-2d.Csv and Table 3.3.18. Mani (1980) has presented the Ångström turbidity data for Indian locations. For post-monsoon season β for Chennai is reported to be 0.042. The equivalent Linke turbidity is 2.39. Using the above turbidity data obtain estimates for global and diffuse irradiation.

Using Prog3-2d.For and default values of u_o (0.3 atm-cm) and p-atm (1013.25 h Pa) the solution may be obtained. Table 3.3.18 enables a comparison of predicted and measured data. Reasonable concordance is to be seen between the respective data sets, especially in

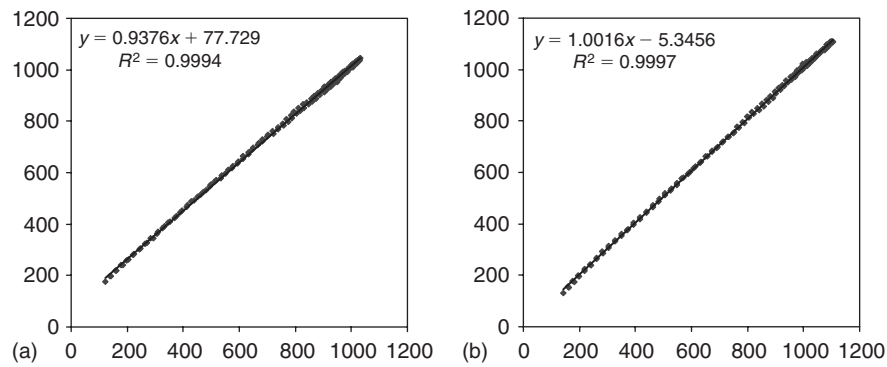

Figure 3.3.10 *Performance of Yang model (left) and MRM (right) for predicting clear-sky irradiance: Bahrain data. Units for both axes are W/m²*

Table 3.3.18 Evaluation of Yang's model for Chennai, India: 11°N on 16 September 1990

				Irradiation data (W/m^2)					
		Temperature (°C)		Measured		Computed from $\beta = 0.042$		Computed from $T_{LK} = 2.39$	
Hour	Minute	DBT	WBT	I_G	I_D	I_G	I_D	I_G	I_D
8	30	28.6	24.0	319	200	293	139	293	139
9	30	30.1	24.7	514	197	522	161	522	162
10	30	31.2	25.4	769	153	717	173	716	174
11	30	33.2	26.2	903	169	853	180	853	181
12	30	33.3	26.6	969	142	921	183	920	184
13	30	33.3	27.1	892	253	913	183	912	183
14	30	33.4	27.6	900	231	830	178	830	179
15	30	32.3	27.2	703	233	680	170	680	171
16	30	31.2	26.8	394	239	480	157	479	157
17	30	30.2	26.4	128	119	250	132	249	132

view of the fact that the standard ozone and atmospheric data have been used rather than locally observed values.

In this section models based on sunshine and cloud-cover data were presented. In view of their inter-dependence, and in conclusion, programs that enable estimation of these meteorological variables are presented in Prog3-2e.For and Prog3-2f.For. Note that the required input data file for these programs, In3-2.Prn, has the following data fields for any given day's data: hour, global, diffuse irradiation (W/m^2), sunshine fraction, cloud cover in oktas, dry- and wet-bulb temperatures, atmospheric pressure (h Pa) and solar altitude (degrees).

3.4 Hourly horizontal diffuse irradiation

Sections 3.2 and 3.3 respectively dealt with the estimation of hourly diffuse irradiation from monthly-averaged daily irradiation and meteorological records. The hourly diffuse irradiation on a horizontal surface can be determined more precisely from the records of hourly global irradiation, if validated regression equations relating the two quantities are available. Following the approach of Liu and Jordan (1960), of regressing D/G against K_t, it is logical to correlate hourly diffuse ratio I_D/I_G and hourly clearness index K_t. One such plot for Camborne (UK), based on Muneer's work (1987), is shown in Figure 3.4.1. One of the first team to attempt a regression between the hourly values of the above two quantities was Orgill and Hollands (1977). Their study was based on 4 years of data for Toronto in Canada.

Erbs et al. (1982) followed the procedure of Orgill and Hollands to develop a regression model for the US locations. They used 65 months data for four locations (Fort Hood, Texas; Maynard, Massachusetts; Raleigh, North Carolina and Livermore, California) with a latitude range of 31–42°N. A single correlation, for the four locations, showed close agreement

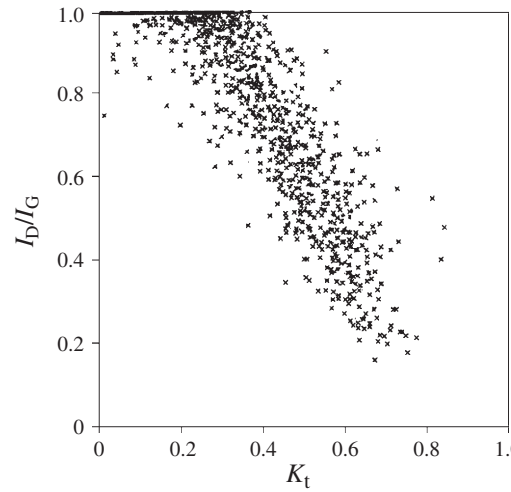

Figure 3.4.1 *Hourly diffuse ratio versus clearness index for Camborne, UK*

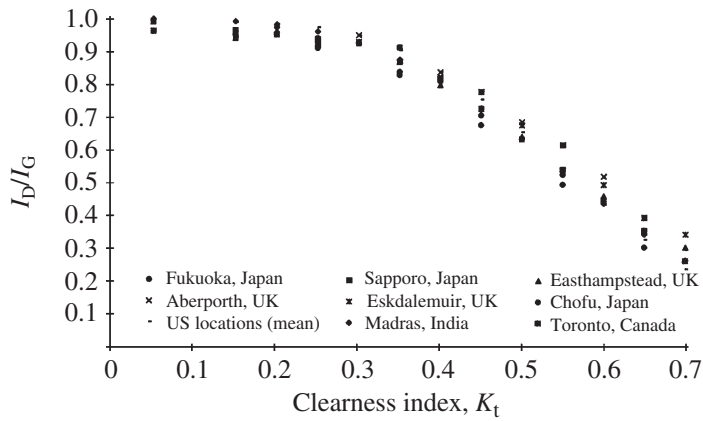

Figure 3.4.2 *Hourly diffuse ratio versus clearness index for worldwide locations*

with the above-mentioned Toronto fit. They also checked the applicability of their regression equation using 3 years of data obtained for Highett, Australia (latitude 38°S). Erbs et al. proposed that their regression equation was location dependent. In a study for five Australian locations, Spencer (1982) found a similar latitude effect. Spencer compared the performance of models due to Bugler (1977), Boes et al. (1976), Bruno (1978) and Orgill and Hollands (1977). He found the Orgill–Hollands' approach to be the best.

Muneer et al. (1984) used 2 years of hourly diffuse and global irradiation data from New Delhi to develop an Orgill–Hollands type regression model. The latter study provides a link between the works of Orgill and Hollands (1977) and Erbs et al. (1982) for North America and that of Spencer (1982) for Australia. The regression curve for New Delhi was found to lie between the curves for Australia and North America thus strengthening the assertion of Spencer on location dependency.

Regression curves for worldwide locations are presented in Figure 3.4.2. Muneer et al. (1996) have provided Eq. (3.4.1) which was fitted for the mean global curve and this may

be used to estimate the horizontal diffuse irradiance in the absence of any specific regression model for a candidate location:

$$I_D/I_G = 1.006 - 0.317K_t + 3.1241K_t^2 - 12.7616K_t^3 + 9.7166K_t^4 \quad (3.4.1)$$

Bugler (1977) has followed an alternate approach to obtain the diffuse component from measured global irradiation. Using a year's data for Melbourne, Bugler developed plots of I_D/I_E versus I_G/I_E for a range of solar altitudes. From these, a general set of curves was obtained which showed a linear relationship between I_D/I_E and I_G/I_E. Further, a regression between I_D/I_G and I_G/I_C was obtained, I_C being the hourly clear-sky irradiation. Bugler claims that, in this form, the regression equations are independent of location. Although Bugler's method is more involved its performance has been found to be inferior to that of Orgill and Hollands (1977) as reported by Spencer (1982). Moreover, Bugler's procedure requires monthly data of precipitable water vapour and dust content, a clear disadvantage over the simpler approach of Orgill and Hollands.

The method of Boes et al. (1976) is altogether different from those discussed so far. This method provides regression equations for determining the normal incidence radiation I_0 from the hourly clearness index. The diffuse component is then obtained by subtracting the horizontal component of I_0 from I_G.

During the 1990s there have been some attempts, e.g. Jeter and Balaras (1990), Perez et al. (1991) and Lam and Li (1996), to reduce the scatter for the type of regression shown in Figure 3.4.1. The scope of the former studies has been rather limited and therefore does not warrant universal applicability. For example, it was shown by Jeter and Balaras (1990) that using the air mass as an additional parameter improves the regression. That study was based on data from one US location. However, other studies, such as the one by Muneer and Saluja (1986) based on data from five UK locations, have specifically shown that solar altitude and hourly sunshine fraction have a bearing on the relation between the diffuse ratio and clearness index. Perez et al. (1991) have examined the newer developments in the possible refinements in diffuse (or beam) ratio predictions. Based on data obtained from 14 sites in Europe and the US, they have proposed Maxwell's model (Maxwell, 1987) as the overall best. Maxwell model is given by:

$$I_{B,n} = I_0\{K_{nc} - [A + B\exp(mC)]\} \quad (3.4.2a)$$

$I_{B,n}$ is normal incidence irradiance.

$$K_{nc} = 0.866 - 0.122m + 0.0121m^2 - 0.000\,653m^3 + 0.000\,014m^4 \quad (3.4.2b)$$

A, B and C are obtained as follows:

If $K_t \leqslant 0.6$:
$$A = 0.512 - 1.560K_t + 2.286K_t^2 - 2.222K_t^3$$
$$B = 0.370 + 0.962K_t$$
$$C = -0.280 + 0.932K_t - 2.048K_t^2$$

For $K_t > 0.6$:
$$A = -5.743 + 21.770K_t - 27.490K_t^2 + 11.560K_t^3$$
$$B = 41.400 - 118.500K_t + 66.050K_t^2 + 31.900K_t^3$$
$$C = -47.010 + 184.200K_t - 222.000K_t^2 + 73.810K_t^3$$

Lam and Li (1996) have proposed to split the above regression with a regression between beam irradiation and clearness index used for $K_t < 0.5$. For the remainder of the K_t range the diffuse ratio – clearness index regression was suggested.

Reindl et al. (1990) have also examined the influence of other climatic variables to improve the accuracy of the above Orgill–Holland classical approach. They used hourly data from five European and North American locations to develop improved diffuse ratio correlations based on four parameters: K_t, SOLALT, dry-bulb temperature T_{db} and RH. Reindl et al. have shown that this approach reduces the residual sum of squares statistic by 14% when compared to Orgill–Holland type model. In essence Reindl et al.'s work is similar to the MRM model (Section 3.3.4) which estimates the diffuse as well as beam transmission of the short-wave radiation from the latter three of the above parameters. It was shown in Section 3.3.4 that the non-overcast diffuse irradiance may be estimated with an acceptable accuracy from other meteorological data. Thus, Reindl's model shows promise and may be a candidate for further evaluation.

Reindl et al's model is given as follows:

$$I_D/I_G = 1.000 - 0.232K_t + 0.0239 \sin \text{SOLALT} - 0.000\,682T_{db} + 0.0195\text{RH}, \quad K_t \leqslant 0.3, \quad I_D/I_G \geqslant 1.0 \tag{3.4.3a}$$

$$I_D/I_G = 1.329 - 1.716K_t + 0.2670 \sin \text{SOLALT} - 0.003\,570T_{db} + 0.1060\text{RH}, \quad 0.3 < K_t < 0.78, \quad I_D/I_G \leqslant 0.97 \quad \text{and} \quad I_D/I_G \geqslant 0.1 \tag{3.4.3b}$$

and:

$$I_D/I_G = 0.426K_t - 0.2560 \sin \text{SOLALT} + 0.003\,49T_{db} + 0.0734\text{RH} \quad K_t \leqslant 0.78, \quad I_D/I_G \geqslant 0.1 \tag{3.4.3c}$$

Example 3.4.1

Hourly global irradiance values were provided for London, UK in Table 3.3.5. Use Eqs (3.4.1) and (3.4.2) to obtain the corresponding diffuse irradiance estimates. Evaluate these estimates against those obtained in Example 3.3.1 using the MRM procedure.

Prog3-3.For may be used to obtain the above estimates for I_D. These estimates are also included in Table 3.3.5. It is evident that using the present diffuse ratio regressions improves I_D estimates. However, given the fact that MRM does not require any irradiation values as a starting point, its reasonable performance is noteworthy.

3.5 Hourly horizontal illuminance

Recent developments in technology have shown that significant savings in electrical consumption within the building sector are possible through exploitation of daylight. One such lighting control schematic which would enable such exploitation is shown in Figure 3.5.1. Modern buildings frequently employ designs and equipment which enable maximum exploitation of solar heat and light with the added possibility of glare and overheat avoidance using weather sensitive, controlled blinds. One such building is the new European Court of

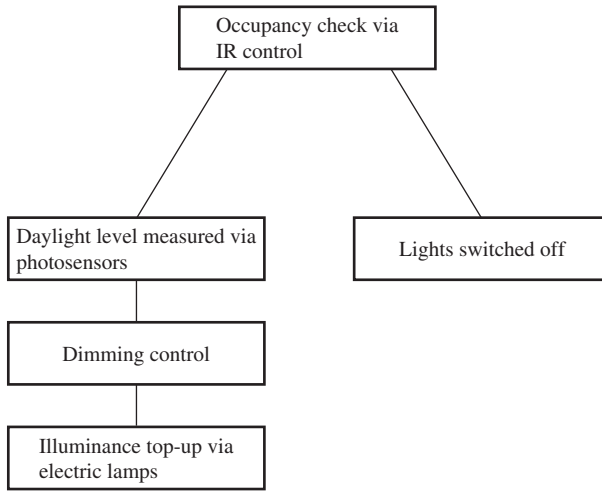

Figure 3.5.1 *Lighting control schematic*

Human Rights in Strasbourg which, on demand, can provide up to 92% protection against solar heat (*Building Services and Environmental Engineer*, 1996).

In the UK the latest update of the building regulations aims to improve the lighting efficiency (CIBSE, 1996). To satisfy the new regulation, the designer is prompted to encourage the maximum use of daylight. Efficient and more precise design of windows in buildings requires the development of inclined surface illuminance models. These in turn require values of horizontal global and diffuse illuminance. In the absence of measurements it is necessary to resort to luminous efficacy models to obtain an estimate of global and diffuse illuminance from other measured or estimated atmospheric parameters. Several approaches have been adopted, including the use of solar altitude, water vapour content, Linke turbidity factor and many other atmospheric parameters.

The global luminous efficacy of daylight K_G is expressed as the ratio of luminance (lx) to irradiance (W/m^2) which can be found through the integration of the whole spectrum, i.e.:

$$K_G = \left[680\int_{400\text{ nm}}^{700\text{ nm}} V(\lambda)I_G(\lambda)\mathrm{d}\lambda\right] \Big/ \left[\int_0^{\infty} I_G(\lambda)\mathrm{d}\lambda\right] \tag{3.5.1}$$

where $V(\lambda)$ is the CIE spectral sensitivity of the human eye and $I_G(\lambda)$ is the solar spectral irradiance.

Note that under the aegis of the 'International project to realise the lumen', work has been undertaken to ascertain the luminous flux equivalence of 1 W radiation. The latter study has determined that a unit Watt of radiation emitted at a frequency of 540.1012 Hz (wavelength = 555 nm) and having the largest efficacy is equivalent to 683 lumen (abbreviated as lm). The latter equivalence represents the direct relation between radiometric and light quantities (Ivanov et al., 2002).

3.5.1 Atmospheric parameters used in luminous efficacy estimations

Luminous efficacy values enable daylight illuminance to be derived from solar radiation measurements. The problem has been tackled in many different ways by previous

researchers. Methods vary by the differing approaches used to account for the absorption and scattering processes that radiation encounters as it passes through the atmosphere. The following note describes the terms and processes occurring in the atmosphere and their effect on luminous efficacy.

In Section 3.3 it was shown that the attenuation of irradiance or daylight is a function of the quantity of atmospheric water vapour and aerosol particles. The presence of dust and soot particles is the result of man-made pollution and natural phenomena. A significant contributor is volcanic eruption which may expel millions of tonnes of soot high into the atmosphere where jet streams disperse the particles across the earth. The following paragraphs describe the terms and processes occurring in the atmosphere and their effect on luminous efficacy.

Particles such as soot and dust are defined as aerosols. The density of dust particles varies with location and season, with higher densities located over land in warmer seasons. A turbid (or hazy) atmosphere is renowned for possessing high levels of aerosols resulting in the attenuation or scattering of solar radiation. The scattering process and its effects are discussed in the following sub-sections and in more detail in Chapter 5.

The concept of Ångström's turbidity coefficient, β was introduced in Section 3.3.3.2. As a very crude approximation β may be obtained by assuming an average value of $\alpha = 1.3$ and using visibility measurements *vis* (expressed in km), obtainable from the local meteorological office by:

$$\beta = 0.55^{\alpha}(3.912/vis - 0.011\,62)[0.024\,72(vis - 5) + 1.132] \tag{3.5.2}$$

3.5.1.1 Linke turbidity factor

In Section 3.3.7 it was shown that the Linke turbidity factor T_{LK} allows the estimation of irradiance. However, its use may be extended to estimate illuminance as given by:

$$IL_{\mathrm{B}} = I_{\mathrm{E}} \exp(-\alpha_{\mathrm{IL}} m T_{\mathrm{ILK}}) \tag{3.5.3}$$

where IL_{B} is the horizontal beam illuminance.

Navvab et al. (1988) developed an illuminance turbidity coefficient T_{ILK} (Eq. (3.5.4)) which utilises the Ångström turbidity coefficient β. They have shown that the illuminance turbidity factor may be more sensitive to atmospheric conditions than T_{ILK}. T_{ILK} is related to the Ångström turbidity coefficient as follows:

$$T_{\mathrm{ILK}} = 1 + 21.6\beta \tag{3.5.4}$$

Note that there are a whole host of other similar relationships that relate various turbidity parameters. The relevant discussion was presented in Section 3.3.7. Note that a detailed treatment of illuminance turbidity has been presented by Gueymard and Kambezidis (1997).

3.5.1.2 Clouds

The effect of cloud cover for daylight calculations is important. Clouds are good attenuators of solar radiation. It is fair to assume that nearly all the energy removed by the water droplets is in turn scattered.

Tregenza (1980) developed a scheme to estimate illuminance from clouds for use in daylight factors. This method involves, among other considerations, the geometry of clouds. As

scattering due to cloud cover will increase the path length of light, the luminous efficacy of an overcast sky will be slightly higher than that of a clear sky with values averaging around 110–120 lm/W.

3.5.2 Beam luminous efficacy models

As shown in Section 3.3.3, beam irradiance undergoes strong attenuation as it enters the atmosphere. This process, known as Rayleigh scattering, is prevalent at low solar altitudes. Rayleigh scattering by air molecules tends to be wavelength dependent and in particular affects the visible spectrum. It is estimated that between 10% and 15% of the beam radiation is absorbed as a result of Rayleigh scattering. Another process responsible for the reduction of beam radiation is the effect of Ångström's turbidity coefficient. Again this is most sensitive in the visible waveband. Attenuation of beam radiation is also effected by water vapour absorption. This absorption process is mainly confined to the IR region of the solar spectrum. The overall effect of these processes is the reduction of beam radiation reaching the earth and the reduction of luminous efficacy. Many authors have utilised the physics of these processes in the development of luminous efficacy models and produced good correlations with measured data.

Navvab et al. (1988) developed a semi-empirical formula for a range of turbidities and produced a relationship for the estimation of beam luminous efficacy K_B:

$$K_B = 104.59[1 - \exp(-9.39\text{SOLALT})] \tag{3.5.5}$$

Table 3.5.1 displays the statistical results of all the luminous efficacy models presented herein. Aydinli and Krochmann (1983) developed a polynomial relationship between beam luminous efficacy and solar altitude:

$$\begin{aligned} K_B = {} & 17.72 + 4.4585\text{SOLALT} - 8.7563 \times 10^{-2}\text{SOLALT}^2 \\ & + 7.3948 \times 10^{-4}\text{SOLALT}^3 - 2.167 \times 10^{-6}\text{SOLALT}^4 \\ & - 8.4132 \times 10^{-10}\text{SOLALT}^5 \end{aligned} \tag{3.5.6}$$

Table 3.5.1 Comparison of luminous efficacy models against Edinburgh data

	r^2	MBE (lx)	RMSE (lx)
Direct luminous efficacy			
Navvab et al. (1988)	0.973	−258	2339
Aydinli and Krochmann (1983)	0.97	−718	2381
Average (104 lm/W)	0.973	−247	2319
Global luminous efficacy			
Aydinli and Krochmann (1983)	0.987	−3016	4351
Chroscicki (1971)	0.985	−5378	6915
Littlefair (1985)	0.987	−767	2842
Average (110 lm/W)	0.987	−1667	3277
Diffuse luminous efficacy			
Littlefair (1985)	0.989	−945	1580
Average (120 lm/W)	0.986	−82	1870

A simple, yet robust model is the use of a single, averaged value of luminous efficacy, a technique that has been adopted by several authors (Littlefair, 1985). An average value of between 93 and 115 1m/W is quoted for beam luminous efficacy. Table 3.5.1 provides the accuracy evaluation of a luminous efficacy value of 104 lm/W.

3.5.3 Global and diffuse luminous efficacy models

Drummond and Ångström (1971) have shown that precise determination of illuminance may be obtained via pyranometric measurements with broadband filters such as the Schott RG8 filter which gives irradiation, $I_{G,\,0-700\,nm}$ in the $0 < \lambda < 700$ nm interval. This way all visible wavebands are included but the effects of water vapour in the NIR region are excluded. The above authors have proposed a precise equation, with an average error of 1%, to obtain global illuminance:

$$IL_G = 215 I_{G,\,0-700}(1 + 0.102\,nm) \tag{3.5.7}$$

The luminous efficacy of daylight depends upon the way in which the radiant energy is shared between the visible and invisible (IR and UV) parts of the spectrum. This in turn depends upon a number of factors including the state of the sky (clear, overcast or average) and the altitude of the sun. In particular, the luminous efficacy is different for the sun alone, the sky alone and for the global radiation (sun plus sky).

Determinations have been made by workers in different parts of the world of the luminous efficacy of daylight from simultaneous measurements of the illuminance and irradiance. Worthy of note among the earliest measurement efforts are Pleijel (1954) in Scandinavia, Blackwell (1954) at Kew, England, Dogniaux (1960) at Uccle, Belgium and Drummond (1958) at Pretoria in South Africa. Pleijel showed that clear and overcast skies vary little in luminous efficacy with solar altitude (and thus with time of year) but that there is a marked decrease in the efficacy of the sun's beam radiation at solar altitudes less than 30°. Blackwell's measurements were related to global radiation with clear, overcast and average skies. The mean efficacies were found to be 119, 120 and 116 lm/W, respectively. With average skies, the global efficacy was found to vary between 105 and 128 lm/W.

Moon's (1940) empirical spectral distribution curves for sunlight give an almost constant luminous efficacy of about 117 lm/W for solar altitudes greater than 25°, decreasing to 90 lm/W at 7.5°.

Blackwell does not provide figures for the diffuse luminous efficacy but by combining his sky irradiance measurements at Kew with corresponding illuminance measurements reported by McDermott and Gordon-Smith (1951) for neighbouring Teddington, a constant value of 125 lm/W has been deduced by Hopkinson et al. (1966).

Traditionally, researchers have modelled global luminous efficacy for clear and overcast skies. Notable among these are Aydinli and Krochmann (1983) and Chroscicki (1971) who developed formulae relating clear-sky global luminous efficacy to solar altitude. However, it is highly desirable to obtain luminous efficacies under all sky conditions. Such models are presented in the following sections.

3.5.4 Littlefair model

The estimation of global luminous efficacy K_G due to Littlefair (1988) involves weighing the sky diffuse K_D, ground-reflected diffuse K_{gr} and beam luminous efficacies with cloud

cover. Diffuse luminous efficacy was reported to be sensitive to cloud cover *CC*. Littlefair's model is summarised below:

$$K_G = R_B K_B + R_D K_D + R_g K_{gr} \tag{3.5.8}$$

$$K_B = 51.8 + 1.646\text{SOLALT} - 0.01513\text{SOLALT}^2 \tag{3.5.9}$$

and:

$$K_D = 144 - 29CC/8 \tag{3.5.10}$$

where, *CC* is the cloud cover in oktas and may be obtained via its reported relationship with sunshine probability σ:

$$CC/8 = 1 - 0.55\sigma + 1.22\sigma^2 - 1.68\sigma^3$$

K_{gr} in Eq. (3.5.8) is taken as 86 1m/W.

R_B, R_D and R_g respectively represent the beam, sky diffuse and ground-reflected fractions of the global illuminance (or irradiance). A modified version of the above model (Eq. (3.5.10)), which does not require sunshine probability, was evaluated by Muneer and Angus (1993; 1995):

$$K_D = (1 - R_D)K_{cl} + R_D K_{oc} \tag{3.5.11}$$

where K_{cl} is the clear-sky luminous efficacy (=144 1m/W) and K_{oc} the overcast-sky luminous efficacy (=115 lm/W). The values of global and diffuse illuminance are then obtained by the multiplication of the appropriate efficacies by the respective irradiance measure. The performance of this modified model was first presented by Muneer and Angus (1993) for Garston data.

Littlefair's (1988) diffuse luminous efficacy model is represented by Eq. (3.5.11). Table 3.5.1 shows the evaluation of this model. Once again good agreement between the estimated and measured data has been found.

3.5.5 Perez et al. model

The Perez et al. (1990) model has a more involved structure and is considered to be more sophisticated. The model is given by:

$$K_G \text{ or } K_D = a_i + b_i l_w + c_i \cos z + d_i \ln(\Delta) \tag{3.5.12}$$

where a_i, b_i, c_i and d_i are the coefficients of a 4×8 matrix given in Table 3.5.2. ε represents the sky clearness from overcast sky through partly cloudy conditions to clear skies:

$$\varepsilon = \left[\left\{\left(I_D + I_{Bn}\right)/I_D\right\} + kz^3\right] \Big/ \left[1 + kz^3\right] \tag{3.5.13}$$

where I_{Bn} is the normal incidence irradiance, z the solar zenith angle and k is a constant equal to 1.041 for z in radians.

Table 3.5.2 Coefficients for Perez et al. luminous efficacy and zenith luminance model (Eq. (3.5.12))

ε (bin): i	1	2	3	4	5	6	7	8
lower bound	1.000	1.065	1.230	1.500	1.950	2.800	4.500	6.200
upper bound	1.065	1.230	1.500	1.950	2.800	4.500	6.200	–
Global luminous efficacy								
a_i	96.6251	107.5371	98.7277	92.7210	86.7266	88.3516	78.6240	99.6452
b_i	−0.4703	0.7866	0.6972	0.5591	0.9763	1.3891	1.4699	1.8569
c_i	11.5010	1.7899	4.4046	8.3579	7.1033	6.0641	4.9305	−4.4555
d_i	−9.1555	−1.1892	−6.9483	−8.3063	−10.9361	−7.5967	−11.3703	−3.1465
Diffuse luminous efficacy								
a_i	97.2375	107.2129	104.9660	102.3945	100.7100	106.4200	141.8800	152.2300
b_i	−0.4597	1.1508	2.9605	5.5890	5.9400	3.8300	1.9000	0.3500
c_i	11.9962	0.5840	−5.5334	−13.9510	−22.7500	−36.1500	−53.2400	−45.2700
d_i	−8.9149	−3.9490	−8.7793	−13.9052	−23.7400	−28.8300	−14.0300	−7.9800
Zenith luminance								
a_i	40.8646	26.5790	19.3462	13.2425	14.4716	19.7665	28.3923	42.9198
b_i	26.7766	14.7298	2.2895	−1.3987	−5.0932	−3.8843	−9.6634	−19.6247
c_i	−29.5863	58.4662	100.0029	124.7992	160.0932	154.6061	151.5770	130.8072
d_i	−45.7562	−21.2447	0.2547	15.6529	9.1255	−19.2028	−69.3941	−164.0794

Perez et al. (1990) regard the variations in ε as reflecting the changing atmospheric turbidity, and the sky brightness coefficient Δ as denoting the optical transparency of the cloud cover. The equation for sky brightness is:

$$\Delta = I_D m / I_E \tag{3.5.14}$$

The atmospheric precipitable water content l_w is obtained from Eq. (3.3.2).

Perez model was derived empirically on the basis of data recorded at 10 US and three Central European sites operating mainly hourly, with some stations recording at 15 min intervals. The periods of measurements ranged from 6 months to 3 years.

Muneer and Angus (1993) have evaluated the above all-sky models (Littlefair, 1988; Perez et al. 1990) using data obtained from Watford (north London). Figure 3.5.2 and Table 3.5.3 present the plots of measured and modelled horizontal illuminance. The Littlefair model has a tendency to under-estimate global illuminance. Some over-estimation of the diffuse illuminance is also evident. The data scatter in either of the two cases, i.e. Perez and Littlefair, is of the same order. Perez model was reported to perform exceptionally well in both the global and diffuse illuminance estimations. Moreover the data scatter is minimal. Statistical tests for the above models are given in Table 3.5.1.

Average luminous efficacy models also show promise, at least for the temperate belt of the globe. Muneer and Angus (1995) have shown that for UK locations the respective average luminous efficacies of 110 and 120 lm/W for global and diffuse components give results which are comparable with most of the diffuse illuminance models presented herein. In this respect attention is drawn towards Figures 3.5.3 and 3.5.4 and Table 3.5.4.

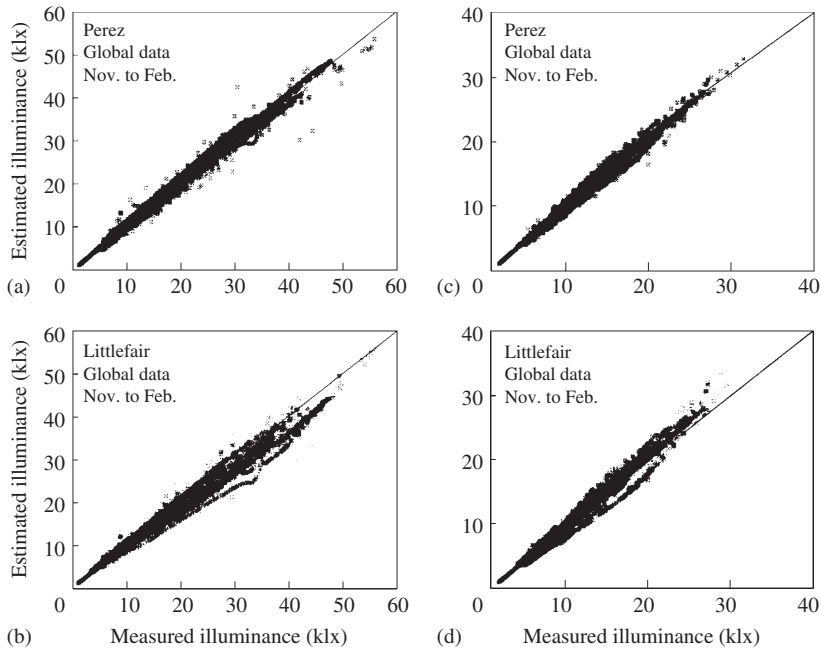

Figure 3.5.2 *Performance of luminous efficacy models*

Table 3.5.3 Performance of Perez and Littlefair luminous efficacy models – north London data

		Illuminance	
Model	Statistic (lx)	Global	Diffuse
Perez et al.	MBE	410	180
	RMSE	1160	660
Littlefair	MBE	−1120	100
	RMSE	2210	990

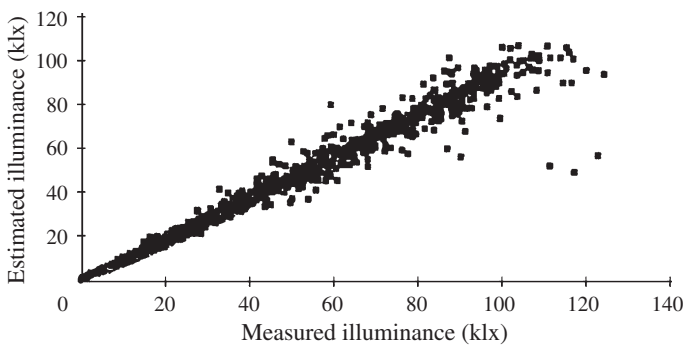

Figure 3.5.3 *Performance of average global luminous efficacy model (luminous efficacy = 110 lm/W)*

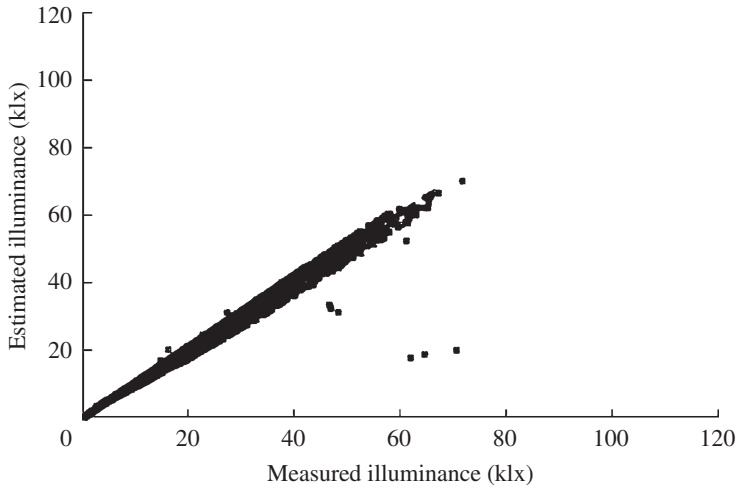

Figure 3.5.4 *Performance of average diffuse luminous efficacy model (luminous efficacy = 120 lm/W)*

Table 3.5.4 Input/output data for Example 3.5.1: north London data, 1 April 1992

		Input (measured) data					Output (computed) data		
Hour	Minute	I_G (W/m^2)	I_D (W/m^2)	IL_G (klx)	IL_D (klx)	L_Z (Cd/m^2)	IL_G (klx)	IL_D (klx)	L_Z (Cd/m^2)
9	0	483	191	50 578	23 403	3579	51 171	25 086	4061
9	5	502	204	52 334	24 877	3798	52 963	26 523	4399
9	10	516	222	52 788	26 314	4643	54 103	28 468	4869
9	15	547	236	56 389	27 579	4909	57 130	29 971	5250
9	20	521	230	54 087	26 752	3885	54 692	29 396	5132
9	25	386	229	40 863	26 391	4143	41 699	28 011	5381
9	30	392	245	42 205	27 278	6938	42 206	29 763	5865
9	35	286	237	31 695	25 488	9056	31 885	27 121	7385
9	40	186	178	20 320	19 217	6674	21 477	20 652	7757
9	45	144	135	15 939	14 815	4749	17 010	16 013	6242
9	50	352	244	37 223	26 839	6463	39 017	28 798	6452
9	55	455	294	47 040	31 908	8647	49 899	34 238	7830
						MBE	983	1932	262
						RMSE	171	486	139

Source: data collected by the Building Research Establishment, Garston, UK.

3.5.6 DuMortier–Perraudeau–Page model

This model has been used in the preparation of the ESRA (CEC, 1996) and *CIBSE Guide J* (CIBSE, 2002). The diffuse K_D, beam K_B and global K_G luminous efficacy models, validated by Littlefair (1996), are given below.

Luminous efficacy of diffuse irradiance is obtained via the work undertaken by Chauvel (1993). The pseudo cloud cover *CC* is given by:

$$CC = 1 - 0.55NI + 1.22NI^2 - 1.68NI^3 \tag{3.5.15}$$

where *NI* is the nebulosity index (DuMortier 1994a,b):

$$\text{for } h > 5^\circ, \quad K_D = 144 - 29CC \tag{3.5.16}$$

$$\text{else}, \quad K_D = 120 \tag{3.5.17}$$

The following steps highlight the computation of the nebulosity index *NI*. The air mass *m* is given by:

$$m = [\sin \text{SOLALT} + 0.505\,72 \exp\{-1.6364 \ln(\text{SOLALT} + 6.079\,95)\}]^{-1}$$

The Rayleigh scattering coefficient *Ar* is given by:

$$Ar = \{5.4729 + m[3.0312 + m\{-0.6329 + m(0.091 - 0.005\,12m)\}]\}^{-1}$$

The theoretical horizontal diffuse illuminance for clear sky $I_{D,cl}$ is given by:

$$I_{D,cl} = 0.0065 + (0.255 - 0.138 \sin \text{SOLALT})\sin \text{SOLALT}$$

The theoretical cloud ratio *CR* for the clear sky with turbidity factor of 4 is given by:

$$CR = I_{D,cl}/[I_{D,cl} + \exp(-4mAr)\sin \text{SOLALT}]$$

Finally:

$$NI = [1 - (I_D/I_G)]/(1 - CR)$$

Luminous efficacy of beam irradiance is based on the work of Page (CEC, 1996) as follows:

$$K_B = 62.134 - 0.758\,85\text{SOLALT} + 0.277\,49\text{SOLALT}^2 - 0.012\,108\text{SOLALT}^3 + 0.000\,205\,2\text{SOLALT}^4 - 1.2278 \times 10^{-6}\text{SOLALT}^5, \quad \text{SOLALT} \leqslant 50^\circ \tag{3.5.18a}$$

$$K_B = 103 + 0.2(\text{SOLALT} - 50), \quad 50^\circ < \text{SOLALT} \leqslant 60^\circ \tag{3.5.18b}$$

$$K_B = 105, \quad \text{SOLALT} > 60^\circ \tag{3.5.18c}$$

Luminous efficacy of global irradiance is obtained as weighted average of K_B and K_D:

$$K_G = (K_B I_B + K_D I_D)/I_G \tag{3.5.19}$$

3.5.7 Other approaches

Delaunay (1995) and Muneer (1995) have shown that for improved precision over an average-value model the global and diffuse efficacies may be regressed against the instantaneous clearness index, K_t.

It has been reported in the literature that the average values of the above efficacies vary with the geographic location. Whereas Littlefair (1988) cites an average overcast and clear-sky diffuse luminous efficacy of 115 and 144 lm/W respectively, Koga et al. (1993a) report a range of 100–140 lm/W for overcast conditions and 153–165 lm/W for clear skies.

Figure 3.5.5 shows the variation of global and diffuse efficacies plotted against the clearness index, K_t for a Japanese location (Fukuoka, 33.5°N and 130.5°E). Further plots for other Japanese locations have been presented by Muneer (1995). Herein, four points are worth noting:

(a) There is a definite relationship between the dependent quantities (global and diffuse luminous efficacies) and the independent parameter K_t.
(b) The global efficacy shows a decreasing trend (see Figure 3.5.5a). As reported by Perez et al. (1990) the increase in global efficacy for overcast conditions is attributable to the increase in water vapour absorption. For the US and Swiss locations

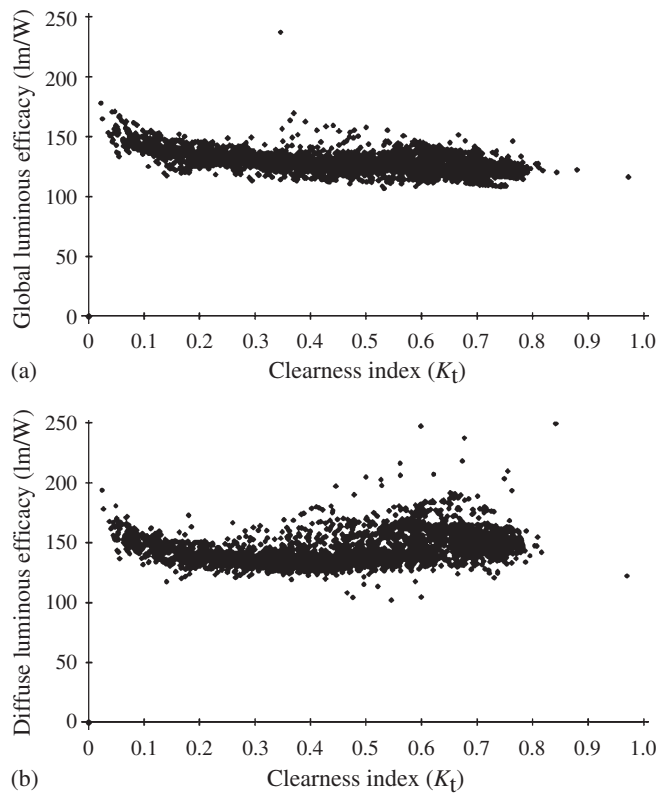

Figure 3.5.5 *Relationship between (a) global and (b) diffuse luminous efficacy and clearness index (Fukuoka)*

the global efficacy was shown to rise up to 140 lm/W. This trend has also been noted by Littlefair (1988). On the other hand the efficacy in the absence of any atmosphere is 97 lm/W.

(c) Japanese locations display a higher value of efficacy for the overcast conditions than found elsewhere. This was also the conclusion drawn by Koga et al. (1993a,b).

(d) The diffuse efficacy displays a sag in the middle section of the plot (part-overcast conditions) with higher values at the two extremes of heavy overcast and clear skies. The increase in the diffuse efficacy of clear skies has been explained due to the increased contribution of molecular (Rayleigh) scattering. This was confirmed to be the case for the US and Swiss locations (Perez et al., 1990). It was noted by Muneer (1995) that $K_t = 0.4$ was the local threshold for the onset of thin overcast. As explained above, increase in the cloud cover (bright thin clouds to heavy overcast) results in the increase of the diffuse luminous efficacy (once the sky is overcast the global and diffuse efficacies are identical). This phenomenon explains the sagging curves shown in Figure 3.5.5b.

It is clear from the above analysis that one single fit for the efficacy models, to cover all geographic areas of the globe, would pose difficulties. Muneer (1995) has evaluated the validity of the above Perez model. Figure 3.5.6 shows its performance for estimating global and diffuse illuminance from their respective irradiance measures. The model consistently underpredicts both global and diffuse illuminance. However, the low scatter indicates that the model would perform adequately if it is fitted against local data. The MBE and RMSE obtained for Perez model against Fukuoka data were 12% and 13% (Muneer, 1995). A further point of interest noted by Muneer (1995) was that the use of a constant value of $l_w = 2$ cm does not have any appreciable influence on the sensitivity of Perez model.

3.5.8 Muneer–Kinghorn model for luminous efficacy

The philosophy behind these models is that the luminous efficacy is most significantly influenced by the sky clearness index (Muneer and Kinghorn, 1997). Thus:

$$K_G = 136.6 - 74.541K_t + 57.3421K_t^2 \tag{3.5.20}$$

and:

$$K_D = 130.2 - 39.828K_t + 49.9797K_t^2 \tag{3.5.21}$$

The above models have been rigorously evaluated against an extensive set of measured data gathered from a variety of locations across the UK as part of the International Daylight Measurement Programme. Findings confirm that in the event of unavailability of long-term measured illuminance data, using measured irradiance values in conjunction with a luminous efficacy model, is one of the most reliable method of synthetically generating an illuminance database.

In conclusion, all of the above luminous efficacy models, e.g. Average value, Littlefair, Perez and Muneer–Kinghorn are good estimators, so long as their performance has been evaluated against (at least) short-term data for any given location. They are not, however, universal in their nature and thus may need fitting against the local conditions. For the

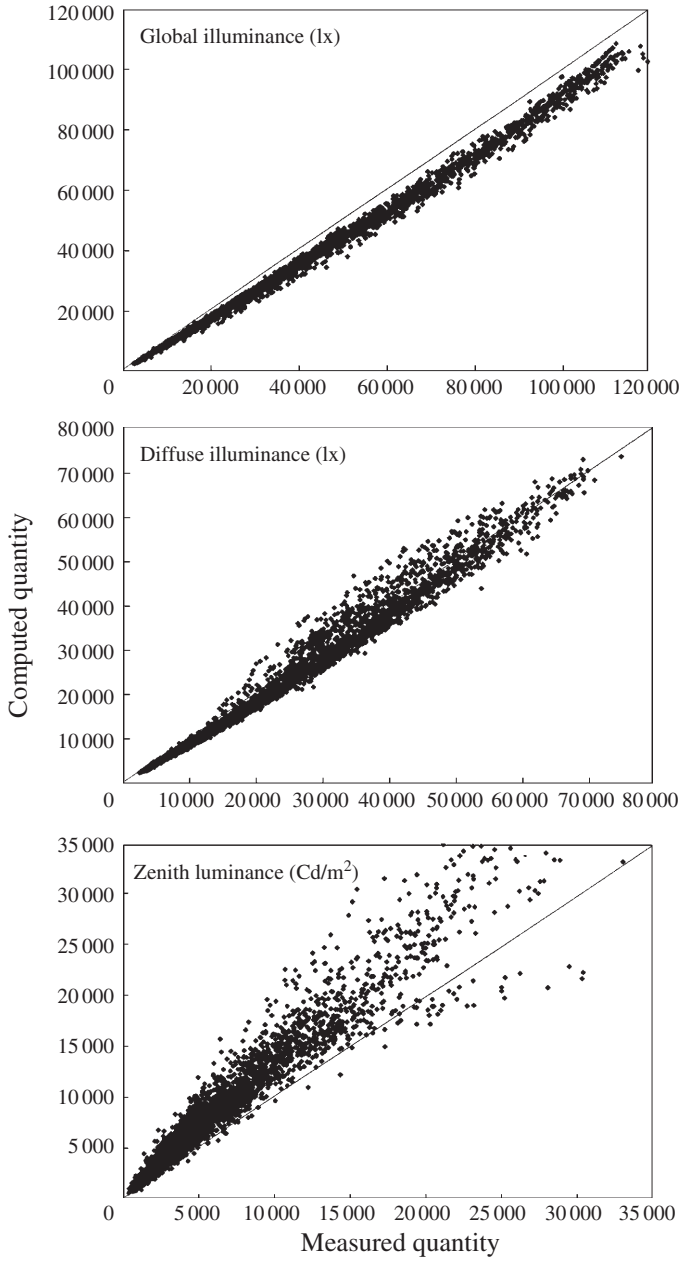

Figure 3.5.6 *Evaluation of Perez et al. model against Fukuoka data (1994)*

climates of North America and Europe, Perez and Muneer–Kinghorn models may respectively be used with confidence. Prog3-4a.For and Prog3-4b.For respectively provide routines for Perez and Muneer–Kinghorn models. The routines enable estimation of global and diffuse illuminance from the corresponding irradiance data.

3.5.9 Zenith luminance

Zenith luminance is an important design parameter and is also required to obtain the absolute luminance distribution of the sky hemisphere. The sky radiance and luminance distributions will be discussed in Chapter 4. A number of researchers have proposed zenith luminance models for clear skies. Notable among these are Kittler (1970), Krochmann (1970), Nagata (1970), Liebelt (1975), Dogniaux (1979), Karayel et al. (1983), Nakamura and Oki (1986) and Rahim et al. (1993). Some of the above models are not applicable in the tropical belt as they use a tangent function of the solar altitude (Rahim et al., 1993). The latter team has also demonstrated the site-specific nature of many of the older models.

The relative luminance distribution of the CIE standard clear sky (CIE, 1973) is expressed as the ratio of the luminance of any given sky patch to the zenith luminance. Zenith luminance may then be used to obtain the corresponding absolute quantities.

Hopkinson et al. (1966) and more recently Littlefair (1994) have shown that under dark, overcast skies the Moon and Spencer (1942) proposed CIE overcast-sky model shows good agreement with measurements. Under such conditions the zenith luminance may be obtained as:

$$L_z = (9/7\pi) I L_G \tag{3.5.22}$$

3.5.9.1 Perez et al. model

Perez et al. (1990) have developed an all-sky zenith luminance model which has been tested against extensive data from five locations in North America. The model is represented by Eq. (3.5.15):

$$L_z/I_D = a_i + b_i \cos z + c_i \exp(-3z) + d_i \Delta \tag{3.5.23}$$

This model claims to be site and season independent. With an overall bias error around 1% and RMSEs ranging between 0.7 kcd/m^2 for clear skies and 1.5 kcd/m^2 for the intermediate sky, it represents a significant improvement over the above models. Prog3-4a.For may be used to obtain Perez modelled zenith luminance given horizontal irradiance data as will be demonstrated below.

Example 3.5.1

Five-minute averaged horizontal global and diffuse irradiance values are provided for Watford, north London (51.71°N and 0.37°W) in Table 3.5.4. Use Perez model to compute horizontal global and diffuse illuminance and the zenith luminance. Evaluate these estimates against the corresponding measured values which are included in Table 3.5.4.

Prog3-4a.For may be used to obtain the above estimates for IL_G, IL_D and L_z. These are shown in Table 3.5.4. The MBEs for the horizontal global illuminance indicate an average error of 2.5%. The corresponding error in estimating zenith luminance is 7%.

3.5.10 Muneer–Kinghorn model for zenith luminance

It will be shown in Chapter 4 that the sky luminous distribution index *b* provides an indication of the relative brightness of the sky vault. It has been shown by Muneer (1987) that

the radiance, or luminance, distribution of each half of the sky vault, e.g. 'sun facing' (by the sun) and 'shaded' (opposite sun), may be represented by a unique value of b. These indices are denoted by b_{sf} and b_{sh} respectively.

Equation (4.3.3.1) presents the generalised form of the Moon–Spencer model. Integration of this equation allows the development of a relationship between sky diffuse illuminance IL_D (lx) and the zenith luminance (cd/m^2).

Refer to Figure 4.3.1a which shows a sketch of a hemispherical sky whose luminance distribution is described by Eq. (4.3.3.1). Let the radius of the hemisphere be R.

The illuminance on a horizontal plane at the centre of the hemisphere due to the light from the hemisphere will be proportional to $1/R^2$ and to the luminance of the hemisphere. An elemental ring of the hemisphere of angular width $\mathrm{d}\theta$ at an angle of elevation θ above the horizon will have an area $(R\,\mathrm{d}\theta)(2\pi R\cos\theta)$. The luminance of the ring will be given by the product of this area and its luminance L_θ, i.e. $2\pi R^2\cos\theta\,\mathrm{d}\theta\,L_\theta$. The illuminance at the centre of the hemisphere IL_D due to the ring will be given by the product of this luminance, the cosine of the angle between the perpendicular at the reference point (the centre of the hemisphere) and the radius of the hemisphere, $\cos(90-\theta)$ and the inverse square of the distance.

Hence, this will be $L_\theta 2\pi\sin\theta\cos\theta\,\mathrm{d}\theta$.

Thus, by substituting for L_θ from Eq. (4.3.3.1):

$$IL_D = \frac{\pi L_z}{1+b} I$$

where:

$$I = \int_0^{\pi/2} \sin 2\theta(1 + b\sin\theta)\mathrm{d}\theta$$

or:

$$I = \int_0^{\pi/2} \sin 2\theta + b\sin\theta\sin 2\theta\,\mathrm{d}\theta$$

$$I = \int_0^{\pi/2} \sin 2\theta + \frac{b}{2}(\cos\theta - \cos 3\theta)\mathrm{d}\theta$$

$$I = \left\{\left[-\frac{1}{2}\cos 2\theta\right]_0^{\pi/2} + \frac{b}{2}\left[\frac{\sin\theta}{1}\right]_0^{\pi/2} - \frac{b}{2}\left[\frac{1}{3}\sin 3\theta\right]_0^{\pi/2}\right\}$$

Hence:

$$I = \left[1 + \frac{4b}{6}\right]$$

or:

$$IL_D = \frac{\pi L_z(3+2b)}{3(1+b)} \tag{3.5.24}$$

Substitution of Moon and Spencer overcast sky luminance distribution index of $b = 2$ in Eq. (3.5.24) leads to Eq. (3.5.22).

Using Eq. (3.5.24) the zenith luminance L_z is then calculated in the following manner as a function of these indices and the corresponding diffuse illuminance of the sky vault:

$$L_z = \frac{6\,IL_D}{\pi}\left[\left(\frac{3+2b_{sh}}{1+b_{sh}}\right)+\left(\frac{3+2b_{sf}}{1+b_{sf}}\right)\right]^{-1} \tag{3.5.25}$$

Note that to enable zenith luminance computations, values of b_{sh} and b_{sf} have to be determined from their clearness index dependent functions (see Section 4.4.3).

Prog3-4b.For is an easy means of obtaining zenith luminance via Muneer–Kinghorn model provided horizontal global and diffuse irradiance are available. The computations undertaken by Prog3-4b.For will be demonstrated via Example 4.4.2.

3.6 Daylight factor

In design studies it has become customary to specify interior daylighting in terms of daylight factor. The daylight Factor is the ratio of the internal illuminance to the external illuminance, available simultaneously. It is usually expressed as a percentage. The daylight factor is divided into three components: the direct skylight (sky component), the externally reflected component and the internally reflected component.

The sky component is the ratio of illuminance at any given point that is received from a sky of known luminance distribution to the horizontal illuminance under an unobstructed sky hemisphere. Likewise, the external- and internal-reflected components are, respectively, the ratios of the illuminance received after reflections from external and internal surfaces to the horizontal illuminance under an unobstructed sky hemisphere. An electronic look-up table for the sky component, based on the CIE standard overcast sky, is provided in Prog3-5.For. This table was originally published by Hopkinson et al. (1966). The BRE protractor and the accompanying literature (Building Research Establishment, 1986) enables the estimation of the above three components.

It is worth mentioning that Prog3-5.For requires the datafile In3-5.Csv. The user must load the two files Prog3-5.For and In3-5.Csv in a common directory in their PC.

The BRE sky component tables may be used to obtain the daylight level at a reference point in a horizontal plane if the height H and width $2W$ of the window and the distance D of the reference point is known. Figure 3.6.1 shows these details. The electronic look-up table, Prog3-5.For, gives the sky component at the intersections of the ratio H/D and W/D. The geometric construction has to be such that the horizontal and vertical planes drawn through the given point to meet the window wall perpendicularly form two bounding edges of the window. If the window sill is above the reference plane, the height of the sill above the reference plane must also be taken into account. The following example demonstrates the use of Prog3-5.For.

Example 3.6.1

Consider the case of a single-glazed rectangular window shown in Figure 3.6.1. The external obstruction runs along the entire length of the room. Obtain the sky component using Prog3-5.For.

With reference to Figure 3.6.1 we compute the following:

$$W/D = \tan 20^\circ = 0.364, \quad H_1/D = \tan 45^\circ = 1.0, \quad H_2/D = \tan 35^\circ = 0.7$$

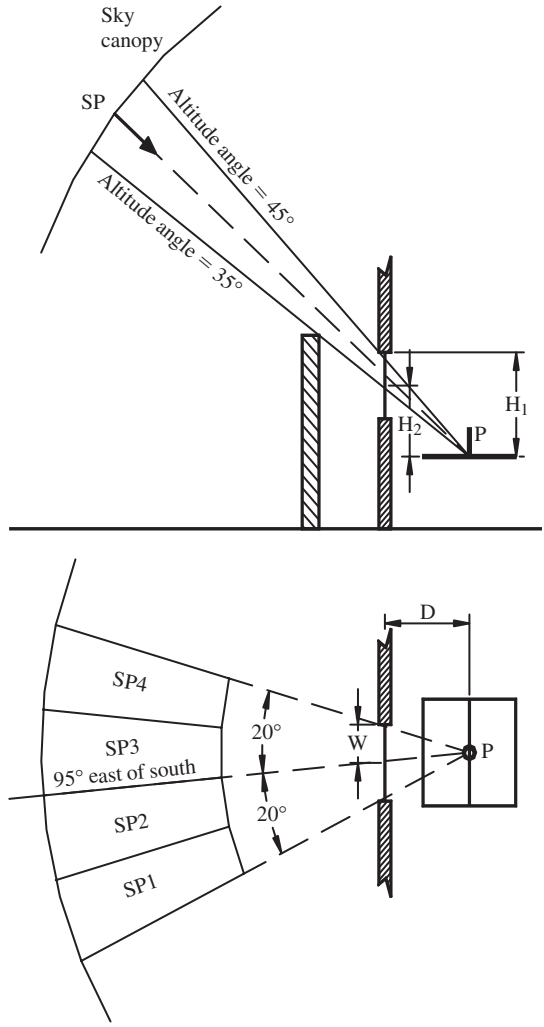

Figure 3.6.1 *Window schematic for Example 3.6.1*

For the H_1/D, W/D pair Prog3-5.For gives the sky component = 2.02, and for the H_2/D, W/D pair the value of 1.18 is obtained. The actual sky component is then obtained by subtraction of the above two values and then doubling the result (due to symmetry).

Thus,

sky component at point $P = 2 \times 0.84 = 1.68\%$

It must be borne in mind that the above computation of sky component does not take into account the effects of window orientation, e.g. sun facing or shaded aspects. It is therefore only an approximate method of obtaining internal illuminance. In Chapter 4, more precise procedures are presented which take into account the window aspect and the real sky luminance distributions.

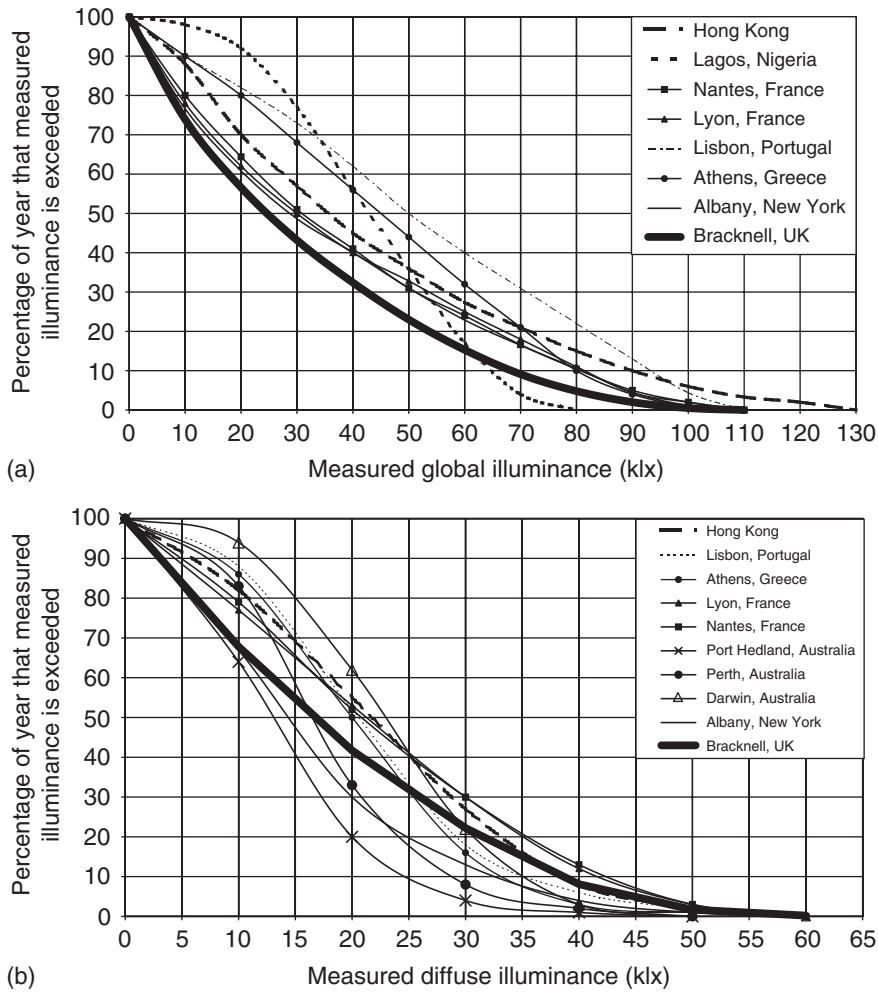

Figure 3.6.2 *Frequency of occurrence of illuminance for worldwide locations*

However, owing to its simplicity the above procedure for sky-component estimation is widely used. Hopkinson et al. (1966) have enumerated the advantages of daylight factor as follows. Firstly, it represents the effectiveness of the window as a lighting provider. Secondly, the daylight factor remains constant even though the outdoor illuminance may fluctuate. Constancy is associated with the concept of adaptation. Appreciation of brightness is governed not only by the actual luminance of the habitated environment, but also by the brightness of the surroundings which governs the level of visual adaptation. As a result, visual appreciation of the interior of a room does not change radically even though the actual luminance will be higher as a result of the greater amount of daylight penetration coming under brighter skies.

At any given point the daylight factor will result in wide variations in internal illuminance. Acceptance of a given illuminance level as the criterion of an appropriate visual

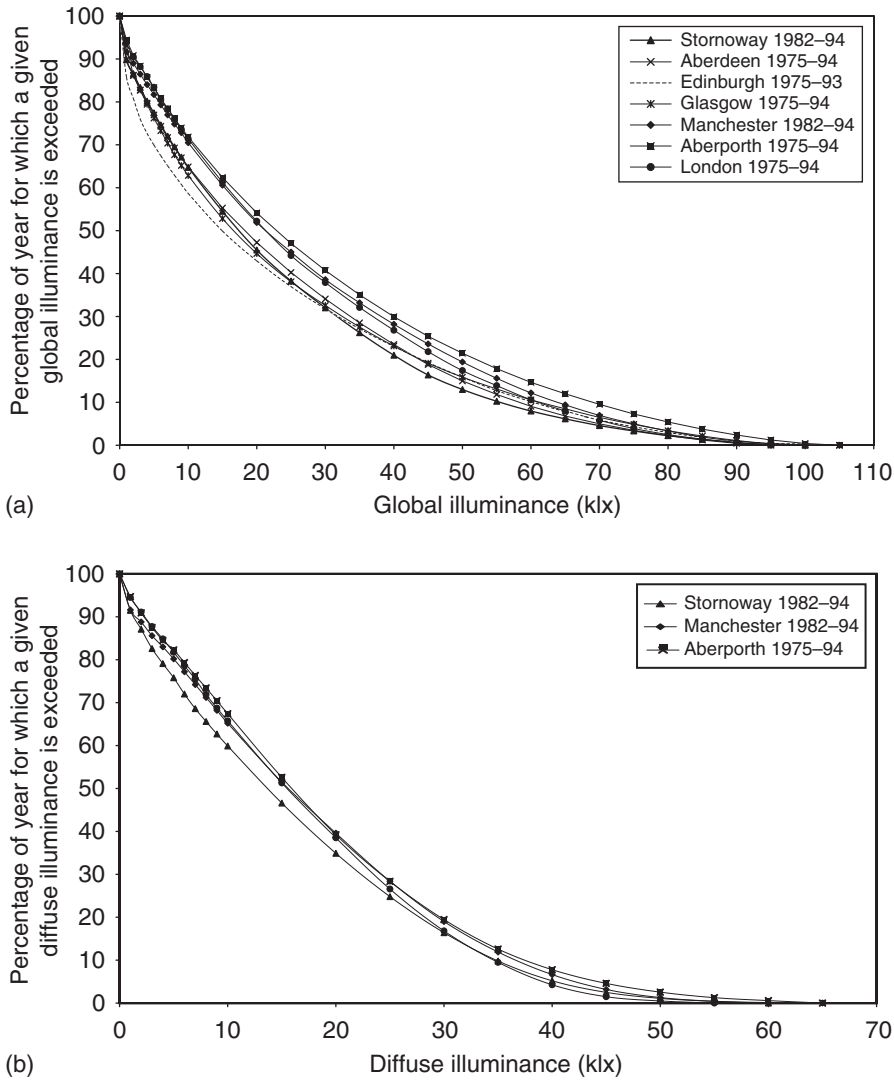

Figure 3.6.3 *Frequency of occurrence of illuminance for UK locations*

environment poses a problem in relation to the variability of available daylight. One solution is to design in such a way that the recommended level of internal illuminance is attained during a certain agreed proportion of the working period throughout the year. An example of this type of approach is to be found in the work of Hunt (1979) for Bracknell and Kew in the UK. It is possible to undertake illuminance frequency analysis for other locations too, using the procedure laid out in the following section.

Figures 3.6.2 and 3.6.3, extracted from Pilkington's (1993) design book and the work of Kinghorn (1999), show the global and diffuse illuminance frequency distributions for worldwide as well as UK locations.

3.7 Solar climate characterisation

In Section 3.3.7 information regarding turbidity and its use in the classification of the radiation climate was presented. Besides turbidity there are other measures that can be used for such characterisation. In this section other such measures are presented.

3.7.1 Frequency distribution of irradiation

Prediction of solar energy-system performance can be achieved via detailed computer simulations using hourly or sub-hourly weather data or by simpler methods which are based on statistical analysis of long-term measurements. The frequency of occurrence of various levels of daily (and indeed hourly) irradiation is of interest not only from the above viewpoint, but also to enable the determination of the monthly-averaged correlations between diffuse and global quantities. For example, it was shown in Section 2.6 that the latter regression curve may be obtained from the regression for daily diffuse fraction if the frequency distribution of global irradiation during any month was known.

If for any given location the frequency of occurrence of days with various values of K_T is plotted, the resulting distribution would appear like that shown in Figure 3.7.1. This distribution was presented by Hawas and Muneer (1984b), based on long-term measurements for 18 Indian locations. Here it may be seen that the probability of occurrence of K_T between 0.65 and 0.75 is 85%. The shape of this curve depends on the average value of K_T, i.e. lower values of $\bar{K}_T$ would produce curves skewed to the left and vice versa. When the data of Figure 3.7.1 is used to plot cumulative distribution curves, plots such as Figure 3.7.2 are obtained. This figure shows the long-term cumulative frequency f of the daily clearness indices for six Indian locations. It is clear that a set of generalised curves may be obtained for the above locations. As a matter of fact the above technique was originally developed by Liu and Jordan (1963), based on an earlier work of Whillier (1956). Later extensions of this work were undertaken by Bendt et al. (1981) for the US, Hawas and Muneer (1984b)

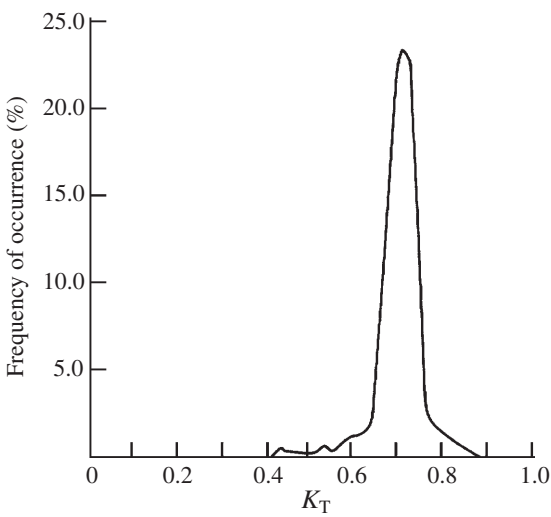

Figure 3.7.1 *Frequency of occurrence of* K_T *for an Indian location*

for India and Lloyd (1982) for the UK. More recently Saunier et al. (1987) have drawn the same conclusions as the latter group of researchers that the above distributions are indeed unique for a given geographic area but by no means universal. This point is demonstrated via Figures 3.7.3 and 3.7.4 which shows disparate distributions for the US, Indian and UK locations.

Figures 3.7.5–3.7.7 show the K_T distributions, respectively, for the US, India and the UK. These curves, also known as generalised K_T curves, present the insolation character for the respective regions. The curves enable querying the availability of solar energy above a given threshold. For example, for Indian locations, during a month for which $\bar{K}_T = 0.7$, $K_T \leqslant 0.73$ for 70% fractional time, and $K_T \leqslant 0.68$ for 20% of the time. In contrast the corresponding figures for the US are, respectively, 56% and 30%. It is therefore evident that the distributions for the Indian locations are flatter. This means that for the Indian sub-continent the daily clearness index K_T varies in a narrower range.

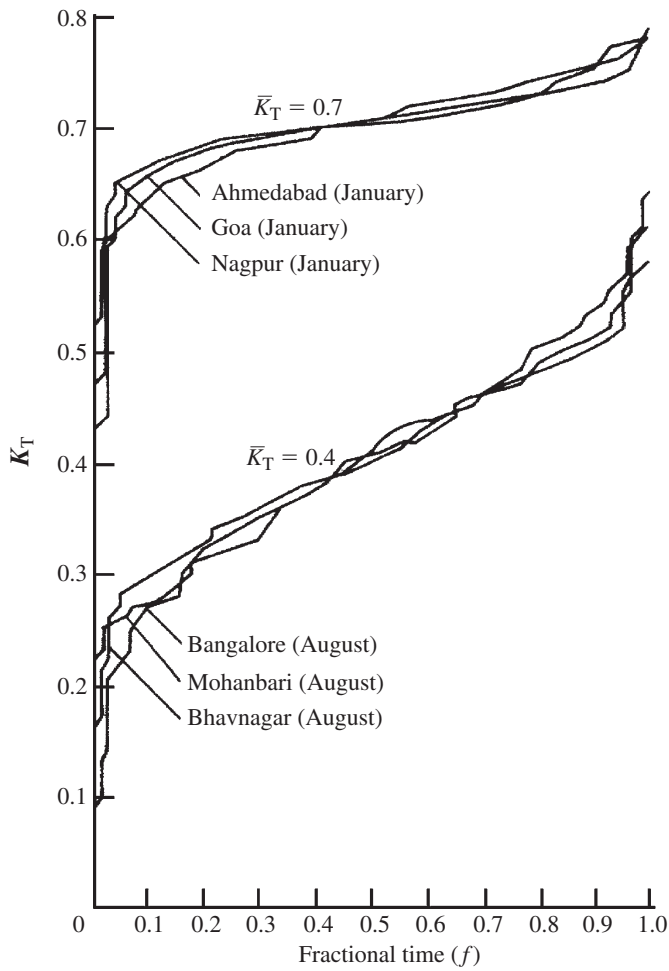

Figure 3.7.2 *Individual* K_T *curves for Indian locations*

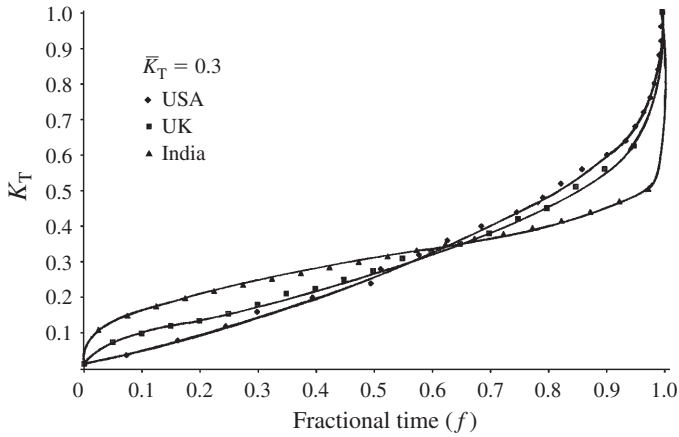

Figure 3.7.3 *Comparison of* K_T *curves for average clearness index = 0.3*

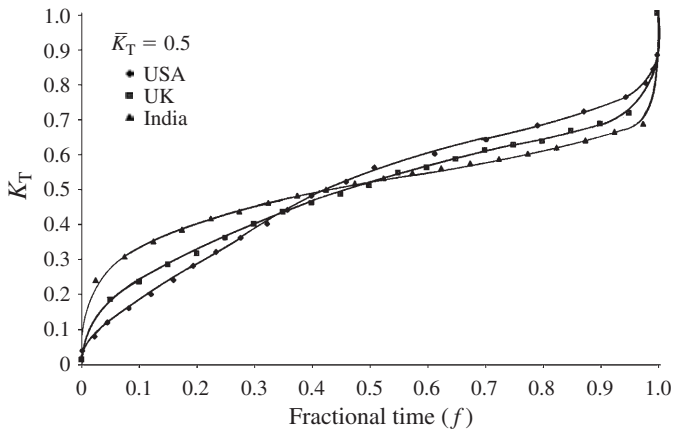

Figure 3.7.4 *Comparison of* K_T *curves for average clearness index = 0.5*

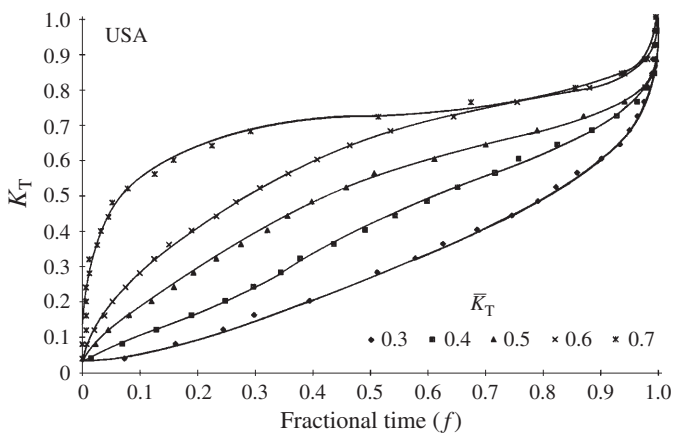

Figure 3.7.5 *Generalised* K_T *curves for USA*

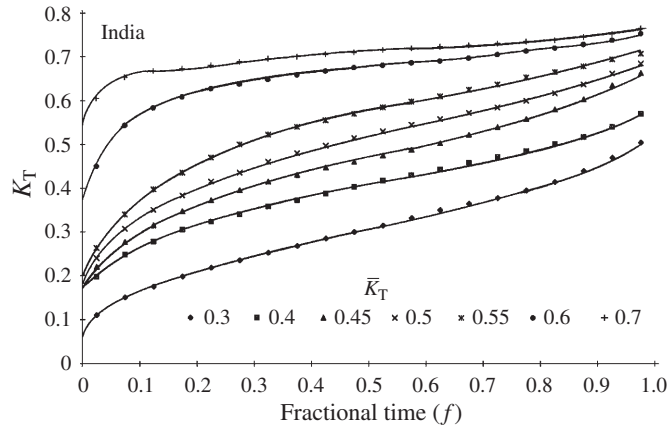

Figure 3.7.6 *Generalised* K_T *curves for India*

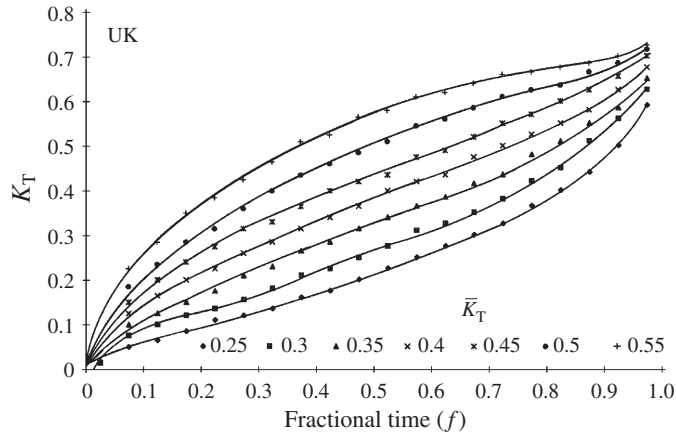

Figure 3.7.7 *Generalised* K_T *curves for UK*

Udo (2000) has further confirmed the above assertion that the K_T distributions are not universal. Furthermore, comparing the findings of Udo for three Niegrian locations – Ilorin, Ibadan and Kumasi – against the Indian sites (see Figure 3.7.8) we note that even for tropical locations no generalisation exist for K_T distributions. Attempts have however been made to provide a generalised formulation and one such work has been presented later on in this section.

Strictly speaking the above insolation frequency distributions are for daily based quantities. However, Whillier (1953) has shown that the hourly and daily distribution curves are very similar to each other. Thus the above curves may also be used to obtain the frequency occurrence of hourly global irradiation.

Curve fitting of the above data is quite involved. Attempts have been made by Bendt et al. (1981) to obtain a model using an exponential form. However, as pointed out by Duffie and Beckman (1991) the computations are tedious. Presently, computer look-up tables in FORTRAN have been prepared for ease of use. These are included as Prog3-6.For (for the US and North American locations), Prog3-7.For (for Indian and other tropical locations)

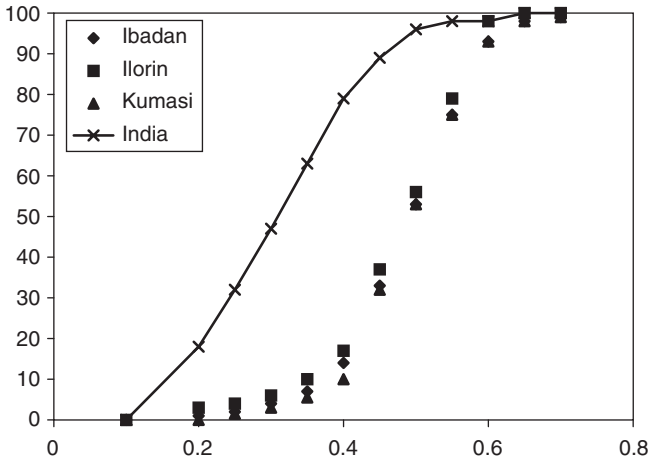

Figure 3.7.8 *Frequency of occurrence of* K_T *for Nigerian and Indian locations: a comparison*

and Prog3-8.For (for the UK and northern Europe). In these programs the required input is K_T and $\bar{K}_T$, which in turn may be obtained via Prog3-1.For. The following example demonstrates the use of generalised K_T curves.

Example 3.7.1

An office building situated in London, UK is designed to utilise daylight via on–off controls. The working-plane daylight factor is estimated to be 2% and the design illuminance level is set at 500 lx. Using bright sunshine data for London given in Table B1, prepare a table of the frequency of occurrence of internal illuminance exceeding the above design value. Perform computations for mid-hour for the normal range of working hours (9–17 h) for the month of May.

To achieve an internal illuminance of 500 lx, the required external global illuminance would be 25 klx. We assume an approximate and conservative value of 100 lm/W for the global luminous efficacy. Thus, what is required is the frequency of occurrences when horizontal global irradiation exceeds 250 W/m^2.

We note from Table B1 that the average daily bright sunshine hours for May are 6.56. Using Prog2-1.For and providing the respective values of 0.13 and 0.65 for the '*a*' and '*b*' coefficients of Eq. (2.1.1) (Table 2.1.2), the following output is obtained for 16 May:

Day-length = 15.379 h
Monthly-averaged extraterrestrial irradiation = 10.511 kW h/m^2
Averaged global irradiation = 4.28 kW h/m^2 (Page and Lebens (1986) gives this value as 4.33 kW h/m^2)
$\bar{K}_T = 0.407$

Now Prog3-3 and Prog3-8.For may be used to respectively obtain the hourly clearness index K_t and f, the hourly frequency of occurrence when the mid-hour irradiance was

below the required threshold of 250 W/m^2. These are tabulated as follows:

Hour	K_t	f	f_1	f_2
9.5	0.260	0.245	24.5	75.5
10.5	0.236	0.204	20.4	79.6
11.5	0.225	0.186	18.6	81.4
12.5	0.225	0.186	18.6	81.4
13.5	0.236	0.204	20.4	79.6
14.5	0.260	0.245	24.5	75.5
15.5	0.310	0.330	33.0	67.0
16.5	0.398	0.483	48.3	51.7

f_1: frequency of occurrences when internal illuminance is below 500 lx, %.
f_2: frequency of occurrences when internal illuminance exceeds 500 lx, %.

Sarath-Babu and Satyamurty (2001) describe the development of a truly generalised set of frequency distributions. In their article they examine the suitability of a new parameter, $\hat{\bar{K}}_T$, and a variable, $\hat{K}_T$, to depict generalised clearness index distributions. $\hat{\bar{K}}_T$ is a normalised monthly average daily clearness index, while $\hat{K}_T$ is a normalised daily clearness index. These normalised clearness indices comprise maximum and minimum daily clearness indices ($K_{T,max}$ and $K_{T,min}$) in a month in addition to monthly average daily clearness index $\bar{K}_T$ and daily clearness index K_T. Regressions have been developed to predict $K_{T,max}$ and $K_{T,min}$ needed in the absence of data. The distributions have been tested for over 70 locations with latitudes ranging from 8°N to 64°N. The daily clearness index values have been predicted within a standard deviation of 0.034 with the expressions developed in their study. The 70 locations employed in developing and validating their distributions were based on the measurements made by the US National Solar Radiation Data Base (NSRDB) during 1961–90. A reduced version of the latter database may be accessed at http://rredc.nrel.gov.solar/old_data/nsrdb/tmy2/.

The variables and the relevant parameters are defined in Eqs (3.7.1)–(3.7.3):

$$\hat{K}_T = \frac{K_T - K_{T,min}}{K_{T,max} - K_{T,min}} \tag{3.7.1}$$

$$\hat{\bar{K}}_T = \frac{\bar{K}_T - K_{T,min}}{K_{T,max} - K_{T,min}} \tag{3.7.2}$$

$\hat{K}_T$ is related to $\hat{\bar{K}}_T$ and f by:

$$\hat{K}_T = (-3.94 f + 10.49 f^2 - 8.60 f + 3.044) + (9.97 f - 20.93 f^2 + 16.57 f - 5.61 f^4)\, \hat{\bar{K}}_T \tag{3.7.3}$$

3.7.2 Other measures of characterising solar climate

Other useful methods for the characterisation and inter-comparison of sites with regard to their suitability for utilisation of solar energy based upon the statistical analysis of their

solar radiation intensities have been presented by Ianetz et al. (2000). In those methods each monthly data set of the daily global, horizontal beam and diffuse radiation intensities is analysed with the view to obtain monthly average daily radiation intensity, coefficient of variation (see Chapter 1), skewness and kurtosis. While *skewness* represents the degree of asymmetry about the central value of a distribution, *kurtosis* is the degree to which a distribution is sharply peaked at its centre.

The values of the skewness and kurtosis may then be used to describe the distribution curves for any given radiation intensity data set. In addition, the same type of statistical analysis is applied to the monthly average daily ratios of the horizontal beam to global radiation, diffuse to global and the clearness index. The solar climate of a given location is thus characterised with regard to the distribution of their intensity levels. An intersite comparison can then be made for the suitability of solar climate for any given application.

Ianetz et al. (2000) have argued that:

(a) The monthly average daily radiation intensity values are nonpareil in importance with regard to the design of solar energy conversion systems. Information regarding the monthly-averaged daily magnitude of the beam radiation is critical in determining, first, if a site is amenable to concentrating solar conversion systems and, secondly, for their design, i.e. sizing. Similarly, such information regarding the global radiation is required for non-concentrating solar conversion systems.

(b) The coefficient of variation, reported as a per cent, is a measure of the variation in a parameter, e.g. the daily radiation intensity, during a particular time interval, a month, and is defined as the ratio of the standard deviation to the average monthly value. In other words, it is a measure of the stability of the parameter during the time interval under consideration. Consequently, a small coefficient of variation is desirable in order to facilitate the sizing of a solar conversion system. A relatively small coefficient of variation ensures that the number of days for which the system is either oversized, under-utilised or oversized, resulting in possible dumping of the converted solar energy is minimised.

(c) The values for the skewness and kurtosis are utilised to define the frequency distribution type for each database, i.e. to describe the breadth of the distribution curve, its degree of asymmetry and its shape relative to that for a normal distribution curve. The frequency distribution types as a function of the skewness and kurtosis values are defined in Table 3.7.1. It is argued that the preferred types of distribution that are suitable for solar energy conversion systems, in descending order are as follows: V $>$ IV $>$ I $>$ VI $>$ II and III. The reasoning behind this order of preference of the distribution types will now be explained. Statistically, a type V distribution frequency has a higher occurrence of values greater than the average value, 35–40%, relative to a normal distribution (type I), whereas a type IV has a higher occurrence of values greater than the average value, 25%, relative to a normal distribution. Consequently, if types V and IV possess the same average value as a normal distribution type, I, they will both afford a greater number of days with values in excess of the average value relative to that afforded by a normal distribution. Types II and III are both characterised by a relatively low average value and are, therefore, much less preferred for solar conversion systems.

Table 3.7.1 Solar radiation frequency distribution characterisation

Distribution type number	Distribution curve	Skewness	Kurtosis
I	Normal	−0.4 to 0.4	−0.8 to 0.8
II	Almost normal with positive trail	0.4	−0.8 to 0.8
III	Narrow peak with positive trail	0.4	−0.8 to 0.8
IV	Almost normal with negative trail	−0.4	−0.8 to 0.8
V	Narrow peak with negative trail	−0.4	0.8
VI	Bimodal, symmetrical with flat peak	−0.4 to 0.4	−0.8

3.8 Frequency distribution of illuminance

A more direct method for obtaining the frequency distributions of global and diffuse illuminance was presented by Tregenza (1986). In this work the above distributions were derived in relation to solar altitude using empirically developed functions. The estimated cumulative frequency distributions were found to be in good agreement with the measurements carried out at Nottingham (52.9°N), Garston (51.6°N) in the UK and Uccle (50.8°N) in Belgium.

The procedure to be followed for obtaining the above daylight illuminance distributions (in units of lx) is as follows. Empirical models, given by Eqs (3.8.1) and (3.8.2), are used to obtain the mean global and diffuse illuminance:

$$IL_G = 10.5(\text{SOLALT} + 5)^{2.5} \quad -5 < \text{SOLALT} \leqslant 2.5 \tag{3.8.1a}$$

$$IL_G = 73\,700 \sin^{1.22} \text{SOLALT} \quad 2.5 < \text{SOLALT} \leqslant 60 \tag{3.8.1b}$$

$$IL_D = 10.5(\text{SOLALT} + 5)^{2.5} \quad -5 < \text{SOLALT} \leqslant 5 \tag{3.8.2a}$$

$$IL_D = 48\,800 \sin^{1.105} \text{SOLALT} \quad 5 < \text{SOLALT} \leqslant 60 \tag{3.8.2b}$$

The solar altitude is then calculated (using say Prog1-6.For) on intervals during the day and regular dates throughout the year. At each time the mean illuminance is then computed from the above models. The relative frequencies of illuminance of 0.125, 0.375, 0.625, 0.875, … , 2.375 times the mean are obtained from the values illustrated in Figure 3.8.1. At each calculated instance 10 values of frequencies are obtained which may be treated to be statistically similar to time-based measurements.

The above procedure has the advantage that it extends its application to daylight as well as civil twilight band. Figure 3.8.2 compares the estimated illuminance frequency for Uccle using the method under discussion with those obtained by Dogniaux (1985).

Hunt (BRE, 1989) has analysed several years of records from Kew, Bracknell and five other UK locations to produce graphs and tables of the frequency distribution of horizontal global and diffuse illuminance. This type of information is a useful aid for the daylight designers for exploring the potential for energy savings via modern photoelectric controls (see Figure 3.5.1). Figures 3.8.3 and 3.8.4 provide a comparison of Tregenza's

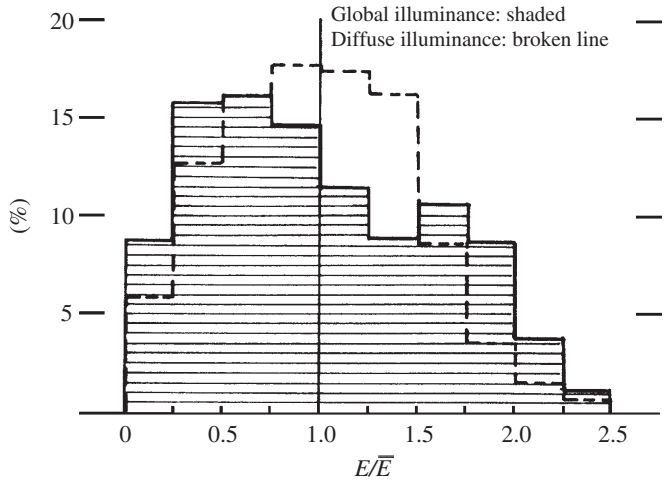

Figure 3.8.1 *Frequency of occurrence of a given horizontal illuminance as a fraction of the mean illuminance*

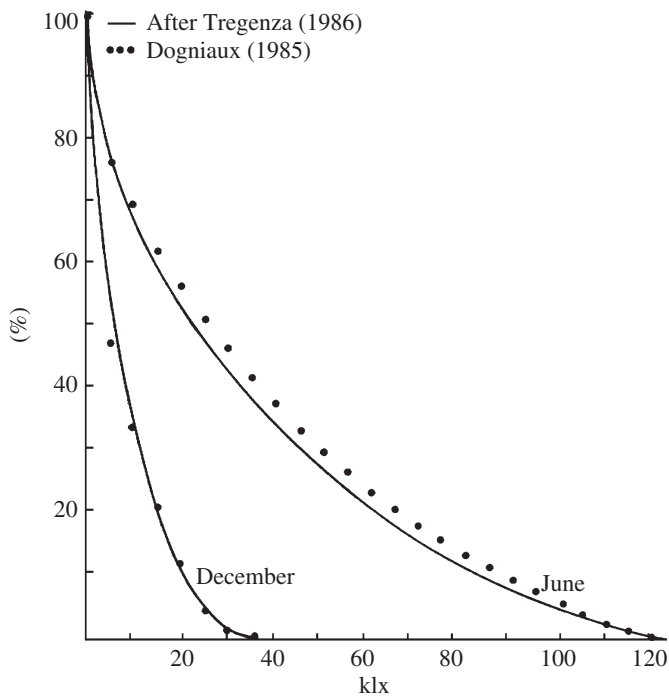

Figure 3.8.2 *Derived cumulative distributions of global illuminance at Uccle for June (18 h) and December (9.3 h)*

(1986) method and the data presented by Hunt (BRE, 1979) for Kew. The agreement is highly satisfactory for the global illuminance. Reasonably good agreement may also be noted, bar the intermediate level illuminance, for the diffuse component. It is well known that the diffuse illuminance from a part-overcast sky exhibits most pronounced scatter.

Using the procedure outlined in the present and the preceding sections it is therefore possible to obtain the frequency of occurrence of a given daylight level for other locations.

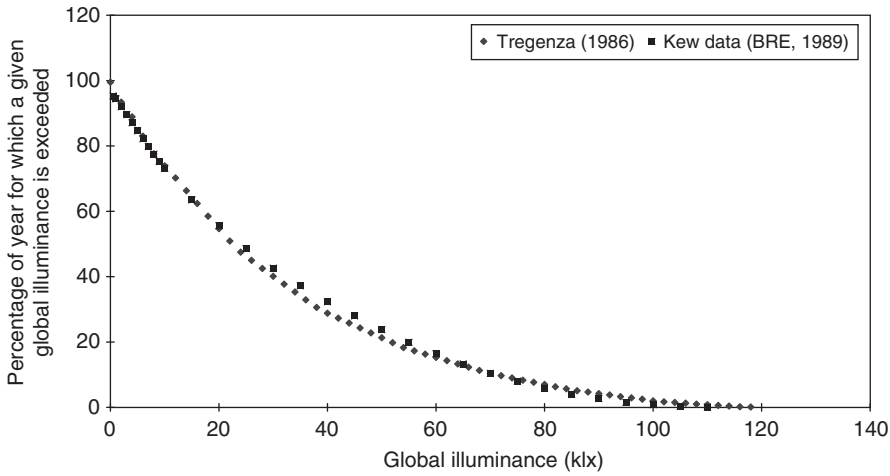

Figure 3.8.3 *Standard working year daylight availability: cumulative global illuminance frequency*

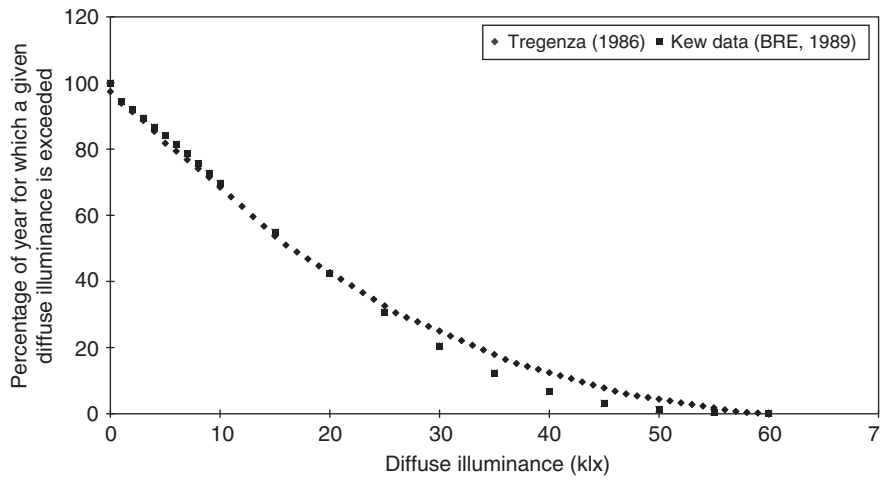

Figure 3.8.4 *Standard working year daylight availability: cumulative diffuse illuminance frequency*

One such plot, obtained via Prog3-9.For, is shown in Figure 3.8.5. Prog3-9.For performs stepwise computation of:

(a) solar altitude at each 15 min increment for each day of the year;
(b) the relative occurrence of illuminance equal to 0.125, 0.375, … , 2.375 times the mean;
(c) the cumulative frequency distribution of horizontal global and diffuse illuminance.

The only input required to execute the above routine is the latitude and longitude of the location for which the above illuminance distributions are required. For any geographic region,

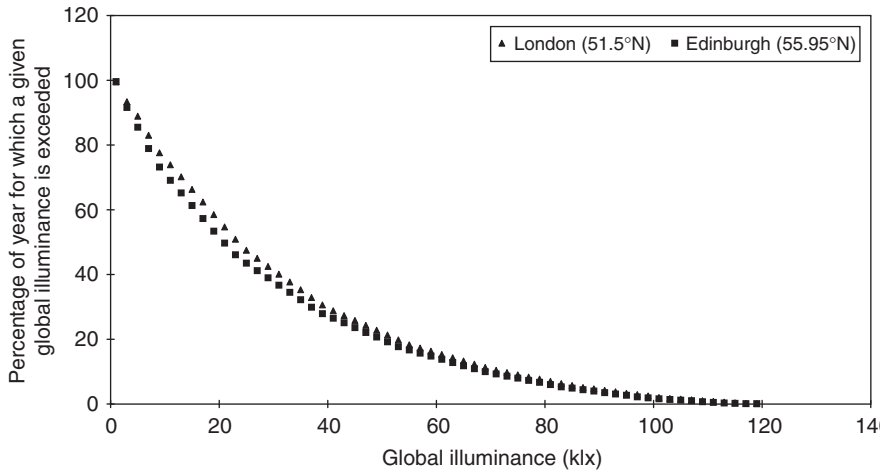

Figure 3.8.5 *Standard working year daylight availability: cumulative global illuminance frequency (London and Edinburgh)*

Table 3.8.1 Frequency of occurrence of a given horizontal illuminance* (after Tregenza, 1986)

Fraction of mean illuminance†	Frequency of occurrence	
	Global	Diffuse
0.125	8.87	5.96
0.375	15.78	12.86
0.625	16.15	16.19
0.875	14.67	17.65
1.125	11.45	17.39
1.375	8.87	16.27
1.625	10.62	8.63
1.875	8.68	3.55
2.125	3.79	0.80
2.375	1.12	0.70

* Any irregularities in the frequency of measured occurrences may be due to the conditions in the relevant period. Longer-term data may be represented by a smoother curve.
† Mid-point of frequency band.

subject to the availability of fractional mean frequencies such as those shown in Figure 3.8.1 and Table 3.8.1, the following daylight design tables and charts may be produced:

(a) global and diffuse illuminance frequency distributions;
(b) occurrence of a given illuminance level on a monthly or mean-hourly basis;
(c) effect of latitude;
(d) effect of summer time shift, office and school operating hours and lunch breaks on daylight use.

The sociological and energetic implications of a shift in the clock time are significant. In the UK for instance, an experiment of maintaining the British Summer Time (BST) through the winter was conducted from 1968 to 1971. A study of the associated costs and benefits of that experiment were published by the Policy Studies Institute (1988). A rigorous and updated review of this subject was carried out by Hillman (1993). The latter work examines the effects of Double British Summer Time (DBST) and putting the clock forward from end of summer to the beginning of spring. It has been shown that such a change would have a direct bearing on road accidents, security, health and leisure, agricultural activities as well as fuel consumption due to lighting of domestic and office buildings. The tools presented in this section, e.g. Prog3-9.For, enable such impacts to be quantified.

3.9 Exercises

3.9.1 Ten-year monthly-averaged data for Bracknell, UK are given in Tables 3.3.6 and 3.3.7. Using Liu and Jordan's regression models (Eqs (3.1.1) and (3.2.1)) obtain hourly values of global and diffuse irradiation from monthly-averaged daily data (Table 3.3.7). Compare your estimates against the MRM predictions which are also provided in Table 3.3.6.

3.9.2 Using the sunshine data for Stornoway and Bracknell, UK given in Table 3.3.7, obtain monthly-averaged daily estimates of global irradiation using Eq. (2.1.1). You may then proceed to obtain monthly-averaged daily diffuse irradiation using Eq. (2.2.2). Compare these with the estimates of MRM given in Table 3.3.7.

3.9.3 Hourly synoptic (weather) and irradiance data for Easthampstead, UK (51.383°N) are given in Table 3.9.1. Prepare the input file In3-2.Csv containing the data fields for year, month, day, hour, dry- and wet-bulb temperatures, atmospheric pressure and sunshine fraction (columns 3, 4, 5 and 6). Hence execute Prog3-2a.For (or Prog3-2a.Exe) to obtain hourly horizontal global and diffuse irradiation (columns 7 and 8). Compare your estimates against the measured data which are included in Table 3.9.1. Prepare the MBE and RMSE statistic for your estimates.

Hourly global and diffuse radiation, fractional sunshine, cloud cover (in Oktas), dry- and wet-bulb temperatures, atmospheric pressure and solar altitude data for Bracknell, England are provided in file In3-3.Prn. Use the MRM, CRM and PRM procedures (with the relevant software) to compute the irradiation quantities and compare them against the measured data reported within the file.

Save your results for the computation of slope irradiation (see Exercise 4.7.3) from your estimated values of horizontal irradiation. (Hint: You may use a spreadsheet medium, such as Excel, to prepare In3-2.Csv file and to import Out3-2.Dat. The MBE and RMSE statistic may then be obtained in Excel).

3.9.4 Use Prog3-3.For, based on Eqs (3.4.1) and (3.4.2), to compute hourly horizontal diffuse irradiation using the global irradiation values given in Table 3.9.1. Comment on the accuracy of the presently computed estimates against those obtained in Exercise 3.9.3.

Table 3.9.1 Synoptic and radiation data for Easthampstead, UK (51.383°N), June 1991

Day	Hour	Dry-bulb temp. (°C)	Wet-bulb temp. (°C)	Atmosphere pressure (mbar)	SF	I_G (W/m^2)	I_D (W/m^2)	$I_{G,TLT}$ (W/m^2)	$I_{G,N}$ (W/m^2)	$I_{G,E}$ (W/m^2)	$I_{G,S}$ (W/m^2)	$I_{G,W}$ (W/m^2)
11	0	0.0	0.0	1018.0	0.0	0	0	0	0	0	104	93
11	1	0.0	0.0	1018.5	0.0	0	0	0	0	0	95	87
11	2	0.0	0.0	1018.8	0.0	0	0	0	0	0	82	77
11	3	0.1	0.1	1019.0	0.0	1	1	0	2	0	82	79
11	4	5.0	3.1	1018.9	0.2	23	106	14	181	15	84	80
11	5	17.7	6.7	1018.9	1.0	57	217	34	534	32	89	85
11	6	31.7	7.8	1019.1	1.0	152	142	47	685	38	100	93
11	7	41.2	22.2	1019.1	0.5	301	112	115	516	79	120	105
11	8	32.2	27.2	1019.5	0.2	257	107	131	199	97	140	114
11	9	23.8	22.5	1019.3	0.0	186	91	96	118	83	150	110
11	10	23.4	23.2	1019.6	0.0	173	96	88	96	89	150	110
11	11	33.9	32.7	1019.5	0.0	260	121	133	122	130	139	116
11	12	40.4	39.0	1018.9	0.0	326	139	175	157	147	130	104
11	13	24.9	24.5	1017.9	0.0	187	100	96	102	95	148	113
11	14	25.0	24.7	1017.4	0.0	188	98	96	100	98	152	114
11	15	19.8	19.5	1017.1	0.0	148	78	75	84	72	148	114
11	16	13.2	13.1	1016.7	0.0	93	56	46	55	50	145	116
11	17	8.6	8.5	1016.0	0.0	62	35	31	33	34	146	118
11	18	2.8	2.7	1015.7	0.0	18	11	9	11	10	142	115
11	19	1.1	1.0	1014.8	0.0	7	4	3	3	3	141	117
11	20	0.1	0.1	1014.4	0.0	0	0	0	0	0	137	120
11	21	0.0	0.0	1013.9	0.0	0	0	0	0	0	135	120
11	22	0.0	0.0	1013.2	0.0	0	0	0	0	0	134	122
11	23	0.0	0.0	1012.4	0.0	0	0	0	0	0	132	125
12	0	0.0	0.0	1011.4	0.0	0	0	0	0	0	130	124
12	1	0.0	0.0	1010.8	0.0	0	0	0	0	0	130	124
12	2	0.0	0.0	1010.2	0.0	0	0	0	0	0	130	124
12	3	0.0	0.0	1009.4	0.0	0	0	0	0	0	128	123
12	4	1.3	1.3	1008.6	0.0	9	5	4	5	5	128	123
12	5	2.9	2.9	1008.4	0.0	21	12	10	11	11	129	124
12	6	6.4	6.3	1007.5	0.0	46	27	23	27	25	132	126
12	7	19.4	18.0	1007.5	0.2	150	76	77	126	61	135	129
12	8	43.6	24.1	1007.3	0.8	379	95	181	397	70	145	134
12	9	61.5	25.5	1007.3	1.0	570	102	290	432	89	159	135
12	10	55.7	35.3	1006.9	1.0	503	128	270	264	125	170	131
12	11	77.3	29.1	1006.8	1.0	743	112	399	199	126	176	130
12	12	51.2	31.2	1006.2	1.0	478	114	262	132	168	184	134
12	13	21.3	19.4	1005.5	0.1	179	79	98	86	83	195	136
12	14	18.5	17.3	1005.2	0.2	129	77	61	62	98	185	136
12	15	33.2	20.2	1005.4	0.4	281	76	136	80	237	165	130
12	16	15.0	14.1	1004.8	0.2	118	54	62	59	74	175	135
12	17	7.9	7.3	1004.7	0.0	56	38	29	28	59	165	130
12	18	13.9	9.7	1005.0	0.5	68	123	38	38	258	155	122
12	19	2.6	2.5	1005.2	0.0	20	15	11	11	17	144	120
12	20	0.1	0.1	1005.2	0.0	1	0	0	0	0	141	113
12	21	0.0	0.0	1005.4	0.0	0	0	0	0	0	139	113
12	22	0.0	0.0	1005.6	0.0	0	0	0	0	0	129	108
12	23	0.0	0.0	1005.3	0.0	0	0	0	0	0	124	111

$I_{G,TLT}$: irradiance on a south-facing surface at the local latitude angle.
$I_{G,N}$, $I_{G,E}$, $I_{G,S}$, $I_{G,W}$: irradiance on a north-, east-, south- and west-facing vertical surface.

3.9.5 Make appropriate modifications to Prog3-3.For so that Eq. (3.4.3) is replaced in place of Eq. (3.4.2). Execute this program after estimating the hourly RH data from the corresponding dry- and wet-bulb temperatures using Prog7-1.Exe. Compare on the accuracy of diffuse irradiation estimates obtained from the three models, e.g. Eqs (3.4.1–3.4.3).

3.9.6 Use Prog3-4a.For, based on Perez luminous efficacy model, to compare its performance against 5 min averaged (measured) data provided in File3-1.Csv. Recall that this file contains Edinburgh data for April 1993.

3.9.7 Compare the accuracy of the above estimates against the Page–Perraudeau–Dumortier Model presented in Section 3.5.6.

3.9.8 Refer to Figure 3.6.1 and Example 3.6.1. Assume that the distance of the reference point at which the sky component was computed is 2.75 m from the window. Use Prog3-5.For to obtain the sky components successively for points which are positioned at linear distances of 0.5, 1 and 1.5 m away from the original position shown in Figure 3.6.1.

3.9.9 Using Prog3-8.For and monthly-averaged data provided in Table 3.1.1 obtain the frequency distribution of global irradiance and illuminance for 10 and 11 h. (Hint: You may use an average global luminous efficacy of 110 lm/W).

3.9.10 Compare the above frequency distribution of global illuminance against the distribution computed via Tregenza model given in Section 3.8. Comment on any differences you may notice between the two frequency distributions.

References

Abdelrahman, M., Said, S. and Shuaib, A. (1988) Comparison between atmospheric turbidity coefficients of desert and temperate climates. *Solar Energy* 40, 219.

Ångström, A. (1929) On the atmospheric transmission of sun radiation and on dust in the air. *Geografis. Annal*. 2, 156.

Ångström, A. (1930) On the atmospheric transmission of sun radiation. *Geografis. Annal*. 2 and 3, 130–59.

ASHRAE (2002) *Handbook of Fundamentals*. American Society of Heating, Refrigerating and Air conditioning Engineers, New York.

Aydinli, S. and Krochmann, J. (1983) *Data on Daylight and Solar Radiation: Guide on Daylight*. Draft for CIE TC 4.2, Commission Internationale de l.Eclairage, Paris.

Bannon, J. and Steel, L. (1960) Meteorological office. *Geophysical Memoirs* 13, 102. HMSO, London.

Barbaro, S., Coppolino, S., Leone, C. and Sinagra, E. (1979) An atmospheric model for computing direct and diffuse solar radiation. *Solar Energy* 22, 225.

Bendt, P., Collares-Pereira, M. and Rabl, A. (1981) The frequency distribution of daily radiation values. *Solar Energy* 27, 1.

Bennett, I. (1969) *Correlation of Daily Insolation with Daily Total Sky Cover, Opaque Sky Sky Cover and Percentage of Possible Sunshine. Solar Energy* 12, 391.

Bird, R.E. and Hulstrom, R.L. (1979) *Application of Monte Carlo Technique to Insolation Characterisation and Prediction.* US SERI Tech. Report TR-642-761, 38.

Bird, R.E. and Hulstrom, R.L. (1981) *A Simplified Clear-Sky Model for the Direct and Diffuse Insolation on Horizontal Surfaces*. US SERI Tech. Report TR-642-761, 38.

Blackwell, M.J. (1954) *Five Years Continuous Recordings of Total and Diffuse Solar Radiation at Kew Observatory*. Met. Res. Publication 895, Met. Office, London.

Boes, E.C., Hall, I.J., Prarie, R.R., Stromberg, R.P. and Anderson, H.E. (1976) *Report SAND 76-0411*. Sandia Nat. Lab., Albuquerque, New Mexico.

Brinsfield, R., Yaramangolu, M. and Wheaton, F. (1984) Ground level solar radiation prediction model including cloud cover effects. *Solar Energy* 33, 493–9.

Bruno, R. (1978) A correction procedure for separating direct and diffuse insolation on a horizontal surface. *Solar Energy* 20, 97.

Bugler, J.W. (1977) The determination of hourly insolation on an inclined plane using a diffuse irradiance model based on hourly measured global horizontal. *Solar Energy* 19, 477.

Building Research Establishment (1986) *Estimating Daylight in Buildings: Parts I and II*. BRE Digests 309, 310. Building Research Establishment, Watford, UK.

Building Research Establishment (1989) *Designing for Natural and Artificial Lighting* (Availability of daylight: D.R.G. Hunt). Building Research Establishment, Watford, UK.

Building Services and Environmental Engineer (1996) *News International*, p. 5, March 1996. Building Services and Environmental Engineer, London.

CEC (1996) *European Solar Radiation Atlas*, eds W. Palz and J. Grief. Springer-Verlag, Berlin.

Chandrasekhar, S. (1950) *Radiative Transfer*. Oxford University Press, London.

Chandrasekhar, S. and Elbert, D.D. (1954) The illumination and polarization of the sunlit sky on Rayleigh scattering. *Trans. Amer. Phil. Soc*. 44, 643.

Chartered Institution of Building Services Engineers (2002) *CIBSE Guide J: Weather & Solar Data*. CIBSE, London.

Chauvel, P. (1993) *Dynamic Characteristics of Daylight Data and Daylighting Design in Buildings*. Final Report JOUE CT 90-0064, CEC, Brussels.

Chroscicki, W. (1971) Calculation methods of determining the value of daylight's intensity on the ground of photometric and actinometric measurements. *Proc. CIE Barcelona Conf*. 71, 24.

CIBSE (1996) *Building Services Supplement*, May 1996. Chartered Institute of Building Services Engineers, London.

Collares-Pereira, M. and Rabl, A. (1979) The average distribution of solar radiation – correlations between diffuse and hemispherical and between daily and hourly insolation values. *Solar Energy* 22, 155.

Commission Internationale de l'Eclairage (1973) Standardization of luminance distribution of clear skies. CIE No. 22 (TC-4.2).

Coulson, K.L. (1959) Characteristics of radiation emerging from the top of a Rayleigh atmosphere. *Planet Space Sci*. 1, 265.

Dave, J.V. (1964) Importance of higher order scattering in a molecular atmosphere. *J. Opt. Soc. Amer*. 54, 307.

Dave, J.V. (1979) Extensive data sets of the diffuse radiation in realistic atmospheric models with aerosols and common absorbing gases. *Solar Energy* 21, 361–9.

Davies, J.A., Schertzer, W. and Nunez, M. (1975) Estimating global solar radiation. *Boundary-Layer Meteorol*. 9, 33–52.

Delaunay, J.J. (1995) *Development and Performance Assessment of Luminous Efficacy Models.* Internal Report. Fraunhofer Institute for Solar Energy Systems, Freiburg, Germany.

Dogniaux, R. (1960) Donnees Meteorologiques concernant l'Ensoleillement et l'Eclairage Naturel. *Cah. Cent. Sci. Batim.* 44, 24.

Dogniaux, R. (1979) *Variations qualitatives et quantitatives des composante du rayonment solaire sue une surface horizontale par ciel serein enfonction du trouble atmospherique*. Publication IRM, Serie b(62), Institut Royal Meteorologique de Belgique, Brussels.

Dogniaux, R. (1985) *Disponibilite de la lumiere du jour.* Institut Royal Meteorologique de Belgique, Brussels.

Drummond, A.J. (1958) Notes on the measurement of natural illumination II. Daylight and skylight at Pretoria: the luminous efficacy of daylight. *Arch. Met. Wien*, Series B(9), 149.

Drummond, A.J. and Ångström, A.K. (1971) Derivation of the photometric flux of daylight from filtered measurements of global (sun and sky) radiant energy. *Appl. Opt.* 10, 2024.

Duffie, J.A. and Beckman, W.A. (1991) *Solar Engineering of Thermal Processes*. Wiley, New York.

Dumortier, D. (1994a) *Modelling Global and Diffuse Horizontal Irradiances under Cloudless Skies with Different Turbidities.* Report for JOULE 2 Project, CEC, Brussels.

Dumortier, D. (1994b) *Discussion on the Prediction of Irradiances for Clear Sky Conditions*. Report for JOULE 2 Project, CEC, Brussels.

Erbs, D.G., Klein, S.A. and Duffie, J.A. (1982) Estimation of the diffuse fraction of hourly, daily and monthly average global radiation. *Solar Energy* 28(6), 293–302.

ESRA (2000) *European Solar Radiation Atlas Ecole des Mines*, Paris.

Goody, R.M. (1964) *Atmospheric Radiation I: Theoretical Basis*. Oxford University Press, London.

Grenier, J., de la Casiniere, A. and Cabot, T. (1994) A spectral model of Linke's turbidity factor and its experimental implications. *Solar Energy* 52, 303.

Grindley, P.C., Batty, W.J. and Probert, S.D. (1995) Mathematical model for predicting the magnitudes of total, diffuse and direct-beam insolation. *Appl. Energy* 52, 89.

Gueymard, C. (1993a) Critical analysis and performance assessment of clear sky solar irradiance models using theoretical and measured data. *Solar Energy* 51, 121.

Gueymard, C. (1993b) Mathematically integrable parameterization of clear-sky beam and global irradiances and its use in daily irradiation applications. *Solar Energy* 50, 385.

Gueymard, C. (1994) Analysis of monthly average atmospheric precipitable water and turbidity in Canada and northern United States. *Solar Energy* 53, 57.

Gueymard, C. (1995) *SMARTS2, a Simple Model of the Atmospheric Radiative Transfer of Sunshine: Algorithms and Performance Assessment.* Report FSEC-PF-270-95, Florida Solar Energy Center, Cocoa, USA.

Gueymard, C. (1998) Turbidity determination from broadband irradiance measurements: a detailed multi-coefficient approach. *J. Appl. Met.* 37, 414.

Gueymard, C. (2000) Prediction and performance assessment of mean hourly global radiation. *Solar Energy* 68, 285.

Gueymard, C. (2003) Direct solar transmittance and irradiance predictions with broadband models. Part I: detailed theoretical performance assessment. *Solar Energy* 74, 355.

Gueymard, C. and Kambezidis, H. (1997) Illuminance turbidity parameters and atmospheric extinction in the visible spectrum. *Q. J. Roy. Met. Soc*. 123, 679.

Gul, M.S. and Muneer, T. (1998) Models for obtaining solar radiation from other meteorological data. *Solar Energy* 64, 99–108.

Haurwitz, B. (1945) Insolation in relation to cloudiness and cloud density. *J. Met.* 2, 154–66.

Haurwitz, B. (1948) Insolation in relation to cloud type. *J. Met.* 5, 110–13.

Hawas, M. and Muneer, T. (1984a) Study of diffuse and global radiation characteristics in India. *Energy Conv. Mgmt*. 24, 143.

Hawas, M. and Muneer, T. (1984b) Generalized monthly K_T-curves for India. *Energy Conv. Mgmt*. 24, 185.

Hay, J.E. (1976) A revised method for determining the direct and diffuse components of the total shortwave radiation. *Atmosphere* 14, 278.

Hay, J.E. (1979) Calculation of monthly mean solar radiation for horizontal and inclined surfaces. *Solar Energy* 23, 301.

Hillman, M. (1993) *Time for a Change – A New Review of the Evidence*. Policy Studies Institute, London.

Hopkinson, R.G., Petherbridge, P. and Longmore, J. (1966) *Daylighting*. Heinemann, London.

Hunt, D.R.G. (1979) *Availability of Daylight*. Building Research Establishment, Garston, UK.

Ianetz, A., Lyubansky, V., Setter, I., Evseev, E. and Kudish, A. (2000) A method for characterisation and inter-comparison of sites with regard to solar energy utilisation by statistical analysis of their solar radiation data as performed for three sites in the Israel Negev region. *Solar Energy* 69, 283.

Ineichen, P. and Perez, R. (2002) A new air mass independent formulation for the Linke turbidity coefficient. *Solar Energy* 73, 151.

Iqbal, M. (1979) Prediction of hourly diffuse solar radiation from measured hourly global radiation on a horizontal surface. *Solar Energy* 24, 491.

Iqbal, M. (1983) *An Introduction to Solar Radiation*. Academic Press, Toronto.

Ivanov, V., Sapritsky, V., Ogarev, S., Parfentyev, N., Samoylov, M., Khlevnoy, B., Goodman, T., Khromchenko, V., Ohno, Y., Sauter, G. and Stolyarevskaya, R. (2002) International project to realize the lumen. *Light Eng.* 10, 9.

Jeter, M. and Balaras, C.A. (1990) Development of improved solar radiation models for predicting beam transmittance. *Solar Energy* 44, 149.

Kambezidis, H. and Papanikolaou, N. (1989) Total solar irradiance on inclined surfaces with arbitrary orientations in Greece. *Proc. of the General Assembly of the European Geophysical Society*, Barcelona, Spain, 13–17 March 1989.

Kambezidis, H., Founda, D. and Papanikolaou, N. (1993) Linke and Unsworth-Monteith turbidity parameters in Athens. Q.J.R. Meteorol. Soc. 119, 367.

Kambezidis, H., Psiloglou, B. and Synodinou, B. (1997) Comparison between measurements and models for daily solar irradiation on tilted surfaces in Athens, Greece. *J. Renew. Energy* 10, 505.

Kambezidis, H., Founda, D. and Papanikolaou, N. (1998a) Linke and Unsworth–Monteith turbidity parameters in Athens. *Q. J. Roy. Met. Soc*. 119, 367.

Kambezidis, H., Katevatis, E., Petrakis, M., Lykoudis, S. and Asimakopoulos, D. (1998b) Estimation of Linke and Unsworth–Monteith turbidity factors in the visible spectrum application for Athens, Greece. *Solar Energy* 62, 39.

Kambezidis, H., Adamopoulos, A. and Zevgolis, D. (2001) *Determination of Anstrom and Scheupp's Parameters from Ground-based Spectral Measurements of Beam Irradiance in the Ultraviolet and Visible Spectrum in Athens, Greece*.

Karayel, M., Navvab, M., Neeman, E. and Selkowitz, S. (1983) Zenith luminance and sky luminance distribution for daylighting applications. *Energy Build.* 6, 3.

Kasten, F. (1993) Discussion on the relative air mass. *Light. Res. Tech*. 25, 129

Kasten, F. and Czeplak, G. (1980) Solar and terrestrial radiation dependent on the amount and type of cloud. *Solar Energy* 24, 177–89.

Kimball, H.H. (1919) Variations in the total and luminous solar radiation with geographical position in the United States. *Mon. Weather Rev*. 47, 769–93.

Kimura, K. and Stephenson, D.G. (1969) *Solar Radiation on Cloudy Days*. Research paper no. 418. Division of building research, National Research Council, Ottawa, 9.

Kinghorn, D. (1999) *Daylight Modelling for the United Kingdom*. PhD thesis, Napier University, Edinburgh.

Kittler, R. (1970) *Some Considerations Concerning the Zenith Luminance of the Cloudless Sky*. Circular No. 11, CIE E-3.2.

Koga, Y., Nakamura, H. and Rahim, M.R. (1993a) Study on luminous efficacy – The relation to cloud cover. *Proc. Lux Europa 1993*, Edinburgh, 4–7 April 1993, vol II, pp. 799–803.

Koga, Y., Nakamura, H. and Rahim, M.R. (1993b) Daylight and solar radiation data in Ujung Pandang, Indonesia *Proc. Second Lux Pacifica Lighting Conf*., Bangkok, 10–13 November 1993, pp. C85–90.

Kondratyev, K.Ya. (1969) *Radiation in the Atmosphere*. Academic Press, New York.

Krochmann, J. (1970) Uber die horizontal beleuchtungs-starke und die zenitleuchtdichte des klaren himmels. *Lichttechnik* B22, 551.

Lacis, A.A. and Hansen, J.E. (1974) A parameterisation for the absorption of solar radiation in the earth's atmosphere. *J. Atmos. Sci*. 31, 118–32.

Lam, J. and Li, D. (1996) Correlation between global solar radiation and its direct and diffuse components. *Build. Environ.* 31, 527.

Lam, J. and Li, D. (1998) Correlation analysis of solar radiation and cloud cover. *Int. J. Ambient Energy* 19, 187.

Li, D. and Lam, J. (2002) A study of atmospheric turbidity for Hong Kong. *Renew. Energy* 25, 1.

Liebelt, C. (1975) Leuchtdichte-und strahldichteverteilung durch tageslicht. *Gesundsheitsingenieur* 96, 127.

Linke, F. (1922) Transmission-Koeffizient und Trubungsfaktor. *Beitraege Phy. Atmos.* 10, 91.

Littlefair (1996) *Internal Report*. Building Research Establishment, Garston, UK.

Littlefair, P.J. (1985) The luminous efficacy of daylight: a review. *Light. Res. Technol*. 17, 162.

Littlefair, P.J. (1988) Measurement of the luminous efficacy of daylight. *Light. Res. Technol.* 20, 177.

Littlefair, P.J. (1994) A comparison of sky luminance models with measured data from Garston, United Kingdom. *Solar Energy* 53, 315.

Liu, B.Y.H. and Jordan, R.C. (1960) The inter-relationship and characteristic distribution of direct, diffuse and total solar radiation. *Solar Energy* 4, 1.

Liu, B.Y.H. and Jordan, R.C. (1963) The long-term average performance of flat plate solar energy collectors. *Solar Energy* 7, 53.

Lloyd, P.B. (1982) *A Study of Some Empirical Relations Described by Liu and Jordan*. Report no. 333, Solar Energy Unit, University College, Cardiff, July 1982.

Lumb, F.E. (1964) The influence of cloud on hourly amounts of total solar radiation at sea surface. *Q. J. Roy. Met. Soc*. 90, 43–56.

Lunde P.J. (1980) *Solar Thermal Engineering*, Wiley, New York.

Mani, A. (1980) *Handbook of Solar Radiation Data for India*. Allied Publishers, New Delhi, India.

Mani, A. and Rangarajan, S. (1983) Techniques for the precise estimation of hourly values of global, diffuse and direct solar radiation. *Solar Energy* 31, 577.

Maxwell, E.L. (1987) *A Quasi-Physical Model for Converting Hourly Global Horizontal to Direct Normal Insolation*. Report SERI/TR-215-3087. Solar Energy Research Institute, Golden, Colorado.

McDermott, L.H. and Gordon-Smith, G.W. (1951) Daylight illumination recorded at Teddington. *Proc. Build. Res. Congr*., Division 3, Part III, 156.

Meteorological Office (1980) *Solar Radiation Data for the United Kingdom*. Meteorological Office Report 912, Bracknell, United Kingdom.

Moon, P. (1940) Proposed standard solar radiation curves for engineering use. *J. Franklin Inst*. 230, 583.

Moon, P. and Spencer, D.E. (1942) Illumination from a non-uniform sky. *Trans. Illum. Eng. Soc*., London 37, 707.

Muneer, T. (1987) *Solar Radiation Modelling for the United Kingdom*. PhD thesis, Council for National Academic Awards, London.

Muneer, T. (1995) Solar irradiance and illuminance models for Japan II: luminous efficacies. *Light. Res. Tech*. 27, 223.

Muneer, T. and Saluja, G.S. (1986) Correlation between hourly diffuse and global solar radiation for the UK. *BSER&T* 7, 37.

Muneer, T. and Angus, R.C. (1993) Daylight illuminance models for the United Kingdom. *Light. Res. Tech*. 25, 113.

Muneer, T. and Angus, R.C. (1995) Luminous efficacy: Evaluation of models for the United Kingdom. *Light. Res. Tech*. 27, 71.

Muneer, T. and Kinghorn, D. (1997) Luminous efficacy of solar irradiance: improved models. *Light. Res. Tech*. 29, 185.

Muneer, T. and Gul, M. (1998) Detailed evaluation of a meteorological radiation model using long-term data from UK locations. *Energy Conv. Mgmt* 38, 303.

Muneer, T., Gul, M. and Kambezidis, H. (1998) Models for obtaining solar radiation from other meteorological data. *Solar Energy* 64, 33.

Muneer, T. and Gul, M. (2000) Evaluation of sunshine and cloud cover based models for generating solar radiation data. *Energy Conv. Mgmt*. 41, 461.

Muneer, T. and Hawas, M.M. and Sahili, K. (1984) Correlation between hourly diffuse and global radiation for New Delhi. *Energy Conv. Mgmt*. 24, 265.

Muneer, T., Gul, M., Kambezedis, H. and Alwinkle, S. (1996) An all-sky solar radiation model based on meteorological data. *Proc. CIBSE/ASHRAE Joint Annual Conf.*, Harrogate, United Kingdom.

Nagata, T. (1970) Luminance distribution of clear skies. Part 2 – Theoretical considerations. *Trans. Arch. Inst.*, Japan, 186, 41.

Nakamura, H. and Oki, M. (1986) The mean sky composition, its dependence on the absolute luminance of the sky elements and its application to the daylighting prediction. *Proc. Int. Daylighting Conf.*, Long Beach, California, p. 61.

Navvab, M., Karayel, M., Neeman, E. and Selkowitz, S. (1988) Luminous efficacy of daylight. *Proc. CIBSE Nat. Light. Conf.*, p. 409.

Orgill, J.F. and Hollands, K.G.T. (1977) Correlation equation for hourly diffuse radiation on a horizontal surface. *Solar Energy* 19, 357.

Page, J.K. and Lebens, R. (1986) *Climate in the United Kingdom*. HMSO, London.

Paltridge, G. and Platt, C. (1976) *Radiative Processes in Meteorology and Climatology*. Elsevier, Amsterdam.

Parker, D.E. (1971) The effect of cloud on solar radiation receipt at the tropical ocean surface. *Met. Mag*. 100, 232–40.

Perez, R., Ineichen, P. and Seals, R. (1990) Modelling daylight availability and irradiance components from direct and global irradiance. *Solar Energy* 44, 271–89.

Perez, R., Ineichen, P., Maxwell, E., Seals, R. and Zelenka, A. (1991) Dynamic global-to-direct irradiance conversion models. *Proc. ISES World Congress*, Denver, Colorado.

Pilkington plc (1993) *Glass in Buildings*, eds D. Button and B. Pye. Pilkington plc, Prescott Road, St Helens, United Kingdom.

Pisimanis, D., Notaridou, V. and Lalas, D.P. (1987) Estimating direct, diffuse and global radiation on an arbitrarily inclined plane in Greece. *Solar Energy* 39(3), 159.

Pleijel, G. (1954) The computation of natural radiation in architecture and town planning. *Meddelande Bull., Statens Namnd for Byggnadsforskning*, Stockholm 25, 30.

Policy Studies Institute (1988) *Making the Most of Daylight Hours*. Policy Studies Institute, London.

Power, H. (2001) *Atmos. Environ.* 35, 125.

Rahim, M.R., Nakamura, H., Koga, Y. and Matsuzawa, T. (1993) The modified equation for the zenith luminance of the clear sky. *Proc. 2nd Lux Pacifica Conf.*, Bangkok, 10–13 November 1993.

Red Book (1992) *Ozone Data for the World*. Atmospheric Environment Service, Downsview, Ontario, Canada, in cooperation with the World Meteorological Organisation, 33, no. 6, November–December 1992.

Reindl, D.T., Beckman, W.A. and Duffie, J.A. (1990) Diffuse fraction correlations. *Solar Energy* 45, 1–7.

Reitan, C.H. (1963) Surface dew-point and water vapor aloft. *J. Appl. Met.* 2, 776.

Robinson, N. (1966) *Solar Radiation*. Elsevier, Amsterdam.

Rodger, G., Souster, C. and Page, J. (1981). *Department of Building Science Report BS 28 (Revised)*. University of Sheffield, England.

Saluja, G.S. and Robertson, P. (1983) Design of passive solar heating in the northern latitude locations. *Proc. Solar World Congress*, Perth, Australia, p. 40.

Sarath-Babu, K. and Satyamurty, V. (2001) Frequency distribution of daily clearness indices through generalized parameters. *Solar Energy* 70, 35.

Saunier, G.Y., Reddy, T.A. and Kumar, S. (1987) A monthly probability distribution function of daily global irradiation values appropriate for both tropical and temperate locations. *Solar Energy* 38, 169.

Schuepp, W. (1949) Die Bestimmung der Komponenten der atmospharischen Trubung aus Aktinometermessungen. *Archiv fur Meteorologie, Geophysik und Bioklimatologie* B1, 257.

Sekera, Z. (1956) Recent developments in the study of the polarization of skylight. *Adv. Geophys*. 3, 43.

Shettle, E.P. and Fenn, R.W. (1975) Models of the atmospheric aerosol and their optical properties, *Proc. AGARD Conf. no 183 on 'Optical Propagation in the Atmosphere'*, pp. 2.1–2.16.

Spencer, J.W. (1982) Correlation equation for hourly diffuse radiation on a horizontal surface. *Solar Energy* 29, 19.

Tregenza, P.R. (1980) A simple mathematical model of illumination from a cloudy sky. *Light. Res. Tech*. 12, 121.

Tregenza, P.R. (1986) Measured and calculated frequency distributions of daylight illuminance. *Light. Res. Tech*. 18, 71.

Udo, S. (2000) Sky conditions at Ilorin as characterised by clearness index and relative sunshine. *Solar Energy* 69, 45.

Unsworth, M.H. and Monteith, J.L. (1972). Aerosol and solar radiation in Britain. *Q. J. Roy. Met. Soc*. 98, 778.

US Standard Atmosphere (1976) US Government Printing Office, Washington, DC.

Van Heuklon, T.K. (1979) Estimating atmospheric ozone for solar radiation models. *Solar Energy* 22, 63–8.

Whillier, A. (1953) *Solar Energy Collection and Its Utilization for House Heating.* PhD thesis, MIT, Cambridge, MA.

Whillier, A. (1956) The determination of hourly values of total radiation from daily summations. *Arch. Met. Geoph. Biokl. Series B*, 7, 197.

Won, T.K. (1977) The simulation of hourly global radiation from hourly reported meteorological parameters. *3rd Conf., Canadian Solar Energy society*, Edmonton, Alberta.

Wright, J., Perez, R. and Michalsky, J.J. (1989) Luminous efficacy of direct irradiance: variations with insolation and moisture conditions. *Solar Energy* 42, 387.

Yang, K., Huang, G.W. and Tamai, N. (2001) A hybrid model for estimating global solar radiation. *Solar Energy* 70, 13.

Valko, P. (1966) *Arch. Met. Geophys. Biobl*. B14, 336.

4 HOURLY SLOPE IRRADIATION AND ILLUMINANCE

Introduction

In the previous sections, models for incident horizontal diffuse and global irradiation and illuminance were discussed. Having obtained these quantities, the next step is to obtain the incident slope beam and diffuse energy. Diffuse irradiance or illuminance on any sloping surface consists of sky-diffuse and ground-reflected components. While the latter will be discussed at length in Chapter 6, the former, i.e. sky-diffuse component, will be discussed presently.

The task of computing beam (direct) energy on a slope when its value on the horizontal is known is a matter related to solar geometry. Computation of the diffuse component on a surface of given orientation and tilt is, however, not as simple. Chapter 1 provides the equations and FORTRAN programs related to solar geometry. Most programs in this chapter, which enable computation of the slope beam, sky-diffuse and isotropic ground-reflected components, have been developed on Prog1-6.For platform which is a convenient and precise routine for solar geometry.

Historically, the development of sky-diffuse models initiated with the work of Moon and Spencer (1942) who used measured data from Kiel in Germany, and Chicago and Washington DC to demonstrate the anisotropic nature of the luminance distribution of overcast skies. Figure 4.0.1 presents their findings.

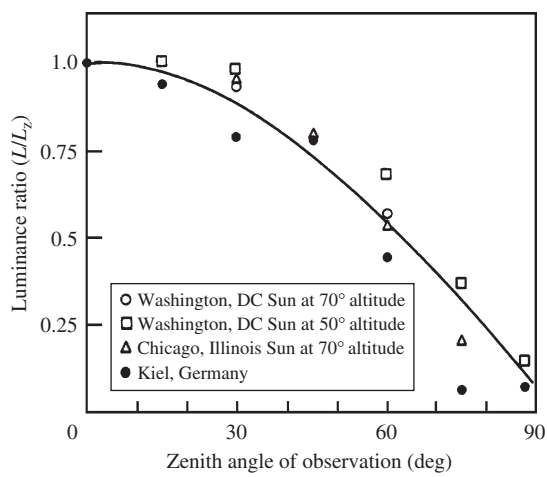

Figure 4.0.1 *Luminance distribution for overcast skies (Moon and Spencer, 1942)*

The irradiance model development has, however, been rather slow, e.g. even in the early seventies Liu and Jordan's (1960) isotropic model was employed in very many studies. In the present chapter the irradiance model development is categorised in three sections, referred as the first, second and third generation models. The development of slope illuminance models will be examined in Section 4.4. The radiance and luminance distributions of the sky have evolved from a 'discrete' to a 'continuous' mode and these will be presented in Section 4.5.

Dubayah and Rich (1995) have presented an overview of the effects of topography and plant canopies on solar radiation. One of the important aspects of that work is the presentation of the effects of shade and shadowing on the land mass surrounding hills. The corresponding impact on the biophysical processes, soil heating and water balances was also presented. It will be shown herein that new developments in slope irradiance modelling enables such intricate details to be incorporated in large scale applications such as geometeorology as well as building design.

4.1 Slope beam irradiance and illuminance

As shown in Section 2.7, the daily slope beam irradiation is obtained from horizontal beam irradiation by multiplying it with the beam conversion factor R_B. Similarly, the hourly or instantaneous slope beam irradiance is obtained via,

$$I_{B,TLT} = I_B\, r_B \tag{4.1.1a}$$

$$r_B = \max[0,\ \cos \text{INC}/\sin \text{SOLALT}] \tag{4.1.1b}$$

If measured directly, I_B can be observed as the difference between the hourly, or instantaneous, horizontal global I_G and diffuse irradiance I_D.

4.2 Sky clarity indices

In Section 3.4, the concept of hourly clearness index, $K_t = I_G/I_E$, and diffuse ratio, $K = I_D/I_G$, was introduced. Many anisotropic sky-diffuse models use one form or another of sky clarity index to describe the prevailing condition. Under non-overcast conditions the constituent components of sky-diffuse irradiance are a circumsolar (sun's aureole) part and background diffuse irradiance. The sky clarity indices are used to 'mix' the above-mentioned components. Some of these indices will be presented herein.

The most common of all the sky clarity indices is the 'clearness function' F, given by:

$$F = (I_G - I_D)/I_E \tag{4.2.1}$$

I_E is the horizontal extraterrestrial irradiance (W/m^2). Equation (3.3.7) and Prog4-1.For enable computation of I_E. Note that using Eq. (3.4.1) a relationship may be established between F and K_t that takes the form as:

$$F = K_t\,[1 - \text{function}\,(K_t)]$$

Using the above relationship and by observation of recorded irradiance data it may be shown that when $K_t < 0.2$ a complete overcast sky is observed. K_t values of 0.5, 0.7 and 0.9 are associated with intermediate, clear and very clear sky respectively. The corresponding values of F for the above K_t are, respectively, 0.18, 0.51 and 0.61. Note that for $K_t < 0.2$, F assumes a value of naught.

The index proposed by Klucher (1979) is of the form:

$$F' = 1 - (I_D/I_G)^2 \tag{4.2.2}$$

To identify cloudless conditions, Perez et al. (1990) have proposed the following criterion: $K_t' \geqslant 0.7$, where,

$$K_t' = \frac{K_t}{1.031 \exp\left[\frac{-1.4}{0.9 + 9.4/m_r}\right] + 0.1} \tag{4.2.3}$$

On the other hand Batlles et al. (1998) have introduced the following criterion that is based on solar altitude, global and diffuse irradiation:

$$K_{tt} = -0.3262 - 0.0032\,\text{SOLALT} + 0.6843 \log \text{SOLALT} \tag{4.2.4a}$$

$$K_k = 1.0827 - 0.3893 \log \text{SOLALT} \tag{4.2.4b}$$

where solar altitude is in degrees. A cloudless sky is defined as one under which the following conditions are met: $K_t > K_{tt}$ and $K < K_k$.

In Eqs (3.5.13) and (3.5.14) the Perez sky clearness (ε) and brightness factors (Δ) were respectively introduced. These factors are, respectively, functions of cloud conditions and cloud thickness or aerosol loading. For the respective ranges of 1–1.065, 1.065–1.2 and >6.0 the ε value indicates heavy overcast, average overcast and very clear conditions. An approximate ε value of 2.0 is the mid-point for intermediate skies. $\Delta < 0.1$ indicates very dark sky, whereas $0.1 < \Delta < 0.3$ suggests average sky and $\Delta > 0.48$ very bright sky.

The French research team headed by Perraudeau has suggested a nebulosity index FP that is also a useful measure of the sky clarity (Kambezidis et al., 1998). FP actually represents the status of sky cloud cover and takes values in the range (0,1). Specifically, $0 < F < 0.05$ indicates an overcast sky, $0.05 < F < 0.2$ intermediate overcast sky, $0.2 < F < 0.7$ intermediate blue sky, $0.7 < F < 0.9$ intermediate sky and $0.9 < F < 1$ a blue (cloudless) sky.

The following steps enable computation of FP:

$$\text{FP} = (1 - \text{CRM})/(1 - \text{CRT})$$

CRM is ratio of measured diffuse to measured global horizontal irradiance while CRT is ratio of the same parameters for a completely cloudless sky. Thus,

$$\text{CRM} = I_D/I_G \quad \text{and} \quad \text{CRT} = \text{ISC}/(\text{ISC} + I_B)$$

$$\text{ISC} = \text{ISCA} \times \text{ISCB}$$

where

$$\text{ISCA} = 0.5528 + 0.8785m - 0.013\,22m^2 + 0.000\,343\,4m^3$$

$$\begin{aligned}\text{ISCB} = {} & 6.9731 + 0.042\,496m - 0.000\,853\,75m^2 - 0.000\,086\,088m^3 \\ & + 0.000\,001\,984\,8m^4 - 0.000\,000\,016\,222m^5 \\ & + 0.000\,000\,000\,047\,823m^6\end{aligned}$$

$$I_{\text{B}} = \text{ISC}[1 + 0.033\cos(360\ \text{DN}/365)]\exp(-K_{\text{P}}mT_{\text{LK}})$$

$$K_{\text{P}} = 1/(6.5567 + 1.7513m - 0.1202m^2 + 0.0065m^3 - 0.000\,13m^4)$$

Prog4-1.For enables computation of the key sky clarity indices and this will be demonstrated via the following example.

Example 4.2.1

The hourly-averaged receipt of global and diffuse irradiance at Bracknell, England (51.4°N) on 22 August 1990 at 1130 h solar time (mid-point of the recording interval) was 747 and 272 W/m^2 respectively. The bright sunshine fraction for this hour was noted to be 1.0 and the cloud amount was 1 okta. Compute the above cited sky clarity indices given the Linke turbidity is 3.5.

Execution of Prog4-1.For provides the following results:

Air-mass calculations:

Kasten air mass = 1.308 (refer Prog4-1.For)
Gueymard air mass = 1.307 (refer Prog4-1.For)

Sky clarity calculations:

Perradeau FP = 0.823
Clearness index $K_{\text{t}} = 0.73$
Perez modified clearness index $K'_{\text{t}} = 0.71$
Clearness function $F = 0.46$
Batlles $K_{\text{tt}} = 0.68$
Batlles $K_{\text{k}} = 0.42$

Diffuse ratio $K\ (=I_{\text{D}}/I_{\text{G}}) = 0.36$

Note that three of the above five indices, i.e. Perez K'_{t}(Eq. (4.2.3)), Batlles formulation (Eq. (4.2.4)) and clearness index K_{t} indicate the existence of a nearly clear sky. This is confirmed by the observed SF = 1.0 and cloud cover of 1 okta.

4.3 Sky-diffuse irradiance models

With the exception of clear skies, very often the sky-diffuse irradiance is the dominant component. Precise estimation of it is therefore important for all solar energy related work. The three sub-sections presented below, though not exhaustive, outline the historical development of the relevant models. A FORTRAN program which enables computation of instantaneous slope beam, sky-diffuse and ground-reflected irradiance is provided in Prog4-1.For. The program estimates sky-diffuse irradiance for seven selected models, the selection being made to reflect their general currency and rigorous validations undertaken in the past, e.g. Kambezedis et al. (1994).

4.3.1 First generation models

As the name suggests, these are the earliest and simplest of all models. Although easy to use, owing to their imprecise nature, they are increasingly being replaced by more sophisticated second and third generation models.

4.3.1.1 Isotropic model

The simplest of all slope irradiance models is the one which assumes an isotropic sky. The following equation may easily be derived using the radiation configuration analysis:

$$I_{D,TLT} = I_D \cos^2(TLT/2) \tag{4.3.1.1}$$

However, diffuse irradiation is not isotropic in nature and is an angular function of the solar altitude and azimuth. Kondratyev and Manolova (1960) have made an excellent study of the nature of diffuse and reflected radiation. They measured the radiation intensity in 37 directions for the tilt angles of 15°, 40° and 65° in every 30° of azimuth and the zenith. The anisotropic nature of sky radiance was thus demonstrated.

The following are the broad conclusions drawn from the study of Kondratyev and Manolova (1960):

(a) Measurements of diffuse and reflected irradiation show that the distribution is a function of the azimuth and solar altitude.
(b) In the case of overcast skies (dense cloudiness) the isotropic condition proves to be satisfactory.
(c) However, when the clouds are not uniform and partial transparency exists, the isotropic condition is unrealistic.

4.3.1.2 Circumsolar model

Another simple model which belongs to the first generation set is the circumsolar model which assumes that the sky-diffuse radiation, as well as the beam radiation, emanates from the direction of the solar disc (Iqbal, 1983). Mathematically, this may be expressed as,

$$I_{D,TLT} = I_D r_B \tag{4.3.1.2}$$

The above model may only be adopted under exceptionally clear-sky conditions. Even under those conditions it will only approximately represent the radiance distribution and, as such, never been a serious contender.

4.3.2 Second generation models

These models differentiate between the radiance distribution of clear and overcast skies. However, they do not completely divorce their generic development from the isotropic sky and as such revert to the latter under overcast conditions. In terms of accuracy they offer a fair improvement over the first generation models.

4.3.2.1 Temps–Coulson model

Temps and Coulson (1977) have suggested an anisotropic modification to the clear-sky diffuse radiance model. They used clear-sky measurements to demonstrate the anisotropic nature of diffuse irradiation.

The findings of Temps and Coulson for clear-sky radiance distribution may be summarised as follows:

(a) The main deficiency in the isotropic model seems to be due to the fact that an increased intensity exists near the horizons and in the circumsolar region of the sky.
(b) Observations showed that skylight intensity is about 40% greater at horizons than at zenith. This gradient was strongest at low solar altitudes.
(c) Introduction of the factor $[1 + \sin^3(\mathrm{TLT}/2)]$ takes into account the effect of horizon brightening.
(d) Introduction of the factor $[(1 + \cos^2 \mathrm{INC}) \sin^3 Z]$ takes into account the effect of circumsolar radiation also known as sun's aureole, Z being the zenith angle of the sun.

Temps and Coulson's clear-sky diffuse irradiance model may be expressed as:

$$I_{\mathrm{D,TLT}} = I_{\mathrm{D}} \cos^2(\mathrm{TLT}/2)[1 + \sin^3(\mathrm{TLT}/2)](1 + \cos^2 \mathrm{INC}) \sin^3 Z \qquad (4.3.2.1)$$

4.3.2.2 Klucher's model

Klucher (1979) progressed the work of Temps and Coulson (1977) by developing an anisotropic model for all-sky conditions. He used hourly measured radiation values for New York for a 6-month period on surfaces tilted towards the equator at 37° and 60° angles. He found that the Liu–Jordan isotropic model gives good results under overcast skies, but underestimates insolation under clear and part-overcast conditions. Klucher noted that the Temps–Coulson model provides a good prediction for clear-sky conditions but overestimates overcast insolation.

Klucher's results may be put explicitly as follows:

(a) The Liu–Jordan model provides a good fit for low intensities ($<300\,\mathrm{W/m^2}$), such values being associated with overcast skies. However, for intensities greater than $500\,\mathrm{W/m^2}$, the Liu–Jordan model underestimates insolation by as much as $80\,\mathrm{W/m^2}$ at 37° tilt and up to $100\,\mathrm{W/m^2}$ at 60° tilt.
(b) The Temps–Coulson model provided results which are highly consistent with the entire 6 months data for clear skies. However, for other days, the model overpredicted insolation by about $120\,\mathrm{W/m^2}$ in winter and up to $50\,\mathrm{W/m^2}$ in summer.

Klucher's model is given by:

$$I_{\mathrm{D,TLT}} = I_{\mathrm{D}} \cos^2(\mathrm{TLT}/2)[1 + F' \sin^3(\mathrm{TLT}/2)][1 + F' \cos^2 \mathrm{INC} \sin^3 Z] \qquad (4.3.2.2)$$

where F' is the modulating function, given by Eq. (4.2.2). Under overcast skies, F' becomes zero, thereby reducing Klucher's model to that of Liu–Jordan, and under clear skies, F' approaches unity, thus approximating the Temps–Coulson model.

4.3.2.3 Hay's model

Hay's model (Hay, 1979; Hay and Davies, 1980; Hay and McKay, 1988) assumes diffuse radiation incident on a horizontal surface to be composed of circumsolar and uniform background sky-diffuse components. The two components are weighted accordingly, as given by:

$$I_{D,TLT} = I_D[Fr_B + (1 - F)\cos^2(TLT/2)] \tag{4.3.2.3}$$

Ma and Iqbal (1983) have used a year's measured data for Woodbridge, Ontario to compare the performance of Klucher–Hay models. Two statistical measures of error, the root mean square error (RMSE) and mean bias error (MBE), were used to evaluate the accuracy of the models. Ma and Iqbal have presented their results for measured and predicted global irradiation on south-facing slopes of 30°, 60° and 90°. Global slope irradiation was calculated as the sum of beam, diffuse and ground-reflected components; the last, in turn, was calculated using a daily value of measured ground-reflected irradiation. The conclusions of Ma and Iqbal may be listed as follows:

(a) The RMSEs for all three models increase with the slope.
(b) For all slopes, the models are reasonably accurate during the summer months.
(c) The errors are maximum in winter months when the sky-diffuse component forms a significant proportion of the total irradiation.
(d) The highest RMSE for the isotropic model is 30%. Hay–Klucher models are much alike with maximum RMSEs of 20% on 90° slopes and 15% on 60° slopes.

4.3.2.4 Skartveit–Olseth model

This model was primarily developed for the higher latitudes (Skartveit and Olseth, 1986) and may be expressed as:

$$I_{D,TLT} = I_D[Fr_B + B\cos TLT + (1 - F - B)\cos^2(TLT/2)] \tag{4.3.2.4}$$

where $B = \max[(0.3 - 2F), 0]$.

4.3.2.5 Reindl's model

Reindl et al. (1990) have used the work of Hay and Davies (1980) and Klucher (1979) to propose:

$$I_{D,TLT} = I_D\{(1 - F)\cos^2(TLT/2)[1 + f\sin^3(TLT/2)] + Fr_B\} \tag{4.3.2.5}$$

F is defined by Eq. (4.2.1) and $f = (I_B/I_G)^{0.5}$.

4.3.3 Third generation models

These models treat the sky-diffuse component as anisotropic. Most models under this category decompose non-overcast irradiance as the sum of two components, i.e. circumsolar and background sky diffuse, an exception being the Perez et al. (1990) model which consists of three components.

Three all-sky models which belong to this category, e.g. Gueymard (1987), Muneer (1987) and Perez et al. (1990) will be described herein. The first two of the above models owe their development to the works of Moon and Spencer (1942) and Steven and Unsworth (1979; 1980) which will be presented first.

4.3.3.1 Moon–Spencer model

Moon and Spencer (1942) used measured data to demonstrate a relationship between the luminance of a patch of an overcast sky and its zenith angle, θ. Their proposed relationship was given as:

$$L_\theta = L_z(1 + b\cos\theta)/(1 + b) \tag{4.3.3.1}$$

Figure 4.3.1a shows a sketch of a hemispherical sky whose luminance distribution is described by Eq. (4.3.3.1). The parameter b in the above equation is the luminance

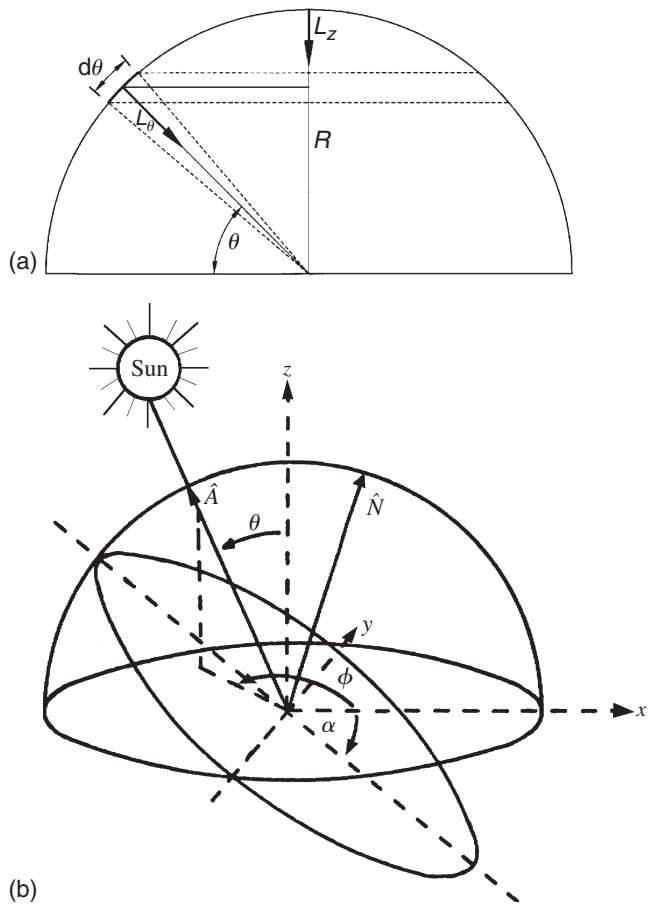

Figure 4.3.1 *(a) A hemispherical sky whose luminance distribution is described by Eq. (4.3.3.1). (b) Solar geometry for an inclined surface*

(or radiance) distribution index. Moon and Spencer obtained the value of $b = 2$ which was later adopted to define the CIE standard overcast sky.

Kondratyev (1969) has also reported that the radiance and luminance distributions are rather similar and azimuthaly independent for an overcast sky.

A further discussion on radiance and luminance distribution of overcast skies is provided in Section 4.5.

4.3.3.2 Steven–Unsworth model

Steven and Unsworth (1980) measured the overcast sky radiance at Sutton Bonnington (52.8°N) by using nine pyrheliometers, eight of which faced north, east, south and west at angles of 30° and 60° to the zenith and the remaining one faced the zenith. Radiance distribution of the sky was found to be similar to Eq. (4.3.3.1) but they obtained the average value of $b = 1.23$. Steven and Unsworth attributed the difference in the value of b, in the two studies, to the difference between radiance and luminance distribution of the overcast sky. Steven (1977a,b) has also measured the radiance distribution of a clear sky and reported its anisotropic nature. Steven and Unsworth (1979) used Steven's (1977a,b) measurements to predict irradiation on an inclined surface as given by:

$$I_{D,TLT} = I_{DC}\, r_B + I_{DB} \tag{4.3.3.2}$$

where I_{DC} and I_{DB} are, respectively, the circumsolar and background-sky components of the hourly diffuse irradiation. I_{DC} was assumed to be proportional to I_D as given by:

$$I_{DC} = sI_D \tag{4.3.3.3}$$

where s is a proportionality constant which varies with the sky clarity.

Steven (1977a) integrated Eq. (4.3.3.1), replacing luminance by radiance to obtain:

$$\frac{I_{DB}}{I_D} = \cos^2\frac{\mathrm{TLT}}{2} + \frac{2b}{\pi(3+2b)}\left[\sin \mathrm{TLT} - \mathrm{TLT}\cos \mathrm{TLT} - \pi \sin^2\frac{\mathrm{TLT}}{2}\right] \tag{4.3.3.4}$$

The mathematical proof for the above equation is given below. The computation of hourly tilted surface irradiation thus requires I_D and the values of s and b. Steven and Unsworth (1979) have calculated these values for a range of zenith angles between 35° and 65°. For all zenith angles, taken together, they obtained $s = 0.51$ and $b = -0.87$.

Derivation of Eq. (4.3.3.4) for sky-diffuse irradiance on a tilted surface

The analysis, originally due to Steven (1977b), has been presented by Usher and Muneer (1989). Consider the solar geometry for a surface having a slope of angle α to the horizontal and normal $\hat{N}$ (Figure 4.3.1b). Let $\hat{A}$ be a unit vector in the direction of the sun, θ be the zenith angle and ϕ be the azimuth angle. With respect to the Cartesian co-ordinates x, y, z in the horizontal plane:

$$\hat{A} = (\sin\theta\cos\phi,\ \sin\theta\sin\phi,\ \cos\theta)$$

$$\hat{N} = (\sin\alpha,\ 0,\ \cos\alpha)$$

If $I(\theta, \phi)$ denotes the radiance distribution then the flux of radiation on the tilted surface is given by:

$$I_{D\alpha} = \iint_{\text{Visible region of sky}} I(\theta,\phi)\hat{A}\hat{N}\,d\Omega$$

$\hat{N}$ is the vector drawn normal to the elemental sky patch $d\Omega$.

$$I_{D\alpha} = \iint I(\theta,\phi)\,(\sin\theta\cos\phi\sin\alpha + \cos\theta\cos\alpha)\sin\theta\,d\theta\,d\phi \tag{4.3.3.5}$$

This integral may be simplified as follows. First consider the projection of the unit vector $\hat{A}$ onto the inclined surface, the projected sector **B** being given by:

$$\mathbf{B} = \hat{A} - (\hat{A}\cdot\hat{N})\hat{N}$$

Now consider the transformation corresponding to the rotation of the inclined surface through an angle α about the *y*-axis which maps the vector **B** into a vector **C** in the horizontal *xy*-plane. The matrix of this transformation is given by:

$$R_\alpha = \begin{pmatrix} \cos\alpha & 0 & -\sin\alpha \\ 0 & 1 & 0 \\ \sin\alpha & 0 & \cos\alpha \end{pmatrix}$$

$$\mathbf{C} = R_\alpha\mathbf{B}$$

It may then be shown that:

$$\mathrm{C} = \begin{pmatrix} \cos\alpha\sin\theta\ \cos\phi\ -\sin\alpha\ \cos\theta \\ \sin\theta\sin\phi \\ 0 \end{pmatrix}$$

Thus, consider co-ordinates in the tilted plane given by:

$$x' = \cos\alpha\sin\theta\cos\phi - \sin\alpha\cos\theta$$
$$y' = \sin\theta\sin\phi$$

With these co-ordinates Eq. (4.3.3.5) reduces to:

$$I_{D\alpha} = \iint_{R'} I(\theta(x',y')\phi(x',y'))\,dx'\,dy' \tag{4.3.3.6}$$

where the region R' is the projection of the sky hemisphere on the tilted plane. For negative x', i.e. $\pi/2 \leqslant \phi \leqslant 3\pi/2$, the region R' is a semi-circle of unit radius. However, for positive x', i.e. $-\pi/2 \leqslant \phi \leqslant \pi/2$, the region R' is bounded by an ellipse which is determined by

the projection of the unit semi-circle, $\pi/2 \leqslant \phi \leqslant \pi/2$, in the horizontal xy-plane, onto the sloped $x'y'$-plane. The parametric equation of this ellipse will be given by:

$$x' = \cos\alpha \cos\phi, \quad -\pi/2 \leqslant \phi \leqslant \pi/2$$
$$y' = \sin\phi, \qquad -\pi/2 \leqslant \phi \leqslant \pi/2$$

For subsequent evaluation of the integral in Eq. (4.3.3.6) it is convenient to transform to polar co-ordinates (r, η). Thus:

$$I_{\mathrm{D}\alpha} = \iint_{R'} I(\theta(r,\eta)\phi(r,\eta))\, r\, \mathrm{d}r\, \mathrm{d}\eta \tag{4.3.3.7}$$

A suitable expression for the radiance distribution $I(\theta, \phi)$ is now required. It may be assumed that:

(a) I is independent of ϕ,
(b) I varies linearly with $\cos\theta$.

Thus, let $I(\theta) = I_{90}(1 + b\cos\theta)$, where I_{90} and b are constants to be determined. It may be shown that if the flux on a horizontal surfaces is I_{D} then:

$$I(\theta) = \frac{I_{\mathrm{D}}}{\pi(1 + 2b/3)}(1 + b\cos\theta) \tag{4.3.3.8}$$

Using this expression for the radiance distribution and the appropriate polar co-ordinate transformation, Eq. (4.3.3.7) becomes:

$$I_{\mathrm{D}\alpha} = \iint_{R'} \left\{1 + \mathrm{b}\left[-r\cos\eta\sin\alpha + \cos\alpha\sqrt{1 - r^2}\right]\right\} \frac{I_{\mathrm{D}}}{\pi(1 + 2b/3)}\, r\, \mathrm{d}r\, \mathrm{d}\eta$$

The limits of integration are found to be given by:

$$0 \leqslant r \leqslant 1 \quad \text{for} \quad \pi/2 \leqslant \eta \leqslant 3\pi/2$$
$$0 \leqslant r \leqslant q \quad \text{for} \quad -\pi/2 \leqslant \eta \leqslant \pi/2$$

where

$$q = \cos\alpha \Big/ \sqrt{1 - \sin^2\alpha \sin^2\eta} \tag{4.3.3.9}$$

Algebraic manipulation leads to:

$$\frac{I_{\mathrm{D}\alpha}}{I_{\mathrm{D}}} = \cos^2\left(\frac{\alpha}{2}\right) + \frac{2b}{3\pi(1 + 2b/3)}\left[\sin\alpha - \alpha\cos\alpha - \pi\sin^2\left(\frac{\alpha}{2}\right)\right] \tag{4.3.3.10}$$

The subscript α has been introduced to signify that this is the sky-diffuse irradiation on a surface inclined at an angle α to the horizontal. When $b = 0$, Eq. (4.3.3.10) reduces to the isotropic case.

Note that α used in the above derivation is more commonly known as the surface tilt angle TLT.

As mentioned above, Eq. (4.3.3.10) enables estimation of sky-diffuse irradiation on any tilted surface given the value of the radiance distribution index *b*. Steven and Unsworth (1979; 1980) have provided the value of '*b*' for the overcast- and clear-sky conditions. Their approach therefore falls short of an all-sky model. The above analysis has nevertheless been used effectively by Gueymard (1987) and Muneer (1987; 1990a,b) to obtain an anisotropic model which enables computation under the varying sky conditions.

4.3.3.3 Gueymard's model

It was shown above that the sky-diffuse irradiance received on any surface is physically related to the radiance distribution. For a tilted receiving surface r_D may be defined as:

$$r_D = I_{D,TLT} / I_D \tag{4.3.3.11}$$

The main assumption used in the derivation of Gueymard's model (1987) is that the radiance of a partly cloudy sky may be considered as a weighted sum of radiances of a clear and an overcast sky. Using the work of Steven and Unsworth (1979), Gueymard has introduced the concept of weighted normalised radiances which may be translated into an equation for the slope factor corresponding to general sky conditions:

$$r_D = (1 - N_{pt})\, r_{d0} + N_{pt}\, r_{d1} \tag{4.3.3.12}$$

where subscripts 0 and 1 refer to the opacity (0: clear; 1: overcast). r_{d0} and r_{d1} may be obtained if the corresponding distributions of normalised radiances are available. r_{d0} is obtained as the sum of a circumsolar component (dependent on INC and SOLALT) and an hemispheric component (dependent on TLT and SOLALT) via polynomial regression:

$$r_{d0} = \exp(a_0 + a_1 \cos \text{INC} + a_2 \cos^2 \text{INC} + a_3 \cos^3 \text{INC}) + F(\text{TLT})\, G(\text{SOLALT}) \tag{4.3.3.13}$$

where

$$a_0 = -0.897 - 3.364h' + 3.960h'^2 - 1.909h'^3 \tag{4.3.3.14}$$

$$a_1 = 4.448 - 12.962h' + 34.601h'^2 - 48.784h'^3 + 27.511h'^4 \tag{4.3.3.15}$$

$$a_2 = -2.770 + 9.164h' - 18.876h'^2 + 23.776h'^3 - 13.014h'^4 \quad (4.3.3.16)$$

$$a_3 = 0.312 - 0.217h' - 0.805h'^2 + 0.318h'^3 \quad (4.3.3.17)$$

$$F(\mathrm{TLT}) = [1 + b_0 \sin^2(\mathrm{TLT}) + b_1 \sin(2\mathrm{TLT}) + b_2 \sin(4\mathrm{TLT})]/[1 + b_0] \quad (4.3.3.18)$$

$$G(\mathrm{SOLALT}) = 0.408 - 0.323h' + 0.384h'^2 - 0.170h'^3 \quad (4.3.3.19)$$

where $h' = 0.01$SOLALT (degrees), $b_0 = -0.2249$, $b_1 = 0.1231$ and $b_2 = -0.0342$.

Overcast sky condition

In this case $r_D = r_{d1}$ (refer Eq. (4.3.3.12)). r_{d1} is the ratio of the short-wave energy received on the tilted surface to that which is incident on the horizontal. It is thus equal to the right hand side of Eq. (4.3.3.4). The limit value $b = 0$ in Eq. (4.3.3.4) would correspond to an isotropic sky. However, most theoretical and experimental determinations of b lie in the range 1.0–2.0. A mean value of $b = 1.5$ has been adopted by Gueymard.

Part-overcast sky condition

In the general case of a part-overcast sky, Eq. (4.3.3.12) applies, where r_{d0} is obtained from Eq. (4.3.3.13) and r_{d1} from the right hand side of Eq. (4.3.3.4). It was shown by Gueymard that b decreases with cloudiness. To take this effect into account b is assumed to be a linear function of the cloud opacity, such that $b = 0.5 + N_{pt}$.

If no cloud observation is available, but hourly possible sunshine (SF) is measured, the following relationship is suggested:

$$N_{pt} = 1 - \mathrm{SF} \quad (4.3.3.20)$$

If hourly sunshine is not available, N_{pt} is to be estimated from horizontal diffuse ratio thus:

$$N_{pt} = \max\{\min(Y, 1), 0\} \quad (4.3.3.21)$$

where:

$$Y = 6.6667(I_D/I_G) - 1.4167, \quad (I_D/I_G) \leqslant 0.227 \quad (4.3.3.22)$$

$$\text{otherwise, } Y = 1.2121(I_D/I_G) - 0.1758 \quad (4.3.3.23)$$

4.3.3.4 Perez et al.'s model

The Perez et al. (1990) model is based on a three-component treatment of the sky-diffuse irradiance and illuminance. The incident diffuse energy on any tilted surface is given by:

$$I_{D,TLT} = I_D[(1 - F_1)\cos^2(\mathrm{TLT}/2) + F_1(a_0/a_1) + F_2 \sin \mathrm{TLT}] \quad (4.3.3.24)$$

where F_1 and F_2 are circumsolar and horizon brightness coefficients, and a_0 and a_1 are terms that account for the respective angles of incidence of circumsolar radiation on the titled and horizontal surfaces. The circumsolar radiation is considered to be from a point source:

$$a_0 = \max[0,\ \cos \mathrm{INC}]$$
$$a_1 = \max[\cos 85°,\ \cos z] \tag{4.3.3.25}$$

With these definitions, a_0/a_1 becomes r_B.

The brightness coefficients F_1 and F_2 are functions of three parameters that describe the sky conditions, the zenith angle z, sky clearness ε and a brightness Δ. ε is a function of I_D and the normal incidence beam irradiation $I_{B,n}$:

$$\varepsilon = \{[I_D + I_{B,n}/I_D] + 5.535 \times 10^{-6} z^3\}/\{1 + 5.535 \times 10^{-6} z^3\} \tag{4.3.3.26}$$

where z is in degrees, and

$$\Delta = mI_D/I_{E,n} \tag{4.3.3.27}$$

where m is the air mass and $I_{E,n}$ is the extraterrestrial normal incidence radiation. The brightness coefficients F_1 and F_2 are obtained via Table 4.3.1 and the following equations:

$$F_1 = \max[0,\ \{F_{11} + F_{12}\Delta + (\pi/180)\, z F_{13}\}] \tag{4.3.3.28}$$

Table 4.3.1 Coefficients for Perez et al. (1990) slope irradiance and illuminance model (refer Eq. (4.3.3.24))

ε (bin)	1	2	3	4	5	6	7	8
Lower bound	1.000	1.065	1.230	1.500	1.950	2.800	4.500	6.200
Upper bound	1.065	1.230	1.500	1.950	2.800	4.500	6.200	–
Irradiance								
F_{11}	−0.0083	0.1299	0.3297	0.5682	0.8730	1.1326	1.0602	0.6777
F_{12}	0.5877	0.6826	0.4869	0.1875	−0.3920	−1.2367	−1.5999	−0.3273
F_{13}	−0.0621	−0.1514	−0.2211	−0.2951	−0.3616	−0.4118	−0.3589	−0.2504
F_{21}	−0.0596	−0.0189	0.0554	0.1089	0.2256	0.2878	0.2642	0.1561
F_{22}	0.0721	0.0660	−0.0640	−0.1519	−0.4620	−0.8230	−1.1272	−1.3765
F_{23}	−0.0220	−0.0289	−0.0261	−0.0140	0.0012	0.0559	0.1311	0.2506
Illuminance								
F_{11}	0.0113	0.4296	0.8093	1.0141	1.2818	1.4257	1.4848	1.1695
F_{12}	0.5707	0.3634	−0.0535	−0.2522	−0.4205	−0.6533	−1.2139	−0.2998
F_{13}	−0.0820	−0.3066	−0.4422	−0.5311	−0.6888	−0.7789	−0.7837	−0.6149
F_{21}	−0.0947	0.0499	0.1809	0.2750	0.3802	0.4247	0.4111	0.5180
F_{22}	0.1579	0.0080	−0.1686	−0.3498	−0.5586	−0.7851	−0.6292	−1.8924
F_{23}	−0.0177	−0.0650	−0.0918	−0.0957	−0.1144	−0.0966	−0.0822	−0.0551

$$F_2 = F_{21} + F_{22}\Delta + (\pi/180)\, z F_{23} \tag{4.3.3.29}$$

4.3.3.5 Muneer's model

Muneer's model (Muneer, 1987; 1990b; 1995; Saluja and Muneer, 1987) treats the shaded and sunlit surfaces separately and further distinguishes between overcast and non-overcast conditions of the sunlit surface. In this model the slope diffuse irradiation for surfaces in shade and sunlit surfaces under overcast sky is computed as

$$I_{D,\,TLT} = I_D[TF] \tag{4.3.3.30}$$

Equation (4.3.3.30) suggests that for any sloped surface in shade (facing away from sun) there is a linear relationship between $I_{D,\,TLT}$ and I_D. Moreover, the value of b, the radiance (or luminance) distribution index (refer Eq. (4.3.3.31)), may easily be obtained by finding a linear curve fit between a vertical surface irradiance and horizontal diffuse irradiance. Figure 4.3.2 shows such a plot for Chofu in Japan. The scatter points shown in this figure represent 10-min averaged data. The slope of the best-fit lines for Chofu as well as many other locations worldwide were obtained by Muneer (1987; 1990a,b; 1995). Some of these best-fit values are shown in Figure 4.3.3.

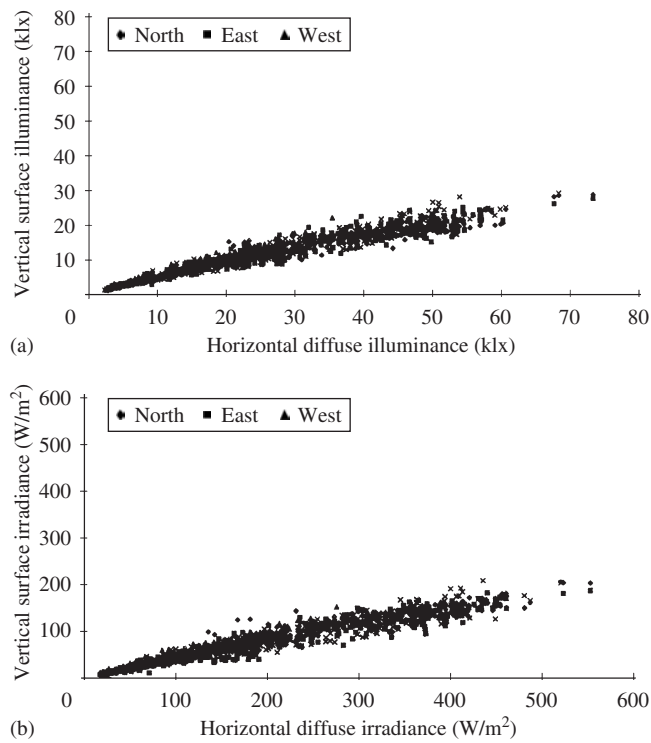

Figure 4.3.2 *Relationship between shaded vertical and horizontal diffuse: (a) illuminance and (b) irradiance (Chofu)*

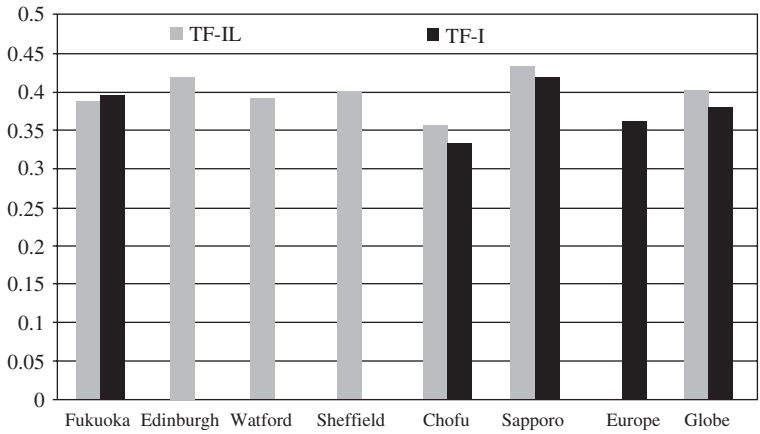

Figure 4.3.3 *Ratio of shaded vertical surface to horizontal diffuse incident energy*

A sunlit surface under non-overcast sky is modelled as:

$$I_{\mathrm{D,TLT}} = I_{\mathrm{D}}[\mathrm{TF}(1 - F) + Fr_{\mathrm{B}}] \tag{4.3.3.31}$$

TF is obtained from Eq. (4.3.3.4) using a value of b which corresponds to the appropriate sky and azimuthal condition. For the European climate a shaded surface is modelled with $b = 5.73$, while $b = 1.68$ for sun-facing surfaces under overcast sky (Muneer, 1990b). On a worldwide basis, Figure 4.3.3 suggests an average value of $b = 2.5$. Non-overcast skies, on the other hand, exhibit a continuously decreasing behaviour of b and therefore the following equations, obtained via data from 14 worldwide locations (Muneer, 1990b; 1995) are recommended:

$$2b\{\pi(3 + 2b)\}^{-1} = 0.003\,33 - 0.415F - 0.6987F^2 \text{ [for northern Europe]} \tag{4.3.3.32a}$$

$$2\mathrm{b}\{\pi(3 + 2b)\}^{-1} = 0.002\,63 - 0.712F - 0.6883F^2 \text{ [for southern Europe]} \tag{4.3.3.32b}$$

$$2b\{\pi(3 + 2b)\}^{-1} = 0.080\,00 - 1.050F - 2.8400F^2 \text{ [for Japan]} \tag{4.3.3.32c}$$

$$2b\{\pi(3 + 2\mathrm{b})\}^{-1} = 0.040\,00 - 0.820F - 2.0260F^2 \text{ [for the globe]} \tag{4.3.3.32d}$$

A sample plot for Fukuoka, Japan which demonstrates the curvilinear relationship suggested by Eq. (4.3.3.32) is shown in Figure 4.3.4. Data from many other locations are presented in Figure 4.3.5. These plots confirm the validity of the findings reported by Temps and Coulson (1977) and Steven and Unsworth (1979). Prog4-2.For enables slope irradiance computation using the procedure laid out for seven of the above models. These models are isotropic (first generation); Hay, Skartveit–Olseth and Reindl (second generation); and Gueymard, Perez and Muneer (third generation).

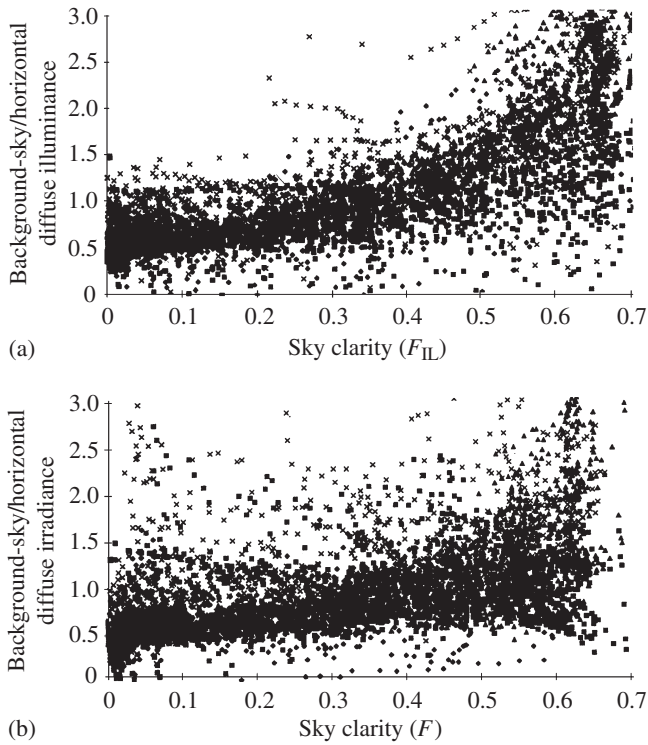

Figure 4.3.4 *Relationship between vertical, sun-facing background sky diffuse: (a) illuminance and (b) irradiance fraction and sky clarity (Fukuoka)*

Example 4.3.1

Using the isotropic sky-diffuse model, calculate the beam and diffuse irradiance on a vertical surface facing south in Edinburgh (55.95°N and 3.20°W) at 1120 h on 10 August 1993. The 5-min averaged value for horizontal global and diffuse irradiance, centred at 1120 h are, respectively, 552 and 267 W/m^2. Note: Ground-reflected radiation was excluded in the above measurements.

For the above conditions:

$$I_E = 980.15\ \mathrm{W/m^2}$$

$$\mathrm{SOLALT} = 48°, \quad \mathrm{INC} = 51.4°$$

$$\mathrm{TF} = \cos^2(\mathrm{TLT}/2) = 0.5$$

$$r_B = \cos \mathrm{INC}/\sin \mathrm{SOLALT} = 0.8385$$

$$I_{B,TLT} = (G - D)r_B = (552 - 267) \times 0.8385 = 239\ \mathrm{W/m^2}$$

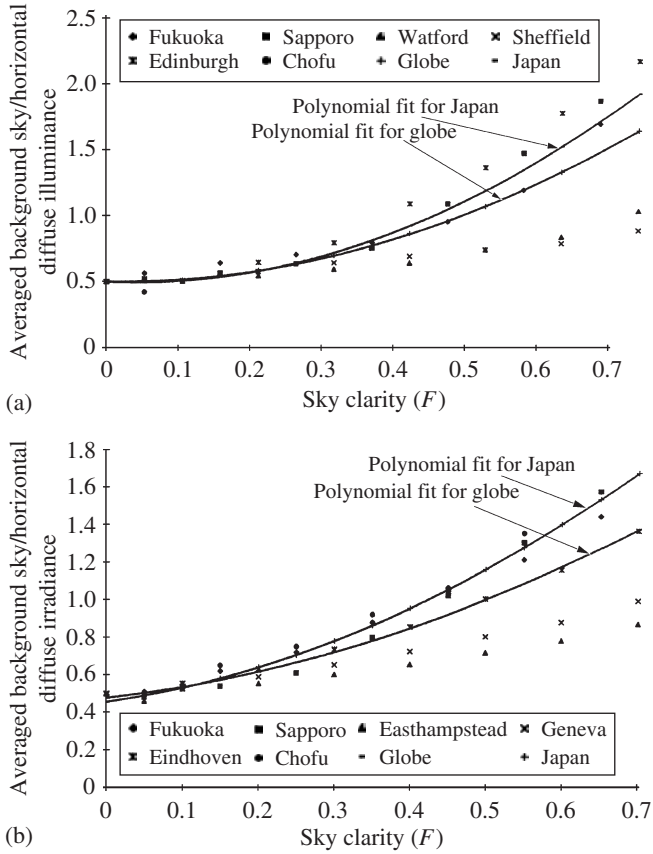

Figure 4.3.5 *Averaged background sky diffuse: (a) illuminance and (b) irradiance fraction*

$$I_{D,TLT} = I_D \mathrm{TF} = 267 \times 0.5 = 133.5\ \mathrm{W/m^2}$$

$$I_{TLT} = 372.5\ \mathrm{W/m^2}$$

The corresponding measured value is 379 W/m^2.

Example 4.3.2

Using Hay's model, perform calculations on the data given in Example 4.3.1.

We note from the preceding example that $I_E = 980.15\ \mathrm{W/m^2}$, TF = 0.5, $r_B = 0.8385$ and $I_{B,TLT} = 239\ \mathrm{W/m^2}$. Then,

$$F = (I_G - I_D)/I_E = 0.291$$

$$I_{D,TLT} = I_D[Fr_B + (1 - F)\mathrm{TF}] = 267[0.291 \times 0.8385 + 0.709 \times 0.5] = 160\ \mathrm{W/m^2}$$

$$I_{TLT} = 399\ \mathrm{W/m^2}$$

The corresponding measured value is 379 W/m^2.

Example 4.3.3

Using Skartveit–Olseth model, perform calculations on the data given in Example 4.3.1.

In this case, $B = \max[(0.3 - 2F), 0] = 0.0$, TF $= 0.5$ and $r_B = 0.8385$. Then,

$$I_{D,TLT} = 267[0.291 \times 0.8385 + 0.0 \times 0.0 + (1 - 0.291)0.5] = 160 \text{ W/m}^2$$

$$I_{TLT} = 399 \text{ W/m}^2$$

The corresponding measured value is 379 W/m^2.

Example 4.3.4

Using Reindl's model, perform calculations on the data given in Example 4.3.1.

We note that $F = 0.291$, $f = 0.719$. Then,

$$I_{D,TLT} = 267[(1 - 0.291) \times 0.5 \times (1 + 0.719 \times 0.3535) + 0.291 \times 0.8385] = 184 \text{ W/m}^2$$

$$I_{TLT} = 423 \text{ W/m}^2$$

The corresponding measured value is 379 W/m^2.

Example 4.3.5

Using Gueymard's model, perform calculations on the data given in Example 4.3.1.

We note that SOLALT $= 48°$, $h' = 0.48$. Using Eqs (4.3.3.14)–(4.3.3.19),

$a_0 = -1.81$, $a_1 = 2.26$, $a_2 = -0.78$, $a_3 = 0.0573$ and $G(\text{SOLALT}) = 0.323$ since TLT $= 90°$, $F(\text{TLT}) = 1.00$.

than r_{d0} and r_{d1} are obtained (note: INC $= 51.4°$) as:

$$r_{d0} = 0.8244 \quad \text{and} \quad r_{d1} = 0.4314$$

Now $N_{pt} = 0.4105$ as $Y = 0.4105$. Then Eq. (4.3.3.11) is now used to obtain:

$$I_{D,TLT} = 177 \text{ W/m}^2$$

$$I_{TLT} = 416 \text{ W/m}^2$$

The corresponding measured value is 379 W/m^2.

Example 4.3.6

Using Perez et al.'s model, perform calculations on the data given in Example 4.3.1.

The data on I_B, I_E, cos INC, sin SOLALT and r_B from Example 4.3.2 is used here. Thus:

$$Z = 90 - \text{SOLALT} = 42°$$

$$m = 1.343$$

$$\varepsilon = 2.019 \qquad \text{Eq. (4.3.3.26)}$$

$$\Delta = 0.26231 \qquad \text{Eq. (4.3.3.27)}$$

We note from Table 4.3.1 that the above value of ε lies in the fifth bin. Using the values of F_{11} to F_{23}, we obtain:

$$F_1 = 0.505\,33,\ F_2 = 0.105\,28$$

$$a = \max(0,\ \cos \text{INC}) = 0.6234$$

$$b = \max(\cos 85°,\ \sin \text{SOLAT}) = 0.7435$$

Then, using Eq. (4.3.3.24):

$$I_{D,TLT} = I_D[(1-F_1)\cos^2(\text{TLT}/2) + F_1(a_0/a_1) + F_2 \sin \text{TLT}] = 207\ \text{W/m}^2$$

$$I_{TLT} = 446\ \text{W/m}^2$$

The corresponding measured value is 379 W/m^2.

Example 4.3.7

Using Muneer's model, perform calculations on the data given in Example 4.3.1.

First of all from Eqs (4.3.3.32) and (4.3.3.4) we find TF = 0.6, then using Eq. (4.3.3.31) and noting the values of F and $I_{B,\,TLT}$ from the above examples:

$$I_{D,TLT} = I_D[\text{TF}(1 - F) + Fr_B] = 139\ \text{W/m}^2$$

$$I_{TLT} = I_{D,TLT} + I_{B,TLT} = 418\ \text{W/m}^2$$

The corresponding measured value is 379 W/m^2.

The electronic data file File3-1.Csv, contained in the CD, provides 5 min averages of horizontal and vertical irradiance and illuminance for Edinburgh for 11 and 12 August 1993

(respectively, an overcast and a clear day). Based on these data Figures 4.3.6 and 4.3.7 have been prepared to enable performance evaluation of the above seven slope irradiance models. Further, Figures 4.3.8–4.3.11 provide a finer examination of the models for a non-overcast day (12 August 1993). Tables 4.3.2 and 4.3.3 present the statistical evaluation of the models. The present analysis suggests that the accuracy of instantaneous predictions improves significantly when the isotropic model is replaced with most of the second generation and all of the third generation models. The shortcomings of most of the second generation models are noticeable in handling shaded surfaces (surfaces facing away from the sun), e.g. northern aspects in the northern hemisphere and vice versa. This is due to their assumption of isotropicity for such situations which is contrary to the measured evidence, as shown above.

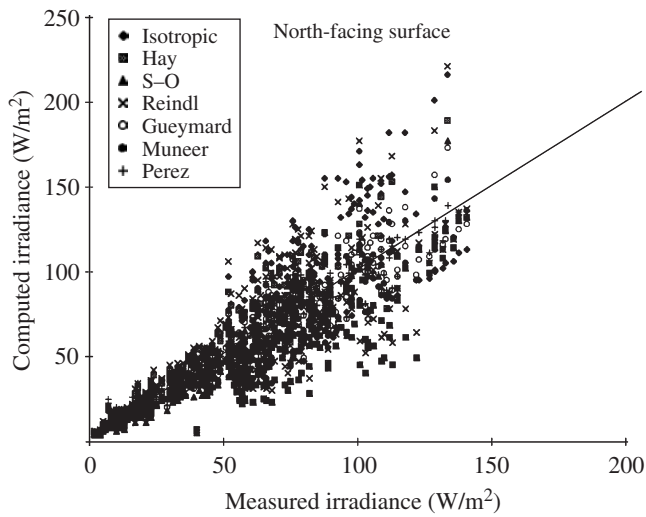

Figure 4.3.6
Evaluation of slope irradiance models for a north-facing surface

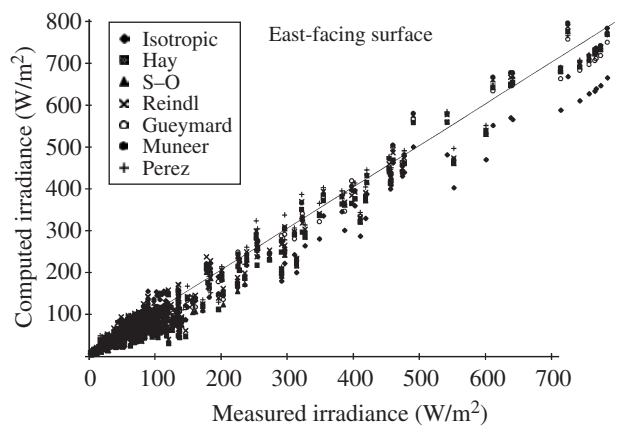

Figure 4.3.7
Evaluation of slope irradiance models for an east-facing surface

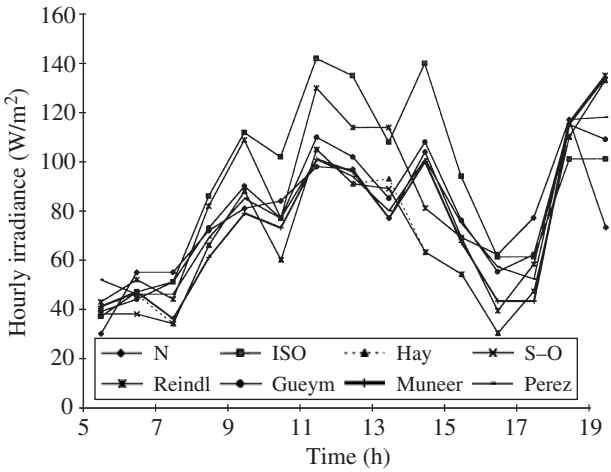

Figure 4.3.8
Measured and estimated irradiance, north-facing surface

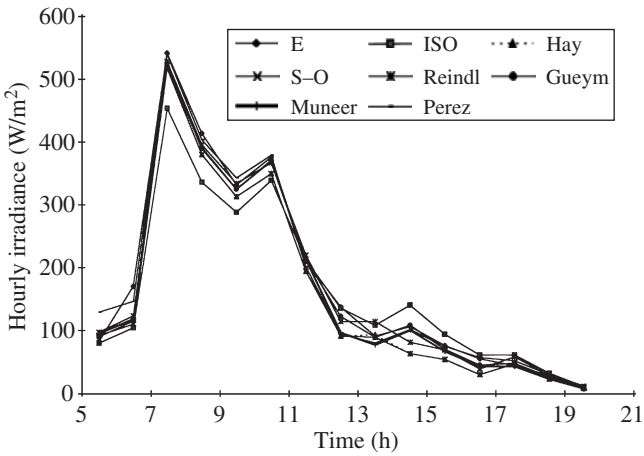

Figure 4.3.9
Measured and estimated irradiance, east-facing surface

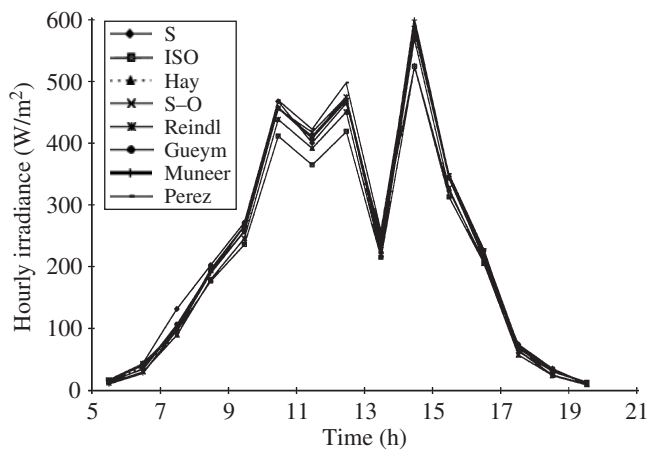

Figure 4.3.10
Measured and estimated irradiance, south-facing surface

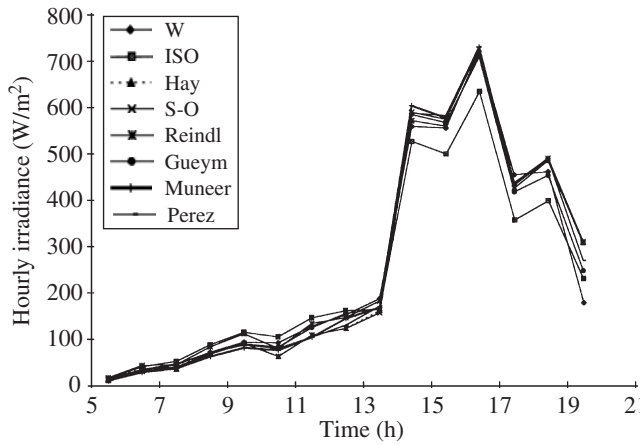

Figure 4.3.11
Measured and estimated irradiance, west-facing surface

Table 4.3.2 Evaluation of slope irradiance models at an hourly level, Edinburgh (55.95°N), August 1993 data (W/m^2)

		North	East	South
Isotropic	MBE	10	−5	10
	RMSE	24	36	25
Hay	MBE	−5	−8	−5
	RMSE	23	28	24
Skartveit and Olseth	MBE	−13	−16	−13
	RMSE	22	30	28
Reindl et al.	MBE	4	−1	4
	RMSE	24	25	24
Gueymard	MBE	−1	−7	−3
	RMSE	12	22	24
Muneer	MBE	−7	−6	1
	RMSE	13	22	27
Perez et al.	MBE	−2	−3	2
	RMSE	10	19	24

Example 4.3.8

Long-term averaged measured horizontal and slope irradiation data is available for Easthampstead, UK (Meteorological Office, 1980). Table 4.3.4 presents such data for June (top part):

(a) Using the daily totals (bold figures) compute the hourly horizontal global and diffuse irradiation. Compare these with given hourly data.
(b) Compute the vertical irradiation for north and south using the above computed hourly horizontal global and diffuse irradiation. Perform the estimations using at least one model from each of the above three generation groups (Sections 4.3.1–4.3.3).

Table 4.3.3 Measured and computed slope irradiation for Edinburgh (55.95°N), 12 August 1993 (W/m^2)

Hour	*G*	*D*	*North*	*Iso*	*Hay*	*S–O*	*Reindl*	*Gueymard*	*Muneer*	*Perez*
5.5	38	31	30	37	41	38	43	39	41	52
6.5	96	80	55	47	46	38	52	44	47	46
7.5	269	102	55	51	34	34	44	51	36	46
8.5	329	172	72	86	66	66	82	73	61	69
9.5	391	223	81	112	88	88	109	90	79	85
10.5	581	204	84	102	60	60	77	77	73	77
11.5	542	284	98	142	105	105	130	110	101	101
12.5	594	269	97	135	91	91	114	102	96	94
13.5	340	215	77	108	93	89	114	85	77	80
14.5	763	280	104	140	63	63	81	108	100	101
15.5	507	187	69	94	54	54	69	76	67	75
16.5	422	121	62	61	30	30	39	55	43	57
17.5	221	122	77	61	47	47	58	62	43	52
18.5	132	64	117	101	110	110	116	115	115	117
19.5	32	22	73	101	133	133	135	109	134	118

Hour	*G*	*D*	*East*	*Iso*	*Hay*	*S–O*	*Reindl*	*Gueymard*	*Muneer*	*Perez*
5.5	38	31	83	80	95	92	97	90	95	129
6.5	96	80	170	104	118	110	123	115	118	146
7.5	269	102	542	454	518	518	528	519	527	540
8.5	329	172	414	336	380	380	396	392	390	404
9.5	391	223	332	288	313	313	334	325	325	343
10.5	581	204	376	339	350	350	367	371	370	379
11.5	542	284	210	212	194	194	220	213	213	201
12.5	594	269	137	135	91	91	114	122	96	94
13.5	340	215	91	108	93	89	114	89	77	80
14.5	763	280	106	140	63	63	81	108	100	101
15.5	507	187	76	94	54	54	69	70	67	75
16.5	422	121	55	61	30	30	39	45	43	57
17.5	221	122	44	61	47	47	58	48	43	52
18.5	132	64	29	32	23	23	29	26	23	30
19.5	32	22	8	11	9	9	11	9	8	12

Hour	*G*	*D*	*South*	*Iso*	*Hay*	*S–O*	*Reindl*	*Gueymard*	*Muneer*	*Perez*
5.5	38	31	13	16	15	12	17	13	11	15
6.5	96	80	44	40	38	30	43	35	28	34
7.5	269	102	131	96	89	89	98	106	97	102
8.5	329	172	202	176	179	179	195	192	189	190
9.5	391	223	271	235	245	245	266	256	257	265
10.5	581	204	467	411	438	438	455	456	457	469
11.5	542	284	400	364	391	391	417	407	410	422
12.5	594	269	464	418	450	450	474	468	472	497
13.5	340	215	250	214	224	219	244	233	230	257
14.5	763	280	524	523	568	568	585	580	599	583
15.5	507	187	322	312	326	326	342	344	345	349
16.5	422	121	209	205	204	204	213	224	217	227
17.5	221	122	73	68	56	56	67	71	63	61
18.5	132	64	34	32	23	23	29	31	23	30
19.5	32	22	9	11	9	9	11	9	8	12

(*continued*)

Table 4.3.3 *Continued*

Hour	*G*	*D*	*West*	*Iso*	*Hay*	*S–O*	*Reindl*	*Gueymard*	*Muneer*	*Perez*
5.5	38	31	11	16	15	12	17	13	11	15
6.5	96	80	31	40	38	30	43	33	28	34
7.5	269	102	44	51	34	34	44	39	36	46
8.5	329	172	70	86	66	66	82	67	61	69
9.5	391	223	91	112	88	88	109	87	79	85
10.5	581	204	89	102	60	60	77	80	73	77
11.5	542	284	124	142	105	105	130	121	101	101
12.5	594	269	148	157	119	119	142	151	140	126
13.5	340	215	182	159	157	152	177	161	163	166
14.5	763	280	554	522	567	567	585	580	599	583
15.5	507	187	550	494	554	554	569	562	572	577
16.5	422	121	716	628	711	711	720	703	724	725
17.5	221	122	448	350	419	419	430	411	426	431
18.5	132	64	454	391	478	478	483	446	482	482
19.5	32	22	170	222	300	300	302	239	301	261

Iso: Isotropic.
S–O: Skartveit and Olseth.

(c) Sum the computed hourly vertical surface irradiation to obtain corresponding daily totals.

Comment on the accuracy obtained via the above calculation chain, e.g. horizontal daily total to horizontal hourly irradiation, hourly slope calculation and then summing to obtain daily slope irradiation.

Table 4.3.4 shows the results for the computational chain, e.g. from horizontal daily to horizontal hourly to slope hourly values. The comparison of daily totals for slope irradiation shows a good performance for all three models: isotropic, Reindl and Muneer. Note that the isotropic model is on par with the other two models considered herein. This is due to the considerable dampening effect in the averaging of data over very many days. However, on an instantaneous or an hour-by-hour level, the isotropic model does generate the order of errors shown above, e.g. Figures 4.3.8–4.3.11 and Table 4.3.3.

4.4 Slope illuminance models

In Chapter 3 models were presented which enable horizontal diffuse and global illuminance to be estimated from the corresponding irradiance quantities. The next stage in the analysis is to predict slope illuminance. Slope illuminance models may be used effectively to characterise the dynamic variations of the internal illuminance in buildings. The building simulation package SERI-RES (Haves, 1988) uses such a scheme.

The concept of the CIE overcast sky daylight factor was introduced in Chapter 3. It was shown in Section 4.3 that under non-overcast conditions, the sky is brighter in the vicinity of the sun and horizon. Orientation factors, such as those given in *CIBSE Guide A2*

Table 4.3.4 Evaluation of r_G (Eq. (3.1.1)), r_D (Eq. (3.2.1)), isotropic (Eq. (4.3.1.1)), Reindl et al. (Eq. (4.3.2.5)) and Muneer (Eq. (4.3.3.31)) models

	Hour															
	5.5	6.5	7.5	8.5	9.5	10.5	11.5	12.5	13.5	14.5	15.5	16.5	17.5	18.5	Daily totals	Error (%)
Measured data for June																
G	108	214	325	411	483	533	547	539	514	467	392	306	208	111	5224	
D	67	117	164	206	239	269	283	281	267	244	214	169	122	72	2767	
North	100	100	83	86	92	97	100	100	97	92	86	81	97	97	1405	
South	31	53	94	164	231	269	283	275	253	208	150	89	53	31	2205	
Computed values																
G	116	203	299	393	476	538	571	571	538	476	393	299	203	116	5192	
D	74	122	167	208	242	265	278	278	265	242	208	167	122	74	2712	
North																
Isotropic	98	93	84	104	121	133	139	139	133	121	104	84	93	98	1541	9.7
Reindl et al.	115	102	83	102	116	125	130	130	125	116	102	83	102	115	1544	9.9
Muneer	110	95	60	74	86	94	99	99	94	86	74	60	95	110	1237	−12.0
South																
Isotropic	37	61	92	159	221	269	296	296	269	221	159	92	61	37	2268	2.8
Reindl et al.	39	63	93	170	240	295	325	325	295	240	170	93	63	39	2448	11.0
Muneer	26	44	85	161	231	286	316	316	286	231	161	85	44	26	2297	4.1

(CIBSE, 1982), may be used to take account of windows facing the sun. However, orientation factors fail to take account of the dynamic variations in daylight as pointed out by Haves and Littlefair (1988). The latter team has introduced a procedure to address the above-mentioned shortcomings of the CIE daylight factor. Haves and Littlefair's (1988) procedure to obtain internal illuminance is summarised as follows:

$$IL_{\text{in}} = IL_{\text{TLT}}\, r \tag{4.4.1}$$

where IL_{in} is the desired horizontal internal illuminance and IL_{TLT} the external slope illuminance. r is defined as the modified daylight factor, it being the ratio of the internal to external illuminance in the plane of the window with a tilt angle of TLT:

$$r = d\,/\,d_{\text{TLT}} \tag{4.4.2}$$

where d is the standard CIE daylight factor (see Chapter 3) and d_{TLT} is the ratio of the exterior illuminance in the plane of the window to the exterior horizontal illuminance under CIE overcast sky conditions. For an unshaded vertical window, $d_{\text{TLT}} = 0.396 + 0.5\rho$. The procedure for obtaining ρ the albedo of the underlying land mass, is presented in Chapter 6. Two models which enable estimation of IL_{TLT} are presented below.

4.4.1 Perez et al.'s model

The Perez et al. (1990) illuminance model is based on the same principles as its irradiance counterpart. Thus, Eqs (4.3.3.24)–(4.3.3.29) are applicable with IL_{G} and IL_{D} respectively substituted for I_{G} and I_{D}. The required coefficients are given in Table 4.3.1.

4.4.2 Muneer–Angus Model

This model (Muneer and Angus, 1993; Muneer, 1995) is along the lines of Muneer's (1990b) work on solar irradiance modelling. Thus, Eqs (4.4.3) and (4.4.4) are analogous to the corresponding slope irradiance relationships (see Section 4.3.3.5):

$$IL_{\beta} = (IL_{\text{G}} - IL_{\text{D}})r_{\text{B}} + IL_{\text{D}}[(1 - F_{\text{IL}})\text{TF} + F_{\text{IL}} r_{\text{B}}] \tag{4.4.3}$$

where

$$F_{\text{IL}} = (IL_{\text{G}} - IL_{\text{D}})/IL_{\text{E}} \tag{4.4.4}$$

TF is obtained from Eq. (4.3.3.4) after estimating b as follows:

$$\frac{2b}{\pi(3 + 2b)} = 0.111F_{\text{IL}} - 4.317F_{\text{IL}}^2 \tag{4.4.5}$$

IL_{E} in Eq. (4.4.4) is the horizontal extraterrestrial illuminance, the product of extraterrestrial irradiance and its luminous efficacy of 96.8 lm/W (Muneer and Angus, 1993).

Prog4-3.For enables computation of slope illuminance based on Perez et al. and Muneer–Angus models.

Example 4.4.1

Table 4.4.1 provides the measured horizontal and slope illuminance data for Edinburgh (55.95°N and 3.2°W). Obtain vertical surface illuminance for the principal aspects and compare these with the above measured values.

The computed values of slope illuminance, obtained via Prog4-3.For, have been included in Table 4.4.1 to enable the required comparison. The MBEs show a remarkable performance of both models. As a matter of fact the errors involved with the above-mentioned third generation irradiance and illuminance models are of the order of the measurement uncertainties, as also pointed out by Perez et al. (1990). A fuller discussion on the measurement errors is provided in Chapter 1.

4.4.3 Kinghorn–Muneer model

The Kinghorn and Muneer (2000) model is a further development of the Muneer–Angus model introduced in Section 4.4.2. Recall that for any sloped surface of angle β, TF represents the ratio of background-sky illuminance on a slope to the horizontal diffuse illuminance:

$$\mathrm{TF} = \frac{IL_{\mathrm{TLT}}}{IL_{\mathrm{D}}} = \cos^2\frac{\beta}{2} + \left\{\frac{2b}{\pi(3+2b)}\left[\sin\beta - \beta\cos\beta - \pi\sin^2\frac{\beta}{2}\right]\right\} \tag{4.4.6}$$

Kinghorn and Muneer have shown that for the respective cases, i.e. shaded (sh) and sun-facing (sf) components of the sky vault, the tilt factor varies with clearness index K_{t}. The respective tilt factors are obtained from:

$$\mathrm{TF}_{\mathrm{sh}} = 0.4 - 0.0014K_{\mathrm{t}} - 0.0793K_{\mathrm{t}}^2 \tag{4.4.7}$$

$$\mathrm{TF}_{\mathrm{sf}} = 0.4 + 0.1991K_{\mathrm{t}} + 0.4755K_{\mathrm{t}}^2 \tag{4.4.8}$$

Once TF values are obtained, values of b_{sf} and b_{sh} are routinely returned from Eq. (4.4.6). Note that in the present context b_{sf} and b_{sh} are the luminance distribution indices of the sky vault. The latter indices are also used to obtain the zenith luminance (see Eq. (3.5.25)) and their use for obtaining the quantities under discussion is demonstrated via the following example.

Example 4.4.2

Tables 4.4.2 and 4.4.3 respectively present measured data for slope illuminance and zenith luminance. In each case the horizontal global and diffuse illuminance data are provided. Use the Kinghorn and Muneer (2000) model to estimate the above quantities and compare them against the measured data set.

Table 4.4.1 Comparison of measured and computed illuminance for Edinburgh, 12 August 1993

Hour	I_G (W/m^2)	I_D (W/m^2)	IL_G (klx)	IL_D (klx)	IL_N (klx)	IL_E (klx)	IL_S (klx)	IL_W (klx)	North		East		South		West	
									Muneer	Perez	Muneer	Perez	Muneer	Perez	Muneer	Perez
8.5	329	172	37.9	22.0	10.0	46.3	25.7	9.2	7.8	8.6	44.4	47.9	22.7	22.8	7.8	8.6
9.5	391	223	44.8	28.0	11.1	38.1	34.3	11.8	10.0	10.2	37.1	41.5	29.9	32.0	10.0	10.2
10.5	581	204	66.5	27.0	11.7	43.8	59.1	12.1	9.6	9.4	46.8	45.2	56.6	55.9	9.6	9.4
11.5	542	284	62.1	35.9	13.6	25.0	50.7	17.0	12.8	11.9	27.2	24.3	48.5	51.5	12.8	11.9
12.5	594	269	67.6	34.4	13.1	16.8	58.9	20.1	12.3	10.8	12.3	10.8	56.6	60.0	20.5	14.6
13.5	340	215	37.9	26.7	10.7	11.4	31.3	23.0	9.5	9.3	9.5	9.3	24.7	31.5	18.3	20.0
14.5	763	280	85.5	37.3	14.1	13.5	66.4	69.6	13.3	12.2	13.3	12.2	75.2	67.3	75.2	67.2
15.5	507	187	57.0	24.7	10.2	9.6	41.4	67.8	8.8	9.3	8.8	9.3	42.6	40.2	67.2	65.9
16.5	422	121	48.3	16.4	9.5	7.6	28.8	86.3	5.8	7.3	5.8	7.3	28.6	26.1	85.9	81.2
								MBE	−1.6	−1.7	−0.8	−0.5	−1.2	−1.0	−1.1	−3.1

Table 4.4.2 Input/Output data for Example 4.4.2: Garston, 1 August 1991

Hour	Minute	I_G (W/m^2)	I_D (W/m^2)	I_{LG} (klx)	I_{LD} (klx)	Measured data (klx)				Computed data (klx)			
						I_{LN}	I_{LE}	I_{LS}	I_{LW}	I_{LN}	I_{LE}	I_{LS}	I_{LW}
8	30	505	132	58.3	21.2	8.4	76.2	30.8	5.7	7.8	67.0	28.5	7.8
9	30	653	217	73.2	31.3	10.0	63.0	46.4	10.8	11.3	58.7	44.5	11.3
10	30	428	307	50.8	37.3	11.7	26.6	33.4	11.6	14.4	26.7	29.7	14.4
11	30	309	286	37.6	35.0	11.8	21.9	22.2	12.8	13.8	17.4	19.1	13.8
12	30	515	390	60.5	46.9	12.7	19.6	34.6	18.5	17.9	27.7	37.4	17.9
13	30	98	88	13.0	12.1	5.4	5.3	6.0	7.1	4.8	4.8	5.7	5.5
14	30	810	324	89.9	41.4	11.5	11.6	52.0	64.1	14.1	14.1	57.8	75.4
15	30	229	219	27.4	26.1	10.6	9.2	11.2	15.0	10.2	10.2	13.5	14.9
16	30	443	270	49.9	35.0	13.6	10.0	18.9	55.1	12.6	12.6	24.7	66.0

Table 4.4.3 Input/Output data for Example 4.4.2: Garston, 1 August 1991

				Measured data			Muneer–Kinghorn			Perez et al.		
Hour	Minute	I_G (W/m^2)	I_D (W/m^2)	IL_G (klx)	IL_D (klx)	L_z (kcd/m^2)	IL_G (klx)	IL_D (klx)	L_z (kcd/m^2)	IL_G (klx)	IL_D (klx)	L_z (kcd/m^2)
11	0	500	355	59.5	42.3	16.9	57.2	43.5	13.1	55.8	41.3	12.9
11	5	455	319	48.6	37.8	13.8	53.1	39.0	13.1	51.1	37.4	11.7
11	10	364	307	44.8	36.7	14.8	43.5	37.7	13.5	40.8	35.3	12.8
11	15	277	249	33.4	29.9	8.9	34.0	30.8	11.6	31.1	28.9	10.7
11	20	205	193	25.0	23.5	11.2	25.8	24.1	9.3	24.8	23.5	9.7
11	25	228	219	27.9	26.6	8.5	28.5	27.3	10.4	27.4	26.4	10.8
11	30	309	286	37.6	35.0	8.4	37.6	35.3	13.1	34.7	33.0	12.3
11	35	703	373	76.8	46.0	16.6	79.3	46.1	11.5	77.3	43.8	14.1
11	40	592	283	67.8	36.5	9.4	67.6	34.7	10.3	65.0	35.9	11.0
11	45	295	258	37.6	33.0	9.8	36.1	31.9	11.9	33.1	29.9	11.3
11	50	350	299	43.7	37.0	12.5	42.1	36.8	13.4	39.3	34.5	12.8
11	55	400	336	47.7	40.6	16.6	47.5	41.2	14.6	44.8	38.6	14.2

The required comparisons are provided in the above-mentioned tables, the computations having been obtained via execution of Prog3-4b.For. Note that in Table 4.4.3 estimates from Perez et al. zenith luminance model have additionally been provided.

4.4.3.1 Slope irradiance and illuminance for low solar altitudes

It was mentioned in Chapter 3 that low solar altitudes pose a special problem for the computation of irradiation. Slope energy calculations share this difficulty, wherein an unusually high value may be returned for the slope beam quantity. This is due to the 1/sin(SOLALT) term in Eq. (4.1.1b). Some slope diffuse irradiance as well as slope illuminance models may also be affected by the above mathematical function. It is conventional that for instances when SOLALT $< 5°$ the slope irradiance or illuminance is set to a nil value. However, an alternate solution would be to set the slope beam energy to nil and use the isotropic model for obtaining the slope diffuse energy. Bearing in mind that during instances of low solar altitude (sunrise and sunset times) most slope surfaces are in shade. This assumption is quite justifiable.

4.5 Radiance and luminance distributions

The diffuse irradiance of sloping surfaces may be either measured, or calculated from the angular sky radiance distribution. Direct measurements, however, often include a component of radiation reflected onto the slope from neighbouring surfaces. This reflected radiation can be a large fraction of the diffuse irradiance, particularly on steep slopes and under cloudless skies when the ratio of diffuse to global radiation is small. On the other hand, separation of direct and diffuse solar radiation components by instruments with shade rings or discs excludes a fraction of circumsolar radiation which depends on shade-ring dimensions. The alternative approach of calculating the diffuse irradiance of a sloping plane by integrating the radiance distribution of the sky 'seen' by the plane is attractive.

On the daylighting front, recent advances in computer graphics technology allow the realistic modelling of complex building interiors with a minimal training time. One such modelling and visualisation package is the RADIANCE lighting simulation system (Ward, 1994). The main features of RADIANCE have been enumerated by Mardaljevic (1995) as follows:

(a) It is a physically based program which allows precise estimation of interior illuminance.
(b) It has the capability to model geometries with realistic, luminance distributions.
(c) It supports a wide variety of reflection and transmission models.
(d) It can import building scene descriptions from CAD systems.
(e) It can estimate daylight factors using real sky luminance distributions, rather than assuming the worst case scenario used by the CIE overcast sky model.

Mardaljevic (1995) has undertaken the first comparison of RADIANCE results to actual room illuminances under a real sky. Using 700 scans of measured sky luminance measurements, undertaken by the Building Research Establishment at Watford, illuminance predictions were found to agree quite favourably with the internal illuminances.

The RADIANCE system is free, copyrighted UNIX-based software produced at the Lawrence Berkeley Laboratory in California. Details of acquiring this software have been given by Mardaljevic (1995).

With the ever increasing processing power of PCs, more development and simulation tools such as RADIANCE will be used by architectural practices and building services engineers. The main engine in packages such as RADIANCE is the sky luminance distribution model. A discussion of some of these models follows.

4.5.1 Overcast sky distributions

Several authors have described the radiance distribution of overcast skies by an equation similar in form to Eq. (4.3.3.1):

$$R_\theta = R_z(1 + b\cos\theta)/(1 + b) \tag{4.5.1}$$

where R_θ and R_z are expressed in W/sr-m^2. R_θ and R_z are the respective radiance counterparts of L_θ and L_z.

The number $1 + b$ is the ratio of radiance at the zenith to that at the horizon. The standard overcast sky (Moon and Spencer, 1942) uses this formula with $b = 2$ but Walsh (1961) suggested that $b = 1.5$ fitted the mean overcast sky more accurately. Goudriaan (1977) and Fritz (1955) gave a theoretical foundation for this form of distribution on the basis of an analysis of scattering and attenuation in clouds. Goudriaan's analysis shows that the value of b depends on surface albedo, ρ, according to $b = 2(1 - \rho)/(1 + 2\rho)$. For a typical range of surface albedo of 0.1–0.2, b should vary between 1.5 and 1.14. Fritz derived the relationship of b with ρ as $b = 1.5(1 - \rho)/(1 + \rho)$. With the same range of surface albedo, 0.1–0.2 the value of b according to the Fritz formula varies between 1.23 and 1.0.

Table 4.5.1 summarises the results obtained by the above authors.

The angular distribution of overcast radiation was measured in detail by Steven and Unsworth (1980). Their averaged $b = 1.23$ is smaller than Moon and Spencer's value given above.

Under overcast skies Grace (1971) has noted rapid changes of radiance distribution when instantaneous measurements are carried out. However, hourly averages are less variable, e.g. Steven and Unsworth (1980) have shown that the coefficient of variation for b is typically about 0.2.

Table 4.5.1 Values of coefficient *b* (Eq. (4.5.1)), overcast sky

Isotropic sky	0
Moon and Spencer (1942)	2
Fritz (1955)	1.0 to 1.23
Walsh (1961)	1.5
Goudriaan (1977)	1.14 to 1.5
Steven and Unsworth (1980)	1.12 to 1.36
Gueymard (1987)	1.5
Muneer (1987)	1.68

Nagata (1990a) has undertaken a series of radiance distribution measurements at Fukui, Japan. Based on several years of data, he has proposed the following equation for overcast sky radiance distribution:

$$R_\theta = R_z(2 + 3\sin\theta)/5 \tag{4.5.2}$$

Integrating the above distribution results in:

$$I_G = (4\pi/5)R_z \tag{4.5.3}$$

from which R_z may be obtained if the value of I_G is available. Nagata (1990b) has also provided clear-sky radiance distribution functions. These functions are similar in nature to those proposed by Steven and Unsworth (1979). The clear-sky radiance distributions are given below.

4.5.2 Clear-sky distributions

Measurements of the photometric or luminance distribution of a clear-sky have been reported by Kimball and Hand (1921), Peyre (1927), Hopkinson (1954), Dogniaux (1954) and Kondratyev (1969). Most of these published results represent only one or two positions of the sun in the sky on a limited number of occasions. However, the distribution of diffuse radiation is strongly dependent on the solar zenith distance and varies to some extent with atmospheric turbidity.

The distribution of clear-sky diffuse radiation was first explained theoretically by Lord Rayleigh (1871). Since then a number of attempts have been made to fit the theory to the observed distributions. In Pokrowski's (1929) formulation, R is expressed as a function of zenith angle θ and azimuth ϕ of a sky patch (SP) and ζ, the angle between the point (θ, ϕ) and the sun:

$$R(\theta,\xi) = S\{(1 + \cos^2\xi)/(1 - \cos\xi) + k\}\{1 - \exp(-\rho_s \sec\theta)\} \tag{4.5.4}$$

where S is a scaling factor, ρ_s is a scattering coefficient and k an empirical constant to allow for multiple scattering. Pokrowski proposed the values 0.32 and 5 for ρ_s and k respectively. Hopkinson (1954), however, found better agreement with measured luminance distributions with the arbitrary constant omitted, i.e. with $k = 0$ and $\rho_s = 0.32$.

Steven (1977a) measured the radiance from cloudless skies at Sutton Bonnington on a large number of days of a wide range of turbidities. When the measurements of radiance were normalised with respect to the diffuse irradiance of a horizontal surface, they were found to be independent of turbidity. On this basis standard distributions of radiance from cloudless skies were proposed as:

$$R(\theta,\xi) = \pi^{-1}\{d_1 + d_2\exp(d_3\xi) + d_4\cos 2\xi\}\{1 - \exp(d_5\sec\theta)\} \tag{4.5.5}$$

Table 4.5.2 provides the coefficients for the above model.

Table 4.5.2 Coefficients to be used in Eq. (4.5.5)

	Solar zenith angle (deg)			
	35	45	55	65
d_1	0.61	0.65	0.73	0.76
d_2	11.90	10.70	11.10	13.00
d_3	−2.97	−2.82	−2.97	−3.09
d_4	−0.12	−0.20	−0.07	−0.17
d_5	−0.45	−0.48	−0.48	−0.42

4.5.3 Intermediate-sky distributions

The CIE overcast sky estimates the minimum luminance daylight quantity as it represents only those conditions when the sky is completely covered with thick and dark clouds. However, it is hardly the representative design condition for locations such as those lying within or near the tropical belt. For example, in Japan the frequency of occurrences of the clear, the intermediate and the overcast skies were respectively found to be 5%, 70% and 25% (Nakamura et al. 1985). The CIE standard overcast sky was thus found to be inadequate to describe the real interior daylit environment. It has been argued that for fuller exploitation of daylight in buildings prediction tools should be based upon the real, rather than a conservative estimate of the sky luminance distribution.

Based on a 10 year measurement programme in Japan, an intermediate sky has been proposed by Nakamura et al. (1985). The varying luminance distributions were found to lie in between the CIE standard clear sky and the CIE standard overcast sky.

Tables 4.5.3–4.5.9 show the above-mentioned measured luminance ratios of the given sky elements and the zenith.

4.5.4 All-sky distributions

Skylight is a non-uniform extended light source. Its intensity and spatial distribution vary as a function of prevailing sky conditions. In addition to direct sunlight, sky luminance angular distribution is the necessary and sufficient information required for calculating daylight penetration into any properly described environment. Because actual sky luminance distribution data are available only in a handful of locations, it is essential to be able to estimate skylight distribution from routine measurements such as irradiance. In the following section luminance distributions for all-sky conditions are presented.

4.5.4.1 Perez et al.'s model

Perez et al. (1993) have presented an all-sky model which is a generalisation of the CIE standard clear-sky formula (CIE, 1973). This expression includes five coefficients that can be adjusted to account for luminance distributions ranging from totally overcast to clear skies. The relative luminance l_v defined as the ratio between the sky luminance at the considered point L_v and the luminance of an arbitrary reference point is given by:

$$l_v = f(\theta, \xi) = [1 + a \exp(b/\cos\theta)][1 + c \exp(\mathrm{d}\xi) + e \cos \xi^2] \tag{4.5.6}$$

Table 4.5.3 Measured luminance distribution data for intermediate sky, SOLALT = 10° (Nakamura et al., 1985)

	Altitude angle of the sky patch (deg)									
AS (deg)	0	10	20	30	40	50	60	70	80	90
0	2.82	3.44	3.81	3.60	2.80	1.97	1.50	1.26	1.10	1.00
10	2.68	3.20	3.54	3.33	2.62	1.95	1.50	1.25	1.09	1.00
20	2.42	2.80	3.04	2.93	2.43	1.91	1.50	1.25	1.08	1.00
30	2.13	2.46	2.73	2.60	2.20	1.81	1.47	1.24	1.08	1.00
40	1.91	2.19	2.38	2.30	2.03	1.75	1.45	1.22	1.08	1.00
50	1.79	1.98	2.10	2.06	1.90	1.68	1.42	1.21	1.07	1.00
60	1.70	1.80	1.89	1.90	1.80	1.59	1.39	1.19	1.07	1.00
70	1.60	1.71	1.79	1.80	1.70	1.52	1.34	1.16	1.06	1.00
80	1.40	1.60	1.71	1.72	1.62	1.44	1.27	1.13	1.05	1.00
90	1.20	1.43	1.60	1.63	1.52	1.34	1.20	1.10	1.03	1.00
100	1.06	1.25	1.43	1.46	1.38	1.23	1.11	1.04	1.01	1.00
110	0.97	1.09	1.20	1.24	1.22	1.10	1.01	0.98	0.98	1.00
120	0.95	1.00	1.06	1.06	1.01	0.96	0.94	0.94	0.96	1.00
130	0.94	0.94	0.95	0.94	0.91	0.92	0.91	0.92	0.95	1.00
140	0.93	0.92	0.90	0.90	0.91	0.91	0.90	0.91	0.95	1.00
150	0.92	0.90	0.91	0.94	0.94	0.92	0.90	0.91	0.94	1.00
160	0.90	0.92	0.98	1.01	0.99	0.94	0.91	0.90	0.94	1.00
170	0.93	0.96	1.01	1.05	1.04	0.98	0.92	0.90	0.94	1.00
180	0.94	0.97	1.03	1.07	1.05	1.00	0.93	0.90	0.93	1.00

AS: Azimuthal separation between the sky patch and sun.

Table 4.5.4 Measured luminance distribution data for intermediate sky, SOLALT = 20° (Nakamura et al., 1985)

	Altitude angle of the sky patch (deg)									
AS (deg)	0	10	20	30	40	50	60	70	80	90
0	2.53	5.00	14.00	5.10	3.49	2.51	1.87	1.42	1.17	1.00
10	2.37	4.26	5.23	4.50	3.41	2.46	1.83	1.40	1.16	1.00
20	2.08	3.28	3.81	3.72	3.10	2.37	1.75	1.38	1.15	1.00
30	1.83	2.53	3.00	3.00	2.70	2.15	1.67	1.35	1.14	1.00
40	1.65	1.92	2.30	2.49	2.34	1.95	1.60	1.33	1.13	1.00
50	1.53	1.73	1.95	2.08	2.02	1.80	1.54	1.31	1.11	1.00
60	1.42	1.61	1.73	1.83	1.80	1.68	1.46	1.25	1.10	1.00
70	1.29	1.52	1.65	1.70	1.64	1.52	1.34	1.18	1.08	1.00
80	1.08	1.35	1.53	1.58	1.52	1.37	1.21	1.10	1.03	1.00
90	0.98	1.16	1.33	1.40	1.33	1.21	1.10	1.03	1.01	1.00
100	0.94	1.00	1.11	1.20	1.16	1.07	1.00	0.98	0.99	1.00
110	0.90	0.92	0.98	1.02	1.00	0.95	0.93	0.94	0.96	1.00
120	0.86	0.88	0.90	0.89	0.88	0.88	0.88	0.90	0.94	1.00
130	0.84	0.84	0.83	0.81	0.81	0.82	0.83	0.86	0.92	1.00
140	0.83	0.83	0.81	0.80	0.80	0.80	0.81	0.84	0.90	1.00
150	0.83	0.82	0.80	0.81	0.81	0.81	0.81	0.83	0.90	1.00
160	0.82	0.81	0.80	0.81	0.81	0.81	0.80	0.82	0.89	1.00
170	0.82	0.81	0.81	0.82	0.82	0.81	0.80	0.82	0.89	1.00
180	0.81	0.80	0.82	0.83	0.82	0.81	0.80	0.82	0.89	1.00

AS: Azimuthal separation between the sky patch and sun.

Table 4.5.5 Measured luminance distribution data for intermediate sky, SOLALT = 30° (Nakamura et al., 1985)

	Altitude angle of the sky patch (deg)									
AS (deg)	0	10	20	30	40	50	60	70	80	90
0	2.09	3.00	5.20	11.50	5.08	2.93	2.04	1.56	1.25	1.00
10	2.00	2.72	4.20	5.20	4.12	2.86	2.03	1.55	1.24	1.00
20	1.70	2.24	2.86	3.25	2.95	2.48	1.96	1.53	1.23	1.00
30	1.52	1.86	2.23	2.56	2.46	2.17	1.86	1.49	1.12	1.00
40	1.40	1.66	1.89	2.15	2.19	2.02	1.73	1.41	1.18	1.00
50	1.30	1.53	1.71	1.89	1.94	1.78	1.53	1.29	1.22	1.00
60	1.19	1.38	1.55	1.66	1.68	1.56	1.34	1.19	1.08	1.00
70	1.03	1.23	1.39	1.46	1.47	1.38	1.21	1.11	1.05	1.00
80	0.94	1.09	1.21	1.30	1.28	1.20	1.13	1.07	1.03	1.00
90	0.87	0.98	1.08	1.15	1.11	1.06	1.04	1.02	1.00	1.00
100	0.82	0.90	0.95	0.97	0.96	0.95	0.94	0.95	0.97	1.00
110	0.78	0.82	0.83	0.83	0.84	0.85	0.86	0.90	0.95	1.00
120	0.75	0.75	0.75	0.74	0.75	0.77	0.80	0.85	0.92	1.00
130	0.73	0.71	0.70	0.69	0.70	0.72	0.75	0.81	0.89	1.00
140	0.70	0.69	0.68	0.68	0.68	0.69	0.72	0.79	0.87	1.00
150	0.68	0.67	0.67	0.67	0.68	0.68	0.71	0.77	0.86	1.00
160	0.66	0.66	0.66	0.67	0.68	0.67	0.70	0.76	0.85	1.00
170	0.64	0.65	0.66	0.68	0.68	0.67	0.69	0.76	0.85	1.00
180	0.63	0.65	0.67	0.68	0.68	0.67	0.69	0.75	0.84	1.00

AS: Azimuthal separation between the sky patch and sun.

Table 4.5.6 Measured luminance distribution data for intermediate sky, SOLALT = 40° (Nakamura et al., 1985)

	Altitude angle of the sky patch (deg)									
AS (deg)	0	10	20	30	40	50	60	70	80	90
0	1.53	1.87	2.26	3.30	7.60	3.50	2.26	1.63	1.29	1.00
10	1.50	1.82	2.16	2.94	3.95	3.08	2.19	1.62	1.27	1.00
20	1.40	1.72	1.95	2.40	2.65	2.45	2.04	1.57	1.24	1.00
30	1.30	1.57	1.72	1.93	2.60	2.03	1.80	1.48	1.21	1.00
40	1.19	1.42	1.59	1.74	1.79	1.75	1.59	1.38	1.18	1.00
50	1.08	1.28	1.43	1.54	1.60	1.53	1.42	1.28	1.13	1.00
60	0.96	1.16	1.30	1.37	1.42	1.36	1.27	1.18	1.08	1.00
70	0.85	1.03	1.16	1.26	1.27	1.22	1.16	1.10	1.05	1.00
80	0.75	0.91	1.04	1.13	1.14	1.12	1.09	1.06	1.03	1.00
90	0.64	0.80	0.92	1.01	1.03	1.02	1.02	1.01	1.00	1.00
100	0.57	0.71	0.80	0.86	0.89	0.90	0.91	0.94	0.97	1.00
110	0.53	0.62	0.69	0.74	0.77	0.79	0.83	0.88	0.94	1.00
120	0.50	0.57	0.62	0.65	0.68	0.71	0.76	0.82	0.91	1.00
130	0.48	0.53	0.57	0.60	0.63	0.66	0.70	0.77	0.87	1.00
140	0.46	0.51	0.54	0.56	0.59	0.62	0.67	0.74	0.85	1.00
150	0.44	0.49	0.52	0.54	0.56	0.59	0.64	0.72	0.83	1.00
160	0.43	0.48	0.51	0.52	0.54	0.57	0.62	0.70	0.82	1.00
170	0.42	0.47	0.50	0.51	0.53	0.56	0.61	0.69	0.81	1.00
180	0.42	0.47	0.49	0.51	0.52	0.55	0.60	0.68	0.80	1.00

AS: Azimuthal separation between the sky patch and sun.

Table 4.5.7 Measured luminance distribution data for intermediate sky, SOLALT = 50° (Nakamura et al., 1985)

	Altitude angle of the sky patch (deg)									
AS (deg)	0	10	20	30	40	50	60	70	80	90
0	1.11	1.47	1.67	2.03	2.82	5.60	3.05	2.02	1.39	1.00
10	1.10	1.44	1.67	2.00	2.60	3.45	2.80	1.95	1.35	1.00
20	1.05	1.36	1.58	1.87	2.25	2.59	2.35	1.85	1.34	1.00
30	1.00	1.22	1.45	1.67	1.93	2.06	1.99	1.67	1.31	1.00
40	0.95	1.07	1.23	1.43	1.62	1.72	1.66	1.50	1.25	1.00
50	0.90	0.98	1.06	1.21	1.34	1.43	1.42	1.32	1.18	1.00
60	0.84	0.92	0.97	1.06	1.15	1.22	1.23	1.18	1.08	1.00
70	0.75	0.84	0.87	0.92	1.00	1.07	1.10	1.08	1.04	1.00
80	0.65	0.73	0.78	0.81	0.86	0.92	0.99	1.02	1.03	1.00
90	0.53	0.62	0.68	0.72	0.77	0.82	0.89	0.96	0.99	1.00
100	0.47	0.55	0.61	0.64	0.68	0.72	0.80	0.90	0.96	1.00
110	0.42	0.50	0.55	0.58	0.61	0.65	0.72	0.82	0.92	1.00
120	0.38	0.46	0.51	0.53	0.56	0.60	0.67	0.75	0.88	1.00
130	0.36	0.43	0.47	0.49	0.52	0.56	0.62	0.70	0.84	1.00
140	0.35	0.41	0.45	0.47	0.49	0.52	0.58	0.66	0.81	1.00
150	0.34	0.40	0.44	0.45	0.47	0.50	0.55	0.64	0.78	1.00
160	0.34	0.39	0.43	0.44	0.46	0.49	0.54	0.62	0.77	1.00
170	0.33	0.39	0.42	0.43	0.45	0.48	0.53	0.62	0.76	1.00
180	0.33	0.39	0.42	0.43	0.44	0.47	0.53	0.61	0.76	1.00

AS: Azimuthal separation between the sky patch and sun.

Table 4.5.8 Measured luminance distribution data for intermediate sky, SOLALT = 60° (Nakamura et al., 1985)

	Altitude angle of the sky patch (deg)									
AS (deg)	0	10	20	30	40	50	60	70	80	90
0	0.53	0.67	0.82	1.08	1.57	2.55	4.00	2.48	1.45	1.00
10	0.52	0.67	0.82	1.06	1.50	2.29	3.16	2.27	1.42	1.00
20	0.50	0.66	0.80	1.00	1.35	1.92	2.32	1.97	1.38	1.00
30	0.48	0.63	0.77	0.94	1.15	1.48	1.76	1.70	1.32	1.00
40	0.45	0.59	0.72	0.86	1.00	1.21	1.40	1.42	1.22	1.00
50	0.40	0.53	0.66	0.78	0.88	1.05	1.18	1.22	1.15	1.00
60	0.36	0.47	0.59	0.69	0.80	0.92	1.04	1.11	1.09	1.00
70	0.32	0.42	0.52	0.60	0.72	0.84	0.94	1.02	1.05	1.00
80	0.30	0.38	0.46	0.53	0.63	0.75	0.88	0.97	1.00	1.00
90	0.29	0.35	0.42	0.48	0.55	0.65	0.78	0.90	0.97	1.00
100	0.28	0.34	0.40	0.45	0.51	0.58	0.70	0.82	0.94	1.00
110	0.27	0.33	0.38	0.42	0.47	0.52	0.62	0.76	0.90	1.00
120	0.27	0.32	0.36	0.40	0.44	0.49	0.57	0.69	0.85	1.00
130	0.26	0.31	0.35	0.38	0.42	0.46	0.53	0.64	0.82	1.00
140	0.26	0.30	0.34	0.37	0.40	0.44	0.50	0.61	0.79	1.00
150	0.25	0.29	0.33	0.36	0.38	0.42	0.48	0.59	0.76	1.00
160	0.25	0.29	0.32	0.35	0.38	0.41	0.47	0.57	0.75	1.00
170	0.25	0.29	0.32	0.34	0.37	0.41	0.46	0.56	0.74	1.00
180	0.25	0.29	0.32	0.34	0.36	0.40	0.46	0.56	0.74	1.00

AS: Azimuthal separation between the sky patch and sun.

Table 4.5.9 Measured luminance distribution data for intermediate sky, SOLALT = 70° (Nakamura et al., 1985)

	Altitude angle of the sky patch (deg)									
AS (deg)	0	10	20	30	40	50	60	70	80	90
0	0.33	0.43	0.54	0.74	0.90	1.07	1.48	2.70	1.54	1.00
10	0.33	0.42	0.53	0.73	0.89	1.05	1.43	1.90	1.48	1.00
20	0.33	0.41	0.51	0.69	0.87	1.02	1.30	1.55	1.35	1.00
30	0.32	0.39	0.48	0.63	0.82	0.97	1.17	1.34	1.26	1.00
40	0.31	0.38	0.45	0.58	0.76	0.93	1.05	1.18	1.19	1.00
50	0.30	0.37	0.43	0.52	0.69	0.86	0.97	1.08	1.10	1.00
60	0.29	0.35	0.40	0.47	0.61	0.79	0.92	1.00	1.05	1.00
70	0.27	0.32	0.38	0.43	0.52	0.70	0.86	0.96	1.00	1.00
80	0.23	0.29	0.35	0.40	0.46	0.57	0.78	0.93	0.99	1.00
90	0.20	0.26	0.32	0.37	0.42	0.48	0.66	0.85	0.96	1.00
100	0.18	0.24	0.29	0.34	0.38	0.44	0.54	0.74	0.91	1.00
110	0.17	0.22	0.27	0.32	0.36	0.41	0.49	0.65	0.87	1.00
120	0.16	0.21	0.26	0.30	0.34	0.39	0.47	0.60	0.82	1.00
130	0.15	0.20	0.25	0.29	0.33	0.37	0.45	0.57	0.78	1.00
140	0.15	0.19	0.24	0.28	0.32	0.36	0.43	0.55	0.75	1.00
150	0.15	0.19	0.23	0.27	0.31	0.35	0.42	0.54	0.73	1.00
160	0.15	0.19	0.23	0.27	0.30	0.34	0.41	0.53	0.72	1.00
170	0.15	0.18	0.23	0.27	0.29	0.34	0.41	0.52	0.72	1.00
180	0.15	0.18	0.22	0.26	0.29	0.34	0.40	0.52	0.72	1.00

AS: Azimuthal separation between the sky patch and sun.

For $x = a, b, c, d$ and e, using Table 4.5.10, where ε is sky clearness:

$$x = x_1 + x_2 z + \Delta[x_3 + x_4 z], \quad \text{for } \varepsilon \text{ ranges } 2\text{–}8 \tag{4.5.7a}$$

else,

$$c = \exp\{(\Delta[c_1 + c_2 z])c_3\}^{-1} \tag{4.5.7b}$$

$$d = -\exp\{\Delta[d_1 + d_2 z]\} + d_3 + \Delta d_4 \tag{4.5.7c}$$

The coefficients a, b, c, d and e are adjustable functions of irradiance conditions. Table 4.5.10 provides the required information for obtaining the above functions.

Perez et al.'s (1993) experimental data set included more than 16 000 full-sky scans from Berkeley, California covering a wide range of conditions from overcast to clear through intermediate skies. Perez et al.'s all-sky model has been incorporated in RADIANCE software package by the Fraunhofer Institute for Solar Energy Systems in Freiburg, Germany (Sick, 1994) and by Mardaljevic at DeMontfort University in Leicester, UK (Mardaljevic, 1996). The latter has evaluated the performance of four sky luminance distribution models by comparing their estimates against vertical illuminance measurements. The models evaluated were (i) CIE overcast sky (Moon and Spencer,

Table 4.5.10 Coefficients for Perez et al. (1993) all-sky luminance distribution model (sky clearness ε) (Eqs (4.5.6) and (4.5.7))

Range	From	To								
			a_1	a_2	a_3	a_4	b_1	b_2	b_3	b_4
1	1.000	1.065	1.3525	−0.2576	−0.2690	−1.4366	−0.7670	0.0007	1.2734	−0.1233
2	1.065	1.230	−1.2219	−0.7730	1.4148	1.1016	−0.2054	0.0367	−3.9128	0.9156
3	1.230	1.500	−1.1000	−0.2515	0.8952	0.0156	0.2782	−0.1812	−4.5000	1.1766
4	1.500	1.950	−0.5484	−0.6654	−0.2672	0.7117	0.7234	−0.6219	−5.6812	2.6297
5	1.950	2.800	−0.6000	−0.3566	−2.5000	2.3250	0.2937	0.0496	−5.6812	1.8415
6	2.800	4.500	−1.0156	−0.3670	1.0078	1.4051	0.2875	−0.5328	−3.8500	3.3750
7	4.500	6.200	−1.0000	0.0211	0.5025	−0.5119	−0.3000	0.1922	0.7023	−1.6317
8	6.200	9999.999	−1.0500	0.0289	0.4260	0.3590	−0.3250	0.1156	0.7781	0.0025
			c_1	c_2	c_3	c_4	d_1	d_2	d_3	d_4
1	1.000	1.065	2.8000	0.6004	1.2375	1.0000	1.8734	0.6297	0.9738	0.2809
2	1.065	1.230	6.9750	0.1774	6.4477	−0.1239	−1.5798	−0.5081	−1.7812	0.1080
3	1.230	1.500	24.7219	−13.0812	−37.7000	34.8438	−5.0000	1.5218	3.9229	−2.6204
4	1.500	1.950	33.3389	−18.3000	−62.2500	52.0781	−3.5000	0.0016	1.1477	0.1062
5	1.950	2.800	21.0000	−4.7656	−21.5906	7.2492	−3.5000	−0.1554	1.4062	0.3988
6	2.000	4.500	14.0000	−0.9999	−7.1406	7.5469	−3.4000	−0.1078	−1.0750	1.5702
7	4.500	6.200	19.0000	−5.0000	1.2438	−1.9094	−4.0000	0.0250	0.3844	0.2656
8	6.200	9999.999	31.0625	−14.5000	−46.1148	55.3750	−7.2312	0.4050	13.3500	0.6234
			e_1	e_2	e_3	e_4				
1	1.000	1.065	0.0356	−0.1246	−0.5718	0.9938				
2	1.065	1.230	0.2624	0.0672	−0.2190	−0.4285				
3	1.230	1.500	−0.0156	0.1597	0.4199	−0.5562				
4	1.500	1.950	0.4659	−0.3296	−0.0876	−0.0329				
5	1.950	2.800	0.0032	0.0766	−0.0656	−0.1294				
6	2.800	4.500	−0.0672	0.4016	0.3017	−0.4844				
7	4.500	6.200	1.0468	−0.3788	−2.4517	1.4656				
8	6.200	9999.999	1.5000	−0.6426	1.8564	0.5636				

1942), (ii) CIE clear sky (CIE, 1973), (iii) intermediate sky (Matsuura and Iwata, 1990) and (iv) Perez et al. (1993) all sky. The reported results may be enumerated as follows:

(a) The CIE overcast sky model shows an overall negative bias in the predictions of illuminances due to north- and east-facing windows.
(b) The CIE clear-sky model is the worst of all four models with MBEs, respectively, being three to four times those associated with the intermediate sky model and almost 10 times more than Perez et al.'s all-sky model.
(c) For all but one aspect Perez et al.'s model generates single digit MBEs.

Prog4-4.For and Prog4-5.For, which respectively use the relative and absolute coordinate scheme for the SP, enable computation of the sky luminance distribution. It must be borne in mind that both of the above-mentioned FORTRAN programs require the coefficients data file In4-3.Csv, which is appended in the book's web site. Presently, in Prog4-4.For and Prog4-5.For the dimensionless parameter l_v has been normalised against zenith luminance. In relative scheme, the azimuth of any given SP is its angular separation from the sun. The other scheme allows the user to obtain the luminance distribution in

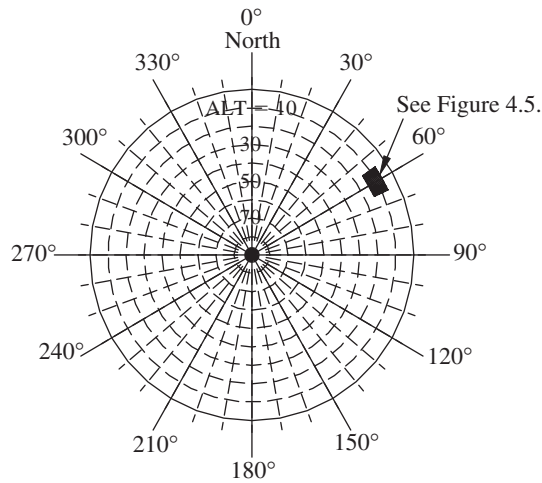

Figure 4.5.1 *Geometry of the sky elements for computation of luminance distribution*

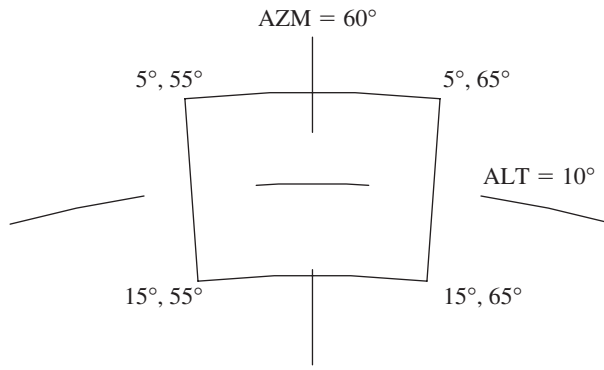

Figure 4.5.2 *Detail of the SP shown in Figure 4.5.1*

the absolute frame. Details of the sky element grid adopted for these computations are shown in Figures 4.5.1 and 4.5.2. This fine resolution grid was adopted in accordance with the measurement scheme followed by Nakamura et al. (1985). Figure 4.5.3 shows a recording map of CIE adopted scheme for sky luminance distribution measurements.

Owing to the large output array, respective electronic data files Lumdist3.Dat and Lumdist4.Dat are generated. These files may then be imported in any spreadsheet packages, e.g. Microsoft Excel and further manipulation may be performed to present the output in the form of a matrix. This procedure is demonstrated via the following example.

Example 4.5.1

In Table 4.5.5 measured luminance distribution for an intermediate sky for SOLALT = 30° were presented. Use Prog4-4.For to compute luminance distributions under thin overcast, heavy overcast and clear skies, and compare them against measured data sets.

Prog4-4.For is used for this purpose. The routine prompts the user to provide the details of time and location. The luminance distribution l_v is then provided as a function of the SP

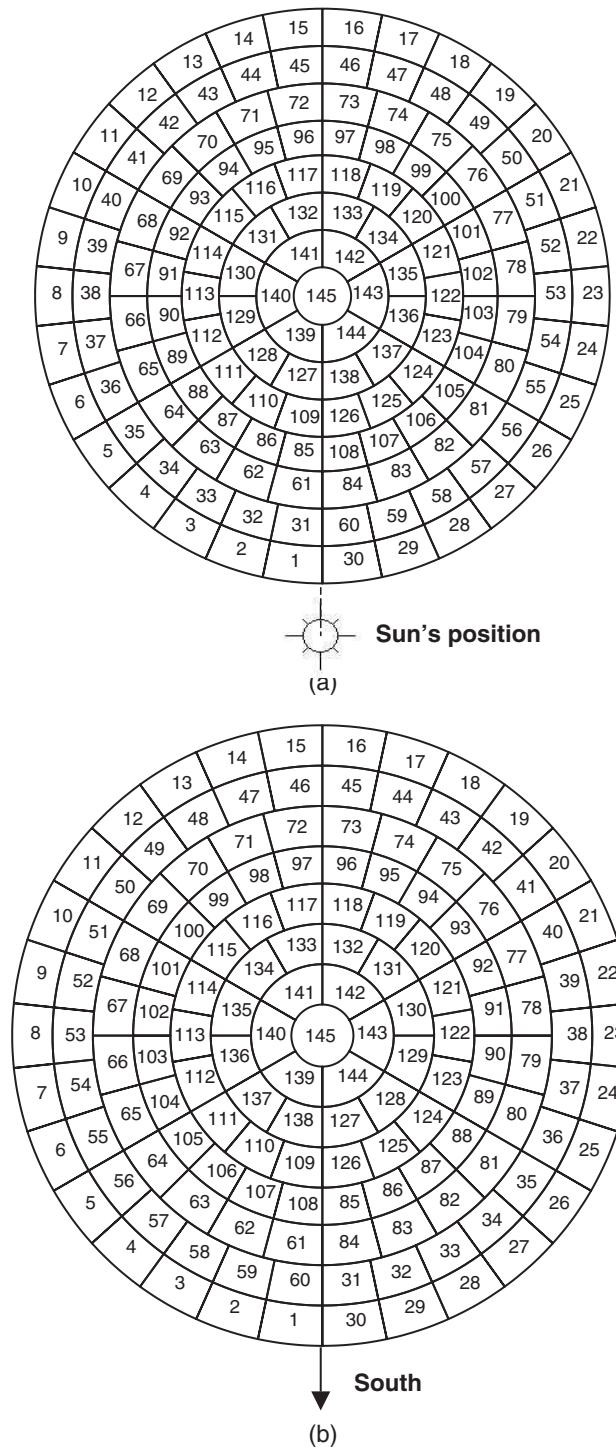

Figure 4.5.3 *Sky scan recording map for (a) Garston and Sheffield (PRC Krochmann scanner: relative co-ordinate system) and (b) Fukuoka (EKO scanner: absolute co-ordinate system)*

azimuth and altitude. The column-wise output may be imported in a matrix table such as Table 4.5.11. The latter table shows good agreement between the measured and computed data sets. Furthermore, software packages such as GINO may be used to produce plots such as those shown in Figure 4.5.4 to enable a visual comparison between computed and measured data sets.

4.5.4.2 Kittler et al.'s model

More recently, Kittler et al. (1999) have proposed a new range of standard skies. It is a set of mathematical equations that describes 15 alternate sky luminance distributions, covering the range of conditions from overcast to clear sky. Kittler's team used measured data sets from Berkeley, California; Tokyo and Sydney to derive a new generation of CIE sky standards. The influence of solar altitude, turbidity, luminance and illuminance parameters as well as typical daylight conditions were specified and their functional relations modelled. Kittler et al. have proposed the following formula for defining the relative luminance distribution of any given standard sky:

$$\frac{L}{L_Z} = \frac{f(\xi)\phi(Z)}{f(Z_S)\phi(0^o)} \tag{4.5.8}$$

where L is the luminance of any arbitrary sky element and both ϕ are indicatrix functions given by Eq. (4.5.9). Likewise, both f indicatrices are described by Eq. (4.5.10):

$$\frac{\phi(Z)}{\phi(0^o)} = [1 + a\exp(b/\cos Z)]/(1 + \exp(b)] \tag{4.5.9}$$

$$f(\xi) = 1 + c[\exp(\xi) - \exp(\mathrm{d}\pi/2)] + e\cos^2\xi \tag{4.5.10}$$

The corresponding parameters a, b, c, d and e are provided in the standard sky luminance distributions (SSLD) in Table 4.5.12. Note that a and b are called the standard gradation parameters as they describe the luminance gradation of any SP with respect to zenith, and c, d and e are standard indicatrix parameters.

Tregenza (1999) has evaluated the above alternate skies using data from maritime climates and concluded that a total of four of the above subsets were adequate to describe the luminance distributions of such (maritime) locations.

Tregenza's conclusions may be summarised more expressly as follows:

(a) The standard set gives a good overall framework for categorising actual skies.
(b) Subsets of four luminance distribution models were adequate to describe the skies that occurred at each (of the maritime) site.
(c) Inhomogeneity of actual skies in maritime climates leads to uncertainty in interior daylight predictions. For 80% of the time the computed room illuminance may lie between 0.8 and 1.3 times the real value. For a 95% frequency of occurrence the above range changes to 0.5–1.5.
(d) The above error range was found to be significantly lower than when calculations were based on an overcast sky alone.

Table 4.5.11 Comparison of Perez et al. (1993) luminance distribution model against measured data from Japan (Nakamura et al., 1985)

	Measured data Altitude angle of the sky patch (deg)										Computed data Altitude angle of the sky patch (deg)									
AS (deg)	0	10	20	30	40	50	60	70	80	90	0	10	20	30	40	50	60	70	80	90
0	2.09	3.00	5.20	11.50	5.08	2.93	2.04	1.56	1.25	1.00	3.10	4.53	6.61	9.59	6.47	3.81	2.38	1.61	1.18	1.00
10	2.00	2.72	4.20	5.20	4.12	2.86	2.03	1.55	1.24	1.00	2.95	4.20	5.78	6.92	5.55	3.58	2.31	1.59	1.17	1.00
20	1.70	2.24	2.86	3.25	2.95	2.48	1.96	1.53	1.23	1.00	2.60	3.47	4.35	4.73	4.15	3.05	2.13	1.53	1.16	1.00
30	1.52	1.86	2.23	2.56	2.46	2.17	1.86	1.49	1.12	1.00	2.19	2.74	3.19	3.33	3.06	2.49	1.90	1.45	1.14	1.00
40	1.40	1.66	1.89	2.15	2.19	2.02	1.73	1.41	1.18	1.00	1.83	2.16	2.40	2.44	2.30	2.01	1.66	1.35	1.11	1.00
50	1.30	1.53	1.71	1.89	1.94	1.78	1.53	1.29	1.22	1.00	1.56	1.76	1.87	1.88	1.80	1.65	1.45	1.25	1.07	1.00
60	1.19	1.38	1.55	1.66	1.68	1.56	1.34	1.19	1.08	1.00	1.37	1.49	1.54	1.52	1.46	1.38	1.27	1.16	1.04	1.00
70	1.03	1.23	1.39	1.46	1.47	1.38	1.21	1.11	1.05	1.00	1.23	1.31	1.32	1.29	1.24	1.19	1.13	1.07	1.01	1.00
80	0.94	1.09	1.21	1.30	1.28	1.20	1.13	1.07	1.03	1.00	1.14	1.19	1.18	1.14	1.09	1.06	1.03	1.00	0.97	1.00
90	0.87	0.98	1.08	1.15	1.11	1.06	1.04	1.02	1.00	1.00	1.09	1.12	1.09	1.04	0.99	0.96	0.95	0.94	0.94	1.00
100	0.82	0.90	0.95	0.97	0.96	0.95	0.94	0.95	0.97	1.00	1.05	1.07	1.04	0.97	0.92	0.89	0.89	0.89	0.91	1.00
110	0.78	0.82	0.83	0.83	0.84	0.85	0.86	0.90	0.95	1.00	1.03	1.04	1.00	0.93	0.88	0.85	0.84	0.86	0.89	1.00
120	0.75	0.75	0.75	0.74	0.75	0.77	0.80	0.85	0.92	1.00	1.02	1.02	0.98	0.91	0.85	0.81	0.81	0.82	0.87	1.00
130	0.73	0.71	0.70	0.69	0.70	0.72	0.75	0.81	0.89	1.00	1.02	1.01	0.96	0.89	0.83	0.79	0.78	0.80	0.85	1.00
140	0.70	0.69	0.68	0.68	0.68	0.69	0.72	0.79	0.87	1.00	1.02	1.01	0.96	0.88	0.81	0.77	0.76	0.78	0.84	1.00
150	0.68	0.67	0.67	0.67	0.68	0.68	0.71	0.77	0.86	1.00	1.02	1.01	0.96	0.87	0.81	0.76	0.75	0.77	0.83	1.00
160	0.66	0.66	0.66	0.67	0.68	0.67	0.70	0.76	0.85	1.00	1.02	1.01	0.96	0.87	0.80	0.76	0.74	0.76	0.82	1.00
170	0.64	0.65	0.66	0.68	0.68	0.67	0.69	0.76	0.85	1.00	1.02	1.02	0.96	0.87	0.80	0.75	0.74	0.76	0.82	1.00
180	0.63	0.65	0.67	0.68	0.68	0.67	0.69	0.75	0.84	1.00	1.02	1.02	0.96	0.87	0.80	0.75	0.74	0.75	0.82	1.00

AS: Azimuthal separation between the sky patch and sun.

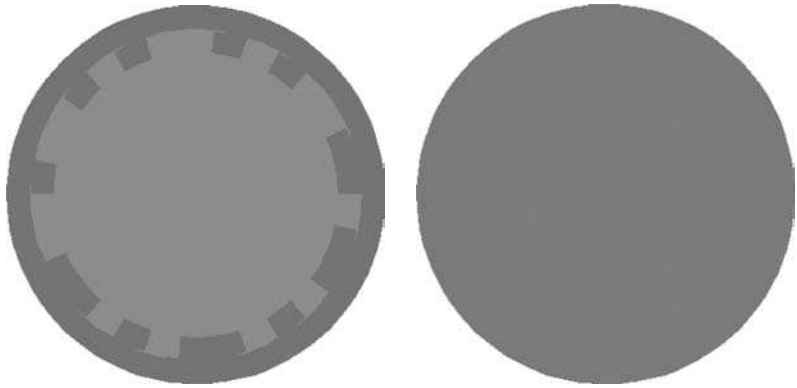

Measured Computed

Heavy overcast sky 15 January 1992, 1105 h

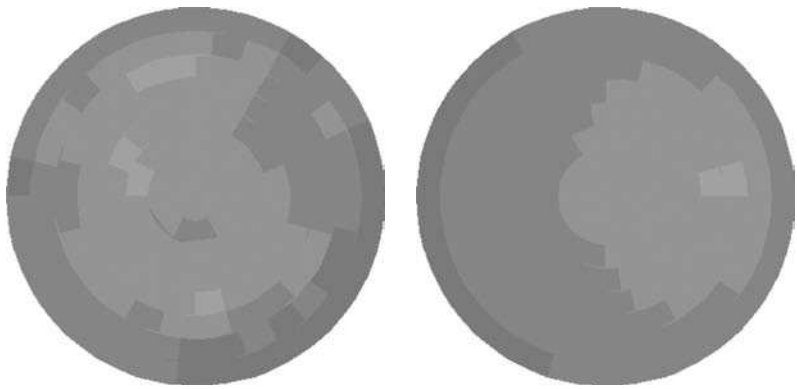

Measured Computed

(a) Thin overcast sky 17 March 1992, 1340 h

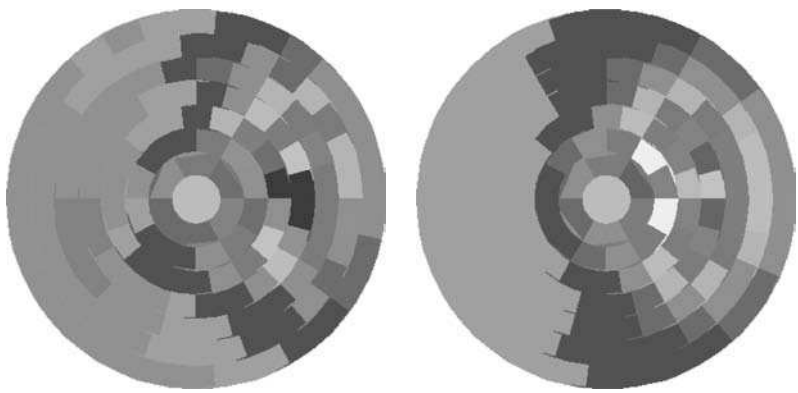

Measured sky scan Computed sky scan

(b) Sky luminance distribution for Garston data – 28 June 1992, 1145 h GMT

Figure 4.5.4 *Luminance distribution plot for Garston, UK: (a) overcast sky and (b) clear sky*

Table 4.5.12 SSLD

Code	Type of sky	Standard gradation parameters	Standard indicatrix parameters	Linke turbidity range	Gradation standard (zenith to horizon)
I.1	Overcast with steep gradation and azimuthally uniform	$a = 4$ $b = -0.7$	$c = 0$ $d = -1$ $e = 0$	From 20 to 40	1:0.3
I.2	Overcast with a steep gradation and slight brightening towards sun	$a = 4$ $b = -0.7$	$c = 2$ $d = -1.5$ $e = 0.15$	Over 15	1:0.3
II.1	Overcast moderately gradated, azimuthally uniform	$a = 1.1$ $b = -0.8$	$c = 0$ $d = -1$ $e = 0$	Around 20	1:0.66
II.2	Overcast moderately gradated with slight brightening towards sun	$a = 1.1$ $b = -0.8$	$c = 2$ $d = -1.5$ $e = 0.15$	Around 20	1:0.66
III.1	Overcast overall uniform	$a = 0$ $b = -1$	$c = 0$ $d = -1$ $e = 0$	Around 20	1:0.1
III.2	Cloudy or quasi-overcast with a uniform gradation and slight brightening towards sun	$a = 0$ $b = -1$	$c = 2$ $d = -1.5$ $e = 0.15$	Around 15	1:0.1
III.3	Cloudy or quasi-overcast with a brighter circumsolar effect and uniform gradation	$a = 0$ $b = -1$	$c = 5$ $d = -2.5$ $e = 0.3$	Around 10	1:0.1
III.4	Cloudy, rather uniform with a clear solar corona	$a = 0$ $b = -1$	$c = 10$ $d = -3$ $e = 0.45$	From 6 to 15	1:0.1
IV.2	Partly cloudy with a shaded sun position	$a = -1$ $b = -0.55$	$c = 2$ $d = -1.5$ $e = 0.15$	Over 15	1:0.3
IV.3	Cloudy with brighter circumsolar effect	$a = -1$ $b = -0.55$	$c = 5$ $d = -2.5$ $e = 0.3$	From 6 to 12	1:2.5
IV.4	Cloudy or partly cloudy with a clear solar corona	$a = -1$ $b = -0.55$	$c = 10$ $d = -3$ $e = 0.45$	From 1.5 to 4	1:2.5
V.4	Very clear with clear solar corona	$a = -1$ $b = -0.32$	$c = 10$ $d = -3$ $e = 0.45$	From 1.5 to 4	1:3.5
V.5	Cloudless polluted with a broader solar corona	$a = -1$ $b = -0.32$	$c = 16$ $d = -3$ $e = 0.3$	From 3 to 8	1:3.5
VI.5	Cloudless turbid with a broader solar corona	$a = -1$ $b = -0.15$	$c = 16$ $d = -3$ $e = 0.3$	From 4 to 10	1:7
VI.6	Quasi-cloudy and turbid with a wide solar corona effect	$a = -1$ $b = -0.15$	$c = -24$ $d = -2.8$ $e = 0.15$	From 6 to 12	1:7

Table 4.5.13 Distribution of best-fit standard skies for maritime climates

Site	Latitude	Longitude	Predominance of sky types (refer Table 4.5.12)
Singapore	1.5°N	104.0°E	1, 4, 8, 13
Fukuoka, Japan	33.5°N	130.5°E	1, 3, 5
Garston, England	51.7°N	0.4°W	1, 3, 8, 13
Sheffield, England	53.5°N	1.5°W	1, 3, 8, 11

Tregenza's work may be quantitatively summarised by means of Table 4.5.13.

Tregenza's work has also been validated by Li et al. (2003) who used a 36 month measured data set from Hong Kong to investigate the frequency of occurrence of Kittler's sky types. The latter team report that sky types 1, 3, 6, 11 and 13 were adequate to describe the luminance distributions of the southern China maritime climate.

4.6 Luminance transmission through glazing

Hopkinson et al. (1966) has presented daylight transmission curves for single, double and triple glazings of clear float-glass design. The CIE sky component tables, presented in Chapter 3, incorporate transmission loss for a single glazing. For double and triple glazings the BRE Digest (1986) recommends respective correction factors of 0.9 and 0.8 to be multiplied to the total daylight factor. This is certainly a simple but approximate approach. In the present context, it is possible to investigate the fine detail of daylight penetration through multiple glazings without any loss of serious accuracy by combining the above luminosity estimates with the glazing transmission characteristics. This material is presented in the following sections.

4.6.1 Incidence angle of luminance from a given sky patch

In order to obtain the transmission of luminance from any given SP discussed above, the angular separation of the SP and a normal to the window glazing is required. Prog4-6.For enables such computations to be performed quite easily. This is demonstrated via the following example.

Example 4.6.1

Refer to Figure 3.6.1 wherein the four SPs, SP1–SP4 are shown. Compute the incidence angle between a normal to the window and the luminance emanating from these SPs.

Prog4-6.For prompts as follows:

Enter altitude and azimuth of the first point

At this point the respective altitude and azimuth (measured from true north) of the centre of SP1 is to be provided as 40.0 and 90.0. Prog4-6.For further prompts as:

Enter altitude and azimuth of the second point

The altitude and azimuth of the normal to the window is now provided as 0.0 and 95.0.

The routine then provides the answer as:

42.3°

Using a similar procedure the incidence angle for SP2 is obtained as 40.3°. SP3 and SP4 are then obtained from consideration of symmetry.

4.6.2 Transmission of luminance (or radiance) through multi-glazed windows

Presently, Prog4-7.For is provided which enables computation of transmission of luminance through multiple glazings. Four types of glazings have been modelled herein, e.g. Float-glass single, double and triple panes, and Pilkington Kappafloat double glazing. The latter design, owing to its energy efficiency features, is predominantly being used in new buildings.

Example 4.6.2

Refer to Example 4.6.1 in which the incidence angles of the luminance emanating from the four SPs, SP1–SP4 were computed. Estimate the luminance transmission through the window shown in Figure 3.6.1. The window may be assumed to be single glazed.

Using the incidence angles obtained in Example 4.6.1, Prog4-7.For enables the required transmissivities to be computed as follows:

Transmissivity, τ of luminance emanating from SP1 = 0.905
Transmissivity, τ of luminance emanating from SP2 = 0.908

Example 4.6.3

Refer to Table 3.5.4 which provides illuminance data for Watford, north London. Using Perez et al.'s all-sky luminance distribution model Eq. (4.5.6), obtain the internal illuminance for the reference point shown in Figure 3.6.1 for 0930 h. Use data obtained in the above two examples.

Figure 4.6.1 shows a sketch of the sky hemisphere and the geometry for any given SP. A derivation for estimating the illuminance on a horizontal surface due to the given SP is now presented.

Area of SP $= (r\,\mathrm{d}\alpha)\,(r\,\mathrm{d}\psi)$

Where $\mathrm{d}\alpha$ and $\mathrm{d}\psi$ determine the size of the SP. In Prog4-4.For and Prog4-5.For these values are each set at 10° ($\pi/18$ rad).

Let $\Delta(IL)$ represent the internal horizontal illuminance at the reference point P due to the given SP. The total internal illuminance due to sky may then be obtained by summing the contributions of all relevant SPs.

It may easily be shown that:

$$\Delta(IL) = \tau L(r\,\mathrm{d}\alpha)(r\,\mathrm{d}\psi)\sin\alpha/r^2 \qquad (4.6.1)$$

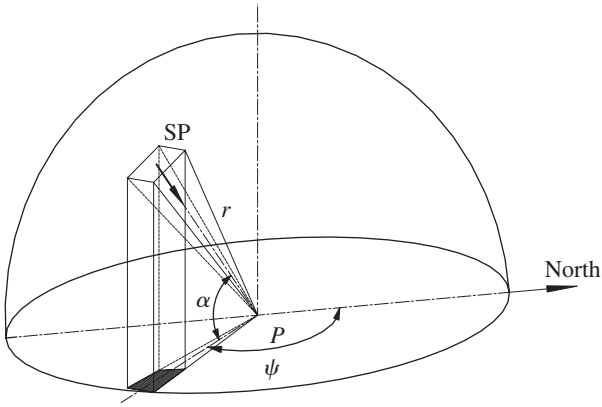

Figure 4.6.1 *Geometry of a given SP*

where L is the luminance of the SP in cd/m^2. Using the above fixed values of $\pi/18$ for dα and dψ used in Prog4-4.For and Prog4-5.For:

$$\Delta(IL) = \tau L(\pi/18)^2 \sin\alpha \tag{4.6.2}$$

Based on Examples 4.6.1 and 4.6.2, an average incidence angle of 41.3° and an average τ of 0.906 may be assumed for the above four SPs. Recall that in Example 3.5.1 $L_{z,\text{comp}}$ was obtained as 5865 cd/m^2 (see Table 3.5.4). The following table summarises the output from Prog4-4.For and the rest of the computations.

SP (Figure 3.6.1)	L/L_z Prog4-5.For (lx)	$L_{z,\text{comp}}$ (cd/m^2)	$L_{z,\text{comp}} \times (L/L_z)$ cd/m^2	$\Delta(IL)$ lx Eq. (4.6.2)
SP1	1.72	5865	10 090	179
SP2	2.19	5865	12 840	228
SP3	2.90	5865	17 010	302
SP4	3.95	5865	23 170	411
Total internal illuminance				1120

4.7 Quality control of cloud cover, sunshine, solar radiation and daylight data

It was shown in Chapter 1 that measurement of solar radiation and daylight is susceptible to errors due to equipment uncertainty and also due to operational errors. Worldwide there has been a revival of data collection and quality control and this task has been led by CIBSE in the UK National Renewable Energy Laboratory (NREL) and ASHRAE in the US, European Solar Radiation Atlas (ESRA) in the European Union (EU) and CIE for the globe.

During the preparation of *CIBSE Guides A* (CIBSE, 1999) and *J* (CIBSE, 2002) a series of tests were developed to evaluate the quality of data collected from four principal UK sites – London Weather Centre, Bracknell, Aughton and Mylnefield. The latter station only measures global irradiation so the tests were restricted to that component. The lessons

learnt from the above data processing have been summarised by Muneer and Fairooz (2002). Additionally, the lessons learnt from the ESRA (Terzenbach, 1995; ESRA, 2000) were also used for the quality control checks performed by the CIBSE's solar data task group. These tests were undertaken for over 50 worldwide locations. In this section results obtained from 5 min averaged data for Bahrain, Arabian Gulf are used as demonstration. The tests were developed on the basis of the CIE recommendations (1994) and those developed expressly for the CIBSE Guides A and J work. A considerable amount of work has also been taken by the NREL staff in Colorado (Myers et al., 2002).

4.7.1 Cloud cover and sunshine fraction data

Historically, during daytime cloud cover has been measured by use of the most intelligent sensor, i.e. available on earth – the human eye! Within the UK, cloud cover at night is measured via use of laser cloud base recorders. These, primarily, record the height of cloud passing overhead, but they are also used on automatic weather stations to calculate cloud amount (on the assumption that what passes overhead is representative of the rest of the sky). For heights up to about 1200 m the observer would also have the aid of a non-laser cloud base recorder and a cloud spotlight and 'alidade'. The latter shines a beam vertically upwards, illuminating a spot on the cloud base. The alidade, located some distance away, is used by the observer to measure the angle of the spot from the vertical. By trigonometry, the angle of the spot allows the height of the cloud base to be calculated.

The two synoptic parameters, cloud cover and sunshine duration, provide an approximate means of generating those solar radiation data that are missing from a time series or have clearly been identified as being suspect. There are advantages as well as disadvantages in the use of cloud cover as a means of estimating solar irradiation. The advantage is that the reported value is very reliable, it being observed by a trained observer and thus free from instrumentation misalignment or calibration errors. The disadvantage is that the amount of cloud does not indicate whether the solar disc was obscured or not. Under a broken cloud, with the sun shining through, global irradiance may actually be greater than clear-sky receipt, as beam and sky-diffuse components are augmented by reflection of the clouds. A detailed validation of cloud- and sunshine-based irradiance models was undertaken by Gul et al. (1998), Muneer et al. (1998) and Muneer and Gul (2000) for UK, Japan and Swiss data. That study has shown that sunshine data fares better than its cloud-based counterpart and that is due to the reasons highlighted above.

In many countries, diurnal duration of bright sunshine is measured at a wide number of places. However, in view of the rather poorer quality of sunshine records generated by Campbell–Stokes sunshine recorders, in many instances, it may be desirable to estimate the latter, or indeed fill in the missing series of data using a validated procedure. Towards this end fundamental research work was undertaken by Page (*CIBSE Guide J*, 2002). A summary of procedures for filling in sunshine data, generated from measured cloud-cover information and vice versa, is presented below.

Page showed that the two observed variables, cloud cover and sunshine fraction, are statistically interlinked, but in a more complex way than is often perceived. The relationship depends on solar altitude. A new study of this relationship had to be developed through research on observed concurrent sunshine and cloud data. Using a complete year's hourly data from a closely monitored location in England (Bracknell is the headquarter of the

Table 4.7.1 Coefficients for use in Eqs (4.7.1b) and (4.7.2)

	Solar altitude (deg)					
Coefficient	8–15	15–25	25–35	35–45	45–55	>55
a_0	1.041	0.980	0.970	0.943	0.908	0.903
a_1	−0.088	−0.007	0.043	0.090	0.124	0.121
a_2	−0.006	−0.015	−0.021	−0.026	−0.030	−0.029
b_0	7.38	7.46	7.42	7.44	7.44	7.48
b_1	−2.82	−3.18	−0.42	0.27	1.06	1.00
b_2	−3.13	−1.73	−4.12	−4.28	−5.61	−5.60

UK Meteorological Office), a second order banded polynomial relationship between cloud cover (cc, expressed as octa) and sunshine fraction (sf) was produced:

$$\text{If cc} \leqslant 1, \quad \text{sf} = 1 \tag{4.7.1a}$$

$$\text{For } 1 < \text{cc} < 8 \text{ octa}, \quad \text{sf} = a_0 + a_1\text{cc} + a_2\text{cc}^2 \tag{4.7.1b}$$

if sf $>$ 1, then sf $=$ 1.

$$\text{If sf} = 8, \text{ sf} = 0. \tag{4.7.1c}$$

Table 4.7.1 provides banded coefficients for use with Eq. (4.7.1b).

Page has also provided a procedure for estimating missing cloud cover from sunshine records and that model is provided below for the sake of completion:

$$\text{cc} = b_0 + b_1\text{sf} + b_2\text{sf}^2 \tag{4.7.2}$$

Table 4.7.1 provides banded coefficients for use with Eq. (4.7.2).

4.7.2 Quality control of irradiance data

Level 1 tests

These involve rough absolute checks that ensure that no major problems exist:

Test 1.1 $\quad 0 < I_G < 1.2I_E$

Test 1.2 $\quad 0 < I_D < 0.8I_E$

I_E is the normal incidence extraterrestrial irradiance.

Level 2 tests

These include two consistency tests between diffuse and global, and between global and horizontal extraterrestrial irradiation:

Test 2.1 $\quad I_G < I_E$

Test 2.2 $\quad I_D < I_G$

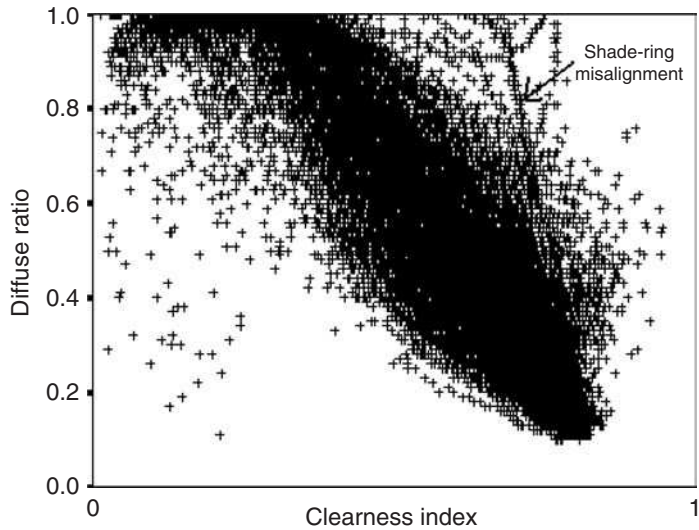

Figure 4.7.1 *Diffuse ratio–clearness index plot for Bahrain. Five-minute averaged data (28 March–30 September 2000)*

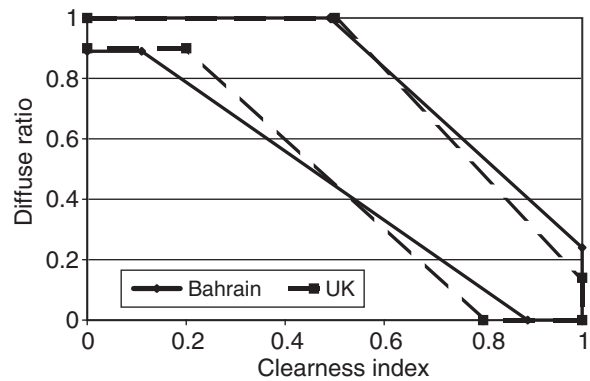

Figure 4.7.2 *Boundaries of the expected diffuse ratio–clearness index envelopes*

Level 3 tests

Test 3.1

The third category includes tests based on established and expected diffuse ratio I_D/I_G – clearness index K_t regression envelope. Note that 'K' is often used instead of I_D/I_G. A sample plot for Bahrain is provided in Figure 4.7.1, with the boundaries of the expected diffuse ratio–clearness index envelopes for Bahrain and UK sites shown in Figure 4.7.2. The boundaries of this envelope of 'acceptance' are given in terms of the clearness index–diffuse ratio co-ordinates.

For Bahrain: (0,1), (0.49,1), (1,0.24), (1,0), (0.89,0), (0.11,0.89), (0,0.89) and (0,1)
For UK: (0,1), (0.5,1), (1,0.14), (1,0), (0.8,0), (0.2,0.9), (0,0.9) and (0,1)

Test 3.1 involves a check that the diffuse irradiation data conforms to the limits set out by the above envelope.

Test 3.2
A further check on the quality of diffuse irradiance may be undertaken by comparing its value with the diffuse irradiance regime's two extreme conditions, i.e. very clear- and heavily-overcast sky. Clear-sky irradiance may be obtained by setting the air mass 2 Linke turbidity to 2.5. In this respect the reader is referred to Section 3.3.6. The overcast irradiance is obtained by setting it equal to 572 times the solar altitude expressed in radian. The computational chain is fairly involved. Reference is herein made to Muneer et al. (2000) and Prog 4-7a.For. The latter monograph also contains a CD with the necessary software (in MS-Excel).

Level 4 test
Test 4.1
As a final measure of check on global and diffuse irradiance data, turbidity may be calculated for the given time series. Once again, Muneer et al. (2000) may be used for such calculations. A Linke turbidity value, i.e. less than 1.5 (obtained under exceptionally clear skies), or greater than 12 (obtainable under dust storm conditions) would demand close inspection of data. A sample turbidity frequency histogram for Bahrain is shown in Figure 4.7.4. Note that Prog4-7a.For provides computation of the Linke turbidity.

Example 4.7.1

The data file Bahrain.zip contains 5 min averaged data for Bahrain, Arabian Gulf. An extract of one day's data from that file is presented in the file In4-7a.Csv. Use Prog4-7a.For to evaluate the quality of data contained within In4-7a.Csv.

Note that the input data file contains the time stamp (year, month, day, hour and minute) and 5 min averaged measured data for horizontal global followed by vertical irradiance on north-, east-, south- and west-facing surfaces. Horizontal diffuse irradiance is the last recorded quantity and is not corrected for shade-ring effects. The output file Out4-7a.Dat contains the following elements.

Time stamp (year, month, day, hour and minute) and horizontal global followed by vertical irradiance on north-, east-, south- and west-facing surfaces. Corrected horizontal diffuse irradiance is the next element. Solar geometry, SOLALT and SOLAZM and K_t values then follow, followed by the shade-ring correction factor (obtained via the Muneer–Zhang formulation provided in Section 4.8) and the uncorrected diffuse irradiance. Flags assigned to the results of five quality control tests are then reported.

These tests are as follows:

(a) if solar altitude $> 7°$, Flag 1 = 2, else Flag 1 = 1,
(b) if $K_t < 1.0$, Flag 2 = 2, else Flag 2 = 1,
(c) if $I_D < I_G$, Flag 3 = 2, else Flag 3 = 1,
(d) if $(I_G - I_D) <$ clear-sky beam irradiance, Flag 4 = 2, else Flag 4 = 1,
(e) if clear-sky diffuse irradiance $< I_D <$ upper limit diffuse irradiance, Flag 5 = 2, else Flag 5 = 1.

The last two of the above tests were based on the work of ESRA (2000). The final three quantities within the output file are the clear-sky beam irradiance (obtained by setting the

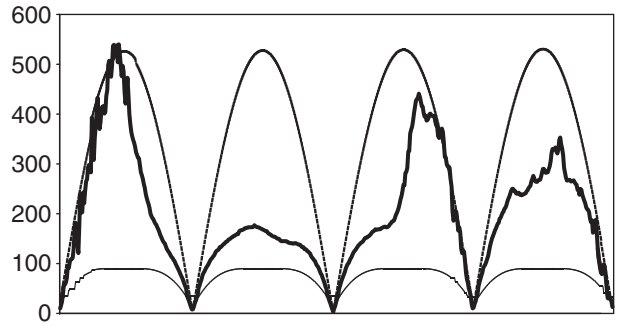

Figure 4.7.3 *Quality control of horizontal diffuse irradiance data: measured data (thick line) ought to lie between computed overcast (dotted line) and clear-sky (thin line) data.* x*-axis: time and* y*-axis: irradiance (W/m²)*

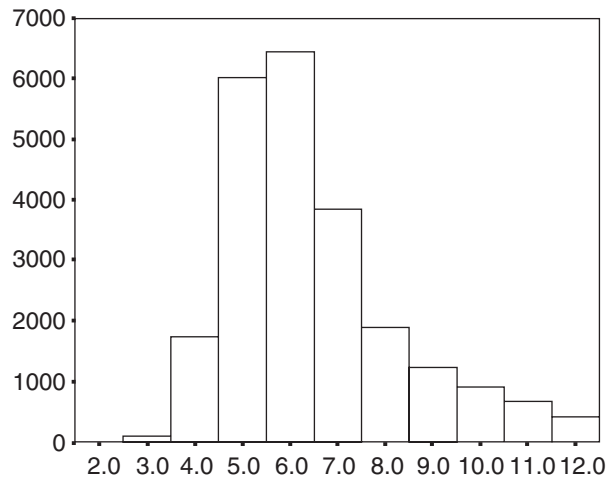

Figure 4.7.4 *Turbidity histogram for Bahrain data (28 March 2000–30 September 2000).* x*-axis: turbidity and* y*-axis: frequency of occurrence*

Linke turbidity to 2.5), the air-mass 2 Linke turbidity and the Ineichen–Perez modified Linke turbidity (see Chapter 3 for further details).

Line number 14 within the FORTRAN code provides the ratio of the given shade-ring width to its radius (the variable BOVR). For a Kipp and Zonen CM5 shade ring this ratio is 0.2.

Figure 4.7.3 shows the variation of measured diffuse irradiance along with the upper and lower bounds, respectively represented by overcast and clear-sky irradiance (refer Test 4).

Tests developed by US NREL

The US-based NREL has developed alternate procedures and software for performing post-measurement quality assessment of solar radiation data. The assessments are also performed on the uncertainty of measured solar radiation data. In this respect a quality assessment software package (SERI QC) was developed by NREL to address the above needs. Chapter 8 provides the web link for NREL and other useful web sites.

SERI QC is based on the establishment of boundaries or limits within which acceptable data are expected to lie. This is similar to previous quality assessment procedures that use

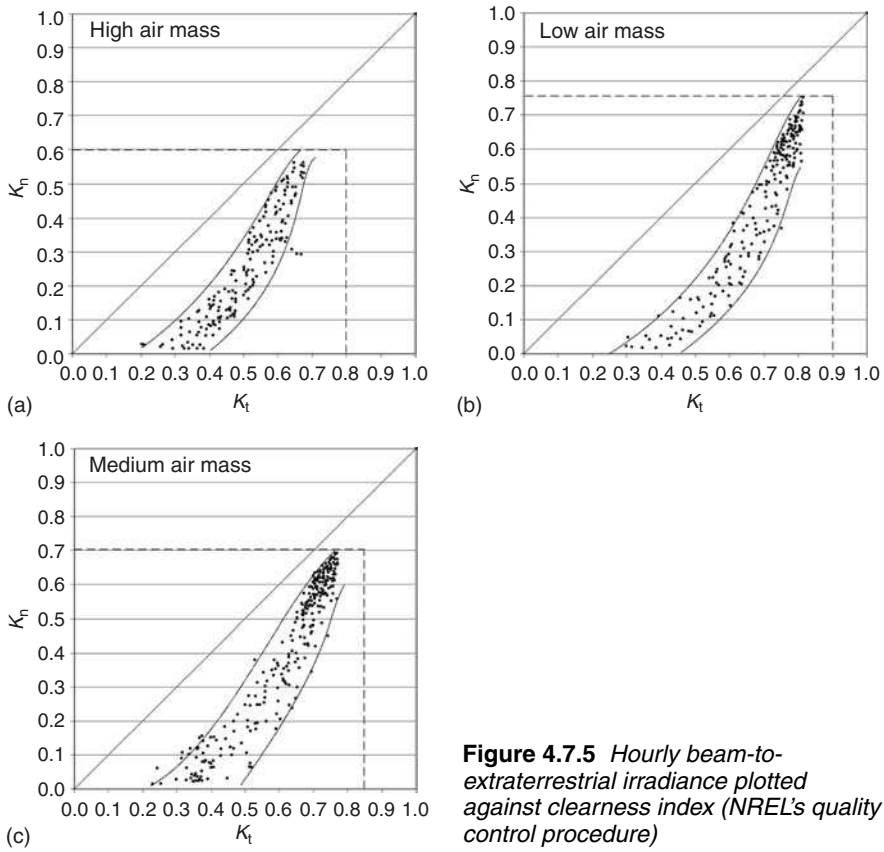

Figure 4.7.5 *Hourly beam-to-extraterrestrial irradiance plotted against clearness index (NREL's quality control procedure)*

extraterrestrial values for the upper limit and zero for the lower limit within which solar radiation data were expected to lie. SERI QC increases the sophistication of the latter approach by establishing much more restrictive boundaries specific to each station month.

SERI QC operates in a dimensionless space, i.e. solar radiation normalised to extraterrestrial values. An example of the expected limits and boundaries established by SERI QC is given in Figure 4.7.5. The variables that form the abscissa and ordinate in this figure are defined according to the following additional expressions. Note that K_t was defined earlier on in this chapter:

$$k_B = I_B/(I_E \sin \text{SOLALT}) \quad \text{and} \quad k_D = I_D/(I_E \sin \text{SOLALT})$$

where k_B is the atmospheric transmission of the direct beam radiation from the solar disc and k_D could be referred to as the effective diffuse transmittance.

The hourly data values plotted in Figure 4.7.5 are the actual data collected by NREL for Nashville, Tennessee for the period April 1978–April 1980. Established empirical limits and boundaries of acceptable data for this station are also shown within the latter figure.

The heavy dashed lines represent the expected maximum global horizontal, and direct normal values and the curved boundaries around the scatter plot of the data were

empirically determined by these data. This was implemented by positioning a limited set of boundary shapes around the data. The position of the boundaries was adjusted by NREL in K_t increments of 0.025 such that up to 5% of the data lay outside the boundaries. This criterion was based both on the assumption that some of the data were in error and a desire to limit the acceptance of erroneous data to small percentages.

When empirical maximum values for K_t and K_n are imposed, the area of acceptability is reduced to the area outlined by the heavy dashed lines shown in Figure 4.7.5. The maximum limits are based on the maximum values achieved by good quality data, as shown in the figure. Values approaching zero are not found on these plots because data from times just after sunrise and just before sunset have been excluded from these plots. The latter procedure was also incorporated by the present author in the production of *CIBSE Guides A* (CIBSE, 1999) and *J* (CIBSE, 2002) wherein all irradiation values corresponding to solar altitude less than 7° were dropped and instead synthetically generated values obtained via Tregenza's work incorporated in Chapter 3 were filled in.

The three parts of Figure 4.7.5 show data, maximum–minimum limits and boundaries for three different air masses. SERI QC assigns limits and boundaries for three air mass ranges (low: 1.0–1.25, medium: 1.25–2.5 and high: 2.5–5.58). Changes in limits and boundary positions with smaller changes in air mass are not significant.

When all three of the solar radiation elements are available (global horizontal, direct normal and diffuse horizontal) redundancies may be used to further reduce the uncertainty of the data. This is accomplished by calculating the global from the direct normal and diffuse, and by comparing the calculated global with the measured global. This comparison provides a direct indication of the accuracy of all three measurements. It is possible, of course, that offsetting measurement errors could partially invalidate this comparison. Nevertheless, when hourly values of global horizontal, direct normal and diffuse horizontal agree within a specified error limit, the lowest possible uncertainty for solar radiation data can be assigned.

In addition to determining whether the solar radiation data fall within expected boundaries, SERI QC calculates the distance in *K*-space by which data fall outside the boundaries. The flagging system used by SERI QC records these distances and indicates whether one-element, two-element or three-element data were involved and whether the data point was below or above expected boundaries. The SERI QC flags, therefore, permit the assignment of uncertainties that are dependent on the nature of the test performed (one, two or three components) and the distance by which the data point exceeds expected limits. A more detailed description of SERI QC can be found in the *User's Manual for Quality Assessment of Solar Radiation Data*. In this respect the reader is referred to NREL's web site link provided in Chapter 8.

A point worth mentioning is that once the above filtering process has been completed and the erroneous data removed, there is a need to fill in the 'holes' within the data set. Unless this procedure is undertaken the time series would be incomplete and building energy simulation programs in particular are prone to hick-ups with such problems. Gaps identified within the data set may either be filled by generation of irradiation data from other synoptic data such as sunshine or cloud cover, or data averaging techniques. Rymes and Myers (2001) have presented a method for smoothly interpolating averaged (coarsely resolved) data into data with a finer resolution, while preserving the deterministic mean of the data. Their technique claims to preserve the component relationship between

direct, diffuse and global solar radiation when values for at least two of the components are available. Their method is primarily a simplification of the Markov moving averages auto-regression approach.

Web-based test procedures and tools

Geiger et al. (2002) have described the availability of a web-based service for quality control of solar radiation data. The service is available through the web site www.helioclim.net. The quality control procedure is part of an on-going effort of the Group 'Teledetection and Modelisation' of the Ecole des Mines de Paris/Armines to provide free-of-charge valuable tools and information to the solar radiation community through the most known and used media, namely the worldwide web. The object of that service is not to perform a precise and fine control but to perform a likelihood control of the data and to check their plausibility. This is achieved by comparing observations with some expectations based upon the extra-terrestrial irradiation and a simulation of the irradiation for clear skies. It offers a means to check time series of irradiation data. Inputs are provided via an HTML page by a copy and paste procedure and the return is also via similar means. Suspicious data are flagged upon return.

The user is requested to provide information to compute the quality control procedure: geographical co-ordinates, elevation and dates (if single value). HTML pages are available to better understand and fill the forms for each quality control procedure. Documents explaining the algorithm used in the calculation and references to articles, web sites of interest and publications on solar radiation topics are also provided.

The quality control procedure has been divided into four HTML documents:

(a) Daily irradiation for a single day: one value is to be examined.
(b) Daily irradiation for several days: several daily values spread over several months and years can be analysed.
(c) Hourly irradiation for a single hour: one value is analysed.
(d) Hourly irradiation for several hours: several hourly values spread over several days, months and years can be tested.

Geiger et al. (2002) quote the WMO published figures for the achievable relative uncertainties at the 95% confidence level for solar radiation measurements. These are about 3%, 8% and 20% for operational pyranometers of high, good and moderate quality in case of hourly sums. In case of daily sums, relative uncertainties of 2%, 5% and 10% are quoted. These figures are incorporated in relation to interpretation of quality control results. Note that in Chapter 1 similar figures were quoted based on the work of Coulson (1975).

Molineaux and Ineichen (2003) describe the availability of yet another web-based facility for quality control of solar radiation data. Their computer programs allow validation limits to be set on the tests so as to enable the user to increase the precision of the tests. The program reads an input file based on the ASCII format and in turn creates an output file in the same format with AQC flags. Visualisation of the comparisons between measured and predicted values (based on well established solar radiation models) is used to trace the errors. Their program carries out a series of coherence tests which is then followed by the creation of a number of plots based on comparisons between modelled/calculated and measured values.

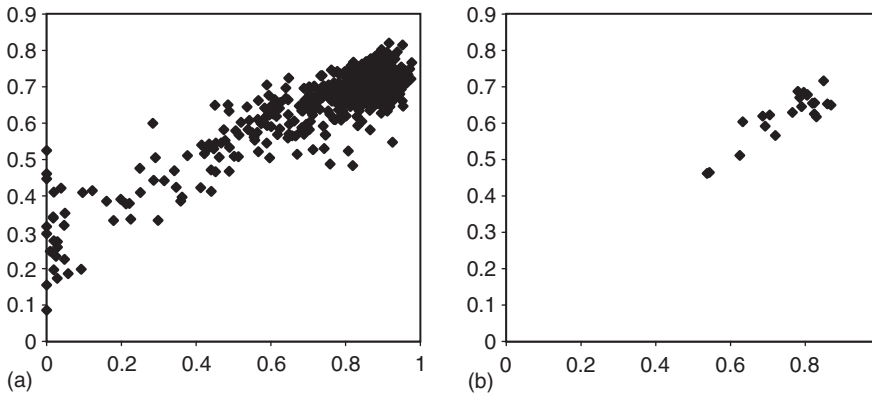

Figure 4.7.6 *(a) Daily clearness index plotted against daily sunshine fraction, Bahrain data (28 March 2000–23 January 2002). (b) Monthly-averaged clearness index plotted against monthly-averaged sunshine fraction, Bahrain data*

4.7.3 Daily- and monthly-averaged daily sunshine and irradiation data

A great deal of work has been undertaken by the ESRA team (Terzenbach, 1995; ESRA, 2000) in checking the quality of daily totals of sunshine and global irradiation using Ångström-type plots, i.e. a cross-plot of daily clearness index and daily sunshine fraction. This work may also be extended to a cross-plot of the above parameters on a monthly-averaged time scale. Furthermore, the type of analysis presented in Section 4.7.1 for hourly or sub-hourly diffuse ratio may also be extended, once again, for monthly-averaged daily totals. Plots prepared along these lines using Bahrain data are presented in Figure 4.7.6(a) and (b).

In ESRA (2000) examples for filtering out suspect data for two locations – Norderney, Germany and Puntijarka, Croatia – are presented. The procedure adopted by the ESRA team was to obtain Ångström relationship between daily clearness index and daily sunshine fraction with and without the suspect data. The suspect data were identified in the latter work as being those with an ordinate deviation greater than 0.3. However, a better filtration process may be carried out using established statistical procedures and one such procedure is described below.

4.7.4 Outlier analysis

In Section 1.11.5 it was pointed out that often in solar radiation studies one encounters data that lie unusually far removed from the bulk of the data population. Such data are called ‘outliers’. Statistical tests to ascertain whether a suspect datum is indeed an outlier were also presented in the above-mentioned section.

A high number of outliers in any given data set signifies that either the observations have a high degree of variability or that the station is operated poorly. For example, the ESRA team has reported significant differences between the monthly-averaged solar radiation standard deviation (σ) values for two European locations: Norderney (root mean square $= 0.061$) and Puntijarka ($\sigma = 0.152$).

With reference to Figure 4.7.6(a) the influence of any outlier such as that identified as the point bearing co-ordinates 0.468 and 0.301 may be investigated. If a narrow band of

data that fall within the daily clearness index band of 0.45–0.50 are considered, the interquartile range is obtained as 0.133. The lower limits (y-value) of near- and far-outliers would thus be 0.411 and 0.212, respectively. The datum under investigation is thus a near-outlier. The two sets of coefficient of determination (r^2-value), with and without the suspect point, are 0.81 and 0.82. This is a significant improvement considering removal of a single suspect datum out of a total of population of 664 points.

For a more rigorous discussion on outlier analysis reference is made to Draper and Smith (1998) and Montgomery and Peck (1992).

In Section 4.7.2 (Level 3 tests) a graphical (visual) procedure was presented as a means of quality control. In addition to the above outlier analysis Claywell et al. (2003) have proposed a new standard deviation-based procedure. Their procedure for identification of outliers using standard deviation categorises diffuse ratio (K)–clearness index (K_t) data in bands of K_t. Their proposed 'standard deviation' method identifies outliers by defining an envelope of acceptance, i.e. of $\overline{k} \pm 2\sigma\ k$ boundaries for any given K_t band. Any datum outside the described envelope of acceptance is potentially an outlier and needs to be queried. Based on Bahrain data, Figure 4.7.7(a) presents banded mean and median values of K along with the respective envelopes for $\overline{k} \pm 2\sigma\ k$ and the limits for near-outliers. For comparison

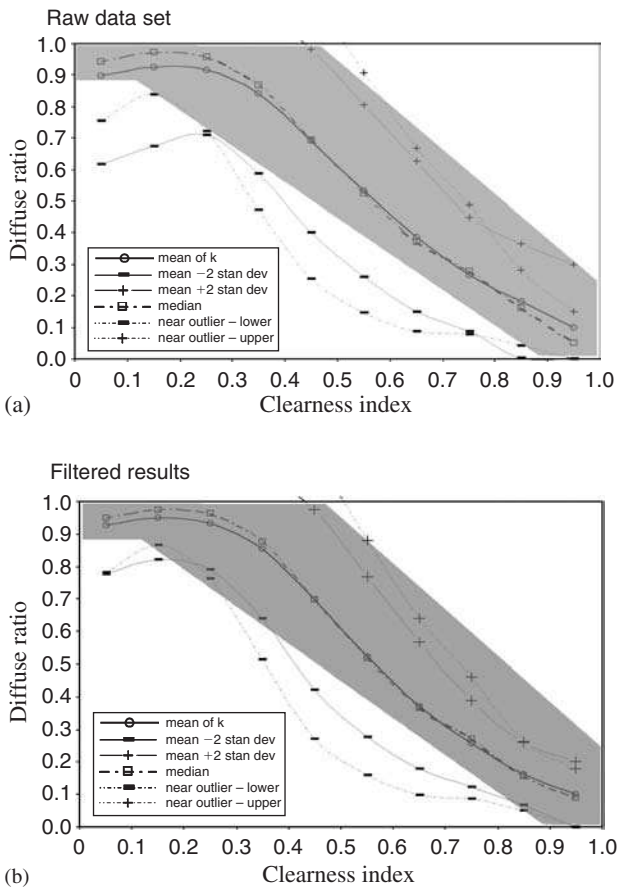

Figure 4.7.7 *Near outlier, standard deviation and Bahrain visual envelopes (highlighted area): (a) for raw data set and (b) after filtering*

(the standard area), the 'hand drawn' envelope for Bahrain is included in both Figures 4.7.7(a) and (b). After the suspect data are excluded the same analysis is repeated to see the impact of the removal of all data lying outside the +/−two standard deviation limits. This is shown in Figure 4.7.7(b). The new $\bar{k} \pm 2\sigma\, k$ method, described here, provides a very quick and efficient quality control and filtering methodology for large data sets, and outperforms the quartile analysis in terms of ease of programming and computation. FORTRAN program Prog4-7b.For enables execution of the above quality control procedure via K–K_t data provided in In4-7b.Txt file. Table 4.7.2 presents the output of Prog4-7b.For and its explanation.

4.7.5 Slope irradiation data

The outlier analysis introduced in the above section may easily be extended to quality control slope irradiation data. The usual practice of meteorological offices is to log these data on an hourly basis. However, more recent data recorded by academic and other research institutions are increasingly being measured and reported at 5 or 10 min averaged frequencies. Such data may be quality controlled by using any one of the recent, validated slope irradiation models, then comparing the difference between measured and expected slope irradiation. A similar technique was employed within the CIE (1994) quality control procedures applied on daylight illuminance data. Presently, demonstration is provided via the use of Muneer's (1990) established and widely validated slope irradiation model to undertake the task under discussion. The argument for this selection is that the latter procedure is the *CIBSE Guide J* (CIBSE, 2002) and ESRA (2000) reference model. In this respect a brief extract from ESRA (2000) text is presented below.

The EU ESRA (2000) programme was funded to the tune of $1 million and took 5 years for completion. The scientific co-ordinators for the ESRA programme were J. Page and R. Dogniaux. The ESRA team used data from 22 meteorological organisations representing the 15 EU member states and Russia to evaluate leading slope radiation models. Their findings are quoted herein: 'A review of the literature and preliminary comparative tests of the performance of existing models led to the selection of nine models for testing'. These were the Liu and Jordan (1960) basic isotropic model, the Bugler (1977), Klucher (1979), Hay (1979) and Reindl et al. (1990) representing a first generation of anisotropic models already describing the sky dome as incorporating circumsolar and/or horizon band enhancing of diffuse irradiance, the Gueymard (1987), Skartveit and Olseth (1986), Perez et al. (1990) and Muneer (1990a) models representing a second generation of yet more sophisticated models.

The models were ranked accordingly to the yearly averages of each of the above three performance parameters (MBE, RMSE and mean absolute bias error) in order to select a best model for each site and orientation. A 'geographical' average is performed to select a best model for each orientation. The models were sorted by the average rank for each site, new ranks were computed and averaged for the available sites. Finally, the model ranks for the various orientations were averaged as a group to select an overall best model, but in this case weights were applied based on an estimate of the relative importance of data for practical applications: weight 3 for south-facing surfaces, 2 for east- and west-facing surfaces and 1 for north-facing surfaces.

The Skartveit and Osleth (1986) and Muneer (1990a) models proved the best overall performers, followed by a group including the Reindl et al. (1990), Hay (1979), Perez et al.

Table 4.7.2 Sample output from Prog4-7b.For

Clearness index			Diffuse ratio							
Lower limit	Upper limit	No. of points	Lowest value	1st quartile	Median	3rd quartile	Highest value	Mean	Wt. mean	Standard deviation of wt. mean
0.045	0.09	175	0.1	0.875	0.938	0.966	0.988	0.872	0.874	0.158
0.09	0.135	218	0.167	0.922	0.962	0.979	0.993	0.905	0.925	0.15
0.135	0.18	241	0.189	0.929	0.965	0.981	0.994	0.922	0.937	0.13
0.18	0.225	383	0.108	0.875	0.955	0.981	0.996	0.904	0.914	0.124
0.225	0.27	501	0.31	0.868	0.953	0.982	0.997	0.909	0.916	0.108
0.27	0.315	855	0.438	0.857	0.933	0.977	0.997	0.902	0.905	0.099
0.315	0.36	1508	0.393	0.798	0.897	0.959	0.997	0.867	0.87	0.111
0.36	0.405	2250	0.254	0.708	0.817	0.912	0.998	0.8	0.802	0.132
0.405	0.45	2768	0.238	0.623	0.736	0.84	0.996	0.728	0.729	0.14
0.45	0.496	3090	0.299	0.558	0.661	0.77	0.99	0.662	0.662	0.141
0.496	0.541	3678	0.245	0.483	0.577	0.677	0.99	0.584	0.583	0.137
0.541	0.586	4338	0.177	0.421	0.508	0.599	0.996	0.517	0.516	0.13
0.586	0.631	5446	0.187	0.367	0.442	0.526	0.996	0.454	0.453	0.122
0.631	0.676	7627	0.167	0.313	0.375	0.446	0.997	0.39	0.388	0.113
0.676	0.721	12595	0.125	0.258	0.317	0.381	0.99	0.332	0.331	0.106
0.721	0.766	18011	0.111	0.219	0.261	0.309	0.994	0.273	0.272	0.083
0.766	0.811	11582	0.103	0.178	0.207	0.243	0.978	0.219	0.218	0.07
0.811	0.856	1973	0.086	0.118	0.139	0.168	0.822	0.169	0.167	0.099
0.856	0.901	94	0.079	0.087	0.374	0.468	0.755	0.332	0.336	0.193

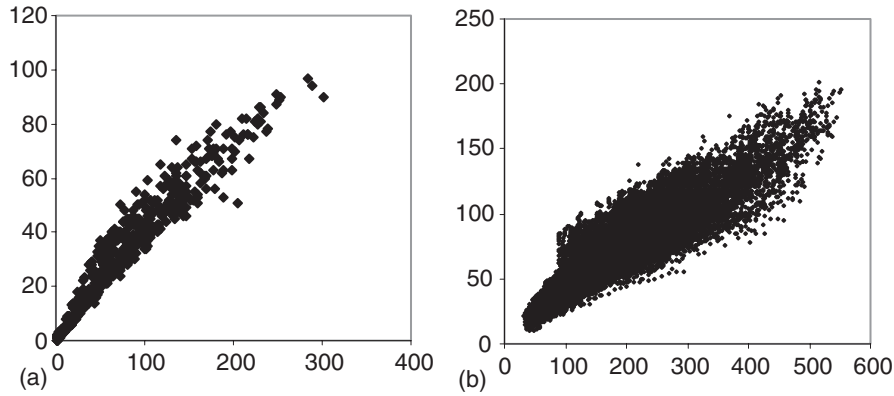

Figure 4.7.8 *Relationship between diffuse irradiance on a vertical surface facing away from sun and horizontal diffuse irradiance: (a) Bracknell hourly data and (b) Bahrain 5 min data. Both axes in W/m²*

(1990) and isotropic models. Finally, the fact that the Muneer (1990a) diffuse model seemed also to have a sounder theoretical basis, and thus more potential for improvement was additionally taken into account. This model was therefore selected for generation of slope irradiance.

Findings similar to the one mentioned above regarding the Perez et al.'s model have been reported by Kambezidis et al. (1994) and Li and Lam (1999). Their findings suggest that the Perez et al.'s model requires construction of localised coefficients based on local measurements and therefore poses limitations on the use of the latter model. However, once fitted with localised coefficients the latter model provides optimised results.

Muneer's model differentiates between sloping (or vertical) surfaces facing away from sun (labelled as 'shaded' surfaces) and those that face the sun ('sunlit' or 'sun-facing' surfaces). It has been shown that for worldwide locations there is a linear regression between shaded and horizontal diffuse irradiance. Figure 4.7.8 demonstrates this feature for two disparate locations. For sunlit surfaces the Muneer's model uses a two-component approach to predict slope irradiance, details of which are provided in Section 4.3.3.5. Figure 4.7.9 presents such a plot for Bahrain. Similar plots for other worldwide locations are provided in Muneer (1995). A banded outlier analysis may hence be applied on data presented in Figures 4.7.8 and 4.7.9 to identify any suspect data. The approach would be similar to that demonstrated with respect to Figure 4.7.6. Alternatively, Prog4-7b.For may be used for automating the identification of outliers.

4.7.6 Checking for completeness of time series

Once the above quality control procedures have been completed and any erroneous data replaced a check for the completeness of time series is required. This is particularly the case for stations that are operated by part-time staff when the station down times may be considerable. Prog4-7c.For, Prog4-7d.For and Prog4-7e.For may prove to be of value in this respect. These programs, respectively designed for hourly (Prog4-7c.For and Prog4-7d.For) and 5 min (Prog4-7e.For) data files, require In4-7c.Dat, In4-7d.Dat and In4-7e.Csv files.

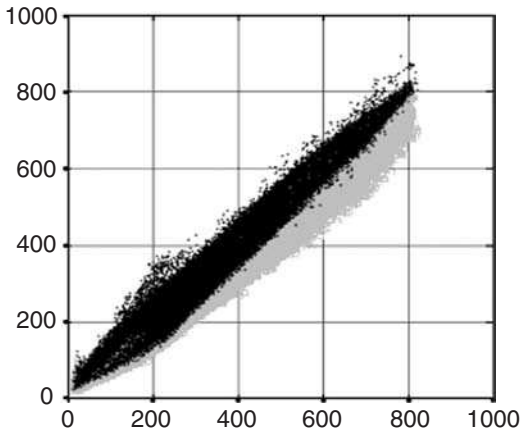

Figure 4.7.9 *Computed irradiance on a south-facing vertical surface plotted against measured data for Bahrain. Both axes in W/m²*

Checks for the continuity of hourly data and any discontinuities are identified by a gap in the running counter, i.e. generated in the first column of the output file (In4-7d.Dat). Furthermore, the program for hourly data Prog4-7d.For takes the latter file In4-7d.Dat to the next stage whereby an output file Out4-7d.Dat is produced with any missing time slots being filled in with a −99 code.

The above operations are demonstrated via Example 4.7.2

Example 4.7.2

The data file In4-7c.Dat contains hourly global and diffuse radiation records (provided in the last two columns within the file) for 7 years for a given European location. The irradiation data are provided at an hour-ending basis. Close examination of the file shows that data for the 16th hour for 11 December, 1997 are missing. Furthermore, data for the first hour of the day for the period 12–30 December 1997 are also missing as is the data for the last day of December 1997. Use Prog4-7c.For and Prog4-7d.For to respectively identify the missing periods and then fill the gaps with a prescribed coded number (−99 has been presently chosen).

The above tasks may be achieved by executing Prog4-7c.For and Prog4-7d.For. The former FORTRAN program creates an output file with the name In4-7d.Dat which is in turn required by the latter program. The format for In4-7d.Dat is identical to that of file In4-7c.Dat with the exception that an additional first column contains a running counter. The final output file Out4-7d.Dat contains a complete time series with the missing data identified with the −99 code.

The program Prog4-7e.For requires file In4-7e.Csv for its execution. The latter data file contains 5 min data for CIE-IDMP first class station with six illuminance sensor and six pyranometer readings for each time record. The program may be altered for other time frequency or sensor arrangements. The program outputs the line at which it identifies any break in the time series. Presently, with the given input file the output identifier shows that there is missing data for the time record (year, month, day, hour and minute):

1993 4 2 12 25

4.8 Shadow band (shade ring) diffuse irradiance correction factor

For solar energy application design, global and diffuse horizontal irradiance and beam normal irradiance are the three most important quantities. The important role that diffuse irradiance plays in a solar energy system design cannot be overemphasised. It was reported by Drummond (1956) and others that the long-term average ratio of diffuse to global irradiance can be as high as 0.65. Therefore, to provide a precise estimation of the solar energy available for a given application, an accurate measurement of diffuse irradiance is required.

The relationship between I_G, I_D and $I_{B,n}$ is:

$$I_G - I_D = I_{B,n} \sin \text{SOLALT} \tag{4.8.1}$$

Therefore, diffuse irradiance can either be calculated from measurement of I_G and $I_{B,n}$ or measured directly. Measurements of beam normal irradiance are made using a pyrheliometer. Unfortunately, the collection of pyrheliometric data can be very expensive. The direct equipment cost alone is almost six times the expense of alternate collection methods. For example, prices quoted for Kipp and Zonen, premium grade equipment (ISO 9000 standard) in February 2003, were \$18 909 for a pyrheliometric system and \$3245 for a pyranometer with a shadow band. The overall expense is most certainly directly related to the equipment cost, but has a significant indirect cost which is linked to the high level of daily maintenance associated with pyrheliometric system. An alternate and relatively inexpensive approach that is often employed is to use a pyranometer with an occulting device, to block the beam direct component from reaching the sensor. The most commonly used occulting devices are shadow bands or shade rings. All shading devices are usually coated with a low albedo black paint to reduce any reflected radiation from the shadow band. The shadow bands are aligned and fixed parallel to the earth's polar axis matching the sun's track in the sky. This method produces a constant shadow on the pyranometer's sensor, effectively blocking the beam direct irradiance and theoretically leaving only the diffuse irradiation. Shadow band use is economical and effectively shades direct beam irradiation. Regrettably, shadow bands also shade a portion of the sky and the corresponding reduced measured diffuse irradiance. This shading thus introduces errors that can markedly influence the accuracy of measurements. It has been shown that shading errors can lead to a maximum error of up to 24% in the true diffuse irradiance value and hence a correction factor needs to be introduced. An energy audit can derive the correction factor for the physical amount of sky that is blocked by the shadow band and the amount of diffuse irradiance that is representative of that blocked portion. Figure 4.8.1 is a pictorial representation of the view of the sky as seen from a pyranometer with a shade ring. The latter picture was taken by staff at University of Gerona, Spain to whom credit is hereby given.

The correction factor of the diffuse irradiance can be calculated by using the simple geometric method given by Drummond (1956). This geometric method calculates the proportion of the sky area that is subtended by the shadow band f and then derives the correction factor as $1/(1 - f)$. However, as shown in the earlier part of Chapter 4, real sky-diffuse distribution is not isotropic, an anisotropic factor must be taken into consideration to obtain a correction factor. The necessity of applying an anisotropic correction factor has been widely investigated. Kudish and Ianetz (1993) have reported that, for

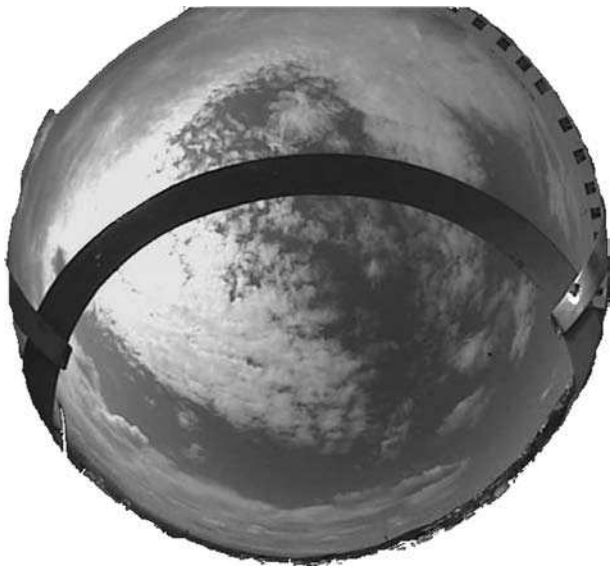

Figure 4.8.1 *View of the sky as seen from the pyranometer end of a diffuse irradiance measurement set up with properly aligned shadow band*

Beer Sheva, Israel, the anisotropic correction factor varies from 2.9% to 20.9%, whereas the geometric (isotropic) correction factor varies only from 5.6% to 14.0%. Painter (1981) compared the diffuse irradiance measured by both an occulting disc and a shadow band pyranometer. He concluded that the anisotropic correction factor has a significant seasonal deviation. Vartiainen's study (1998) showed that the deviation of the monthly isotropic correction factor with respect to total correction factor ranges from 1% for winter to 7.5% for summer months.

During the past decade several investigators have undertaken work relating the development of an anisotropic diffuse irradiance correction method. Ineichen et al. (1984) reported their method of combining two simple models to determine the total correction factor: one was the isotropic geometric model and the other was based on the diffuse radiation expressed as a function of solar altitude. Kasten et al. (1983) considered the influence of three parameters that were most relevant in determining the anisotropic correction factor, namely the ratio of the diffuse to global radiation, the solar declination and the coefficient for beam radiation transmission. Siren's (1987) investigation and evaluation, based on a two-component sky radiation model, showed that the total correction factor appeared to be a function of the shadow band geometry, location of the shadow band and the sky radiation distribution. LeBaron et al. (1990) presented a model employing the parameter scheme method put forward by Perez et al. (1990). This parameter scheme is represented as a 256-grided values of the zenith angle of sun, the isotropic correction factor, the sky's clearness index and the sky's brightness index.

In the following sections four methods for correcting the shadow band diffuse correction factor are presented and a synopsis of their performance inter-compared. For a fuller treatment of the relevant validation procedure the reader is referred to the studies undertaken by Muneer and Zhang (2002), Muneer et al. (2003) and Lopez et al. (2003a,b).

4.8.1 Drummond's method

Drummond (1956) gave the following formula based on geometrical analysis to calculate the isotropic shadow band diffuse correction factor C_D:

$$C_D = 1/(1 - f) \tag{4.8.2}$$

where f is the proportion of diffuse irradiance obstructed by the shadow band. Note that C_D is to be multiplied with the uncorrected value of diffuse irradiance as measured with shadow band to provide the corrected diffuse irradiance. f can be calculated by:

$$f = X/T = 2(W/\pi)\cos^3 \text{DEC}(\omega_s \sin \text{LAT} \sin \text{DEC} + \cos \text{LAT} \cos \text{DEC} \sin \omega_s) \tag{4.8.3}$$

where X is the diffuse irradiance shaded by shadow band, T is the total (true) diffuse irradiance. Equation (4.8.3) is derived from the integration of Eqs (4.8.4) and (4.8.5), based on the assumption that the sky-diffuse radiance distribution is uniform. Note that the sunrise/sunset hour angle ω_s is given by Eq. (2.7.9):

$$X = IW \cos^3 \text{DEC} \int_{\omega_s=\text{sunrise}}^{\omega_s=\text{sunset}} \sin \text{SOLAT} \, d\omega \tag{4.8.4}$$

$$T = \pi I \tag{4.8.5}$$

where I is the radiation intensity of the sky and W is the shadow band width. However, as the real sky-diffuse radiance distribution is anisotropic, a more accurate correction factor is obtained when the I value is treated as a variant.

4.8.2 LeBaron et al's method

LeBaron's model (1990) builds on methods developed by Drummond (1956) and Perez et al. (1990). LeBaron's correction model uses four parameters to describe both isotropic and anisotropic sky conditions. The first of these parameters is C_D while the other three parameters describe the anisotropic contribution to the total shadow band correction. These parameters are, the zenith angle θ_z, used to index the position of the sun in the vertical plane, ε, and Δ. Recall that ε and Δ are dimensionless parameters that index the sky's clearness and brightness, respectively. ε is primarily a function of the cloud conditions and Δ a function of the cloud thickness or aerosol loading. In LeBaron's model, ε is a simplification of the term used by Perez et al. (1990) in that it is not corrected for the solar zenith angle.

Using the four parameters in order, θ_z, C_D, ε and Δ, the model clusters the data according to 256 separate categories, so the final LeBaron correction factor C_L is actually 'looked up' in Table 4.8.1 and applied to the shadow band measured I_d with the following equation:

$$I_{d\text{LeBaron}} = C_L I_d$$

Table 4.8.1 LeBaron et al. (1990) shadow band correction factors for the parameterised catagories (*i* = zenith, *j* = geometric, *k* = epsilon, *l* = delta)

(*i*, *j*,1,1)

i =	*j* = (,1)	(,2)	(,3)	(,4)
(1,)	1.051	1.082	1.117	1.173
(2,)	1.051	1.104	1.115	1.163
(3,)	1.069	1.082	1.119	1.140
(4,)	1.047	1.063	1.074	1.030

(*i*, *j*,2,1)

i =	*j* = (,1)	(,2)	(,3)	(,4)
(1,)	1.051	1.082	1.117	1.248
(2,)	1.051	1.082	1.117	1.184
(3,)	1.161	1.161	1.147	1.168
(4,)	1.076	1.078	1.104	1.146

(*i*, *j*,3,1)

i =	*j* = (,1)	(,2)	(,3)	(,4)
(1,)	1.051	1.082	1.117	1.156
(2,)	1.051	1.082	1.117	1.156
(3,)	1.051	1.082	1.117	1.156
(4,)	1.187	1.167	1.139	1.191

(*i*, *j*,4,1)

i =	*j* = (,1)	(,2)	(,3)	(,4)
(1,)	1.051	1.082	1.117	1.181
(2,)	1.051	1.082	0.990	1.104
(3,)	1.015	1.016	0.946	1.027
(4,)	0.925	0.967	0.977	1.150

(*i*, *j*,1,2)

i =	*j* = (,1)	(,2)	(,3)	(,4)
(1,)	1.051	1.082	1.117	1.176
(2,)	1.051	1.095	1.130	1.162
(3,)	1.073	1.089	1.115	1.142
(4,)	1.058	1.076	1.117	1.156

(*i*, *j*,2,2)

i =	*j* = (,1)	(,2)	(,3)	(,4)
(1,)	1.051	1.082	1.117	1.211
(2,)	1.051	1.082	1.186	1.194
(3,)	1.086	1.130	1.168	1.177
(4,)	1.074	1.102	1.118	1.174

(*i*, *j*,3,2)

i =	*j* = (,1)	(,2)	(,3)	(,4)
(1,)	1.051	1.082	1.117	1.237
(2,)	1.051	1.082	1.203	1.212
(3,)	1.080	1.195	1.211	1.185
(4,)	1.140	1.098	1.191	1.181

(*i*, *j*,4,2)

i =	*j* = (,1)	(,2)	(,3)	(,4)
(1,)	1.051	1.082	1.117	1.217
(2,)	1.051	1.082	1.120	1.180
(3,)	1.182	1.115	1.081	1.111
(4,)	1.057	1.119	1.133	1.033

(*i*, *j*,1,3)

i =	*j* = (,1)	(,2)	(,3)	(,4)
(1,)	1.051	1.082	1.117	1.182
(2,)	1.051	1.082	1.128	1.159
(3,)	1.076	1.088	1.131	1.129
(4,)	1.060	1.085	1.103	1.156

(*i*, *j*,2,3)

i =	*j* = (,1)	(,2)	(,3)	(,4)
(1,)	1.051	1.082	1.117	1.221
(2,)	1.051	1.171	1.180	1.213
(3,)	1.135	1.148	1.176	1.197
(4,)	1.092	1.119	1.143	1.182

(*i*, *j*,3,3)

i =	*j* = (,1)	(,2)	(,3)	(,4)
(1,)	1.051	1.082	1.117	1.238
(2.)	1.051	1.160	1.207	1.230
(3,)	1.169	1.191	1.193	1.210
(4,)	1.150	1.133	1.180	1.156

(*i*, *j*,4,3)

i =	*j* = (,1)	(,2)	(,3)	(,4)
(1,)	1.051	1.082	1.117	1.156
(2,)	1.051	1.082	1.117	1.156
(3,)	1.051	1.082	1.117	1.156
(4,)	1.089	1.194	1.216	1.064

(*i*, *j*,1,4)

i =	*j* = (,1)	(,2)	(,3)	(,4)
(1,)	1.051	1.082	1.117	1.191
(2,)	1.051	1.105	1.143	1.168
(3,)	1.085	1.093	1.117	1.156
(4,)	1.069	1.082	1.117	1.156

(*i*, *j*,2,4)

i =	*j* = (,1)	(,2)	(,3)	(,4)
(1,)	1.051	1.082	1.117	1.238
(2,)	1.051	1.148	1.195	1.230
(3,)	1.132	1.160	1.183	1.210
(4,)	1.118	1.116	1.150	1.185

(*i*, *j*,3,4)

i =	*j* = (,1)	(,2)	(,3)	(,4)
(1,)	1.051	1.082	1.117	1.232
(2,)	1.051	1.206	1.210	1.238
(3,)	1.144	1.178	1.226	1.216
(4,)	1.117	1.155	1.178	1.167

(*i*, *j*,4,4)

i =	*j* = (,1)	(,2)	(,3)	(,4)
(1,)	1.051	1.082	1.117	1.156
(2,)	1.051	1.082	1.117	1.156
(3,)	1.051	1.082	1.117	1.156
(4,)	1.024	1.025	1.162	1.142

* The shaded numbers are 'mean' factors, derived using Drummond's geometric formula.
Boundaries for the parameters in the above table – index (3,4,1,3) would be (*i*) 50–60 zenith angle, (*j*) geometric screening > 13.2%, (*k*) overcast skies and (*l*) average to high sky brightness

Cuts	1	2	3	4	
i	0.000	35.00	50.00	60.00	90.00
j	1.000	1.068	1.100	1.132	–
k	0.000	1.253	2.134	5.980	–
l	0.000	0.120	0.200	0.300	–

4.8.3 Batlles et al.'s method

The Batlles et al. (1995) model utilises a multiple linear regression employing the four parameters in LeBaron's (1990) approach. The correction factor C_B is then expressed as an analytical function of C_D, θ_z and Δ, which is parameterised against ε. The set of equations is:

$$\varepsilon \leqslant 3.5 \quad C_B = 1.178C_D + 0.207 \log \Delta + 0.122/\exp(m) \tag{4.8.6}$$

$$3.5 < \varepsilon \leqslant 8 \quad C_B = 1.454C_D + 0.655 \log \Delta + 0.4756/\exp(m) \tag{4.8.7}$$

$$8 < \varepsilon \leqslant 11 \quad C_B = 1.486C_D + 0.495 \log \Delta \tag{4.8.8}$$

$$\varepsilon > 11 \quad C_B = 1.384C_D + 0.363 \log \Delta \tag{4.8.9}$$

Measurements of diffuse irradiance are then corrected using:

$$I_{d^{Batlles}} = C_B I_d \tag{4.8.10}$$

4.8.4 Muneer–Zhang method

With reference to Eq. (4.3.3.1) Muneer and Zhang (2002) developed mathematical relationship between b and K_t as follows:

$$\text{For } K_t > 0.2, \quad \frac{2b_1}{\pi(3 + 2b_1)} = 0.382 - 1.11K_t \text{ (for southern half of sky hemisphere)} \tag{4.8.11a}$$

$$\text{and} \quad \frac{2b_2}{\pi(3 + 2b_2)} = 0.166 + 0.105K_t \text{ (for northern half of sky hemisphere)} \tag{4.8.11b}$$

For $K_t \leqslant 0.2$, $b_1 = b_2 = 1.68$, after Muneer (1990a).

A point worth mentioning here is that, strictly speaking, the sky radiance distribution is two dimensional, a function of any given SP geometry (SP altitude and azimuth) and the position of the sun. Equation (4.8.11) represents a compromise between simplicity (represented by an isotropic model) and complexity (represented by a two-dimensional model such as those described above). Another feature of Eq. (4.8.11) is that due to its relative simpler formulation it also tends to be robust (covering all-sky conditions) and of general applicability.

The total sky-diffuse irradiance can be obtained through a numerical integration based on Moon and Spencer's sky-diffuse distribution model. If the zenith radiance is termed L_z, then the horizontal diffuse irradiance I_D can be calculated using:

$$I_D = \int_0^{\pi/2} (\pi \sin\theta \cos\theta)(L_{\theta_1} + L_{\theta_2})\,\mathrm{d}\theta \tag{4.8.12}$$

where $L_{\theta_1} = L_z(1 + b_1\cos\theta)/(1 + b_1)$, and $L_{\theta_2} = L_z\,(1 + b_2\cos\theta)/(1 + b_2)$. L_{θ_1} is defined as the sky-diffuse radiance emanating from any given patch of the southern half of the sky vault, and $L_{\theta 2}$ the corresponding radiance from the northern half of the sky hemisphere. Thus:

$$I_D = \pi L_z\left\{\left[\int_0^{\pi/2}(\sin\theta\cos\theta + b_1\sin\theta\cos^2\theta)/(1 + b_1)\mathrm{d}\theta\right] + \left[\int_0^{\pi/2}(\sin\theta\cos\theta + b_2\sin\theta\cos^2\theta)/(1 + b_2)\mathrm{d}\theta\right]\right\} \tag{4.8.13}$$

So:

$$I_D = (\pi L_z/6)[\{(3 + 2b_1)/(1 + b_1)\} + \{(3 + 2b_2)/(1 + b_2)\}] \tag{4.8.14}$$

If F_Δ is defined as the diffuse irradiance that is obscured by the shadow band, then F_Δ may be calculated by:

$$F_\Delta = W\cos^3\mathrm{DEC}\int_{\omega_s=\text{sunrise}}^{\omega_s=\text{sunset}} L_{\theta_1}\sin\mathrm{SOLAT}\,\mathrm{d}\omega \tag{4.8.15}$$

The result of the above integration is:

$$F_\Delta = 2WL_z\cos^3\mathrm{DEC}(I_1 + b_1I_2)/(1 + b_1) \tag{4.8.16}$$

$$I_1 = \cos\mathrm{LAT}\cos\mathrm{DEC}\sin\omega_s + \omega_s\sin\mathrm{LAT}\sin\mathrm{DEC}$$

$$I_2 = \omega_s\sin^2\mathrm{LAT}\sin^2\mathrm{DEC} + 2\sin\omega_s\sin\mathrm{LAT}\cos\mathrm{LAT}\sin\mathrm{DEC}\cos\mathrm{DEC} + \cos^2\mathrm{LAT}\cos^2\mathrm{DEC}[\omega_s/2 + (\sin 2\omega_s)/4]$$

The Muneer–Zhang shadow band diffuse irradiance correction factor, C_{M-Z}, can now be obtained:

$$C_{M-Z} = 1/(1 - F_\Delta/I_D) \tag{4.8.17}$$

4.8.4.1 Evaluation of shadow band diffuse irradiance correction factors

Validation of the above procedures was undertaken by Muneer and Zhang (2002) and Lopez et al. (2003a,b) using data for Bracknell, England (51.4°N and 0.8°W), Beer Sheva, Israel (31.3°N and 34.8°E) and Almeria, southern Spain (36.83°N and 2.45°W).

The true correction factor F_{true} is obtained by:

$$F_{\text{true}} = (I_G - I_{B,n}\sin\mathrm{SOLALT})/I_{D,\text{uncorrected}} \tag{4.8.18}$$

Figure 4.8.2 shows that Drummond's isotropic correction factor ranges from 1.010 to 1.128, whereas the true correction factor ranges from 1.001 to 1.480. It is therefore confirmed that, in the case of hourly diffuse irradiance measurement, Drummond's method significantly underestimates the shade-ring correction factor.

Results based on the work of Muneer and Zhang (2002) and Lopez et al. (2003a,b) on the evaluation of the performance of the models are shown by means of graphical and statistical

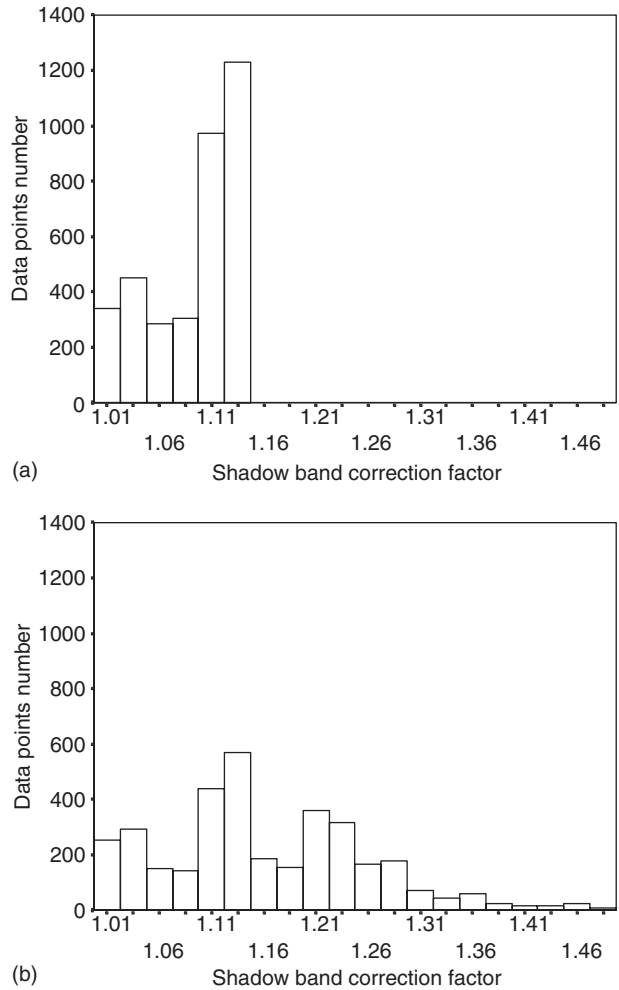

Figure 4.8.2 *Diffuse irradiance correction factor given by: (a) Drummond's method and (b) actual results*

techniques. Figures 4.8.3–4.8.6 show these results. Corrected diffuse irradiance is shown plotted against true diffuse irradiance. Figure 4.8.5 shows the residual differences, calculated as corrected diffuse irradiance minus true diffuse irradiance values and expressed as percentage of the mean value of true diffuse irradiance for each interval of K_t.

Furthermore, Table 4.8.2 shows the statistical results for the performance of each model for correcting diffuse irradiance under varying regimes of cloud cover. In order to analyse the models performance under different sky conditions the data set was split into two subsets, one corresponding to cloudless skies and the other corresponding to cloudy to part-cloudy skies. To identify cloudless conditions, the radiometric criterion proposed by Batlles et al. (2000) was used (see Eq. (4.2.4)).

Statistical evaluation was carried out based on the regression analysis of corrected diffuse irradiance versus true diffuse irradiance values, in terms of the coefficient of determination R^2, RMSE and MBE. Both RMSE and MBE have been expressed as a percentage of the mean value of true diffuse irradiance.

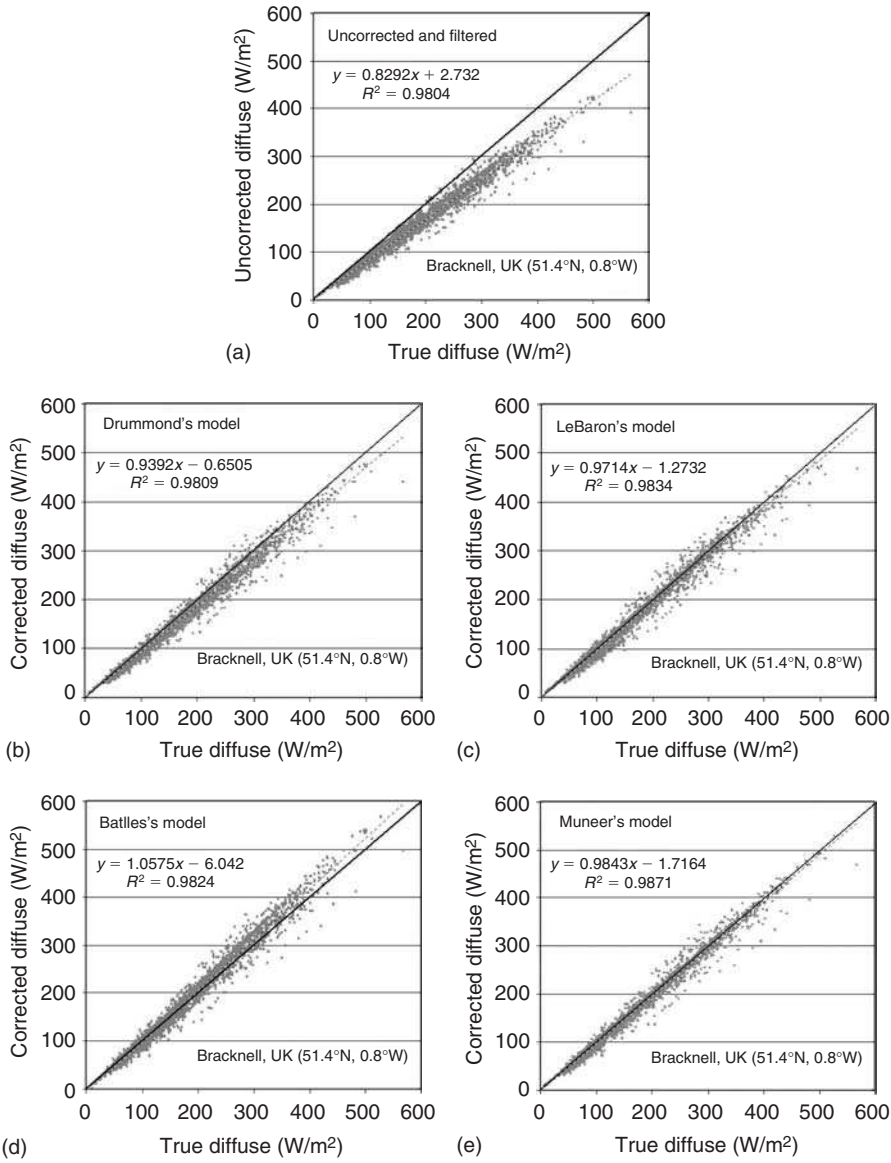

Figure 4.8.3 *Evaluation of diffuse irradiance correction models, Bracknell data*

It is noted that the rather simple Drummond's model shifts the measured diffuse irradiance data points quite significantly towards the one-to-one relationship between corrected- and true-diffuse irradiance under regimes of high diffuse irradiance values. Nevertheless, we note that the other three models perform better. Drummond's model improves the measurements. For example, for Almeria, the reduction of the RMSE and MBE is around 10% with respect to uncorrected diffuse irradiance. Nevertheless, diffuse irradiance measurements corrected by Drummond's model produces an underestimation of the true diffuse

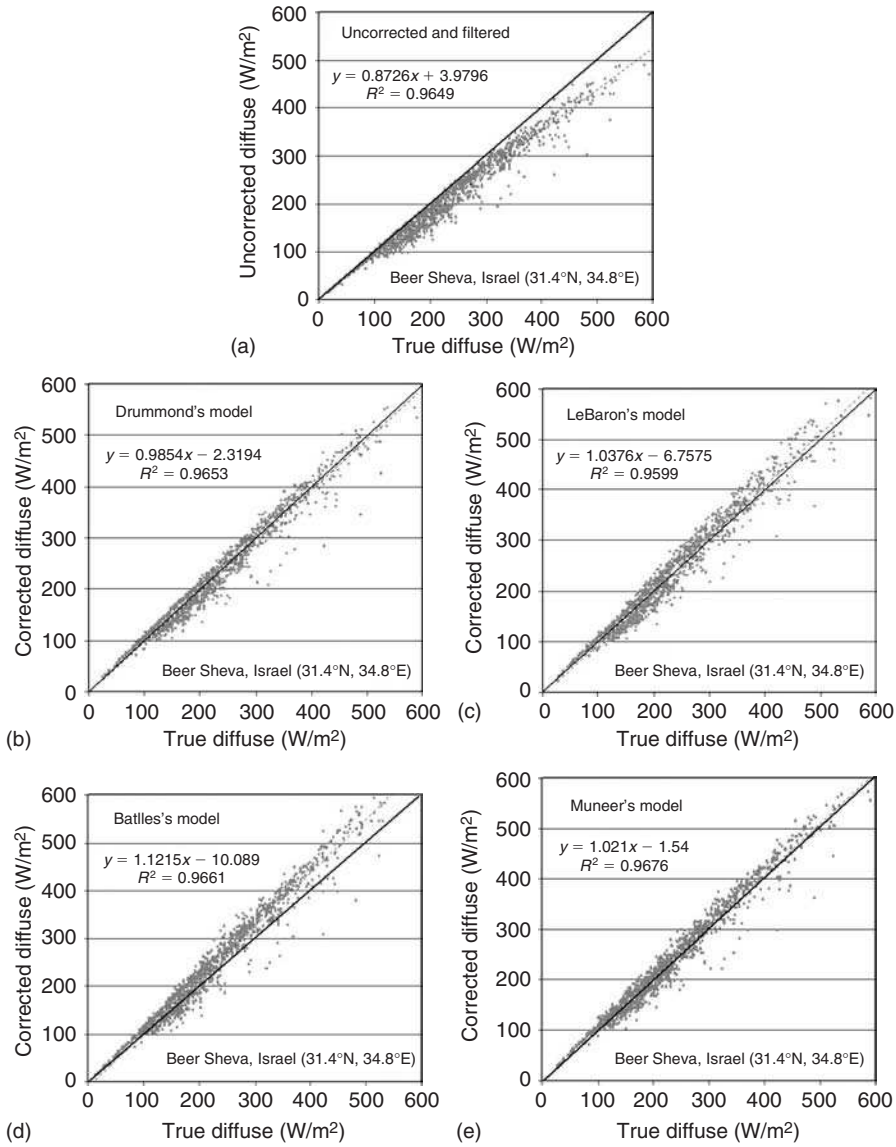

Figure 4.8.4 *Evaluation of diffuse irradiance correction models, Beer Sheva data*

values of around −10%. Models based on anisotropic conditions perform better than Drummond's isotropic model as RMSE and MBE values prove. Among these models, LeBaron's model presents the highest values of both RMSE and MBE. Thus, LeBaron's model provides an accentuated underestimation. Batlles and Muneer–Zhang models provide the lowest MBE and RMSE. The coefficient of determination is very high in all cases.

Given the information presented in Figures 4.8.3–4.8.6 it may be noted that uncorrected measurements of diffuse irradiance present underestimation ranging from −10% for low K_t

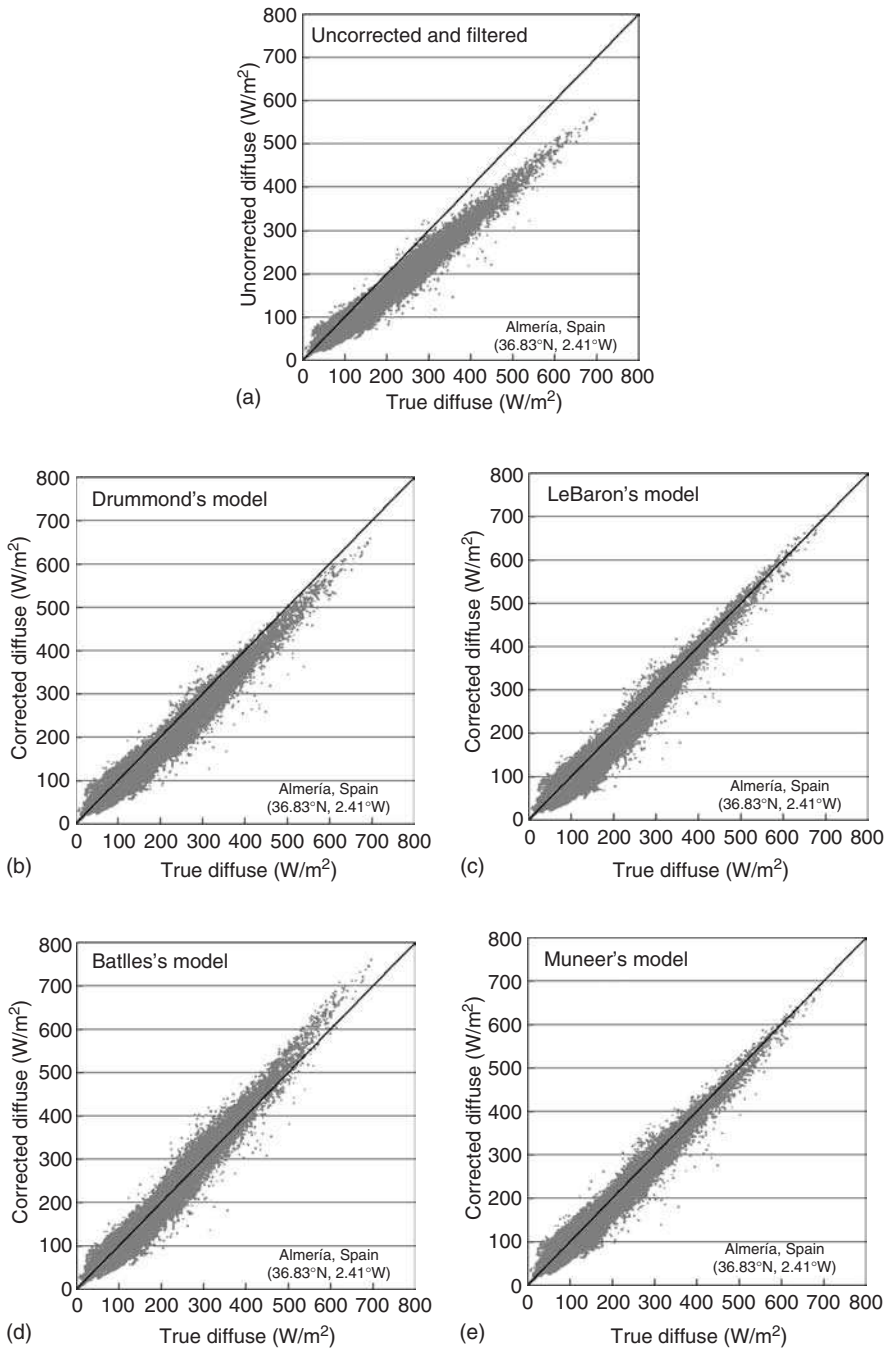

Figure 4.8.5 *Evaluation of diffuse irradiance correction models, Almeria data*

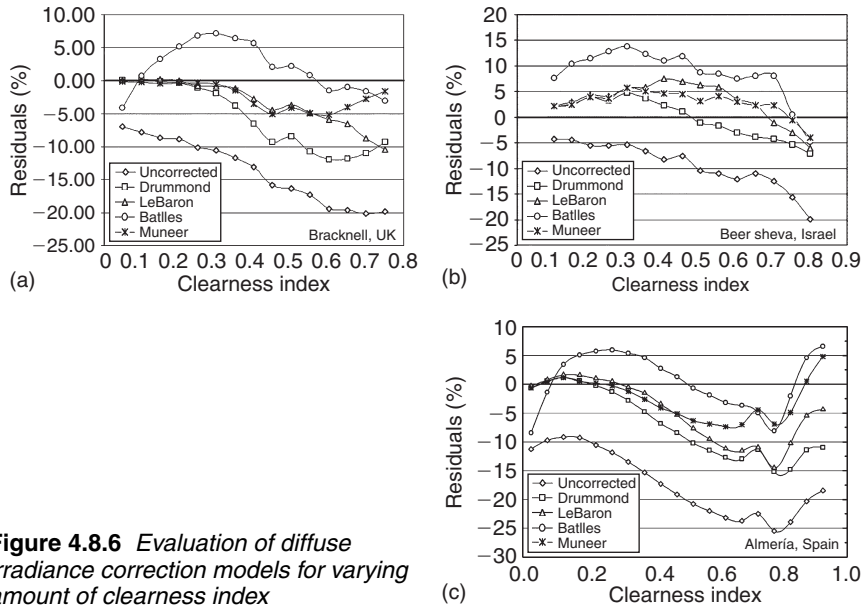

Figure 4.8.6 *Evaluation of diffuse irradiance correction models for varying amount of clearness index*

Table 4.8.2 Evaluation of shadow band diffuse irradiance correction models

		All-sky conditions			Overcast to part-cloudy			Clear sky conditions		
Site	Model	R^2	MBE	RMSE	R^2	MBE	RMSE	R^2	MBE	RMSE
Bracknell										
	Uncorrected	0.98	−26	32.9	0.98	−25.1	32.9	0.99	−28.3	32.7
	Drummond	0.98	−10.9	17.7	0.98	−8.5	16.9	0.99	−16.3	19.5
	LeBaron	0.98	−5.2	15.6	0.98	−0.6	13.4	0.98	−16.1	19.7
	Batlles	0.98	3.7	15.3	0.98	6.9	16.7	0.98	−3.8	11.2
	Muneer	0.99	−4.3	11.8	0.99	−3.6	12.5	0.99	−5.9	10.3
Beer Sheva										
	Uncorrected	0.96	−25	33.2	0.97	−24.2	34	0.92	−26.2	31.9
	Drummond	0.97	−4	18.8	0.97	−0.7	19	0.93	−8.5	18.4
	LeBaron	0.96	0.2	21.2	0.97	6.4	22.2	0.91	−8.4	19.7
	Batlles	0.97	17.6	30.7	0.97	26	35.5	0.91	5.8	22.4
	Muneer	0.97	4.5	18.8	0.98	7.1	19.8	0.92	0.8	17.3
Almeria										
	Uncorrected	0.96	−20.9	26.8	0.97	−18	23.5	0.89	−23.5	29.4
	Drummond	0.96	−10.2	16.6	0.98	−7.2	12.4	0.89	−13	20.5
	LeBaron	0.96	−8.7	15.8	0.98	−3.1	8.9	0.87	−13.9	21.7
	Batlles	0.96	−2.1	13.6	0.98	2.2	9.7	0.88	−6	17.2
	Muneer	0.96	−4.9	12.9	0.98	−3.6	9	0.89	−6.1	16.4

values to −24% for K_t values around 0.78. Residuals from the isotropic Drummond's model present no deviation for $K_t < 0.3$, whereas an accentuated underestimation is noted for $K_t > 0.6$ with residuals higher than −10%. These results show that under cloudy conditions, diffuse irradiance can be considered isotropic, and thus, a correction factor accounting only for isotropic conditions, such as the one proposed by Drummond, leads to fairly accurate corrections. Under cloudless conditions, sky anisotropy plays a major role and an isotropic correction factor is not sufficient. It is interesting to note that as the clearness index increases beyond 0.8, the underestimation of uncorrected measurements is reduced. Higher values of clearness index are principally associated to part-cloudy skies (Vázquez et al., 1991) and the sky anisotropy is thus expected to decrease. Lebaron's model, which incorporates both isotropic and anisotropic conditions in the correction factor, presents residual deviations similar to that due to Drummond's model with a slight improvement for the central range of K_t (associated with part-cloudy skies) and for $K_t > 0.8$.

Prog4-8.For enables computation of the above four shade-ring correction factors.

4.9 Exercises

4.9.1 File3-1.Csv contains 5 min averaged, horizontal and slope irradiance as well as illuminance data for Edinburgh (55.95°N and 3.2°W). Use the horizontal irradiance data to compute slope irradiation using the seven all-sky models presented in Section 4.3. Compare your estimates against the measured values using MBE and RMSE statistics as well as scatter plots for the deviations. Comment on the adequacy of the above models using the criteria laid out in Chapter 1. You may use Prog4-1.For for this task.

You may repeat the above exercise using horizontal and slope irradiance data for Bracknell, England provided at this book's web site.

4.9.2 Using File3-1.Csv perform computations for slope illuminance using Perez et al. and Muneer–Angus models. Compare your estimates against the measured values using MBE and RMSE statistics as well as scatter plots for the deviations. Comment on the adequacy of the above models using the criteria laid out in Chapter 1. You may use Prog4-1.For for this task.

4.9.3 Measured luminance distribution data for Japan were given in Tables 4.5.3–4.5.9. Using Prog4-5.For (or Prog4-5.Exe) obtain the computed luminance distributions. Compare the estimates against the reported values.

4.9.4 Refer to Exercise 3.9.8. Compute the transmission of illuminance for all the above-mentioned points for which the sky components were obtained using the procedure presented in Example 4.6.3.

References

Batlles, F.J., Alados-Arboledas, L. and Olmo, F. (1995) On shadowband correction methods for diffuse irradiance measurements. *Solar Energy* 54, 105.

Batlles, F.J., Barbero, J., López, G., Pérez, M., Rodrigo, F. and Rubio, M.A. (1998) 'Fundamentos de la radiación solar y aspectos climatológicos de Almería, 1990–1996', ed. Servicio de Publicaciones de la Universidad de Almería (in Spanish).

Batlles, F.J., Olmo, F.J., Tovar, J. and Alados-Arboledas, L. (2000) Comparison of cloudless sky parameterizations of solar irradiance at various Spanish midlatitude locations. *Theor. Appli. Climatol.* 66, 81.

BRE (1986) *Estimating Daylight in Buildings: Part 2*. BRE Digest, Building Research Establishment, Watford, UK.

Bugler, J.W. (1977) The determination of hourly insolation on an inclined plane using a diffuse irradiance model based on hourly measured global horizontal insolation. *Solar Energy* 19, 477.

CIBSE Guide A (1999) Chartered Institution of Building Services Engineers, London, UK.

CIBSE Guide A2 (1982) Chartered Institution of Building Services Engineers, London.

CIBSE Guide J (2002) Chartered Institution of Building Services Engineers, London, UK.

CIE (1994) *Guide to Recommended Practice of Daylight Measurement*. Technical report, CIE 108.

Claywell, R., Muneer, T. and Asif, M. (2003) An efficient method for assessing the quality of large solar irradiance datasets. *ASME: JSEE* (communicated).

Commission Internationle de l'Eclairage (1973) Standardisation of luminous distribution on clear skies. *International Conference on Illumination*, Paris.

Coulson, K.L. (1975) *Solar and Terrestrial Radiation*. Academic Press, New York.

Dogniaux, R. (1954) Etude du climat de la radiation en Belgique. *Inst. R. Met. Belg. Contr.* 18, 54.

Draper, N. and Smith, H. (1998) *Applied Regression Analysis*, 3rd edn. Wiley, New York.

Drummond, A. (1956) On the measurement of sky radiation. *Arch. Met. Geophys. Bioklim.* 7, 413–36.

Dubayah, R. and Rich, P.M. (1995) Topographic solar radiation models for GIS. *Int. J. Geog. Informa. Sys.* 9, 405.

ESRA (2000) *European Solar Radiation Atlas, vol 2: Database and Exploitation Software*. Ecole des Mines de Paris, Paris, France.

Fritz, S. (1955) Illuminance and luminance under overcast skies. *J. Opt. Soc. Am.* 45, 820.

Geiger, M., Diabaté, L., Ménard, L. and Wald, L. (2002) A web service for controlling the quality of measurements of global solar irradiation. *Solar Energy* 73, 475.

Goudriaan, J. (1977) *Crop Micrometeorology: A Simulation Study.* Centre for Agricultural Publishing and Documentation, Wageningen, The Netherlands.

Grace, J. (1971) The directional distribution of light in natural and controlled environment conditions. *J. Appl. Eco.* 8, 155.

Gueymard, C. (1987) An anisotropic solar irradiance model for tilted surfaces and its comparison with selected engineering algorithms. *Solar Energy* 38, 367. Erratum, *Solar Energy* 40, 175.

Gul, M., Muneer, T. and Kambezidis, H. (1998) Models for obtaining solar radiation from other meteorological data. *Solar Energy* 64, 99.

Haves, P. (1988) *SERI-RES Building Thermal Simulation Model Version 1.2*. ETSU/HMSO, UK.

Haves, P. and Littlefair, P.J. (1988) Daylight in dynamic thermal modelling programs: case study. *BSER&T* 9, 183.

Hay, J.E. (1979) Calculation of monthly mean solar radiation for horizontal and inclined surfaces. *Solar Energy* 23, 301.

Hay, J.E. and Davies, J.A. (1980) Calculation of the solar radiation incident on an inclined surface, *Proc. First Canadian Solar Radiation Data Workshop*. Ministry of Supply and Services, Canada, p. 59.

Hay, J.E. and McKay, D.C. (1988) *Calculation of Solar Irradiances for Inclined Surfaces: Verification of Models which Use Hourly and Daily Data.* IEA Task IX Final Report, Atmospheric Environment Service, Downsview, Canada.

Hopkinson, R.G. (1954) Measurements of sky luminance distribution at Stockholm. *J. Opt. Soc. Am*. 44, 455.

Hopkinson, R.G., Petherbridge, P. and Longmore, J. (1966) *Daylighting*. Heinemann, London.

Ineichen, P., Gremaud, J., Guisan, O. and Mermoud, A. (1984) Study of the corrective factor involved when measuring the diffuse solar radiation by using the ring method. *Solar Energy* 44, 249.

Iqbal, M. (1983) *An Introduction to Solar Radiation*. Academic Press, New York.

Kambezedis, H.D., Psiloglou, B.E. and Gueymard, C. (1994) Measurements and models for total solar irradiance on inclined surface in Athens, Greece. *Solar Energy* 53, 177.

Kambezidis, H., Katevatis, E., Petrakis, M., Lykoudis, S. and Asimakopoulos, D. (1998) Estimation of Linke and Unsworth–Monteith turbidity factors in the visible spectrum application for Athens, Greece. *Solar Energy* 62, 39.

Kasten, F., Dehne, K. and Brettschneider, W. (1983) Improvement of measurement of diffuse solar radiation. *Solar Rad. Data Ser. F.2*, 221.

Kimball, H.H. and Hand, I.F. (1921) Sky brightness and daylight illumination measurements. *Mon. Weath. Rev*. 49, 481.

Kinghorn, D. and Muneer, T. (2000) All-sky zenith luminance model for the UK. *Light. Res. Tech.* 31, 49.

Kittler, R., Darula, S. and Perez, R. (1999) A set of standard skies characterising daylight conditions for computer and energy conscious design. *Final report of American-Slovak grant project US-SK92052*.

Klucher, T.M. (1979) Evaluation of models to predict insolation on tilted surfaces. *Solar Energy* 23, 111.

Kondratyev, K.Y. (1969) *Radiation in the Atmosphere*. Academic Press, London.

Kondratyev, K.Y. and Manolova, M.P. (1960) The radiation balance of slopes. *Solar Energy* 4, 14.

Kudish, A.I. and Ianetz, A. (1993) Analysis of diffuse radiation data for Beer Sheva: measured (shadow ring) versus calculated (global-horizontal beam) values. *Solar Energy* 51, 495–503.

LeBaron, B., Perez, Michalsky, J. and Perez, R. (1990) A simple procedure for correcting shadowband data for all sky conditions, *Solar Energy* 44, 249.

Li, D. and Lam, J. (1999) Evaluation of Perez slope irradiance and illuminance models against measured Hong Kong data. *Int. J. Ambient Energy* 20, 193.

Li, D., Lau, C. and Lam, J. (2003) A study of 15 sky luminance patterns against Hong Kong data. *Archit. Sci. Rev.* 46, 61.

Liu, B.Y.H. and Jordan, R.C. (1960) The inter-relationship and characteristic distribution of direct, diffuse and total solar radiation. *Solar Energy* 4, 1.

Lopez, G., Muneer, T. and Claywell, R. (2003a) Comparative study of four shadow band diffuse irradiance correction algorithms for Almeria, Spain. *ASME: JSEE* (communicated).

Lopez, G., Muneer, T. and Claywell, R. (2003b) Assessment of four shadow band correction models using beam normal irradiance data from the United Kingdom and Israel. *Energy* (communicated).

Ma, C.C.Y. and Iqbal, M. (1983) Statistical comparison of models for estimating solar radiation on inclined surfaces. *Solar Energy* 31, 313.

Mardaljevic, J. (1995) Validation of a lighting simulation program under real sky conditions. *Light. Res. Tech.* 27, 181.

Mardaljevic, J. (1996) *Private Communication*. DeMontfort University, Leicester, UK.

Matsuura, K. and Iwata, T. (1990) A model of daylight source for the daylight illuminance calculations on all weather conditions. *Proc. Third Int. Daylighting Conference*, Moscow.

Meteorological Office (1980) *Solar Radiation Data for the United Kingdom* 1951–75. MO 912. Meteorological Office, Bracknell.

Molineaux, B. and Ineichen, P. (2003) Automatic quality control of daylight measurement: Software for IDMP stations. Available from http://idmp.entpe.fr/

Montgomery, D. and Peck, E. (1992) *Introduction to Linear Regression Analysis*, 2nd edn. Wiley, New York.

Moon, P. and Spencer, D.E. (1942) Illumination from a non-uniform sky. *Trans. Illum. Engng. Soc. NY*. 37, 707.

Muneer, T. (1987) *Solar Radiation Modelling for the United Kingdom*. PhD thesis, Council for National Academic Awards, London.

Muneer, T. (1990a) Further evaluation of the Muneer's solar radiation model. *BSER&T* 11, 77.

Muneer, T. (1990b) Solar radiation model for Europe. *BSER&T* 11, 153.

Muneer, T. and Angus, R.C. (1993) Daylight illuminance models for the United Kingdom. *Light. Res. Tech.* 25, 113.

Muneer, T. (1995) Solar irradiance and illuminance models for Japan I: sloped surfaces. *Light. Res. Tech.* 27, 209.

Muneer, T. and Gul, M. (2000) Evaluation of sunshine and cloud cover based models for generating solar radiation data. *Energy Conv. Mgmt*. 41, 461.

Muneer, T. and Fairooz, F. (2002) Quality control of solar radiation and sunshine measurements – lessons learnt from processing worldwide databases. *BSER&T* 23, 151.

Muneer, T. and Zhang, X. (2002) A new method for correcting shade-ring diffuse irradiation data. *ASME, J. Sol. Energy Eng.* 124, 34.

Muneer, T., Gul, M. and Kambezidis, H. (1998) Evaluation of an all-sky meteorological radiation model against long-term measured hourly data. *Energy Conv. Mgmt*. 39, 303.

Muneer, T., Abodahab, N., Weir, G. and Kubie, J. (2000) *Windows in Buildings: Thermal, Acoustic, Visual and Solar Performance (with CD)*. Butterworth-Heinemann, Oxford.

Muneer, T., Fairooz, F. and Zhang, X. (2003) Sky luminance and radiance distributions: a comparison based on data from Bahrain, Israel, Japan and Europe. *Light. Res. Tech.* 35, 11.

Myers, D., Stoffel, T., Reda. I., Wilcox, S. and Andreas, A. (2002) Recent progress in reducing the uncertainty in and improving pyranometer calibrations. *ASME: JSEE* 124, 44.

Nagata, T. (1990a) *Radiance Distribution on Overcast Skies*. Internal Report. Department of Architecture and Civil Engineering, Fukui University, Fukui, Japan.

Nagata, T. (1990b) Radiance distribution on clear skies. *Trans. Hokuriku Branch Arch. Inst. Japan* 33, 213.

Nakamura, H., Oki, M. and Hayashi, Y. (1985) Luminance distribution of intermediate sky. *J. Light Visual Environ.* 9, 6.

Painter, H. (1981) The performance of a Campbell–Stokes sunshine recorder compared with a simultaneous record of the normal incidence irradiance. *Met. Mag.* 110, 102.

Perez, R., Ineichen, P. and Seals, R. (1990) Modelling daylight availability and irradiance components from direct and global irradiance. *Solar Energy* 44, 271.

Perez, R., Seals, R. and Michalsky, J. (1993) Modelling skylight angular luminance distribution from routine irradiance measurements. *J. Illum. Eng. Soc. Winter* 10.

Peyre, J. (1927) Mesure de la brillance du ciel diurne. *Revue d'Optique* 6, 73.

Pokrowski, G.I. (1929) Uber einen scheinbaren Mie-Effect und seine mogliche Rolle in der Atmospharenoptik. *A. Phys.* 53, 67.

Rayleigh, Lord J.W.S. (1871) On the light from the sky, its polarisation and colour. *Phil. Mag*. 41, 107.

Reindl, D.T., Beckman, W.A. and Duffie, J.A. (1990) Evaluation of hourly tilted surface radiation models. *Solar Energy* 45, 9.

Rymes, M. and Myers, D. (2001) Mean preserving algorithm for smoothly interpolating averaged data. *Solar Energy* 71, 225.

Saluja, G.S. and Muneer, T. (1987) An anisotropic model for inclined surface solar irradiation. *Proc. Inst. Mech. Eng*. 201(C1), 11.

Sick, F. (1994) *Private Communication*. Fraunhofer Institute for Solar Energy Systems, Freiburg, Germany.

Siren, K. (1987) The shadow band correction for diffuse irradiation based on a two-component sky radiance model. *Solar Energy* 39, 433.

Skartveit, A. and Olseth, J.A. (1986) Modelling slope irradiance at high latitudes. *Solar Energy* 36, 333.

Steven, M.D. (1977a) Standard distribution of clear sky radiance. *Q. J. Roy. Met. Soc*. 103, 457.

Steven, M.D. (1977b) *Angular Distribution and Interception of Diffuse Solar Radiation*. PhD thesis, Nottingham University, UK.

Steven, M.D. and Unsworth, M.H. (1979) The diffuse solar irradiance of slopes under cloudless skies. *Q. J. Roy. Met. Soc*. 105, 593.

Steven, M.D. and Unsworth, M.H. (1980) The angular distribution and interception of diffuse solar radiation below overcast skies. *Q. J. Roy. Met. Soc*. 106, 57.

Temps, R.C. and Coulson, K.L. (1977) Solar radiation incident upon slopes of different orientations. *Solar Energy* 19, 179.

Terzenbach, U. (1995) *European Solar Radiation Atlas: Quality Control Algorithms for Solar Radiation Data. EC-Contract No. JOU2-CT94-0305*, Task II – Algorithms, Regional Consulting Office, Frahmredder 95, Hamburg, Germany.

Tregenza, P.R. (1999) Standard skies for maritime climates. *Light. Res. Tech*. 31(3), 97–106.

Usher, J.R. and Muneer, T. (1989) Case studies in solar radiation modelling. *Math. Comput. Model*. 12, 1155.

Vartiainen, E. (1998) An anisotropic shade ring correction method for the horizontal diffuse irradiance measurements. *Renew. Energy* 17, 311.

Vázquez, M., Ruiz, V. and Perez, R. (1991) The roles of scattering, absorption, and air mass on the diffuse-to-global correlations, *Solar Energy* 47, 181–8.

Walsh, J.W.T. (1961) *The Science of Daylight*. Macdonald, London.

Ward, G.J. (1994) The RADIANCE lighting simulation and rendering system. *Computer Graphics Proceedings*, Annual Conference Series.

5 SOLAR SPECTRAL RADIATION

C.A. Gueymard

H.D. Kambezidis

When solar radiation enters the earth's atmosphere it is attenuated by scattering and absorption processes, which, in many instances, change abruptly with wavelength and therefore modify the incident solar spectrum in both quantity and quality. The knowledge of these *spectral* processes and more particularly of spectral irradiance (direct and diffuse) is important for many scientific disciplines as well as engineering and biological applications.

In this chapter an up-to-date review of the relevant work will be discussed and various recent tools and sources of information will be presented. The material covered is oriented toward the building environment and applications such as daylighting and solar energy systems, rather than atmospheric sciences and fundamental knowledge. For this reason, the minute details of atmospheric extinction (that could easily take a whole textbook rather than just a single chapter) have been avoided for clarity and conciseness. The interested reader can find these missing details in the literature appropriately mentioned. More importantly, solved examples are provided to demonstrate the use of spectral radiative codes in typical applications. Therefore the reader can jump onto the spectral bandwagon and make detailed and useful calculations even if he or she does not fully understand the underlying physics.

5.1 Instruments and measurements

5.1.1 Radiometry

Radiometry refers to the measurement of the properties of *radiant energy* (whose international system of units (SI) is Joule, symbol J), which is one of the many interchangeable forms of energy. The rate of flow of radiant energy, in the form of electromagnetic (EM) wave, is called *radiant flux* (whose SI unit is Watt, symbol W, with definition $1\,\mathrm{W} = 1\,\mathrm{J/s}$). For more details on SI units, see e.g. Page and Vigoureux (1977). Radiant flux can be measured as it flows from the *source* (e.g. the sun), through at least one reflecting, absorbing, scattering and transmitting layer (e.g. the earth's atmosphere or a plant canopy) to the *receiving surface* of interest, such as a solar collector or photosynthesising leaf (McCree, 1981). Table 5.1.1 gives a description of the various terms used in radiometry and their units. Note that, for completeness, some of these terms refer to *broadband* radiation, as opposed to spectral radiation which is the purpose of this chapter. Note also that the main focus of this chapter is the solar spectrum from 0.3 to 4 μm (Figure 5.1.1). Almost no solar radiation is transmitted by the atmosphere beyond these limits. However, from 4 μm to about 100 μm measurable radiation still exists in the terrestrial domain. It corresponds to what we usually refer to as

Table 5.1.1 Radiometric terminology and units

Term	Description	Unit
Absorptance	The fraction of the incident flux absorbed by a medium	Dimensionless
Diffuse solar (or sky) radiation	The downward scattered short-wave radiation coming from the whole hemisphere, with the exception of the solid angle subtended by the sun's disc. It can be measured with a *pyranometer* (see Table 5.1.4) protected from the sun by a shadow band or shading disc. It can also be calculated as the difference between global and direct solar radiation	W/m^2
Direct solar radiation	The short-wave radiation emitted from the solid angle of the sun's disc, comprising only un-scattered solar radiation. It is measured by a *pyrheliometer* (see Table 5.1.4)	W/m^2
Global solar radiation	The total (direct + diffuse) short-wave solar irradiance received on a horizontal or tilted surface. It is measured by an unshaded pyranometer	W/m^2
IR (or terrestrial or long wave, or thermal) irradiance	The irradiance emanating from the sky and/or sun at wavelengths larger than about 4 μm. It is measured with a pyrgeometer (see Table 5.1.5)	W/m^2
Irradiance	The radiant flux incident on a receiving surface from all directions per unit area of this surface	W/m^2
Radiance	The radiant flux emitted by a unit solid angle of a source or scatterer (e.g. the sky vault), incident on a unit area of a surface	W/m^2 sr
Radiant flux	The amount of radiation emanating from a source per unit time	W
Radiant intensity	The radiant flux leaving a source point per unit solid angle of space surrounding the point	W/sr
Reflectance	The fraction of radiant flux reflected by a surface	Dimensionless
Spectral irradiance	All properties of radiant flux normally depend on wavelength. The prefix spectral is added when the wavelength dependency is being described. Thus, the spectral irradiance is the irradiance at a given wavelength per unit wavelength interval. The irradiance within a given spectral band is the integral of the spectral irradiance with respect to wavelength (McCree, 1981). Spectral radiation is measured with spectrometers, spectroradiometers or sunphotometers	W/m^2 nm or W/m^2 μm
Transmittance	The fraction of radiant flux transmitted by an atmospheric layer or a non-opaque body	Dimensionless

IR: Infrared.

'heat' (or lack thereof) because this radiation is felt like that by our skin. It emanates from the earth (in the −50 to 50 °C temperature range), objects at 'room temperature' (20 °C), humans or animals (≈37 °C) and heating devices (30–100 °C). This terrestrial (or far infrared, FIR) radiation has important applications in the building environment (e.g. heat transfer, thermal losses by radiation and thermography) but is outside the scope of this book.

5.1.2 Photometry

The visible spectrum extends from about 380 to 780 nm, where the familiar gamut of colours originates (Table 5.1.2). The visible spectrum occupies a narrow range of wavelengths around the peak of the solar spectrum (Figure 5.1.1). Photometry refers to the measurement of this *visible radiation* (or simply 'light') with a sensor having a spectral response

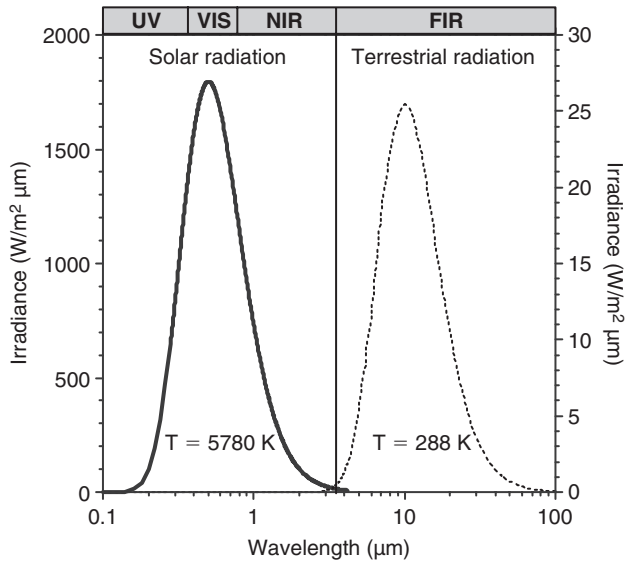

Figure 5.1.1 *The theoretical EM spectrum between 0.1 and 100 μm showing the spectral distributions of solar radiation (left curve) and terrestrial (or thermal) radiation (right curve), and the corresponding spectral bands: UV, visible (VIS), NIR and FIR. Note the limit between the solar domain and the terrestrial domain around 4 μm and the different scales*

Table 5.1.2 Equivalence between colour and wavelength in the visible

Colour	Wavelength (nm)
Violet	390–455
Dark blue	455–485
Light blue	485–505
Green	505–530
Yellow–green	550–575
Yellow	575–585
Orange	585–620
Red	620–760

simulating that of an average human eye. Photometry is used to describe lighting conditions where the eye is the primary sensor, such as illumination for work places, interior lighting, road lighting, monitor screens, etc. Although photometric measurements have been historically used in plant science as well, the next section presents more appropriate methods and definitions in this case.

The spectral response curve of the standard human eye under typical lighting conditions (daylight) is called the *standard photopic curve* and covers the visible band (see Table 1.10.1 for low-resolution data). It has been established by the *Commission Internationale de l'Eclairage* (CIE, International Commission on Illumination) from a large number of experimental measurements. The human eye responds differently to light of different colours and reaches its maximum sensitivity at 555 nm (yellow–green). Under night-time

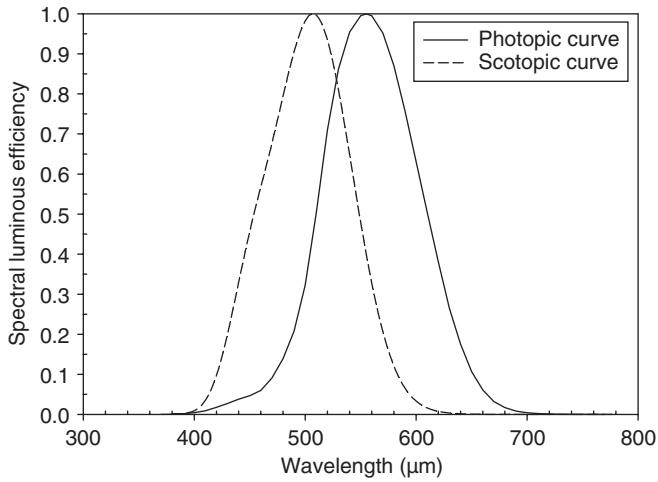

Figure 5.1.2 *CIE standard photopic and scotopic curves*

conditions this sensitivity shifts to smaller wavelengths (with a peak at about 500 nm) resulting in the *scotopic* curve (Figure 5.1.2). For accurate photometric measurements of various colours of light or from differing types of light sources, the photometric sensor's spectral responsivity curve must match the CIE photopic curve very closely. The terminology and units of photometry are indicated in the Introduction. Luminance is the photometric equivalent of radiance in radiometry. Similarly, illuminance is the photometric equivalent of irradiance. The ratio of illuminance and irradiance is called *luminous efficacy* and expresses the lighting efficiency of a radiant source like the sun. More information can be found in textbooks on photometry (e.g. McCluney, 1994).

5.1.3 Photosynthetically active radiation

Photosynthetically active radiation (PAR) is the radiant power that plants can use to activate photosynthesis. This process is limited to the visible (400–700 nm), so that all other wavelengths are essentially lost in this respect. In the past, there has been a disagreement concerning units and terminology related to plant science. Nevertheless, it is sensible to adopt those recommended by international organisations, such as the CIE, the International Bureau of Weights and Measures (IBWM) or the International Committee on Radiation Units (ICRU). Note that two different ways of referring to PAR and its measurement are used concurrently: irradiance and photon flux. The latter refers to quantum theory and can be relative to either a plane surface (collecting photons from the hemisphere it sees) or a sphere (collecting photons from all directions). These are respectively called the photosynthetic photon flux density (PPFD) and the photosynthetic photon flux fluence rate (PPFFR). Table 5.1.3 gives the PAR terminology and units. See (McCree, 1972) for more details. For a collimated beam at normal incidence, PPFFR = PPFD. For perfectly diffuse radiation, PPFFR = 4PPFD. In practice, $1 < \text{PPFFR/PPFD} < 4$.

5.1.4 Instruments of solar radiation

Radiometric instrumentation is critical in any solar radiation fixed station or short-term measurement campaign. (Solar radiation stations are sometimes called *actinometric*

Table 5.1.3 PAR terminology and units

Term	Description	Unit
PAR	Photosynthetically active radiation, or radiation within the 400–700 nm waveband that plants can use (Figure 5.1.1). PAR can be described in either energy terms (see PI below) or quantum terms (see PPFD and PPFFR).	
PI	Photosynthetic irradiance, i.e. the radiant energy in the 400–700 nm waveband incident on a unit surface per unit time	W/m^2
PPFD	Photosynthetic photon flux density, also known as quantum flux energy. This defines the number of photons in the 400–700 nm waveband incident on a unit surface per unit time	The recommended unit is $\mu mol/cm^2 s$
PPFFR	Photosynthetic photon flux fluence rate, also known as quantum scalar irradiance or photon spherical irradiance. It measures the number of photons from all directions incident on an imaginary unit sphere per unit time	The recommended unit is $\mu mol/cm^2 s$

stations, an older terminology.) Radiometers can be divided into two main categories, those measuring in a certain band and spectrally-integrating radiation from all wavelengths it contains (*broadband instruments*), and those which measure radiation at specified wavelengths (*spectral instruments*). The first category includes pyranometers, pyrheliometers, pyrgeometers, UVmeters, rotating shadow band radiometers (RSR) and albedometers, while the second includes scanning filter photometers (SFP) or sky scanners, sunphotometers, multi-filter rotating shadow band radiometers (MFRSR), rotating shadow band spectrometers (RSS), spectroradiometers, interferometers and grating spectrometers. Table 5.1.4 gives the characteristics of the short wave (0.3–4.0 μm) measuring devices, whereas Table 5.1.5 is for long-wave instrumentation.

5.1.5 Measurement of solar radiation

Because of the difficulties frequently encountered when measuring solar radiation and the resultant unknown quality of some solar radiation data, considerable effort has been devoted to develop procedures and software for performing post-measurement quality assessment of the data. Such an assessment is needed to ensure that the data selected for model development or other applications are of the highest possible quality, and to evaluate the uncertainty in the measured solar radiation data. The quality control (QC) procedure recommended by CIE (1994) is frequently used. Its criteria to test the quality of broadband data are detailed in Chapter 4, both for solar radiation and illuminance.

Another QC procedure which is frequently used in North America is known as SERI-QC (NREL, 1993). It is aimed at solar radiation measurements and is most powerful when all three components of radiation (direct, diffuse and global) are recorded simultaneously (for more information, see Chapter 4 and http://rredc.nrel.gov/solar/pubs/seri_qc/). Rather than completely eliminating data points with values not meeting minimum quality requirements, such values are rather conserved but flagged more or less severely. This allows to keep track of instrumental problems over long periods of time, and maintains the possibility of correcting the data at a later date. In some cases, missing data can be interpolated

Table 5.1.4 Short-wave measuring instruments

Name	Measuring spectrum	Characteristics
Broadband instruments		
Pyranometer	Usually 0.285–2.8 μm. Glass filters can be added to reduce the spectral ranges to 0.525–2.8 μm, 0.630–2.8 μm, 0.700–2.8 μm, 0.780–2.8 μm and their combinations if using collocated instruments with different coloured domes	Measurement of global radiant flux (W/m^2). Temperature and cosine-effect sensitivity can be compensated for. Nominal measurement uncertainty of less than ±2%, increasing with zenith angle. Time constant of about 30 s. Calibration against reference instruments or secondary standards
Pyrheliometer	Usually 0.285–4 μm for field instruments with quartz window. All wavelengths can be measured with a reference instrument with no window, called an active cavity radiometer (ACR). Various spectral regions are possible with filters, e.g. 0.525–2.8 μm (OG530 filter, ex-OG1), 0.630–2.8 μm (RG630 filter, ex-RG2) and 0.695–2.8 μm (RG695 filter, ex-RG8). All three filters can be mounted on a wheel and used in succession to obtain a combination of shorter bands	Measurement of direct solar radiation (W/m^2) at normal incidence. Nominal uncertainty of less than ±1% under laboratory conditions to ±3% under field conditions. Time constant is about 1 min. Calibration against ACR traceable to the world radiometric reference (WRR). The latter is dynamically maintained to within ±0.1% by a group of reference ACRs
UVmeter	To measure total radiation in either one of two UV bands measurable at the earth's surface: UV-A (0.315–0.400 μm) or UV-B (0.280–0.315 μm). Some UV instruments (often called 'biometers') have a built-in filter to simulate the erythemal action spectrum	Measurement of UV radiation (W/m^2). Temperature and cosine-effect sensitivity must be corrected, usually a posteriori. Nominal measurement uncertainty of less than ±2% for low zenith angles. Time constant of several msec. Calibration against reference instrument
RSR	Usually 0.3–1.1 μm (silicon-based instrument)	Quasi-simultaneous measurement of the global and diffuse radiation components (W/m^2) with a rotating shade. Direct irradiance is calculated as their difference. Cosine correction necessary. Spectral correction needed to compensate for the insensitivity to IR radiation. Very fast response. Overall accuracy better than 6% under favourable conditions. Calibration against a reference pyranometer
Spectral instruments		
SFP or sky scanner	Various spectral or broadband regions	Measurement of the spatial distribution of radiance (W/m^2sr) or luminance (cd/m^2). Precision

(*continued*)

Table 5.1.4 *Continued*

Name	Measuring spectrum	Characteristics
		~1%. Calibration against an absolute-cavity radiometer
Multi-wavelength sunphotometer	0.3–1.1 μm	Measurement of spectral direct radiation within a few nanometers of a filter's central wavelength, with usually 2–10 channels. Calibration against a standard lamp or at specific facilities (usually at high altitudes) using the Langley-plot technique or by comparison with a reference instrument
MFRSR	0.3–1.1 μm	Quasi-simultaneous measurement of the global and diffuse solar components ($W/m^2\mu m$) with up to seven filters. Calibration with Langley technique on a semi-annual basis or on a continuous basis (Harrison et al. 1994)
RSS	0.3–1.1 μm	Quasi-simultaneous measurement of the global and diffuse solar components ($W/m^2\mu m$) at hundreds of wavelengths. Calibration against standard lamp on a semi-annual basis
Spectroradiometer	Usually 0.3–1.1 μm for a silicon detector. It can be extended to the IR with other detectors	Measurement of global solar radiation ($W/m^2\mu m$). Direct and diffuse radiation can also be measured with attachments. Accuracy better than 8%. Calibration against standard lamp on a semi-annual basis

Table 5.1.5 Long-wave measuring instruments

Name	Measuring spectrum	Characteristics
Broadband instruments		
Pyrgeometer	Nominally 4–50 μm	Measurement of IR radiation (W/m^2). Accuracy better than 2%. Calibration against blackbody emission source on a semi-annual basis
Spectral instruments		
Interferometer	Usually 4–50 μm	Measurement of IR radiation ($W/m^2\mu m$), using laser-beam technology
Grating spectrometer	Usually in various regions within 4–50 μm	Measurement of IR radiation ($W/m^2\mu m$)

or replaced by modelled data if it is important to have a serially complete data set. Such 'artificial' data must be flagged accordingly. There is no equivalent, widely accepted QC procedure for spectral measurements.

The degree of accuracy of a measuring sensor is transferred to the actual measurement. Therefore, a data set of solar radiation values (usually with a time step of a few minutes to one hour) that has passed the QC procedure must be examined for its uncertainty. Each measurement contains errors. The instantaneous error is the difference between the measured or reported value and the true value of the quantity in question. There are two categories of errors: (i) the systematic or biased (fixed offset) errors and (ii) the random (precision or repeatability) errors. The latter errors are assumed to follow a Gaussian (normal) distribution due to their random nature. The calculation of uncertainties requires identification, classification (bias or random) and quantification of every significant source of error. This quantification in turn requires assignment of a justifiable value to each identified and classified error source. This step is usually based on empirical tests, measured data, instrument specifications, calibration results, etc. When no such data is available, engineering judgement, experience or previous knowledge must be used to estimate the magnitude of the error. The bias and random error magnitudes are then combined into total bias and random components of uncertainty, which are in turn used to evaluate the total uncertainty.

Random errors are the result of independent influences on the measurement process and environment, which both change with each measurement. They are recorded as an integral part of the data, varying with each individual measurement. Their magnitudes are estimated from the standard deviation (σ) of repeated measurements. Because of their statistical (random) nature, increasing the sample size (N) normally results in a reduction in the magnitude of these errors.

Bias errors are those that are fixed and present in every measurement using specific procedures and instruments. For example, if an instrument has been mis-calibrated, each measurement made with that sensor exhibits the same error resulting from this mis-calibration. The fact that calibration standards themselves contain bias errors (contributing in turn to measurement errors) is often overlooked.

Once all errors have been identified and quantified, they are combined to provide an estimate of uncertainty. The P_{95} method (i.e. the interval around the reported measured value that is expected to contain the true value, 95% of the time (ASME, 1985)) is used for combining solar radiation measurement errors. Therefore, P_{95} is defined as:

$$P_{95} = \sqrt{\sum_{i=1}^{N}(B_i)^2 + \sum_{i=1}^{N}(2\sigma_{ri})^2} \tag{5.1.1}$$

where B_i is the ith bias error and σ_{ri} is the standard deviation of the ith random error.

Improvements in the measurement accuracy can be achieved by averaging a series of measurements (Barry, 1978). In the case of monthly means of daily solar radiation data the uncertainty is calculated as:

$$P_{95\mathrm{m}} = \left[\sum_{i=1}^{N}(B_i)^2 + \sum_{i=1}^{N}(2\sigma_{ri})^2 / \sqrt{30}\right]^{1/2} \tag{5.1.2}$$

In the case of annual solar radiation data the accuracy is improved even more, as the following formula shows:

$$P_{95y} = \left[\sum_{i=1}^{N} (B_i)^2 + \sum_{i=1}^{N} (2\sigma_{ri})^2 / \sqrt{365} \right]^{1/2} \tag{5.1.3}$$

A fuller treatment of QC of solar radiation data is provided in Section 4.7.

5.1.6 Calibration of solar spectral instruments

Table 5.1.4 describes five widely used spectral apparatus. An SFP is equipped with one or more sensors that rotate to scan the sky's radiance and/or its luminance. A complete scan (about 150 points throughout the sky dome) usually takes a few minutes. Spectroradiometers can measure global irradiance (and direct or diffuse irradiance with appropriate attachments) in the ultraviolet (UV), visible and near infrared (NIR) regions. They normally scan the spectrum at fixed spectral intervals, and a complete scan usually takes a few minutes. The RSS is a particular kind of spectroradiometer as it measures global and diffuse irradiance in rapid succession with a solid-state spectral detector, hence without scanning, and therefore, almost instantaneously. Sunphotometers measure direct normal irradiance through a small number (2–10) of interference filters in the UV, visible and NIR region of the solar spectrum. The MFRSR constitutes a simplified version (with considerably less spectral channels) of the RSS. They both use the same automatic shadow band attachment to successively shade and unshade the sun, thus obtaining global and diffuse irradiance, from which the direct irradiance is readily computed.

In order to maintain these instruments at their optimal level of performance, frequent calibration is necessary (at least once per year). This is particularly important for sunphotometers and MFRSR because their interference filters tend to degrade relatively rapidly over time. A conventional calibration method is against standard lamps in the laboratory, but their own uncertainty is not negligible ($\pm 2\%$), they have a short lifetime and they are very expensive. An alternative method, the *Langley technique*, has therefore been perfected to use the sun as a free and more stable ($\pm 0.2\%$) light source. Both methods have advantages and inconveniences but can be used in alternation for best results (Schmid and Wehrli, 1995).

The Langley technique is named after Samuel P. Langley of the Smithsonian Institution (USA) and is based on his work (during the early 1900s) aimed at determining the 'solar constant', i.e. the total amount of incident solar energy at the top of the earth's atmosphere per unit area. Langley knew that the atmospheric attenuation of solar energy depends exponentially on the total amount of attenuators (more precisely, their optical depth OD) along the path, according to the cornerstone law attributed to Bouguer, Beer or Lambert (hereafter, Beer's law). He then realised that the transmitted solar energy can also decrease if the OD is constant, but the path length increases. Therefore, if V_S (in Volts) is the measured signal of the instrument at the surface of the earth and V_0 its virtual (because inaccessible) reading at the top of the atmosphere, then Beer's law can be employed to relate V_S and V_0:

$$V_S(\lambda) = SV_0(\lambda)\exp[-m\tau(\lambda)] \tag{5.1.4}$$

where m is the air mass (assumed equal to the optical mass of all absorption and scattering processes for this simplified derivation), S is the sun–earth distance correction factor

(see Sections 2.1 and 5.3.1) and τ the total OD for wavelength λ (Thomason et al., 1983; Schmid and Wehrli, 1994). Taking the logarithm on both sides of Eq. (5.1.4), one derives the relationship:

$$\ln V_S(\lambda) = \ln[SV_0(\lambda)] - \tau(\lambda)m \tag{5.1.5}$$

From a series of measurements of V_S (in the form of voltage or 'counts') at different moments (i.e. various values of m) during a day, $\ln V_S$ can be plotted against m for the centre wavelength of each filter. The data points should lie on a straight line of the form $Y = a - b\,m$, whose coefficients a and b can easily be found with a least-squares regression technique. By setting $m = 0$ in Eq. (5.1.5) V_0 is readily obtained as the intercept of the fitted straight line with the y-axis. Furthermore, the total OD of the atmosphere for the centre wavelength of the filter is obtained as coefficient b, i.e. the slope (in absolute value) of this same straight line.

The essential requirements of the Langley method are that (i) the atmospheric constituents (and more essentially, the aerosol mixture) remain constant during the calibration measurements (at least half a day) and (ii) that these measurements are made outside any strong water vapour absorption band. To circumvent the first limitation, sunphotometers are usually sent to an elevated site with low aerosol burden for calibration. This, however, implies long downtimes and sizeable expenses. A modified Langley-plot technique has been proposed to obtain accurate calibration even if the aerosol burden varies during the day (Forgan, 1994), which is the usual case. Similarly, Schmid and Wehrli (1995) and Adamopoulos et al. (1999) have proposed a modified Langley method for estimating V_a, the voltage of the sunphotometer measured at the surface of the earth if aerosols were the only atmospheric attenuator of solar radiation. In this method, Eq. (5.1.5) is modified to:

$$\ln V_a(\lambda) = \ln[SV_0(\lambda)] - \tau_a(\lambda)m_a \tag{5.1.6}$$

where m_a is the optical aerosol mass.

Equation (5.1.6) can be used to estimate $\tau_a(\lambda)$ as an alternative to other methods.

Moreover, the Langley technique can be modified even further to calibrate sunphotometers or MFRSR within water vapour bands (Reagan et al., 1987; Bruegge et al., 1992; Thome et al., 1994).

Figure 5.1.3 gives an example of conventional Langley plots obtained with a sunphotometer at NREL, Golden, USA (altitude 1829 m). The results for only two channels (500 and 862 nm) are shown for clarity. As is clearly demonstrated by the variation in slope for each channel, the aerosol burden is higher in the afternoon and less stable than before noon. This can be explained by the added turbulence when the air temperature rises in the afternoon, and by the proximity of a big city (Denver) with significant pollution. This also explains the slight difference in the V_0 values that are obtained with the morning and afternoon data, the latter having a higher uncertainty. Also, the slopes of the 500 nm linear fits are steeper than those of the 862 nm fits, indicating that the total OD is larger at shorter wavelengths.

5.1.7 Variations in the solar spectrum

Due to the variability in atmospheric conditions (aerosol burden and water vapour, principally) the depletion of solar radiation varies in space and time. When the atmosphere is dry and clean the attenuation (absorption and scattering) is expected to be low. The opposite

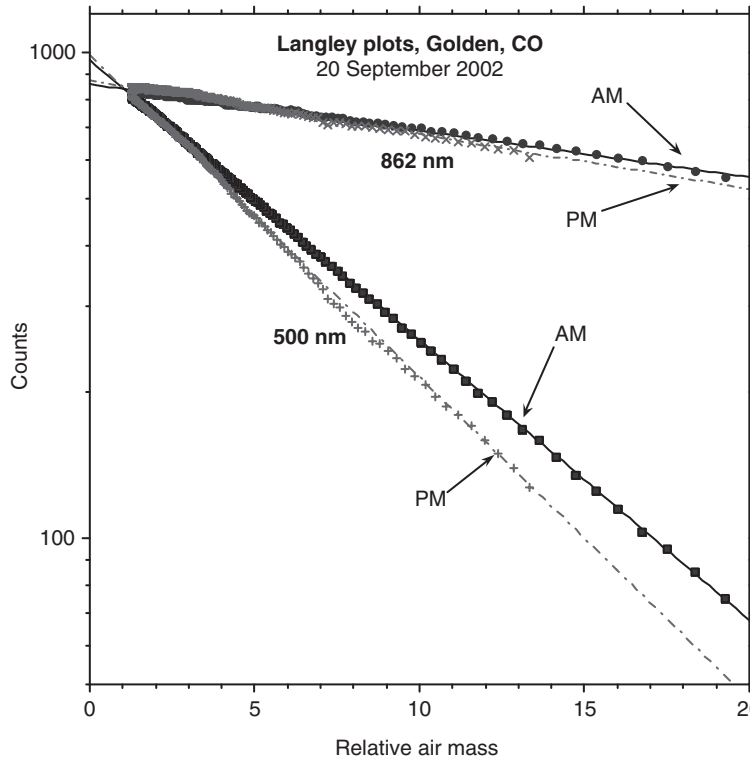

Figure 5.1.3 *Langley plots for two different wavelengths of a sunphotometer at Golden, CO, USA (altitude 1829 m). The bottom points are for the 500 nm channel and the top ones for the 862 nm channel. The former channel senses a larger total OD than the latter. Note the morning/afternoon difference in both slope and intercept of the fitted lines. The raw voltage of the instrument here is expressed as 'counts'*

occurs when the atmosphere contains a larger quantity of scatterers and/or absorbers. As an example, Figure 5.1.4 shows the variation in solar spectral irradiance versus wavelength for morning and mid-day measurements during 'clean' (1 October 2002) and 'dirty' (22 September 2002) atmospheric conditions in Athens, Greece.

In both figures it is observed that the 'cleaner' the atmosphere, the higher the spectral irradiance. For example, the mid-day spectral peak at around 550 nm is about 1.5 W/m^2 nm for the 'clean' day of 1 October 2002 and only 1.2 W/m^2nm for the 'dirtier' day of 22 September 2002, i.e. a loss of 20% in the latter case compared to the former.

The absorption bands shown in both figures can be explained as follows: (i) 300–450 nm, absorption by ozone (O_3); (ii) 720 nm, absorption by water vapour; (iii) 760 nm, absorption by oxygen (O_2) and (iv) around 820 and 940 nm, absorption by water vapour.

The O_3 absorption bands are multiple and of great importance in the short-wave spectrum. The *Hartley band* (200–310 nm) protects life against harmful UV-B and UV-C radiation. The *Huggins band* (310–350 nm) similarly attenuates UV-A radiation, and in the *Chappuis band* (400–850 nm), O_3 attenuates the visible, but with a lesser intensity than in the UV bands. For any site at the surface of our planet, the Hartley band virtually

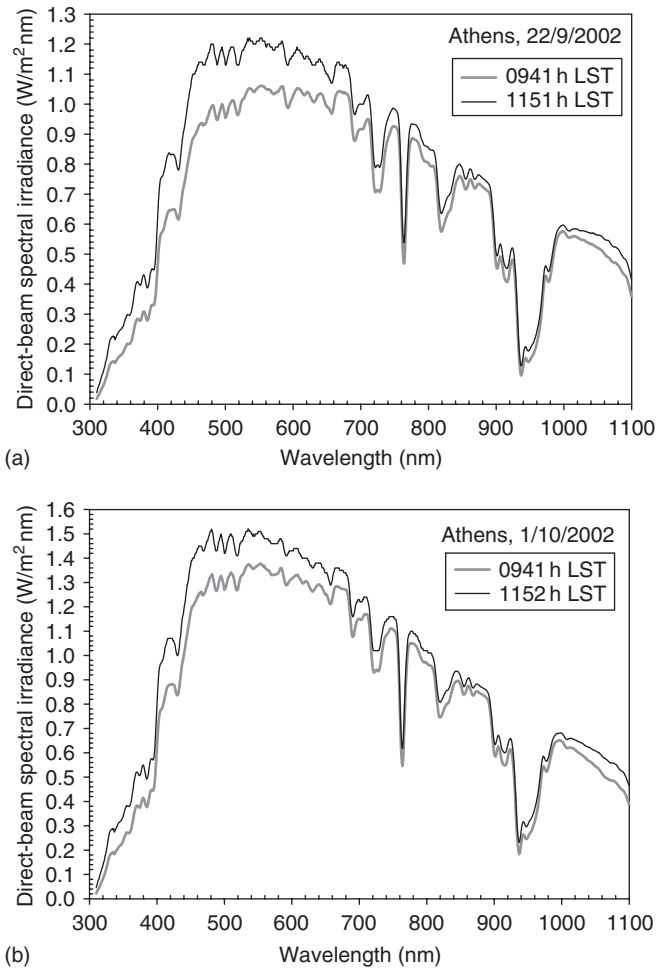

Figure 5.1.4 *Solar spectral irradiance versus wavelength at Athens on: (a) 22 September 2002 and (b) 1 October 2002*

eliminates all radiation below 300 nm. More details about the absorption by O_3 and other gases will be given in Section 5.4.5.

Substantial variations (and most importantly, reductions) in stratospheric O_3 have been measured during the last decades, especially around the poles and in the southern hemisphere. Episodes of very low O_3 are referred to as 'ozone holes' and can be extremely detrimental to life forms because of the concomitant increase in damageable UV radiation. However, the net energetic effect on the *total* short-wave irradiance is minor in relative terms because UV represents only a small part of the total irradiance.

Example 5.1.1

Calculate the power received per m^2 (normal to the solar rays) at the distance that corresponds to the orbit of planet Mars. Take into account that the total power received at the top of the earth's atmosphere from the Sun is 1366.1 W/m^2 and that the Sun–Mars and Sun–Earth distances are $r_{SM} = 225 \times 10^6$ km and $r_{SE} = 150 \times 10^6$ km, respectively.

Consider a sphere with radius r_{SE} equal to the Sun–Earth distance and having its centre at the centre of the Sun. The total power received at the boundaries of the earth's atmosphere is: $\pi(2r_{SE})^2 \times 1366.1 = 17\,166.9r_{SE}^2$. For a new sphere also centred on the Sun but with radius r_{SM}, the power received at the surface of Mars is: $\pi(2r_{SM}^2) \times P_M = 12.57P_M r_{SM}^2$, where P_M is the irradiance at the distance r_{SM} from the Sun. The two powers must be equal, i.e. $17\,166.9r_{SE}^2 = 12.57P_M r_{SM}^2$, giving $P_M = 1365.7$ $(150 \times 10^6/225 \times 10^6)^2 = 607\,W/m^2$. This is less than half the Sun's irradiance received by the earth.

Example 5.1.2

Calculate the total solar irradiance (TSI) received on earth at ground level knowing that the overall planetary albedo is 0.3. How much solar energy is absorbed by the various mechanisms in the atmosphere-ground system?

With an overall albedo (on reflectance) of 0.3, the earth absorbs 0.7 (or 70%) of the energy it receives from the Sun. Therefore the average energy absorbed will be: $1366.1 \times 0.7 = 956.3\,W/m^2$.

Example 5.1.3

Table 5.1.6 details a series of hypothetical measurements of global horizontal and diffuse horizontal irradiance during a specific day. Apply the QC criteria of Section 4.7 to see which data points would pass these QC tests. Take into account that the values in column 4 (direct normal irradiance) are calculated from the other data of the table.

Since the data refers to irradiance only, the QC criteria of Section 4.7.2 is applicable. The values to be computed are: $SI_E = 0.98 \times 1366.1 = 1338.8\,W/m^2$, $1.2SI_E = 1.2 \times 0.98 \times 1366.1 = 1606.5\,W/m^2$ and $0.8SI_E = 0.8 \times 0.98 \times 1366.1 = 1071\,W/m^2$. Note that S refers to the earth–sun distance correction factor (see Sections 2.1 and 5.3.1). Table 5.1.7 indicates the acceptable data points with '•' and the unacceptable values with 'x'.

The results in the above Table 5.1.7 show that the measurements corresponding to $Z = 25°$, 35° and 45° do not pass the QC tests and must, therefore, be flagged as 'out of bounds'.

Table 5.1.6 Dataset of solar radiation measurements*

Z (deg)	I_G (W/m^2)	I_D (W/m^2)	$I_{B,n} = (I_G - I_D)/\cos Z$ (W/m^2)
80	150	60	518.3
75	185	165	77.3
70	290	110	526.3
65	400	150	591.6
60	450	170	560
55	530	190	592.8
50	750	220	824.5
45	1810	280	2163.7
40	860	300	731
35	880	1305	−518.8
30	920	330	681.3
25	1275	45	695.1

* for all $S = 0.98$.

Table 5.1.7 QC test results for the measurements of Table 5.1.6

Z (deg)	$0 \leqslant I_G \leqslant 1606.5$	$0 \leqslant I_D \leqslant 1071$	$0 \leqslant I_D \leqslant 1.1H_g$	$0 \leqslant I_{B,n} \leqslant 1338.8$	$10\,W/m^2 \leqslant I_G$
80	•	•	•	•	•
75	•	•	•	•	•
70	•	•	•	•	•
65	•	•	•	•	•
60	•	•	•	•	•
55	•	•	•	•	•
50	•	•	•	•	•
45	**x**	•	•	**x**	•
40	•	•	•	•	•
35	•	•	**x**	**x**	•
30	•	•	•	•	•
25	•	•	•	**x**	•

Table 5.1.8 Langley equations for various channels

λ (nm)	Equation
340	$\ln V_S = 8.915 - 0.6251m$
500	$\ln V_S = 8.008 - 0.1682m$
670	$\ln V_S = 5.102 - 0.0781m$
1020	$\ln V_S = 3.603 - 0.0255m$

Example 5.1.4

Table 5.1.8 gives the equations of the straight lines obtained with the Langley technique by linearly fitting Eq. (5.1.5) for various channels of a commercial sunphotometer being calibrated at an elevated site. Prepare a diagram containing the plots for all channels and comment on it.

The Langley plots are shown in Figure 5.1.5. It is observed that the lower the wavelength, the larger the slope of the straight line, i.e. the higher the total OD. The latter increases considerably below 500 nm.

Example 5.1.5

Considering that a large number of Langley plots have been made with the same instrument as in Example 5.1.4, estimate the uncertainty in the aerosol optical depth (AOD) caused solely by errors in the V_0 determination, when the ODs of all other constituents are those listed in Table 5.1.9. Assume that $Z = 33.6°$ and that the uncertainty in the Langley determinations of V_0 is $\pm 2\%$ for all channels.

Applying Eq. (5.1.5) separately for the true value of V_0 and for the possible value $V_0' = V_0 + \Delta V_0$, the following is obtained:

$$\ln V_S(\lambda) = \ln S + \ln V_0(\lambda) - \tau_1(\lambda)m$$
$$\ln V_S(\lambda) = \ln S + \ln V_0'(\lambda) - \tau_2(\lambda)m$$

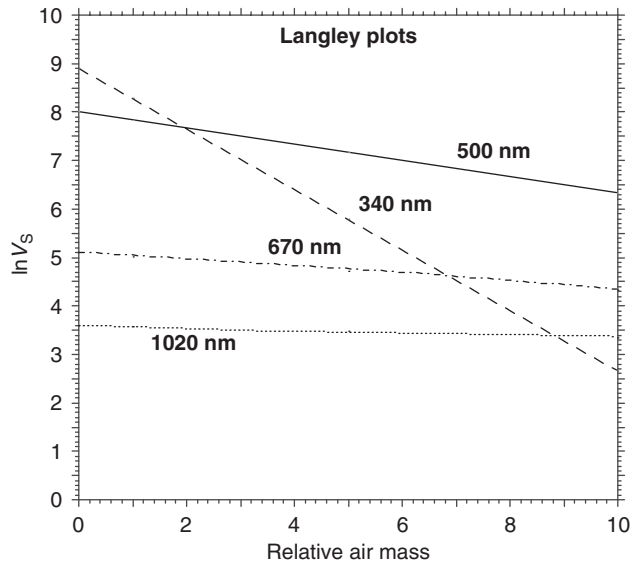

Figure 5.1.5 *Langley plots for selected wavelengths*

Table 5.1.9 ODs of various atmospheric constituents at specified wavelengths*

λ(nm)	Molecules (Rayleigh scattering)	O_3	NO_2	Total
340	0.5344	0.0107	0.0212	0.5663
500	0.1076	0.0110	0.0092	0.1278
670	0.0326	0.0156	0.0000	0.0482
1020	0.0060	0.0000	0.0000	0.0060

*for all water vapour OD = 0.

After subtraction and differentiation, an expression for the absolute error in the total OD, $\Delta\tau(\lambda)$ can be derived as:

$$\Delta\tau(\lambda) = (1/m)\ln[1 + \Delta V_0/V_0] \tag{5.1.7}$$

For $Z = 33.6°$ (hence $m \approx 1/\cos Z = 1.2$) and $\Delta V_0/V_0 = 0.02$, $\Delta\tau(\lambda)$ is equal to (1/1.2) ln(1.02) = 0.0165. This is also the absolute error in AOD if it assumed that the total OD of the atmosphere (excluding aerosols, last column of Table 5.1.9) is perfectly known, hence $\Delta\tau_a(\lambda) = 0.0165$. For the conditions of Example 5.1.4, $\tau(\lambda)$ is equal to the slope of each straight line in Table 5.1.8. This is reported in the column 2 of Table 5.1.10. The AOD, $\tau_a(\lambda)$, is obtained by subtracting the ODs from all non-aerosol constituents from $\tau(\lambda)$. The results are reported in column 4 of Table 5.1.10. Finally, the uncertainty in $\tau_a(\lambda)$ is obtained by dividing $\Delta\tau_a(\lambda)$ by $\tau_a(\lambda)$, and this appears in the last column of Table 5.1.10.

It can be concluded that an apparently reasonable 2% error in V_0 results in a far larger uncertainty in the desired AOD results. This is why extreme care must be devoted to the

Table 5.1.10 OD of various atmospheric constituents at specified wavelengths

λ (nm) (1)	Observed $\tau(\lambda)$, from Table 5.1.8 (2)	Calculated OD, from Table 5.1.9 (excluding aerosols) (3)	$\tau_a(\lambda) = (2)–(3)$ (4)	$\Delta\tau_a(\lambda)$ (5)	$\Delta\tau_a(\lambda)/\tau_a(\lambda) = 100(5)/(4)$ (%) (6)
340	0.6251	0.5663	0.0588	0.0165	28.1
500	0.1682	0.1278	0.0404	0.0165	40.8
670	0.0781	0.0482	0.0299	0.0165	55.2
1020	0.0255	0.0060	0.0195	0.0165	84.6

calibration of sunphotometers by the Langley technique so that the uncertainty in V_0 can be reduced to 1% or less.

5.2 The earth's atmosphere

5.2.1 The structure of the atmosphere

The actual composition and concentration of the constituents of clean air vary with geographic location, elevation and time of the year. Table 3.3.1 shows the normal composition of the US Standard Atmosphere (Anon, 1976).

From Table 3.3.1 it is seen that the earth's atmosphere is composed mainly (99%) of molecular nitrogen (N_2) and molecular O_2. It also contains water vapour and aerosols (particulate matter) such as meteoric dust, sand and dust particles, smoke from forest fires or agricultural and slash burning, water droplets, ice crystals, sea spray, volcanic ash and man-made pollutants (e.g. heavy metals and total suspended particulates). Water vapour and aerosols are highly variable in space and time. Therefore, in order to examine how opaque the atmosphere is to solar rays, the atmospheric constituents are divided into *dry air molecules*, *water vapour* and *aerosols*. Solar radiation is attenuated (scattered and/or absorbed) by each of these three species. These attenuation processes are discussed in general terms in the next section, and in more details in Section 5.4.

Figure 5.2.1 shows a typical variation of mean air temperature with altitude. It is usually assumed that the earth's atmosphere keeps its characteristics up to an altitude of 100 km above sea level. As seen from the figure, the atmosphere's temperature profile presents one maximum at the *stratopause* (approximately at 50 km), as well as two minima: one above the *tropopause* (around 15 km) and an other above the *mesopause* (at 85 km).

Simulation efforts for deriving more detailed mean summer and winter temperature profiles during the GAIA project (http://www.iti.gr/db.php/en/projects/GAIA.html) resulted in calculating the variation of this parameter in the various global climates of the earth (i.e. tropical, sub-tropical, temperate, maritime, continental, desert and polar). Their profiles are shown in Figure 5.2.2. In terms of other gases, O_3 presents a minimum at the tropopause for mid-latitudes on average and a maximum well below the stratopause, water vapour diminishes above the troposphere, while the mixed gases (carbon monoxide (CO), N_2, O_2 mainly) have a rather constant concentration vertical profile. Aerosols, on the contrary, are extremely variable in space and time. Volcanic eruptions, e.g. produce ash that can reach the stratosphere and remain there for considerable time until its deposition

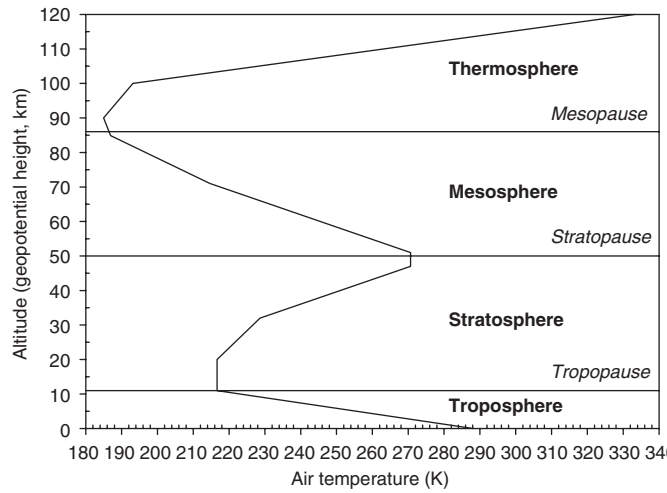

Figure 5.2.1 *Normal temperature profile in the earth's atmosphere. The sea-level temperature is taken at 283 K (15 °C), the atmospheric pressure at 1013.25 h Pa and the air density at 1.2 kg/m^3*

on the surface of the earth. Atmospheric pressure decreases exponentially with altitude: at 30 km it is about 10 h Pa and at 90 km it is only ≈0.001 h Pa.

5.2.2 Depletion of solar radiation

The spectral distribution of solar radiation at the top of the earth's atmosphere is shown in Figure 5.2.3. There are three mechanisms that deplete solar radiation during its passage through the atmosphere: *absorption*, *reflection* and *scattering*. If 100 energy units enter the atmosphere, 24 (20 and 4) of them are reflected by the clouds and the ground, respectively, 21 (6 and 19) are scattered and absorbed by the atmosphere, respectively, and the rest 51 units are absorbed by the ground (see http://www.oswego.edu/Acad_Dept/a_and_s/earth.sci/geo_geochem/sw/G335_2f/tsld003.htm). The earth and its atmosphere as a whole therefore globally absorb 51 + 19 = 70 units, which corresponds exactly to the planetary albedo value of 0.3 mentioned in Example 5.1.2. More details and discussions about the relationship between the earth's energy balance and global climate change can be found at, e.g. http://cgee.hamline.edu/rivers/Resources/Voices/aiken2.htm.

Figure 5.2.4 outlines these mechanisms schematically. The scattered energy is called *diffuse radiation*. Whereas many gases absorb radiation, only air molecules and particles can scatter it. In doing so, they also produce the different shades of blue of the clear sky. Cloud particles (water droplets or ice crystals) also absorb and scatter, producing a large range of greys, depending on their optical thickness.

Natural aerosol particles have diameters in the range 0.002–200 μm. The smallest particles are called *Aitken particles* and range from 0.002–0.2 μm, while the large particles have diameters in the range 0.2–2 μm. The extremely large particles are called *giant particles* and their size varies in the range 2–200 μm. They can be a danger for human health if their diameter is less than 10 μm and particularly around 2.5 μm; they are referred to as PM_{10} and $PM_{2.5}$, respectively, in the international literature dealing with air quality and air pollution.

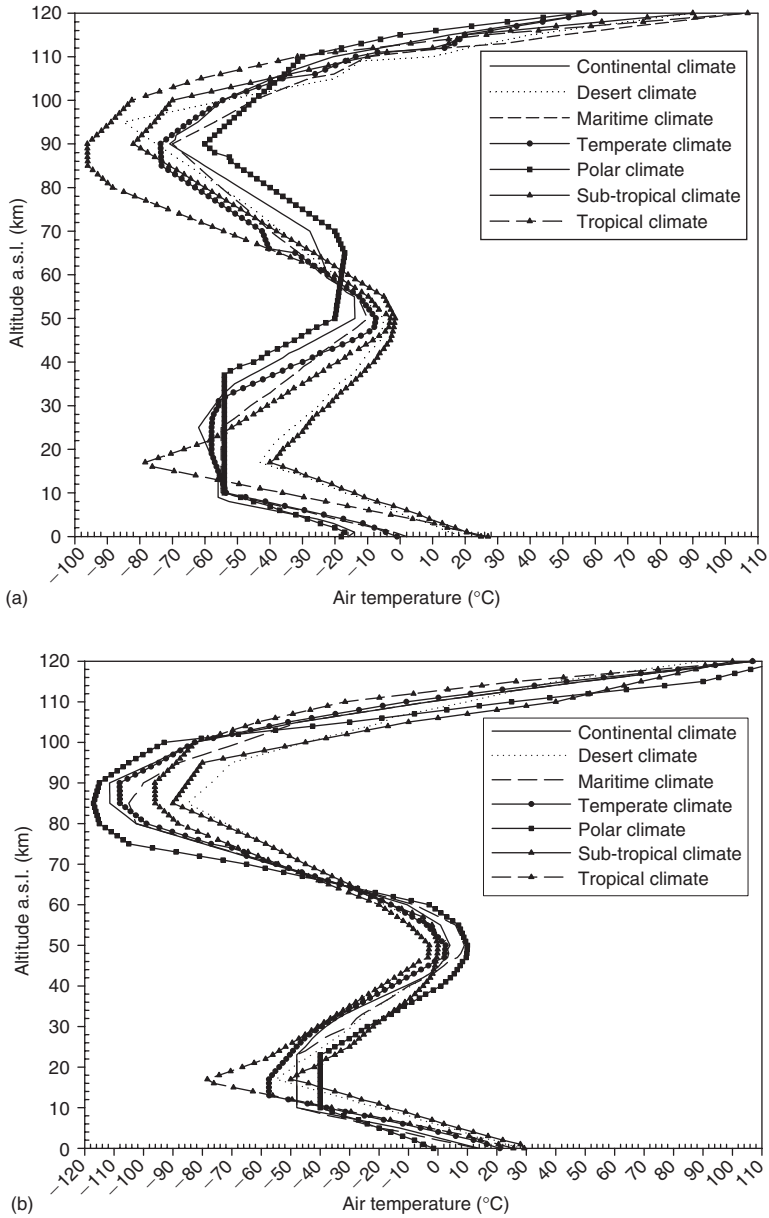

Figure 5.2.2 *Mean (a) winter and (b) summer air temperature profiles for various climatic conditions on earth*

5.2.3 Scattering

When EM radiation falls on a particle (called *scatterer*), part of its incident energy is scattered in various directions. Scattering by air molecules was initially investigated by

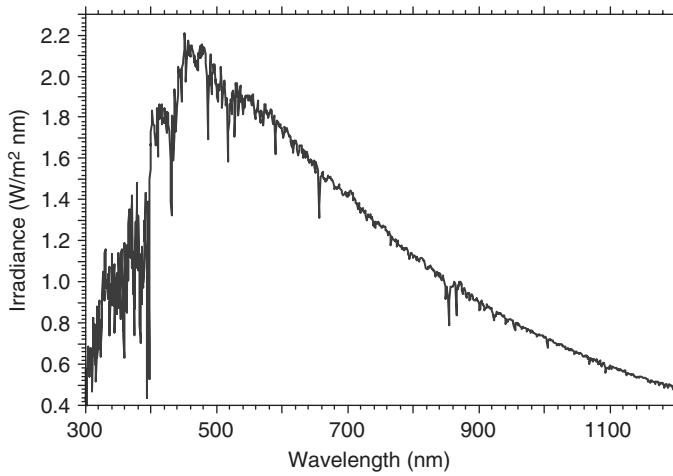

Figure 5.2.3 *Solar spectrum outside the earth's atmosphere*

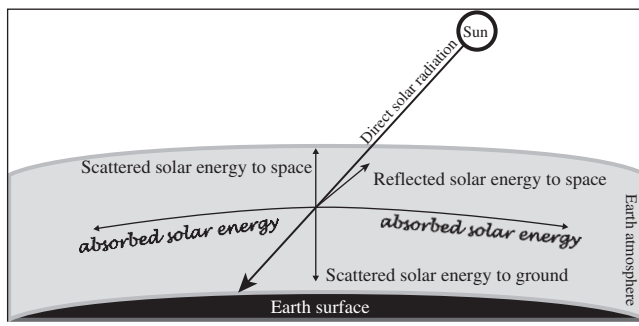

Figure 5.2.4 *Schematic diagram for the absorption and scattering mechanisms of solar energy in the cloud-free earth atmosphere*

Lord Rayleigh (born J.W. Strutt) and in his honour it is usually referred to as *Rayleigh scattering*. Rayleigh's theory gives solution to the simplified problem of scattering of the incident EM energy on spherical particles of size smaller than the wavelength λ of the EM wave. The solution for particles of size equal or greater than the EM wave's wavelength is attributed to Gustav Mie and therefore is called *Mie scattering* to honour him. According to the generalised Mie theory (in which Rayleigh scattering can be considered a particular case) the following criteria occur in nature (Siegel and Howell, 1981):

(a) When $\pi d/\lambda < 0.6/n$ (where d is the diameter of the scattering particle in μm and n its refractive index) Rayleigh scattering dominates. The incident energy is scattered in two directions: forward and backward.

(b) If $0.6/n < \pi d/\lambda < 5$, Mie scattering prevails. The incident energy is mostly forward scattered but also small side lobes appear. Forward scattering becomes more and more dominant as the ratio $\pi d/\lambda$ shifts from the lower to the upper limit of the

inequality. The more aerosols the atmosphere contains, the more *hazy* it looks, and the more forward scattering results. This, in turn, causes a noticeable increase in the size and brightness of the solar aureole (a small sky annulus around the sun). This produces 'circumsolar radiation', which, despite its diffuse nature, behaves like direct radiation.

(c) The condition $\pi d/\lambda > 5$ is seldom satisfied in the earth's atmosphere. This mechanism is mainly a diffuse reflection process.

The depletion of solar energy in the earth's atmosphere is caused by a number of different scatterers: air molecules (Rayleigh scattering), aerosols (Mie scattering) and absorbers: water vapour, many other gases, dust and clouds.

Air molecules

Scattering by air molecules occurs mainly in the spectrum from the UV to the NIR. More precisely, this effect decreases strongly with wavelength, so that it is most intense in the UV and blue parts of the spectrum, which explains the colour of the sky. Lord Rayleigh was the first to propose a physical explanation for this. See Section 5.4.3 for more details.

Aerosols, turbidity and visibility

To evaluate the AOD, the simple turbidity formula expressed by Eq. (3.3.10) or Eq. (5.4.11) and suggested long ago (Ångström, 1929; 1930) is still widely used. Contrarily to molecules, whose total density above a site is completely determined by the latter's barometric pressure, the concentration and optical characteristics of aerosols is highly variable in both space and time, depending on meteorological conditions (Smirnov et al., 1994). Aerosols can be either of natural origin (sea salt, soil dust, sand particles, forest fires, volcanic dust, etc.) or from anthropogenic origin ('pollution', voluntary biomass burning). The Ångström turbidity coefficient β is a measure of the aerosol concentration in the atmosphere, whereas the wavelength exponent α is a function of their size. The values of α and β that appear in Eq. (3.3.10) or Eq. (5.4.11) can be derived from spectral measurements using a multi-wavelength sunphotometer or other spectrometer, as discussed in more detail in Sections 5.1.7 and 5.4.4. Worldwide networks with such instruments have greatly expanded in the last decades but are still too scarce. Turbidity observations by remote sensing (using satellite-based spectrometers) are still not very accurate. Therefore, as a first approximation, it might be useful to estimate β from visibility observations which are usually done routinely at airports and other meteorological stations. Visibility (or 'visual range') observations are subjective by nature (unless they are made by an automatic instrument), are not continuous in time and space, and are subject to a number of limitations. For these reasons, the relationship between visibility and turbidity shows considerable scatter, and might need a posteriori site-specific corrections, so that it is mostly useful on a climatological basis (Husar et al., 2000).

Furthermore, human observers need markers at known distance to estimate visibility in different directions, so that visibilities of more than a few tens of km cannot be reported correctly. Observations are therefore biased toward low visibility/high turbidity conditions. Visibility and turbidity have an inverse relationship, which can be investigated either empirically or physically. In the latter case, precise definitions of the target's contrast and observing conditions are used based on the seminal work of Koschmieder

(1924). Meteorological range V_r is the theoretical equivalent of visibility V, but these two quantities are not equal. They are related by:

$$V_r = 1.306V \tag{5.2.1}$$

A simple relationship between V_r and turbidity has been derived (King and Buckius, 1979) based on an early aerosol model, using extinction coefficients for reference meteorological ranges of 5–23 km (McClatchey et al., 1972; Selby and McClatchey, 1972), and linear interpolation and extrapolation to other conditions:

$$\beta = 0.55^{\alpha}(3.912V_r^{-1} - 0.011\,62)[0.024\,72\,(V_r - 5) + 1.132] \tag{5.2.2}$$

A more thorough analysis using an extended sample of meteorological ranges between 1 and 400 km, more recent aerosol models (Shettle and Fenn, 1979) and more realistic, season-dependent vertical profiles of various aerosol species (Shettle, 1989) leads to a more robust stepwise expression (Gueymard, 2003a):

$$\begin{aligned}
&\beta = 0.55^{\alpha}\ \exp[(a_0 + a_1\tau_r + a_2\tau_r^2)/(1 + a_3\tau_r + a_4\tau_r^2)], && \text{if } V_r < 100 \text{ km} \\
&\beta = 0.55^{\alpha}(a_5 + a_6\tau_r + a_7\tau_r^{\,2}), && \text{if } 100 \leqslant V_r \leqslant 320 \text{ km} \\
&\beta = 0.55^{\alpha}(a_8 + a_9\tau_r), && \text{if } V_r > 320 \text{ km}
\end{aligned} \tag{5.2.3}$$

where $\tau_r = V_r^{-1} - 0.001$, and the necessary coefficients appear in Table 5.2.1.

Other fundamental developments regarding atmospheric turbidity have been those presented by Schüepp (1949), Linke (1922; 1929) and Unsworth and Monteith (1972). Schüepp's turbidity parameter B is associated with α and β of Ångström via:

$$B = 0.4343\beta 2^{-\alpha} \tag{5.2.4}$$

The main difference between B and β is that their reference wavelength does not coincide: it is $\lambda = 0.5\,\mu$m (visible) for Schüepp's turbidity coefficient and $\lambda = 1\,\mu$m (NIR) for Ångström's coefficient. Furthermore, Schüepp's B refers to the decadic logarithmic scale, rather than the natural logarithmic scale in more general use. This might explain why this turbidity coefficient is not in much use anymore.

Table 5.2.1 Coefficients for Eq. (5.2.3)

Coefficient	Spring/summer	Fall/winter	Coefficient	Spring/summer	Fall/winter
a_0	−3.2998	−3.6629	a_5	0.026 483	0.010 149
a_1	−5.3700	−6.5109	a_6	7.1330	6.7705
a_2	156.14	165.85	a_7	−6.6238	−1.7703
a_3	42.389	44.857	a_8	0.039 987	0.023 339
a_4	48.957	51.968	a_9	0.439 28	0.279 28

A broadband (rather than spectral) approach in the derivation of the other two turbidity indices has been followed by Linke and Unsworth–Monteith. Linke defines his turbidity parameter T_L as the number of ideally clean-dry atmospheres that would be radiatively equivalent to the real atmosphere:

$$I_{B,n} = S\, I_E \exp(-m \tau_c T_L) \tag{5.2.5}$$

where τ_c is the OD of the ideal clean-dry atmosphere (i.e. containing no water vapour or aerosols), m is the optical air mass, I_E is the solar constant, $I_{B,n}$ is the beam irradiance at the earth's surface (W/m^2) and S is the sun–earth distance correction factor. As a result of this definition, the minimum value of T_L is 1. Under hazy conditions, values of 10 and more have been observed.

Over the years, many authors have proposed successive refinements in the determination of τ_c (e.g. Kasten, 1980; 1996; Louche et al., 1986; Grenier et al., 1994; Molineaux et al., 1995; Gueymard, 1998). However, most of these determinations relied on simple extinction data and generally ignored the intricate effects of pressure and O_3. A recent and more rigorous determination (Gueymard, 2003d) includes all these refinements:

$$\tau_c = (a_0 + a_1 m + a_2 m^2)/(1 + a_3 m) \tag{5.2.6a}$$

where m is the *relative* air mass (i.e. non-pressure corrected) and coefficients a_0–a_3 depend on both a pressure correction factor $q = 1 - p/p_0$, where p is the site pressure and $p_0 = 1013.25$ h Pa and an O_3 correction factor $\eta = l_o - 0.3$, where l_o is the columnar O_3 amount in atm-cm:

$$a_0 = \exp(-1.7093 - 0.627\,52q + 0.006\,077\,5q^2) + \eta(0.029\,532 + 0.051\,649\eta)/(1 + 2.5681\eta) \tag{5.2.6b}$$

$$a_1 = \exp(-3.6146 + 0.359\,39q + 1.1274q^2) + \eta(0.002\,735\,1 - 0.017\,222\eta)/(1 + 2.2476\eta) \tag{5.2.6c}$$

$$a_2 = -\exp(-7.4771 + 0.399\,57q + 0.930\,46q^2) + \eta(-0.000\,229\,43 + 0.000\,131\,7\eta)/(1 + 2.0855\eta) \tag{5.2.6d}$$

$$a_3 = \exp(-0.655\,73 + 0.407\,33q + 1.5799q^2) - \eta(0.063\,569 + 0.393\,93\eta)/(1 + 2.2912\eta - 0.931\,09\eta^2) \tag{5.2.6e}$$

For many decades, the Linke coefficient proved to be very useful in many applications because of its simplicity and its reliance on broadband irradiance data. It has the merit of its simplicity, but has also some important drawbacks. First, it is not a true turbidity coefficient because it also depends on water vapour. Second, it is subject to virtual variations during a day even if aerosol conditions are constant, caused by its parasitic dependence on air mass. For these reasons, and the rapid development of sources of data of far greater

potential (ground-based sunphotometer networks and satellite measurements, see Section 5.4.4), its role is now more limited, e.g. to secular variations in aerosol climatology.

Unsworth and Monteith defined another broadband (or 'integral') turbidity factor T_{UM} with an expression similar to Eq. (5.2.5):

$$I_{B,n} = I_{CWA} \exp(-mT_{UM}) \tag{5.2.7a}$$

where I_{CWA} is the virtual beam irradiance that would be measured on the surface of the earth after solar rays have passed through an ideal 'clean-wet' atmosphere, i.e. the real atmosphere with water vapour but without aerosols. Unfortunately, the original authors did not provide a specific formulation for I_{CWA}. It can be calculated from the following relationship (Kambezidis et al., 1998):

$$I_{CWA} = S\, I_E\, T_R\, T_O\, T_G\, T_W \tag{5.2.7b}$$

where T_R, T_O, T_G and T_W are the broadband transmittances due to Rayleigh scattering and absorption by O_3, mixed gases and water vapour, respectively. Similar derivations have been proposed by other authors (e.g. Freund, 1983; Uboegbulam and Davies, 1983; Hay and Darby, 1984; Maxwell, 1998), who often refer to T_{UM} as the 'broadband AOD', usually denoted as τ_a. Under most conditions, T_{UM} varies in the range 0–1. Because the extinction effects of water vapour are integrated into I_{CWA}, it is obvious that T_{UM} is closer to the reality of a turbidity coefficient than T_L. However, T_{UM} is not devoid of parasitic fluctuations due to residual air-mass dependence (Gueymard, 1998). This inconvenience almost completely disappears when T_{UM} is rather defined on a limited wavelength range like the visible, where it can be integrated very effectively into illuminance calculations (Gueymard and Kambezidis, 1997; Kambezidis et al., 1998).

Example 5.2.1

Find the values of β with two approaches when the observed airport visibility is $V = 10$ km and $\alpha = 1.3$. Compare the results.

It follows from Eq. (5.2.1) that $V_r = 13.06$ km, hence $\beta_1 = 0.176$ from Eq. (5.2.2) and, from Eq. (5.2.3), $\tau_r = 0.075\,57$ and $\beta_2 = 0.245$ for spring/summer conditions or $\beta_2 = 0.232$ for fall/winter conditions. It is found that $\beta_1 < \beta_2$ for all seasons.

Example 5.2.2

Repeat previous calculations for a series of visibilities with values of 1, 2, 5, 10, 20, 30, 50 and 100 km. Draw a diagram of β_1 and β_2 versus visibility, compare the results and fit the results to an equation of the form $(a_0 + a_1V)/(1 + a_2V)$.

With calculations performed as before, values for β_1 and β_2 are found and shown in Table 5.2.2. The comparison is made in Figure 5.2.5. It is seen that both formulae provide qualitatively comparable results. However, β_1 has smaller values than β_2 for visibilities less than 30–50 km and slightly greater values above this limit, depending on season. In many clean environments, β is measured to be 0.02 or less, which corresponds to visibilities that should exceed 100 km, but cannot be observed in practice with conventional means.

Table 5.2.2 Calculation of β_1 and β_2 values

V (km)	V_r (km)	β_1	τ_r	β_2 (spring/summer)	β_2 (fall/winter)
1	1.306	1.427	0.7647	1.777	1.764
2	2.612	0.733	0.3818	0.941	0.927
5	6.530	0.316	0.1521	0.434	0.420
10	13.060	0.176	0.0756	0.245	0.232
20	26.120	0.105	0.0373	0.133	0.120
30	39.180	0.080	0.0245	0.092	0.080
50	65.300	0.058	0.0143	0.058	0.048
100	130.600	0.036	0.0067	0.034	0.027

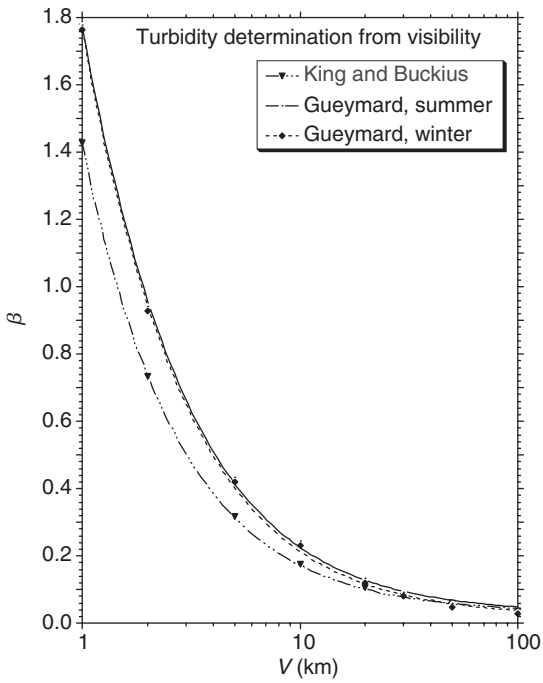

Figure 5.2.5 *Dependence of turbidity coefficient β upon horizontal visibility*

Fitting the results to the equation proposed (as shown in Figure 5.2.5) provides $a_0 = 64.981$, $a_1 = 1.3697$ and $a_2 = 45.504$ for β_1; $a_0 = 13.849$, $a_1 = 0.197\,98$ and $a_2 = 6.9228$ for β_2 with spring/summer conditions and $a_0 = 14.583$, $a_1 = 0.135\,68$ and $a_2 = 7.3624$ for β_2 and fall/winter conditions.

Clouds

Solar radiation is absorbed by water vapour and water droplets inside clouds, but is mainly scattered by them in all directions. A part of the incident energy goes back to space and another part reaches the surface of the earth. Scattering of solar energy by clouds is a complex mechanism, which is extremely difficult to model because the optical characteristics

of clouds are changing very rapidly over time, are not spatially uniform and cannot be measured easily. These optical characteristics must be heavily parameterised to obtain manageable solar radiation models. The simplest case is that of a completely covered sky by a uniform cloud layer (overcast), whereas the most complicated one consists in a partially covered sky with clouds of various kinds and at various altitudes. Because of the complexity of these phenomena, there is currently no simple solar radiation model able to predict the instantaneous spectral irradiance under any sky condition with reasonable accuracy. Therefore, the rest of this chapter will focus on clear-sky conditions only.

5.2.4 Absorption

Although scattering of solar radiation by air molecules and particulate matter is a continuous function of wavelength, absorption of solar radiation by atmospheric gases is a *selective process*. This means that these gases absorb solar energy in selective narrow spectral bands and not equally over the entire solar spectrum. The main short-wave absorbers are: water vapour, carbon dioxide (CO_2), O_3, nitrous oxide (N_2O), CO, O_2, methane (CH_4), N_2 and N_2O, and the minor absorbers are: HNO_3, ammonia (NH_3), nitric oxide (NO), nitrogen dioxide (NO_2), and sulphur dioxide (SO_2). More details on absorption are provided in Section 5.4.5.

Water vapour

Water exists in nature in three different physical states: liquid, gas and ice. In its gaseous state, it is called water vapour. The amount of water vapour in the atmosphere can be expressed in different ways, like molecular concentration and mixing ratio. In solar radiation studies, it is more common to express it in terms of *precipitable water*. This is defined as the height (in cm) of a column of liquid water with a section of 1 cm^2, which would be ideally formed if all water vapour in the zenith direction from the ground up could be condensed. Because, by definition, 1 cm^3 of water weighs 1 g, precipitable water can be alternatively expressed as a height (in cm) or as a specific mass (in g/cm^2) with the same number.

Water vapour is concentrated in the troposphere and becomes negligible above the tropopause. Its concentration decreases rapidly with altitude, so that precipitable water over mountainous areas is significantly less than above low-elevation areas. Figures 5.2.6 shows typical water vapour vertical density profiles for the various global climates that were considered during the GAIA project.

Although water vapour absorbs radiation without scattering, it has an indirect effect on aerosols. In most cases, these are made of a mix of hygroscopic particles that can both scatter and absorb. When relative humidity increases (particularly above 80%), their size grows and their extinction cross-section in turn may increase considerably (Shettle and Fenn, 1979). However, the resulting effect is exactly what turbidity measurements will sense, so that no further corrections are necessary.

Example 5.2.3

Calculate T_L for five sites at different elevations corresponding to atmospheric pressures of 1000, 900, 800, 700 and 600 h Pa for the same solar position ($Z = 30°$) and the average

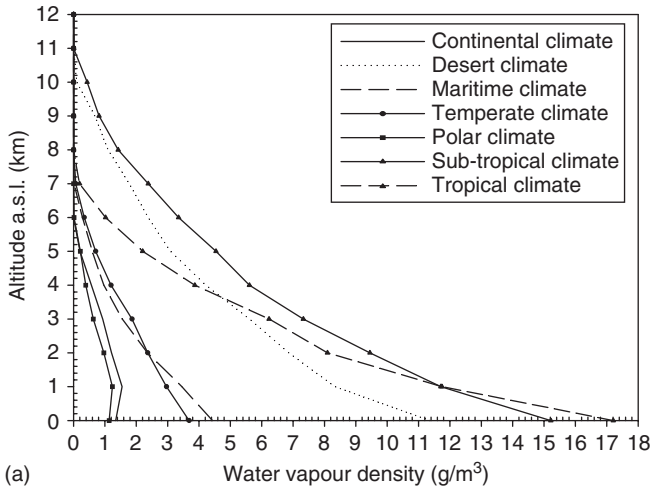

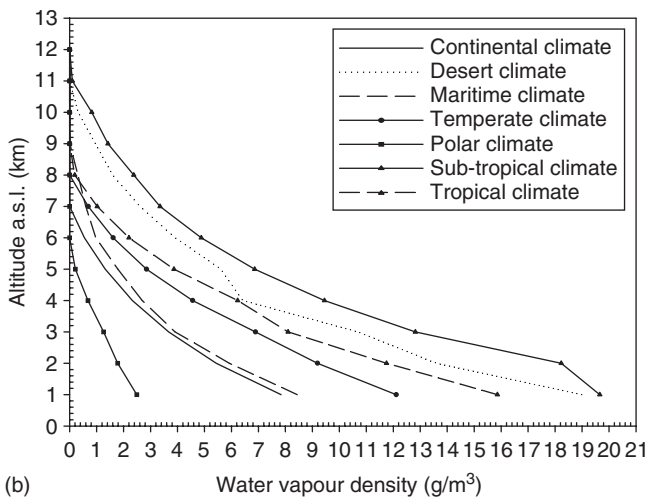

Figure 5.2.6 *Mean (a) winter and (b) summer water vapour density profiles within the earth's troposphere*

sun–earth distance. A beam irradiance $I_{B,n} = 850\,\mathrm{W/m^2}$ is measured at the lowest elevation, and is assumed to increase in steps of $20\,\mathrm{W/m^2}$ when p decreases by 100 h Pa. Consider two possible O_3 amounts, $l_o = 0.15$ and 0.45 atm-cm and $I_E = 1366.1\,\mathrm{W/m^2}$.

First, m must be calculated for a zenith angle of 30°. Equation (5.4.7) can be employed but for low zenith angles the approximation $m \approx 1/\cos Z$ is sufficient, and this gives $m = 1.155$. Finally, the various values of T_L are shown in Table 5.2.3 for the two O_3 cases. It is seen that T_L decreases by nearly 10% when the O_3 amount increases. This can be explained by the fact that, in the latter situation, the irradiance under an ideal clean-dry atmosphere decreases, which in turn must be compensated for by a larger irradiance after aerosol and water vapour extinction, thus leading to a lower apparent turbidity.

Table 5.2.3 Calculation of T_L with intermediate results

p (h Pa)	p/p_0	$I_{B,n}$ (W/m^2)	$l_o = 0.15$		$l_o = 0.45$	
			τ_c	T_L	τ_c	T_L
1000	0.9869	850	0.1128	3.64	0.1214	3.38
900	0.8882	870	0.1044	3.74	0.1129	3.46
800	0.7895	890	0.0956	3.88	0.1039	3.57
700	0.6908	900	0.0867	4.06	0.0948	3.71
600	0.5922	910	0.0778	4.28	0.0857	3.89

Table 5.2.4 Calculation of T_{UM} and intermediate results

p (h Pa)	p/p_0	T_R	T_O	T_G	T_W	I_{CWA} (W/m^2)	$I_{B,n}$ (W/m^2)	T_{UM}
1000	0.9869	0.926	0.980	0.950	0.870	1025.0	850	0.162
900	0.8882	0.933	0.980	0.955	0.900	1074.1	870	0.182
800	0.7895	0.946	0.980	0.960	0.920	1119.0	890	0.198
700	0.6908	0.962	0.980	0.965	0.940	1168.5	900	0.216
600	0.5922	0.977	0.980	0.970	0.960	1218.1	910	0.234

Example 5.2.4

With the same data as in the previous problem, calculate T_{UM}. The values of the required transmittances are given in Table 5.2.4 (columns 3–6). A single O_3 amount ($l_o \approx 0.35$ atm-cm) is considered here.

First, I_{CWA} values are derived through Eq. (5.2.7b); they are given in column 7. The calculated results are shown in the last column of Table 5.2.4.

5.3 Extraterrestrial spectrum

Precise knowledge of the extraterrestrial spectrum (ETS) is necessary whenever terrestrial spectra need to be predicted using appropriate radiative transfer codes or spectral radiation models (see Sections 5.4 and 5.5). As a first and very rough approximation, the sun can be considered as a blackbody radiating at a temperature $T \approx 5780$ K. The corresponding spectral irradiance can thus be estimated from Planck's law, which is described in many textbooks on radiative heat transfer, radiometry or photometry (Sparrow and Cess, 1978; Siegel and Howell, 1981; McCluney, 1994). In reality, the sun's energetic output exhibits noticeable departure from the smooth Planck spectral curve, particularly at wavelengths below 800 nm. These accidents are related to numerous absorption and emission solar lines, so that direct experimental measurements of ETS are needed to obtain terrestrial spectra of sufficient accuracy.

For the last decades, continuous monitoring of the sun's energetic output with spaceborne instruments has demonstrated that ETS is variable on a day-to-day basis according to solar activity. As a general rule, the shorter wavelengths (e.g. UV) are more affected than longer ones (e.g. visible or IR). Day-to-day variations in ETS are normally negligible in

periods of minimum activity (between two successive 11 year solar cycles), and very noticeable around the peak of a solar cycle. However, because these variations are small in the spectral range of interest to terrestrial applications, they will be neglected in what follows and a representative ETS corresponding to moderate solar activity (thus a period approximately half way between a solar cycle minimum and maximum) will only be considered.

5.3.1 Total solar irradiance and solar constant

Because of the day-to-day variations in ETS mentioned above, the integrated irradiance at normal incidence over the whole spectrum (as seen from the earth), or TSI, also varies. These variations may in turn trigger reactions in the earth's atmosphere with possible effects on global climate (Hoyt and Schatten, 1997). Between November 1978 (the date the modern era of direct monitoring TSI from space-borne radiometers began) and January 2003, the extreme values of TSI have been 1363 and 1368 W/m^2 (Fröhlich, 2004). Under the average solar activity conditions mentioned above, the solar constant I_E can be obtained as the average value of TSI, defined as the arithmetic mean between the minimum and maximum values of TSI after a 27 day smoothing filter is applied to dampen the sun's rotation effect. The most recent determination of I_E thus obtained is 1366.1 W/m^2 (ASTM, 2000; Gueymard, 2004), with an uncertainty of about $\pm 0.1\%$. Daily excursions in TSI being only a maximum of about $\pm 0.2\%$ of I_E, most engineering calculations may ignore them and simply replace daily values of TSI by I_E.

Because the earth's orbit around the sun is elliptical and not circular, the value of the solar constant is always given for the average sun–earth distance, i.e. 1 Astronomical unit or 1.496×10^{11} m. This average distance is reached around 3 April and 5 October each year. For any other day, the sun–earth distance correction S, whose value is up to $\pm 3.5\%$, needs to be used to obtain the daily extraterrestrial irradiance at normal incidence I_{0n} from the solar constant, according to:

$$I_{0n} = SI_E \tag{5.3.1}$$

For moderately accurate calculations, a second-order Fourier series of the day number (as the only variable) can be used to obtain S (Spencer, 1971). For more accurate results, its calculation must be coupled with that of the exact position of the sun, which is also needed to obtain its declination, zenith angle, azimuth, refraction and the equation of time. A complete package for all these calculations is provided in Prog1-6.For.

5.3.2 Spectral irradiance

Considering ideal average solar activity conditions in all what follows, the following relationship must hold between the spectral irradiance at normal incidence $I_{0\lambda}$ and the solar constant:

$$I_{SC} = \int_0^\infty I_{0\lambda}\, d\lambda \tag{5.3.2}$$

Although it is theoretically equivalent to measure I_E directly or to measure $I_{0\lambda}$ and then perform the spectral integration described by Eq. (5.3.2), the latter method does not provide

a good approximation of I_E because the uncertainty in current spectral measurements is at least an order of magnitude greater than that in broadband measurements. Furthermore, no spectrometer can sense irradiance over the whole spectrum (contrarily to active cavity radiometers used to measure TSI), hence data measured through different time periods by different instruments with different resolutions and from different space platforms or terrestrial locations need to be assembled to constitute a complete ETS. In practice, this assemblage also involves scaling factors of up to a few per cents in different spectral bands to remove discontinuities between them, and sometimes a supplementary overall scaling factor to force the integrated irradiance described by the right hand side of Eq. (5.3.2) into a predetermined value of I_{SC}. This method has been used for the development of two widely used four-band spectra (Wehrli, 1985; ASTM, 2000). A more recent nine-band spectrum, which integrates to 1366.1 W/m^2 without any overall scaling, is recommended here (Gueymard, 2004). It covers the spectral region 0–1 000 000 nm (or 0–1000 μm) and is available in file Data5-1.Txt. This ETS is represented in Figure 5.3.1 for

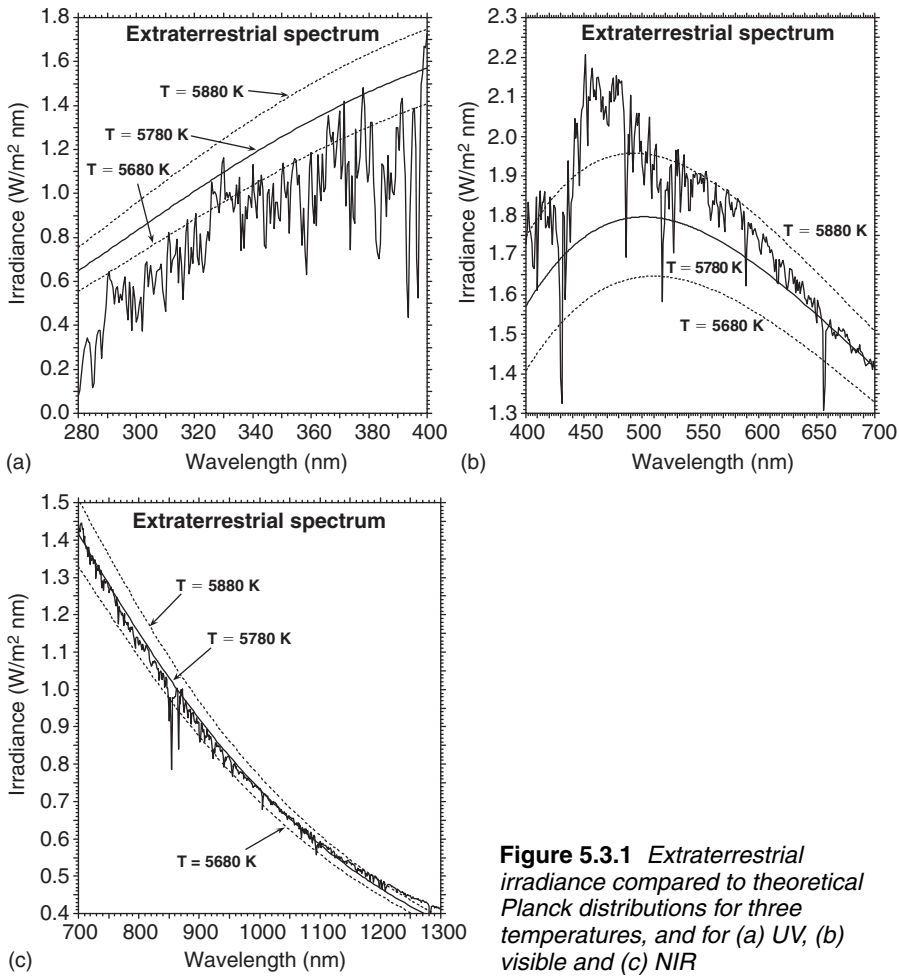

Figure 5.3.1 *Extraterrestrial irradiance compared to theoretical Planck distributions for three temperatures, and for (a) UV, (b) visible and (c) NIR*

three parts of the spectrum, which are essential in terrestrial applications: UV (280–400 nm; resolution 0.5 nm), visible (400–700 nm; resolution 1 nm) and NIR (700–1300 nm; resolution 1 nm). For illustrative purposes it is also compared to ideal Planck distributions for $T = 5680$, 5780 and 5880 K.

Like for the solar constant, the spectral irradiance at any wavelength must be corrected by S to obtain its correct value for any day of the year.

5.4 Spectral modelling

Many biological, chemical and physical processes are activated more powerfully at some wavelengths than at others. In the building environment, typical examples of such spectrally-selective processes include glazings, photovoltaic (PV) devices (to produce electricity) and materials degradation (e.g. fading). Usually, these processes cannot be experimentally monitored because of the technical difficulties and prohibitive costs associated with spectral measurements. Moreover, it is often necessary to evaluate or predict the performance of such systems at the design stage, long before they are eventually installed (if at all). The only way to perform such predictions is through the use of mathematical models, which must include a description of the spectral characteristics of the incident radiation. Different spectral radiation models or 'radiative transfer models' of varied complexity and accuracy may provide this spectral information (see Sections 5.4.1 and 5.5). Because atmospheric processes are themselves selective by nature, it is always more physically sound to model such processes on a spectral basis than on a broadband basis. As an indirect consequence of this, another interesting use of these spectral models is to provide benchmarks to test the performance of broadband radiation models, such as those reviewed in Chapters 3 and 4 (Gueymard, 1993a; 2003b).

5.4.1 Types of spectral models

A large variety of spectral models have been presented in the literature. Most models are tailored for a specific application and can generally not be converted to accept other inputs or satisfy other uses. A detailed list of spectral codes, mostly for atmospheric applications, is given in Section 5.5 and Table 5.5.1.

Atmospheric radiative transfer models are generally the most complex of them all. Not only they solve the equations of radiative transfer wavelength by wavelength, but also layer by layer in the atmosphere. Furthermore, the scattering processes that create diffuse radiation (either under clear or cloudy skies) require sophisticated modelling and elaborate numerical solutions. A typical application of these models is the analysis of signals from earth-observing satellite sensors. Examples of this type of radiative transfer model include the Santa Barbara DISORT atmospheric radiative transfer code (SBDART) and the moderate resolution transmission code (MODTRAN). SBDART (Ricchiazzi et al., 1998), developed at the University of California at Santa Barbara, is relatively simpler to use than MODTRAN, is freely accessible, and even has a convenient user interface online (http://arm.mrcsb.com/sbdart/). MODTRAN (Berk et al., 1999), developed by the Air Force Geophysical Laboratory (AFGL), has a much higher resolution and is considered a de facto standard in atmospheric applications. It is now a commercial software and is available from the Ontar Corporation (http://www.ontar.com). See Section 5.5 and Table 5.5.1 for further details.

These models, however, are not convenient for solar energy or other engineering-type applications. For such uses, two models with different capabilities are recommended: the spectral model of the atmospheric radiative transfer of sunshine (SMARTS) and Bird's simple spectral model (SPCTRAL2). Even though these models are limited to clear-sky conditions, they can also be empirically modified to predict spectra under cloudy conditions, at least to some extent (Bird et al., 1987; Nann and Riordan, 1991).

SMARTS was originally developed to investigate the effect of varying atmospheric conditions on the performance of spectrally-selective glazings, but the model evolved into a versatile radiative transfer code adaptable to a variety of applications (Gueymard, 2003d). The derivation of earlier versions is detailed elsewhere (Gueymard, 1995b; 2001). In recent years, the model received considerable improvements and was subjected to extensive validation. Its version 2.9.2 has been chosen to define reference direct and global irradiance spectra at air mass 1.5 (Gueymard et al., 2002), which have been eventually standardised (ASTM, 2003). See Section 5.6.1 for more details. The model can be used to predict clear-sky direct, diffuse and global irradiance incident on any horizontal or tilted surface at 2002 wavelengths from 280 to 4000 nm, as well as illuminances, luminous efficacy, UV action spectra, circumsolar irradiance and broadened irradiances (to simulate the output of actual spectroradiometers). The FORTRAN code and its documentation are available from http://rredc.nrel.gov/solar/models/SMARTS/.

The SPCTRAL2 model was developed in the early 1980s (Bird, 1984; Bird and Riordan, 1986) but has not been updated ever since. Hence, its features and accuracy appear now relatively limited compared to SMARTS, for instance. Still, SPCTRAL2 can be useful for very rapid estimates of the clear-sky direct, diffuse and global irradiance on horizontal or tilted surfaces, for 122 wavelengths between 300 and 4000 nm. The code exists in FORTRAN and C, and also as an electronic spreadsheet. All these versions are available from http://rredc.nrel.gov/solar/models/spectral/.

5.4.2 Spectral modelling bases

Direct radiation undergoes different attenuation processes on its path from the top of the atmosphere to the earth's surface. As mentioned in Section 5.2, the main processes involved are scattering and absorption. Radiation scattered out of the direct beams creates the diffuse sky radiance. Radiation absorbed in different layers of the atmosphere is their source for heating, which in turn drives different meteorological processes. At the spectral level, the attenuation generated by these processes can generally be described by the pivotal Beer's law already mentioned in Section 5.1.6. If, for instance, the whole atmosphere can be considered homogeneous for a given extinction process, the direct irradiance at the bottom of the atmosphere and for wavelength λ, $I_{\mathrm{Bn}\lambda}$, is related to the irradiance at the top of the atmosphere, $I_{0\lambda}$, through:

$$I_{\mathrm{Bn}\lambda} = I_{0\lambda} \exp(-k_\lambda L) \tag{5.4.1}$$

where k_λ is the spectral extinction coefficient (per unit length) for this attenuating medium and L is the total path length through the atmosphere.[1] An equivalent, but

[1]Note that this law is also applicable to non-atmospheric extinction processes, such as solar absorption through glass.

generally more practical way of using Eq. (5.4.1) is to rewrite it as:

$$I_{\mathrm{Bn}\lambda} = I_{0\lambda} \exp(-\tau_\lambda m) \tag{5.4.2}$$

where τ_λ is the spectral OD (or optical thickness) for the attenuating medium and m is its optical mass, i.e. its slant path length relative to an exactly vertical path length. The optical mass is mainly a function of the sun's zenith angle Z but also of the vertical distribution of the attenuating medium under scrutiny; it is exactly 1 for a zenith sun and close to $1/\cos Z$ when Z is less than about 75°. Equation (5.4.1) is generally used in atmospheric radiative transfer models because they calculate the extinction for all atmospheric layers (possibly of different heights and different refraction properties) separately. For simpler spectral models such as SMARTS or SPCTRAL2 – where only one layer of each extinction process is considered for the whole atmosphere – Eq. (5.4.2) is rather used. As the optical mass is mostly a geometric coefficient, the main difficulty in Eqs (5.4.1) and (5.4.2) resides in the determination of k_λ or τ_λ for each specific process. These processes can be separated into three main groups: (i) molecular (or Rayleigh) scattering; (ii) aerosol extinction (Mie scattering + absorption) and (iii) gaseous absorption.

Another pivotal law of radiative transfer is that, again at the monochromatic level, different attenuation processes can be treated independently as if they appeared in successive order. For n extinction processes with OD $\tau_{i\lambda}$ and optical mass m_i, this implies that:

$$I_{\mathrm{Bn}\lambda} = I_{0\lambda} \exp[-(\tau_{1\lambda} m_1 + \tau_{2\lambda} m_2 + \cdots + \tau_{n\lambda} m_n)] \tag{5.4.3}$$

or:

$$I_{\mathrm{Bn}\lambda} = I_{0\lambda} T_{1\lambda} T_{2\lambda} \cdots T_{n\lambda} \tag{5.4.4}$$

where each $T_{i\lambda}$ represents the atmospheric transmittance for extinction process i. In practice, calculations cannot be done at the ideal monochromatic level, so that they are rather performed at specific wavelengths with a finite bandwidth (or 'resolution'). The equations above are still valid at this relaxed spectral level, with the notable exception of water vapour absorption. This gas presents extreme variations from one absorption line to the other, and this is compounded by non-linear saturation properties. These features cannot be resolved with a finite bandwidth, so that Eqs (5.4.1) and (5.4.2) cannot be used in this case either. Equation (5.4.4) can still be used but the water vapour transmittance must be calculated separately. This is basically how the direct irradiance is predicted with SMARTS, for instance.

5.4.3 Rayleigh scattering

Since Lord Rayleigh demonstrated that the scattering effect of molecules was roughly an inverse function of the fourth power of wavelength, many refinements have been proposed. A typical simple expression for the Rayleigh OD (Leckner, 1978) is such that:

$$\tau_{\mathrm{R}\lambda} = 0.008\,735(p/p_0)\lambda^{-4.08} \tag{5.4.5}$$

where λ is wavelength in μm, p is the atmospheric pressure at site level and p_0 is the reference sea-level pressure, 1013.25 h Pa. A more elaborate expression is used in SMARTS:

$$\tau_{R\lambda} = (p/p_0)/[a_0\,(\lambda/\lambda_0)^4 + a_1(\lambda/\lambda_0)^2 + a_2 + a_3\,(\lambda/\lambda_0)^{-2}] \tag{5.4.6}$$

where $\lambda_0 = 1\,\mu$m, $a_0 = 117.3405$, $a_1 = -1.5107$, $a_2 = 0.017\,535$ and $a_3 = -8.7743 \times 10^{-4}$.

Along with the following expression for the optical air mass, or 'relative air mass', m_R:

$$m_R = 1/[\cos Z + b_0 Z^{b_1}(b_2 - Z)^{b_3}] \tag{5.4.7}$$

where $b_0 = 0.483\,53$, $b_1 = 0.095\,846$, $b_2 = 96.741$ and $b_3 = -1.754$, the Rayleigh transmittance becomes:

$$T_{R\lambda} = \exp(-\tau_{R\lambda} m_R) \tag{5.4.8}$$

If the site-level pressure is not measured, it can be estimated from the site's altitude (in km) z and the site's latitude (in degrees) ϕ according to (Gueymard, 1993b):

$$p = p_0\,F_p \exp(0.001\,77 - 0.119\,63z - 0.001\,36z^2) \tag{5.4.9}$$

where, for latitudes other than $\pm 45°$:

$$F_p = 0.993 + 2.0783 \times 10^{-4}\,|\phi| - 1.1589 \times 10^{-6}\phi^2 + (8.855 \times 10^{-3} - 1.5236 \times 10^{-4}\,|\phi| - 9.2907 \times 10^{-7}\phi^2)z \tag{5.4.10}$$

Figure 5.4.1 compares the Rayleigh transmittance for a site at sea level ($p = p_0$) and a site at 3.4 km altitude ($p = 680$ h Pa) for air masses of 1.5 and 5.0 ($Z = 48.2°$ and 78.7°, respectively).

Example 5.4.1

Calculate m_R, $\tau_{R\lambda}$ and $T_{R\lambda}$ for $Z = 80°$, $\lambda = 0.5\,\mu$m at Mauna Loa Observatory, Hawaii (latitude 19.539°N and altitude 3397 m).

Using $z = 3.397$ km, Eqs (5.4.9) and (5.4.10) provide $F_p = 1.021\,26$ and $p = 679.7$ h Pa. From Eqs (5.4.6) to (5.4.8), these results are obtained:

$$\tau_{R\lambda} = 0.096\,24,\ m_R = 5.5897,\ T_{R\lambda} = 0.583\,94.$$

For comparison purposes, the average measured pressure for 1992–99 was 680.0 h Pa at Mauna Loa, which is very close to the calculated value. However, the absolute minima

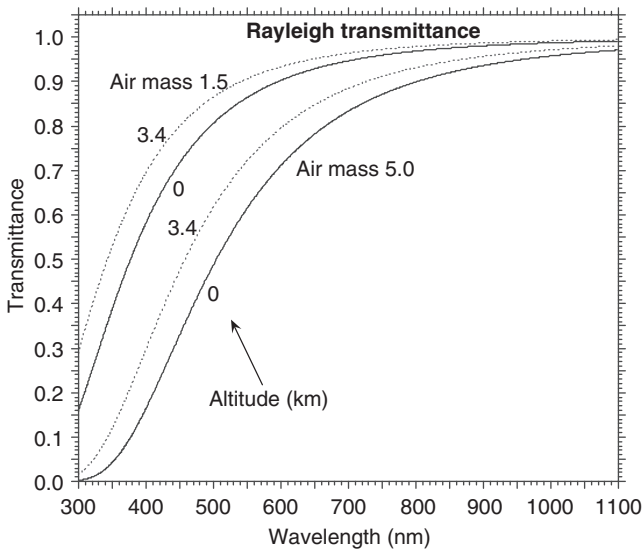

Figure 5.4.1 *Rayleigh transmittance for either a sea-level site (continuous curves) or a high-altitude site (dotted curves), and two air masses: 1.5 (top two curves) and 5.0 (bottom two curves)*

and maxima were 666 and 686 h Pa, respectively, showing that daily errors of up to about $\pm 2\%$ in $\tau_{R\lambda}$ can occur if pressure is not routinely measured and is therefore considered artificially constant in time-dependent calculations.

5.4.4 Aerosol extinction

Under clear skies, aerosol extinction generally represents the largest attenuation for direct radiation. This extinction is mainly scattering, and the rest is absorption. The exact balance between scattering and absorption is not of a concern when modelling direct irradiance (but it is an important consideration in the case of diffuse irradiance, see Section 5.4.6). Mie scattering theory (see Section 5.2.3) and early observations reported by Ångström showed that the spectral behaviour of aerosol extinction was comparable to that of Rayleigh scattering, but with a reduced wavelength exponent. The two-variable Ångström formula, Eq. (3.3.10), is a very convenient way to evaluate the AOD (also referred to as the aerosol optical thickness, AOT). For further developments, it is rewritten here as:

$$\tau_{a\lambda} = \beta(\lambda/\lambda_0)^{-\alpha} \tag{5.4.11}$$

where the Ångström turbidity coefficient β is the AOD at $\lambda_0 = 1\,\mu$m. This coefficient is proportional to the aerosol loading, or 'turbidity', of the atmosphere. It normally varies between 0 and about 0.5. The wavelength exponent α mainly depends on the size distribution of the aerosol particles. Under most conditions, a normal average value is $\alpha = 1.3$, for aerosols of rural or continental origin (Ångström, 1929), and it is frequently used when no more precise data are available. Nevertheless, α can take far lower and larger values, between about -0.6 and 2.6. Larger particles (sand, volcanic dust and sea salt) are associated with low α values and vice versa. For example, in Athens, Greece, mean annual α values have been found to vary in the range -0.6 to 1.8 during the period 1975–95 (unpublished results). During the same period, β varied between 0.3 and 1.2, values which are characteristic of

very turbid or hazy conditions. Measurements in other parts of the world have also shown that β can be >1 under severe sand storms and plumes from forest fires. To the other extreme, β can be frequently <0.01 at remote and elevated sites such as Mauna Loa, Hawaii or Antartica.

Equation (5.4.11) has the merit of its simplicity and is generally of acceptable accuracy between 0.4 and 1 μm, but, in reality, α is not always constant over the whole spectrum, resulting in a more or less pronounced curvature in log-log coordinates (Weller and Leiterer, 1988; Eck et al., 1999). As a good compromise between accuracy and complexity, both SPCTRAL2 and SMARTS (see Section 5.4.1) provide the option of using a two-tier formula with a separation at 0.5 μm, using values α_1 below 0.5 μm and α_2 above. This separation at 0.5 μm is convenient because AOD is often reported at 0.5 μm rather than 1 μm. From Eq. (5.4.11), the AOD at 0.5 μm, $\tau_{a0.5}$, is equal to $\beta 2^{\alpha}$, and $\tau_{a\lambda}$ can be expressed as a function of $\tau_{a0.5}$ rather than β using:

$$\tau_{a\lambda} = \tau_{a0.5}(2\lambda/\lambda_0)^{-\alpha} \tag{5.4.12}$$

The optical aerosol mass m_a is slightly different from m_R in Eq. (5.4.7) because aerosols are concentrated in the mixing layer, i.e. in the first few kilometres above the surface. Equation (5.4.7) can still be used to calculate m_a, but with these alternate coefficients: $b_0 = 0.168\,51$, $b_1 = 0.181\,98$, $b_2 = 95.318$ and $b_3 = -1.9542$.

Figure 5.4.2 compares the aerosol transmittance at air mass 1.5 and 5.0 for a rural aerosol with $\beta = 0.02$ (low turbidity) and an urban aerosol with $\beta = 0.50$ (high turbidity, e.g. pollution episode).

To accurately calculate AOD, the main difficulty resides in the determination of the correct values of β and α to use in Eq. (5.4.11). To better address this problem, the purpose of the intended spectral calculations needs to be considered. Two main cases can be envisioned: (i) generic, or ideal, atmospheric conditions are contemplated, e.g. to define reference spectra or (ii) time series of hourly spectral irradiance corresponding to actual atmospheric conditions are required, e.g. for the simulation or testing of a spectrally-selective device during a specific period of time.

The first case is the easiest to solve because various aerosol models exist. For instance, SMARTS has a library of 10 aerosol models for which α, α_1 and α_2 have been pre-calculated as a function of relative humidity if necessary. A typical value of β or $\tau_{a0.5}$ is then all what is needed to evaluate Eq. (5.4.11) or Eq. (5.4.12). This value is generally chosen to characterise a particular region for which some knowledge of the aerosol climatology is available. Section 5.6.1 presents more information on the development of reference spectra.

Case (ii) involves the knowledge of time series of both α and β (or $\tau_{a0.5}$) on a short-term (e.g. hourly) basis. Such data can be indirectly obtained from two possible sources: ground-based sunphotometers from turbidity networks or experimental sites and gridded data sets derived from space-borne spectrometer measurements. The international NASA network AERONET (http://aeronet.gsfc.nasa.gov) is a good example of the first source of data, with hundreds of sites reporting $\tau_{a\lambda}$ at seven wavelengths every 15 min (or less) whenever the sun is clear and Z is less than about 80°. To obtain the needed synthetic results a simple technique can be advantageously used. Equation (5.4.11) can be rewritten as:

$$\ln \tau_{a\lambda} = \ln \beta - \alpha \ln(\lambda/\lambda_0) \tag{5.4.13}$$

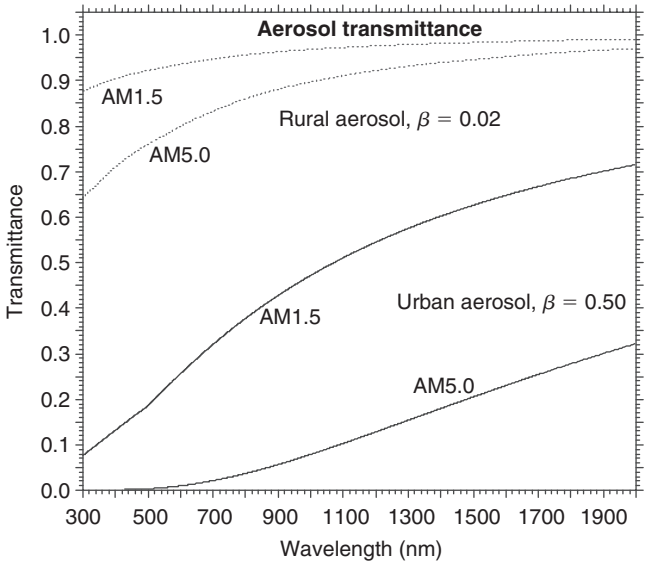

Figure 5.4.2 *Aerosol transmittance for low turbidity conditions (upper two curves) and high turbidity conditions (lower two curves) and two air masses: AM1.5 and AM5.0*

which corresponds to a linear equation in log–log co-ordinates, with a slope $-\alpha$ and an intercept equal to $\ln\beta$. The pairs of data $(\lambda, \tau_{a\lambda})$ can therefore be fitted to Eq. (5.4.13) with a regular least-squares method, and this can be done simply from within an electronic spreadsheet (which is convenient because AERONET files are in spreadsheet-ready format). This technique can also be adapted to other sunphotometric data sets. Figures 5.4.3–5.4.5 present time series of α and β thus obtained for three sites in very different climates: Bondville, Illinois (latitude 40.06°N, longitude 88.37°W and elevation 213 m); Mauna Loa, Hawaii (latitude 19.54°N, longitude 155.58°W and elevation 3397 m) and Solar Village, Saudi Arabia (latitude 24.91°N, longitude 46.41°E and elevation 650 m). It is obvious that the climatologies of α and β are very different from one site to the other and that large daily and seasonal variations do occur in both variables, due in particular to local pollution outbreaks, dust storms or long-range aerosol transport. Pollution outbreaks from the northeast U.S. and the urban Chicago area can explain most turbidity excursions at Bondville. Elevated turbidity episodes at Mauna Loa are a well-known yearly phenomenon caused by long-range transport of dust from violent Asian sand storms in the Spring. Finally, frequent regional dust storms explain the spikes in β at Solar Village.

Gridded data sets from space-borne spectral measurements – the second source of turbidity data – are still in their infancy. The first data sets of this kind, from instruments such as AVHRR over oceans or MODIS over both oceans and continents, suffer from a number of problems: instrument degradation, calibration difficulties, cloud contamination, interference from highly reflecting surfaces, etc. Nevertheless, progress is extremely rapid in this domain, with considerably improved multi-channel instruments being launched to space, and refined retrieval algorithms being developed. All this activity should bear fruit within a few years and should provide spectral AOD information on a fine grid size (e.g. 10 km $\times$ 10 km) over the whole world. Research is also oriented towards the development of merged data sets, using advanced optimisation techniques to combine retrieved data

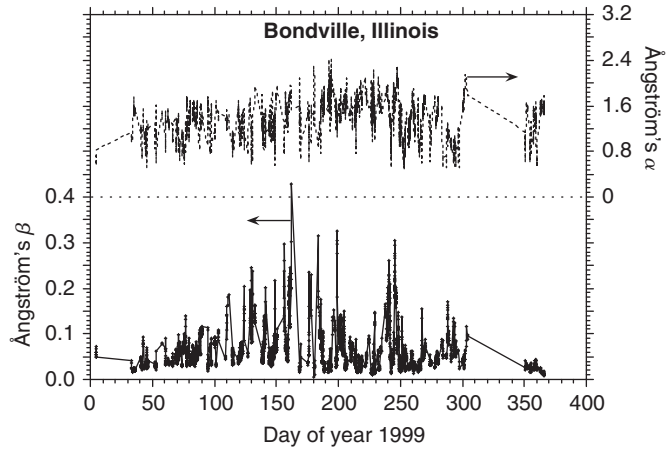

Figure 5.4.3 *Time series of α (top panel) and β (bottom panel) for Bondville, Illinois in 1999*

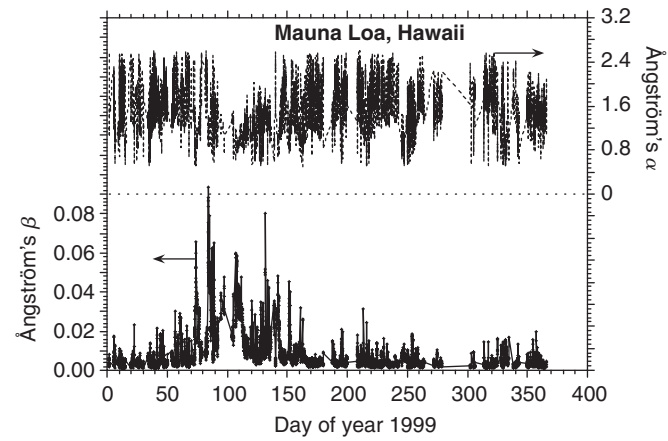

Figure 5.4.4 *Time series of α (top panel) and β (bottom panel) β for Mauna Loa, Hawaii in 1999*

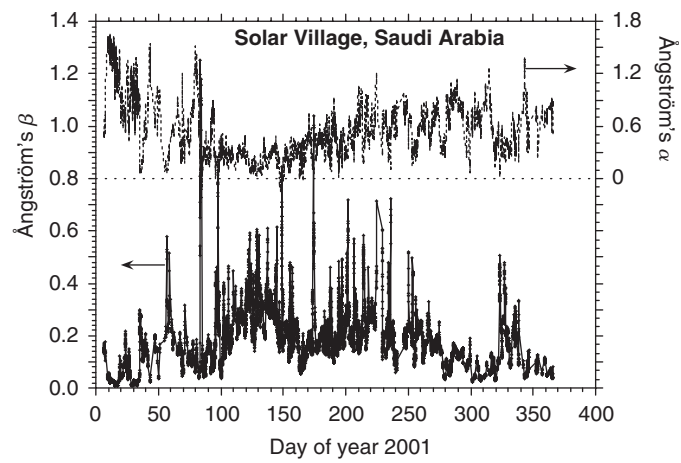

Figure 5.4.5 *Time series of α (top panel) and β (bottom panel) for Solar Village, Saudi Arabia in 2001*

Table 5.4.1 Estimation of $\tau_{a\lambda}$ as a function of λ for various values of α and β

λ	$\beta = 0.02$					$\beta = 0.40$				
(μm)	$\alpha = 0.5$	$\alpha = 1.0$	$\alpha = 1.3$	$\alpha = 2.0$	$\alpha = 2.6$	$\alpha = 0.5$	$\alpha = 1.0$	$\alpha = 1.3$	$\alpha = 2.0$	$\alpha = 2.6$
0.3	0.0365	0.0667	0.0957	0.2222	0.4576	0.7303	1.3333	1.9134	4.4444	9.1526
0.4	0.0316	0.0500	0.0658	0.1250	0.2166	0.6325	1.0000	1.3164	2.5000	4.3322
0.5	0.0283	0.0400	0.0492	0.0800	0.1213	0.5657	0.8000	0.9849	1.6000	2.4251
0.6	0.0258	0.0333	0.0389	0.0556	0.0755	0.5164	0.6667	0.7771	1.1111	1.5096
0.7	0.0239	0.0286	0.0318	0.0408	0.0506	0.4781	0.5714	0.6360	0.8163	1.0111
0.8	0.0224	0.0250	0.0267	0.0313	0.0357	0.4472	0.5000	0.5346	0.6250	0.7145
0.9	0.0211	0.0222	0.0229	0.0247	0.0263	0.4216	0.4444	0.4587	0.4938	0.5261
1.0	0.0200	0.0200	0.0200	0.0200	0.0200	0.4000	0.4000	0.4000	0.4000	0.4000

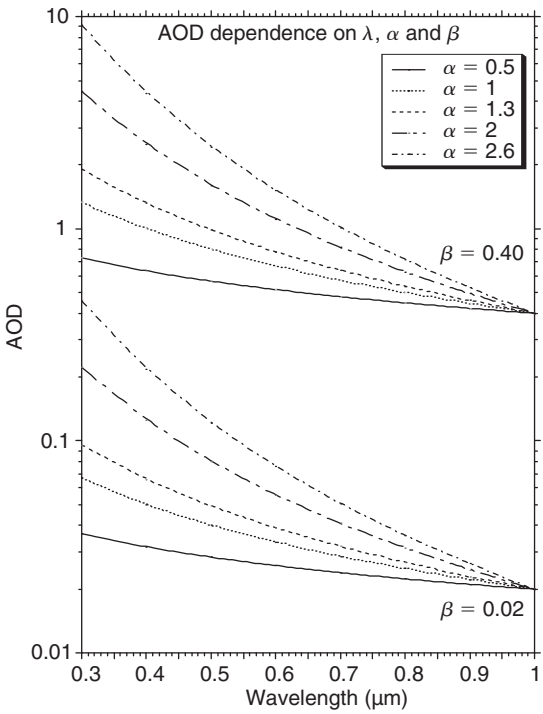

Figure 5.4.6 *Dependence of the AOD upon wavelength for various values of Ångström's turbidity parameters* α *and* β

from satellite instruments, predictions from chemical transport models and sunphotometric ground truth (Yu et al., 2003).

Example 5.4.2

Obtain $\tau_{a\lambda}$ for various values of α (0.5, 1, 1.3, 2 and 2.6) as a function of λ ($0.3 < \lambda < 1.0$ μm, step = 0.1 μm) considering $\beta = 0.02$ (very clear conditions) and $\beta = 0.40$ (hazy conditions).

Using Eq. (5.4.11) the aerosol extinction coefficient is calculated and tabulated in Table 5.4.1. As the concentration of the aerosols gets greater so does their OD. A visualisation of the results in Table 5.4.1 appears in Figure 5.4.6. The AOD can be fairly high in the UV

under hazy conditions, thus considerably reducing direct irradiance to the benefit of diffuse irradiance.

Example 5.4.3

The following table contains actual data of $\tau_{a\lambda}$ at Bondville, Illinois, as measured with a multi-wavelength sunphotometer of AERONET. The second line is for the last data point of 9 February 1999 (at 22:15:51 UT or 16:15:51 LST) and the third line is for the first data point of the next day (at 14:07:58 UT or 08:07:58 LST). For these two moments, calculate α, α_1, α_2, β and $\tau_{a\lambda}$ at $\lambda = 0.55\,\mu m$. Furthermore, compare the measured value of $\tau_{a0.5}$ to the values calculated from β and α or α_2:

Date	$\tau_{a\lambda}$	1.02 μm	0.87 μm	0.67 μm	0.50 μm	0.44 μm	0.38 μm	0.34 μm
9 February 1999	22:15:51	0.031 006	0.030 501	0.032 711	0.057 721	0.071 997	0.098 305	0.099 939
10 February 1999	14:07:58	0.080 759	0.075 356	0.070 551	0.092 420	0.109 579	0.134 808	0.131 679

The first step, shown in the table below, is to calculate $\ln\lambda$ (line 2) and $\ln\tau_{a\lambda}$ (lines 3 and 4) for each wavelength and each data point:

λ	1.02 μm	0.87 μm	0.67 μm	0.50 μm	0.44 μm	0.38 μm	0.34 μm
$\ln\lambda$	0.019 802 63	−0.139 262 1	−0.400 477 6	−0.693 147 2	−0.820 980 6	−0.967 584	−1.078 809 7
22:15:51	−3.473 574 5	−3.489 995 8	−3.420 043 9	−2.852 134 2	−2.631 130 8	−2.319 680 4	−2.303 195 3
14:07:58	−2.516 285 9	−2.585 531 7	−2.651 419 4	−2.381 411 9	−2.211 109 5	−2.003 903 7	−2.027 388 1

In the second and last step, the data points just calculated are fitted to Eq. (5.4.13). Coefficients α, α_1 and α_2 can be obtained with the *slope* function of an electronic spreadsheet, whereas $\ln\beta$ can be obtained with the *intercept* function. Ångström's α (column 2) and β (column 3) are obtained here using all seven channels, whereas α_1 (column 4) is obtained with four points (0.34–0.50 μm) and α_2 (column 5) also with four points (0.50–1.02 μm). The AOD at 0.55 μm (column 6) and at 0.5 μm (column 7) are calculated from Eq. (5.4.11) using α and β in columns 2 and 3, respectively. Finally, the alternate AOD at 0.5 μm (column 8) is calculated from the same equation but with α_2 from column 5. The measured $\tau_{a0.5}$ (last column) is roughly the average of these two calculated values. The significant variation in aerosol conditions that takes place during the short period of 16 h that separates the two data points is remarkable, but not isolated.

						$\tau_{a0.5}$		
UT	α	β	α_1	α_2	$\tau_{a0.55}$	From α	From α_2	Measured
22:15:51	1.222	0.0263	1.521	0.855	0.0545	0.0613	0.0510	0.0577
14:07:58	0.551	0.0699	0.989	0.174	0.0972	0.1024	0.0849	0.0924

5.4.5 Gaseous absorption

Contrarily to the scattering processes reviewed above, gaseous absorption is highly spectrally selective and can be hardly predicted by pure theory. Therefore, progress in this field is

Table 5.4.2 Coefficients for the calculation of optical masses with Eq. (5.4.7). The maximum value of the optical mass (for $Z = 90°$) appears in the last column

Constituent	Description	b_0	b_1	b_2	b_3	m (max.)
Molecules	Rayleigh scattering	0.483 53	0.095 846	96.741	−1.7540	38.18
Aerosols	Aerosol extinction	0.16851	0.181 98	95.318	−1.9542	68.55
BrO	Bromine monoxide[1]	1.065 1	0.637 90	101.80	−2.2694	14.41
CH_4	Methane[2]	0.493 81	0.355 69	98.230	−2.1616	38.91
CH_2O	Formaldehyde[1]	0.616 96	0.060 787	96.632	−1.8279	39.16
$ClNO_3$	Chlorine nitrate[1]	1.121 2	1.613 2	111.55	−3.2629	14.08
CO	Carbon monoxide[2]	0.505 0	0.063 191	95.899	−1.9170	44.75
CO_2	Carbon dioxide[2]	0.657 86	0.064 688	96.974	−1.8083	38.08
HNO_2	Nitrous acid[1]	1.044 0	0.784 56	103.15	−2.4794	16.69
HNO_3	Nitric acid[1]	1.044 0	0.784 56	103.15	−2.4794	16.69
H_2O vapour	Water vapour	0.106 48	0.114 23	93.781	−1.9203	72.22
N_2	Nitrogen[2]	0.381 55	8.871×10^{-5}	95.195	−1.8053	51.30
NH_3	Ammonia[1]	0.321 01	0.010 793	94.337	−2.0548	60.49
NO	Nitric oxide[1]	0.777 38	0.110 75	100.34	−1.5794	31.28
NO_2	Nitrogen dioxide[1]	1.121 2	1.613 2	111.55	−3.2629	14.08
NO_3	Nitrogen trioxide[1]	1.121 2	1.613 2	111.55	−3.2629	14.08
N_2O	Nitrous oxide[2]	0.616 96	0.060 787	96.632	−1.8279	39.16
O_2	Oxygen[2]	0.657 79	0.064 713	96.974	−1.8084	38.09
O_3	Ozone	1.065 1	0.637 9	101.80	−2.2694	14.41
SO_2	Sulphur dioxide[1]	0.634 54	$9.919\,8 \times 10^{-3}$	95.804	−2.0573	56.15

[1] Trace gas; [2] Uniformly mixed gas.

through more and more sophistication in laboratory measurements carried out with spectroscopic methods, and in atmospheric detection of variable gases and 'trace' gases by radiometry or chemical sampling. The former task aims at a more accurate description of the spectral absorption coefficient of each gas, whereas the latter task aims at quantifying the vertical profile of the concentration of each gas, or at least the total content of a vertical column extending from the ground to the top of the atmosphere. For terrestrial applications in the building environment, only this vertical column content, or abundance, is of interest. With reference to Eq. (5.4.2) the OD at wavelength λ for absorption by a specific gas i, $\tau_{i\lambda}$, is simply equal to the product of its absorption coefficient, $A_{i\lambda}$, by its abundance, C_i. The latter is not a function of wavelength but may be variable over time, space and elevation. The former is a characteristic of the gas but is also generally a slight function of temperature and pressure. For most gases, the spectral transmittance after absorption can be obtained as:

$$T_{i\lambda} = \exp(-A_{i\lambda} C_i m_i) \tag{5.4.14}$$

where, as before, m_i is the optical mass for gas i, and can be expressed with specific coefficients in Eq. (5.4.7). Table 5.4.2 provides these coefficients for the most radiatively-active gases.

For all these gases, various sources of spectroscopic data at high resolution with temperature dependence (if applicable) have been proposed. However, their spectral range is generally limited so that, in many cases, different sources of absorption coefficients or

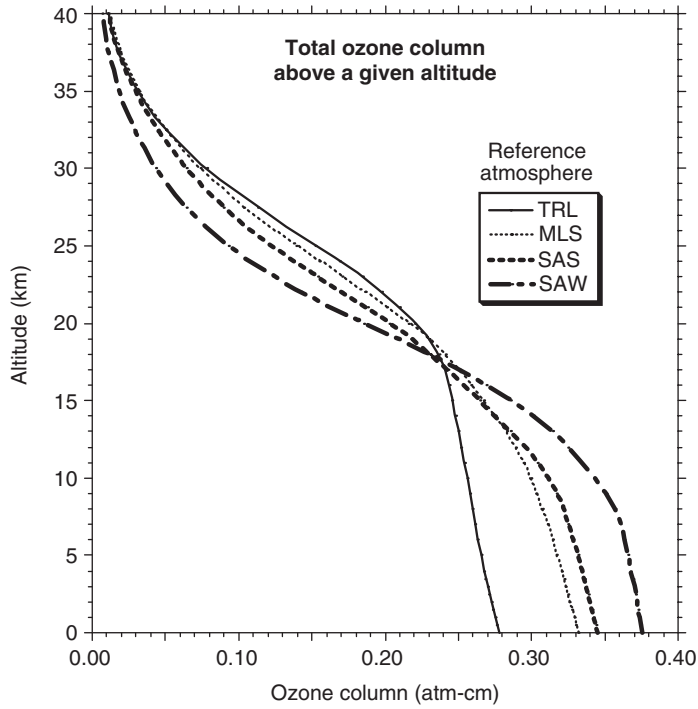

Figure 5.4.7 *Ozone abundance above a given altitude for four reference atmospheres*

cross-sections must be assembled into a composite spectrum. Also, their original resolution must usually be degraded to that of the target radiative transfer model. Because of the complexity of some phenomena and the large quantity of numbers involved (e.g. the value of $A_{i\lambda}$ for each gas and each wavelength), only general indications will be given here. For detailed calculations in practice, the reader is referred to complete models, such as those reviewed in Sections 5.4.1 and 5.5.

O_3 is extremely absorbing in the UV (fortunately for life on earth), and moderately in the visible and IR. The recommended sources of absorption and temperature dependence data are: Daumont et al. (1992) and Malicet et al. (1995) for 280–345 nm; Bogumil et al. (2000; 2003) for 345–405, 523–610 and 761–1000 nm; Burrows et al. (1999) for 391–522 nm; Burkholder and Talukdar (1994) for 611–760 nm and Anderson et al. (1993) for 1001–1091 nm. O_3 is concentrated in the stratosphere at about 20 km altitude. Its abundance is variable in time and space, but as a general rule it is lower in the tropics and around the poles, and higher at mid-latitudes. Model atmospheres include typical vertical profiles of its concentration, from which it is possible to calculate its total abundance l_o along a vertical column. Figure 5.4.7 presents the results of this exercise for four different reference atmospheres (Anderson et al., 1986): tropical (TRL), mid-latitude summer (MLS), sub-arctic summer (SAS) and sub-arctic winter (SAW). Under realistic, day-to-day conditions the ozone abundance can be as low as 0.1 atm-cm (or 100 Dobson units, DU; 1 atm-cm = 1000 DU) near the poles (an 'ozone hole' occurs when it is below 100 DU) to about 0.5 atm-cm at mid- to high latitudes. Sources of daily data include ground measurements at hundreds of sites from the World Ozone and Ultraviolet Data Center network

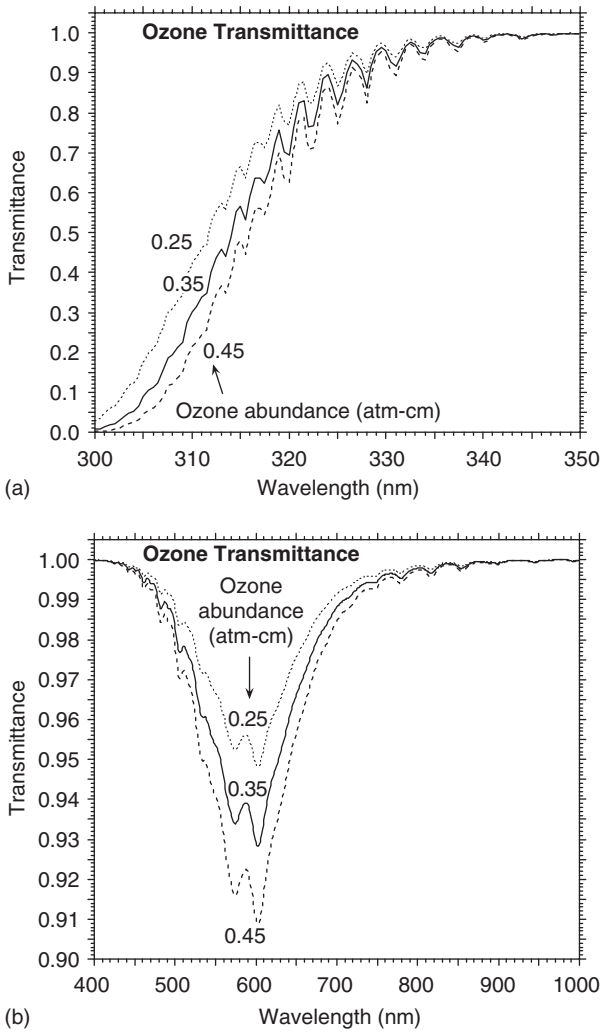

Figure 5.4.8 *Ozone transmittance for three typical ozone abundances and an air mass of 1.5 for: (a) UV region, (b) visible and NIR regions. Note the different scales*

(http://www.woudc/.org), and space-borne measurements from a few satellites such as TOMS (http://toms.gsfc.nasa.gov/ozone/ozone.html) and GOME (http://www.knmi.nl/gome_fd/index.html). These or other sources can also provide monthly-average data from which the ozone climatology can be evaluated for a specific region. Such sources are preferable to spatiotemporal formulae (Van Heuklon, 1979) which are simplistic in nature and based on older and partial data. Figure 5.4.8 shows the O_3 transmittance $T_{o\lambda}$ as predicted by SMARTS for an air mass of 1.5 ($Z = 48.2°$) and three typical O_3 abundances: 0.25, 0.35 and 0.45 atm-cm.

Water vapour is not absorbing in the UV but becomes extremely active when wavelength increases above 500 nm. In the short-wave region contemplated here (300–4000 nm), it is by far the main absorber in magnitude. Considerable progress has been done in the determination of its absorption features since earlier engineering-type

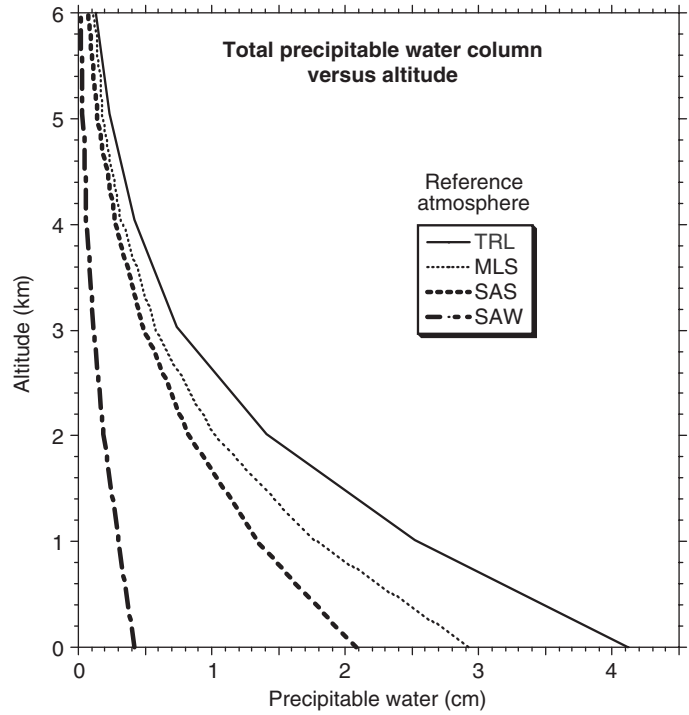

Figure 5.4.9 *Precipitable water over a given altitude for four reference atmospheres*

spectral models were proposed (e.g. Leckner, 1978). There is still very active ongoing research in spectroscopy to obtain more accurate absorption data, discover possible new weak absorption bands and settle controversies about the exact magnitude of the continuum (a slowly varying broad and weak absorption feature, which is normally masked by the strong and rapidly varying selective absorption). The basic line absorption data are regularly compiled in huge databanks such as HITRAN (Rothman et al., 1998; Rothman et al., 2003; see also http://www.hitran.com) and GEISA (Jacquinet-Husson et al., 1999). This information, however, can only be used *directly* by extremely sophisticated line-by-line atmospheric radiative models, or *indirectly* (with a somewhat degraded resolution) by other models such as MODTRAN. Water vapour transmittance results purposefully obtained from the latter can be in turn used as the basis to obtain the parameterised water vapour ODs of SMARTS (for instance), because, as mentioned above, water vapour absorption does not obey Beer's law at the spectral level envisioned here.

These ODs are intricate functions of pressure, optical mass and precipitable water w (see definition in Section 5.2.4.). As mentioned in Section 5.2.4 and shown in Figure 5.2.6, water vapour is concentrated in the lower troposphere. Precipitable water is obtained by integrating these profiles between a given altitude and the top of the atmosphere. Results of such calculations are shown in Figure 5.4.9 for the same four reference atmospheres as in Figure 5.4.7, using published water vapour concentration data (Anderson et al., 1986). By comparison with Figure 5.4.7, it is obvious that the ways w and l_o decrease with altitude are completely different. As a general rule, typical daily values of w range from less than 0.5 cm at high latitudes in winter or elevated sites, to 5 cm and more in tropical climates.

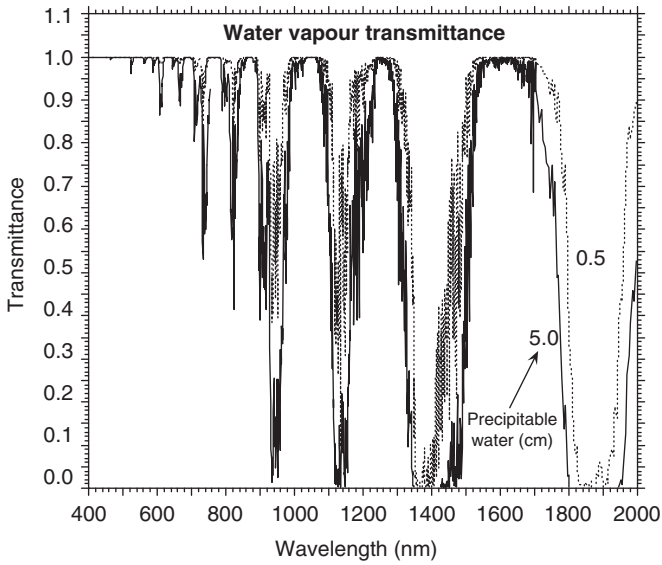

Figure 5.4.10 *Water vapour transmittance for $w = 0.5$ cm (dry conditions, top curve) or 5 cm (humid conditions, lower curve) and an air mass of 1.5*

Large short-term and seasonal variations in w exist, so that locally measured or estimated data of w are necessary for accurate predictions of its transmittance.

Sources of measured data include thousands of radiosonde sites in the worldwide network (but there are usually two soundings per day only, and w then needs to be calculated from each sounding by integrating the vertical distribution of humidity – a cumbersome task), radiometric measurements by sunphotometric networks such as AERONET (see Section 5.4.4), global positioning system (GPS) delay measurements (http://www.gpsmet.noaa.gov/jsp/index.jsp, http://www.gst.ucar.edu/gpsrg/realtime.html), gridded data sets from remote sensing from space and, finally, assimilated gridded data sets combining remote-sensed data and radiosonde soundings, such as in the NASA Water Vapour Project or NVAP (Randel et al., 1996); http://eosweb.larc.nasa.gov/GUIDE/dataset_documents/base_nvap_dataset.html). When none of these resources is appropriate, it is possible to estimate w from local surface data of temperature and humidity, using an empirical model (Smith, 1966; Leckner, 1978; Gueymard, 1994), but the random error with such estimates is very high – of the order of 50% on an hourly basis – because of the frequent decoupling between surface conditions and vertical humidity profile. Figure 5.4.10 shows the water vapour transmittance $T_{w\lambda}$ calculated by SMARTS for an air mass of 1.5 and two largely different values of w, 0.5 and 5 cm. This figure also indicates that saturation effects are normally maximum in strong bands (e.g. around 1400 and 1850 nm) and minimum in weak bands (e.g. around 600, 700 and 1700 nm).

Uniformly mixed gases are a series of gases (CH_4, CO, CO_2, N_2, N_2O and O_2) whose concentration is roughly constant with altitude. Their vertical distribution resembles that of air molecules, so that their optical mass is similar to that of Rayleigh scattering (Table 5.4.2). Also, they normally follow Beer's law at the spectral level, and their abundance is mostly a function of pressure. The abundance of CO_2 has seasonal variations, and, as a major greenhouse gas, is slowly increasing over time. Its current concentration is about 370 ppm. However, these variations have only very limited effect on spectral irradiance

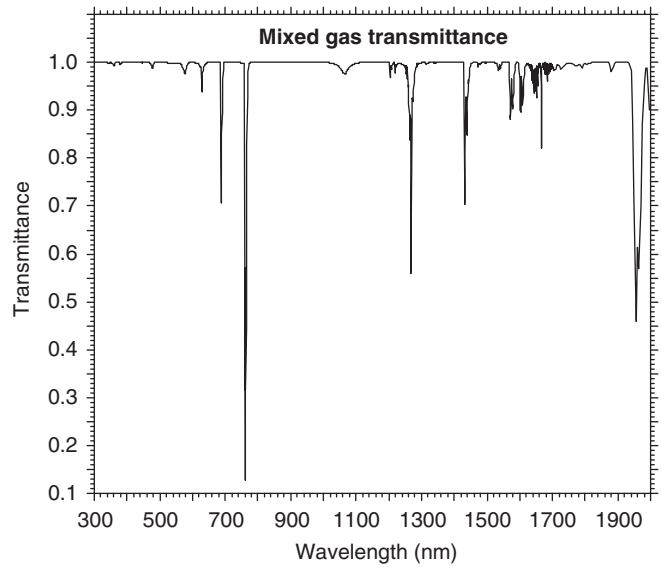

Figure 5.4.11 *Mixed gas transmittance for a sea-level site and an air mass of 1.5*

below about 1900 nm because this gas mostly absorbs in the IR. Figure 5.4.11 shows the mixed gas transmittance $T_{g\lambda}$ for an air mass of 1.5 and a sea-level site. The sharp O_2 absorption feature around 760 nm is clearly visible.

Finally, there are some trace gases whose absorption is normally very small if not negligible. However, some of them (NO, NO_2 and SO_2 in particular, but O_3 as well, even though it is not treated here as a trace gas) might be in unusually large concentrations in the mixing layer over polluted sites. The difficulty in this case is to estimate their abundance, but it can be done if their concentration is monitored for air quality reasons, which is often the case at least for the four main gases mentioned above. This concentration can be assumed constant over the height of the mixing layer, but the latter is variable (generally between 0.5 and 2 km) and therefore the conversion to the needed abundance is generally not accurate. The trace gas transmittance $T_{t\lambda}$ under severely polluted conditions (such that the NO_2 abundance is 0.02 atm–cm) appears in Figure 5.4.12 for air masses 1.5 and 5, with most absorption caused by NO_2 – peaking at around 400 nm and extending over both the UV and visible regions.

In summary, direct irradiance is dependent upon many spectral features that introduce a lot of perturbations in its spectrum. For illustrative purposes, Figure 5.4.13 compares three spectra relative to widely different conditions: a 'best case' characterising an elevated site ($z = 2$ km and $p = 790$ h Pa) with dry and clean conditions ($w = 0.5$ cm and $\beta = 0.02$, no pollution), normal O_3 (0.30 atm-cm) and a moderate air mass ($m_R = 1.5$); an 'average case' for a site at 0.5 km altitude ($p = 950$ h Pa), an air mass of 2.0 and otherwise typical conditions ($w = 1.5$ cm, $\beta = 0.10$, no pollution, 0.30 atm-cm O_3) and a 'worst case' for a sea-level site with moderate humidity ($w = 2.5$ cm) and moderate pollution with significant turbidity ($\beta = 0.4$), average O_3 (0.35 atm-cm) and a low sun ($m_R = 5.0$). The worst-case scenario exhibits a considerable decrease in magnitude, but also a significant red shift, compared to the other scenarios. This red shift characteristically results from an increase in either air mass or turbidity.

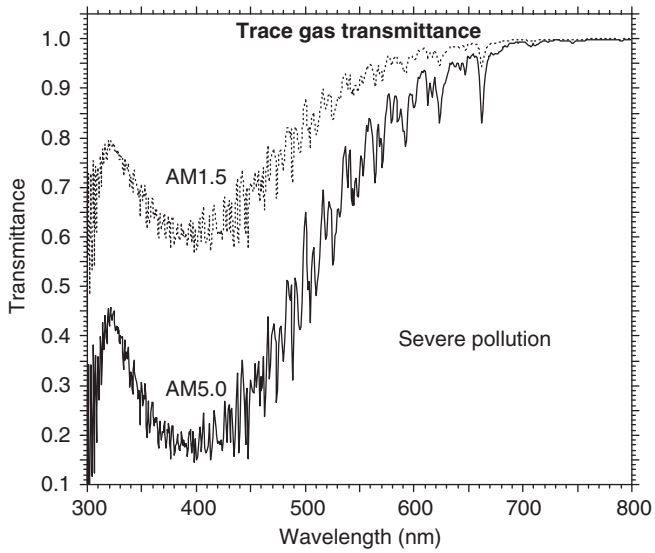

Figure 5.4.12 *Trace gas transmittance for air masses of 1.5 and 5 under severe pollution*

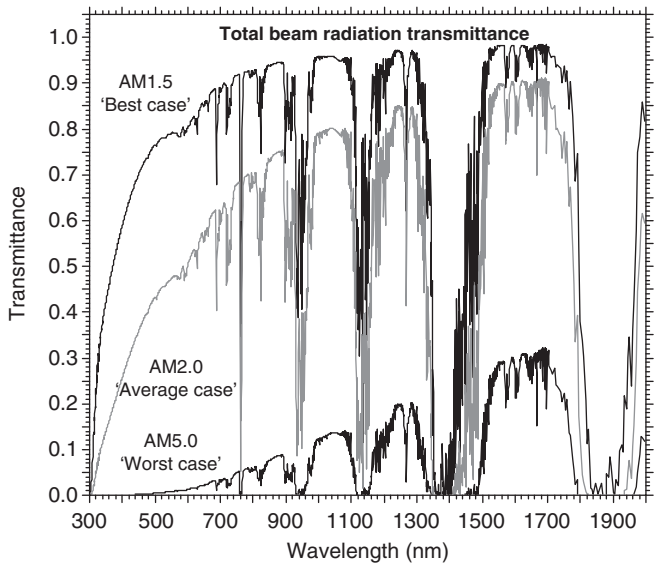

Figure 5.4.13 *Spectral beam transmittance for a 'best case' (top curve), an 'average case' (middle curve) and a 'worst case' (bottom curve)*

5.4.6 Diffuse irradiance

The two scattering processes that have been reviewed in Sections 5.4.3 and 5.4.4 contribute to the radiation that emanates from the whole sky hemisphere – in short, diffuse irradiance. Aerosol scattering is usually the most important source of diffuse radiation for two reasons: (i) the AOD is normally larger than the Rayleigh OD, thus scatters away more photons from the direct beam and (ii) aerosols scatter considerably more in the forward direction than all others, whereas molecules scatter in all directions almost equally,

so that a large fraction of the radiation scattered by aerosols, and only half of the radiation scattered by the molecules, reach the ground.

It is common observation that, under clear skies, the sky looks brighter in two areas: the aureole around the sun and the horizontal annulus close to the horizon. The increase in radiance and luminance in these areas is directly related to the aerosols optical characteristics, to the point that spectral measurements in the aureole can provide detailed information about the AOD and size distribution of the aerosols. If this spectral radiance were known at each point of the sky's hemisphere, a spatial integration over the dome would provide the spectral diffuse irradiance. This method, however, would require considerable calculations, and thus is not used in practice. Models such as MODTRAN and SBDART, which were mentioned in Section 5.4.1, solve the equation of radiative transfer for each atmospheric level and calculate the diffuse irradiance in the upward and downward directions through an appropriate numerical method; in this case, discrete ordinate radiative transfer method (DISORT) (Stamnes et al., 1988). This method is still too computationally intensive for engineering models such as SPCTRAL2 or SMARTS, which thus rather rely on parameterised solutions based on the same transmittance functions as used to calculate the direct irradiance in the previous section.

In this simplified approach, the Rayleigh diffuse component can be calculated as:

$$I_{\mathrm{DR}\lambda} = I_{0\lambda} T_{\mathrm{g}\lambda} T_{\mathrm{w}\lambda} T_{\mathrm{t}\lambda} T_{\mathrm{aa}\lambda} (1 - T_{\mathrm{R}\lambda}^{0.9}) F_{\mathrm{R}\lambda} \Gamma_{\mathrm{o}\lambda} \cos Z \tag{5.4.15}$$

where $I_{0\lambda}$ is the extraterrestrial irradiance (duly corrected for the sun–earth distance), $T_{\mathrm{g}\lambda}$, $T_{\mathrm{w}\lambda}$ and $T_{\mathrm{t}\lambda}$ are the transmittances for the uniformly mixed gases, water vapour and trace gases discussed in the previous section, respectively, and $T_{\mathrm{R}\lambda}$ is the Rayleigh transmittance from Eq. (5.4.9). $F_{\mathrm{R}\lambda}$ is the molecular forward scatterance, i.e. the fraction of the total energy scattered by molecules that is actually scattered in the forward direction and may reach the ground. Its maximum value is 0.5, but decreases at shorter wavelengths and large values of $\tau_{\mathrm{R}\lambda}$ due to multiple-scattering effects (Skartveit and Olseth, 1988). $T_{\mathrm{aa}\lambda}$ is the transmittance of the aerosol absorption process, which is defined by:

$$T_{\mathrm{aa}\lambda} = \exp(-m_{\mathrm{a}} \tau_{\mathrm{aa}\lambda}) = T_{\mathrm{a}\lambda} / T_{\mathrm{as}\lambda} \tag{5.4.16}$$

where $T_{\mathrm{as}\lambda}$ is the transmittance for the aerosol-scattering process and $\tau_{\mathrm{aa}\lambda}$ is the OD for aerosol absorption, related to the AOD and the OD for aerosol scattering $\tau_{\mathrm{as}\lambda}$ according to:

$$\tau_{\mathrm{aa}\lambda} = \tau_{\mathrm{a}\lambda} - \tau_{\mathrm{as}\lambda} \tag{5.4.17}$$

with, when defining the aerosol single-scattering albedo as $\omega_{0\lambda} = \tau_{\mathrm{as}\lambda}/\tau_{\mathrm{a}\lambda}$:

$$\tau_{\mathrm{aa}\lambda} = (1 - \omega_{0\lambda}) \tau_{\mathrm{a}\lambda} \tag{5.4.18}$$

The single-scattering albedo is a slight function of wavelength and relative humidity, with values normally in the 0.60–0.98 range. (In other words, aerosol extinction is always dominated by scattering processes.) Finally, the $\Gamma_{\mathrm{o}\lambda}$ term in Eq. (5.4.15) represents an effective O_3 diffuse transmittance, which accounts for the fact that most of the Rayleigh-scattering process occurs below the O_3 layer. Therefore, $\Gamma_{\mathrm{o}\lambda}$ is normally of far greater magnitude than $T_{\mathrm{o}\lambda}$ in the UV, and is an intricate function of the O_3 OD and of its optical mass.

The aerosol diffuse component is obtained in a similar manner:

$$I_{\mathrm{Da}\lambda} = I_{0\lambda} T_{\mathrm{g}\lambda} T_{\mathrm{w}\lambda} T_{\mathrm{t}\lambda} T_{\mathrm{aa}\lambda} T_{\mathrm{R}\lambda} (1 - T_{\mathrm{as}\lambda}) F_{\mathrm{a}\lambda} \Gamma_{\mathrm{o}\lambda} \cos Z \tag{5.4.19}$$

where $F_{\mathrm{a}\lambda}$ is the aerosol forward scatterance, an intricate function of wavelength, aerosol-scattering OD and zenith angle.

5.4.7 Global irradiance

The sum of $I_{\mathrm{DR}\lambda}$ and $I_{\mathrm{Da}\lambda}$ represents the diffuse irradiance that is incident on an ideally non-reflecting ground. For such a surface or receiver, assumed horizontal, the global irradiance would be:

$$I_{\mathrm{G0}\lambda} = I_{\mathrm{DR}\lambda} + I_{\mathrm{Da}\lambda} + I_{\mathrm{Bn}\lambda} \cos Z \tag{5.4.20}$$

In reality, however, the ground has a non-zero reflectance, $\rho_{\mathrm{g}\lambda}$, so that a fraction of the incident irradiance is reflected back to the sky as diffuse radiation. The sky has also a finite reflectance, $\rho_{\mathrm{s}\lambda}$, so that a backscattered component returns to the ground and that the total diffuse irradiance is:

$$\begin{aligned} I_{\mathrm{D}\lambda} &= I_{\mathrm{DR}\lambda} + I_{\mathrm{Da}\lambda} + \rho_{\mathrm{s}\lambda}\rho_{\mathrm{g}\lambda} I_{\mathrm{G0}\lambda} / (1 - \rho_{\mathrm{s}\lambda}\rho_{\mathrm{g}\lambda}) \\ &= (I_{\mathrm{DR}\lambda} + I_{\mathrm{Da}\lambda} + \rho_{\mathrm{s}\lambda}\rho_{\mathrm{g}\lambda} I_{\mathrm{Bn}\lambda} \cos Z)/(1 - \rho_{\mathrm{s}\lambda}\rho_{\mathrm{g}\lambda}) \end{aligned} \tag{5.4.21}$$

Therefore, the real global irradiance is:

$$I_{\mathrm{G}\lambda} = I_{\mathrm{D}\lambda} + I_{\mathrm{Bn}\lambda} \cos Z \tag{5.4.22}$$

The spectral reflectance of various surfaces appear in Figure 5.4.14. The reflectance of a specific surface may vary from one site to the other, as well as with its dryness or the sun's zenith angle. Most vegetative surfaces have a very low reflectance in the UV, typically below 0.1. Note also that the 'surface' considered here for the calculation of Eq. (5.4.21) extends within a radius of at least 10 km around the site under scrutiny. Because natural surfaces are rarely homogeneous over such a large area, but constitute a mosaic, a weighted average of all reflectance spectra involved should be performed. This can amount to a formidable task, which is almost never done in practice, so that a single representative surface has usually to be defined instead. Details about the calculation of $\Gamma_{\mathrm{o}\lambda}$, $\omega_{0\lambda}$, $F_{\mathrm{a}\lambda}$, $\rho_{\mathrm{s}\lambda}$, and of diffuse and global irradiance on tilted surfaces, can be found in Gueymard (1995b).

Example 5.4.3

Calculate and evaluate the spectra for direct normal irradiance, diffuse horizontal irradiance, global horizontal irradiance and global irradiance incident on a sun-facing vertical surface for the 'average case' of Figure 5.4.13.

This case is completely treated as *Example 11* in the Example library of the SMARTS code. A ready-to-use input file, as well as the corresponding output files, are provided, so that no extra calculations are needed. When the spectral output file is imported into a plotting program, the four spectra appear as in Figure 5.4.15. The difference in magnitude between these different spectra is particularly evident.

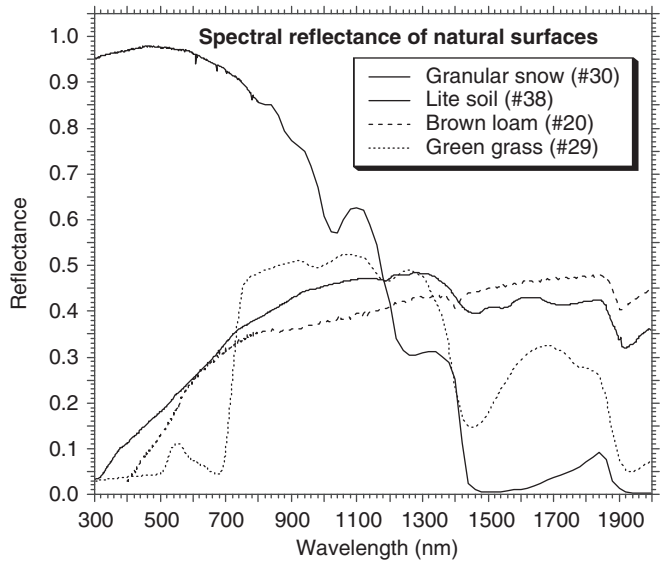

Figure 5.4.14 *Spectral reflectance of a few natural surfaces. Numbers refer to the specific call number in the albedo library of SMARTS*

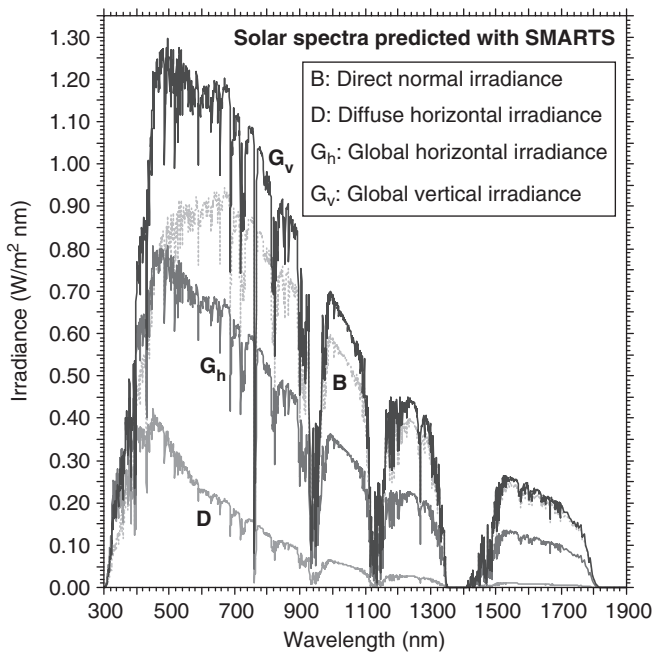

Figure 5.4.15 *Comparison of direct normal irradiance, diffuse and global irradiance on a horizontal surface, and global irradiance on a vertical surface facing the sun for the average case in Figure 5.4.13*

5.5 Validation

Several *spectral transfer radiative codes* have been developed over the past 30 years. They are listed in Table 5.5.1 with a brief description of the application areas each of them covers and their availability.

Table 5.5.1 Spectral atmospheric radiative transfer codes in alphabetical order as for their abbreviations

Code name	Code developer(s)	Code processing method	Code description
6S	D. Tanré et al.	Single-scattering	6S is one of the best codes for satellite spectral radiance simulations with heavy documentation. Available from ftp://loaser.univ-lille1.fr/ or ftp://kratmos.gsfc.nasa.gov/6S/
ATRAD	W. Wiscombe	Adding doubling	W. Wiscombe does not support this code any more. The code is based on the adding and doubling technique.
CliRad SW and CliRad LW	M.D. Chou	2-stream 1-D	Radiative transfer codes used in global circulation models and mesoscale models developed at NASA, Goddard.
Column radiation model (CRM)	NCAR		CRM is a stand-alone version of the radiation model used in the NCAR community climate model (CCM).
DISORT	K. Stamnes, S.C. Tsay, W. Wiscombe	1-D discrete ordinates method (DOM)	DISORT is a solver only. Available from ftp://climate.gsfc.nasa.gov/pub/wiscombe/Disc_Ord. Description of the code: http://imk-msa.fzk.de/msa-public/softaware-tools/modtran/science/disort.htm
DOM	J. Haferman	DOM	The code is available from ftp://iihr.uiowa.edu/pub/hml/haferman
Discrete ordinates optical simulator (DOORS)	C. Godsalve	DOM	DOORS uses aerosol data from LOWTRAN (see below) and gaseous absorption data from 6S (see above).
FASCODE	AFGL	Line-by-line	Instructions and download at http://www2.bc.edu/~sullivab/soft/fascode.html
FluxNet	J. Key	Neural networks	FluxNet is the neural network version of STREAMER (see below). Given a set of input data consisting of surface, cloud and atmospheric characteristics, FluxNet calculates upwelling and downwelling surface flux in either short wave or long wave. While it is not as flexible as STREAMER, FluxNet is faster by two to four orders of magnitude, making it ideal for large batch jobs and image processing.

Fu-Liu v. 0602b	Q. Fu, K.N. Liou	K-distribution, two-stream	The code was popular in the past but has poor documentation. It is a two-stream solver with good molecular package. Available from http://snowdog.larc.nasa.gov/rose/flp/ (on-line computation) or http://snowdog.larc.nasa.gov/rose/fu0602/ (documentation and source code download).
GENSPECT	University of Toronto, atmospheric physics (now as a commercial product)	Line-by-line	GENSPECT is a radiative transfer toolbox under MATLAB to calculate gas absorption and emissivity, emission and transmission for a wide range of atmospheric gases from NUV to NIR. For more information, see http://www.genspect.com
Line-by-line radiative transfer model (LBLRTM)	Atmospheric and environmental research inc.		Documentation and download of LBLRTM from http://www.rtweb.aer.com/lblrtm_frame.html. The code needs some input data, which can be taken from the output of the LNFL code (http://www.rtweb.aer.com).
libRadtran	A. Kylling and B. Mayer		libRadtran is a collection of C and FORTRAN functions and programmes for calculation of solar and thermal radiation in the earth's atmosphere. Free download of source code and instructions are available from http://www.libradtran.org
LidarPC			Information is available from http://www.optics.arizona.edu/Palmer/PDF/atmosoft.pdf
LOWTRAN	AFGL	Band model approximation of line-by-line	LOWTRAN is a lower-resolution code than its successor, MODTRAN. One should prefer to use MODTRAN instead. LOWTRAN source code is freely available from http://www1.ncdc.noaa.gov/pub/software/lowtran/
Monte Carlo modelling in multi-layer media (MCML)	L.H. Wang and S.L. Jacques	Monte Carlo	MCML is a steady-state Monte Carlo simulation programme intended for multi-layered turbid media. Each layer has its own optical properties of absorption, scattering, anisotropy and refractive index. MCML code and documentation can be found at http://omlc.ogi.edu/pubs/abs/wang95c.html
MODTRAN	AFGL (Berk et al., 1999)	Band model approximation of line-by-line, and DOM	Newer versions of MODTRAN include multiple scattering. It is considered as one of the best codes because its molecular package (based on HITRAN) is often updated. Older versions can be downloaded from http://www2.bc.edu/~sullivab/soft/instruct.html, where a non-disclosure agreement must be signed. MODTRAN's original report as a postscript file can be found at http://imk-msa.fzk.de/msa-public/software-tools/modtran/science/modrep.htm. Recent versions are distributed on a commercial basis by Ontar Corp., http://www.ontar.com
Moderate spectral atmospheric radiance and transmittance (MOSART)	AFGL	Band-model approximation	MOSART is a unified computer code for calculating atmospheric transmission and radiance at low altitudes for line-of-sight paths within the atmosphere and for paths that intersect the earth's surface. Download of code can be done through http://www2.bc.edu/~sullivab/soft/NDA_MOSART.txt, after a non-disclosure, agreement is signed.

(*continued*)

Table 5.5.1 *Continued*

Code name	Code developer(s)	Code processing method	Code description
mc-layer	A. Macke	Monte Carlo	A radiative transfer code for multiple scattering in vertically inhomogeneous atmospheres.
Polarised radiative transfer (PolRadTran)	F. Evans		PolRadTran is a plane-parallel fully polarised atmospheric radiative transfer model. It is available from http://nit.colorado.edu/~evans/polrad.html
SAMM	AFGL		A combination of SHARC and MODTRAN to calculate the IR radiance. The source code is available from http://www2.bc.edu/~sullivab/soft/NDA_SAMM.txt. A non-disclosure agreement must be signed first.
SBDART	P. Ricchiazzi, S. Yang and C. Gautier	1-D code using the DOM	SBDART is a FORTRAN computer code for the analysis of a wide variety of radiative transfer problems in satellite remote sensing and atmospheric energy budget studies. The source code can be downloaded from http://arm.mrcsb.com/sbdart, while a description of SBDART can be found at http://crisp.nus.edu.sg/research/links/rs-arm.html
SCIATRAN	IFE/IUP University of Bremen	Line-by-line or correlated-k methods, plane-parallel mode or pseudo-spherical mode	SCIATRAN has been designed to allow fast and accurate simulation of radiance spectra as measured or expected to be measured from space with the passive remote sensing UV–visible–NIR spectrometers: Global ozone monitoring experiment (GOME) and SCIAMACHY. SCIATRAN is designed to be the forward model for retrieval of atmospheric constituents from GOME/SCIAMACHY satellite data. Available from http://www.iup.physik.uni-bremen.de/sciatran/. A licensing agreement must be signed
Synthetic High-Altitude Radiance Code SHARC	AFGL		Simulates IR high-altitude background radiation. The source code is available from http://www2.bc.edu/~sullivab/soft/NDA_SHARC.txt. A non-disclosure agreement must be signed first.

Spherical harmonics discrete ordinate for 3-D atmospheric radiative transfer (SHDOM)	F. Evans	3-D DOM	This code computes unpolarised monochromatic or spectral-band radiative transfer in a 1-, 2- or 3-D medium for either collimated solar and/or thermal emission sources of radiation. It is probably one of the best 3-D codes available. A description of the code can be found at http://nit.colorado.edu/~evans/shdom
SIG			The source code is available from http://www2.bc.edu/~sullivab/soft/NDA_SIG.txt. A non-disclosure agreement must be signed first.
Simplified method for atmospheric corrections (SMAC)	R. Rahman and G. Dedieu	Semi-empirical approximation	SMAC works over the whole solar spectrum. Available from ftp://www.cesbio.ups-tlse.fr
Simple model of the atmospheric radiative transfer of sunshine (SMARTS)	C. Gueymard	Transmittance parameterisations	The code calculates total as well as partial atmospheric transmittances, irradiances and illuminances. SMARTS and its documentation are available from http://www.nrel.gov/solar/models/SMARTS, after a password is given to download the code and an agreement is signed. A detailed description of early versions of SMARTS can be found in Gueymard (1995b; 2001).
Simple spectral model (SPCTRAL2)	R.E. Bird and C. Riordan	Transmittance parameterisations	Details of the code can be found in Bird (1984). The code is freely available from http://rredc.nrel.gov/solar/models/spectral/spectrl2 and is available in different versions (C, FORTRAN or spreadsheet)
System for transfer of atmospheric radiation (STAR)	H. Schwander, A. Kaifel, A. Ruggaber and P. Koepke		Details of the code can be found in Schwander et al. (2001). The code, as a Java application, is available from http://www.meteo.physik.uni-muenchen.de/strahlung/uvrad/Star/starprog.html. An agreement must be signed first
STREAMER	J. Key	DOM	Radiative transfer model that can be used for computing either radiances or irradiances for a wide variety of atmospheric and surface conditions. It is a 1-D radiative transfer solver with molecular package. Its molecular package is not often updated, however.

A comparison between FASCODE, MODTRAN and LOWTRAN can be found at http://imk-msa.fzk.de/msa-public/software-tools/modtran/science/fa-mo-lo.htm. Many of the above spectral codes use the absorption-line database of HITRAN, which is regularly updated. To obtain the database an electronic application is required at http://www.hitran.com. The codes used here for validation against solar spectral measurements, in alphabetical order, are: MODTRAN, SMARTS and SPCTRAL2. Before the comparisons are presented, a more specific description of the codes than those in Table 5.5.1 is given in the following sections.

5.5.1 MODTRAN

The code is used here in its commercial form (PCModWin) available from Ontar Corp. (http://www.ontar.com). MODTRAN is an atmospheric code developed at the US Air Force Phillips Laboratory (also known as AFGL). MODTRAN is partly based on the LOWTRAN model (Kneizys et al., 1988) and is considered its direct successor. It is used in the calculation of transmission and/or radiance in a specified path in the atmosphere. MODTRAN is written in FORTRAN77 programming language and can be used as either stand-alone program or a separate routine in other larger system codes. The source code of older MODTRAN versions is free software (see Table 5.5.1). Newer versions are distributed by Ontar.

MODTRAN works in the wave number range 50–50 000 cm^{-1}, i.e. for wavelengths between 0.2 and 200 μm. Its maximum spectral resolution is 2 cm^{-1}, adequate for many applications. The geometry routine of the code considers effects caused by atmospheric refraction and the curvature of the earth. The atmosphere is simulated by a stack of 33 distinct layers, starting at the surface of the earth up to 100 km altitude. Various parameters, such as air temperature, barometric pressure, gaseous absorption, extinction coefficients, aerosol optical characteristics and refraction, are defined for each layer. Standard atmospheres are used or realistic vertical profiles can be alternatively supplied by the user. Aerosol and cloud models can also be used to take into account the effect of various particulates along the path. MODTRAN calculates the effects from the various atmospheric components of interest, which are combined over the optical path for each wave number.

The code uses different aerosol models depending on altitude above ground: (i) *boundary-layer aerosols* (BLA, 0–2 km), (ii) *upper-troposphere aerosols* (UTA, 2–10 km), (iii) *lower-stratosphere aerosols* (LSA, 10–30 km) and (iv) *stratospheric aerosols* (SA, 30–100 km). For BLA, four main types of aerosol distribution can be selected: rural, urban, desert and maritime aerosols. UTA has a much more uniform distribution of aerosols than BLA. Aerosols in LSA are dominated by seasonal changes in the altitude of the tropopause between seasons; these aerosols exhibit a uniform global distribution. Volcanic eruptions can contribute significantly in this layer after such an event. Finally in the SA case, the most important attenuating factor is meteoric dust. Humidity is also taken into account by MODTRAN calculations as this parameter has an important influence upon the extinction caused by aerosols.

The standard atmospheres used by MODTRAN are the following: (i) the *1976 US standard atmosphere* (representative of mid-latitudes), (ii) the *TRL atmosphere* (applied to locations around 15°N), (iii) *MLS* (45°N, July), (iv) *mid-latitude winter* (45°N, January), (v) *SAS* (60°N, July) and (vi) *SAW* (60°N, January). Each reference atmosphere

contains concentration profiles of water vapour, O_3, CO, CO_2, CH_4, NO_x, NH_3, O_2, SO_2 and various trace gases up to 100 km.

5.5.2 SMARTS

This code calculates solar short-wave irradiance from spectral transmittance functions for the main extinction processes in the cloudless atmosphere, i.e. Rayleigh scattering, aerosol extinction and absorption by O_3, uniformly mixed gases, water vapour and various other gases including NO_2. The latest versions of the code make calculations for a number of other atmospheric gases ignored by many other radiative code. Temperature-dependent or pressure-dependent extinction coefficients have been developed for all these absorbing gases, based on recent spectroscopic data obtained either directly from the experimental literature, or derived from MODTRAN. Aerosol extinction is evaluated using a two-tier Ångström approach. Parameterisations of the wavelength exponent and single-scattering albedo for different aerosol models are provided as a function of both wavelength and relative humidity. Moreover, aerosol turbidity can be estimated from airport visibility data and vice versa.

Radiative calculations are performed at 2002 wavelengths with fixed 0.5 nm intervals between 280 and 400 nm, 1 nm intervals between 280 and 1700 nm and 5 nm intervals between 1705 and 4000 nm. Various extraterrestrial spectra can be selected by the user, some of them being common with MODTRAN. Incident direct, diffuse and global irradiance (as well as illuminance and PAR) for any plane orientation at ground level (including tracking surfaces) are calculated by the model, with provisions for both multiple-scattering effects, ozone absorption intricacies in the UV and ground reflection processes including diffuse, semi-diffuse and specular reflectance. SMARTS also has an optional circumsolar correction function and two filter-smoothing post-processors, which together allow the simulation of actual spectroradiometers. This facilitates comparison between modelled results and measured data. Finally, optional UV calculations provide the UV index and the results of convolving the predicted irradiance with various biological action spectra.

Detailed performance assessment of the model is provided and consists in comparisons between its predictions and rigorous radiative transfer models for different specific atmospheric conditions in the UV, visible and NIR. High-quality measured data sets in the UV and in other spectral bands (e.g. 290–620 nm and 300–1100 nm) are also used to validate the model by direct comparison. The resultant overall accuracy appears as a significant improvement over existing simplified models, particularly in the UV. Therefore, SMARTS can be used in a variety of applications to predict full terrestrial spectra under any cloudless atmospheric condition.

5.5.3 SPCTRAL2

This model computes clear-sky spectral direct-beam, diffuse and global irradiances on a prescribed receiver plane – tilted or horizontal – at a single point in time. For tilted planes, the user specifies the incidence angle of the direct beam (FORTRAN version) or the tilt and azimuth of the plane (C and spreadsheet versions). The wavelength spacing is irregular, covering 122 wavelengths from 305 to 4000 nm. AOD, precipitable water and O_3 abundance must be specified by the user. No variations in atmospheric constituents or structure are available. There is no separate computation of circumsolar radiation.

The direct-beam spectral irradiance is assumed to contain the circumsolar radiation within a 5° solid angle. No smoothing functions are provided.

5.5.4 Comparison between measurements and model predictions

Assessing the performance of spectral models is normally an inherent part of their development. This ensures that their description of atmospheric processes is realistic, which is essential to guarantee reproducible and accurate predictions not only under ideal conditions but also under realistic atmospheres. Comparisons between predicted and measured spectra can thus be found in the literature (Bird and Riordan, 1986; Wang and Anderson, 1994; Kambezidis et al., 1997a,b; 2000a,b; 2001a,b; Adamopoulos et al., 2000; Gueymard, 2001; 2003d; Gueymard et al., 2002). Note, however, that these comparisons can only be done under very well defined and stable atmospheric conditions. In particular, a clear line of sight (from the instrument to the sun) is needed to perform a correct performance assessment of direct-beam irradiance. Global and diffuse irradiance tests, however, require considerably more stringent conditions, i.e. a cloudless sky (zero cloud cover).

In recent years, the need for spectral information and simulations has tremendously increased. Instruments capable of providing such information have been continuously developed, but their cost is generally too high and their calibration requirements are often too sophisticated for the resources of most institutions. For example, as of this writing, a high-performance, weatherproof spectroradiometer with extended spectral range and various attachments for automatic operation and recording of direct, diffuse and global irradiance would cost more than $100 000. Portable or 'field' instruments may cost less, but their spectral range might be reduced, their resolution lower, etc. Even the most sophisticated instruments have uncertainties that are not negligible, as well as inherent limitations. For example, some spectral bands can be very difficult, if not impossible, to monitor (e.g. below 300 nm or above 2500 nm). Good models can thus help either in testing the spectral accuracy or overall performance of a spectroradiometer (Gueymard et al., 2002), or in extending its measured spectra by filling in the missing bands (Osterwald and Emery, 2000). In other words, measurements of the highest accuracy are needed to test the performance of models and, vice versa, models can be used to test the performance of instruments – at least under clear-sky conditions. This synergetic effect may lead to both better models and measurements.

As an example of possible intercomparisons, spectral measurements at NREL (Golden, Colorado) are compared here with predictions from the three spectral codes reviewed just above: MODTRAN (version 4v1r1), SMARTS (version 2.9.3) and SPCTRAL2 (spreadsheet version). The direct irradiance spectrum was scanned from 300 to 2400 nm with an Optronic OL-750 spectroradiometer (often considered as a reference instrument) on 18 October 2002, 1420 LST, at an air mass of 2.06. Precipitable water (0.45 cm) and AOD (0.067 at 500 nm) were obtained from collocated sunphotometers. An equivalent meteorological range of 123 km was used for MODTRAN. A default rural aerosol submodel (Shettle and Fenn, 1979) was used for both MODTRAN and SMARTS. As equivalence for SPCTRAL2, the default α value of 1.14 was selected. The O_3 amount for that day (0.29 atm-cm) was obtained from TOMS. The measured pressure was 812 h Pa.

The spectroradiometer output can be simulated in MODTRAN and SMARTS (but not in SPCTRAL2) by invoking their smoothing post-processors. In this case the bandwidth

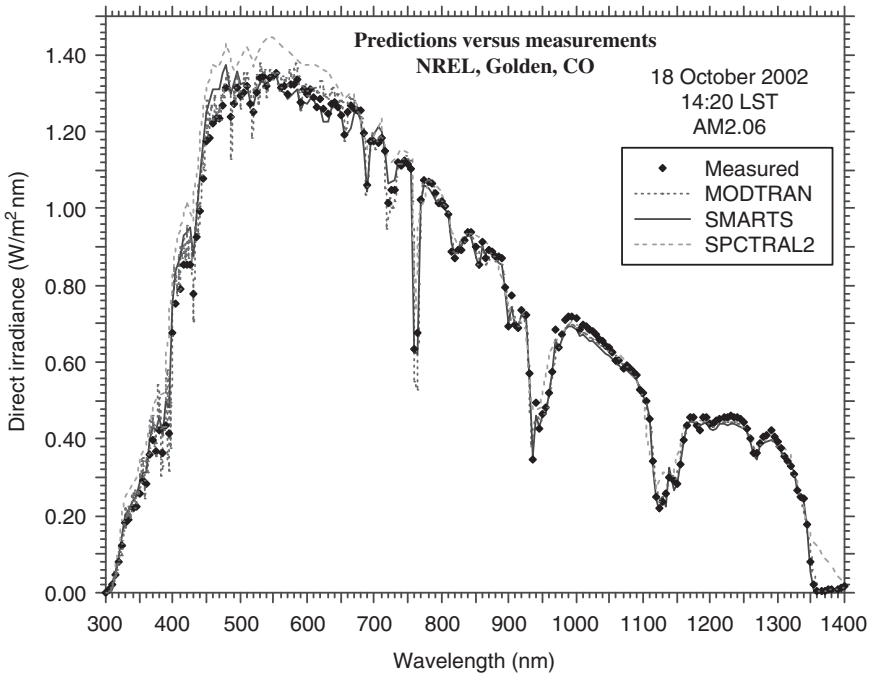

Figure 5.5.1 *Normal-incidence direct-beam solar spectral irradiance at NREL in the 300–1400 nm band, as measured and predicted using three atmospheric radiative codes*

(5 nm) and wavelength step (5 nm) of this spectroradiometer were taken into account by a Gaussian-shaped filter. Furthermore, the circumsolar radiation within a cone of 2.5° around the sun's centre was simulated by SMARTS.

The results of these simulations appear in Figure 5.5.1 for the 300–1400 nm band and in Figure 5.5.2 for the 1350–2450 nm band. Interestingly, the predictions of both MODTRAN and SMARTS appear to be very close to the measured data, with differences normally better than 5%, which is the estimated uncertainty of this instrument over most of the spectrum. This confirms that high-performance instruments and models can be considered as equally valid, with two limitations for the latter: (i) models can only predict with this accuracy under clear and stable conditions and (ii) atmospheric conditions need to be either properly monitored or idealised.

Results from SPCTRAL2 appear less satisfactory, due in part to its limited resolution, particularly in strong absorption bands.

5.6 Applications

Solar spectral models can be used in a variety of applications, as mentioned in Section 5.4. Those applications that are more specifically related to the building environment and solar energy utilisation are discussed in more details in what follows.

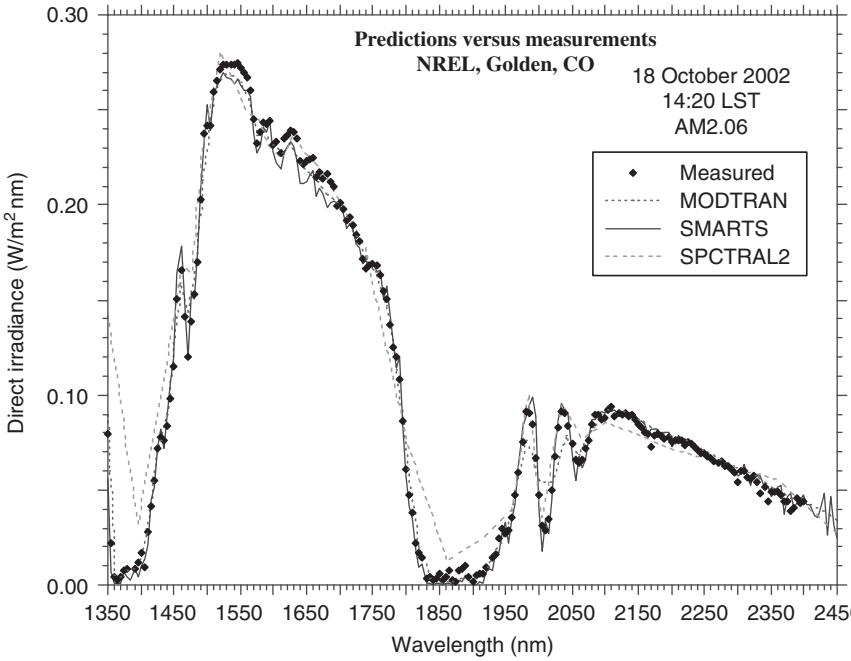

Figure 5.5.2 *Normal-incidence direct-beam solar spectral irradiance at NREL in the 1350–2450 nm band, as measured and predicted using three atmospheric radiative codes*

5.6.1 Reference spectra

Reference spectra are necessary in many disciplines to allow different spectrally-selective systems or devices to be tested or rated against a common benchmark. It is almost an impossible challenge to reconcile the diverging needs of many disciplines and make them use a single reference spectrum, especially when considering the extreme diversity of possible atmospheric or environmental conditions, and of the resulting spectra. In this context, it has been an impressive feat that, since the 1980s, different standardisation bodies agreed on only two reference spectra, one for direct normal irradiance and one for global tilted irradiance (ASTM, 1987a,b; 1998; IEC, 1989; ISO, 1992). The scientific bases, history and limitations of these standards are detailed elsewhere (Gueymard et al., 2002). They have been used extensively in applications such as PV systems performance testing and rating, and as a unique weighting function for the calculation of the spectrally-averaged optical properties of glazings and windows (Rubin et al., 1998; Karlsson, 2001).

In the 20 year interval since the initial publication of these standards, many things have obviously changed, particularly in the fields of PV performance testing and solar radiation modelling. A first essential change has been the realisation by many experimenters that the global reference spectrum (originally, ASTM E892) was relatively satisfying for flat-plate PV systems, but that the direct spectrum (originally, ASTM E891) could not reproduce the real conditions under which concentrating PV systems were deployed in many areas of the world. In other words, the direct spectrum had become obsolete, and this could be traced

back to the fact that this standard was originally designed for sub-optimal turbidity conditions (see Section 5.4.4). A second change was that the original radiative code (BRITE) that had been used to obtain the spectra in these standards had not been maintained and was not available anymore.

A new standard, G173-03 (ASTM, 2003), has been adopted. The main differences with earlier standards are as follows:

(a) The two reference spectra are obtained with the SMARTS code rather than BRITE.
(b) The resolution has been increased and spectral results are now provided at 2002 wavelengths from 280 to 4000 nm, rather than 120 wavelengths between 305 and 4045 nm.
(c) Whereas the old spectra had variable wavelength intervals, which resulted in spectral integration difficulties, the new spectra have three fixed intervals only: 0.5 nm in the UV (280–400 nm), 1 nm in the 400–1700 nm range and 5 nm beyond.
(d) Three important modifications are considered for the atmospheric and environmental conditions: (i) the AOD at 500 nm is decreased from 0.270 to 0.084, affecting the direct spectrum considerably but the global spectrum only marginally; (ii) an increased CO_2 concentration (370 ppm rather than 330 ppm) is used to reflect the current state of the atmosphere (but this has only minor influence on the spectra) and (iii) a more realistic spectral reflectance for a *light sandy soil* is now used (see Figure 5.4.14), along with a non-isotropic reflectance pattern (rather than the simplistic isotropic and fixed 0.2 albedo), affecting global irradiance significantly but not direct irradiance.
(e) The accuracy of the direct irradiance spectrum has been improved by about an order of magnitude, by comparison with benchmark calculations (using version 4 of the MODTRAN code).
(f) The new standard is dynamic rather than static, i.e. experimenters are given the possibility to use SMARTS and perform any number of simulations of their own, e.g. for parametric studies. The main benefit is considerable flexibility in evaluating the effect that non-standard atmospheric or environmental conditions might have on solar irradiance and any spectrally-selective device, while maintaining compatibility and consistency with the standard conditions of G173 for direct comparisons. In the case of PV systems, this opens the possibility to easily evaluate 'spectral mismatch' functions.

The two new reference spectra are shown in Figure 5.6.1. The direct spectrum is now substantially closer to the global spectrum, which is obtained for a sun-facing surface tilted at 37°. However, the direct spectrum is slightly red-shifted compared to the global spectrum (because of the scattering effect induced by molecules and aerosols which is maximum at shorter wavelengths). Therefore, the two spectra are not interchangeable, particularly in the case of highly spectrally-selective devices.

In the building environment, reference spectra might also have other uses. Because of the complexity of the technologies used in the fabrication of current glazings (such as thin film coatings, dyes and electrochromic devices), all optical calculations are now done on a spectral basis for rating and testing purposes. The derivation of the broadband optical properties of these glazings (such as their solar transmittance, visible transmittance or solar

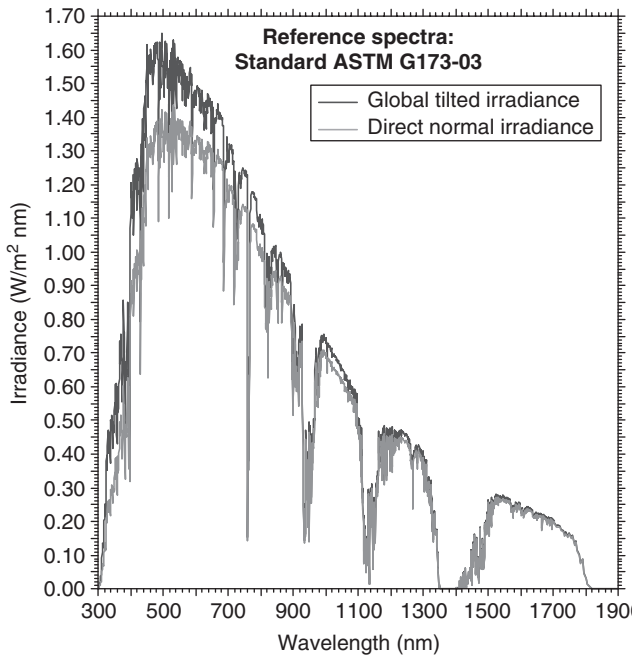

Figure 5.6.1 *Comparison of direct normal irradiance and global irradiance on a 37° tilted sun-facing surface per ASTM G173-03 standard*

heat gain coefficient) is therefore obtained by convolving their spectral properties with an appropriate weighting function. So far, this weighting function has been the global 37° tilted spectrum of the standards mentioned above. This choice might be appropriate for rating purposes (even though one might argue that windows are rarely tilted at 37° on a permanently sun-facing surface), but the instantaneous performance of highly spectrally-selective glazings may be somewhat different from their rated performance (McCluney, 1993; 1996). For instance, Figure 5.6.2 shows different global vertical spectra obtained for the same conditions as in the 'average case' in Figure 5.4.13, except for the ground reflectance. Green grass reflectance data are used here, as plotted in Figure 5.4.14, and three orientations are considered, characterised by relative sun-surface azimuths of 0° (sun facing) $\pm 90°$ and 180°. Figure 5.6.2 illustrates the fact that, under such realistic conditions, very different spectra are obtained, particularly depending on whether or not the sun is illuminating the surface, and on the reflectance characteristics of the environment (note the large increase in irradiance above ≈ 750 nm, caused by the particular spectral behaviour of green grass). Other environmental factors that would complicate the choice of an appropriate spectrum even more are the presence of shading and obstructions to the horizon. The intricate interactions between the solar spectrum and the spectral optical characteristics of windows are discussed in more detail in Section 5.6.4.

5.6.2 Illuminance and luminous efficacy

Chapter 3 presented methods to obtain the luminous efficacy of broadband irradiance and the illuminance for horizontal or tilted surfaces. A drawback of these relatively simple methods is that they are all essentially empirical in nature. In the case of clear skies, the

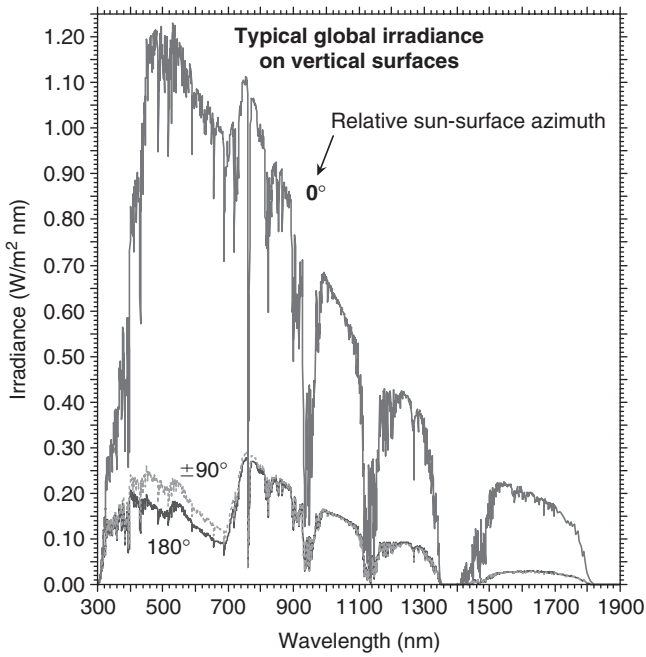

Figure 5.6.2 *Global vertical irradiance for surfaces with azimuths 0°, ±90° and 180° from the sun*

use of a spectral model is more physically sound and can be worth the added complexity. In particular, parametric studies can be conducted to show the effect of various atmospheric variables on either luminous efficacy or illuminance.

The direct, diffuse or global illuminance IL (in lx) is calculated by convoluting the corresponding component of the spectral irradiance I_λ (direct, diffuse or global), with the spectral luminous efficiency function of the human eye or, in short, photopic curve $V(\lambda)$:

$$IL = 683\int_{\lambda_0}^{\lambda_1} V(\lambda) I_\lambda \, d\lambda \tag{5.6.1}$$

where the coefficient 683 lm/W corresponds to the spectral luminous efficacy of radiation at 555 nm (the peak of the photopic curve) in standard air according to a 1977 decision of the International Committee for Weights and Measures (CPIM), and λ_0 and λ_1 are the first and last wavelengths of the photopic curve, respectively. Accordingly, the direct, diffuse or global luminous efficacy K is obtained as the ratio between the illuminance and the corresponding irradiance, i.e:

$$K = IL/I = 683\int_{\lambda_0}^{\lambda_1} V(\lambda) I_\lambda \, d\lambda \Big/ \int_0^\infty I_\lambda \, d\lambda \tag{5.6.2}$$

In practice, the integration limits of the denominator's integral can be 300 and 4000 nm because the energy beyond these limits is negligible in terrestrial applications.

The photopic curve has been standardised by the CIE (http://www.cie.co.at/cie/), but in fact two slightly different spectral data sets exist, the original curve and the modified curve, which have been recommended in 1924 and 1988, respectively (CIE, 1924; 1988; Kaufman, 1984). The original curve of 1924 was later (1931) officially adopted, and is

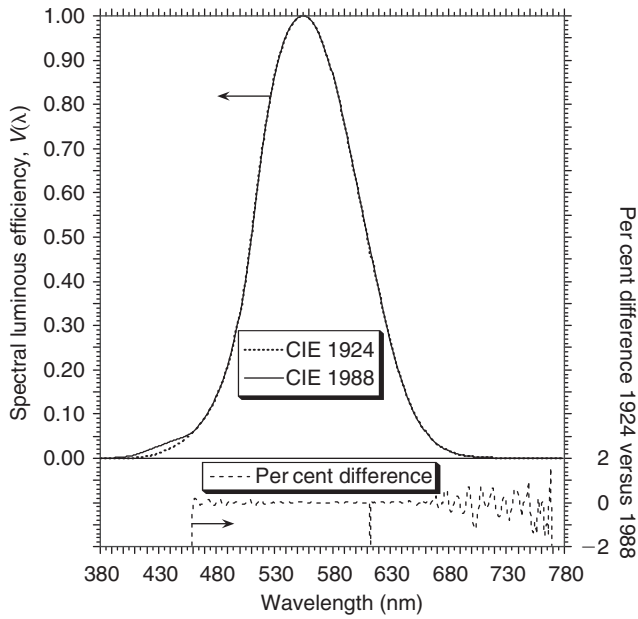

Figure 5.6.3 *CIE's spectral luminous efficiency curves of 1924 and 1988 (top panel) and their per cent relative difference (bottom panel)*

therefore referred to by CIE as the 'standard observer of 1931'. The two curves are shown in Figure 5.6.3. The relative difference between them appears minimal (below $\pm 2\%$) between 460 and 769 nm, but reaches large values beyond these limits. (Note that $\lambda_0 = 380$ nm for the two curves, but that $\lambda_1 = 769$ nm for the 1924 curve and 780 nm for the 1988 curve, respectively.)

To accelerate repetitive calculations that might be needed in practice, the SMARTS code has an option to output the illuminance and luminous efficacy, using one or the other photopic curve (at the user's discretion), in addition to the broadband irradiance that is always calculated. In other words, Eqs (5.6.1) and (5.6.2) are transparent to the user, who can immediately use the results, and, for instance, compare them to those from the empirical models reviewed in Chapters 3 and 4. This is discussed in more detail in Section 5.6.3.

Parametric calculations of illuminance are displayed in Figures 5.6.4–5.6.6. Each figure shows the effect of zenith angle and aerosol turbidity (symbolised by β), the latter being the most important atmospheric variable affecting the direct, diffuse and global horizontal illuminances. All the other variables are ideally fixed in these calculations: Ångström aerosol model ($\alpha = 1.3$), 1.5 cm precipitable water, 0.35 atm-cm O_3, standard pressure, no pollution and a spectrally-constant albedo of 0.2. These variables affect both irradiance and illuminance, but significantly less than turbidity. It should be noted that precipitable water has only a negligible role here because water vapour absorption bands are scarce and weak in the visible. Meanwhile, precipitable water strongly affects irradiance, so that it also affects the luminous efficacy, as demonstrated in Figures 5.6.7 and 5.6.8. (Typical turbidity conditions are then used, $\beta = 0.1$.) As could be expected, turbidity also directly affects luminous efficacy. In particular, the direct efficacy K_B like direct irradiance and direct illuminance is a strong function of turbidity (Figure 5.6.9). The diffuse efficacy K_D is normally larger than the direct efficacy (because diffuse radiation is richer in short/visible

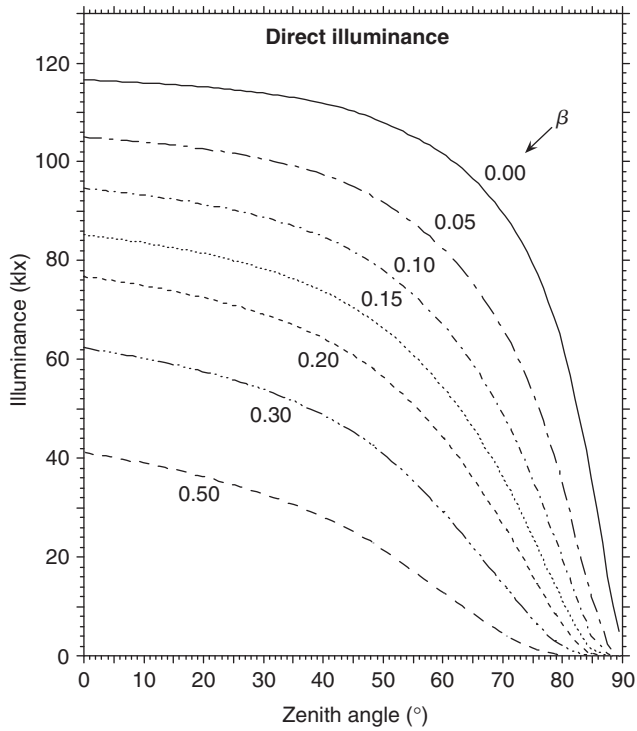

Figure 5.6.4 *Direct illuminance at normal incidence as affected by zenith angle and turbidity* (β) *for otherwise typical conditions*

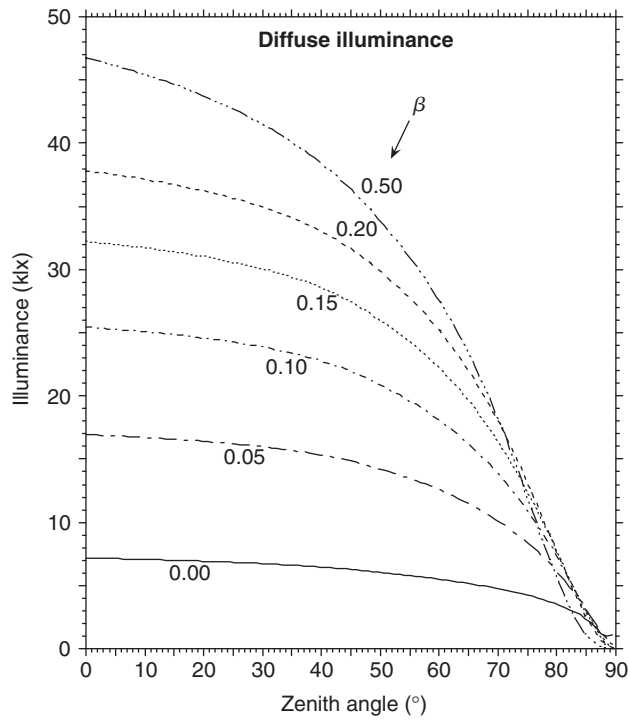

Figure 5.6.5 *Diffuse illuminance on a horizontal surface as affected by zenith angle and turbidity* (β) *for otherwise typical conditions*

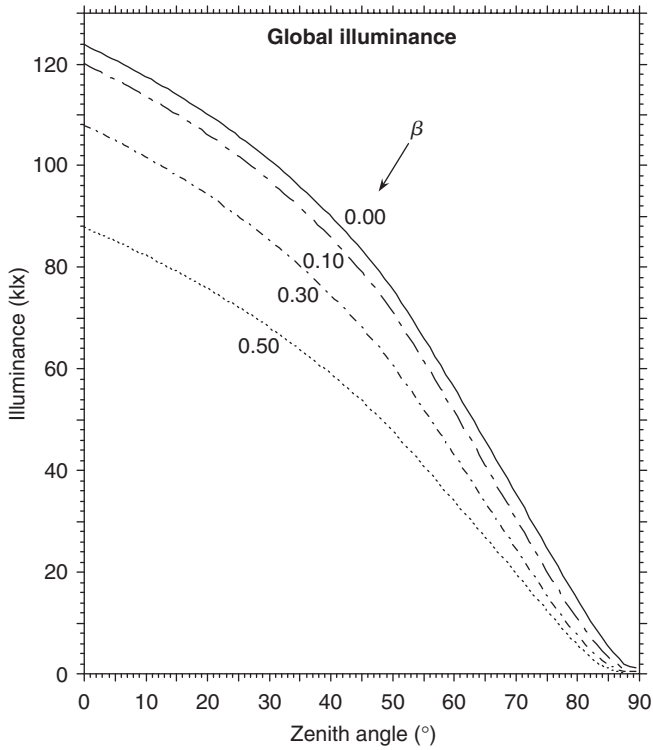

Figure 5.6.6 *Global illuminance on a horizontal surface as affected by zenith angle and turbidity* (β) *for otherwise typical conditions*

wavelengths than direct radiation), and varies with zenith angle in an intricate way (Figure 5.6.10). For Z less than about 40°, K_D normally increases when β increases, which is the opposite as for K_B. At large zenith angles, this behaviour tends to reverse. The net effect of turbidity on the global efficacy is considerably smaller than on K_B (Figures 5.6.11 and 5.6.12). For the typical turbidity conditions considered here ($\beta = 0.1$), the global efficacy is roughly constant at 111.0 lm/W for zenith angles below about 70°. For reference purposes, the direct and diffuse luminous efficacies for the same conditions are 106 and 134 lm/W, respectively. All these values are significantly larger than the efficacy of radiation outside of the atmosphere, calculated to be 98.08 lm/W when using a recent synthetic ETS (Gueymard, 2004) that integrates to 1366.1 W/m^2.

Example 5.6.1

Using SMARTS, evaluate the direct, diffuse and global irradiance, illuminance and luminous efficacy for typical summer (mid-July) cloudless conditions and zenith angles $Z = 30°$ and 60° at Lille (France), Sevilleta (New Mexico, USA), Sherbrooke (Quebec, Canada), Solar Village (Saudi Arabia) and Venice (Italy), which are all AERONET sites. Assume an O_3 amount of 0.35 atm-cm at all sites to simplify calculations.

The first step is to gather the necessary input data from the AERONET web site (http://aeronet.gsfc.nasa.gov). Note that, in some cases, the experimental site is identified by the acronym of the hosting institution rather than by that of the city. This is the case

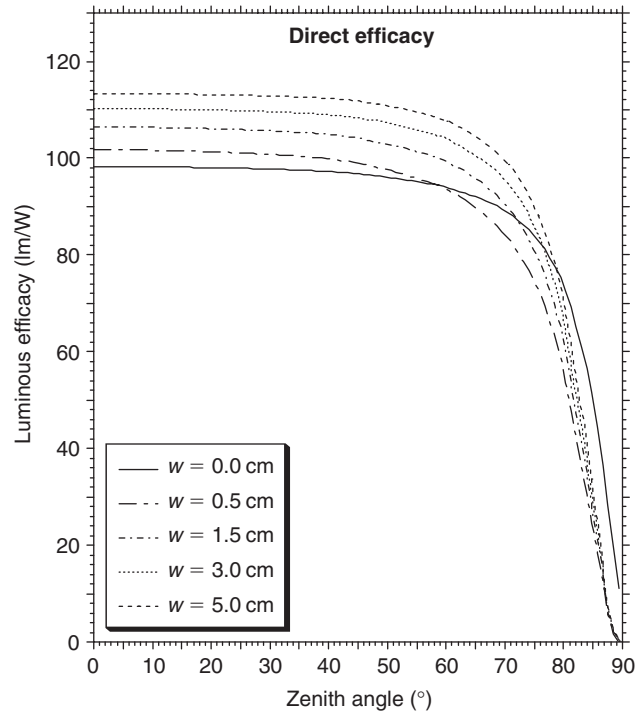

Figure 5.6.7 *Direct luminous efficacy as affected by zenith angle and precipitable water for otherwise typical conditions (in particular,* $\beta = 0.1$*)*

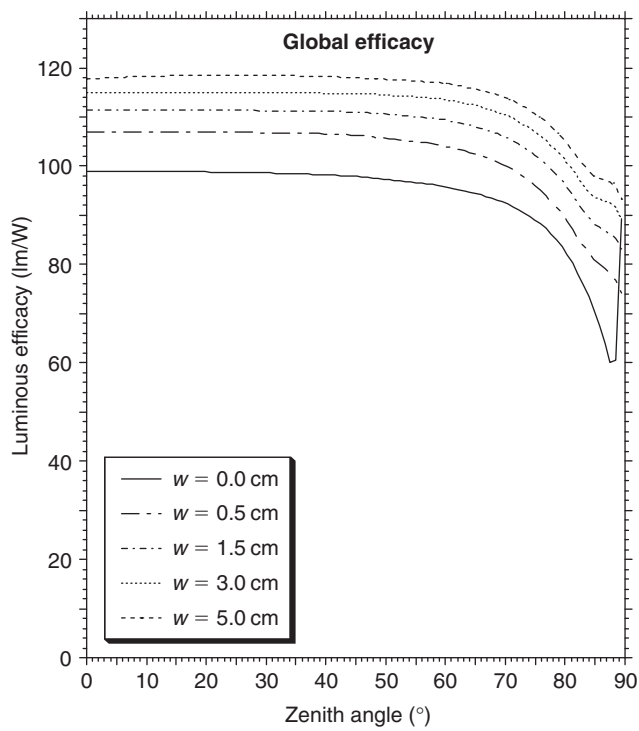

Figure 5.6.8 *Global luminous efficacy as affected by zenith angle and precipitable water for otherwise typical conditions (in particular,* $\beta = 0.1$*)*

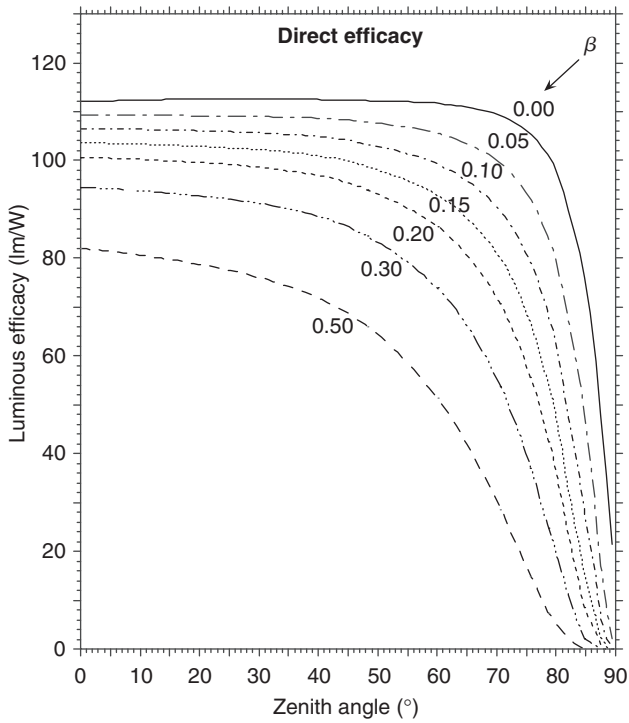

Figure 5.6.9 *Direct luminous efficacy as affected by zenith angle and turbidity (β) for otherwise typical conditions*

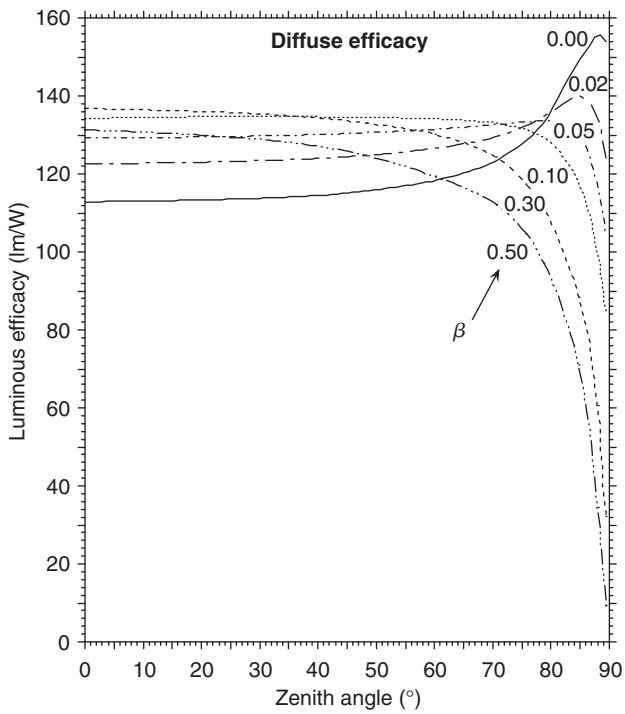

Figure 5.6.10 *Diffuse luminous efficacy as affected by zenith angle and turbidity (β) for otherwise typical conditions*

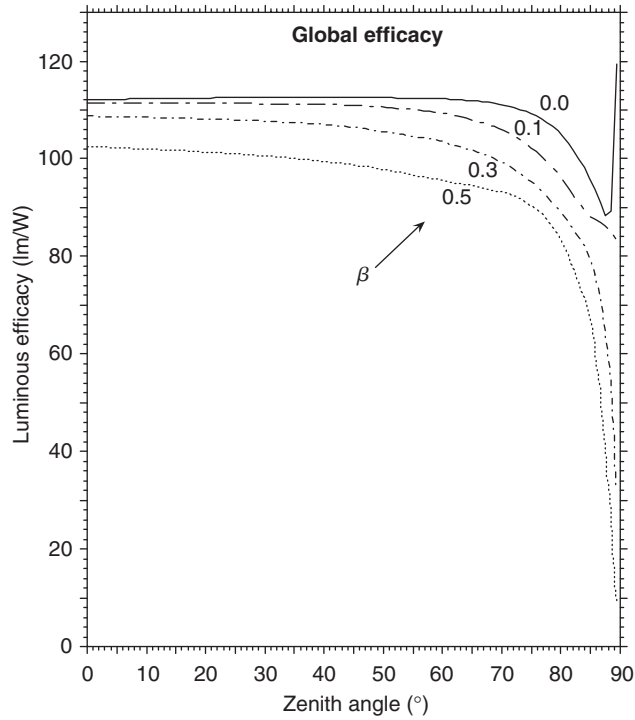

Figure 5.6.11
Global luminous efficacy as affected by zenith angle and turbidity (β) for otherwise typical conditions

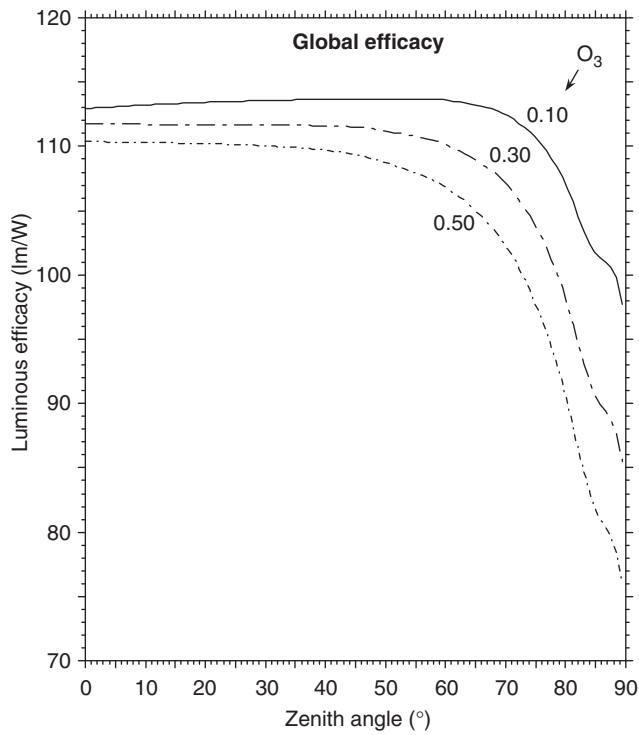

Figure 5.6.12
Global luminous efficacy as affected by zenith angle and the vertical O_3 column for otherwise typical conditions (in particular, $\beta = 0.1$)

for Sherbrooke, which appears under the acronym of CARTEL (a research centre at the University of Sherbrooke). Because typical results are needed, rather than specific results for a particular day, data from the 'AERONET climatology' summary tables will be used for July at all sites, i.e. monthly-average data calculated over the period of measurement. This climatology is slowly changing over time, so that the current values may be slightly different from those reported here, as of July 2003. The following table summarises the data gathered this way.

Geographic name	AERONET name	Latitude	Longitude*	Elevation (m)	$\tau_{a0.5}$	α	w, raw (cm)	w, adjusted (cm)	β
Lille	Lille	50.60	3.13	60	0.37	1.54	2.49	2.24	0.127
Sevilleta	Sevilleta	34.35	−106.88	1477	0.12	1.41	2.26	2.03	0.045
Sherbrooke	CARTEL	45.37	−71.92	300	0.28	1.34	2.38	2.14	0.111
Solar Village	Solar_Village	24.90	46.40	650	0.38	0.59	1.54	1.39	0.252
Venice	Venise	45.30	12.50	10	0.33	1.69	3.24	2.92	0.102

* Negative numbers indicate west longitudes.

The last two columns display results of additional calculations. The adjusted precipitable water is obtained by reducing the raw AERONET values by 10% (Gueymard, 2003c), and β is obtained from the measured $\tau_{a0.5}$ and α by applying Eq. (5.4.11), i.e. $\beta = \tau_{a0.5} 0.5^{\alpha}$. These values of β are indicated here for comparative purposes only because SMARTS also accepts $\tau_{a0.5}$ as an alternative input.

When using the values above as inputs for SMARTS, the following results are readily obtained for $Z = 30°$ and 60°. (It is assumed that $\alpha_1 = \alpha_2 = \alpha, \omega_{0\lambda} = 0.88$, along with a fixed albedo value of 0.2).

Geographic name	Direct normal irradiance (W/m^2)	Diffuse horizontal irradiance (W/m^2)	Global horizontal irradiance (W/m^2)	Direct normal illuminance (klx)	Diffuse horizontal illuminance (klx)	Global horizontal illuminance (klx)	Direct luminous efficacy (lm/W)	Diffuse luminous efficacy (lm/W)	Global luminous efficacy (lm/W)
$Z = 30°$									
Lille	764.8	218.7	881.0	79.2	30.6	99.2	103.6	139.7	112.6
Sevilleta	933.4	117.2	925.5	103.1	15.3	104.5	110.4	130.2	112.9
Sherbrooke	811.7	193.3	896.2	86.4	26.3	101.1	106.4	136.1	112.8
Solar Village	725.6	267.5	895.9	76.2	32.7	98.7	105.1	122.0	110.1
Venice	778.2	200.3	874.2	82.6	28.4	100.0	106.2	141.7	114.3
$Z = 60°$									
Lille	577.0	160.5	449.0	54.2	22.4	49.5	93.9	139.7	110.3
Sevilleta	789.9	91.7	486.6	85.2	12.1	54.7	107.8	131.8	112.3
Sherbrooke	630.8	144.8	460.2	62.8	19.7	51.1	99.6	135.8	111.0
Solar Village	510.5	199.6	454.9	50.6	23.9	49.1	99.1	119.5	108.0
Venice	597.8	147.2	446.1	58.3	21	50.1	97.5	142.7	112.4

Example 5.6.2

For the same five sites and the same typical July conditions as in Example 5.6.1, evaluate the daily-average direct horizontal and global vertical irradiation and illuminance. Consider vertical surfaces facing either north or south and a ground covered with green grass.

Such calculations can be performed easily (without extra manual integration) using the daily-integration capabilities of SMARTS and its own algorithm to obtain radiation on tilted surfaces. Using the same input data as above and an integration time step of 10 min, the following results are readily obtained.

Geographic name	Direct horizontal irradiation (MJ/m^2)	North global vertical irradiation (MJ/m^2)	South global vertical irradiation (MJ/m^2)	Direct horizontal illuminance (klx)	North global vertical illuminance (klx)	South global vertical illuminance (klx)
Lille	19.2	10.0	22.9	49.5	16.6	46.6
Sevilleta	26.1	8.6	10.3	79.0	14.6	19.7
Sherbrooke	21.3	9.6	18.8	58.3	16.5	39.6
Solar Village	19.3	13.8	11.1	53.3	27.8	21.7
Venice	20.4	9.6	19.0	54.8	17.0	40.8

The two examples above illustrate the considerable impact that geographic location and atmospheric conditions (particularly turbidity) have on irradiance and illuminance. Furthermore, it can be observed that, for the low-latitude location of Solar Village in July, the global irradiation and illuminance on a vertical surface is significantly larger when the latter is oriented north than south. This can be explained by the fact that around noon in summer the sun is nearly vertical so that the angle of incidence on a sun-facing vertical surface is large, thus decreasing the impact of direct radiation. Conversely, the angle of incidence on surfaces facing away from the sun is relatively more favourable.

Further material on this topic is provided in Chapter 3.

5.6.3 Clear-sky luminous efficacy calculations in practice

The previous section offered a computerised spectral method to physically obtain the illuminance and luminous efficacy under clear-sky conditions, using only atmospheric variables as inputs. As demonstrated in Chapters 3 and 4, the luminous efficacy under clear or cloudy conditions can also be empirically obtained from broadband global irradiance inputs only (e.g. Muneer's model, Eqs (3.5.20) and (3.5.21)), or from direct and diffuse irradiance supplemented by precipitable water in the case of the more sophisticated Perez et al. model (Eq. (3.5.12)). The widely different *spectral* and *broadband* methodologies partly overlap and their predictions can thus be compared in the important case of clear-sky conditions. A typical procedure to obtain parametric comparisons comprises two steps. The first step consists in using the SMARTS code to predict both the irradiance components and their associated luminous efficacy for fixed atmospheric conditions. In the second step, these predicted irradiances are input to the broadband illuminance or luminous efficacy model under scrutiny.

As indicated in the previous section, the most important atmospheric variable affecting direct and diffuse irradiance, illuminance and luminous efficacy is turbidity. The same parametric data set that was presented in Figures 5.6.9 and 5.6.10 is shown again in Figures 5.6.13 and 5.6.14, but this time as a function of air mass. Using the same basic data, the direct and diffuse irradiance, as well as the sky clearness and sky brightness indices used in the Perez et al. model can be calculated and Eq. (3.5.12) solved for the

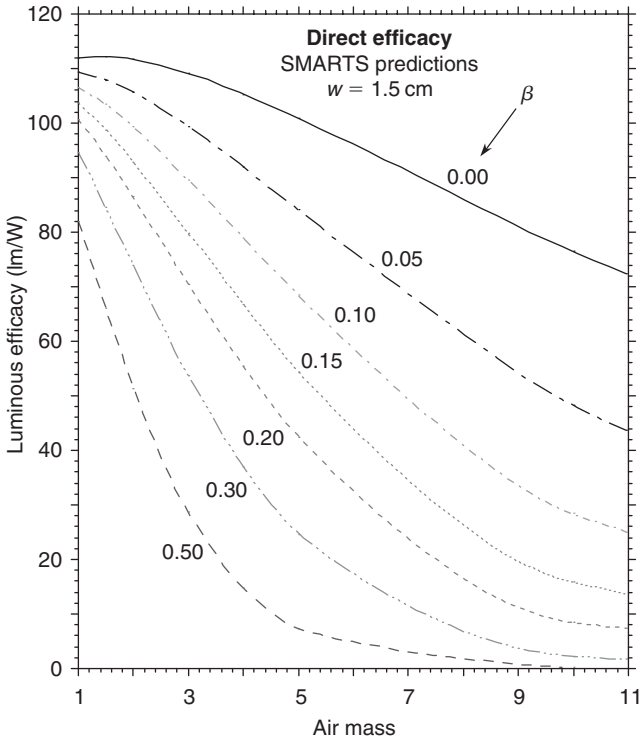

Figure 5.6.13 *Variation of direct luminous efficacy with* m *and* β*, as predicted by SMARTS*

direct and diffuse luminous efficacy, whose values are plotted in Figures 5.6.15 and 5.6.16, respectively. By comparison with the SMARTS predictions of direct efficacy, those from the Perez et al. model look considerably compressed. When turbidity increases and β reaches about 0.2, the efficacy calculated with the Perez et al. model stops its decreasing trend and rather starts to increase. This can be explained by the behaviour of the sky clearness index: it interprets very turbid conditions as cloudy conditions, and the luminous efficacy of the latter is different than that of the former. Moreover, turbid conditions are generally under-represented in the data sets used to derive empirical models of luminous efficacy. Hence the Perez et al. model and others of the same kind are probably not very accurate in tropical or polluted locations where β is frequently greater than 0.2.

For the diffuse efficacy (compare Figures 5.6.14 and 5.6.16), the smooth transition between the increasing effect of m on efficacy for $\beta < 0.05$ and the steeply decreasing efficacy with increasing m for higher turbidities is absent from the predictions with the Perez et al. model, which also does not generate smooth variations with air mass.

It is therefore recommended that, whenever the atmospheric data are available and clear-sky conditions only are envisioned, a physical spectral model be used rather than an empirical broadband model.

Example 5.6.3

Using SMARTS, calculate the direct normal and diffuse horizontal irradiances, and the corresponding luminous efficacies for the five sets of atmospheric conditions in Table 5.6.1.

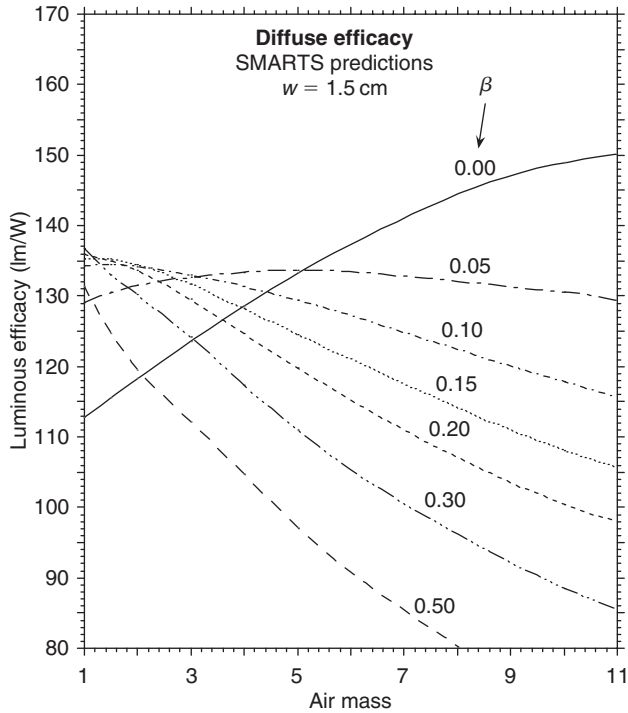

Figure 5.6.14
Variation of diffuse luminous efficacy with m *and* β*, as predicted by SMARTS*

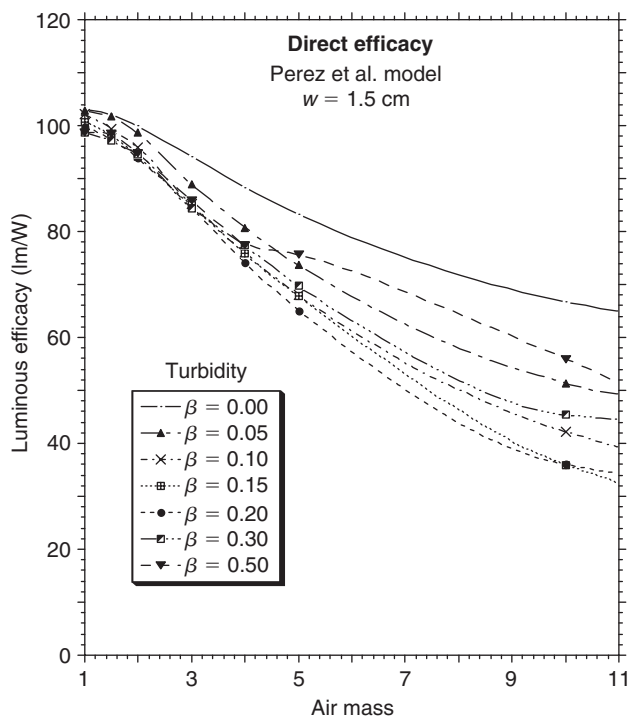

Figure 5.6.15
Variation of direct luminous efficacy with m *and* β*, obtained from the broadband Perez et al. model*

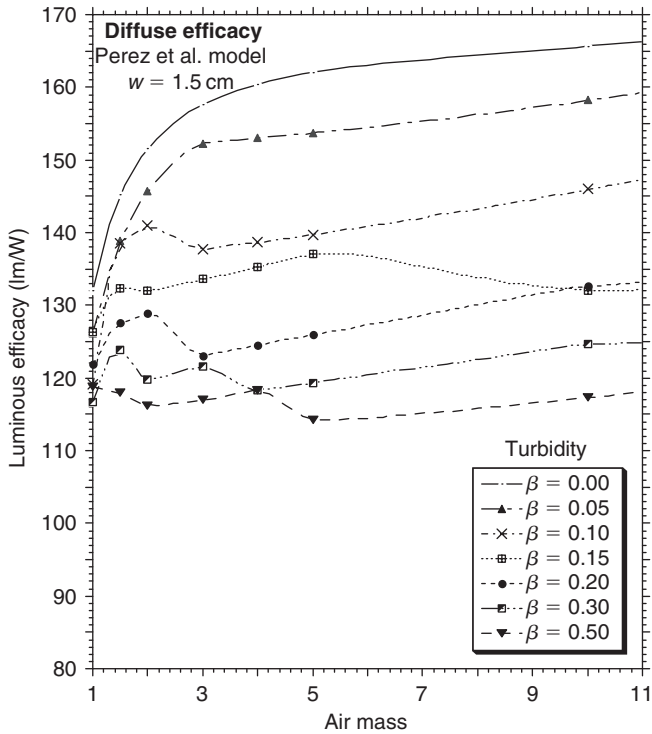

Figure 5.6.16 *Variation of diffuse luminous efficacy with* m *and* β*, obtained from the broadband Perez et al. model*

Table 5.6.1 Variable atmospheric conditions

Case	w (cm)	β	α	p (h Pa)
1	0.5	0.1	1.3	1013.3
2	1.5	0.1	0.5	1013.3
3	1.5	0.1	1.3	795.0
4	1.5	0.3	1.3	1013.3
5	5.0	0.1	1.3	1013.3

Use these values of irradiance and the models of Muneer and Perez et al. described in Chapter 3 to evaluate their luminous efficacies. Use fixed values of 0.35 atm-cm for O_3, 0.2 for the ground albedo, a standard atmosphere with no pollution effect, an extraterrestrial irradiance of 1366.1 W/m^2 at the average sun–earth distance and two air-mass values, 1.5 ($Z = 48.236°$) and 5.0 ($Z = 78.733°$).

For each of these cases, the irradiances and efficacies are readily obtained by SMARTS and are shown in Table 5.6.2. The input to Muneer's model (K_T) is calculated by dividing the calculated global irradiances by 1366.1 W/m^2. The inputs to the Perez et al. model (ε and Δ) are calculated per Eqs (3.5.13) and (3.5.14). All results appear in Table 5.6.2. The Muneer model provides K_D and K_G as a quadratic functions of K_T. To obtain K_B, some manipulation of the basic equations is necessary. It can be shown that:

$$K_B = \left[K_G - K_D\left(I_D/I_G\right)\right] \Big/ \left[1 - \left(I_D/I_G\right)\right] \tag{5.6.3}$$

Table 5.6.2 Irradiance and luminous efficacies calculated by different models

Source	SMARTS						Muneer		Perez et al.			
Case	$I_{B,n}$	I_D	I_G	K_B	K_D	K_T	K_B	K_D	ε	Δ	K_B	K_D
$m = 1.5$												
1	812.5	161.7	702.8	98.2	132.0	0.7724	108.4	129.3	4.100	0.1775	100.6	134.1
2	818.5	134.4	679.6	109.3	121.2	0.7469	109.1	128.3	4.756	0.1475	100.8	136.1
3	792.7	155.1	683.1	103.6	133.4	0.7507	108.4	128.5	4.153	0.1702	99.5	139.1
4	504.5	264.9	600.9	84.5	133.1	0.6604	101.9	125.7	2.175	0.2908	97.1	123.8
5	709.2	153.0	625.4	111.2	138.1	0.6873	107.9	126.4	3.859	0.1679	95.2	152.9
$m = 5.0$												
1	385.2	66.8	142.1	62.1	124.4	0.5323	104.3	123.2	2.558	0.2445	71.9	132.7
2	389.9	61.2	137.4	89.9	118.6	0.5148	105.8	122.9	2.721	0.2241	68.0	140.7
3	368.0	64.8	136.7	71.5	127.9	0.5122	104.9	122.9	2.534	0.2372	68.0	139.3
4	121.3	77.8	101.5	24.7	110.9	0.3803	97.7	122.3	1.421	0.2848	69.7	119.3
5	300.1	59.6	118.2	77.2	135.8	0.4428	107.2	122.4	2.362	0.4428	54.2	162.1

As could be expected from the discussion above in this section, the results in Table 5.6.2 demonstrate that large differences exist between a model's predictions and the other, especially for a low sun (or high air mass).

5.6.4 Spectral irradiance transmitted by windows

In the building environment, one of the most important applications of solar radiation calculations obviously is to predict the energy transmitted by windows, depending on their orientation and optical characteristics, on the position of the sun and on the atmospheric conditions. For decades, these calculations could be easily done using measured or modelled data of *broadband* irradiance because the spectral transmittance of ordinary clear glass (still in use in most dwellings) was essentially constant with wavelength. This methodology is described in many textbooks (e.g. Threlkeld, 1970; Duffie and Beckman, 1980; Siegel and Howell, 1981). However, recent technological advances, particularly in the domains of coatings, thin films and electrochromic devices, have in turn pushed the development of glazings considerably more sophisticated than clear glass. Most windows now specified for new commercial buildings result from the assemblage of one or more *spectrally-selective* panes, often designed to maximise (or control) light transmission and minimise solar heat gains, heat transfer and, ultimately, heating and cooling loads.

Because of the intricacies involved in calculating the optical characteristics of such sophisticated fenestration systems, the most recent calculation methods involve rigorous spectral calculations (Rubin et al., 1998). In practice, building engineers need to perform repetitive calculations before they can actually select the most appropriate fenestration system for their projects. These calculations not only involve the solar and visible transmittance properties of glazings, but also their thermal properties. To perform such calculations on a routine basis, software programs have been developed by different institutions, such as Lawrence Berkeley Laboratory's Windows and Daylighting group. Modern user-friendly computer programs such as OPTICS and WINDOW[2] are recommended.

[2]Available from http://windows.lbl.gov/Default.htm.

Even though this kind of sophisticated software performs spectral calculations, only a single standard spectrum is used to evaluate broadband optical properties, as a weighted average of their spectral properties. For example, the average solar transmittance at normal incidence T_S is obtained as:

$$T_S = \int_{\lambda_0}^{\lambda_1} T_\lambda I_\lambda \, d\lambda / \int_{\lambda_0}^{\lambda_1} I_\lambda \, d\lambda \tag{5.6.4}$$

where T_λ is the window's spectral transmittance and I_λ is the incident spectral irradiance at wavelength λ. The default I_λ is the standard global irradiance spectrum on a 37° tilted surface facing the sun. In practice, the integration can be performed between $\lambda_0 = 0.3\,\mu m$ and $\lambda_1 = 3\,\mu m$ because both glass transmittance and incident radiation are negligible beyond these limits.

These calculations are helpful to compare the performance of various windows under common standard conditions, but not to evaluate the effect of changing atmospheric conditions on their overall properties. To illustrate the latter effect, which can be important when considering modern spectrally-selective glazings, four different simplified window arrangements – made of a single pane only – are considered. The necessary transmittance data (T_λ) is available in the spectral database of hundreds of commercial basic glass panes and coatings that is used by the OPTICS and WINDOW software programs. The code names of the spectrally-selective glazings selected here for demonstration purposes are C155.AFG, VA235.VIR and VE785.VIR. Additionally, a conventional glass pane (3 mm clear float glass) is also selected for reference. Three different spectra are considered. Two of them are shown in Figure 5.6.2 (global vertical irradiance for surfaces whose azimuths are 0° and 180° from the sun). The third one is the standard irradiance spectrum for global radiation on a 37° tilted surface facing the sun in Figure 5.6.1 as per ASTM G173-03. Results clearly show that the distribution of energy throughout the visible spectrum varies greatly from one window to the other, and from one incident spectrum to the other. This induces a potential *visual comfort* issue: chromatic differences and colour rendition may or may not please the eye, and may or may not be appropriate for some type of activity within the building. Such an issue is best addressed by a lighting expert. The building engineer is more concerned with the calculation of cooling loads, which are directly a function of solar heat gains and therefore of the solar transmittance of the fenestration system. (Heating loads are calculated without solar gains.)

Assuming that the reference solar transmittance of each window is obtained with the global standard spectrum in Figure 5.6.1, it is possible to calculate the resulting 'reference' T_S by application of Eq. (5.6.4), as well as the per cent differences that result from rather using the two alternate global vertical spectra. The results of this exercise are graphically displayed in Figure 5.6.17. They show a gradual increase in the deviation from the reference solar transmittance with increasing spectral selectivity of the window. The deviation is also significantly greater for windows facing away from the sun. In this case, the maximum deviation reaches −21% for VE785.VIR. This deviation could be even larger if highly spectrally-selective fenestration systems (with two or three panes of different optical characteristics) were considered. More detailed discussions on the spectral effect on sophisticated multi-pane spectrally-selective glazings are presented elsewhere (McCluney, 1993; 1996).

Whereas clear float glass is almost insensitive to spectral effects, the latter's magnitude cannot be neglected with most other glazings. These spectral effects are a complex function of the sun's position relative to the window, of the atmospheric conditions, and of the

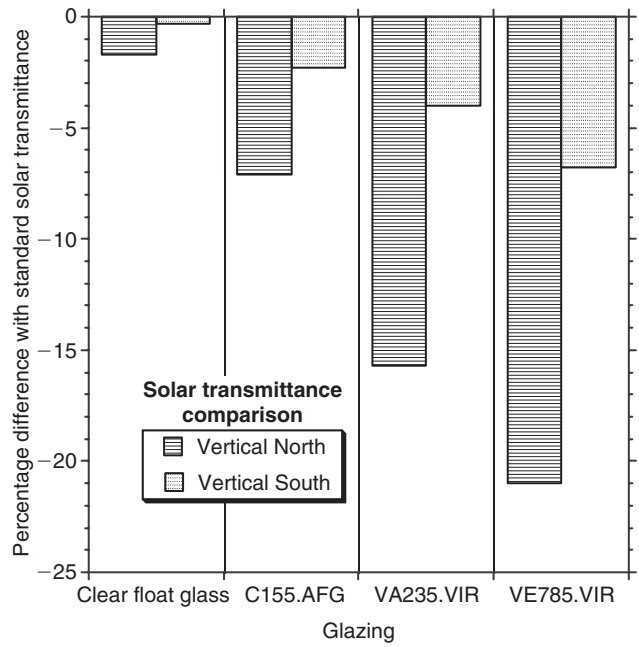

Figure 5.6.17 *Per cent difference in overall solar transmittance depending on the glazing's spectral selectivity and incident spectrum*

building environment (e.g. ground albedo and shading). Because of the complexity of these interactions and of the lack of spectral radiation model allowing the simulation of real-world cloudy conditions, it is still not possible to study how the spectral selectivity of windows affect their solar or light transmittance on a seasonal or yearly basis. When these necessary simulation tools become finally available, it will be possible to refine the existing simplified analyses of building energy consumption as a function of window size, orientation and climatic conditions (Gueymard and McCluney, 1992; Crooks et al., 1995; Gueymard, 1995a; Holte, 1995).

References

Adamopoulos, A.D., Kambezidis, H.D., Zevgolis, D., Topalis, F.B. and Djepa, V. (1999) Aerosol optical thickness through modified Langley-plots in the atmosphere of Athens, Greece. *Proc. EuroSun98*, vol 1, eds A. Goetzberger and A. Krainer Portoroz, Slovenia, pp. 1–7.

Adamopoulos, A.D., Kambezidis, H.D., Zevgolis, D. and Topalis, F.B. (2000) Estimation of total ozone column over Athens using ground-based beam solar irradiance measurements. *Fres. Environ. Bull.* 9, 201–8.

Anderson, G.P., Clough, S.A., Kneizys, F.X., Chetwynd, J.H. and Shettle, E.P. (1986) *AFGL Atmospheric Constituent Profiles (0–120 km).* Rep. AFGL-TR-86-0110, Air Force Geophysics Laboratory, Hanscom AFB, MA.

Anderson, S.M., Hupalo, P. and Mauersberger, K. (1993) Ozone absorption cross section measurements in the Wulf bands. *Geophys. Res. Lett.* 20, 1579–82.

Ångström, A. (1929) On the atmospheric transmission of sun radiation and on dust in the air. *Geografis. Annal.* 2, 156–66.

Ångström, A. (1930) On the atmospheric transmission of sun radiation. *Geografis. Annal.* 2 and 3, 130–59.

Anon (1976) *US Standard Atmosphere.* NOAA/NASA/USAF, US Government Printing Office, Washington, DC. Online version at http://nssdc.gsfc.nasa.gov/space/model/atmos/us_standard.html.

ASME (1985) *Supplement on Instruments and Apparatus. Part 1: Measurement Uncertainty.* PTC 19.1, American Society of Mechanical Engineers.

ASTM (1987a) *Standard Tables for Terrestrial Direct Normal Solar Spectral Irradiance for Air Mass 1.5.* Standard No. E891-87, American Society for Testing and Materials, Philadelphia, PA.

ASTM (1987b) *Standard Tables for Terrestrial Solar Spectral Irradiance at Air Mass 1.5 for a 37° tilted surface.* Standard No. E892-87, American Society for Testing and Materials, Philadelphia, PA.

ASTM (1998) *Standard Tables for Reference Solar Spectral Irradiance at Air Mass 1.5: Direct Normal and Hemispherical for a 37° Tilted Surface.* Standard G159-98, American Society for Testing and Materials, West Conshohocken, PA.

ASTM (2000) *Standard Solar Constant and Zero Air Mass Solar Spectral Irradiance Tables.* Standard E490-00. American Society for Testing and Materials, West Conshohocken, PA.

ASTM (2003) *Standard Tables for Reference Solar Spectral Irradiances: Direct Normal and Hemispherical on 37° Tilted Surface.* Standard G173-03, American Society for Testing and Materials http://www.astm.org.

Barry, S.A. (1978) *Errors in Practical Measurements in Science, Engineering and Technology.* John Wiley & Sons, Inc., New York.

Berk, A. et al. (1999) MODTRAN4 radiative transfer modeling for atmospheric correction. *Proc. Optical Spectroscopic Techniques and Instrumentation for Atmospheric and Space Research III, SPIE*, vol 3756, Society of Photo-optical Instrumentation Engineers.

Bird, R.E. (1984) A simple, solar spectral model for direct-normal and diffuse horizontal irradiance. *Solar Energy* 32, 461–71.

Bird, R.E. and Riordan, C. (1986) Simple solar spectral model for direct and diffuse irradiance on horizontal and tilted planes at the Earth's surface for cloudless atmospheres. *J. Clim. Appl. Met.* 25, 87–97.

Bird, R.E., Riordan, C.J. and Myers, D.R. (1987) *Investigation of a Cloud-Cover Modification to SPCTRAL2, SERI's Simple Model for Cloudless-Sky, Spectral Solar Irradiance.* Rep. SERI/TR-215-3038, Solar Energy Research Institute (now NREL), Golden, CO.

Bogumil, K., Orphal, J. and Burrows, J.P. (2000) Temperature dependent absorption cross sections of O_3, NO_2, and other atmospheric trace gases measured with the SIAMACHY spectrometer. *Proc. ERS-ENVISAT Symposium*, Gothenburg 2000, ESA-ESTEC, Noordwijk.

Bogumil, K. et al. (2003) Measurements of molecular absorption spectra with the SIAMACHY pre-flight model: instrument characterization and reference data for atmospheric remote-sensing in the 230–2380 nm region. *J. Photochem. Photobiol.* 157A, 167–84.

Bruegge, C.J. et al. (1992) Water vapor column abundance during FIFE. *J. Geophys. Res.* 97, 18759–68.

Burkholder, J.B. and Talukdar, R.K. (1994) Temperature dependence of the ozone absorption spectrum over the wavelength range 410 to 760 nm. *Geophys. Res. Lett.* 21, 581–4.

Burrows, J.P. et al. (1999) Atmospheric remote-sensing reference data from GOME: 2. Temperature-dependent absorption cross sections of O_3 in the 231–794 nm range. *J. Quant. Spectros. Radiat. Transf.* 61, 509–17.

CIE (1924) *Proceedings.* Cambridge University Press.

CIE (1988) *Spectral Luminous Efficiency Functions Based upon Brightness Matching for Monochromatic Point Sources 2° and 10° Fields.* Publ. CIE 75-1988, Commission Internationale de l'Eclairage.

CIE (1994) *Guide to Recommended Practice of Daylight Measurement.* CIE Publication No. 108, Commission Internationale de l' Eclairage.

Crooks, B., Larsen, J., Sullivan, R., Arasteh, D. and Selkowitz, S. (1995) Progress in the development of NFRC's residential fenestration annual energy rating methodology. *Proc. Window Innovations Conf. '95*, Toronto, Canada, pp. 202–17.

Daumont, D., Brion, J., Charbonnier, J. and Malicet, J. (1992) Ozone UV spectroscopy. I. Absorption cross-sections at room temperature. *J. Atmos. Chem.* 15, 145–55.

Duffie, J.A. and Beckman, W.A. (1980) *Solar Engineering of Thermal Processes.* John Wiley, New York.

Eck, T.F. et al. (1999) Wavelength dependence of the optical depth of biomass burning, urban, and desert dust aerosols. *J. Geophys. Res.* 104D, 31333–49.

Forgan, B.W. (1994) General method for calibrating sun photometers. *Appl. Opt.* 33, 4841–50.

Freund, J. (1983) Aerosol optical depth in the Canadian Arctic. *Atmos. Ocean* 21, 158–67.

Fröhlich, C. (2004) Solar irradiance variability, in: *Solar Variability and Its Effect on Climate*, ed. J.M. Pap et al., Geophysical Monograph 141, American Geophysical Union.

Grenier, J.C., de la Casinière, A. and Cabot, T. (1994) A spectral model of Linke's turbidity factor and its experimental implications. *Solar Energy* 52, 303–14.

Gueymard, C. (1993a) Critical analysis and performance assessment of clear sky solar irradiance models using theoretical and measured data. *Solar Energy* 51, 121–38.

Gueymard, C. (1993b) Mathematically integrable parameterization of clear-sky beam and global irradiances and its use in daily irradiation applications. *Solar Energy* 50, 385–97. *Erratum*: 51, 525.

Gueymard, C. (1994) Analysis of monthly average atmospheric precipitable water and turbidity in Canada and Northern United States. *Solar Energy* 53, 57–71.

Gueymard, C. (1995a) Annual energy performance of residential advanced windows related to climate, window area, and orientation. *Proc. Window Innovations '95*, Toronto, Canada.

Gueymard, C. (1995b) *SMARTS2, Simple Model of the Atmospheric Radiative Transfer of Sunshine: Algorithms and Performance Assessment.* Rep. FSEC-PF-270–95, Florida Solar Energy Center, Cocoa, FL.

Gueymard, C. (1998) Turbidity determination from broadband irradiance measurements: a detailed multicoefficient approach. *J. Appl. Met.* 37, 414–35.

Gueymard, C. (2001) Parameterized transmittance model for direct beam and circumsolar spectral irradiance. *Solar Energy* 71, 325–46.

Gueymard, C. (2003a) *SMARTS Code, Version 2.9.2 User's Manual*. Solar Consulting Services.

Gueymard, C.A. (2003b) Direct solar transmittance and irradiance predictions with broadband models. Part 1: detailed theoretical performance assessment. *Solar Energy* 74, 355–79.

Gueymard, C.A. (2003c) Direct solar transmittance and irradiance predictions with broadband models. Part 2: validation with high-quality measurements. *Solar Energy* 74, 381–95.

Gueymard, C.A. (2003d) Interdisciplinary applications of a versatile spectral solar irradiance model: a review. *Proc. International Expert Conf. on Measurement and Modeling of Solar Radiation*, Edinburgh, Scotland. To be published in *Energy*.

Gueymard, C.A. (2004) The sun's total and spectral irradiance for solar energy applications and solar radiation models. *Solar Energy* 76, 423–453.

Gueymard, C. and Kambezidis, H.D. (1997) Illuminance turbidity parameters and atmospheric extinction in the visible spectrum. *Q. J. Roy. Met. Soc.* 123, 679–97.

Gueymard, C. and McCluney, R. (1992) An analysis of the energy performance of typical office buildings in Florida using daylighting. *Proc. 17th National Passive Solar Conf*, eds S. Burley and M.E. Arden Cocoa Beach, FL, American Solar Energy Society, pp. 126–31.

Gueymard, C., Myers, D. and Emery, K. (2002) Proposed reference irradiance spectra for solar energy systems testing. *Solar Energy* 73, 443–67.

Harrison, L., Michalsky, J. and Berndt, J. (1994) Automated multifilter rotating shadowband radiometer: an instrument for optical depth and radiation measurements. *Appl. Opt.* 33, 5118–25.

Hay, J.E. and Darby, R. (1984) El Chichon – influence on aerosol optical depth and direct, diffuse and total solar irradiances at Vancouver, B.C. *Atmos. Ocean* 22, 354–68.

Holte, D.E. (1995) A parametric study of the impact of high performance windows (and curtain walls) on building heating and cooling loads, energy use and HVAC system design. *Proc. Window Innovations Conf. '95*, Toronto, Canada, pp. 500–8.

Hoyt, D.V. and Schatten, K.H. (1997) *The Role of the Sun in Climate Change.* Oxford University Press, New York.

Husar, R.B., Husar, J.D. and Martin, L. (2000) Distribution of continental surface aerosol extinction based on visual range data. *Atmos. Environ.* 34, 5067–78.

IEC (1989) *Photovoltaic Devices: Part 3. Measurement Principles for Terrestrial Photovoltaic (PV) Solar Devices with Reference Spectral Irradiance Data.* Standard IEC 60904-3, International Electro-Technical Commission.

ISO (1992) *Solar Energy – Reference Solar Spectral Irradiance at the Ground at Different Receiving Conditions, Part 1.* International Standard 9845-1, International Organization for Standardization, Geneva.

Jacquinet-Husson, N. et al. (1999) The 1997 spectroscopic GEISA databank. *J. Quant. Spectros. Radiat. Transf.* 62, 205–54.

Kambezidis, H.D., Petrova, V.D. and Adamopoulos, A.D. (1997a) Radiative transfer. I. Atmospheric transmission monitoring with modelling and ground-based multispectral measurements, *Appl. Opt.* 36, 6976–82.

Kambezidis, H.D., Petrova, V.D. and Adamopoulos, A.D. (1997b) Radiative transfer. II. Impact of meteorological variables and surface albedo on atmospheric optical properties retrieved from ground-based multispectral measurements. *Appl. Opt*. 36, 6983–88.

Kambezidis, H.D., Katevatis, E.M., Petrakis, M., Lykoudis, S. and Asimakopoulos, D.N. (1998) Estimation of the Linke and Unsworth–Monteith turbidity factors in the visible spectrum: application for Athens, Greece. *Solar Energy* 62, 39–50.

Kambezidis, H.D., Adamopoulos, A.D. and Zevgolis, D. (2000a) Case studies of spectral atmospheric transmittance in the ultraviolet and visible regions in Athens, Greece. I. Total transmittance. *Atmos. Res*. 54, 223–32.

Kambezidis, H.D., Adamopoulos, A.D. and Zevgolis, D. (2000b) Case studies of spectral atmospheric transmittance in the ultraviolet and visible regions in Athens, Greece. II. Aerosol transmittance. *Atmos. Res*. 54, 233–43.

Kambezidis, H.D., Adamopoulos, A.D. and Gueymard, C. (2001a) Total NO_2 column amount over Athens, Greece in 1996–97. *Atmos. Res*. 57, 1–8.

Kambezidis, H.D., Adamopoulos, A.D. and Zevgolis, D. (2001b) Determination of Ångström and Schüepp's parameters from ground-based spectral measurements of beam irradiance in the ultraviolet and visible spectrum in Athens, Greece. *Pure Appl. Geophys*. 158, 821–38.

Karlsson, J. (2001) *Windows – Optical Performance and Energy Efficiency*. Ph.D. thesis, Uppsala University.

Kasten, F. (1980) A simple parameterization of the pyrheliometric formula for determining the Linke turbidity factor. *Met. Res.* 33, 124–7.

Kasten, F. (1996) The Linke turbidity factor based on improved values of the integral Rayleigh optical thickness. *Solar Energy* 56, 239–44.

Kaufman, J.E., ed. (1984) *IES Lighting Handbook – Reference Volume*. Illuminating Engineering Society of North America, New York.

King, R. and Buckius, R.O. (1979) Direct solar transmittance for a clear sky. *Solar Energy* 22, 297–301.

Kittler, R., Heyman, S., Ruck, N. and Julian, W. (1992) Daylight measurement data: methods of evaluation and representation. *Light. Res. Technol.* 24, 173–87.

Kneizys, F. et al. (1988) *Users guide to LOWTRAN7*. Rep. AFGL-TR-88-0177, Air Force Geophysics Laboratory, Hanscom AFB, MA.

Koschmieder, H. (1924) Theorie der horizontalen Sichtweite. *Beitr. Phys. Atmos.* 12, 33–53.

Leckner, B. (1978) The spectral distribution of solar radiation at the earth's surface – elements of a model. *Solar Energy* 20, 143–50.

Linke, F. (1922) Transmission koeffizient und trübungsfaktor. *Beitr. Phys. Atmos.* 10, 91–103.

Linke, F. (1929) Messungen der sonnenstrahlung bei vier freiballonfahrten. *Beitr. Phys. Atmos.* 15, 176.

Louche, A., Peri, G. and Iqbal, M. (1986) An analysis of Linke turbidity factor. *Solar Energy* 37, 393–6.

Malicet, J. et al. (1995) Ozone UV spetroscopy. II. Absorption cross-sections and temperature dependence. *J. Atmos. Chem.* 21, 263–73.

Maxwell, E.L. (1998) METSTAT – the solar radiation model used in the production of the National Solar Radiation Data Base (NSRDB). *Solar Energy* 62, 263–79.

McClatchey, R.A., Fenn, R.W., Selby, J.A., Volz, F.E. and Garing, J.S. (1972) *Optical Properties of the Atmosphere, 3rd edn.* Rep. AFCRL-72-0497, Air Force Cambridge Research Laboratory, Hanscom AFB, MA.

McCluney, R. (1993) Sensitivity of optical properties and solar gain of spectrally selective glazing systems to changes in solar spectrum. *Proc. Solar '93, 22nd ASES Conf.* Washington, D.C., American Solar Energy Society.

McCluney, R. (1996) Sensitivity of fenestration solar gain to source spectrum and angle of incidence. *ASHRAE Trans.* 102, pt.2, 112–122.

McCluney, W.R. (1994) *Introduction to Radiometry and Photometry.* Artech House, Boston.

McCree, K.J. (1972) Tests of current definitions of photosynthetically active radiation against leaf photosynthesis data. *Agric. Met.* 10, 443–53.

McCree, K.J. (1981) Photosynthetically active radiation. *Physiological Plant Ecology* vol 12A, eds O.L. Lange et al. Springer-Verlag, Berlin.

Molineaux, B., Ineichen, P. and Delaunay, J.J. (1995) Direct luminous efficacy and atmospheric turbidity – improving model performance. *Solar Energy* 55, 125–37.

Nann, S. and Riordan, C. (1991) Solar spectral irradiance under clear and cloudy skies: measurements and a semiempirical model. *J. Appl. Met.* 30, 447–62.

NREL (1993) *Users Manual for SERI QC Software – Assessing the Quality of Solar Radiation Data.* NREL/TP-463-5608, National Renewable Energy Laboratory, Golden, CO.

Osterwald, C.R. and Emery, K.A. (2000) Spectroradiometric sunphotometry. *J. Atmos. Ocean Technol.* 17, 1171–88.

Page, C.H. and Vigoureux, P. (1977) *The International System of Units (SI).* Rep. No. 330, US Government Printing Office.

Randel, D.L. et al. (1996) A new global water vapor dataset. *Bull. Am. Met. Soc.* 77, 1233–46.

Reagan, J.A., Thome, K., Herman, B. and Gall, R. (1987) Water vapor measurements in the 0.94 micron absorption band: calibration, measurements and data applications. *Proc. Int. Geosci. Remote Sens. Symp., IEEE 87CH2434-9*, pp. 63–7.

Ricchiazzi, P., Yang, S., Gautier, C. and Sowle, D. (1998) SBDART: a research and teaching software tool for plane-parallel radiative transfer in the earth's atmosphere. *Bull. Am. Met. Soc.* 79, 2101–14.

Rothman, L.S. et al. (1998) The HITRAN molecular spectroscopic database and HAWKS (HITRAN Atmospheric Workstation): 1996 edn. *J. Quant. Spect. Radiat. Transf.* 60, 665–710.

Rothman, L.S. et al. (2003) The HITRAN molecular spectroscopic database: edition of 2000 including updates through 2001. *J. Quant. Spect. Radiat. Transf.* 82, 5–44.

Rubin, M., Von Rottkay, K. and Powles, R. (1998) Window optics. *Solar Energy* 62, 149–61.

Schmid, B. and Wehrli, C. (1994) High precision calibration of a sun photometer using Langley plots performed at Jungfraujoch (3580 m) and standard irradiance lamps. *Proc. IGARSS'94* vol IV. Pasadena, CA, USA.

Schmid, B. and Wehrli, C. (1995) Comparison of sun photometer calibration by use of the Langley technique and the standard lamp. *Appl. Opt.* 34, 4500–12.

Schüepp, W. (1949) Die bestimmung der komponenten der atmosphärischen trübung aus aktinometermessungen. *Arch. Met. Geophys. Bioklim.* B1, 257–617.

Schwander, H., Kaifel, A., Ruggaber, A. and Koepke, P. (2001) Spectral radiative transfer modelling with minimized computation time using neural network technique. *Appl. Opt.* 40, 331–5.

Selby, J.E.A. and McClatchey, R.A. (1972) *Atmospheric Transmittance from 0.25 to 28.5 μm: Computer Code LOWTRAN-2.* Rep. AFCRL-72-0745, Air Force Cambridge Research Laboratory, Hanscom AFB, MA.

Shettle, E.P. (1989) Models of aerosols, clouds and precipitation for atmospheric propagation studies. *Proc. AGARD Conf. Proc. No. 454*, paper No. 15.

Shettle, E.P. and Fenn, R.W. (1979) *Models for the Aerosols of the Lower Atmosphere and the Effects of Humidity Variations on their Optical Properties.* Rep. AFGL-TR-79-0214, Air Force Geophysics Lab., Hanscom, MA.

Siegel, R. and Howell, J.R. (1981) *Thermal Radiation Heat Transfer.* McGraw-Hill Co., New York.

Skartveit, A. and Olseth, J.A. (1988) Some simple formulas for multiple Rayleigh scattered irradiance. *Solar Energy* 41, 19–20.

Smirnov, A., Royer, A., O'Neill, N.T. and Tarussov, A. (1994) A study of the link between synoptic air mass type and atmospheric optical parameters. *J. Geophys. Res.* 99D, 20967–82.

Smith, W.L. (1966) Note on the relationship between total precipitable water and surface dew point. *J. Appl. Met.* 5, 726–7.

Sparrow, E.M. and Cess, R.D. (1978) *Radiation Heat Transfer.* Hemisphere Publ., Washington.

Spencer, J.W. (1971) Fourier series representation of the position of the sun. *Search* 2, 172.

Stamnes, K., Tsay, S., Wiscombe, W. and Jayaweera, K. (1988) Numerically stable algorithm for discrete-ordinate-method radiative transfer in multiple scattering and emitting layered media. *Appl. Opt.* 27, 2502–9.

Thomason, L., Herman, B. and Reagan, J. (1983) The effect of atmospheric attenuators with structured vertical distributions on air mass determinations and Langley plot analyses. *J. Atmos. Sci.* 40, 1851–4.

Thome, K.J., Smith, M.W., Palmer, J.M. and Reagan, J.A. (1994) Three-channel solar radiometer for the determination of atmospheric columnar water vapor. *Appl. Opt.* 33, 5811–19.

Threlkeld, J.L. (1970) *Thermal Environmental Engineering, 2nd edn.* Prentice-Hall, Englewood Cliffs, NJ.

Uboegbulam, T.C. and Davies, J.A. (1983) Turbidity in Eastern Canada. *J. Clim. Appl. Met.* 22, 1384–92.

Unsworth, M.H. and Monteith, J.L. (1972) Aerosol and solar radiation in Britain. *Q. J. Roy. Met. Soc.* 98, 778–97.

VanHeuklon, T.K. (1979) Estimating atmospheric ozone for solar radiation models. *Solar Energy* 22, 63–8.

Wang, J. and Anderson, G.P. (1994) Validation of FASCOD3 and MODTRAN3: comparison of model calculations with interferometer observations from SPECTRE and ITRA. *In Passive Infrared Remote Sensing of Clouds and the Atmosphere II*, vol 2309, Society of Photo-Optical Instrument Engineers (SPIE).

Wehrli, C. (1985) *Extraterrestrial Solar Spectrum.* Pub. No. 615, World Radiation Center, Davos, Switzerland.

Weller, M. and Leiterer, U. (1988) Experimental data on spectral aerosol optical thickness and its global distribution. *Contr. Atmos. Phys.* 61, 1–9.

Yu, H. et al. (2003) Annual cycle of global distributions of aerosol optical depth from integration of MODIS retrievals and GOCART model simulations. *J. Geophys. Res.* 108D, 4128, doi:10.1029/2002JD002717.

6 GROUND ALBEDO

Introduction

Solar radiation incident on vertical and inclined surfaces consists of beam, sky-diffuse and ground-reflected components. The ground-reflected component may be significant, particularly in the northern latitudes due to low elevations of the sun and, at times, due to the presence of highly-reflecting snow cover. Accurate estimation of ground-reflected radiation would require knowledge of the foreground type and geometry, its reflectivity, degree of isotropy, the details of the surrounding skyline and the condition of the sky. Little information is available on the interaction of these parameters. The usual approach is to take a constant value of ground reflectance of 0.2 for temperate and humid tropical localities and 0.5 for dry tropical localities (CIBSE, 1982). This is despite the fact that the reflectivity of snow-covered ground could be as high as 0.9.

The term 'ground albedo' or simply 'albedo' is often used interchangeably with 'ground reflectance'. On the other hand, as Monteith (1959) has pointed out, the term 'albedo' or 'whiteness' refers to the reflection coefficient in the visible range of the spectrum, whereas 'reflectance' denotes the reflected fraction of short-wave energy. In this book the term 'albedo' has been used synonymously with reflectance, applying to the total short-wave energy.

The importance of knowing the albedo for the determination of radiation balance of macro- and microclimates is well known. A good estimate of albedo of the surrounding terrain is a prerequisite for representative calculations related to the energy balance of vegetation, amount of potential transpiration, energy interception of walls, windows, roofs and solar energy collectors. Therefore the small- and large-scale variation of albedo is of interest. The variation in albedo is spatial and temporal owing to the changing landscapes of the earth and due to the seasonal presence of snow and to some extent moisture deposition.

There has been some initiative in the past to assess the spatial variability of albedo. Barry and Chambers (1966) have presented a map of summer albedo over England and Wales. The map was prepared on the basis of published values of albedo and data collected at specific sites by means of ground and airborne measurements over southern England.

The aim of this chapter is to present data on albedo values for a variety of surfaces which may be in view of solar energy collection systems and to present techniques for computation of averaged albedo values for any locality. In this respect preliminary maps for UK are also provided which would be useful in estimating the albedo of any land mass for the summer and winter months.

6.1 Estimation of ground-reflected radiation

The two main problems in estimating the ground-reflected radiation are the uncertainty of average reflectance of the neighbouring ground and the lack of an accurate model.

Determination of a reasonably accurate value of albedo is not easy. Furthermore, it is more difficult to specify reflectivity than the other radiative properties such as absorptivity. As indicated by Siegel and Howell (1972), no less than eight types of reflectivity are in current use: bidirectional spectral, directional-hemispherical spectral, hemispherical-directional spectral, hemispherical spectral, bidirectional total, directional-hemispherical total, hemispherical-directional total and hemispherical total. Of these, hemispherical-total reflectivities are sufficient for applications such as meteorology and solar heating design, while spectral reflectivities are required for other applications such as electricity generation by photovoltaic cells, photobiology and solar controlled glazing. Several references including Greiger (1966), Kondratyev (1969), Hay (1970), Eagleson (1970), Meteorological Office (1972), Monteith (1973), Iqbal (1983), Gueymard (1987) and Saluja and Muneer (1988) quote spectral and total values or reflectivities for different landscapes.

Tables 6.1.1–6.1.4 present average hemispherical-total albedo for a number of ground coverings. Kondratyev (1969) has highlighted the possible sources of error in the measurement of albedo. Weather and time-dependent variations of albedo are illustrated in Figures 6.1.1–6.1.4. Figure 6.1.1 shows the variation of albedo of short grass and bare soil as a function of solar altitude and Figure 6.1.2 shows the albedo of water as a function of cloudiness and solar latitude. Figure 6.1.3 shows the effect of ageing in the albedo

Table 6.1.1 Albedo of soil covers

Soil	Albedo (%)
Black earth, dry	14
Black earth, moist	8
Grey earth, dry	25–30
Grey earth, moist	10–12
Ploughed field, moist	14
White sand	34–40
River sand	43
Light clay earth (levelled)	30–31

Table 6.1.3 Albedo of natural surfaces

Surface	Albedo (%)
Fresh snow cover	75–95
Old snow cover	40–70
Rock	12–15
Densely built-up areas	15–25
High dense grass	18–20
Sea ice	36–50
Water surfaces, sea	3–10
Lawn: high sun, clear sky	23
Lawn: high sun, partly cloudy	23
Lawn: low sun, clear sky	25
Lawn: overcast day	23
Dead leaves	30

Table 6.1.2 Albedo of vegetative covers

Class of vegetation	Species at maximum ground cover	Albedo (%)
Farm crops	Grass	24
	Wheat	26
	Tomato	23
	Pasture	25
Natural vegetation and forests	Heather	14
	Bracken	24
	Deciduous woodland	18
	Coniferous woodland	16

of snow and Figure 6.1.4 the variation of that of a snow-covered surface as a function of accumulated temperature index, which is the cumulative value of maximum daily temperatures since the last snowfall.

Hay (1970) has prepared maps of mean monthly albedo for Canada by using the values of albedo reported above and knowledge of a specific dominant surface cover. On the basis of these maps Hay (1976) has tabulated average monthly values of albedo for a number of Canadian locations. Iqbal (1983) has extended Hay's tables to further North American locations.

Kung et al. (1964) carried out a series of 12-monthly flights along a selected path in Wisconsin and a series of four long-range flights over extensive areas of North America. From these measurements they produced three continental albedo maps for North America covering winter, summer and transitional seasons. Barry and Chambers (1966) have produced a map of summer albedo for England and Wales.

Tables 6.1.1–6.1.4 characterise the measured values of albedo of small underlying surfaces. However, in engineering applications, such as solar heating design, a weighted average albedo of a relatively large area of foreground is required. Complication arises as

Table 6.1.4 Albedo of building materials

Surface	Albedo (%)
Weathered concrete	22
Weathered blacktop	10
Bituminous and gravel roof	13
Crushed rock surface	20
Building surfaces, dark (red brick, dark paints, etc.)	27
Building surfaces, light (light brick, light paints, etc.)	60

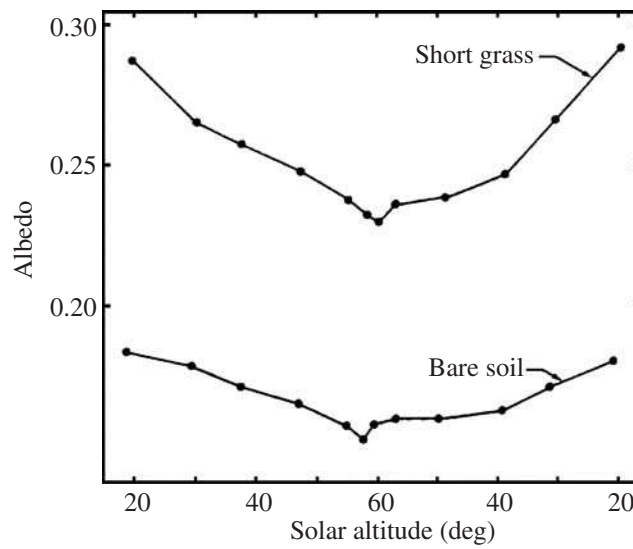

Figure 6.1.1 *Variation of albedo of bare soil and short grass with solar altitude*

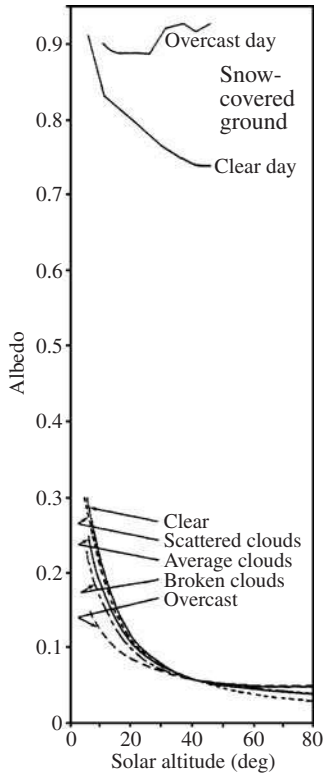

Figure 6.1.2 *Variation of albedo of water surface and snow-covered ground with solar altitude and cloud cover*

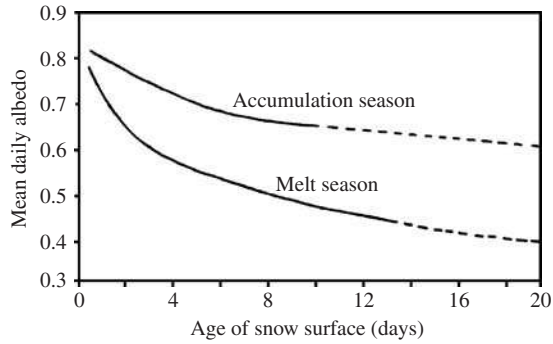

Figure 6.1.3 *Effect of ageing of snow on albedo*

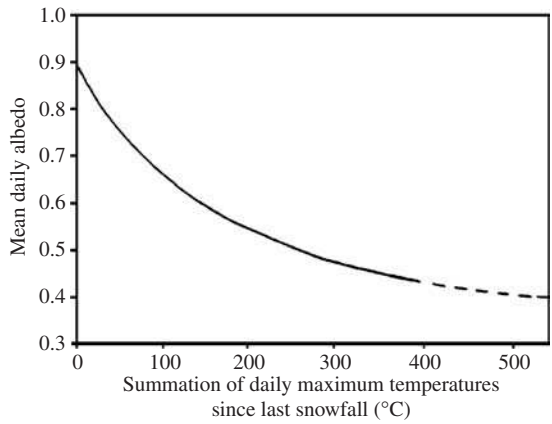

Figure 6.1.4 *Variation of albedo of a snow surface with accumulated temperature index since the last snow fall*

this foreground may consists of patches of different ground cover, each with its own characteristic albedo. In their study of the long-term performance of flat-plate solar collectors, Liu and Jordan (1963) adopted a simple approach by assuming an albedo of 0.2 when the ground was covered with less than 25 mm of snow and 0.7 for snow coverage of 25 mm. They calculated, for each month, an average albedo by using a weighting factor equal to the fractional time during the month when the snow depth exceeded 25 mm. Hunn and Calafell (1977) have questioned the adequacy of such a broad assumption and have used a photographic methods to compute the weighted average albedo of a few winter landscapes for some urban and rural areas of the USA. They concluded that an average albedo of 0.6–0.7, similar to that used by Liu and Jordan, is applicable to rural landscapes in winter where snow cover is prominent, except for locations adjacent to water surfaces where a considerably lower value of albedo is obtained. For urban areas, Hunn and Calafell maintain that no characteristic albedo in winter may be specified owing to the possibility of wide variations in landscape details and its value may vary in the range 0.16–0.49. The field of view in snow cover strongly influences the ground reflectivity.

6.2 Models for ground-reflected radiation

Liu and Jordan (1963) have proposed a simple isotropic model for diffusely-reflected radiation from the ground. For a surface inclined at an angle TLT to the horizontal and for infinite horizontal foreground, the geometric view factor for radiation exchange between the foreground and the surface is $\sin^2(\text{TLT}/2)$. Without any shadow in the foreground, Liu and Jordan's model results in hourly ($I_{g,\text{TLT}}$) and daily (g_{TLT}) reflected irradiation as given by Eqs (6.2.1) and (6.2.2) respectively:

$$I_{g,\text{TLT}} = \rho I_G \sin^2(\text{TLT}/2) \tag{6.2.1}$$

$$g_{\text{TLT}} = \rho G \sin^2(\text{TLT}/2) \tag{6.2.2}$$

where I_G and G are hourly and daily global irradiation on a horizontal surface, ρ the average albedo of the foreground and $I_{g,\text{TLT}}$ and g_{TLT} are respectively the hourly and daily reflected radiation on a sloping surface.

This model provides an easy means of computing the ground-reflected component; however, it does not take into account the anisotropic nature of the reflected radiation. Furthermore, as illustrated by Figures 6.1.1 and 6.1.2, the hemispherical-total reflectivity is a function of the solar elevation. Therefore an adequate model ought to incorporate the following effects:

(a) the variation of albedo of the surfaces in the foreground as a function of solar elevation and cloudiness,
(b) the geometric view factors subtended by the surfaces in the foreground on the inclined plane,
(c) the details of surrounding skyline in order to estimate the shaded fraction of the foreground.

In addition, as Kondratyev (1969) has shown, all surfaces are to some degree selective as to the wavelength of the incident radiation. Thus it is obvious that precise estimation of reflected radiation is a complex task. Temps and Coulson (1977) have reported the angular dependence of grass-reflected radiation. Based on their measurements for one location in California they have proposed the following model for grass-reflected radiation:

$$I_{g,\text{TLT}} = \rho I_G \sin^2(\text{TLT}/2)\{[1 + \sin^2(z/2)]\cos^2 \text{SOLALT}\} \tag{6.2.3}$$

where z is the zenith angle and SOLALT is the solar altitude. This model has only been tested against short-term data on cloudless days.

Gueymard (1987) has proposed more complex models by considering specifically two cases according to the optical characteristics of the reflecting surfaces: the near isotropic reflectance and the pure specular reflectance. The former is of general interest. In this case the reflected radiation can be treated as isotropic in the two half-hemispheres involved. Gueymard has proposed the use of the apparent reflectance as given by Eqs (6.2.4) and (6.2.5):

$$\rho_a = f_B \rho_B K_B + \rho_D(1 - K_B) \tag{6.2.4}$$

where f_B is the shadow factor for the beam irradiance, ρ_B is the beam reflectance, K_B the hourly horizontal beam fraction and ρ_D the reflectance of the diffuse irradiance. ρ_B

is a function of the reflectance of the normal incidence beam irradiance, $\rho_{B,N}$. ρ_D is given by:

$$\rho_D = \rho_N + 0.023(f_{ab} + f_{af}) \tag{6.2.5}$$

where f_{ab} and f_{af} are the anisotropy coefficients which describe the backward and forward reflectance.

Gueymard (1987) has suggested tentative values of the anisotropy coefficients for grass, snow, concrete and other common surfaces.

6.3 Albedo atlas for the UK

An accurate estimate of albedo for the surrounding terrain is desirable for representative calculations related to the heat balance of vegetation, the potential amount of transpiration, energy intercepted by windows and other building surfaces and solar energy collectors. The aim of the present section is to provide preliminary UK maps which would be useful in estimating the albedo of any land mass during the summer and winter months. The methodology presented here may be used with equal effectiveness for other geographical regions.

Snow-covered ground significantly affects the albedo, and hence the incidence of ground-reflected radiation on inclined and vertical surfaces. During snow-free periods albedo is a function of the dominant ground cover and the nature of the surfaces surrounding a building element or a solar collection device. By using the maps of snow cover and monthly-average albedo for snow-free periods, a significant improvement can be made in estimating ground-reflected radiation on inclined and vertical surfaces.

Any detailed study of solar radiation on inclined surfaces would require hourly or daily albedo values. Long-term predictions are usually made by employing monthly averages of daily or hourly irradiation values. As a first step, this study aims at the estimation of average monthly albedo for the UK locations. Albedo-related maps for winter months have been presented. These maps are reproduced from the work of Muneer (1987).

A number of Meteorological Office stations across the UK collect snow data. Published data are available from detailed measurements covering a limited number of locations. The extent of snow cover is observed every day at 0900 GMT. The depth of snow is also measured by ruler in an area of level snow. For most countries in the temperate belt periodically published climatological memoranda give statistical data of snow depth and days with snow lying at various locations. In the UK such information is available from the Meteorological Office. With reference to the latter source, ‘a day of snow falling’ is designated if snow or sleet is observed to fall at the station at any time during the 24 h period, while ‘a day of snow lying’ is defined as one in which snow covers at least half the ground surrounding the observing station at 0900 GMT.

Kung et al. (1964) have shown that the albedo of snow-covered ground is related to the depth of snow. The snow depth data for the UK are only readily available on an annual basis. In the absence of monthly-snow depth data, UK maps are reproduced for the mean number of days on which the snow was lying on the ground for the months of December to March.

The UK maps for November and April were prepared by Muneer (1987) using the following procedure. A correlation was established between snow falling and snow lying on

the ground for the months of December and March. Using the maps of snow falling in November and April and employing the correlation for December and March, respectively, maps of snow lying for November and April were prepared.

The contours of equal numbers of days when the snow was lying on the ground throughout the UK are shown in Figures 6.3.1–6.3.6 for the months between November and April. The rest of the period is considered to be free of snow.

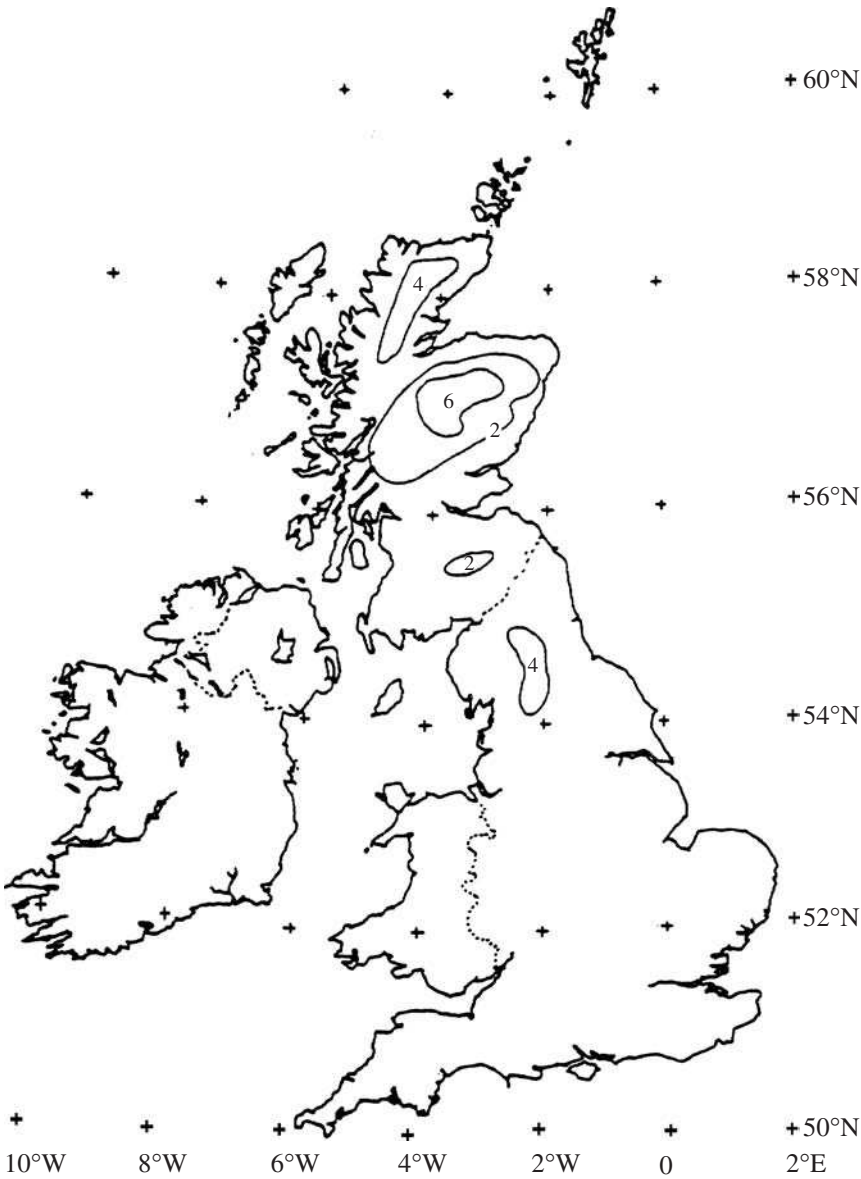

Figure 6.3.1 *Mean number of days with snow lying at 0900 GMT for November*

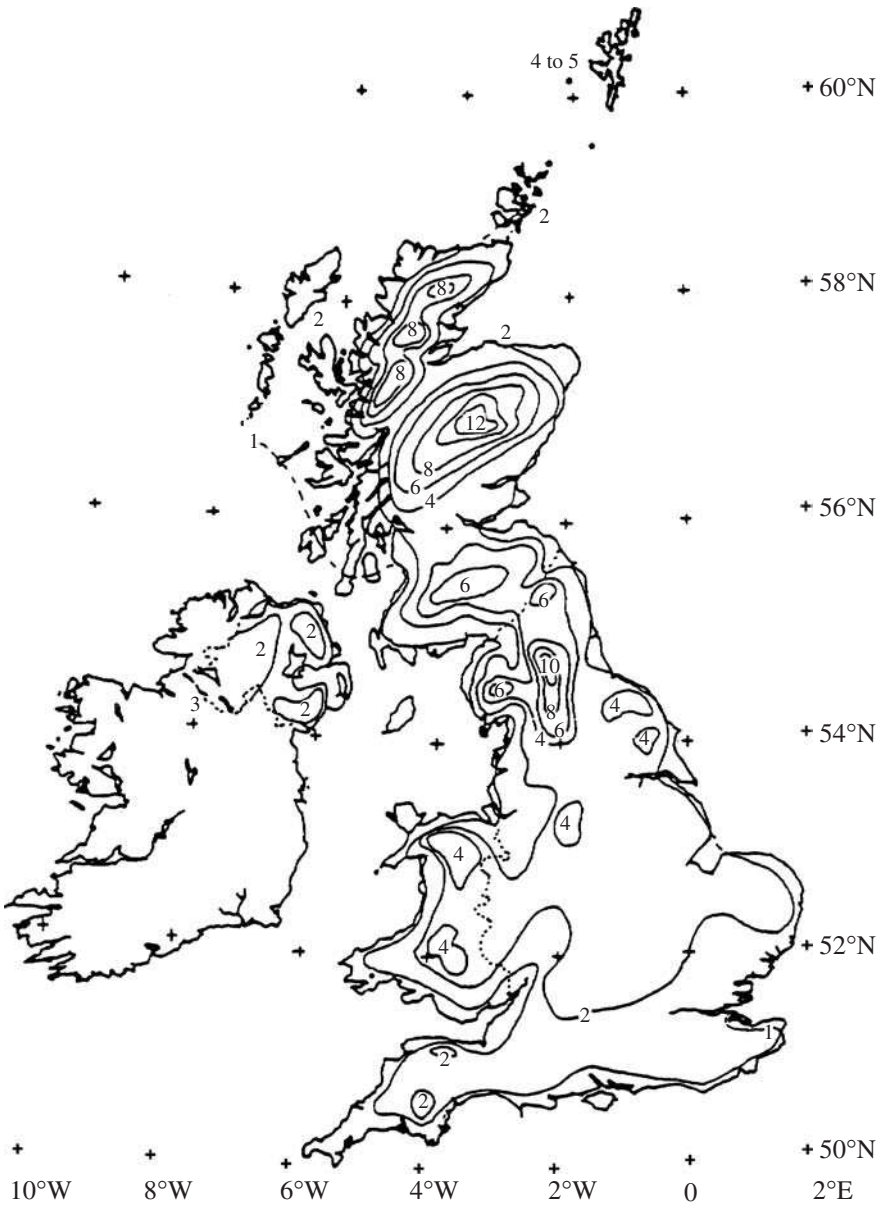

Figure 6.3.2 *Mean number of days with snow lying at 0900 GMT for December*

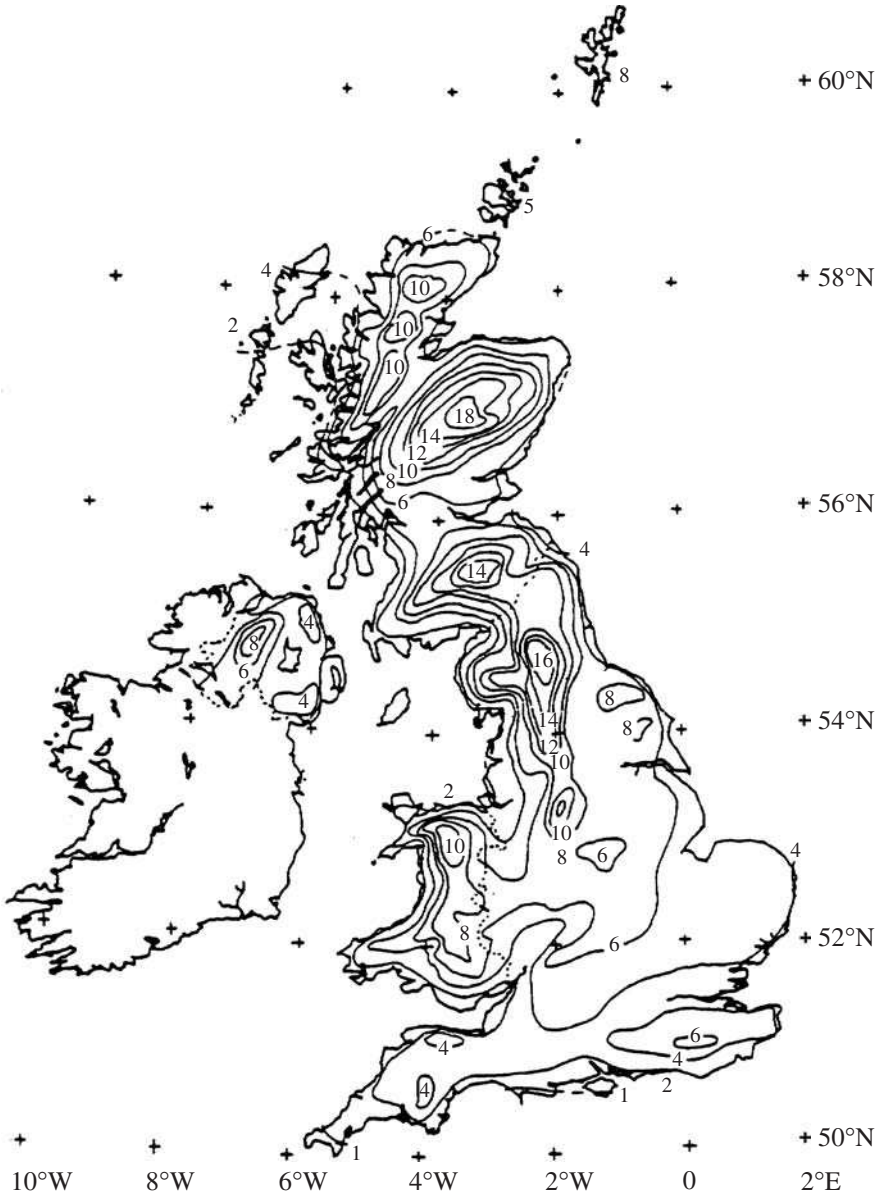

Figure 6.3.3 *Mean number of days with snow lying at 0900 GMT for January*

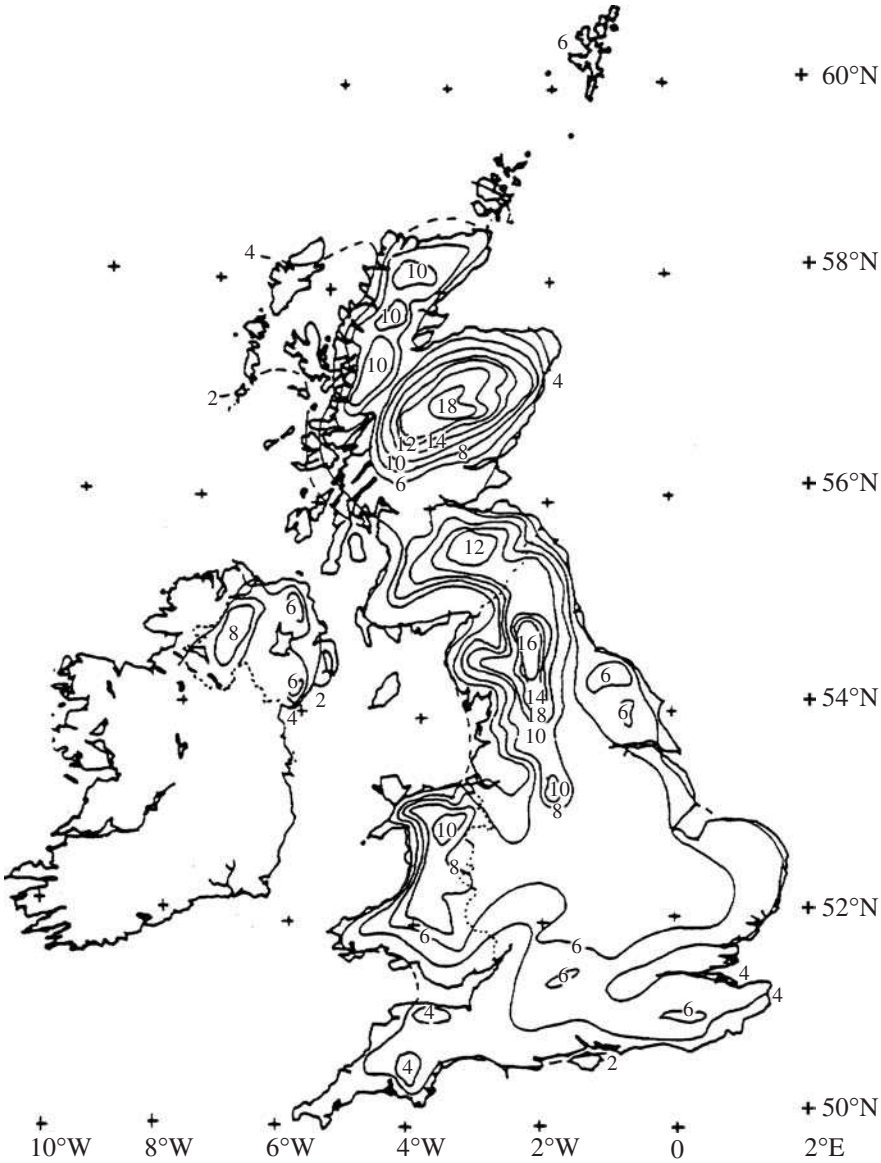

Figure 6.3.4 *Mean number of days with snow lying at 0900 GMT for February*

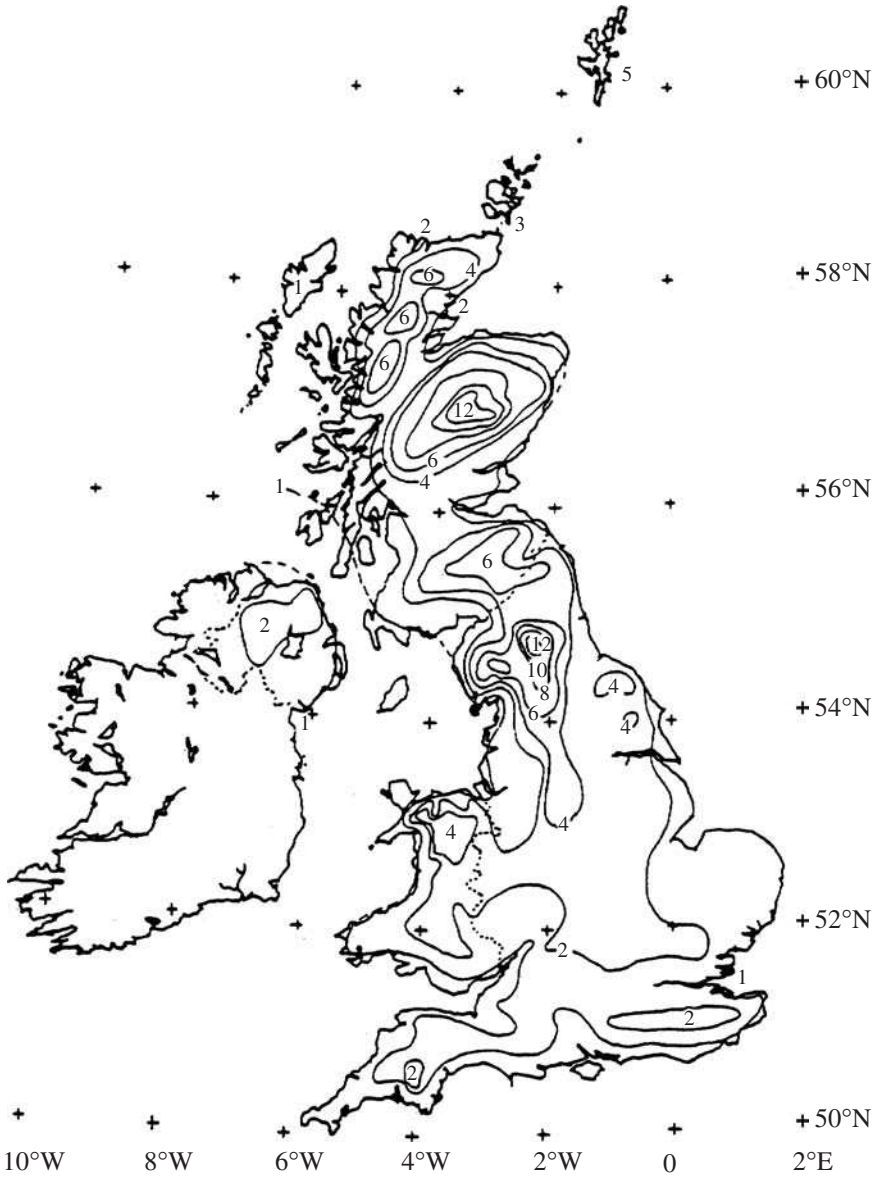

Figure 6.3.5 *Mean number of days with snow lying at 0900 GMT for March*

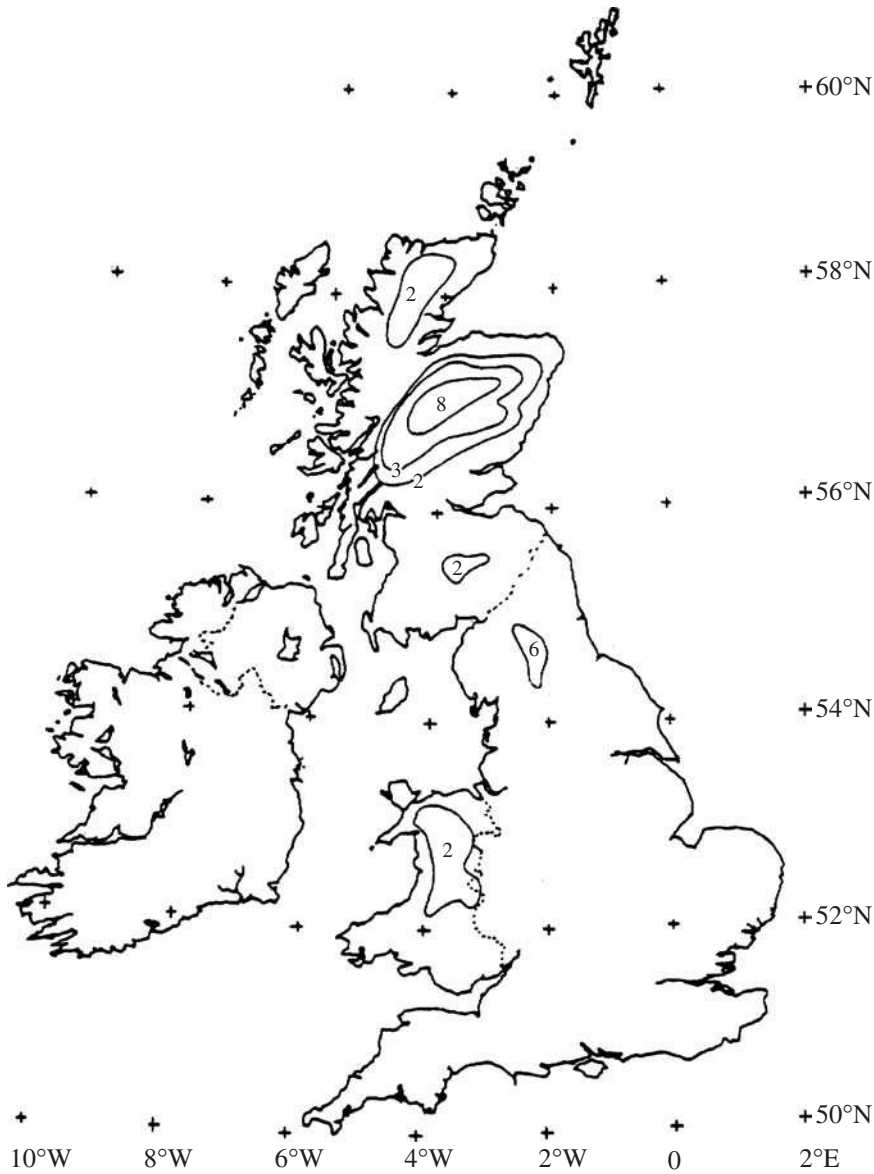

Figure 6.3.6 *Mean number of days with snow lying at 0900 GMT for April*

6.4 Estimation of monthly-averaged albedo

Following the procedure suggested by Liu and Jordan (1963) the monthly-averaged albedo $\bar{\rho}$ for any month is given by:

$$\bar{\rho} = \rho_{\text{snow-free}}(1 - f_{\text{snow}}) + \rho_{\text{snow}}\ f_{\text{snow}} \tag{6.4.1}$$

where f_{snow} is the fractional time during the month when the snow was lying on the ground.

Liu and Jordan (1963) used the period when the snow depth was over 25 mm. A snow albedo of 0.7 (see Figure 6.1.3) may be used for snow which is 2–3 days old. The albedo of grass is in the range 0.23–0.25 (see Tables 6.1.2 and 6.1.3). Monteith (1973), using measurements in the UK, has adopted 0.24 for the albedo value for grass. The albedo for heather has been quoted as between 0.1 and 0.14 while the range of albedo for urban areas has been taken as 0.15–0.25 (see Table 6.1.3). Kung et al. (1964) found the measured albedo for the snow-free period as 0.13–0.17 for the suburban area of Madison, Wisconsin and 0.15–0.18 in the downtown area. Their findings are in agreement with those of Oguntoyinbo (1970) for Nigeria. Saluja and Muneer (1988) have suggested the corresponding value for UK as 0.14–0.18.

Example 6.4.1

Estimate the monthly-averaged albedo for Aviemore (57.2°N and 3.8°W) for the month of February.

For a predominantly heather-covered area, $\rho_{\text{snow-free}}$ may be taken as 0.14. From Figure 6.3.3, the average number of days the snow is lying on the ground is 18. Therefore using Eq. (6.4.1) the monthly-averaged albedo is:

$$\bar{\rho} = 0.14(10/28) + 0.7(18/28) = 0.50$$

References

Barry, R.G. and Chambers, R.E. (1966) A preliminary map of summer albedo over England and Wales. *Q. J. Roy. Met. Soc.* 92, 543.

CIBSE (1982) *CIBSE Guide, Section A2: Weather and Solar Data*. Chartered Institution of Building Services Engineers, London.

Eagleson, P.S. (1970) *Dynamic Hydrology*. McGraw-Hill, New York.

European Solar Radiation Atlas (1984) *Vol 1: Horizontal Surfaces; Vol 2: Inclined Surfaces*, ed. W. Palz. Commission of the European Communities/Tuv Rheinland, Brussells.

Greiger, R. (1966) *The Climate Near the Ground.* Harvard University Press, Cambridge.

Gueymard, C. (1987) An anisotropic solar irradiance model for tilted surfaces and its comparison with selected engineering algorithms. *Solar Energy* 38, 367.

Hay, J.E. (1970) *Aspects of the Heat and Moisture Balance of Canada.* PhD thesis, University of London.

Hay, J.E. (1976) A revised method for determining the direct and diffuse components of the total short-wave radiation. *Atmosphere* 14, 278.

Hunn, B.D. and Calafell, D.O. (1977) Determination of average ground reflectivity for solar collectors. *Solar Energy* 19, 87.

Iqbal, M. (1983) *Introduction to Solar Radiation*. Academic Press, New York.

Kondratyev, K.Y. (1969) *Radiation in the Atmosphere*. Academic Press, New York.

Kung, E.C., Bryson, R.A. and Lenshow, D.H. (1964) A study of a continental surface albedo on the basis of flight measurements and structure of the Earth's surface cover over North America. *Monthly Rev.* 92, 543.

Liu, B.Y.H. and Jordan, R.C. (1963) The long-term average performance of flat-plate solar-energy collectors. *Solar Energy* 7, 53.

Meteorological Office (1972) *Meteorological Glossary*, ed. D.H. McIntosh. HMSO, London.

Monteith, J.L. (1959) The reflection of short-wave radiation by vegetation. *Q. J. Roy. Met. Soc.* 85, 392.

Monteith, J.L. (1973) *Principles of Environmental Physics*. Edward Arnold, London.

Muneer, T. (1987) *Solar Radiation Modelling for the United Kingdom.* PhD thesis, Council for National Academic Awards, London.

Oguntoyinbo, J.S. (1970) Reflection coefficient of natural vegetation, crops and urban surfaces in Nigeria. *Q. J. Roy. Met. Soc.* 96, 430.

Saluja, G.S. and Muneer, T. (1988) Estimation of ground-reflected radiation for the United Kingdom. *BSER&T* 9, 189.

Siegel, R. and Howell, J.R. (1972) *Thermal Radiation Heat Transfer.* McGraw-Hill, New York.

Temps, R.C. and Coulson, K.L. (1977) Solar radiation incident upon slopes of different orientations. *Solar Energy* 19, 179.

7 PSYCHROMETRICS

Introduction

Psychrometrics deals with the study of moist air and its thermodynamic properties. Due to the wide application of psychrometrics in the design and application of building air-conditioning systems, properties are more commonly known as psychrometric properties. The aim of this chapter is to introduce these properties, present models for their computation and provide the relevant FORTRAN routines.

It may be recalled that in Chapter 3 with reference to the meteorological radiation model it was pointed out that for any given hour, the dew-point temperature was required to determine the prevailing atmospheric moisture content. The commonly recorded psychrometric parameters are either the dry- and wet-bulb temperatures, or the dry-bulb temperature and relative humidity. In the UK, e.g. the former two components are recorded at over 500 locations. In many locations these quantities are reported as the daily maximum and minimum temperatures. However, for the recording sites managed by the Meteorological Office hourly data are easily available.

For those sites where only daily maximum and minimum temperatures are recorded a method is required to enable these to be decomposed into hourly, or sub-hourly, values. A procedure and an electronic routine based on ASHRAE (1993) is also provided herein to this effect.

7.1 Psychrometric properties

All models presented in this chapter are those of ASHRAE (1993). Thus the notation of ASHRAE is closely followed in the accompanying text as well as the electronic routines, receptively, presented as Prog7-1.For (given input: dry- and wet-bulb temperatures) and Prog7-2.For (given input: dry-bulb temperature and relative humidity).

If t is the temperature (°C) and T the absolute temperature (K) then $T = t + 273.15$. If W_s is the humidity ratio at saturation, then for a given temperature and pressure, humidity ratio W can have any value from zero to W_s.

We now define v_a as the specific volume of dry air (m^3/kg), h_a the specific enthalpy of dry air (kJ/kg of dry air) and p_{ws} the vapour pressure of water (kPa) in moist air.

The saturation pressure over *ice* for the temperature range of -100 to 0 °C is given by:

$$\ln(p_{ws}) = C_1/T + C_2 + C_3T + C_4T^2 + C_5T^3 + C_6T^4 + C_7 \ln(T) \tag{7.1.1}$$

where $C_1 = -5.674\,535\,9 \times 10^3$, $C_2 = -5.152\,305\,8 \times 10^{-1}$, $C_3 = -9.677\,843\,0 \times 10^{-3}$, $C_4 = 6.221\,570\,1 \times 10^{-7}$, $C_5 = 2.074\,782\,5 \times 10^{-9}$, $C_6 = -9.484\,024\,0 \times 10^{-13}$ and $C_7 = 4.163\,501\,9$.

The range of saturation pressure over *liquid water* for the temperature range of 0–200 °C is given by:

$$\ln(p_{ws}) = C_8/T + C_9 + C_{10}T + C_{11}T^2 + C_{12}T^3 + C_{13}\ln(T) \tag{7.1.2}$$

where $C_8 = -5.800\,220\,6 \times 10^3$, $C_9 = -5.516\,256\,0$, $C_{10} = -4.864\,023\,9 \times 10^{-2}$, $C_{11} = 4.176\,476\,8 \times 10^{-5}$, $C_{12} = -1.445\,209\,3 \times 10^{-8}$ and $C_{13} = 6.545\,967\,3$.

The actual humidity ratio W is given by:

$$W = 0.621\,98\frac{p_w}{p - p_w} \tag{7.1.3}$$

where p_w is the partial pressure of water vapour and p is the atmospheric pressure.

Similarly, the humidity ratio at saturation is given by:

$$W_s = 0.621\,98\frac{p_{ws}}{p - p_w} \tag{7.1.4}$$

The relative humidity may be obtained from:

$$\phi = \frac{p_w}{p_{ws}}\Big|_{t,p} \tag{7.1.5}$$

It may easily be shown that:

$$v = \frac{R_a T(1 + 1.6078W)}{p} \tag{7.1.6}$$

where R_a is the gas-constant for water substance.

The enthalpy of a mixture of gases equals the sum of the individual partial enthalpies of the components. Thus:

$$h = h_a + W_{h_g} \tag{7.1.7}$$

where h_a is the specific enthalpy for dry air and h_g is the specific enthalpy for saturated water vapour at the temperature of the mixture. ASHRAE (1993) recommends:

$$h_a = 1.006t \text{ (kJ/kg)} \tag{7.1.8}$$

$$h_g = 2501 + 1.805t \text{ (kJ/kg)} \tag{7.1.9}$$

$$h = 1.006t + W(2501 + 1.805t) \text{ (kJ/kg)} \tag{7.1.10}$$

where t is the dry-bulb temperature (°C).

For an adiabatic process:

$$h + (W_s^* - W)h_w^* = h_s^* \tag{7.1.11}$$

The properties of W_s^*, h_w^* and h_s^* are functions only of the temperature t^* for a fixed value of pressure. The value of t^*, which satisfies Eq. (7.1.11) for given values of h, W and p, is defined as the thermodynamic wet-bulb temperature.

Substituting the approximate relationship for $h_w^* = 4.186t^*$ in Eq. (7.1.11) and solving for the humidity ratio yields:

$$W = \frac{(2501 - 2.381t^*)W_s^* - (t - t^*)}{2501 + 1.805t - 4.186t^*} \tag{7.1.12}$$

The dew-point temperature t_d is obtainable as follows:

$$t_d = C_{14} + C_{15}\alpha + C_{16}\alpha^2 + C_{17}\alpha^3 + C_{18}(p_w)^{0.1984} \tag{7.1.13}$$

t_d being in the range 0–93 °C. However, when t_d is below 0 °C:

$$t_d = 6.091\,260\alpha + 0.4959\alpha^2 \tag{7.1.14}$$

where $\alpha = \ln(p_w)$, $C_{14} = 6.54$, $C_{15} = 14.526$, $C_{16} = 0.7389$, $C_{17} = 0.094\,86$ and $C_{18} = 0.4569$.

ASHRAE (1993) provides detailed, step-by-step computational procedure for all psychrometric properties for a variety of input combinations. The basic equations for the above task are those which were given above. Use of Prog7-1.For and Prog7-2.For is now demonstrated.

Example 7.1.1

Compute psychrometric properties given the dry- and wet-bulb temperatures (dbt and wbt) of 30 and 20 °C.

Prog7-1.For produces the following output:

relative humidity = 0.398 (39.8%)
humidity ratio = 0.0105 kg water vapour per kg dry air
specific volume = 0.873 m^3/kg dry air
enthalpy of moist air = 57.1 kJ/kg dry air
dew-point temperature = 14.9 °C

Example 7.1.2

Compute psychrometric properties given the dry-bulb temperature = 30 °C and relative humidity = 0.398 (39.8%).

Prog7-2.For produces the following output:

humidity ratio = 0.0105 kg water vapour per kg dry air
specific volume = 0.873 m^3/kg dry air
enthalpy of moist air = 57.1 kJ/kg dry air
dew-point temperature = 14.9 °C
wet-bulb temperature = 20 °C

A psychrometric chart prepared with the execution of Prog7-2.For is shown in Figure 7.1.1. The corresponding data are included in File7-1.Csv. The advantage of this type of database is that it can easily be imported in any of the popular spreadsheet software packages. The

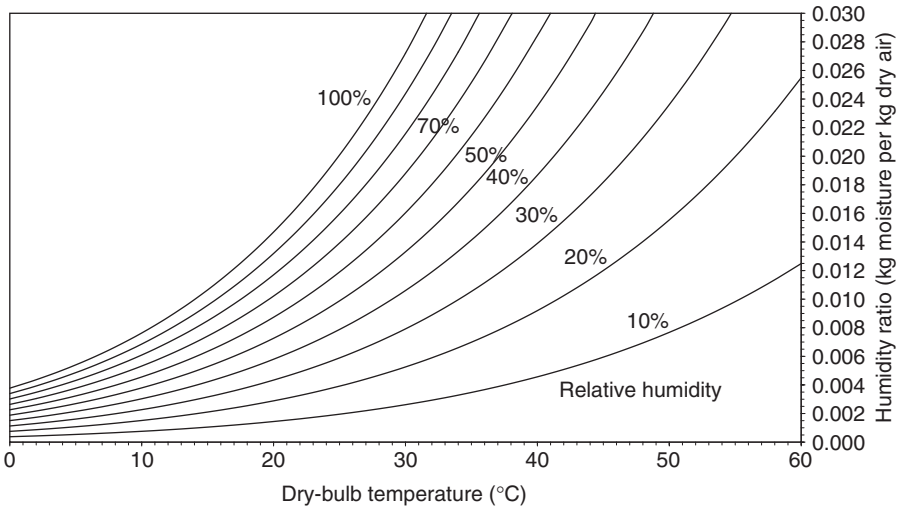

Figure 7.1.1 *Psychrometric chart based on Prog7-1.For*

Table 7.2.1 Diurnal temperature swing

Hour	%	Hour	%
1	87	13	11
2	92	14	3
3	96	15	0
4	99	16	3
5	100	17	10
6	98	18	21
7	93	19	34
8	84	20	47
9	71	21	58
10	56	22	68
11	39	23	76
12	23	24	82

user may then superimpose their own computed data (obtained via one of the presently available routines) to produce charts to display their psychrometric state points or processes.

7.2 Hourly temperature model

As mentioned above, very often daily or monthly-mean maximum and minimum temperatures are available from weather reports. However, for simulation purposes hourly data are required. Towards this end ASHRAE provides a simple model which is presented in the following:

$$\text{Temperature (at any hour)} = \text{daily maximum temperature} - (\text{daily range} \times \text{percentage}) \quad (7.2.1)$$

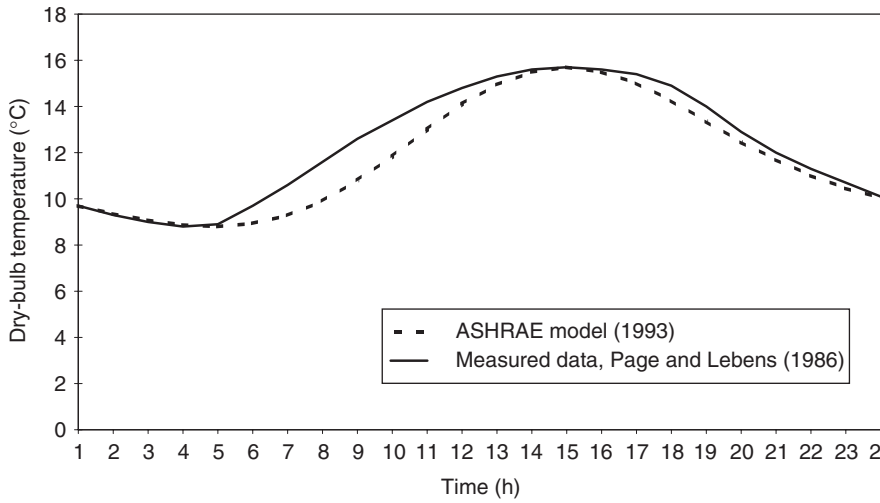

Figure 7.2.1 *Evaluation of ASHRAE hourly temperature model for dry-bulb temperature*

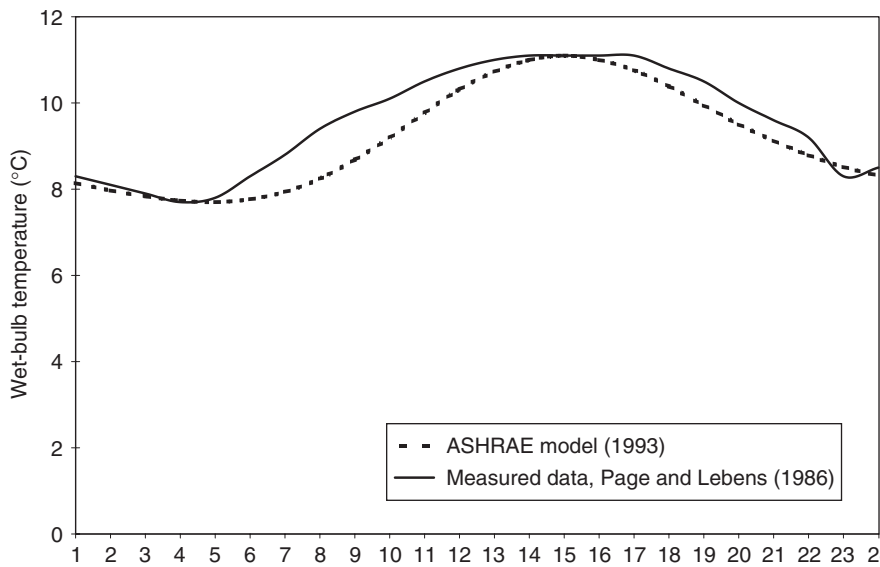

Figure 7.2.2 *Evaluation of ASHRAE hourly temperature model for wet-bulb temperature*

The daily range is the difference between the daily maximum and minimum temperatures, and the percentage is the figure corresponding to each hour given in Table 7.2.1.

Figures 7.2.1 and 7.2.2 enable evaluation of the performance of ASHRAE hourly temperature model against measured data for one location in the UK. The plots show a reasonably good agreement, thus making it possible to obtain the hourly values in the absence of such information.

Example 7.2.1

Compute the dry- and wet-bulb temperatures at 21 h, given the respective daily maximum and minimum temperatures of 15 and 3 °C.

Prog7-3.For enables computation of all 24 h cyclic temperatures. The temperature for 21 h thus obtained is 8 °C.

References

ASHRAE (1993) *Handbook of Fundamentals*. American Society of Heating, Refrigerating and Air-conditioning Engineers, Atlanta, USA.

Page, J.K. and Lebens, R. (1986) *Climate in the United Kingdom*. HMSO, London.

8 SOLAR RADIATION AND DAYLIGHT DATA

This chapter is largely based on the work of Muneer and Kinghorn (1998), Kinghorn (1999), Muneer et al. (2000) and Claywell (2003).

8.1 International Daylight Measurement Programme

The Commission International de l'Éclairage (CIE) declared the year 1991 as the International Daylight Measurement Year (IDMY). As a result, new activity commenced in the field of daylight measurement on a worldwide scale. This activity was later named the International Daylight Measurement Programme (IDMP). In the UK as a result of the CIE call, horizontal and vertical illuminance and irradiance (solar radiation) measurements have been carried out for four sites, i.e. Garston, Manchester, Sheffield and Edinburgh. The measurements at Edinburgh were respectively undertaken at Napier and Heriot-Watt universities. In Japan daylight data were recorded at 14 stations. Details of IDMP stations throughout the world are shown in Table A1.

Measured solar irradiance and illuminance IDMP data for the UK and Japan have been compiled and duly reported (Muneer and Kinghorn, 1998). That data is available separately on a CD-ROM with Muneer et al. (2000). For more extensive data the reader is referred to the following web sites: http://idmp.entpe.fr/ and http://www.cie.co.at/cie/home.html. Other sources of solar radiation data are appended at the end of this chapter.

Most IDMP data are quality controlled in accordance with the rules set out by CIE (1994). The UK quality-controlled data furnished to the author have been rigorously checked, initially by the respective station managers and then by the overall co-ordinator, Professor P.R. Tregenza as part of an EPSRC funded project (Tregenza, 1995). Japanese data were checked for quality by the research team headed by Professor H. Nakamura at Kyushu University. Furthermore, Chapter 4 outlines the quality control procedures that may be applied to any such data set.

8.2 IDMP recorded horizontal and slope data for solar radiation and daylight measurements

Daylight is a highly variable resource and therefore warrants measurement at a short time interval. The solar radiation and daylight data included varies from a frequency of 5 min for three UK stations, i.e. Edinburgh's Napier (55.95°N and 3.20°W), Heriot-Watt (55.93°N and 3.20°W) universities and Garston (51.71°N and 0.38°W) to half-hourly time series for Manchester (53.50°N and 2.25°W) and Sheffield (53.38°N and 1.50°W). Fukuoka (33.52°N and 130.48°E) data are presented by Muneer et al. (2000) as 10 min

Table 8.2.1 Format of slope illuminance data files

Edinburgh sites	Fukuoka	Garston	Manchester	Sheffield
Month	Date	Month	Year	Year
Day	Time	Day	Julian day	Julian day
Year	SOLALT	Year	Hour	Hour
Hour	SOLAZM	Hour	E_{eg}	E_{eg}
Minute	E_{vg}	Minute	E_{ed}	E_{ed}
E_{vg}	E_{vd}	E_{vg}	E_{egn}	E_{egn}
E_{vd}	E_{vb}	E_{vd}	E_{ege}	E_{ege}
E_{vgn}	E_{vgn}	E_{vgn}	E_{egs}	E_{egs}
E_{vge}	E_{vge}	E_{vge}	E_{egw}	E_{egw}
E_{vgs}	E_{vgs}	E_{vgs}	E_{vg}	E_{vg}
E_{vgw}	E_{vgw}	E_{vgw}	E_{vd}	E_{vd}
E_{eg}	E_{eg}	E_{eg}	E_{vgn}	E_{vgn}
E_{ed}	E_{ed}	E_{ed}	E_{vge}	E_{vge}
E_{egn}	E_{eb}	E_{egn}	E_{vgw}	E_{vgs}
E_{ege}	E_{edn}	E_{ege}	E_{vgs}	E_{vgw}
E_{egs}	E_{ede}	E_{egs}	RH	L_{vz}
E_{egw}	E_{eds}	E_{egw}	T_{db}	RH
SOLALT	E_{edw}	SOLALT		T_{db}
SOLAZM	T_{db}	SOLAZM		
$C_{ef}C_{vf}$	T_{dp}	$C_{ef}C_{vf}$		
		L_{vz}		
		RH		
		T_{db}		
		E_{vs}		
		E_{es}		

averages of 1 min spot readings. The format of those files, presented by Muneer et al. (2000) is shown in Table 8.2.1. Solar radiation data from non-IDMP sources are reported as hourly values.

In Section 1.8 threshold values of illuminance for a number of naturally occurring events were presented. This information may be useful in acquiring a sense of the prevailing daylight illuminance levels for the locations under discussion. Tables 8.2.1 and 8.2.2 respectively provide details of the notation, format and structure of the files presented by Muneer et al. (2000). Approximately 1 week of data per month are included for each UK site considered. An attempt has been made to supply these data using the mean day of each month as a centre point for each weekly period. In accordance with the work of Klein (1977), the mean days of each month are reported as those for which daily horizontal extraterrestrial irradiance values are approximately equal to the mean monthly values. This approach provides a simple, yet reliable, method for determination of monthly-average radiation values required in a multitude of solar energy engineering applications. In instances where no measured data are available for the mean day of each month, data for the nearest period to the mean day has been selected.

Solar radiation data from non-IDMP stations are available separately on CD-ROM format and contain the relevant information for Bahrain, Japan, Kuwait and Portugal. Table 8.2.3 provides details of the non-IDMP stations whose data have been processed by the author's research group.

Table 8.2.2 Nomenclature used in slope illuminance data files

CIE abbreviation	Parameter	Units
C_{ef}	Shade ring correction factor for horizontal diffuse irradiance	Dimensionless
C_{vf}	Shade ring correction factor for horizontal diffuse illuminance	Dimensionless
E_{eb}	Direct (beam normal) irradiance	W/m^2
E_{ed}	Diffuse horizontal irradiance	W/m^2
E_{eg}	Global horizontal irradiance	W/m^2
E_{ege}	Vertical irradiance, east facing surface	W/m^2
E_{egn}	Vertical irradiance, north facing surface	W/m^2
E_{egs}	Vertical irradiance, south facing surface	W/m^2
E_{egw}	Vertical irradiance, west facing surface	W/m^2
E_{vb}	Direct (beam normal) illuminance	lx
E_{vd}	Diffuse horizontal illuminance	lx
E_{vg}	Global horizontal illuminance	lx
E_{vge}	Vertical illuminance, east facing surface	lx
E_{vgn}	Vertical illuminance, north facing surface	lx
E_{vgs}	Vertical illuminance, south facing surface	lx
E_{vgw}	Vertical illuminance, west facing surface	lx
L_{vz}	Zenith luminance	Cd/m^2
RH	Relative humidity	%
SOLALT	Solar altitude angle	°
SOLAZM	Solar azimuth angle	°
T_{db}	Dry-bulb temperature	°C
T_{dp}	Dew point temperature	°C

Table 8.2.3 Non-IDMP solar radiation databases available as a separate companion to the present publication (refer Section 8.2)

Country	Location	Latitude	Longitude	Time stamp	Data period (years)	Content*
Bahrain	Bahrain	26.13°N	50.39°E	LCT centred	2000–02	a, b, c, d, e, f
Japan	Chofu	35.65°N	139.55°E	LCT 10 min average	1993	a, b, c, d, e, f
	Fukuka	33.52°N	130.48°E	LCT 10 min average	1992–94	a, b, c, d, e, f
	Sapporo	43.05°N	141.33°E	LCT 10 min average	1991, 1993	a, b, c, d, e, f
	Toyota	35.18°N	137.17°E	LCT 10 min average	1993, 1994	a, b, c, d, e, f
Kuwait	Kuwait	29.22°N	47.98°E	LCT hour beginning	1996–2000	a, b, c, d, e, f
Portugal	Faro	37.02°N	9.15°W	AST centred	1982–86	a, b, c
	Lisbon	38.70°N	9.15°W	AST centred	1982–90	a, b, c

* Information provided.
a: Time stamp.
b: Global irradiance.
c: Diffuse irradiance.
d: Direct (beam) irradiance.
e: Other irradiance data, ERAD, diffuse ratio, clearness index, etc.
f: Other meteorological data, dry bulb, wet bulb, wind, etc.

8.3 Sky scan data

Sky luminance and radiance distribution data from one Japanese and two UK sites were presented by Muneer et al. (2000). Table 8.3.1 presents a summary of radiance and luminance data recorded by sky scanners at Sheffield, Garston and Fukuoka. Since these data are comparatively scarcer than, say, slope data, the information was provided in approximately 5 day blocks around the mean day of each month. The UK data were measured using a PRC Krochmann sky scanner. The Japanese data were recorded using a twin-headed sensor, capable of concurrent luminance and radiance recording, purposely developed by EKO company of Tokyo. A comparative evaluation of these instruments has previously been conducted against IDMP data from Geneva, Switzerland (Ineichen and Molineaux, 1993). Both instruments measure their required parameters by considering individual elements, or patches, of the sky. Each sky patch can be recognised in terms of its solar geometry, i.e. the altitudinal and azimuthal co-ordinates individual to each patch. Note that the geometric relationship between sky patches, solar position and sky zenith was shown in Figure 4.6.1.

Both PRC Krochmann and EKO instruments operate on the following principle. A hemisphere, representing the sky canopy, can be divided into bands of solar altitude. These bands lie parallel to the horizon and represent increments in solar altitude of 12°. Further, each band is azimuthally sub-divided to produce an array of sky patches. A short note on the merit of this technique of sky sub-division is available in the literature (Tregenza, 1987). The azimuthal increments of each band are shown in Table 8.3.2.

Figure 4.5.3(a) and (b) represents the individual sky patches as respectively measured by the PRC Krochmann (German) and EKO (Japanese) sensors. The outer bandwidths are those at the horizon, while the centre point (number 145) relates to the zenith of the sky hemisphere. There exists a slight difference between the numbering of each sky patch.

Table 8.3.1 Sky scan database

	Luminance			Radiance
Month	Fukuoka (1994) Data8-07.xls (Days)	Garston (1992) Data8-08.xls (Julian days)	Sheffield (1993) Data8-09.xls (Days)	Fukuoka (1994) Data8-10.xls (Days)
January	11th–15th	15–21	No data available	11th–15th
February	3rd– 7th	44–50	No data available	3rd–7th
March	1st–5th	76–81	14th–20th	1st–5th
April	1st–5th	103–109	14th–17th	1st–5th
May	1st–5th	133–138	18th–19th	1st–5th
June	2nd–6th	162–168	No data available	2nd–6th
July	5th–9th	191–197	No data available	5th–9th
August	1st–5th	230–236	No data available	1st–5th
September	1st–5th	256–262	17th–19th	1st–5th
October	1st–5th	288–294	15th–21st	1st–5th
November	1st–5th	314–320	18th–24th	1st–5th
December	1st–5th	348–354	20th–26th	1st–5th

Table 8.3.2 Sky patch geometry for UK locations (sun-relative co-ordinate system)*

Patch no.	1	2	3	4	5	6	7	8	9	10
Altitude (°)	6	6	6	6	6	6	6	6	6	6
Azimuth (°)	0	12	24	36	48	60	72	84	96	108
Patch no.	11	12	13	14	15	16	17	18	19	20
Altitude (°)	6	6	6	6	6	6	6	6	6	6
Azimuth (°)	120	132	144	156	168	180	192	204	216	228
Patch no.	21	22	23	24	25	26	27	28	29	30
Altitude (°)	6	6	6	6	6	6	6	6	6	6
Azimuth (°)	240	252	264	276	288	300	312	324	336	348
Patch no.	31	32	33	34	35	36	37	38	39	40
Altitude (°)	18	18	18	18	18	18	18	18	18	18
Azimuth (°)	0	12	24	36	48	60	72	84	96	108
Patch no.	41	42	43	44	45	46	47	48	49	50
Altitude (°)	18	18	18	18	18	18	18	18	18	18
Azimuth (°)	120	132	144	156	168	180	192	204	216	228
Patch no.	51	52	53	54	55	56	57	58	59	60
Altitude (°)	18	18	18	18	18	18	18	18	18	18
Azimuth (°)	240	252	264	276	288	300	312	324	336	348
Patch no.	61	62	63	64	65	66	67	68	69	70
Altitude (°)	30	30	30	30	30	30	30	30	30	30
Azimuth (°)	0	15	30	45	60	75	90	105	120	135
Patch no.	71	72	73	74	75	76	77	78	79	80
Altitude (°)	30	30	30	30	30	30	30	30	30	30
Azimuth (°)	150	165	180	195	210	225	240	255	270	285
Patch no.	81	82	83	84	85	86	87	88	89	90
Altitude (°)	30	30	30	30	42	42	42	42	42	42
Azimuth (°)	300	315	330	345	0	15	30	45	60	75
Patch no.	91	92	93	94	95	96	97	98	99	100
Altitude (°)	42	42	42	42	42	42	42	42	42	42
Azimuth (°)	90	105	120	135	150	165	180	195	210	225
Patch no.	101	102	103	104	105	106	107	108	109	110
Altitude (°)	42	42	42	42	42	42	42	42	54	54
Azimuth (°)	240	255	270	285	300	315	330	345	0	20
Patch no.	111	112	113	114	115	116	117	118	119	120
Altitude (°)	54	54	54	54	54	54	54	54	54	54
Azimuth (°)	40	60	80	100	120	140	160	180	200	220
Patch no.	121	122	123	124	125	126	127	128	129	130
Altitude (°)	54	54	54	54	54	54	66	66	66	66
Azimuth (°)	240	260	280	300	320	340	0	30	60	90
Patch no.	131	132	133	134	135	136	137	138	139	140
Altitude (°)	66	66	66	66	66	66	66	66	78	78
Azimuth (°)	120	150	180	210	240	270	300	330	0	60
Patch no.	141	142	143	144	145	146	147	148	149	150
Altitude (°)	78	78	78	78	90	90	90	90	90	90
Azimuth (°)	120	180	240	300	–	–	–	–	–	–

*See Figure 4.5.3(a).

This is due to the data collection techniques of the respective sky scanners. The EKO sensor used for Japanese data collection operates in the following manner. Staring at a southerly vector, the sensor is elevated to an angle of 6°. Rotating clockwise, the sensor records the properties of each sky patch at 12° intervals until it has returned to its initial starting point. The sensor then rotates counter-clockwise to the next elevation of 18° and records sky patch properties at 12° intervals until it again returns to due south. This clockwise-counter-clockwise rotation continues through further altitudinal and azimuthal divisions of the sky, as shown in Figure 4.5.3, until the sensor is finally vertical. At this point, the sensor measures the properties of the zenith of the sky canopy.

Though both sky scanners consider only 145 sky patches, it is seen that 150 patches are reported during each complete sky recorded by the PRC Krochmann instrument at both UK locations. This is due to the fact that this scanner records an additional five values of zenith luminance during each complete sky scan. The sky scans at Garston and Sheffield sites are respectively reported at 15 and 30 min intervals. Also, zenith luminance is the last patch to be measured. Therefore, when the sensor reaches a vertical position the zenith luminance may have changed since initialisation of that scan. Data for patches 145–150 should be averaged to obtain zenith luminance.

8.4 Web-based sources for accessing solar radiation and weather data

Data on ozone and NO_2
www.woudc.org
http://jwocky.gsfc.nasa.gov/teacher/ozone_overhead.html
http://www.knmi.nl/gome_fd/index.html
www.arm.gov

ASHRAE: The American Society of Heating, Refrigerating, and Air-Conditioning Engineers: http://www.ashrae.org/
Baseline Solar Radiation Network: http://bsrn.ethz.ch/
ASRC: Atmospheric Sciences Research Centre: http://asrc.cestm.albany.edu/
Data on turbidity: http://aeronet.gsfc.nasa.gov/
http://www.gos.udel.edu/ios/GCOS_ios.htm

CIE: International Commission on Illumination: http://www.cie.co.at/cie/home.html
FSEC: Florida Solar Energy Center: www.fsec.ucf.edu and www.logger.fsec.ucf.edu/met/
IDMP-CIE: International Daylight Measurement Programme: http://idmp.entpe.fr/
NASA: National Aeronautics and Space Administration: www.eosweb.lare.nasa.gov/sse

NOAA: The United States – National Oceanic and Atmospheric Administration: http://www.noaa.gov/
NREL: The National Renewable Energy Laboratory: http://rredc.nrel.gov/solar/

S@tel-Light: The European Database of Daylight and Solar Radiation: http://www.satel-light.com/index2.htm

SODA: Solar radiation databases for environmental monitoring: http://www.soda-is.org/
WDC: World Data Centre for Solar-Terrestrial Physics: http://www.wdc.rl.ac.uk/wdcmain/
BADC: British Atmospheric Data Centre

Solar Energy Laboratory, University of Texas: www.me.utexas.edu/~solarlab
Helioclim: http://www.helioclim.net/
(Table 8.4.1 provides a list of UK stations for which data is available from this web site):
http://badc.nerc.ac.uk/home/

Table 8.4.1 UK Meteorological Office hourly solar radiation stations

Station	Latitude (North)	Longitude	Altitude (masl)
Lerwick*	60° 08′	01° 11′W	82
Kirkwall	58° 57′	02°54′W	26
Altnaharra	58° 17′	04°26′W	81
Kinbrace	58°14′	03°55′W	103
Stornoway*	58°13′	06°19′W	9
Glascarnoch	57°43′	04°53′W	265
Skye (LUSA)	57°15′	05°48′W	18
Aberdeen	57°10′	02°05′W	35
Aviemore	57°08′	03°51′W	228
Tulloch Bridge	56°52′	04°42′W	237
Inverbervies	56°51′	02°16′W	134
Tiree	56°30′	06°53′W	9
Dunstaffnage	56°28′	05°26′W	3
Mylnefield†	56°27′	03°04′W	30
Strathallan	56°19′	03°44′W	35
Bishopton	55°54′	04°32′W	59
Edinburgh	55°51′	03°23′W	57
Charterhall	55°42′	02°23′W	112
Prestwick	55°31′	04°35′W	27
Eskdalemuir*	55°19′	03°12′W	242
Ballypatric Forest	55°11′	06°10′W	156
Sunderland	54°54′	01°23′W	56
West Freugh	54°51′	04°57′W	11
Dundrennan	54°48′	04°00′W	114
Durham	54°46′	01°35′W	102
Aldergrove*	54°39′	06°13′W	68
Shap	54°30′	02°42′W	255
Hillsborough	54°27′	06°04′W	38
Leconfield	53°87′	00°43′W	6
St Angelo	54°24′	07°39′W	47
Leeds	53°80′	01°55′W	64
Leeming	54°18′	01°32′W	32
Bramham	53°52′	01°20′W	54
Cawood	53°50′	01°08′W	6
Church Fenton	53°50′	01°12′W	8
Preston	53°45′	02°40′W	44
Manchester	53°28′	02°15′W	33
Valley	53°15′	04°32′W	10
Waddington	53°11′	00°31′W	68
Harwarden	53°10′	02°59′W	10
Nottingham	53°00′	01°15′W	117
Holbeach	52°52′	00°09′E	3
Sutton Bonington	52°50′	01°15′W	48
Shawbury	52°48′	02°40′W	72

(*continued*)

Table 8.4.1 (*continued*)

Station	Latitude (North)	Longitude	Altitude (masl)
Aberdaron	52°47′	04°44′W	95
Coltishall	52°45′	01°21′E	17
Lake Vyrnwy	52°45′	03°28′W	360
Wittering	52°37′	00°27′W	73
Edgbaston	52°28′	01°56′W	163
Winterbourne	52°27′	01°55′W	130
Gogerddan	52°26′	04°01′W	40
Coventry	52°25′	01°32′W	119
Monks Wood	52°24′	00°14′W	41
Church Lawford	52°22′	01°20′W	107
Brooms Barn	52°16′	00°34′E	75
Shobdon	52°15′	02°53′W	99
Bedford	52°13′	00°29′W	85
Aberporth*	52°08′	04°34′W	134
Wattisham	52°07′	00°58′E	89
Woburn	52°01′	00°36′W	89
Little Rissington	51°52′	01°41′W	214
Rothamsted	51°48′	00°21′W	128
Hoddesdon	51°47′	00°00′W	47
Ryemeads	51°47′	00°01′E	29
Filton	51°31′	02°35′W	59
London*	51°31′	00°07′W	77
Long Ashton	51°26′	02°40′W	51
St Athan	51°24′	03°26′W	49
Bracknell Modle*	51°23′	00°47′W	73
Manston	51°22′	01°19′E	44
Herne Bay	51°21′	01°08′E	40
Wisley	51°19′	00°28′W	38
Kenley	51°18′	00°05′W	170
East Malling	51°17′	00°27′E	37
Odiham	51°14′	00°57′W	118
Charlwood	51°09′	00°14′W	67
Liscombe	51°05′	03°36′W	348
Herstmonceux	50°53′	00°19′E	52
Thorney Island	50°49′	00°55′W	4
North Wyke	50°46′	03°54′W	177
Efford	50°44′	01°34′W	16
Bodmin	50°30′	04°40′W	200
Camborne*	50°22′	05°32′W	87
Jersey‡	49°11′	02°11′W	85

* These stations additonally record hourly sky-diffuse irradiation.
† Only daily integrated global irradiation recorded.
‡ Only daily integrated global and sky-diffuse irradiation recorded.

8.5 Satellite based and other sources for accessing solar radiation and weather data

Perez et al. (2002) have presented a model that is capable of exploiting geo-stationary satellite visible images for the production of site/time-specific global and direct irradiances.

Their model features clear sky global and direct irradiance functions, cloud-index-to-irradiance index function as well as global-to-direct-irradiance conversion model. They claim that the grid size of their archive is 0.1° latitude–longitude. However, eventually a resolution of 0.01° is achievable. The following information is available from satellites on an hourly basis: Terrain elevation, climatological Linke turbidity and snow cover.

Marion and George (2001) have presented a methodology for the calculation of solar radiation from surface meteorological observations. DATSAV2 data are surface weather observations archived by the US Air Force and distributed by the National Climatic Data Center (NCDC) in Asheville, NC. The archival of DATSAV2 data began in 1973 and continues today. Worldwide, there are data for more than 20 000 stations. The DATSAV2 database provides the capability to use the METSTAT (meteorological/statistical) model to calculate hourly values of direct normal, diffuse horizontal and global horizontal solar radiation for locations throughout the world. Opaque cloud cover, a key input parameter to the METSTAT model, is derived from the DATSAV2 layered cloud cover information. Resulting multiyear data sets include solar radiation and other meteorological data such as dry bulb temperature, dew point temperature, wind speed and atmospheric pressure. For further details the reader is referred to the above-mentioned article.

References

CIE (1994) *Guide to Recommended Practice of Daylight Measurement*. Technical Report CIE 108-1994. Commission International de l'Eclairage, TC 3.09.

Claywell, R. (2003) *Improved Quality Control Procedures for Solar Radiation Data*. MPhil thesis, Napier University, Edinburgh.

Ineichen, P. and Molineaux, B. (1993) *Characterisation and Comparison of Two Sky Scanners*. PRC Krochmann and EKO instruments IEA Task XVII expert meeting Geneva.

Kinghorn (1999) *Solar Illuminance Models for the UK*. PhD thesis, Napier University, Edinburgh.

Klein, S.A. (1977) Calculation of monthly average insolation on tilted surfaces. *Solar Energy* 19, 325.

Marion, W. and George, R. (2001) Calculation of solar radiation using a methodology with worldwide potential. *Solar Energy* 71, 275.

Muneer, T. and Kinghorn, D. (1998) Solar irradiance and daylight illuminance data for the United Kingdom and Japan. *Renew. Energy* 15, 318.

Muneer, T., Abodahab, N., Weir, G. and Kubie, J. (2000) *Windows in Buildings*. Elsevier, Oxford.

Perez, R., Ineichen, P., Moore, K., Kmiecik, M., Chain, C., George, R. and Vignola, F. (2002) A new operational model for satellite-derived irradiances description and validation. *Solar Energy* 73, 307.

Tregenza, P.R. (1987) Subdivision of the sky hemisphere for luminance measurements. *Light. Res. Technol.* 19, 13.

Tregenza, P.R. (1995) *Standardisation of UK Daylight Data*. Final report for EPSRC research grant GR/K07829, May 1995.

PROJECTS

Chapter 1

P1 Daylight illuminance and irradiance data is available as 5 min averages from worldwide locations given in Table A1. Merge and edit Prog1-6.For and Prog1-7.For to produce a FORTRAN program which enables computation of daily sunrise and sunset times and the sun altitude and azimuth at every 5 min time step, given the latitude and longitude of a location. Enable your program to read/write data via computer files.

P2 Modify Prog1-7.For to produce a year's listing of civil twilight times, given the latitude and longitude of a location.

Chapter 2

P3 Refer to the basic meteorological data available in Table B1. Using the monthly-averaged sunshine duration, prepare tables of monthly-averaged daily global $\bar{G}$ and diffuse $\bar{D}$ irradiation for the given sites. You may modify Prog2-1.For to enable the input/output flow via datafiles.

P4 Using values of $\bar{G}$ and $\bar{D}$ obtained in Project P3, prepare tables for monthly-averaged daily vertical irradiation for the four cardinal aspects using Prog2-2.For as a platform.

Chapter 3

P5 Using computations for $\bar{G}$ and $\bar{D}$ obtained in Project P3, prepare tables for monthly-averaged hourly irradiation, $\bar{I}_{\mathrm{G}}$ and $\bar{I}_{\mathrm{D}}$. Prog3-1.For may be adopted for this task.

P6 Compute monthly-averaged hourly global and diffuse illuminance using the output obtained from P5.

P7 Using Prog3.8.For and closely following the working of Example 3.7.1, prepare monthly-frequency distribution tables for horizontal irradiance and illuminance for Manchester, UK for 9, 10, 11 and 12 h GMT.

Chapter 4

P8 Using the monthly-averaged hourly irradiation, $\bar{I}_{\mathrm{G}}$ and $\bar{I}_{\mathrm{D}}$ obtained in P5, compute vertical irradiation for the four cardinal aspects. You may use Prog4-1.For for this task.

P9 Using the data obtained from P8, obtain hourly illuminances for the respective slopes. Prog4-2.For may be adapted for these computations.

P10 Compute the luminance distribution of the sky canopy for 9 and 12 h GMT for London, UK using Prog4-3.For and the corresponding values of $\bar{I}_G$ and $\bar{I}_D$ obtained in P5. How do these distributions compare with the Japanese data given in Section 4.5?

Chapter 7

P11 Using the ASHRAE hourly temperature model given in Chapter 7, compute the hourly dry- and wet-bulb temperatures for London for the period November to February. Use the monthly-average maximum/minimum temperature data given in Table B1.

P12 Plot the above data points on the electronic psychrometric chart which may be drawn using the data given in File7-1.Csv. You may use any of the popular computer spreadsheets for this task.

APPENDICES

Table A1 International daylight measurement programme (worldwide measurement stations)[†]

Code	Country	Location	Type
J1	Japan	Fukuoka	R
J2	Japan	Kyoto	R
J3	Japan	Sapporo	R
J4	Japan	Uozo	G
J5	Japan	Nagoya (Daido)	G
J6	Japan	Nagoya (Meijo)	G
J7	Japan	Toyota	G
J8	Japan	Suita	S
J9	Japan	Ashikaga	sR
J10	Japan	Tokyo	R
J11	Japan	Chofu	R
J12	Japan	Tshukuba	R
J13	Japan	Kiyose	S
J14	Japan	Osaka	S
GB1	UK	Garston	R
GB2	UK	Edinburgh	G
GB3	UK	Manchester	R
GB4	UK	Sheffield	G
F1	France	Nantes	G
F2	France	Vauix en Velin	G
F3	France	Strasbourg	S
F4	France	Chanbery	S
F5	France	Grenoble	S
S1	Sweden	Norrkoping	R
S2	Sweden	Gavle	G
S3	Sweden	Kiruna	G
RFA1	Germany	Hamburg	G
RFA2	Germany	Freiburg	S
CH1	Switzerland	Geneva	R
NL1	Netherlands	Eindhoven	R
G1	Greece	Athens	G
P1	Portugal	Lisbon	G
IL1	Israel	Bet Dagan	S
SU1	Russia	Voelkovo	G
SU2	Russia	Moscow	S
SU3	Ukraine	Karadag	S
USA1	USA	Ann Arbor	R
USA2	USA	Albany	G
USA3	USA	Cape Canaveral	R
CDN1	Canada	Calgary	G
AUS1	Australia	Sydney	R
RC1	China	Chongquing	G
RC2	China	Beijing	R
RC3	China	Changchun	G
SGP1	Singapore	Singapore	R
SGP2	Singapore	Singapore	G
IND1	India	Roorkee	R

R: research class, sR: simplified research class, G: general class, S: simplified general class.

[†]*Source*: H. Nakamura, Chair CIE-TC3.25.

Table B1 Mean-monthly weather data for selected UK sites

Location* a, a'	Lat. N	Long. W	SH**	Max.†	Min.†	Max.‡	Min.‡	b*	SH**	Max.†	Min.†	Max.‡	Min.‡	b*
			January						*February*					
Aberdeen 24, 15	57.150	2.100	1.61	4.7	−0.2	3.2	−0.2	0.51	2.82	5.4	−0.2	3.3	−0.2	0.51
Dundee 24, 14	56.483	3.000	1.66	5.1	0.1	3.3	0.1	0.51	2.87	5.9	0.2	3.5	0.2	0.51
Edinburgh 23, 14	55.950	3.200	1.33	5.9	0	3.4	0.0	0.51	2.42	6.6	0.2	3.4	0.2	0.51
Glasgow 23, 14	55.867	4.233	1.15	5.5	0.8	3.6	0.8	0.52	2.20	6.3	0.8	3.7	0.8	0.52
Newcastle 24, 15	54.983	1.583	1.37	5.6	2.2	3.2	2.2	0.49	2.36	6.0	2.1	3.5	2.1	0.49
Belfast 25, 15	54.583	5.917	1.43	5.8	1.3	4.0	1.3	0.49	2.40	6.5	1.1	4.1	1.1	0.49
Manchester 25, 16	53.500	2.250	1.27	5.5	1.2	3.8	1.2	0.48	2.19	6.3	1.0	4.0	0.1	0.48
Liverpool 25, 16	53.417	2.917	1.37	6.1	2.1	4.0	2.1	0.48	2.24	6.6	1.9	4.0	1.9	0.48
Sheffield 25, 16	53.383	1.500	1.23	5.6	1.2	3.2	1.2	0.48	1.93	6.0	1.1	3.5	1.1	0.48
Leicester 25, 17	52.633	1.083	1.35	5.8	0.1	3.5	0.1	0.47	2.25	6.5	0.3	3.6	0.3	0.47
Birmingham 25, 17	52.500	1.833	1.38	5.1	1.5	3.5	1.5	0.47	2.03	5.7	1.3	3.6	1.3	0.47
London 23, 14	51.500	0.167	1.54	6.1	2.3	4.7	2.3	0.45	2.28	6.8	2.3	5.0	2.3	0.45
Bristol 26, 17	51.430	2.580	1.45	6.3	1.6	4.3	1.6	0.47	2.24	6.9	1.5	4.4	1.5	0.47
Cardiff 26, 17	51.483	3.217	1.60	6.8	1.5	4.5	1.5	0.48	2.64	6.9	1.5	4.5	1.5	0.48
Plymouth 25, 16	50.383	4.167	1.87	8.0	3.8	6.2	3.8	0.50	2.86	7.9	3.2	6.1	3.2	0.50
			March						*April*					
Aberdeen 24, 15	57.150	2.100	3.43	7.7	1.2	4.4	1.2	0.51	5.09	1.1	0.3	6.2	0.3	0.60
Dundee 24, 14	56.483	3.000	3.29	8.2	1.8	5.1	1.8	0.51	5.02	11.5	3.5	6.8	3.5	0.59
Edinburgh 23, 14	55.950	3.200	3.2	8.7	1.8	5.0	1.8	0.51	4.98	11.7	3.7	6.9	3.4	0.59
Glasgow 23, 14	55.867	4.233	3.04	8.8	2.2	5.1	2.2	0.52	4.90	1.2	0.4	7.3	0.4	0.58
Newcastle 24, 15	54.983	1.583	3.29	7.8	3.1	5.2	3.1	0.49	5.01	1.0	0.5	7.4	0.5	0.58
Belfast 25, 15	54.583	5.917	3.30	9.0	2.4	5.4	2.4	0.49	5.12	1.2	0.4	7.5	0.4	0.56
Manchester 25, 16	53.500	2.250	3.52	9.2	2.3	5.7	2.3	0.48	4.79	1.2	0.4	7.9	0.4	0.56
Liverpool 25, 16	53.417	2.917	3.53	9.5	3.1	5.8	3.1	0.48	4.87	12.4	5.3	8.1	5.3	0.55
Sheffield 25, 16	53.383	1.500	2.98	8.7	2.3	5.2	2.3	0.48	4.3	1.2	0.5	7.4	0.5	0.56
Leicester 25, 17	52.633	1.083	3.24	9.4	1.5	5.2	1.5	0.47	4.67	12.9	3.8	7.6	3.8	0.54
Birmingham 25, 17	52.500	1.833	3.14	8.7	2.6	5.2	2.6	0.47	5.55	1.2	1.5	7.6	1.5	0.54
London 23, 14	51.500	0.167	3.62	9.8	3.4	6.5	3.4	0.45	5.41	1.3	0.6	8.9	0.6	0.52
Bristol 26, 17	51.430	2.580	3.55	9.9	2.6	6.2	2.6	0.47	5.15	13.1	4.8	8.6	4.8	0.54
Cardiff 26, 17	51.483	3.217	3.95	10.0	2.8	5.9	2.8	0.48	5.44	1.3	0.5	8.0	0.5	0.54
Plymouth 25, 16	50.383	4.167	4.23	9.9	4.3	7.1	4.3	0.50	6.07	1.2	0.6	8.8	0.6	0.54
			May						*June*					
Aberdeen 24, 15	57.150	2.100	5.51	12.7	5.0	9.0	5.0	0.60	5.80	16.1	7.9	12.0	7.9	0.60
Dundee 24, 14	56.483	3.000	5.44	14.3	5.8	9.2	5.8	0.59	5.6	17.6	8.9	12.4	8.9	0.59
Edinburgh 23, 14	55.950	3.200	5.69	14.2	6.0	9.4	6.0	0.59	6.08	17.3	9.1	12.5	9.1	0.59
Glasgow 23, 14	55.867	4.233	5.95	15.1	6.2	10.3	6.2	0.58	6.04	17.9	9.3	13.2	9.3	0.58
Newcastle 24, 15	54.983	1.583	5.50	12.2	7.1	10.5	7.1	0.58	6.01	15.7	10.1	13.8	10.1	0.58
Belfast 25, 15	54.583	5.917	6.17	14.7	6.1	10.3	6.1	0.56	5.82	17.4	9.2	13.2	9.2	0.56
Manchester 25, 16	53.500	2.250	5.93	15.7	6.9	11.3	6.9	0.56	6.37	18.8	9.9	14.3	9.9	0.56
Liverpool 25, 16	53.417	2.917	5.91	15.7	7.8	10.8	7.8	0.55	6.57	18.7	10.9	13.8	10.9	0.55
Sheffield 25, 16	53.383	1.500	5.24	15.4	7.2	10.5	7.2	0.56	6.11	18.7	10.3	13.8	10.3	0.56
Leicester 25, 17	52.633	1.083	5.75	16.1	6.1	10.8	6.1	0.54	6.22	19.3	9.1	14.1	9.1	0.54
Birmingham 25, 17	52.500	1.833	5.47	15.4	7.4	10.8	7.4	0.54	6.15	18.7	10.4	14.1	10.4	0.54
London 23, 14	51.500	0.167	6.56	16.8	8.4	12.3	6.4	0.52	7.14	20.2	11.5	15.7	11.5	0.52
Bristol 26, 17	51.430	2.580	6.14	16.1	7.3	11.3	7.3	0.54	6.8	19.2	10.6	14.4	10.6	0.54
Cardiff 26, 17	51.483	3.217	6.34	16.2	7.7	11.0	7.7	0.54	6.92	19.2	10.7	14.0	10.7	0.54
Plymouth 25, 16	50.383	4.167	7.04	14.9	8.2	11.4	8.2	0.54	7.27	17.6	11.1	14.2	11.1	0.54

(*continued*)

Table B1 ***(continued)***

Location* a, a'	Lat. N	Long. W	SH**	Max.†	Min.†	Max.‡	Min.‡	b*	SH**	Max.†	Min.†	Max.‡	Min.‡	b*
			July						*August*					
Aberdeen 24, 15	57.150	2.100	5.19	17.5	9.6	13.7	9.6	0.60	4.52	17.1	9.4	13.6	9.4	0.60
Dundee 24, 14	56.483	3.000	5.08	19.0	10.6	13.1	9.9	0.59	4.44	18.3	10.3	13.4	10.2	0.59
Edinburgh 23, 14	55.950	3.200	5.43	18.6	10.8	13.0	9.9	0.59	4.75	18.2	10.6	13.4	10.3	0.59
Glasgow 23, 14	55.867	4.233	5.14	18.6	10.8	14.3	10.8	0.58	4.60	18.5	10.6	14.2	10.6	0.58
Newcastle 24, 15	54.983	1.583	5.31	17.4	12.0	15.2	12.0	0.58	4.68	17.2	12.0	15.0	12.0	0.58
Belfast 25, 15	54.583	5.917	4.41	18.1	10.7	14.3	10.7	0.56	4.42	18.0	10.5	14.2	10.5	0.56
Manchester 25, 16	53.500	2.250	5.00	19.6	11.7	15.4	11.7	0.56	4.90	19.4	11.5	15.4	11.5	0.56
Liverpool 25, 16	53.417	2.917	5.28	19.6	12.8	15.1	12.3	0.55	4.94	19.5	12.5	14.6	12.2	0.55
Sheffield 25, 16	53.383	1.500	5.15	19.8	12.2	15.2	12.2	0.56	4.58	19.5	11.9	15.0	11.9	0.56
Leicester 25, 17	52.633	1.083	5.43	20.7	11.2	15.7	11.2	0.54	4.96	20.4	10.7	15.3	10.7	0.54
Birmingham 25, 17	52.500	1.833	5.29	19.9	12.1	15.7	12.1	0.54	4.86	19.5	11.9	15.3	11.9	0.54
London 23, 14	51.500	0.167	6.34	21.6	13.4	17.2	13.4	0.52	5.90	21.0	13.1	16.7	13.1	0.52
Bristol 26, 17	51.430	2.580	6.07	20.6	12.4	15.1	12.3	0.54	5.5	20.1	12.1	15.0	0.0	0.54
Cardiff 26, 17	51.483	3.217	6.11	20.4	12.3	15.5	12.3	0.54	5.77	20.1	12.3	15.5	12.3	0.54
Plymouth 25, 16	50.383	4.167	6.53	19.0	12.7	15.7	12.7	0.54	6.09	19.0	12.7	15.8	12.7	0.54
			September						*October*					
Aberdeen 24, 15	57.150	2.100	3.98	15.5	8.0	11.3	8.0	0.60	2.94	12.4	5.8	9.1	5.8	0.51
Dundee 24,1 4	56.483	3.000	3.92	16.4	8.7	12.3	8.7	0.59	2.93	12.9	6.1	10.0	6.1	0.51
Edinburgh 23, 14	55.950	3.200	4.0	16.6	9.0	12.3	9.0	0.59	2.94	13.3	6.5	9.9	6.5	0.51
Glasgow 23, 14	55.867	4.233	3.53	16.3	9.1	12.3	9.1	0.58	2.45	13.0	6.8	9.8	6.8	0.52
Newcastle 24, 15	54.983	1.583	4.03	15.9	10.6	13.0	10.6	0.58	3.00	13.0	8.4	10.0	8.4	0.49
Belfast 25, 15	54.583	5.917	3.47	16.0	9.3	12.4	9.3	0.56	2.53	12.9	7.2	10.2	7.2	0.49
Manchester 25, 16	53.500	2.250	3.97	17.3	10.0	13.4	10.0	0.56	2.98	13.7	7.3	10.5	7.3	0.48
Liverpool 25, 16	53.417	2.917	3.89	17.5	11.0	13.5	11.0	0.55	2.79	14.0	8.4	11.1	8.4	0.48
Sheffield 25, 16	53.383	1.500	3.71	17.4	10.3	13.0	10.3	0.56	2.71	13.7	7.6	10.0	7.6	0.48
Leicester 25, 17	52.633	1.083	3.99	18.0	9.1	13.1	9.1	0.54	2.92	14.2	6.3	10.1	6.3	0.47
Birmingham 25, 17	52.500	1.833	3.92	17.5	10.4	13.1	10.4	0.54	2.81	13.5	7.8	10.1	7.8	0.47
London 23, 14	51.500	0.167	4.77	18.5	11.4	14.5	11.4	0.52	3.29	14.7	8.5	11.6	8.5	0.45
Bristol 26, 17	51.430	2.580	4.29	18.0	10.3	13.9	10.3	0.54	3.01	14.5	7.7	11.6	7.7	0.47
Cardiff 26, 17	51.483	3.217	4.43	18.0	10.7	13.8	10.7	0.54	3.28	14.5	8.0	11.0	8.0	0.48
Plymouth 25, 16	50.383	4.167	4.93	17.5	11.6	14.3	11.6	0.54	3.63	14.8	9.4	12.1	9.4	0.50
			November						*December*					
Aberdeen 24, 15	57.150	2.100	2.01	8.0	2.6	5.2	2.6	0.51	1.42	5.7	1.0	4.4	1.0	0.51
Dundee 24, 14	56.483	3.000	2.04	8.4	2.6	5.4	2.6	0.51	1.47	6.2	1.0	3.1	1.0	0.51
Edinburgh 23, 14	55.950	3.200	1.72	9.0	2.6	5.4	2.6	0.51	1.19	7.0	1.1	3.3	1.1	0.51
Glasgow 23, 14	55.867	4.233	1.55	8.7	3.3	5.5	3.3	0.52	0.98	6.5	1.9	4.3	1.9	0.52
Newcastle 24, 15	54.983	1.583	1.75	8.8	5.1	6.0	5.1	0.49	1.24	6.6	3.2	3.9	3.0	0.49
Belfast 25, 15	54.583	5.917	1.87	8.9	3.9	6.2	3.9	0.49	1.12	6.7	2.5	4.8	2.5	0.49
Manchester 25, 16	53.500	2.250	1.64	8.9	4.0	6.4	4.0	0.48	1.21	6.4	2.2	4.4	2.2	0.48
Liverpool 25, 16	53.417	2.917	1.68	9.5	5.1	6.6	5.1	0.48	1.3	7.1	3.1	4.1	3.1	0.48
Sheffield 25, 16	53.383	1.500	1.45	8.9	4.3	6.0	4.3	0.48	1.14	6.9	2.3	3.9	2.3	0.48
Leicester 25, 17	52.633	1.083	1.7	9.3	3.1	6.2	3.1	0.47	1.22	7.0	1.1	4.0	1.1	0.47
Birmingham 25, 17	52.500	1.833	1.61	8.6	4.5	6.2	4.5	0.47	1.35	6.2	2.7	4.0	2.7	0.47
London 23, 14	51.500	0.167	1.92	9.8	5.3	7.5	5.3	0.45	1.38	7.2	3.4	5.5	3.4	0.45
Bristol 26, 17	51.430	2.580	1.83	9.7	4.5	7.1	4.5	0.47	1.44	7.3	2.9	4.4	2.9	0.47
Cardiff 26, 17	51.483	3.217	2.01	10.2	4.7	7.4	4.7	0.48	1.55	8.0	2.7	5.4	2.7	0.48
Plymouth 25, 16	50.383	4.167	2.30	11.1	6.4	8.8	6.4	0.50	1.82	9.2	4.9	7.0	4.9	0.50

* Coefficients to be used in Eq. (2.4.1).

** Mean daily sunshine hours.

† Mean daily max./min. temperatures.

‡ Mean daily max./min. wet-bulb temperatures.

INDEX

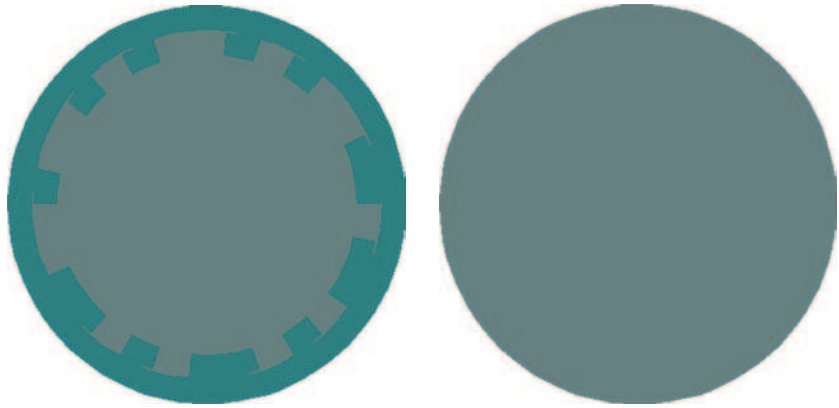

Measured Computed

Heavy overcast sky 15 January 1992, 1105 h

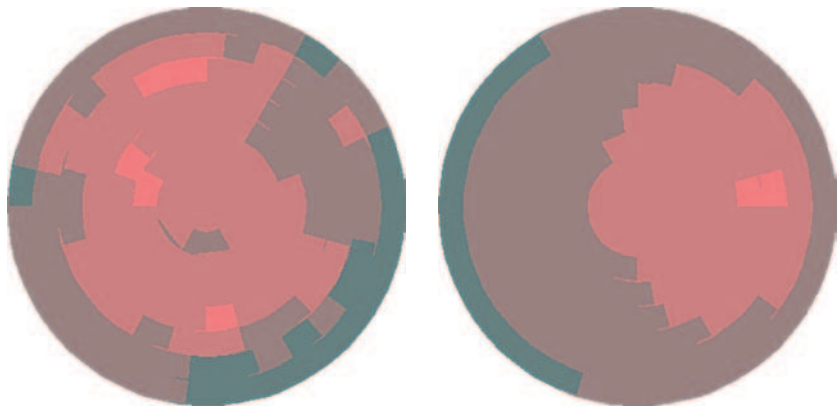

Measured Computed

(a) Thin overcast sky 17 March 1992, 1340 h

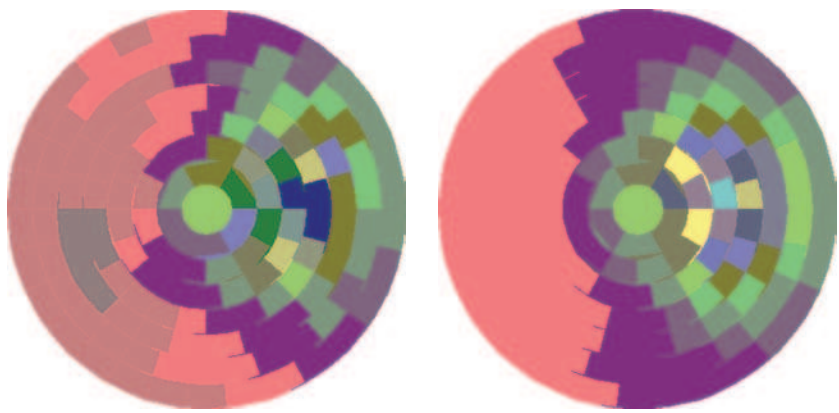

Measured sky scan Computed sky scan

(b) Sky luminance distribution for Garston data – 28 June 1992, 1145 h GMT

Plate 1 *Figure 4.5.4 in colour*